Journal of Heat Transfer

ANNOUNCEMENTS

TECHNICAL PAPERS

(Contents Continued)

TECHNICAL NOTES

DISCUSSION

C. J. Cremers
Department of Mechanical Engineering,
University of Kentucky,
Lexington, Ky. 40506
Fellow ASME

V. K. Mehra
Bishopric Company,
Cincinnati, Ohio

Frost Formation on Vertical Cylinders in Free Convection

Frost growth on a cooled vertical cylinder in free convective flow was studied experimentally. A correlation that is based on heat transfer considerations was found to be effective in predicting frost growth rates particularly at relative humidities equal to or greater than 65 percent and growing times equal to or greater than 60 min.

Introduction

Frost formation is a complicated transient process in which a variety of heat and mass transfer mechanisms are at work simultaneously. The formation of frost on a surface is usually idealized as a moving boundary problem where heat and mass transfer occur across the boundary layer to the growing frost layer. The time scales associated with heat and mass transfer within the frost layer are such that the boundary layer can be considered quasi-steady in relation to it.

In analysis and modeling of the frosting phenomenon, difficulties usually arise in characterizing the internally dynamic frost layer. As it is not possible to study separately the several mechanisms interacting within the frost layer, postulates as to their relative importance can be evaluated only from models that successfully predict measurable physical variables such as temperature and density profiles within the frost layer, frost growth rates, variations in the frost-air interface temperature, and the overall heat flux to the frost surface.

Most of the previous investigations that have been done on the frosting phenomenon are for forced convection conditions. References [1–3] contain complete surveys of the older literature in this area. Recent investigations include extensive studies by Japanese researchers, e.g. [4, 5], for a variety of parameters, including geometrical effects. Perhaps the most notable feature of the latter investigations is the importance given to structural modeling of the frost layer based on photographic observation of frost growth. More recently, Schneider [6] conducted frosting experiments on a horizontal tube for forced convection conditions and presented a crystal growth model that correlates changes in frost thickness versus time to within 10 percent of measured values. He also concludes, as have others [2, 5], that the frost thickness turns out to be independent of the conditions commonly significant to mass transfer, such as arrangement of the test surface, vapor pressure difference between the air stream and the frost surface, and the Reynolds number.

Recent studies of the frosting phenomenon have not been as extensive for natural convection conditions. Ruccia and Mohr [7] conducted tests on a vertical tank filled with liquid oxygen and concluded that the insulating effect of frost depends on time and the partial pressure of water vapor in the atmosphere. Stoecker [8], in his investigation of frosting on

refrigeration coils, concludes that initially the heat transfer coefficient increases because the rough frost surface presents a larger surface area for heat and mass transfer. The same conclusion was reached later by Whitehurst [1] and Tajima et al. [9–12]. Whitehurst's investigation showed that the heat transfer coefficient decreases after the initial increase and then remains constant, however Stoecker did not observe the decrease.

Whereas most of the older work measured overall frost growth, heat flux to the frost layer, and the total mass of frost deposited on a surface, several of the more recent investigations have aimed at probing the internal structure of frost and the mechanisms at work in sustaining continuous growth of the frost layer. Goodman and Kennedy [13], in their work on free convection heat and mass transfer under frosting conditions, report that "as a result of measurements of the frost surface weight and thickness, it must be concluded that in addition to deposition at the frost-air interface, appreciable frost is formed within the frost layer." They also observe that the frost density increases with time and affects the thermal conductivity. Shah [2] showed analytically that the density of the frost layer must increase away from the wall if the vapor and solid phases are in local equilibrium within the frost layer. However, this was not confirmed in his experiments on a horizontal flat plate under forced convection conditions. Cremers et al. [14], using a gamma-ray attenuation technique, found that for frosting under natural convection conditions on a vertical cylinder, the frost density decreases monotonically in the direction away from the wall or with one or more distinct local maxima between the wall and outer edge of the frost layer, depending on ambient conditions.

Tajima et al. [9–12] studied frost formation in natural convection on a flat plate. In their set of four experiments, they positioned the plate facing upwards, downwards, vertically and vertically opposed to another plate and used the enthalpy difference between the humid ambient air and the saturated air at the frost surface to correlate their data. They also present photographs to document changes that occur as the frost layer grows. They suggest that as the layer grows, its surface temperature reaches the triple point and moisture subsequently condenses as droplets of water on the surface. Some of the water seeps into the frost layer by capillarity and freezes. The local thermal conductivity of the frost layer increases as a consequence, and the surface temperature drops below the freezing point. Water present on the surface freezes

---

as an icy layer and fresh crystals of ice grow on the surface. This cycle is then repeated. (White [3] postulated that this three-phase interaction was the cause of a frost thickening that occurred just downstream of the leading edge of a frosting plate in forced convection.) Similarly, Kennedy and Goodman [13, 15], using interferometry to obtain boundary layer temperature distributions around frost growing on a large diameter cylinder, observed cyclic surface temperatures ($\pm 1.5°C$) in their experiment.

The present investigation attempts to fill some gaps in our knowledge of frost layer growth by presenting observations of frost growth on a small diameter vertical cylinder in free convection – an industrially important problem but one which has not, to the authors' knowledge, been studied before. Experiments indicated [14] that this situation, in contrast to all reported cases of frost formation in forced convection as well as free convection on a flat plate, leads to a frost density that varies significantly with distance from the wall. The present experiments were conducted for a variety of ambient humidity and wall temperature conditions. The frost thickness was measured as a function of time and, for some combinations of ambient parameters, the frost layer and boundary layer temperature distributions were also measured. The information obtained from the experiments was used in identifying parameters that influence frost growth. The findings are discussed in the light of previous investigations.

The Experiment

The experiment was conducted using two different test surfaces, one developed for lower wall temperatures (below 250 K) and the other for temperatures above this level. They are described in [14] and [16], respectively. The basic difference between the two test surfaces is that for the former the test surface is on a vertical tube that is internally cooled by liquid nitrogen vented to the atmosphere at the top; while for the latter, the cylindrical surface is on a tube that is part of a closed refrigeration system. This tube has a rounded and well-defined leading edge. In both cases, the moist air entering the test section was preconditioned for temperature and humidity in an entrance plenum.

In our earlier work [14], we found that beyond only two or three tube diameters the frost thickness, density and structure did not seem to vary with distance in the flow direction. Therefore, the axial position for the measurements in each case was chosen for convenience. This was 4 diameters downstream from the leading edge for the high temperature apparatus and 30 diameters for the low-temperature apparatus. The Grashof number for the latter is on the order of 10^7 and the flow is laminar as determined by flow visualization studies using smoke.

The temperature in the frost and in the adjacent boundary layer was measured using a set of 36 AWG butt-welded thermocouples with the junctions arranged radially out from the surface. The thickness of the frost and the distance of the thermocouple junctions from the wall were measured with a traveling microscope.

Experiments were conducted to measure the frost thickness and the internal temperature distribution as functions of time. Related measurements, not of direct importance to this paper, were made of wall heat flux as a function of time. Some of these are reported in [16]. Local density measurements by a

gamma-ray attenuation technique were reported in [14] and are under further development at this time.

Results

The first crystals of frost appear at certain preferred locations such as tube joints and local inhomogeneities on the test surface. However, nucleation soon takes place almost uniformly over the entire surface. As time progresses, these crystals grow like needles, oriented slightly downward, perhaps under the influence of gravity and the downward boundary layer flow. The frost surface is rough at this juncture primarily because of the spacing between adjacent needles and also because some needles are longer than the others. References [4, 5, 9–12] show several stages of the frost layer growth.

As time progresses, a gradual change takes place in the growth pattern. Even though growth still takes place predominantly in the original direction, the crystals begin to branch out and link together forming "tree-like" structures. As a consequence, the frost surface tends to become increasingly uniform with time. Similar growth patterns have been observed during frost formation on flat plates in forced convection [3, 5] and free convection [9–12]. The regularity of the more mature frost layer is so pronounced that such diverse theoretical models – such as a needle-like frost [6], and mixtures of ice cylinders and spheres, or ice planes and air bubbles [17] – can be made to fit observed growth and heat transfer behavior.

For ambient conditions involving low humidity, frost growth continues with little observable change in its physical appearance. However, in situations involving high humidity, after a period of about five or six hours, miniscule droplets of water can be seen on the frost surface. The frost surface tends to become smoother and dense, like that described by Tajima et al. [9–12]. These authors attributed this phenomenon to the freezing of the water on the surface to form ice.

Many of the characteristics of the frosting process that are apparent from the present study have been reported by previous researchers for other flow situations. For example, the irregular character of the frost at growing times on the order of one or two hours has been observed by numerous researchers. The frost surface during that initial period is poorly defined. This leads to rather large uncertainties in the determination of the surface position. The variations in local frost density which arise from the nonuniform growth will in turn lead to difficulties in extrapolating to the frost as a whole the rather local temperature measurements, at least in detail.

Figures 1 and 2 show some typical radial temperature profiles at various times after the beginning of frost growth. These are measured out from the cooled wall and indicate the temperature in both the frost and free-convection boundary layer. By independently measuring the frost surface position, it is possible to interpolate the temperature data to obtain an approximate frost surface temperature. This was done by visually fitting curves to the points known to lie within and outside the frost and taking the surface temperature to be that given by the intersection of the two lines. Such locations are shown by the short vertical lines in Figs. 1 and 2. We have tried, without success so far, to fit a suitable analytical curve to the boundary layer temperature data. The logarithmic

---

_____ **Nomenclature** _____

A = coefficient in equation (1) $(mm/min^{1/2} - K^{1/2})$
b = exponent in equation (1)
T = temperature K

t = time, min
δ = frost thickness
ϕ = relative humidity

Subscripts

a = ambient
δ = frost surface
w = wall
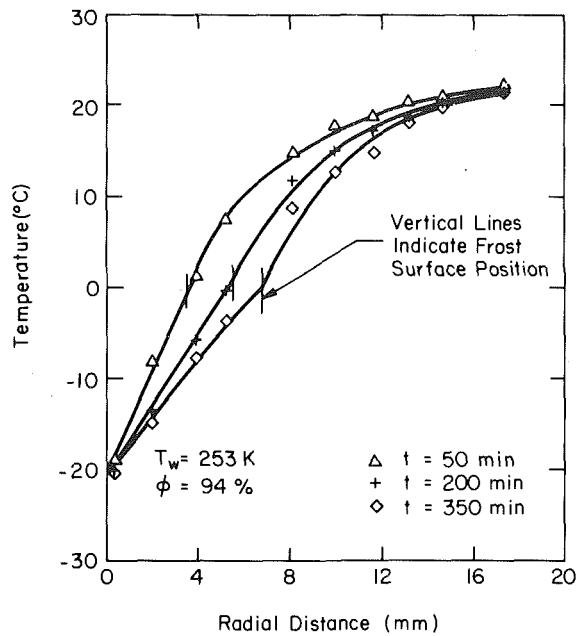
Fig. 1 Temperature in frost and boundary layer – high humidity
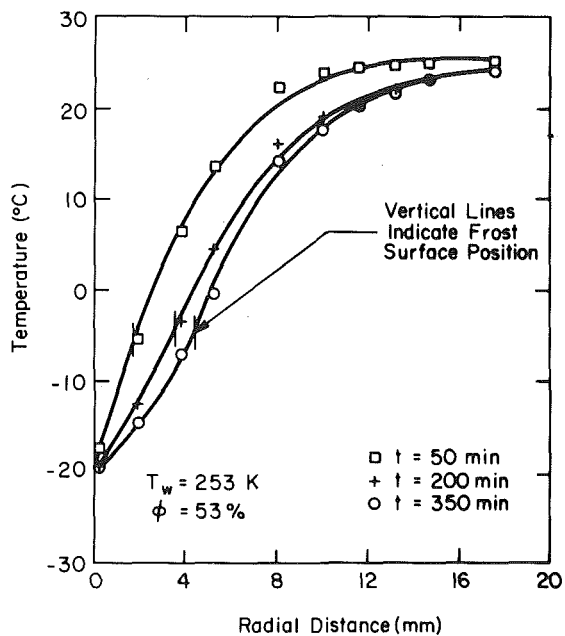
Fig. 2 Temperature in frost and boundary layer – low humidity

Fig. 3 Frost growth, low temperature differences
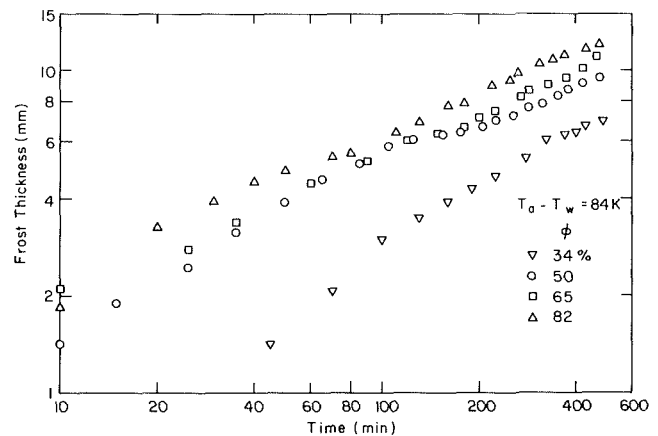
Fig. 4 Frost growth, $(T_a - T_w) = 84$ K
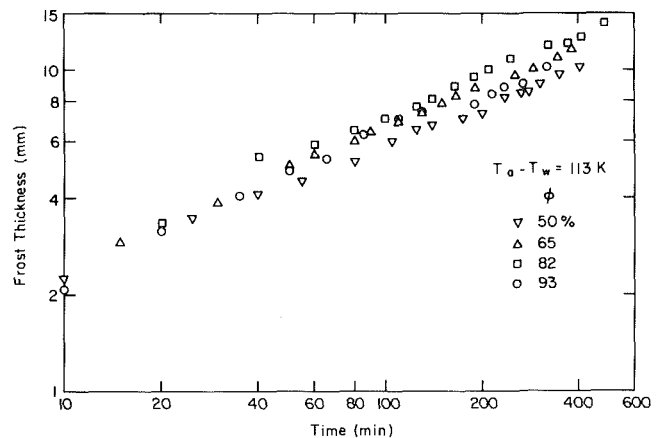
Fig. 5 Frost growth, $(T_a - T_w) = 113$ K

profile, which has been shown by Hama et al. [18] to work well with their small solid-walled cylinders, does not seem to fit the present data as well as the Pohlhausen flat-plate profile [19]. However, agreement with the data, particularly at short times, is not good and so we decided to use the visual fit. The scatter in the frost surface temperature as determined this way is estimated to be on the order of ± 2 K. Superposed on this random error is a systematic correction of the data, for which the maximum value is $+2$ K, caused by heat leakage along the thermocouple lead wires [16]. However, it is still possible to conclude that the surface temperature of frost remains well below the triple-point of water for low-humidity, ambient conditions, such as that for a relative humidity of 53 percent shown in Fig. 2. At high humidities, the frost surface is apparently near or at the triple-point temperature, 0.01 °C.

The data for frost layer growth are somewhat difficult to interpret because their scatter is apparently of the same order

of magnitude as the differences in thickness for different sets of ambient parameters. More serious, and particularly acute because of the cylindrical geometry of the system, is the experimental difficulty in measuring representative thickness. To make these measurements, the traveling microscope was initially focused on the unfrosted surface such that the line of sight was tangent to the surface at the point of observation. Then as the layer grew, the thickness of the layer was determined by adjusting the microscope cross-hair horizontally and normal to the unfrosted surface to the best average position of the frost surface in the field of view. The position of the surface at that time was then recorded. As the frost surface is quite irregular, especially initially, such a method will have the greatest uncertainty at shorter growing times of up to several hours when the layer finally fills out. Before that, the position chosen could correspond to a local
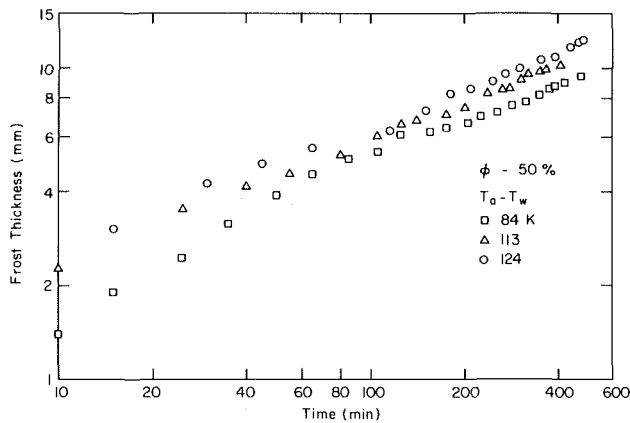
Fig. 6   Frost growth, $\phi = 50$ percent
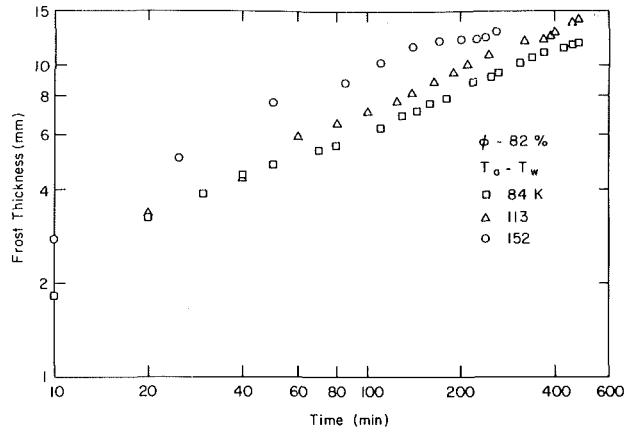
Fig. 8   Frost growth, $\phi = 82$ percent
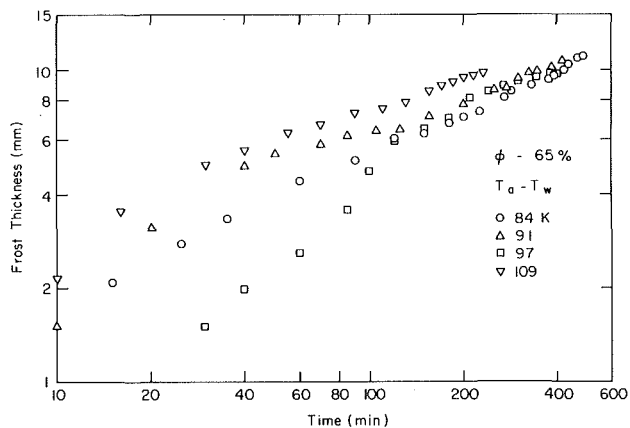
Fig. 7   Frost growth, $\phi = 65$ percent
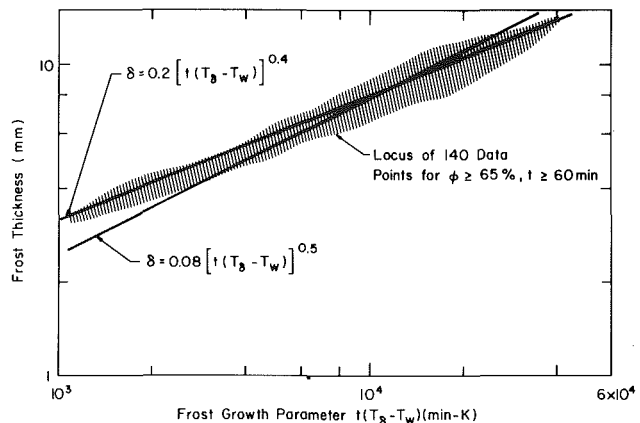
Fig. 9   Frost growth correlations

high or low in the frost thickness. Given the limitations of our optical system there was no way around this difficulty. Consequently, the frost growth data shown in Fig. 3 for the higher wall-temperature experiment, and in Figs. 4–8 for the low-temperature apparatus must be interpreted with caution.

Previous investigations of frosting phenomena in forced convection have shown that frost growth can be predicted by models based on heat transfer rather than on diffusion [3, 6] In reference [3], a model for frost growth over a cooled flat plate in forced convection demonstrated that, for a constant mass flow of vapor to the surface, the layer thickness is proportional to the square-root of the product of time measured from the inception of growth and the difference between the frost surface-temperature and wall temperature. This is described by equation (21) of reference [3] and for present purposes can be rewritten in the form

$$\delta = A[t(T_\delta - T_w)]^{1/2} \qquad (1)$$

Here, δ is the layer thickness, t is the time measured from inception of growth and the $(T_\delta - T_w)$ is the difference between frost surface and wall temperatures. A is a constant derived from ambient parameters. A similar relation was later derived by Schneider [6] for the case of forced convection over a cooled horizontal cylinder. He used a crystal growth model in which heat transfer effects were also dominant. His coefficient A was also obtained by experiment and reflects the ambient parameters of his investigation.

The complete derivation of the above equation was incumbent upon two important assumptions that do not pertain to the present experiment. These are: (a) the frost layer has a constant density, and (b) the vapor diffuses in a parallel fashion rather than converging radially. At present it is not possible to evaluate the influence of these variables because of the complicated nature of the observed density distribution

[14] and the virtual impossibility of measuring the water vapor flux in the frost during the experiment. However, the model may be tried as a data correlation scheme if nothing else.

Figure 9 shows, with the exception of three points, an envelope of 140 data points from Figs. 3–8 (the hatched region) obtained with both apparatuses for humidities and times greater than or equal to 65 percent and 60 min, respectively. The frost thickness in millimeters is plotted against the product of growing time and the difference between wall and frost surface temperatures. The data include a humidity range of 65–94 percent and a range of differences between surface and wall temperatures of 15–121 K; these ranges are considerably greater than those used in references [3] or [6]. The three points excluded are for the case $\phi = 65$ percent, $(T_a - T_w) = 97$ K (see Fig. 7), where only the data for $t > 180$ min are used. Those for shorter times in this particular run can be seen to be anomalously low and probably reflect a situation of nonuniform growth of the frost at short times with the microscope being focused on a low point at the frost surface.

The model of reference [3] as expressed by equation (1) was applied to the data by evaluating A such that the line passed through the centroid of the data which is located at the point (9770, 7.66). This is shown in Fig. 9. Also shown is the line obtained from a least-squares analysis of the data enclosed by the envelope. This resulted in an empirical equation of frost growth under the present conditions of

$$\delta = 0.20t(T_\delta - T_w)^{0.40}, \qquad (2)$$

where δ is in mm. This is also plotted on Fig. 9. The standard deviation (20) of log $[\delta]$ on log $[t(T_\delta - T_w)]$ for this case is 0.030. By comparison, for the flat plate in forced convection

[3], the square-root dependence matched the data quite well for a relative humidity range of about 45 to 90 percent. Exponents obtained by Schneider [6] for the cylinder in forced convection ranged from 0.43 to 0.51 for a relative humidity of 98 percent.

The above data do not include 9 sets for humidities between 34 and 53 percent. If plotted, these all would fall below the envelope shown in Fig. 9 but not in any well-defined manner. The coefficients of these, if averaged would lead to a prediction of

$$\delta = 0.12[t(T_\delta - T_w)]^{0.43}. \tag{3}$$

Here the time span of the data used is arbitrary, but usually greater than 60 min because of wide variations in growth patterns at earlier times. The exponent of equation (3) is appealingly close to those of equations (1) and (2) but this may well be misleading as there are such marked deviations among the individual coefficients. There may be, however, a more general growth law that we are approaching, but which is submerged in the data scatter and realities of experimentation. In any event, all data seem to follow a power law of some sort at growing times long enough to eliminate effects of initial uncertainties in the measurement of representative thicknesses.

The direct experimental uncertainties (95 percent certainty) in the individual measurements were established by test to be ±2 K for the frost-surface temperature and ±0.01 mm for position. The wall temperatures for the high-temperature experiment could be maintained to within ±1 K but for the low-temperature apparatus only ±10 K could be obtained with about 15 min required for corrections to be established. This is probably the cause of some of the long term scatter to be seen in Figs. 4–8.

More significant uncertainties are probably those associated with assigning the measured quantities to the frost layer as a whole. This is because of the difficulty, mentioned previously, of growing a uniform frost layer so that the portion growing at the measurement position represents the frost elsewhere. Surface position and density anomalies can easily develop that we are unable to detect. This is a time dependent problem and is most severe at growing times of less than 2 hr. One might think of this as a systematic error for a given run but a random uncertainty when considering several runs. Taken this way, the uncertainty at 120 min is estimated to be ±0.5 mm in position, with this value decreasing as growing time increases.

Conclusions

Free convective frost formation on a cooled vertical cylinder in room temperature air exhibits a well defined regime of development for relative humidities of 65 percent or greater at growing times beyond those required for local inhomogeneities to smooth out. It appears that at these humidities, the frost-surface temperature is at or near the triple point of water, and the frost growth is predicted reasonably well by the thermodynamic model proposed by White [3] for forced convection over a cooled flat plate. This is similar in final form to a crystal growth model later postulated by Schneider [6] for forced convection past a cooled horizontal cylinder. The frost growth rate seems to be limited by the heat transfer across the boundary layer in this regime.

At low humidities, the frost-surface temperature is below the triple-point temperature, at least for the growing times used in this experiment. The growth rates for the individual experimental runs, on the average, exhibit the same sort of power-law dependence on time and temperature as do the results for high humidities. However, there is excessive variation between runs and the data in general do not group with those corresponding to the high humidities.

References

1 Whitehurst, C. A., "A Survey of Research Efforts in Heat Transfer through Frost Formation," *ASHRAE Journal*, Oct. 1966, pp. 50–55.
2 Shah, Y. T., "Theory of Frost Formation," Sc.D. Thesis, M.I.T., Cambridge, 1968.
3 White, J. E., *"Heat and Mass Transfer in Thick Frost Layers,"* Ph.D Dissertation, University of Kentucky, 1972.
4 Yamakawa, N., and Ohtani, S., "Heat and Mass Transfer in the Frost Layer," *Heat Transfer - Japanese Research*, Vol. 1, No. 3, July-Sept. 1972, pp. 75–82.
5 Hayashi, Y., Aoki, K., and Yuhara, M., "Study of Frost Formation Based on a Theoretical Model of the Frost Layer," *Heat Transfer - Japanese Research*, Vol. 6, No. 3, July-Sept. 1977, pp. 79–94.
6 Schneider, H. W., "Equation of the Growth Rate of Frost Forming on Cooled Surfaces," *International Journal of Heat and Mass Transfer*, Vol. 21, 1978, pp. 1019–1024.
7 Ruccia, R. E., and Mohr, C. M., "Atmospheric Heat Transfer to Vertical Tanks Filled with Liquid Oxygen," *Advances in Cryogenic Engineering*, Vol. 4, Plenum Press, New York, 1960, pp. 307–318.
8 Stoecker, W. F., "Frost Formation on Refrigeration Coils," *ASHRAE Transactions*, Vol. 66, 1960, pp. 71–103.
9 Tajima, O., Yamada, H., Kobayashi, U., and Mizutani, L., "Frost Formation on Air Coolers, Part 1: Natural Convection for a Flat Plate Facing Upwards," *Heat Transfer - Japanese Research*, Vol. 1, No. 2, 1972, pp. 39–48.
10 Tajima, O., Naito, E., Tsutsumi, Y., and Yoshida, H., "Frost Formation on Air Coolers, Part 2: Natural Convection for a Cooled Plate Facing Downwards," *Heat Transfer - Japanese Research*, Vol. 2, No. 2, April-June 1973, pp. 55–76.
11 Tajima, O., Naito, E., Nakashima, K., and Yamamoto, H., "Frost Formation on Air Coolers, Part 3: Natural Convection for the Cooled Vertical Plate," *Heat Transfer - Japanese Research*, Vol. 3, No. 4, Oct.-Dec. 1974, pp. 55–66.
12 Tajima, O., Naito, E., Goto, T., Segawa, S., and Nishimura, K., "Frost Formation on Air Coolers, Part 4: Natural Convection for Two Vertically Opposed Cooled Plates," *Heat Transfer - Japanese Research*, Vol. 4, No. 3, July-Sept. 1975, pp. 21–36.
13 Goodman, J., and Kennedy, L. A., "Free Convection Frost Formation on Cool Surfaces," *Proceedings of 1972 Heat Transfer and Fluid Mechanics Institute*, Stanford University, Palo Alto, 1972, pp. 338–352.
14 Cremers, C. J., Hahn, O. J., and Skorupski, J. H., "Frost Density Measurements on Vertical Cylinders by Gamma-Ray Attenuation," *Advances in Cryogenic Engineering*, Vol. 23, edited by K. D. Timmerhaus, Plenum, New York, 1978, pp. 371–375.
15 Kennedy, L. A., and Goodman, J., "Free Convection Heat and Mass Transfer under Conditions of Frost Deposition," *International Journal of Heat and Mass Transfer*, Vol. 17, 1974, pp. 477–484.
16 Mehra, V. K., "Frost Formation on a Vertical Cylinder with Natural Convection," M.S. Thesis, University of Kentucky, Lexington, 1980.
17 Dietenberger, M., Kumar, P., and Luers, J., "Frost Formation on an Airfoil: A Mathematical Model I," NASA Contractors Report 3129, 1979.
18 Hama, F. R., Recesso, J. V., and Christiaens, J., "The Axisymmetric Free-Convection Temperature Field Along a Vertical Thin Cylinder," *Journal Aero/Space Science*, June 1959, pp. 335–342.
19 Eckert, E. R. G., and Drake, R. M., Jr., *Analysis of Heat and Mass Transfer*, McGraw-Hill, New York, 1972, p. 526.
20 Crandall, K. C., and Seabloom, R. W., *Engineering Fundamentals in Measurement, Probability, Statistics and Dimensions*, McGraw-Hill, New York, 1970.

N. Shamsundar

Associate Professor,
Heat Transfer and
Phase Change Laboratory,
Department of Mechanical Engineering,
University of Houston,
Houston , Texas 77004
Assoc. Mem. ASME

Approximate Calculation of Multidimensional Solidification by Using Conduction Shape Factors

When solidification occurs with conduction controlling and small temperature differences present, quasi-steady models become advantageous. In this paper, the use of conduction shape factors to predict freezing rate and heat transfer in various two-dimensional objects is investigated. Simple equations for calculating these quantities are obtained, and compared to existing results. The use of shape factors to model solidification with time-dependent boundary conditions is illustrated.

Introduction

When solidification takes place in pure substances and eutectics under the control of heat conduction through the solidified part, it often happens that the overall temperature difference driving the phenomenon is moderate or small. Instances of such solidification arise in latent heat recovery and food processing.

In such situations, numerical computations have shown that assuming the temperature field in the solid to be quasi-steady is justifiable and yields sufficient accuracy for practial purposes [1, 2]. It has also been shown that, even when the cooling on the surface of the solid is by convection, the heat transfer rate from the liquid-solid interface to the cooling fluid is expressible in terms of a conduction shape factor, notwithstanding nonuniformities in temperature on the cooled surface [3]. Furthermore, these statements hold whether or not the difference in density between solid and liquid is accounted for [4].

It is profitable to see if solidification can be calculated with the help of the extensively tabulated [5] shape factors for conduction with no change of phase. For, doing so would enable the calculation of solidification for many different geometrical shapes to be made with trivial effort, even if one has to accept modest accuracy as a consequence. This approach is, at first sight, of dubious utility because the solid-liquid interface is a surface of irregular shape, not known *a priori*, and unlikely to be found in a catalogue of shape factors. The counterpoint of this objection is the easily verified observation that the conduction shape factor is not sensitive to slight alterations to the shape of the solid region, and is approximately the same for almost all roundish and squarish shapes with similar boundary conditions. The objective of this paper is to examine the usefulness of the suggested approach by application to specific cases. Prior to doing so, an outline of the method will be provided in general terms.

Analysis

Consider a solidifying substance that is initially all liquid and is separated from the cooling fluid by a thin, highly conducting wall. The cooling fluid may have a time-dependent temperature and heat-transfer coefficient, but the temperature may not differ by a large amount from the melting temperature. If, in an actual problem, the convective coefficient, h, and the coolant temperature, T_f, vary spatially, they are to be replaced by their mean values, $\bar{h}$ and $\bar{T}_f$, over the surface. Adiabatic surfaces may be present, and the limiting caes of $\bar{h} \to \infty$ (uniform surface temperature $T_w(t)$) and $\bar{h} \to 0$ (uniform flux $q_w(t)$) will also be considered. It is assumed that natural convection in the melt plays a negligible role after solidification starts [6]. Although the effects of volume change may be included, as shown in [4], these will be ignored in the present analysis, mainly to keep the presentation simple.

If S is the shape factor between the freezing interface and the cooled wall, the instantaneous heat transfer rate is given by

$$Q = kS[T_{\text{sat}} - \bar{T}_w(t)] = \bar{h}A[\bar{T}_w(t) - \bar{T}_f(t)] \qquad (1)$$

or, after elimination of $\bar{T}_w(t)$,

$$Q = [T_{\text{sat}} - \bar{T}_f(t)]/[1/(kS) + 1/(\bar{h}A)] \qquad (2)$$

Under quasi-steady conditions, the heat-transfer rate must equal the rate at which heat of freezing is released. Thus, if V_s is the volume of solid at time t,

$$Q = \rho\lambda dV_s/dt \qquad (3)$$

which, by expressing V_s in terms of the frozen fraction F, may be written as

$$Q = \rho\lambda V_0 dF/dt \qquad (4)$$

Equating the right hand sides of (2) and (4) gives

$$\rho\lambda V_0 dF/dt = [T_{\text{sat}} - \bar{T}_f(t)]/[1/(kS) + 1/(\bar{h}A)] \qquad (5)$$

As demonstrated mathematically as well as by computational results in [3], the shape factor S is a function only of F for a given geometry. Consequently, the preceding equation is an ordinary differential equation relating F and t, provided $S(F)$ is known. The question of how to obtain $S(F)$ will be taken up later.

The variables in equation (5) are separable only when $\bar{h}$ is independent of time (this includes $\bar{h} = 0$ and $\bar{h} = \infty$). In this case, integration gives

---

Contributed by the Heat Transfer Division for publication in the JOURNAL OF HEAT TRANSFER. Manuscript received by the Heat Transfer Division July 27, 1981.
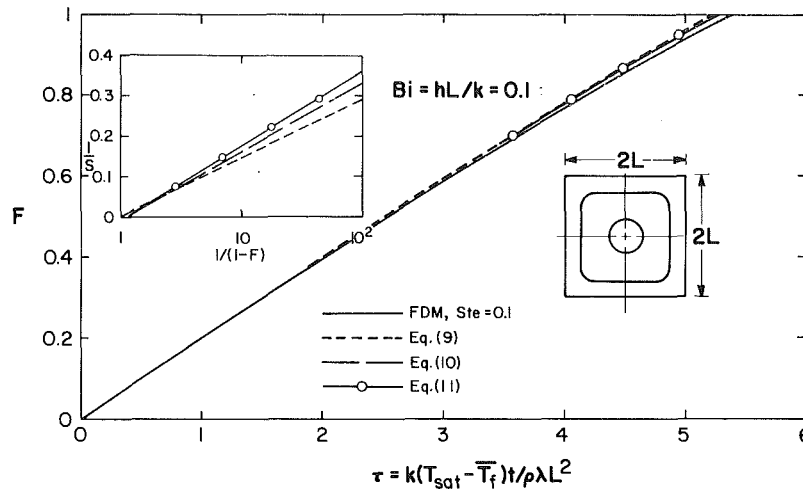
Fig. 1 Schematic of problem, comparison of shape factors, and comparison of results with finite-difference results, solidification of square, Bi = 0.1

$$\int_0^F \left(\frac{1}{S} + \frac{k}{\bar{h}A}\right)dF = \frac{k}{\rho\lambda V_0}\int_0^F [T_{sat} - \bar{T}_f(t)]dt \qquad (6)$$

For the limiting case of infinite convective coefficient, $\bar{T}_f(t) = \bar{T}_w(t)$, and (6) becomes

$$\int_0^F dF/S = (k/\rho\lambda V_0)\int_0^t [T_{sat} - \bar{T}_w(t)]dt \qquad (7)$$

For the other limiting case of $\bar{h} = 0$, the wall flux is specified, and $Q = \bar{q}_w A$. From equation (4),

$$F = (A/\rho\lambda V_0)\int_0^t \bar{q}_w(t)dt \qquad (8)$$

When $\bar{h}$ is specified as being time-dependent, equation (5) will have to be integrated numerically.

Let us now consider finding the shape factor as a function of the frozen fraction. The shape factor can, of course, be found from numerical computations as shown in [3], but that approach is contrary to the thrust of this paper. Instead, tables of shape factors, such as those in [5], should be scanned to identify a stationary geometry (or geometries) which is similar to the geometry of the solidification problem insofar as the shape of the external boundary is concerned. Furthermore, the stationary geometry should have an additional boundary that is similar in shape to the *expected* shape of the evolving solid-liquid interface. This procedure will be made clear during the calculations for specific examples. At this point, let us see what can be accomplished once the shape factor has been identified.

From equations (5–7), F is found as a function of t. Then, from equation (2), Q is obtained as a function of t. If desired, a check on the results is made by examining if the heat flux and frozen fraction results satisfy equation (4), which expresses conservation of energy. Thus, the frozen fraction and heat transfer rate, and other quantities computable from these, are obtained as functions of time. However, interior temperatures, the shape of the solid-liquid interface, or local heat fluxes cannot be obtained.

Solidification Inside a Long Container Of Square Cross-Section With Uniform and Steady Convective Cooling on Sides. This is a simpe two-dimensional solidification problem, for which accurate finite-difference results are available [7]. As shown in the second inset of Fig. 1, the interface is initially square with rounded corners; in later stages, the interface becomes circular. From the table of shape factors in [5], the following formulae are extracted.

$$S \text{ concentric square } = 8/ln(L_0/L_i) \text{ for } L_0/L_i < 1.4$$
$$= 2\pi/[0.93 ln(L_0/L_i) - 0.0502] \text{ for } L_0/L_i > 1.4$$

where

$$2L_0 = \text{side of larger square}$$
$$2L_i = \text{side of smaller square}$$

Since, for concentric squares, $F = 1 - (L_i/L_0)^2$, the above formulae become

$$S = -16/ln(1 - F) \text{ for } F < 0.49 \qquad (9)$$

a,b = coefficients in $1/S = -a ln(1-F) + b$

a_0, b_0 = semi-major and semi-minor axis of elliptical container, respectively

a_i, b_i = semi-major and semi-minor axis of elliptical interface, respectively

A = convectively cooled surface area

Bi = Biot number, hL/k

c = specific heat of solid

C^+ = cooling rate of wall, $-dT_w/dt$

F = frozen fraction = volume of solid/volume of container = V_s/V_0

$\bar{h}(t)$ = mean surface heat transfer coefficient

k = conductivity of solid

L = half-length of side of polygon

$\bar{q}_w(t)$ = mean surface heat flux

Q = heat transfer rate

$S(F)$ = conduction shape factor

$Ste(t)$ = Stefan number = sensible heat/latent heat = $c_p(T_{sat} - \bar{T}_f)/\lambda$

t = time variable

$\bar{T}_f(t)$ = mean temperature of cooling fluid

T_{sat} = solidification temperature

$\bar{T}_w(t)$ = mean surface temperature

V_0 = volume of container

V_s = volume of solid

λ = latent heat

ρ = density of solid

τ = nondimensional time variable, equation (14)

$$S = -2\pi/[0.465ln(1-F) + 0.0502] \text{ for } F > 0.49 \qquad (10)$$

Similarly, for a circle of diameter D within a square of side $2L$,

$$S = 2\pi/[ln(8L/\pi D) - 0.1658] \text{ for } D < 0.2L$$

or, since $F = 1 - (\pi D^2/4)/4L^2$,

$$S = -4\pi/[ln(1-F) + 0.0900] \text{ for } F > 0.99 \qquad (11)$$

For steady $\bar{h}$ and T_f, equation (5) transforms to

$$\int_0^F dF(4/S + 1/2Bi) = \tau,$$

where $\tau = k(T_{sat} - \bar{T}_f)t/\rho\lambda L^2$ and $Bi = \bar{h}L/k$. Writing $1/S = -aln(1-F) + b$, which corresponds to all the three formulae (9-11), we may integrate the preceding equation to obtain

$$\tau = 4(a + b + 1/8Bi)F + 4a(1-F)ln(1-F) \qquad (12)$$

Solidification Inside a Long Container of Square Cross-Section With Uniform Wall-Temperature Decreasing Linearly with Time. Representing the shape factor in terms of the frozen fraction as in the previous case and using equation (7), we obtain

$$(a+b)F + a(1-F)ln(1-F) = C^+ kt^2/8\rho\lambda L^2 = \tau/4 \qquad (13)$$

where $C^+ = -dT_w/dt$ is the rate at which the wall temperature drops, and

$$\tau = (k/\rho\lambda L^2)\int_0^t (T_{sat} - T_w)dt \qquad (14)$$

This problem was solved by Saitoh numerically [8]; he also compared his results to his own earlier experimental results on the freezing of water and found good agreement.

Solidification Inside an Elliptical Container with Uniform Wall-Temperature Decreasing Linearly with Time. This problem is chosen to illustrate using the shape factor approach when the container has an irregular, curved boundary, which is a difficult case to solve by using a finite-difference method. This problem was also solved by Saitoh in the paper just cited.

In attempting to obtain a suitable shape factor formula, two trains of thought obtain. Reference [5] provides a formula for only confocal ellipses. If, somewhat arbitrarily, it is assumed that the interface is not only elliptical but is confocal with the surface, the following formulas are obtained:

shape factor $S = 2\pi/ln[(a_0 + b_0)/(a_i + b_i)]$

confocality condition: $a_0^2 - b_0^2 = a_i^2 - b_i^2$

frozen fraction $F = 1 - a_ib_i/a_0b_0$

By elimination of unwanted variables, the following lengthy expression for S in terms of F is obtained:

$$\frac{1}{S} = \frac{1}{2\pi}ln[(1+b_0/a_0)/\sqrt{\{2(1-F)b_0/a_0} + \sqrt{(1-b_0^2/a_0^2)^2 + 4(1-F)^2b_0^2/a_0^2}] \qquad (15)$$

There is something amiss in this derivation, however. In the early stages, solidification is nearly one-dimensional, and the interface, even if it looks elliptical, will not be confocal since the thickness of the frozen layer must be uniform. Hence, this must be taken into account at least in calculating F. Let us use the same shape factor formula as above, although the confocality condition is violated. In fact, this condition will be replaced by

$$a_i - b_i = a_0 - b_0$$

which represents uniform freezing around the ellipse. The result is the formula

$$\frac{1}{S} = -\frac{1}{4\pi}ln[1 - 4F(b_0/a_0)/(1 + b_0/a_0)^2] \qquad (16)$$
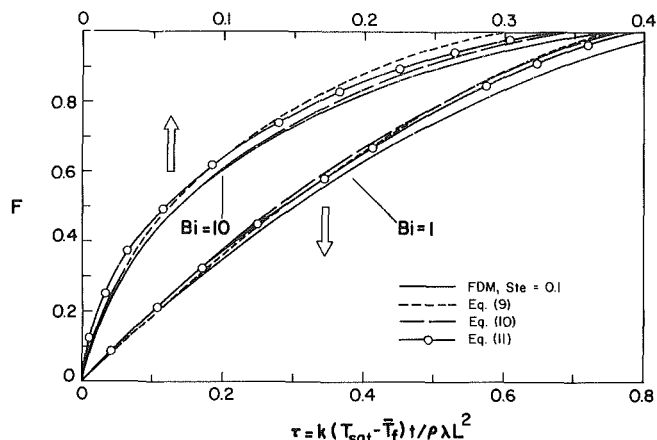
Fig. 2 Comparison of freezing times with finite-difference results, solidification of square, Bi = 1 and 10

It should be noted that, in this second approximation, the only gross assumption is that the shape factor formula may be used even when the interface is not confocal with the container. Since we expect the shape factor to be insensitive to changes in the geometry, we should look for better results from (16), rather than from (15).

As far as the integration of $\int dF/S$ is concerned, the formula (16) leads to the same result as in equation (13), provided the constants a and b are chosen to match (16). Formula (15) is a little more complicated, as it leads to an integral of the form $\int ln(px + \sqrt{p^2x^2 + q^2})dx$, which is equal to $xln(px + \sqrt{p^2x^2 + q^2}) - \sqrt{p^2x^2 + q^2}/p$.

Solidification Inside Polygonal Containers With Steady Convection and Arbitrary Coolant Or Wall Temperature. Since polygons are commonly used shapes, formulas giving $\int dF/S$ for these will be listed. When the frozen layer is thin, heat conduction in it is one-dimensional. Thus, for small F, as for the elliptic container, the formula for S is obtained as

$$S = 4n \tan(\pi/n)/ln[1/(1-F)] \qquad (17)$$

where n is the number of sides of the polygon. For larger F, reference [5] gives, after conversion to our symbols

$$S = 4\pi/\{D_n + ln[1/(1-F)]\} \qquad (18)$$

where

$$D_3, D_4, D_6, D_8, D_\infty = -0.2561, -0.900,$$
$$-0.0234, -0.0090 \qquad (19)$$

The ranges of F for which formulas (18) apply have not been clearly established. We suggest that (18) be used whenever it gives $S > 0$, and (17) otherwise, in evaluating $\int dF/S$. The value of the integral may then be used in formulae (6) and (7) to obtain solidification time, etc.

Results

By employing the equations given above, the frozen fraction was calculated as a function of time. For all the example cases considered, the integrations can be carried out explicitly, leading to formulae that are easily evaluated on a calculator. Taking each case in turn, we shall examine how the results compare to more precisely calculated, published results.

Solidification of a Square with Steady, Uniform Convection on Surface. The results calculated from the approximate equations (9-11) are plotted and compared with the finite-difference results of [7] for Bi = 0.1, 1 and 10 in Figs. 1 and 2. Figure 1 also contains an inset in which the formulae are themselves compared by showing the reciprocal of the shape factor plotted against the logarithm of the liquid
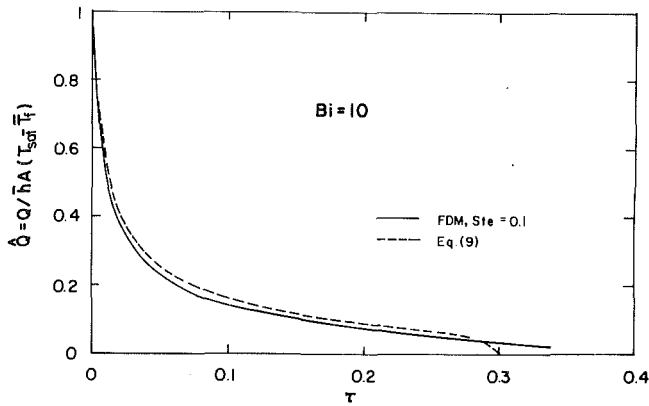
Fig. 3 Comparison of heat transfer rate with finite-difference results, solidification of square, Bi = 10

Fig. 4 Comparison of freezing times for solidification of a square with time-dependent wall temperature

Fig. 5 Comparison of freezing times for solidification of an elliptic cylinder with time-dependent wall temperature

fraction. For Bi = 0.1, the comparison is excellent; but this is no better than expected, since for low Bi the shape factor plays an insignificant role, and even the lumped capacity solution $F = 2Bi$ is sufficiently accurate. For Bi = 1, and even more so for Bi = 10, the conduction resistance becomes important, and the curvature of the freezing line becomes prominent. All the approximate results are in fair agreement over the entire solidification period with the finite-difference results. The curves also fulfill expectations as to their behavior that are based on the nature of the formulae. Formula (9), giving as it does the shape factor between squares, works best up to $F = 0.3$, and gives high values of F later. Similarly, (10) and (11) work better at larger values of F, as they should. Formula (11), listed as being valid for $0.99 \leq F < 1$, works remarkably well for $0 \leq F < 1$, pointing out the insensitivity of the shape factor to the shape.

Although [7] provides results for a Stefan number of 0.01, which are slightly closer to those given by our formulas, the finite-difference results shown here are those for Ste = 0.1, in order to emphasize the low importance of heat capacity effects. The present work, of course, assumes that Ste $\approx$ 0.

The great difficulty and expense involved in obtaining heat transfer results for Bi = 10, as stated in [7], is to be noted. With this in mind, it is gratifying to observe the excellent prediction given by the formula (9), as shown in Fig. 3.

Solidification with Surface Temperature Varying Linearly With Time. For this case, Saitoh [8] conducted experiments and compared them to his numerical results, observing good agreement. The results shown in Fig. 4 by full lines are his numerical results;[1] F was calculated by measuring the areas of the solid regions in his figures with a K & E planimeter. The area measurements were repeated, and the error was less than 0.001 in F.[2] Again, the predictions of the formulas (9-11) are in fair agreement with the numerical (and, therefore, the experimental) results of Saitoh. As before, equation (11) performs much better than expected.

Similar results for the ellipse are shown in Fig. 5. As pointed out earlier, the formula (16), which is for uniform solidification and uses a shape factor for confocal ellipses for ellipses that are not confocal, works better than formula (15). This comparison should point out the need to use due judgment in selecting formulae for shape factors and in assuming the shape of the interface.

These results establish the utility of the shape factor method for treating time-dependent boundary conditions and curved external boundaries.

---

[1] The value of the reference length D in Saitoh's paper is 0.040 m [9].

[2] After this paper was written, Professor Saitoh provided the author with independent measurements of the areas in his figures [9]. The two sets of measurements were found to differ by less than 0.5 percent.
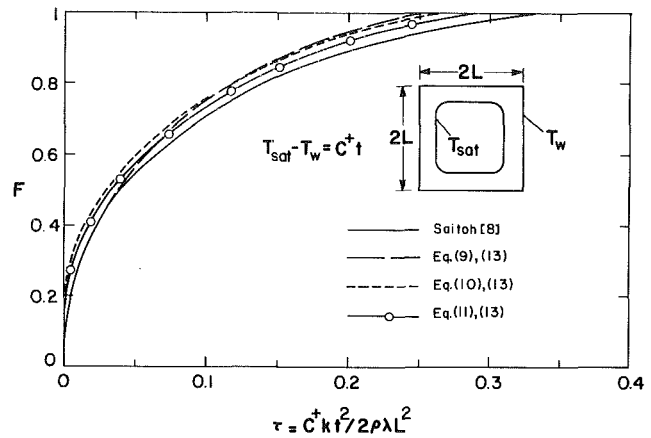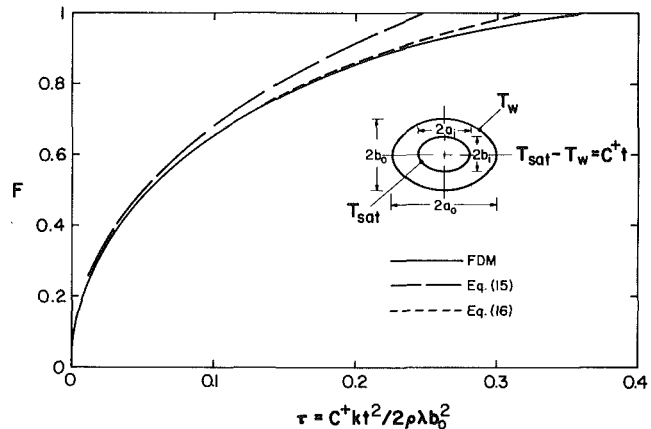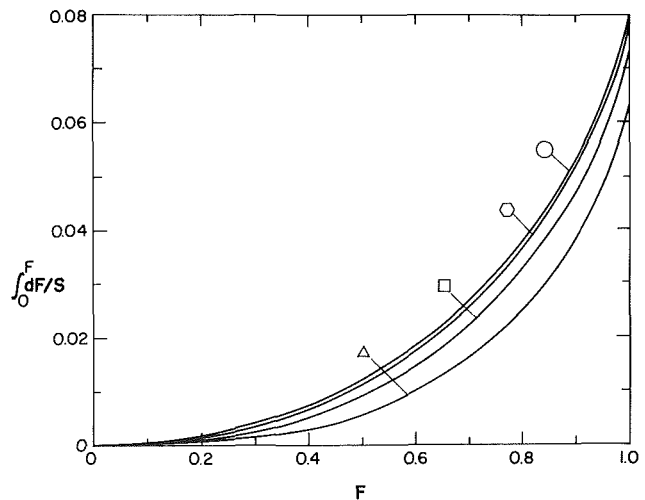
Fig. 6 Thermal resistance contributions to solidification time of various polygonal shapes compared, in terms of frozen fraction

Solidification in Polygonal Containers. The expression $\int_0^F dF/S$ is the contribution of the thermal resistance of the solid to the solidification time. In order to avoid having to account for the effect of the surface convection as well, let us just study the influence of shape on the thermal resistance contribution only. Figure 6 shows $\int_0^F dF/S$ plotted for triangular, square, hexagonal, and octagonal prisms and a cylinder. The area/volume ratio decreases as the number of sides increases, slowing down the solidification rate. For any shape other than

the triangular prism, the use of the simple formula for the cylinder may be sufficiently accurate.

General Rule For Solidification Time. From equation (6), a general rule may be deduced concerning multi-dimensional solidification of objects with time-dependent external cooling. The solidification time consists of two parts. The first part is dependent only on the geometry and the frozen fraction, and is independent of the cooling coefficient and its variation with time. The second part depends on the external convection, and is proportional to $\int dF/\text{Bi}$, Bi being the Biot number. For constant external convection, the rule becomes the following, where f_1 represents $\int dF/S$ and B is a constant.

$$\frac{k(T_{\text{sat}} - T_f)t}{\rho \lambda V_0} = f_1(F, \text{geometry}) + BF/\text{Bi}$$

Interesting particular cases may be derived. At high cooling rates, the internal resistance dominates, and the solidification time is almost independent of the external convective coefficient. At the opposite extreme, as in solidifying metals, the external resistance dominates, and the solidification time becomes independent of the conductivity of the substance, but becomes proportional to $\rho \lambda V_0 / \bar{h} A \Delta T$. This is a rule well-known to metallurgists [10].

Conclusions and Summary

Solidification with slow cooling rates or small temperature differences can be conveniently modeled by using shape factors, even when the boundary temperature, heat flux and convective coefficients are nonuniform and time-dependent. The shape factors need not be exactly calculated, as they are insensitive to moderate changes in the shape. It suffices to identify a shape factor formula for a reasonably similar shape in a tabulation of shape factors. From this formula, a relation between shape factor and frozen fraction can be developed and used with the energy conservation principle to obtain formulae for freezing time and heat transfer rate.

The accuracy of the reults so obtained has been demonstrated by making comparisons to finite-difference results. The simplicity and versatility of the shape factor method recommend it whenever the assumptions behind it are satisfied and one is content to obtain overall results. Extensive tables of shape factors are available to make the application of the method almost effortless. Even if a shape-factor formula is unavailable, modest accuracy can possibly be attained by using the flux-plot technique together with reasonably assumed interface shapes.

The approach described in this paper becomes inadequate if local heat fluxes and details of the interface shape are sought.

References

1 El-Hage, A. A. and Shamsundar, N., "Calculation of Two-Dimensional Solidification by Orthogonal Polynomials," AIAA Paper 81-1050.

2 Shamsundar, N. and Srinivasan, R., "Analysis of Energy Storage by Phase Change in an Array of Cylindrical Tubes," in *Thermal Storage and Heat Transfer in Solar Energy Systems*, edited by F. Kreith, et al. ASME, 1978.

3 Shamsundar, N. and Srinivasan, R., "A New Similarity Method for Analysis of Multi-Dimensional Solidification," ASME JOURNAL OF HEAT TRANSFER, Vol. 101, 1979, pp. 585–591.

4 Shamsundar, N., "Similarity Rule for Solidification Heat Transfer with Change in Volume," ASME JOURNAL OF HEAT TRANSFER, Vol. 103, 1981, pp. 173–175.

5 Hahne, E. and Grigull, U., "Formfactor und Formwiderstand der Stationären Mehrdimensionalen Wärmeleitung," *International Journal of Heat and Mass Transfer*, Vol. 18, 1975, pp. 751–767.

6 Sparrow, E. M., Ramsey, J. W., and Harris, J. S., "The Transition from Natural-Convection-Controlled Freezing to Conduction-Controlled Freezing," ASME JOURNAL OF HEAT TRANSFER, Vol. 103, 1981, pp. 7–12.

7 Shamsundar, N. and Sparrow, E. M., "Analysis of Multi-Dimensional Conduction Phase Change via the Enthalpy Model," ASME JOURNAL OF HEAT TRANSFER, Vol. 97, 1975, pp. 333–340.

8 Saitoh, T., "Numerical Method for Multi-Dimensional Freezing Problems in Arbitrary Domains," ASME JOURNAL OF HEAT TRANSFER, Vol. 100, 1978, pp. 294–299.

9 Saitoh, T., Personal communication, April 1981.

10 Flemings, M. C., *Solidification Processing*, McGraw-Hill, 1974, pp. 12–13.

Analysis of Solidification Interface Shape Resulting From Applied Sinusoidal Heating

R. Siegel

National Aeronautics and
Space Administration,
Lewis Research Center,
Cleveland, Ohio 44135
Fellow ASME

Maintaining a flat solidification interface is important for forming desired crystal structures in certain types of metal casting processes. This has application in new manufacturing techniques for naturally strengthened composite components such as turbine blades. The solidification interface shape will adjust to be compatible with the spatial distribution of energy being transferred to it. The interface shape must be found that satisfies conditions of simultaneously being at the fusion temperature and having an imposed spatially varying heat flux. Specific results are obtained for the heat transfer from the liquid phase varying along the interface in a cosine fashion. Interface shapes are found as a function of the amplitude and wavelength of the imposed heat transfer variations, and the sensitivity of the interface shape to these variations is examined.

Introduction

To form certain types of metallic structures in metal casting, the uniformity of conditions at the solidification interface is very important. By use of a carefully regulated solidification process, strengthened composite structures consisting of a reinforcing phase within a metallic matrix can be obtained by continuous casting. This has potential application in the manufacture of strengthened components such as turbine and compressor blades. One requirement is that the solidification interface be kept planar within a given tolerance. In [1, 2] the interface shape was analyzed in connection with a continuous casting process in which directional solidification is used to form a composite structure directly from a superheated eutectic alloy melt. The interface shape is influenced by the convective heat transfer from the superheated molten metal to the interface. Although for analysis this convection is often assumed uniform, it can vary along the interface as a result of convection currents in the melt. The present paper will analytically examine the sensitivity of the interface shape to spatial variations in the heat transfer from the adjacent liquid. This will indicate how important it is to control external convection currents or temperature variations in the melt as a function of the geometry of the solidified region.

During solidification the shape of the freezing interface responds to the rate at which heat is being locally removed. A steady-state condition will be achieved if the net amount of energy being locally removed becomes zero at all locations along the interface. An example is the shape of a steady-state frozen layer formed on a cold plate immersed in a stream of warm liquid [3, 4, 5]. The frozen layer will form until the local heat conducted through it from the solidification interface to the cold plate is equal to the local heat added to the interface

by the external warm flowing liquid. The spatial variation of the external heat transfer to the interface thus has an important role in determining the frozen layer interface shape.

The present analysis solves an inverse type of problem. The temperature of the solidification interface is fixed at the freezing point. The local heat flux into the interface is also specified by the local external liquid temperature and local heat-transfer coefficient. The result to be obtained is the shape of the steady-state solidification interface. It is desired to examine the sensitivity of the interface shape to the spatial variation in external conditions. This will indicate how carefully external conditions must be controlled to obtain an interface that is flat within a specified tolerance. The results are in terms of parameters involving geometric and heat-transfer quantities.

The inverse problem involving an unknown (or "free") boundary, such as analyzed here, is encountered in many fields. One of the areas where the theory first developed was for groundwater flow in porous soil as given for example in [6]. Another interesting application of the analytical methods is for determining the unknown shape of the cathode tool for electrochemical machining [7, 8]. Some recent numerical techniques for free boundary problems are in [9, 10]. References [6-10] are intended to provide a brief perspective on the wide interest in free boundary problems.

Analysis

A simplified geometry was selected that will provide results that can be applied to a variety of situations of practical interest. This is a layer with the heat transfer from the liquid to the solidification interface varying in a periodic fashion along it in the x direction; this will produce a wavy interface. This situation is also of interest relative to the formation of waves on ice sheets, [11]. The geometry is in Fig. 1(*a*), and from symmetry, only the region between planes A–A and B–B
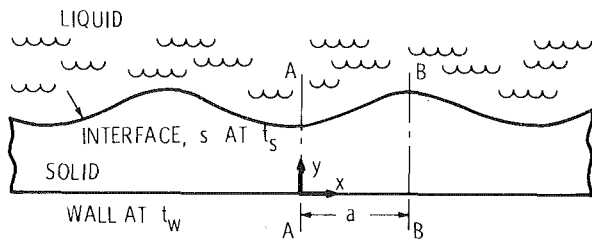
(a) Layer formed as a result of spatially periodic heat transfer from liquid.
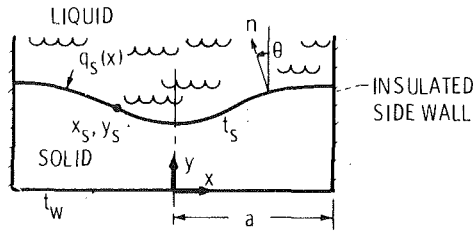
(b) Equivalent region contained between insulated side boundaries.

Fig. 1 Geometry of solidified region

Fig. 2 Solidified region in dimensionless physical plane

need be analyzed. From symmetry, no heat flow passes across these planes so they can also be regarded as insulated boundaries. Hence, the present solution also applies to solidification in a container with side walls insulated, Fig. 1(b). This configuration has application to the shape of the solidification interface in a phase change energy storage device, where free convection in the liquid would provide a variation in heat-transfer coefficient along the freezing boundary. The coefficient would be diminished in the corner region adjacent to the side walls, thereby producing an interface shape as in Fig. 1(b).

The objective of the analysis with regard to metal solidification is to determine the sensitivity of the interface flatness to the heat-transfer conditions. These conditions include the wavelength and amplitude of the periodicity of the convective heat transfer to the interface, and the thermal conductivity of the solid. The results will provide information on the magnitude of the spatial variations in convective heat transfer in the liquid phase that can be permitted without yielding excessive interface distortion.

The region to be analyzed is of width a in Figs. 1(a) and 1(b). The vertical thickness as a function of x is to be determined. The molten liquid above the interface is at a higher temperature than the freezing temperature t_s, which is the temperature along the curved interface. The boundary conditions along the interface are then

$$\frac{\partial t}{\partial n}\bigg|_s = \frac{q_s}{k} \tag{1}$$

$$t(x_s, y_s) = t_s \tag{2}$$

The normal derivative in equation (1) can be resolved into components in the x and y directions to give

$$\frac{\partial t}{\partial x}\bigg|_s = -\frac{\partial t}{\partial n}\bigg|_s \sin\theta = -\frac{q_s}{k}\sin\theta \tag{3a}$$

$$\frac{\partial t}{\partial y}\bigg|_s = \frac{\partial t}{\partial n}\bigg|_s \cos\theta = \frac{q_s}{k}\cos\theta \tag{3b}$$

From the symmetry only the right half of Fig. 1(b) need be considered. Along the cooled wall

$$t = t_w \quad \left(\frac{\partial t}{\partial x} = 0\right) \quad (0 \le x \le a, y = 0) \tag{4}$$

Along the vertical symmetry plane and at the insulated side boundary

$$\frac{\partial t}{\partial x} = 0 \quad x = 0, a (0 \le y) \tag{5}$$

The heat transfer to the interface is specified to have a periodic spatial variation

$$q_s = q_m + \Delta q \cos\frac{\pi x}{a} \tag{6}$$

─────── **Nomenclature** ───────

A = dimensionless parameter and dimensionless length, $(q_m a)/k(t_s - t_w) = a/\gamma$

a = half-wavelength of heating variation along interface

I = imaginary part of inverse tangent, equation (22b)

k = thermal conductivity of solidified material

M = the parameter $\Delta q/q_m$

m = the product $M\delta$

N_0, N_1 = coefficients in Y_s variation, equation (13)

n = normal to the interface, $N = n/\gamma$

q = local convective heat transfer from liquid to interface

Δq = amplitude of periodic variation in q

R = real part of inverse tangent, equation (22a)

t = temperature, $T = (t - t_w)/(t_s - t_w)$

V = intermediate mapping variable, $\xi + i\eta$

W = potential function, $W = -T + i\psi$

x, y = coordinates in the physical plane, $X = x/\gamma$, $Y = y/\gamma$

Y_3, Y_4 = distances given in Fig. 2

z = complex variable in physical plane, $z = x + iy$; $Z = z/\gamma$

α = the quantity $\cos^{-1} m$

γ = length scale quantity, $k(t_s - t_w)/q_m$

δ = a coefficient less than unity in Fig. 4

ζ = complex temperature derivative, $-(\partial T/\partial X) + i(\partial T/\partial Y)$

η = imaginary part of V

θ = angle from vertical to normal direction, Figs. 1(b) and 2

κ = the quantity $\cosh^{-1}(1/\delta)$

ξ = real part of V

ψ = ordinate in W-plane

Subscripts

ℓ = liquid phase

m = mean value

s = at solidification interface

w = cooled wall

$1,2,3,4$ = the four corners of the solid region
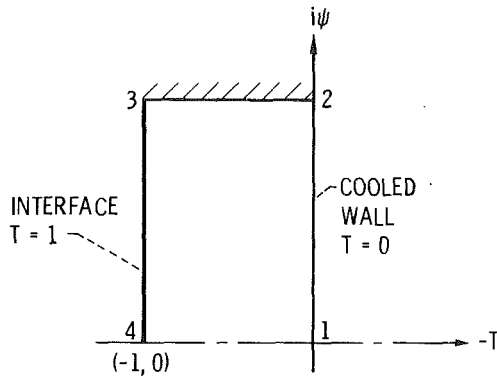
Fig. 3 Solidified region in potential plane, W
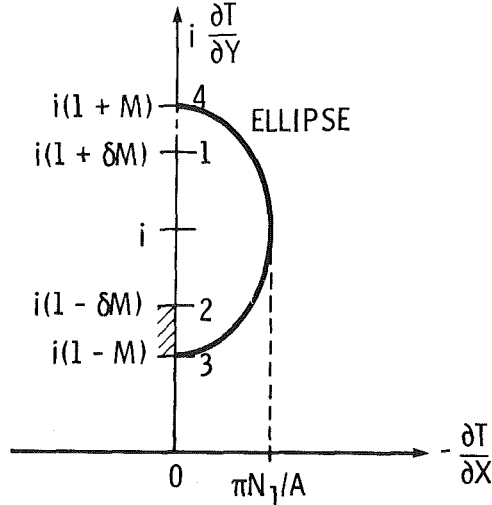
Fig. 4 Region in temperature derivative plane

The steady heat conduction equation

$$\frac{\partial^2 t}{\partial x^2} + \frac{\partial^2 t}{\partial y^2} = 0 \qquad (7)$$

is to be satisfied within the solidified region. The boundary s has its temperature derivatives (equations (3a), (3b), and (6)) specified, and also its temperature, equation (2). The interface shape must be found that will satisfy these conditions with the wall at $y = 0$ cooled so that it is maintained at constant temperature t_w below t_s. An analytical solution will be found provided $\Delta q / q_m$ is small relative to unity. It is desired to find the amplitude of the waviness in surface s relative to the amplitude $\Delta q / q_m$.

A dimensionless temperature is defined as $T = (t - t_w) / (t_s - t_w)$ so that $T = 0$ at the cooled boundary and $T = 1$ along the solidification interface. The physical lengths are all divided by a length quantity, $\gamma = k(t_s - t_w)/q_m$. The quantity $A = a/\gamma$ is a parameter in the problem. A second parameter is $M \equiv \Delta q / q_m$. Equations (3a) and (3b) are placed in dimensionless form after eliminating q_s by use of equation (6),

$$\frac{\partial T}{\partial X}\bigg|_s = - \left(1 + M \cos \frac{\pi X}{A}\right) \sin \theta \qquad (8)$$

$$\frac{\partial T}{\partial Y}\bigg|_s = \left(1 + M \cos \frac{\pi X}{A}\right) \cos \theta \qquad (9)$$

The solid region is shown in the dimensionless physical plane $Z = X + iY$ in Fig. 2.

The solidification interface shape can be obtained by a technique developed in [12]. The gradient of a potential function is proportional to the flow produced in the direction of the gradient. Since heat flows along the gradient of

negative temperature, the $-T$ is a potential function for heat flow. An analytic function W of a complex variable Z can then be defined as

$$W = -T + i\psi \qquad (10)$$

where W satisfies Laplace's equation, and lines of constant T and ψ form an orthogonal curvilinear net in the physical plane.

The derivative of an analytic function is independent of direction so dW/dZ can be written as

$$\frac{dW}{dZ} = -\frac{\partial T}{\partial X} + i \frac{\partial \psi}{\partial X}$$

Using the Cauchy-Riemann equation $\partial \psi / \partial X = \partial T / \partial Y$, the ψ is eliminated to give

$$\frac{dW}{dZ} = -\frac{\partial T}{\partial X} + i \frac{\partial T}{\partial Y} \equiv \zeta \qquad (11)$$

where ζ is the complex temperature derivative. Equation (11) is integrated to yield

$$Z = \int \frac{1}{\zeta} dW + C_1 \qquad (12)$$

As will be shown, the shape of the solidified region is known in the coordinates of W. If ζ can be related to W, the integration can be carried out to obtain the physical region in the Z-plane.

In the W-plane, Fig. 3, the solidified region in Fig. 2 maps into a rectangle where the cooled wall and solidification interface are vertical constant temperature lines. The insulated and symmetry boundaries $\widehat{23}$ and $\widehat{14}$ are normal to the constant temperature lines. If ζ can be found as a function of W, the integration of (12) will yield Z as a function of W. Then the known vertical line $\widehat{34}$ can be transformed into the physical plane to yield the interface shape.

The ζ is an analytic function and can be related to W by conformal mapping if the solidified region can be represented in a ζ-plane. Let us show that if M is small, the interface shape can be found in the ζ-plane as shown in Fig. 4. Along $\widehat{32}$, $\widehat{21}$, $\widehat{14}$, the $\partial T / \partial X = 0$, and $\partial T / \partial Y$ increases from its minimum value at 3 to its maximum at 4. For uniform heat transfer along the interface, equation (6) gives $q_s = q_m$, and the resulting uniform thickness Y_s of the solidified region [as found from the heat balance $q_m = k(t_s - t_w)/y_s$] is $Y_s = 1$. Since the dimensionless temperature difference across the solidified layer is unity, $\partial T / \partial Y = 1$ and $\partial T / \partial X = 0$ throughout the region when q_s is uniform, as can also be obtained from equations (8) and (9) by letting $M = 0$ and $\theta = 0$. Thus the solidified region degenerates to the point $(0, i)$ in the ζ-plane. When M is not zero the region thickness would be expected to respond in a reciprocal way to variations in q_s to yield a shape as in Fig. 2 for positive M. For small M, the $\partial T / \partial Y$ will vary asymmetrically about $(0, i)$ so that the resulting figure in the ζ-plane is symmetric about a horizontal line through this point. At points 3 and 4 the isotherm $T = 1$ in Fig. 2 has a zero slope so from equation (9) with $\theta = 0$, $\partial T / \partial Y|_3 = 1 - M$ and $\partial T / \partial Y|_4 = 1 + M$. For small M, the figure retains symmetry such that points 1 and 2 will be on the axis in Fig. 4 at $(1 + \delta M)i$ and $(1 - \delta M)i$ where δ is an unknown and is less than unity.

The shape of the interface $\widehat{34}$ is now needed in the ζ-plane. This can be found for small M by finding an approximation for θ in equations (8) and (9). In Fig. 2, let $(Y_3 - Y_4)/2 \equiv N_1$ and $N_0 \equiv Y_4 + N_1$. For small M, the interface would be expected to respond in an inverse way to the variations in q_s, so as a first approximation (N_1 is positive)

$$Y_s = N_0 - N_1 \cos \frac{\pi X}{A} + O(N_1^2) \qquad (13)$$
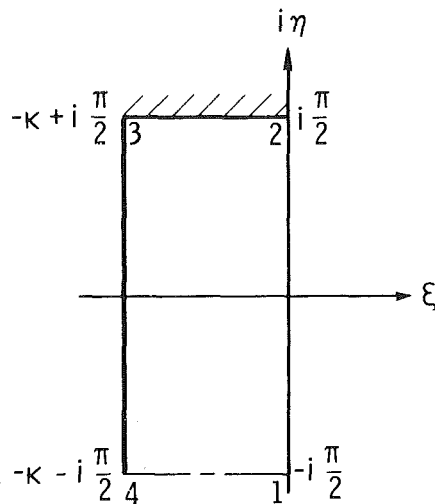
Fig. 5   Region in rectangle in intermediate V-plane

Fig. 6   Amplitude of dimensionless interface distortion relative to amplitude of variation in heat transfer

where $N_0 \approx 1$. This is used to obtain a first approximation for θ, and the interface shape will then be found from equation (12). For small M, the amplitude N_1 is also small, but the ratio N_1/M could be of order unity or smaller. The angle θ will also be small and can be obtained from

$$\tan\theta = \theta + \frac{\theta^3}{3} + \ldots = \frac{dY}{dX}\bigg|_s = N_1 \frac{\pi}{A}\sin\frac{\pi X}{A} \qquad (14)$$

For small θ, equations (8) and (9) are expanded using Maclaurin series, and since M, N_1 and θ are all small this gives

$$\left(\frac{\partial T}{\partial X}\bigg|_s\right)^2 = \theta^2 + 2\theta^2 M\cos\frac{\pi X}{A} + \ldots \qquad (15)$$

$$\left(\frac{\partial T}{\partial Y}\bigg|_s - 1\right)^2 = M^2\cos^2\frac{\pi X}{A} - \theta^2 M\cos\frac{\pi X}{A} + \ldots \qquad (16)$$

where the omitted terms are of 4th or higher order. From equation (14),

$$\theta^2 \approx \left(\frac{\pi N_1}{A}\right)^2 \sin^2\frac{\pi X}{A} = \left(\frac{\pi N_1}{A}\right)^2 \left(1 - \cos^2\frac{\pi X}{A}\right)$$

This is used to eliminate θ^2 from equations (15) and (16), and after retaining only terms to 2nd order, there results

$$\left(\frac{\partial T}{\partial X}\bigg|_s\right)^2 \approx \left(\frac{\pi N_1}{A}\right)^2 \left(1 - \cos^2\frac{\pi X}{A}\right)$$

$$\left(\frac{\partial T}{\partial Y}\bigg|_s - 1\right)^2 \approx M^2 \cos^2\frac{\pi X}{A}$$

These two equations are combined to eliminate the cosine terms, and the result is put in the form

$$\frac{\left(\frac{\partial T}{\partial Y}\big|_s - 1\right)^2}{M^2} + \frac{\left(\frac{\partial T}{\partial X}\big|_s\right)^2}{M^2\left(\frac{\pi}{A}\frac{N_1}{M}\right)^2} = 1 \qquad (17)$$

This is an ellipse about the center (0, 1) and with semi-axes M and $M(\pi/A)$ (N_1/M) as shown in Fig. 4.

There is a known conformal transformation between an ellipse and a rectangle [13]. A convenient rectangle is shown in the V-plane in Fig. 5. The transformation between ζ and V is given by

$$\zeta = M\delta i \sin(iV) + i \qquad (18)$$

where $\cosh\kappa = \dfrac{1}{\delta}$ and $\sinh\kappa = \dfrac{1}{\delta}\dfrac{\pi}{A}\dfrac{N_1}{M}$.

The rectangle in Fig. 5 can also be transformed into Fig. 3 by the relation

$$W = \frac{V}{\kappa} + i\frac{\pi}{2\kappa} \qquad (19)$$

This relates W and ζ through the variable V, and it will be convenient to use the intermediate variable V in what follows.

Equations (18) and (19) are substituted into equation (12) to yield

$$Z = -\frac{1}{\kappa}\int \frac{d(iV)}{M\delta\sin(iV) + 1} + C_1$$

For convenience let $m \equiv M\delta$, and integrate to obtain

$$Z = -\frac{2}{\kappa\sqrt{1-m^2}}\tan^{-1}\left[\frac{\tan\left(\frac{iV}{2}\right) + m}{\sqrt{1-m^2}}\right] + C_1$$

The constant C_1 is evaluated by using the condition that $Z = 0$ at $V = -i\pi/2$, which gives (note that $\kappa = \cosh^{-1}M/m$)

$$Z = \frac{2}{\sqrt{1-m^2}\cosh^{-1}\left(\frac{M}{m}\right)}$$

$$\times\left\{\tan^{-1}\sqrt{\frac{1+m}{1-m}} - \tan^{-1}\left[\frac{\tan\left(\frac{iV}{2}\right) + m}{\sqrt{1-m^2}}\right]\right\} \qquad (20)$$

The quantity m will now be related to the physical quantity A. From Fig. 2, $A = Z_2 - Z_1$; and from Fig. 5, these Z locations correspond to $V_2 = i\pi/2$ and $V_1 = -i\pi/2$. Inserting these into equation (20) gives

$$A = \frac{2}{\sqrt{1-m^2}\cosh^{-1}\left(\frac{M}{m}\right)}\left(\tan^{-1}\sqrt{\frac{1-m}{1+m}} + \tan^{-1}\sqrt{\frac{1+m}{1-m}}\right)$$

which simplifies to (since $\tan^{-1}\beta + \tan^{-1}(1/\beta) = \pi/2$ for any β)

Table 1 Interface amplitude coordinates as a function of parameters A and M

A	M	m	Y_3	Y_4	$(Y_3 - Y_4)/2M$
0.25	0.1	6.9747×10^{-7}	1.0084	0.9924	0.0798
	.2	1.3949×10^{-6}	1.0178	.9855	.0807
	.3	2.0924×10^{-6}	1.0284	.9791	.0821
0.50	0.1	3.7349×10^{-4}	1.0168	0.9848	0.1597
	.2	7.4697×10^{-4}	1.0355	.9710	.1613
	.3	1.1205×10^{-3}	1.0568	.9582	.1642
1	0.1	8.6257×10^{-3}	1.0335	0.9698	0.3182
	.2	1.7245×10^{-2}	1.0709	.9423	.3215
	.3	2.5853×10^{-2}	1.1135	.9171	.3272
2	0.1	0.039808	1.0623	0.9451	0.5861
	.2	.079345	1.1337	.8965	.5930
	.3	.11835	1.2163	.8532	.6050
4	0.1	0.075383	1.0911	0.9230	0.8402
	.2	.15010	1.1999	.8574	.8562
	.3	.22345	1.3318	.8013	.8842
8	0.1	0.092697	1.1051	0.9131	0.9640
	.2	.18503	1.2346	.8403	.9856
	.3	.27658	1.3976	.7787	1.0315
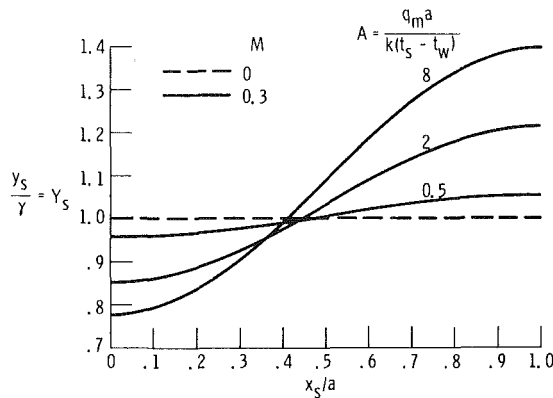
Fig. 7   Typical interface shapes for $M = 0.3$ and various A

$$A = \frac{\pi}{\sqrt{1-m^2}\cosh^{-1}\left(\dfrac{M}{m}\right)} \qquad (21)$$

The coordinates of most interest are those along the solidification interface. Substitute $V = \xi + i\eta$ into equation (20) and expand the tangent function to obtain

$$Z = \frac{2}{\sqrt{1-m^2}\cosh^{-1}\left(\dfrac{M}{m}\right)}$$

$$\times \left\{ \tan^{-1}\sqrt{\frac{1+m}{1-m}} - \tan^{-1}\left[\frac{\dfrac{-\sin\eta + i\sinh\xi}{\cos\eta + \cosh\xi} + m}{\sqrt{1-m^2}}\right] \right\}$$

Let the real and imaginary parts of the inverse tangent be

$$R \equiv \left(\frac{-\sin\eta}{\cos\eta + \cosh\xi} + m\right)\Big/\sqrt{1-m^2} \qquad (22a)$$

$$I \equiv \left(\frac{\sinh\xi}{\cos\eta + \cosh\xi}\right)\Big/\sqrt{1-m^2} \qquad (22b)$$

and take the real and imaginary parts of Z to yield,

$$X = \frac{1}{\sqrt{1-m^2}\cosh^{-1}\left(\dfrac{M}{m}\right)}$$

$$\times \left[2\tan^{-1}\sqrt{\frac{1+m}{1-m}} - \tan^{-1}\left(\frac{2R}{1-R^2-I^2}\right)\right] \qquad (23a)$$

$$Y = \frac{1}{\sqrt{1-m^2}\cosh^{-1}\left(\dfrac{M}{m}\right)} \ln\left[\frac{R^2+(1-I)^2}{R^2+(1+I)^2}\right]^{\frac{1}{2}} \qquad (23b)$$

Along the solidification interface $\widehat{34}$, Figs. 2 and 5 show that the R and I are evaluated using $\xi = -\kappa = -\cosh^{-1}(M/m)$, and $-\pi/2 \le \eta \le \pi/2$. The inverse tangent at the end of equation (23a) should be evaluated in the quadrant corresponding to the individual signs of the numerator and denominator. Then along the interface, X_s and Y_s normalized with respect to A are given by

$$\frac{x_s}{a} = \frac{X_s}{A} = \frac{1}{\pi}$$

$$\times \left[2\tan^{-1}\sqrt{\frac{1+m}{1-m}} - \tan^{-1}\left(\frac{2R_s}{1-R_s^2-I_s^2}\right)\right] \qquad (24a)$$

$$\frac{y_s}{a} = \frac{Y_s}{A} = \frac{1}{\pi}\ln\left[\frac{R_s^2+(1-I_s)^2}{R_s^2+(1+I_s)^2}\right]^{\frac{1}{2}} \qquad (24b)$$

where

$$R_s = \frac{1}{\sqrt{1-m^2}}\left(\frac{-\sin\eta}{\cos\eta + \dfrac{M}{m}} + m\right) \qquad -\frac{\pi}{2}\le\eta\le\frac{\pi}{2}$$

$$I_s = -\frac{1}{\sqrt{1-m^2}}\frac{\left[\left(\dfrac{M}{m}\right)^2-1\right]^{\frac{1}{2}}}{\cos\eta + \dfrac{M}{m}} \qquad -\frac{\pi}{2}\le\eta\le\frac{\pi}{2}$$

Results and Discussion

There are two parameters in the solution: $A = q_m a/k(t_s - t_w)$ and $M = \Delta q/q_m$. For specified values of A and M, the value of m is found from equation (21). Then by using various η values in the range between $-\pi/2$ and $\pi/2$, the X_s and Y_s values can be found along the interface by use of equation (24). The corresponding values of A, M and m are given in Table 1 along with the Y_s values at the end points of the interface. Some of the results from the last column of the table are given in Fig. 6. Typical results for the interface shape are

shown in Fig. 7 for $M = 0.3$. To form a basis for comparison consider first the situation where the heat transfer to the interface is uniform, so that the value of M is zero and the resulting interface is flat. The heat balance $q_m = k(t_s - t_w)/y_s$ yields $y_s/\gamma = Y_s = 1$, so that γ is a convenient characteristic length for normalizing distances in the y-direction. This normalization gives the horizontal line for $M = 0$ in Fig. 7.

When $M > 0$, equations (24a) and (24b) yield curves that are essentially cosine shaped. In the analysis the assumed cosine shape for the interface in equation (13) was used to obtain an approximate relation between $\partial T/\partial X$ and $\partial T/\partial Y$ along the interface. Then a solution satisfying $\nabla^2 T$ was found using this boundary relation. Since the resulting shape of the interface is very close to that originally assumed, the derivative boundary relation, equation (17), used in the approximation was quite accurate and a consistent solution has been found. A small deviation in interface shape from that in equation (13) would perturb the relation used between $\partial T/\partial X$ and $\partial T/\partial Y$ in Fig. 4, but would result in only a higher order correction to the interface shape found in equation (24).

The most important result of the analysis is the magnitude of the solidification interface distortion relative to the magnitude M of the nonuniformity in the imposed heat transfer. The amplitude of the interface distortion is $(Y_3 - Y_4)/2$ and hence the last column in Table 1 is the amplitude ratio; some of these values are plotted in Fig. 6. For each A the ratio is rather insensitive to M.

For small A the amplitude ratio is found to be small; this corresponds to a narrow width of the region in Fig. 2. As shown in Fig. 6, the amplitude ratio in this range can be approximated quite well by the relation A/π, which can be obtained from the theory by noting that for small A the m is very small.

For large A the thickness variation in Fig. 2 becomes stretched out horizontally and the heat conduction tends to become locally one dimensional. In the limit of locally one-dimensional heat flow,

$$q_m + \Delta q \cos\left(\frac{\pi X}{a}\right) = k(t_s - t_w)/y_s$$

which has the dimensionless form

$$\frac{y_s}{\gamma} = Y_s = \cfrac{1}{1 + M \cos\left(\dfrac{\pi X}{a}\right)}$$

Then for a locally one-dimensional heat flow $(Y_3 - Y_4)/2M$

is equal to $(1/2M) [1/(1 - M) - 1/(1 + M)] = 1/(1 - M^2)$ which is greater than 1. This trend with A explains why the value at the bottom of the last column in Table 1 is larger than 1.

Another feature worth noting is that for locally one-dimensonal conditions (large A) the average height $(1/2) (Y_3 + Y_4) = (1/2) [1/(1 - M) + 1/(1 + M)] = 1/(1 - M^2)$ which is greater than unity. This trend persists for smaller A so that the curves in Fig. 7 become centered above unity at $x/a = 0.5$. As a result of the increased surface area of the curved interface as compared to a flat interface, the total heat flow through the layer is somewhat increased when $M \neq 0$. This increase in total heat flow can occur even though the overall location of the interface has moved upward, because the increase in heat flow through the thinner part of the layer more than compensates for the decreased flow through the thicker part.

References

1 Siegel, R., "Shape of Two-Dimensional Solidification Interface During Directional Solidification by Continuous Casting," JOURNAL OF HEAT TRANSFER, Vol. 100, 1978, pp. 3–10.

2 Siegel, R., "Analysis of Solidification Interface Shape During Continuous Casting of a Slab," International Journal of Heat and Mass Transfer, Vol. 21, 1978, pp. 1421–1430.

3 Savino, J. M., and Siegel, R., "Experimental and Analytical Study of the Transient Solidification of a Warm Liquid Flowing over a Chilled Flat Plate," NASA Technical Note D-4015, 1967.

4 Hirata, T., Gilpin, R. R., Cheng, K. C., and Gates, E. M., "The Steady-State Ice Layer Profile on a Constant Temperature Plate in a Forced Convection Flow, Part I: Laminar Regime," International Journal of Heat and Mass Transfer, Vol. 22, 1979, pp. 1425–1433.

5 Hirata, T., Gilpin, R. R., and Cheng, K. C., op. cit., Part II: The Transition and Turbulent Regimes,"pp 1435–1443.

6 DeWiest, R. J. M., ed., Flow Through Porous Media, Academic Press, New York, 1969.

7 Nilson, R. H., and Tsuei, Y. G., "Free Boundary Problem for the Laplace Equation with Application to ECM Tool Design," ASME Journal of Applied Mechanics, Vol. 98, 1976, pp. 54–58.

8 Forsyth, Jr., P., and Rasmussen, H., Perturbation Solutions for Steady Direct and Inverse Electrochemical Machining Problems, International Journal of Engineering Science, Letters, Vol. 17, 1979, pp. 807–812.

9 Meyer, G. H., "The Method of Lines and Invariant Imbedding for Elliptic and Parabolic Free Boundary Problems," SIAM J. Numer. Anal., Vol. 18, 1981, pp. 150–164.

10 Crank, J., and Ozis, T., "Numerical Solution of a Free Boundary Problem by Interchanging Dependent and Independent Variables," J. Inst. Maths. Applics., Vol. 26, 1980, pp. 77–85.

11 Gilpin, R. R., Hirata, T., and Cheng, K. C., "Wave Formation and Heat Transfer at an Ice-Water Interface in the Presence of a Turbulent Flow," ASME Journal of Fluid Mechanics, Vol. 99, 1980, pp. 619–640.

12 Siegel, R., "Conformal Mapping for Steady Two-Dimensional Solidification on a Cold Surface in Flowing Liquid," NASA Technical Note D-4771, 1968.

13 Churchill, R. V., Complex Variables and Applications, 2nd ed., McGraw-Hill, New York, 1960, p. 286.

F. E. Moore[1]

Graduate Student.

Y. Bayazitoglu

Associate Professor.
Assoc. Mem. ASME

Mechanical Engineering and
Materials Science Department,
Rice University,
Houston, Texas 77001

Melting Within a Spherical Enclosure

Melting of a phase change material within a spherical enclosure is considered. The phase change material is initially at its saturation temperature. Suddenly the enclosure temperature is increased to a fixed value. The density of the solid is assumed to exceed the density of the liquid, the implication being that the solid continually drops toward the bottom of the shell as melting progresses. This motion of the solid generates a flow field within the liquid. A mathematical model is developed and confirmed by experimental evidence. The interface positions and the temperature profiles for various Stefan and Fourier numbers are determined, and the energy storage characteristics are studied. It is found that the convective effects can be neglected only at small Stefan numbers.

1 Introduction

Phase change thermal storage devices find application in cases where a large amount of energy must be transferred and stored but only a limited temperature difference is available as the driving potential. The growing number of uses for these systems has encouraged researchers to study the details of the phase change process itself, so that optimum designs can be developed in a systematic fashion.

A survey of the literature reveals that most investigations working with the spherical geometry have restricted themselves to the problem of symmetric melting and/or freezing of a phase change material [1-3]. Riley et al. [1] considered the one dimensional inward solidification of a sphere initially at the fusion temperature and suddenly subjected to a lowering of the wall temperature. They assumed that the liquid remained at the fusion temperature, and used perturbation techniques to solve the problem for the case of small Stefan numbers. Tao [2] presents early numerical results for the freezing of a sphere subject to a constant heat transfer coefficient boundary condition.

This work investigates the melting of a phase-change material initially solid and at its saturation temperature contained within a spherical shell. The solid's density is assumed to exceed that of the liquid, the implication being that the solid will continually descend as material is melted away from its underside. This movement generates a fluid motion which contributes a convective term to the energy equation written for the liquid region. Nicholas and Bayazitoglu [4] were the first to consider the effects of unequal solid and liquid densities in their study of melting within a cylindrical enclosure, but they neglected the convection in the liquid.

2 Analysis

The geometry used to describe the problem is shown in Fig. 1. We consider a phase-change material, initially solid and at its saturation temperature, T_{sat}, which completely fills a spherical shell. The shell is assumed to have negligible thermal
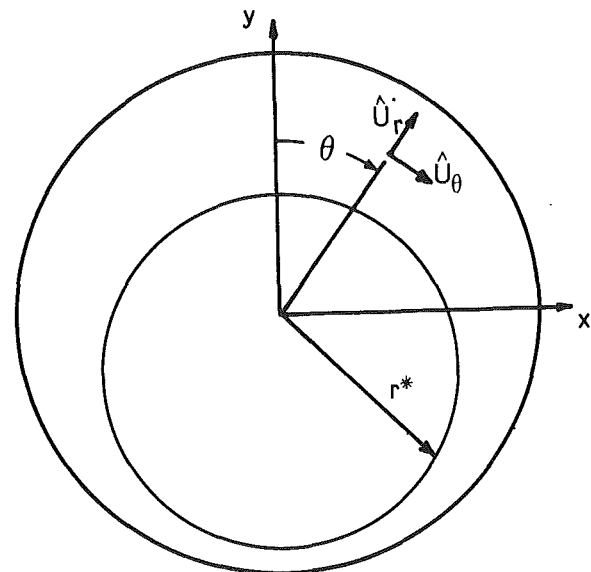
Fig. 1 The geometry

resistance. At time $t = 0$, the temperature of the shell wall is suddenly raised to some value T_W, and melting commences. The boundary separating the liquid and solid phases will henceforth be referred to as the interface, and will be identified by the position vector $r^* \hat{U}_r$. The interface is assumed to be a sharply defined surface; we assume melting occurs at a precise temperature and there is no dendritic structure or slush present at the interface. Constant thermophysical properties are assumed. The difference in density between the solid and liquid phases is considered only so far as it suggests a continual repositioning of the solid toward the bottom of the shell.

The energy equation written for the liquid phase can be expressed nondimensionally as:

$$\frac{\partial \Psi}{\partial Fo} + Re\, Pr \left(v_r \frac{\partial \Psi}{\partial \eta'} + \frac{v_\theta}{\eta'} \frac{\partial \Psi}{\partial \Theta} \right)$$

$$= \frac{\partial^2 \Psi}{\partial \eta'^2} + \frac{\cot\theta}{\eta'^2} \frac{\partial \Psi}{\partial \theta} + \frac{1}{\eta'^2} \frac{\partial^2 \Psi}{\partial \theta^2} + \frac{2}{\eta'} \frac{\partial \Psi}{\partial \eta'} \quad (1)$$

The heat balance written for the interface can be written nondimensionally as [5-7]:

$$\text{VD}\left(\cos\theta + \frac{\sin\theta}{\eta^*}\frac{\partial\eta^*}{\partial\theta}\right) - \frac{\partial\eta^*}{\partial\text{Fo}}$$

$$= \text{Ste}\frac{\partial\Psi}{\partial\eta'}\left[1 + \left(\frac{1}{\eta^*}\frac{\partial\eta^*}{\partial\theta}\right)^2\right] \tag{2}$$

The initial and boundary conditions for the energy equation are:

$$\Psi(\eta',\theta,0) = 0 \tag{3a}$$

$$\Psi(1,\theta,\text{Fo}) = 1 \tag{3b}$$

$$\Psi(0,\theta,\text{Fo}) = 0 \tag{3c}$$

$$\partial\Psi/\partial\theta(\eta',0,\text{Fo}) = 0 \tag{3d}$$

$$\partial\Psi/\partial\theta(\eta',\pi,\text{Fo}) = 0 \tag{3e}$$

The initial and boundary conditions for the interface equation become:

$$\eta^*(F_0 = 0) = \eta_0^* \tag{4a}$$

$$\frac{\partial\eta^*}{\partial\theta}\Bigg|_{\theta=0,\pi} = 0 \tag{4b}$$

The following dimensionless quantities have been introduced:

$$\eta' = r/R; \eta^* = r^*/R; \text{Fo} = \alpha t/R^2; v_\theta = V_\theta/V_D; v_r = V_r/V_D;$$

$$\Psi = (T - T_{\text{sat}})/(T_w - T_{\text{sat}}); \text{Re} = \rho_L V_D R/\mu; \text{Pr} = \mu C_p/k;$$

$$\text{VD} = RV_D/\alpha; \text{Ste} = \left(\frac{\rho_L}{\rho_s}\right)\frac{C_p(T_w - T_{\text{sat}})}{h_{Ls}}$$

The equations developed for the temperature distribution and the interface position only apply so long as the origin of the coordinate system lies within the solid region; otherwise a single radial line would cut the interface in the two locations and an identification problem would arise. Hence we can only hope to predict the interface position up to the time when $\eta^*(\theta = 0) = 0$. For much of this time the lower half of the solid remains roughly spherical, with the gap between the solid and the shell wall nearly constant and on the order of 2 percent of the shell's inner radius. The gap width is seen to change slowly with time. In light of these observations, a quasi-steady-state approximation to the velocity field will be made. The width of the gap is small compared to its curvature, so we will approximate the polar velocity component within the gap as being similar to a pressure induced flow between parallel plates. Since the radial velocity component is never larger than V_D, and must decrease rapidly to zero at the shell wall, it is neglected.

We know that Poiseuille flow is characterized by a parabolic velocity profile. We will calculate the coefficients of this profile by assuming the velocity is zero at the interface and shell wall and must satisfy mass continuity. Essentially, we are assuming that the solid and shell remain fixed, and fluid is injected into the gap with negligible momentum to produce the gap flow. In reality, the velocity of the fluid at the interface must be equal to the solid's velocity.

The first step in calculating the velocity profile at a particular value of θ, say θ_p, is to find the volumetric flow rate through the gap between the interface and the shell wall at that location. Imagine that the motion of the interface during the time dt can be separated into two distinct phases. First, only melting occurs, and the solid velocity is zero. This phase lasts until the final instant of the time interval, whereupon, in the second phase, melting is arrested and the solid suddenly drops to its new equilibrium position. The difference between the volume of fluid that was present at the end of phase one and at the end of phase two will determine the volumetric flow rate.

Knowledge of the velocity distribution will allow us to calculate shear and pressure force distributions. The vertical components of these forces must combine to balance the weight of the solid. The mechanism of achieving a force balance is simple. If the weight is in excess, the solid will drop closer to the shell. This will boost the heat flux and increase the volumetric flow, which must negotiate a more constricted gap than before. Hence, the velocities will increase, and so will the shear and pressure forces. The converse applies if the fluid forces are in excess.

To facilitate computations, we adopt a variable transformation used by Murray and Landis [8]. We replace the variable η' by the variable η, defined as:

$$\eta = \frac{\eta^* - \eta'}{\eta^* - 1} \tag{5}$$

The transformed energy equation becomes:

$$\frac{\partial\Psi}{\partial\text{Fo}} = \text{EN}\frac{\partial\Psi}{\partial\eta} + \text{ENN}\frac{\partial^2\Psi}{\partial\eta^2} + \text{ENT}\frac{\partial^2\Psi}{\partial\eta\partial\theta}$$

$$+ \text{ETT}\frac{\partial^2\Psi}{\partial\theta^2} + \text{ET}\frac{\partial\Psi}{\partial\theta} \tag{6}$$

where

$$\text{EN} = \left[\frac{\eta - 1}{\eta^* - 1}\frac{\partial\eta^*}{\partial\text{Fo}} + \frac{2}{\eta'(1-\eta^*)} + \frac{\cot\theta}{(\eta')^2}\left(\frac{1-\eta}{\eta^*-1}\frac{\partial\eta^*}{\partial\theta}\right)\right.$$

$$+ \frac{1-\eta}{(\eta')^2(\eta^*-1)}\frac{\partial^2\eta^*}{\partial\theta^2} + \frac{2(\eta-1)}{(\eta')^2(\eta^*-1)^2}\left(\frac{\partial\eta^*}{\partial\theta}\right)^2$$

$$\left. - \frac{\text{RePr}v_r}{(1-\eta^*)} + \frac{\text{RePr}v_\theta(1-\eta)}{\eta'(1-\eta^*)}\frac{\partial\eta^*}{\partial\theta}\right] \tag{7a}$$

Nomenclature

c_p	= specific heat			θ	= polar angle
Fo	= Fourier number	v_θ	= dimensionless polar	μ	= dynamic viscosity
h	= enthalpy		velocity	ρ	= density
h_{Ls}	= latent heat of fusion	VD	= dimensionless dropping	ν	= kinematic viscosity
k	= thermal conductivity		velocity	Ψ	= dimensionless temperature
Pr	= Prandtl number	V_D	= dropping velocity		
r	= radial coordinate	V_r	= radial velocity component	**Subscripts**	
r^*	= interface position	V_θ	= polar velocity component	i	= η descriptor
R	= shell radius	α	= thermal diffusivity	j	= θ descriptor
Re	= Reynolds number	η	= transformed coordinate,	L	= liquid
Ste	= Stefan number		equation (5)	n	= time level descriptor
t	= time	η'	= dimensionless radial	s	= solid
T	= temperature		coordinate	sat	= saturation conditions
v_r	= dimensionless radial	η^*	= dimensionless interface	W	= shell wall
	velocity		position	$\circ$	= initial

$$\text{ENN} = \frac{1}{(\eta^* - 1)^2} + \frac{1}{(\eta')^2}\left(\frac{1-\eta}{\eta^*-1}\frac{\partial\eta^*}{\partial\theta}\right)^2 \qquad (7b)$$

$$\text{ENT} = \frac{1}{(\eta')^2}\frac{2(1-\eta)}{\eta^*-1}\frac{\partial\eta^*}{\partial\theta} \qquad (7c)$$

$$\text{ET} = \frac{\cot\theta}{(\eta')^2} - \frac{\text{RePr}v_\theta}{\eta'}, \text{ETT} = \frac{1}{(\eta')^2} \qquad (7d,e)$$

The interface equation becomes:

$$VD\left(\cos\theta + \frac{\sin\theta}{\eta^*}\right) - \frac{\partial\eta^*}{\partial\text{Fo}} = \text{Ste}\frac{\partial\psi}{\partial\eta}\left(\frac{1}{1-\eta^*}\right)$$

$$\times\left[1 + \left(\frac{1}{\eta^*}\frac{\partial\eta}{\partial\theta}\right)^2\right] \qquad (8)$$

Although the boundary conditions do not change, it should be noted that in order to eliminate the temperature discontinuity in the numerical calculations equation, (4a) is given a false start as $\eta^*(\text{Fo}=0) = \eta^*_0 \simeq 1$ at the shell wall.

3 Solution

The energy and interface equations are solved by finite difference techniques. The purpose of the variable transformation is to fix the interface at $\eta = 0$ and the inner shell surface at $\eta = 1$. The transformed plane wherein the solution will be sought is a rectangular region with fixed boundaries and constant mesh spacing.

The Crank-Nicolson procedure, which is a second-order-in-time procedure and is unconditionally stable, is used to solve the energy equation. That is:

$$\frac{\Psi_{ijn+1} - \Psi_{ijn}}{\Delta\text{Fo}} = \frac12\text{EN}_{ij}(\Psi_{ijn+1} + \Psi_{ijn})_\eta$$

$$+ \frac12\text{ENN}_{ij}(\Psi_{ijn+1} + \Psi_{ijn})_{\eta\eta}$$

$$+ \frac12\text{ENT}_{ij}(\Psi_{ijn+1} + \Psi_{ijn})_{\eta\theta}$$

$$+ \frac12\text{ETT}_{ij}(\Psi_{ijn+1} + \Psi_{ijn})_{\theta\theta}$$

$$+ \frac12\text{ET}_{ij}(\Psi_{ijn+1} + \Psi_{ijn})_\theta \qquad (9)$$

where the operators are defined as:

$$(A_{ij})_\eta = (A_{i+1j} - A_{i-1j})/2\Delta\eta \qquad (10a)$$

$$(A_{ij})_{\eta\eta} = (A_{i+1j} - 2A_{ij} + A_{i-1j})/(\Delta\eta)^2 \qquad (10b)$$

$$(A_{ij})_{\eta\theta} = (A_{i+1j+1} - A_{i+1j-1} - A_{i-1j+1}$$
$$+ A_{i-1j-1})/(4\Delta\eta\Delta\theta) \qquad (10c)$$

$$(A_{ij})_{\theta\theta} = (A_{ij+1} - 2A_{ij} + A_{ij-1})/(\Delta\theta)^2 \qquad (10d)$$

$$(A_{ij})_\theta = (A_{ij+1} - A_{ij-1})/2\Delta\theta \qquad (10e)$$

A_{ij} can assume the identity of either Ψ_{ijn+1} or Ψ_{ijn}. Equation (9) contains nine unknowns and would be expensive to solve in a straightforward manner, therefore the alternating direction method [9] as adapted for mixed derivatives [10] is used.

The idea behind the alternating direction procedure is to advance forward one time step by employing one or more intermediate solutions, each of which is implicit in only one space variable. Let Ψ^*_{ij} denote the first approximation, written implicitly in the η direction as:

$$\frac{\Psi^*_{ij} - \Psi_{ijn}}{\Delta\text{Fo}} = \frac12\text{En}_{ij}(\Psi^*_{ij} + \Psi_{ijn})_\eta + \frac12\text{ENN}_{ij}$$

$$(\Psi^*_{ij} + \Psi_{ijn})_{\eta\eta} + \frac12\text{ENT}_{ij}(b\Psi^*_{ij} + a\Psi_{ijn})_{\eta\theta}$$

$$+ \text{ETT}_{ij}(\Psi_{ijn})_{\theta\theta} + \text{ET}_{ij}(\Psi_{ijn})_\theta \qquad (11)$$

where a and b are the weighing factors to be determined and $a + b = 2$.

The second approximation written implicitly in the θ direction becomes:

$$\frac{\Psi_{ijn+1} - \Psi_{ijn}}{\Delta\text{Fo}} = \frac12\text{EN}_{ij}(\Psi^*_{ij} + \Psi_{ijn})_\eta$$

$$+ \frac12\text{ENN}_{ij}(\Psi^*_{ij} + \Psi_{ijn})_{\eta\eta}$$

$$+ \frac12\text{ENT}_{ij}[b\Psi^*_{ij} + a(c\Psi_{ijn+1} + d\Psi_{ijn})]_{\eta\theta}$$

$$+ \frac12\text{ETT}_{ij}(\Psi_{ijn+1} + \Psi_{ijn})_{\theta\theta}$$

$$+ \frac12\text{ET}_{ij}(\Psi_{ijn+1} + \Psi_{ijn})_\theta \qquad (12)$$

where once again the unknown weighing factors are c and d, where $c + d = 1$.

We subtract equation (11) from equation (12), solve for Ψ^* and then substitute this result back into equation (12) to eliminate Ψ^*. We find we can recover the Crank-Nicolson equation [with an additional term which tends to zero as $(\Delta\text{Fo})^2$], if we require that $a+b=2, c+d=1, b+ac=1$, and $ad=1$. There are many solutions to these equations. If we choose $b=0$, we obtain $a=2$, $c=\frac12, d=\frac12$

The working equations are now:

$$\frac{\Psi^*_{ij} - \Psi_{ijn}}{\Delta\text{Fo}} = \frac12\text{EN}_{ij}(\Psi^*_{ij} + \Psi_{ijn})_\eta$$

$$+ \frac12\text{ENN}_{ij}(\Psi^*_{ij} + \Psi_{ijn})_{\eta\eta}$$

$$+ \text{ENT}_{ij}(\Psi_{ijn})_{\eta\theta} + \text{ETT}_{ij}(\Psi_{ijn})_{\theta\theta}$$

$$+ \text{ET}_{ij}(\Psi_{ijn})_\theta \qquad (13)$$

and

$$\frac{\Psi_{ijn+1} - \Psi^*_{ij}}{\Delta\text{Fo}} = \frac12\text{ENT}_{ij}(\Psi_{ijn+1} - \Psi_{ijn})_{\eta\theta}$$

$$+ \frac12\text{ETT}_{ij}(\Psi_{ijn+1} - \Psi_{ijn})_{\theta\theta}$$

$$+ \frac12\text{ET}_{ij}(\Psi_{ijn+1} - \Psi_{ijn})_\theta \qquad (14)$$

The usual case has $\Psi_{ijn+1} = \Psi_{ijn}$ to start with. Equation (13) is used to predict Ψ^*_{ij}. Then equation (14) is applied to give a first approximation to the new Ψ_{n+1}. This predicted value of Ψ_{n+1} is introduced into the mixed derivative term on the right hand side of equation (14), which is then solved to give a corrected value of Ψ_{n+1}. This is compared with the previous prediction for Ψ_{n+1} and equation (14) is solved again until good agreement is reached. The advantage gained by our particular choice of $a, b, c,$ and d is that Ψ^* need only be calculated once. Note that we do not use equation (12), but rather the difference between equation (11) and equation (12); the latter is much simpler algebraically to handle.

The interface equation is written in a finite difference form akin to the Crank-Nicolson approach.

$$VD\left[\cos\theta_j + \frac{2\sin\theta_j}{(\eta^*_{jn+1} + \eta^*_{jn})}\cdot\frac{\partial\eta^*}{\partial\theta}\right]$$

$$- \left(\frac{\eta^*_{jn+1} - \eta^*_{jn}}{\Delta\text{F}_0}\right) + 2\text{Ste}\frac{\partial\Psi}{\partial\eta}\left(\frac{1}{\eta^*_{jn+1} + \eta^*_{jn} - 2}\right)$$

$$\left[1 + \frac{4}{(\eta^*_{jn+1} + \eta^*_{jn})^2}\left(\frac{\partial\eta^*}{\partial\theta}\right)^2\right] = 0 \qquad (15)$$

where

$$\frac{\partial\eta^*}{\partial\theta} \simeq \frac{\eta^*_{j+1\,n+1} - \eta^*_{j-1\,n+1} + \eta^*_{j+1n} - \eta^*_{j-1n}}{4\Delta\theta} \qquad (16)$$

The equation (15) is solved using the modified quasi-linearization algorithm [11], a more robust version of the Newton-Raphson method.

First, we assume that the interface heat flux calculated at time n remains constant throught the time step, and we use this to calculate a first approximation to η^*_{n+1}. The boundary

conditions used to do this are the reflection condition at $\theta = 0$, and the assumption that $\eta^*_{n+1}(\theta = \pi) = \eta^*_n(\theta = \pi)$. (The reflection condition at $\theta = \pi$ is used to calculate VD.) Knowing η^*_{n+1} and η^*_n we can solve for the velocities and ultimately decide whether the solid is in equilibrium, or whether the gap at the bottom must be bigger or smaller. If the gap requires modification, we alter η^*_{n+1} ($\theta = \pi$) accordingly, and recalculate VD and η^*_{n+1}, and eventually the new velocities, shear forces, etc. This is repeated until the solid is balanced. We then return to the energy equation and calculate ψ_{n+1}, by using the average between η^*_{n+1} and η^*_n, wherever η^* is required in the energy equation coefficients. Then the heat flux is recalculated using an average value of ψ_{n+1} and ψ_n, and the balancing routine is reinitiated. This process continues until successive calculations of ψ_{n+1} yield nearly identical results. At this point the time step is said to have converged, and we prepare to calculate ψ_{n+2}. The most successful mesh size used was $\Delta\eta = \Delta\theta = 0.1$. The value of ΔF_0 varied but was usually 0.001.

4 Results and Discussion

Figure 2 shows the interface at various times for a range of Stefan numbers. The development of the interface profile can be studied as follows. The velocity of an arbitrary point on the interface can be separated into two components: the dropping velocity, in the direction of gravity, and the component due to local melting, which is directed into the solid and is normal to the interface. Initially, the interface is everywhere equidistant from the shell wall η^*_0, and the velocity component arising from local melting, which is at its maximum at the onset of melting, is everywhere equal in magnitude, but not in direction. At $\theta = \pi$, for example, the two components are essentially equal in magnitude but opposite in sense, so that the net velocity is zero. Physically speaking, the solid is falling as fast as material is being melted away from its underside. At $\theta = 0$, on the other hand, the two components agree in sense, and the interface recedes from the shell wall. Similar observations can be made for each point on the interface. Eventually, two regions on the liquid side can be distinguished. The upper region is characterized by an ever widening gap between the interface and the shell wall, and the lower region is characterized by a small, nearly constant gap. The two regions join at approximately $\theta = \pi/2$.

The polar velocity component is most significant in the lower region, and it is there that the significant pressure and shear forces are generated. Initially, the temperature profiles taken in the radial direction and the shell wall heat flux are the same for all values of θ. In the upper region, the effect of the receding interface is to diminish the gradient of the temperature profile, resulting in a decrease in the local melting rate and the heat flux at the wall. In the lower region, no such deterioration occurs, and the temperature profile remains constant and essentially linear throughout the melting cycle. Consequently, the local heat flux remains at its initial high rate, so that the lower region increasingly dominates the heat transfer process. Figure 3 shows representative temperature profiles. The change in the gradient of the profiles would be more pronounced if the abscissa had been η' rather than η.

Tests of a qualitative nature were conducted using glass spheres (the type used to make light bulbs) having radii of 3.272 cm and 2.789 cm, and an average wall thickness of 0.15 cm. A well-insulated, ten-gallon water bath was employed to maintain an approximate, constant, wall-temperature boundary condition on the sphere. The sphere could be viewed and photographed through a hole cut through the insulation. The PCM used for testing purposes was n-octadecane wax, chosen because it melts at 28°C and can be readily obtained in a highly purified form. While the solid phase in the sphere melts, the excess volume is accumulated by
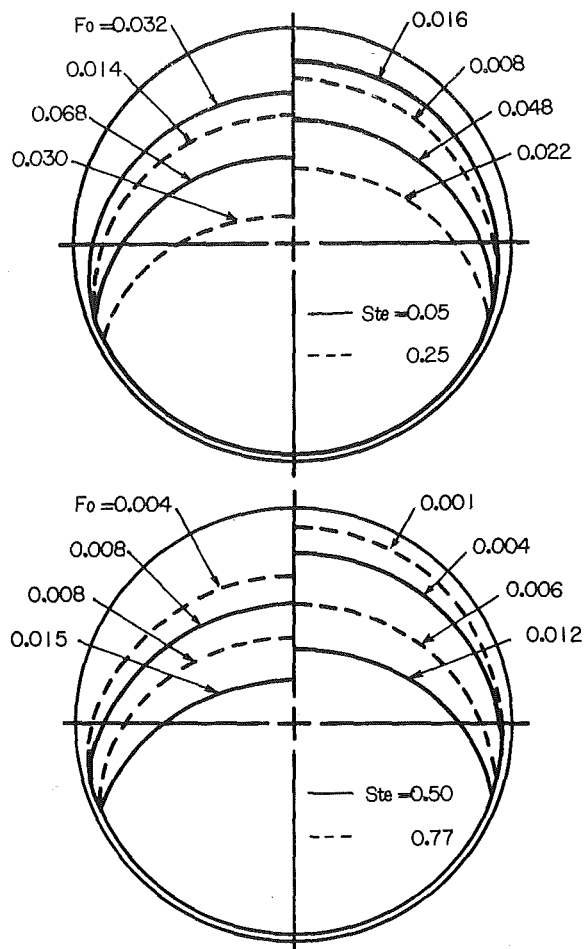
Fig. 2 Interface position at various stages of melting
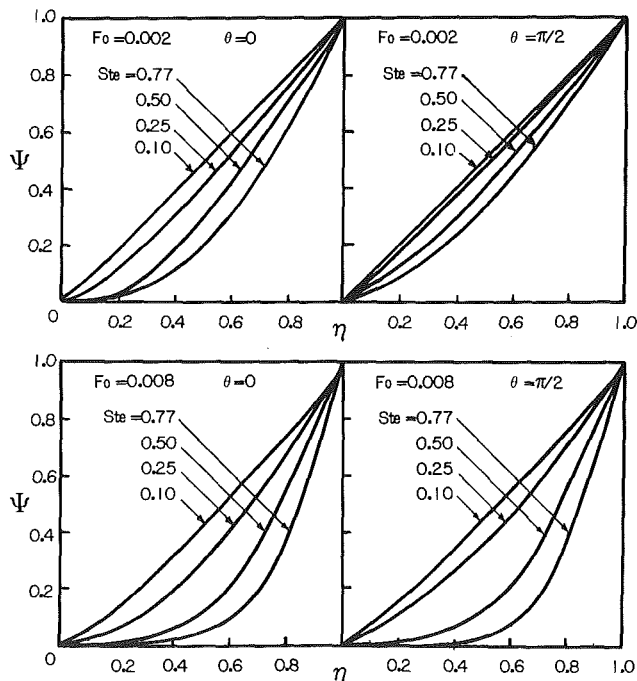
Fig. 3 Temperature profiles in radial direction

the riser of the sphere at the top. This volume increase in n-octadecane wax was about 5-6 percent.

A representative photograph of the interface, one of a sequence [7], is shown in Fig. 4. The dark, irregularly shaped patches visible near the bottom of the solid are flattened air
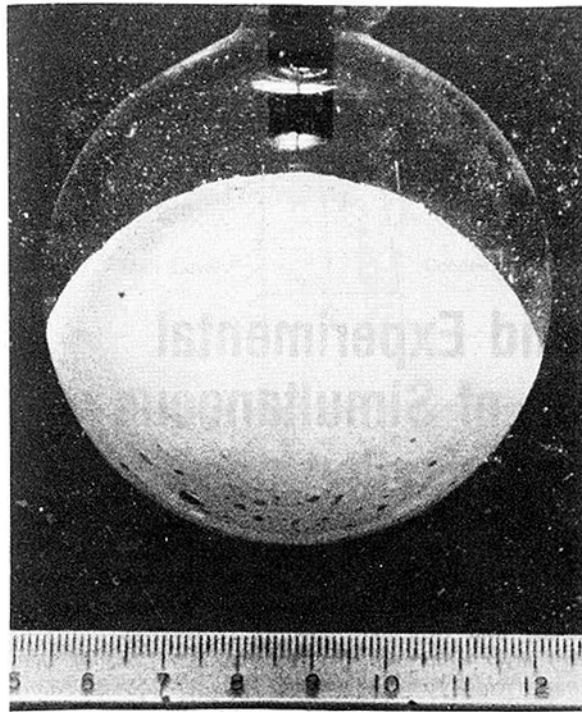
Fig. 4 Interface after 18.5 minutes of melting: $R = 3.272$ cm, $T_w = 34°$C. n-octadecane wax.

Fig. 5 Comparisions of interface position at $\theta = 0$ with experimental data for Ste = 0.05, 0.01, and $R = 3.272$ cm

bubbles working their way to the free surface of the wax. Tkachov [12] reported that trapped air bubbles had no measureable effect on the liquid to solid heat transfer between ice and water, and the same is assumed to apply here. The fact that the bubbles are deformed indicates that the interface is indeed very near to the glass wall and one is not viewing a parallax phenomenon.

A plot of $\eta^*(\theta = 0)$ for Ste = 0.05 and 0.10 is compared to experimental data in Fig. 5. It is apparent that the numerical results are reasonable, at least for small Stefan numbers. This is evident considering the fact that, upon melting, there is an expansion of the liquid at the interface, resulting in an interfacial velocity which may not be quite uniform due to the shape of the interface.

Practical application of the results are exemplified by Fig. 6, which shows the energy stored within a single sphere of 3.272 cm radius containing n-octadecane wax. The solid lines indicate the results obtained by considering conduction in the radial and polar directions, and convection in the polar direction. The dashed lines were generated assuming conduction as the only active mode. It is evident that convective effects can be neglected only at small Stefan numbers.

Acknowledgment

The authors are grateful for numerous enlightening discussions with Professor Herbert W. K. Beckmann. Mr. Bruce A. Ward of General Electric Company is also acknowledged for his providing the bulbs which replaced the clear glass sphere needed for the experimentation.

References

1 Riley, D. S., Smith, F. T., and Poots, G., "The Inward Solidification of Spheres and Circular Cylinders," *International Journal of Heat and Mass Transfer*, Vol. 17, 1974, pp. 1507–1516.

2 Tao, L. C., "Generalized Numerical Solutions of Freezing a Saturated Liquid in Cylinders and Spheres," *AIChE Journal*, Vol. 13, 1967, pp. 165–169.

3 Grimado, P. B., "Symmetric Melting and Solidification of Spheres," Ph.D. dissertation, Columbia University, 1968.

4 Nicholas, D., and Bayazitoglu, Y., "Heat Transfer and Melting Front Within a Horizontal Cylinder," *ASME Journal of Solar Energy Engineering*, Vol. 102, 1980, p. 229.
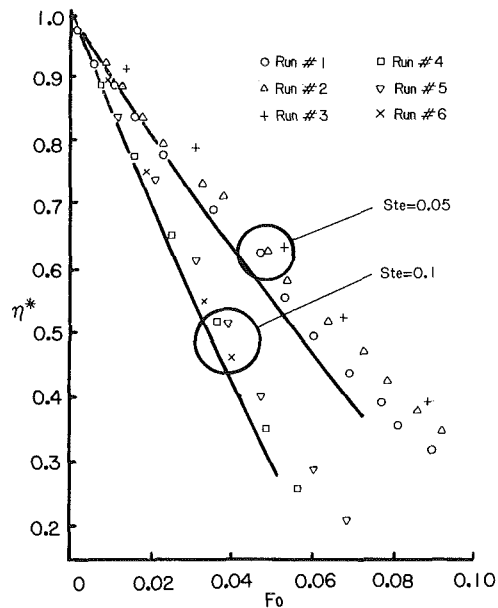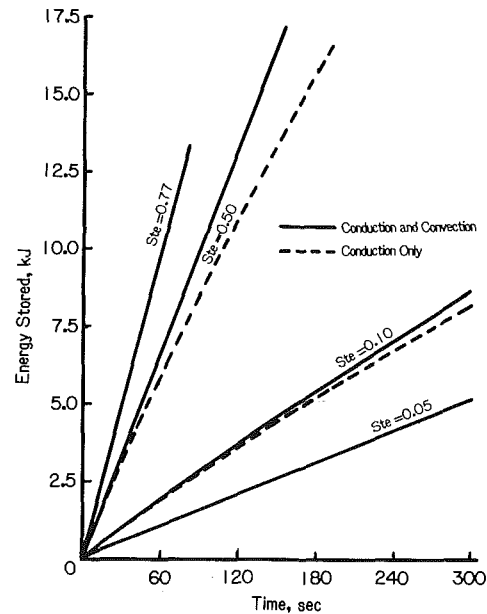
Fig. 6 Energy storage characteristics of n-octadecane wax with a 3.272 cm radius sphere

5 Patel, P. D., "Interface Conditions in Heat Conduction Problems with a Change of Phase," *AIAA Journal*, Vol. 6, 1968, p. 2454.

6 Ozisik, M. N., "A Note on the General Formulation of Phase Change Problem as a Heat Conduction Problem with a Moving Heat Source," ASME JOURNAL OF HEAT TRANSFER, Vol. 100, 1978, p. 370.

7 Moore, F. E., "Melting Within a Spherical Enclosure," M. S. thesis, Rice University, 1981.

8 Murray, W. D., and Landis, F., "Numerical and Machine Solutions of Transient Heat-Conduction Problems Involving Melting or Freezing," *ASME Trans.*, Vol. 81, 1959, pp. 106–112.

9 Douglas, J., "Alternating Direction Methods for Three Space Variables," *Numerische Mathematik*, Vol. 4, 1962, pp. 41–53.

10 Asgarpour, S., "Heat Transfer in Developing Laminar Pipe Flow with or without a Phase Change Material Around the Pipe," Ph.D. dissertation, Rice University, 1981.

11 Miele, A., and Iyer, R. R., "Modified Quasi-linearization Method for Solving Nonlinear, Two-Point Boundary-Value Problems," Aero-Astronautics Report No. 79, Rice University, 1970.

12 Tkachev, A. G., AEC-Tr.-3405, translated from a Publication of the State Power Press, Moscow, Leningrad, 1953.

K. Taghavi-Tafreshi
Student Mem. ASME

V. K. Dhir
Mem. ASME

School of Engineering and Applied Science,
University of California, Los Angeles,
Los Angeles, Calif. 90024

Analytical and Experimental Investigation of Simultaneous Melting-Condensation on a Vertical Wall[1]

Melting of a vertical wall as a result of condensation of saturated vapor is investigated both analytically and experimentally. Employing similarity transformations, full boundary layer equations governing laminar films of melt and condensate are solved numerically for high Prandtl number liquids. Numerical results for the melting and condensation heat transfer and for the melt-condensate interface temperature are obtained. Experiments are conducted by condensing saturated steam on vertical surfaces of slabs made of naphthalene, biphenyl and stearic acid. The data are found to compare well with the predictions. The analysis is extended to condensation on melting surfaces with shapes yielding variable gravity in the direction of flow.

Introduction

When a solid structure is exposed to saturated vapor of a liquid, and the melting temperature of the solid is less than the temperature of the vapor, simultaneous melting-condensation may occur. This phenomenon is of particular interest in nuclear reactor safety and has several applications in the chemical industry. In this work, condensation-driven melting of a vertical wall exposed to saturated vapor of another liquid is studied.

Laminar film condensation on an isothermal vertical wall in the absence of melting was first studied by Nusselt [1] in 1916. With the assumptions that the condensate film was without inertia and a linear temperature profile existed in the film, Nusselt obtained a simple relation for the local Nusselt number at the wall as

$$\text{Nu} = \left[\frac{(\rho_c - \rho_v) g_e h_{fg}' x^3}{4 \nu_c k_c \Delta T_c} \right]^{1/4} \tag{1}$$

where latent heat of vaporization, h_{fg}', corrected for sensible heat is defined as

$$h_{fg}' = h_{fg} + \frac{3}{8} c_{pc} \Delta T_c \tag{2}$$

Subsequently, Rohsenow [2] relaxed Nusselt's assumption of linear temperature profile and accounted for convection terms in the energy equation. The result was to increase the constant in equation (2) from 3/8 to 0.68. Finally, full boundary layer type momentum and energy equations for laminar film condensation on a vertical wall were solved by

Sparrow and Gregg [3]. Their study verified Nusselt's expression with Rohsenow's corrected h_{fg}' as long as $\text{Pr}_c > 1$ and the condensation parameter, $c_{pc} \Delta T_c / h_{fg} < 1$. Later, Dhir and Lienhard studied film condensation in variable gravity fields [4], and on body shapes that yield similar solutions to full boundary layer type equations [5].

Melting of vertical surfaces due to condensation of saturated vapor of the same material was first investigated by Tien and Yen [6]. They obtained similar solutions for the simultaneous condensation-melting, heat-transfer problem in the limit of high Prandtl numbers. Closed-form solutions using an integral technique were also obtained by Tien and Yen and were found to compare well with the similar solutions. Subsequently Epstein and Cho [7] analyzed laminar film condensation on a vertical melting surface when melt and condensate were different immiscible liquids. They formulated the problem using the similarity transformation pioneered by Sparrow and Gregg [3]. Making the assumption that the interface between the melt and condensate layers was flat and parallel to the wall[2], they solved the full boundary layer type equations by using the integral technique. In the integral technique, profiles for velocity and temperature were obtained by satisfying the boundary conditions. The results for the melting rate were presented in terms of six dimensionless parameters, $c_{pm} \Delta T_l / h_{sf}$, $c_{pc} \Delta T_l / h_{fg}$, Pr_m, Pr_c, $(\rho_m \mu_m / \rho_c \mu_c)^{1/2}$, and $(k_m / k_c) \cdot (\nu_c / \nu_m)^{1/2}$. Although the governing equations were set up in a general fashion, results for two-component systems were presented only for melt and condensate Prandtl numbers equal to 4.

Before the results of a two-component, two-layer model can

[2] This assumption was implicitly made in writing the boundary and interfacial conditions.

Copyright © 1982 by ASME

Fig. 1 Physical model for simultaneous melting-condensation on a vertical wall

be applied to a physical situation, it is necessary to assure that the temperature of the interface between the melt and condensate layers is lower than the boiling temperature of the melt and higher than the freezing temperature of the condensate. Epstein and Cho [7], however, neither report the interfacial temperature nor discuss the implications of it.

In this work condensation driven melting of a vertical wall is analyzed for the case when melt and condensate are two different substances, are immiscible and both have Prandtl numbers greater than unity. The governing equations are set up in a manner similar to that employed by Sparrow and Gregg [3] for high Prandtl number film condensation and by Tien and Yen for simultaneous melting-condensation of high Prandtl number one-component system. This approach is much simpler, gives more insight into the problem, and yields information on interface temperatures readily. The effect of existence of an additional layer on melting and condensation heat transfer coefficients is discussed. The heat-transfer results for simultaneous melting-condensation on vertical walls are extended to surfaces that yield variable gravity in the direction of flow. Experiments for simultaneous melting-condensation are conducted by exposing a vertical wall of the slabs made of naphthalene, biphenyl and stearic acid to the saturated steam. The predictions are compared with the data.

Analysis

The physical model used in this study is shown in Fig. 1. A vertical isothermal wall at its melting temperature is exposed to saturated vapor of another immiscible liquid. The melting temperature of the wall is less than the saturation temperature of the vapor such that latent heat of vaporization released

during condensation of vapor leads to melting of the solid. The vapor condenses in the form of a film, and both melt and condensate films flow downwards due to gravitational acceleration. The various assumptions made in analyzing the simultaneous melting-condensation are:

1 During the melting process, which is assumed to be steady, the wall is maintained at its melting temperature. The analysis will be valid for subcooled walls only as long as the rate of diffusion of heat into the solid is faster than the melting rate. For such a situation, the latent heat of fusion can simply be corrected for wall temperature being lower than the melting temperature as

$$h'_{sf} = h_{sf} + c_{ps}\Delta T_s \qquad (3)$$

2 The condensate spreads very easily on the melt layer such that filmwise rather than dropwise condensation occurs. This will be confirmed later with visual observation for the melt-condensate combinations studied in the experiments.

3 The transient times during which condensate and melt layers reach their steady-state thickness are much smaller than times of interest.

4 The leading edge region where surface tension between the two liquids could be important is small and is much less than the height of the melting surface.

5 Since, in the assumed two-film model, the melting rate will be a function of x, the initially vertical wall will start to deviate from its original shape. Thus, the present analysis is valid only for time periods in which the deviation of the melting surface from the original vertical shape is small.

6 The axes are fixed on the wall and move into the solid as the melting front progresses. However, the penetration speed is much smaller than the fluid velocities in the direction of the flow so that each new position of the axes represents a quasistatic state.

7 Prandtl numbers of both the melt and the condensate are much greater than unity. As will be discussed later, the solutions are valid even for Prandtl numbers of about unity as long as melt and condensate parameters are small. Thus, this is not a very restrictive assumption.

Evidently, assumptions 3 and 5 can be conflicting; but, the times at which a significant change in the shape occurs will generally be at least an order of magnitude longer than the times at which melt and condensate layers reach their steady-state thickness.

The steady-state boundary layer equations for either layer are:

$$u_x + v_y = 0 \qquad (4)$$

$$uu_x + vu_y = g_e(\rho - \rho_v)/\rho + \nu u_{yy} \qquad (5)$$

―――――― **Nomenclature** ――――――

A, B = constants used in Appendix, see equation (A8)

c = constant defined in equations (11) and (17)

c_p = specific heat at constant pressure

F = similarity function

g_e = constant gravity

g_{eff} = effective gravity defined in equation (A12)

$g(x)$ = variable gravity

h = heat transfer coefficient

$\bar{h}$ = average heat transfer coefficient,

$$\frac{1}{L}\int_0^L h\,dx$$

h_{fg} = latent heat of vaporization

h_{sf} = latent heat of fusion

h'_{fg} = h_{fg} corrected for sensible heat, $(h_{fg} + r_c c_{pc}\Delta T_c)$

k = thermal conductivity

L = height of the melting surface

Δm = change in the mass of the solid

Nu = Nusselt number, hx/k

Pr = Prandtl number

R_1, R_2, R_3 = constants defined in equations (25), (26) and (28)

r = correction parameter used in equation (47)

T = temperature

T_i = interface temperature

T_{melt} = melting temperature of solid

T_{sat} = saturation temperature of vapor

ΔT_c = temperature difference across condensate layer

ΔT_m = temperature difference across melt layer

T_s = temperature difference between interior of the solid and the melting surface

$$uT_x + vT_y = \alpha T_{yy} \qquad (6)$$

The following boundary and interface conditions are applicable to the layers

$$u_m = 0, \quad T_m = T_{\text{melt}} \qquad \text{at } y = 0 \qquad (7)$$

$$\left. \begin{array}{l} u_m = u_c, \quad v_m = v_c, \quad T_m = T_i, \quad T_c = T_i \\[4pt] \mu_m \partial u_m / \partial y = \mu_c \partial u_c / \partial y, \\[4pt] v_m / u_m = d\delta_m / dx \end{array} \right\} \quad \text{at } y = \delta_m \qquad (8)$$

$$\mu_c = \frac{\partial u_c}{\partial y} = \zeta_c u_c (v_c - u_c \tan\phi_c), T_c = T_{\text{sat}} \text{ at } y = \delta_m + \delta_c \qquad (9)$$

The last interface condition[3] in equation (8) results from the fact that a fluid particle at the interface should follow the interface path line since there is no mass transfer across the interface. The interfacial and boundary conditions listed above do not include the matching of the heat fluxes at the melt-condensate interface. This condition will be used later to determine the temperature of the interface.

Employing a procedure similar to that used in reference [3], a similarity parameter η_m for the melt layer is defined as

$$\eta_m = c_m y / x^{1/4}, \qquad (10)$$

where

$$c_m = \left[\frac{g_e c_{pm} (\rho_m - \rho_v)}{4 \nu_m k_m} \right]^{1/4} \qquad (11)$$

The similarity functions are defined as

$$F_m(\eta_m) = \psi_m / 4\alpha_m c_m x^{3/4}, \quad \theta_m(\eta_m) = (T - T_{\text{melt}})/(T_i - T_{\text{melt}}) \qquad (12)$$

In equation (12), ψ is the stream function. The melt velocities are related to the similarity function, F_m, as

$$u_m = 4\alpha_m c_m^2 x^{1/2} F_m', \quad v_m = \alpha_m c_m x^{-1/4} [\eta_m F_m' - 3F_m] \qquad (13)$$

Using transformations (10-13), the momentum and energy equations (5) and (6) become

$$F_m''' + \frac{1}{\text{Pr}_m} [3F_m'' F_m - 2F_m'^2] + 1 = 0 \qquad (14)$$

$$\theta_m'' + 3F_m \theta_m' = 0 \qquad (15)$$

Similarly the similarity variable and functions for the condensate layer are written as

---

[3] In the analysis of Epstein and Cho [7] the x-axis was aligned with the melt-condensate interface, and the effect of the curvature of the interface was ignored. Such an assumption is not necessary as is shown in the present analysis.

$$\eta_c = c_c (y - \delta_m) / x^{1/4}, \qquad (16)$$

where

$$c_c = \left[\frac{g_e c_{pc} (\rho_c - \rho_v)}{4 \nu_c k_c} \right]^{1/4} \qquad (17)$$

$$F_c(\eta_c) = \psi_c / 4\alpha_c c_c x^{3/4}, \quad \theta_c(\eta_c) = (T - T_i)/(T_{\text{sat}} - T_i) \qquad (18)$$

The condensate velocities in terms of the similarity function F_c are obtained as

$$u_c = 4\alpha_c c_c^2 x^{1/2} F_c', \quad v_c = \alpha_c c_c x^{-1/4} \left[\left(\eta_c + \frac{c_c}{c_m} \eta_{\delta m} \right) F_c' - 3F_c \right] \qquad (19)$$

Using transformations (16-19), governing equations for the condensate layer become

$$F_c''' + \frac{1}{\text{Pr}_c} [3F_c'' F_c - 2F_c'^2] + 1 = 0 \qquad (20)$$

$$\theta_c'' + 3F_c \theta_c' = 0 \qquad (21)$$

The boundary and interface conditions are transformed as

$$F_m' = 0, \quad \theta_m = 0 \qquad\qquad \text{at } \eta_m = 0 \qquad (22)$$

$$\left. \begin{array}{l} F_m' = R_1 F_c', \quad F_c = 0, \quad \theta_m = 1, \quad \theta_c = 0 \\[4pt] F_m'' = R_2 F_c'', \quad F_m = 0 \end{array} \right\} \begin{array}{l} \text{at } \eta_m = \eta_{\delta m} \\ \text{or} \\ \text{at } \eta_c = 0 \end{array} \qquad (23)$$

$$F_c'' + \frac{3}{\text{Pr}_c} F_c' F_c = 0, \theta_c = 1 \qquad \text{at } \eta_c = \eta_{\delta c} \qquad (24)$$

where

$$R_1 = \frac{\alpha_c c_c^2}{\alpha_m c_m^2} \qquad (25)$$

$$R_2 = \frac{\mu_c \alpha_c c_c^3}{\mu_m \alpha_m c_m^3} \qquad (26)$$

Besides the dimensionless parameters R_1 and R_2, which depend on the thermophysical properties of the melt and the condensate materials, there are three other parameters, namely T_i, $\eta_{\delta m}$, and $\eta_{\delta c}$, that are not known a priori. Three relations are needed to determine these unknowns. These relations are the matching of heat fluxes at the interface, and the energy balance for each layer. The matching of heat fluxes yields the interface temperature T_i as

$$\theta_m'(\eta_{\delta m}) = R_3 \frac{T_{\text{sat}} - T_i}{T_i - T_{\text{melt}}} \theta_c'(0) \qquad (27)$$

where

$$R_3 = \frac{k_c c_c}{k_m c_m} \qquad (28)$$

Nomenclature (cont.)

ΔT_t	=	total temperature difference across the layers	η	=	similarity variable defined in equations (10) and (16)
u	=	component of velocity in the x-direction	θ	=	dimensionless film temperature defined in equations (12) and (18)
v	=	component of velocity in the y-direction	μ	=	viscosity
W	=	width of the melting surface	ν	=	kinematic viscosity
x	=	coordinate in the direction of flow	ρ	=	density
			ϕ	=	angle, see Fig. 1
y	=	coordinate normal to the surface			
α	=	thermal diffusivity			
γ	=	coefficient in the expression for the Nusselt number			
δ	=	film thickness			

Superscripts

$*$ = parameter modified for the case of variable gravity, see Appendix

$'$ = derivative of the function with respect to its argument

0 = evaluated at inner edge of the layer

1 = evaluated at outer edge of the layer

$\bar{\ }$ = averaged over the height of the melting surface

Subscripts

c = condensate layer

m = melt layer

Nu = Nusselt's approximation

s = solid

t = total or overall

v = vapor

x = derivative with respect to x

y = derivative with respect to y

The energy balance at the melt front $y = 0$ or $\eta_m = 0$, is written as

$$k_m \frac{\partial T}{\partial y}\bigg|_{y=0} = \rho_m h_{sf} v_m|_{y=0} \qquad (29)$$

In terms of similarity variables, equation (29) transforms to

$$\frac{c_{pm}\Delta T_m}{h_{sf}} = -3\frac{F_m(0)}{\theta'_m(0)} \qquad (30)$$

The energy balance at the free surface, $y = \delta_m + \delta_c$ or $\eta_c = \eta_{\delta c}$, can be written as

$$(\cos \phi_c) k_c (\partial T/\partial y)_{y=\delta_m + \delta_c} =$$

$$-\rho_c h_{fg} [v_c \cos \phi_c - u_c \sin \phi_c]_{y=\delta_m + \delta_c} \qquad (31)$$

Noting that $\tan \phi_c = d(\delta_m + \delta_c)/dx$ ($v_c/u_c \ne \tan \phi_c$ since mass is being transferred across the free surface), and using the similarity variables equation (31) transforms to

$$\frac{c_{pc}\Delta T_c}{h_{fg}} = 3\frac{F_c(\eta_{\delta c})}{\theta'_c(\eta_{\delta c})} \qquad (32)$$

Method of Solution. Only liquids with relatively high Pr are considered here. This will include most of the ordinary liquids except liquid metals. For condensate films of such liquids it has been shown in reference [3] that neglect of the inertia terms in momentum equations imposes little or no error as long as $c_{pc}\Delta T_c/h_{fg}$ is not very large. Thus 1/Pr terms in momentum equations (14) and (20) are assumed to be small and are neglected. This allows direct integration of these equations. Upon integration and using the boundary and interface conditions for the melt and condensate momentum equations, the results are:

$$F_m(\eta_m) = -\frac{1}{6}\eta_m^3 + \frac{1}{2}[F''_m(\eta_{\delta m}) + \eta_{\delta m}]\eta_m^2$$

$$-\frac{1}{2}\eta_{\delta m}^2 F''_m(\eta_{\delta m}) - \frac{1}{3}\eta_{\delta m}^3 \qquad (33)$$

$$F_c(\eta_c) = -\frac{1}{6}\eta_c^3 + \frac{1}{2}\eta_{\delta c}\eta_c^2 + F'_c(0)\eta_c \qquad (34)$$

where

$$F''_m(\eta_{\delta m}) = R_2 \eta_{\delta c} \qquad (35)$$

$$F'_c(0) = \frac{\eta_{\delta m}^2}{R_1}\left(\frac{1}{2} + R_2\frac{\eta_{\delta c}}{\eta_{\delta m}}\right) \qquad (36)$$

Having the relations for F_m and F_c, energy equations can be integrated easily. Since energy equations (15) and (21) along with their boundary conditions have identical form, the subscripts m and c can be dropped to obtain a general result for θ' and θ in terms of F as

$$\theta'(\eta) = e^{-3\int_0^\eta Fd\eta} \bigg/ \int_0^{\eta_\delta} e^{-3\int_0^\eta Fd\eta} d\eta \qquad (37)$$

$$\theta(\eta) = \int_0^\eta e^{-3\int_0^\eta Fd\eta} d\eta \bigg/ \int_0^{\eta_\delta} e^{-3\int_0^\eta Fd\eta} d\eta \qquad (38)$$

Notice that out of the three dimensionless groups, R_1, R_2, and R_3, only the first two are needed to completely solve for functions F and θ. The third dimensionless group, R_3, is needed to determine the temperature of the interface between the two layers. The three dimensionless groups involve several of the same thermophysical property ratios. Thus it is more instructive to obtain the analytical results in terms of the basic property ratios rather than the above mentioned dimensionless groups. For vapor density much less than the melt or condensate density, the basic thermophysical property ratios needed to form the above dimensionless groups are: ρ_c/ρ_m,

c_{pc}/c_{pm}, k_c/k_m and μ_c/μ_m. This may seem somewhat disadvantageous, since the independent parameters have deliberately been increased by one. However, it will be shown in the section on results and discussion that the use of basic thermophysical property ratios for ordinary liquids does not impose any significant penalty.

It must be pointed out that if inertia terms were kept in the momentum equation, the Prandtl number of one of the liquids will be an additional parameter (the second Prandtl number is not needed since the ratio of the two Prandtl numbers is already included in the three dimensionless groups $R_1 = (Pr_m/Pr_c)^{1/2}$). This indeed was the case in the analysis of Epstein and Cho [7].

With three dimensionless groups, R_1, R_2, and R_3, or the four dimensionless property ratios given, and with certain assumed values of $\eta_{\delta m}$ and $\eta_{\delta c}$, the functions F_m and F_c can be obtained from equations (33) and (34). Knowing F_m and F_c, equation (38) can be integrated to obtain the temperature profiles in the melt and condensate layers. Thereafter, the values of $c_{pm}\Delta T_m/h_{sf}$ and $c_{pc}\Delta T_c/h_{fg}$ corresponding to the assumed values of $\eta_{\delta m}$ and $\eta_{\delta c}$ are obtained from equations (30) and (32). Finally, the interface temperature can be obtained by using equation (27).

Using superscripts 0 and 1 to define the heat fluxes at the inner and outer edge of the films, respectively, the local Nusselt numbers for the melt and condensate layers can be written as:

$$Nu_m{}^0 \equiv \frac{x}{\Delta T_m}\frac{\partial T_m}{\partial y}\bigg|_{y=0} = \gamma_m{}^0 \left[\frac{(\rho_m - \rho_v)g_e h_{sf}x^3}{4\nu_m k_m \Delta T_m}\right]^{1/4} \qquad (39)$$

$$Nu_c{}^1 \equiv \frac{x}{\Delta T_c}\frac{\partial T_c}{\partial y}\bigg|_{y=\delta_m + \delta_c} = \gamma_c{}^1 \left[\frac{(\rho_c - \rho_v)g_e h_{fg}x^3}{4\nu_c k_c \Delta T_c}\right]^{1/4} \qquad (40)$$

If only the melting rate of the wall is to be determined, local Nusselt number based on the total temperature difference between the saturated vapor and the melting surface can be defined as

$$Nu_t{}^0 \equiv \frac{x}{\Delta T_t}\frac{\partial T_m}{\partial y}\bigg|_{y=0} = \gamma_t{}^0 \left[\frac{(\rho_m - \rho_v)g_e h_{sf}x^3}{4\nu_m k_m \Delta T_t}\right]^{1/4} \qquad (41)$$

The Nusselt number based on the average heat-transfer coefficient can be simply written as

$$\overline{Nu}_t{}^0 = \frac{4}{3}\gamma_t{}^0 \left[\frac{(\rho_m - \rho_v)g_e h_{sf}x^3}{4\nu_m k_m \Delta T_t}\right]^{1/4} \qquad (42)$$

Equations similar to equations (41) and (42) could also be written for the condensate layer, if one was interested in determining the rate of condensation heat transfer based on the total temperature difference across the two layers. In the above equations $\gamma_m{}^0$, $\gamma_c{}^1$, and $\gamma_t{}^0$ are defined as

$$\gamma_m{}^0 = \left(\frac{c_{pm}\Delta T_m}{h_{sf}}\right)^{1/4}\theta'_m(0) \qquad (43)$$

$$\gamma_c{}^1 = \left(\frac{c_{pc}\Delta T_c}{h_{fg}}\right)^{1/4}\theta'_c(\eta_{\delta c}) \qquad (44)$$

$$\gamma_t{}^0 = \left(\frac{\Delta T_m}{\Delta T_t}\right)\left(\frac{c_{pm}\Delta T_t}{h_{sf}}\right)^{1/4}\theta'_m(0) \qquad (45)$$

Although there are several possible ways to define the Nusselt numbers in the present problem (3 heat fluxes × 3 temperature differences = 9), only three have been chosen. Nusselt numbers defined by equations (39) and (40) are developed for single layers (melt or condensate) and will best show the effect of one layer on the other. Equation (41) yields the heat flux at the melting surface which implicitly requires information from both layers.

Experimental Apparatus and Procedure

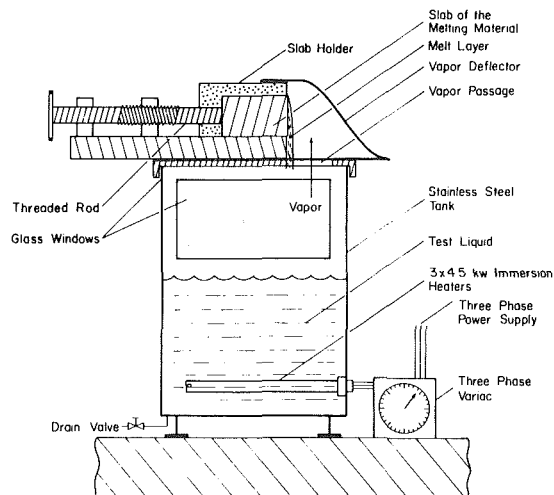Simultaneous melting-condensation experiments were
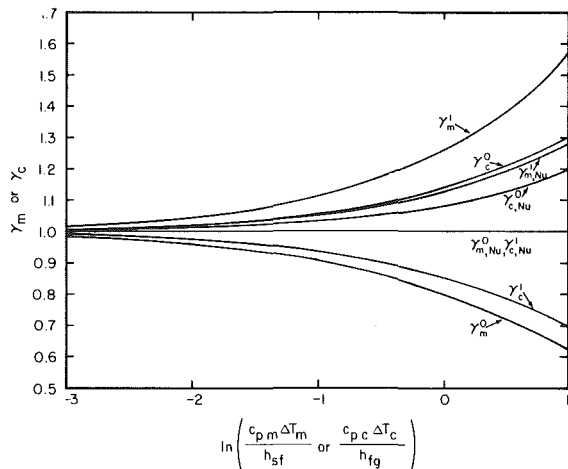
Fig. 2 Test apparatus

Fig. 3 Heat transfer results for high Prandtl number melting or condensation alone

conducted by condensing saturated steam at 1 atmosphere pressure on vertical surfaces made of slabs of naphthalene, biphenyl, and stearic acid. In each run, data for the change in mass of the slab was taken.

Experimental Apparatus. The apparatus used for performing experiments has essentially two parts—the vapor generating tank and the structure for holding the test slab. Figure 2 shows the apparatus with a sectioned view of the holding structure.

The vapor generating tank is made of 1.5-mm thick stainless steel sheet and has dimensions of 25 × 38 × 55 cm. Glass windows are provided in two joining sides of the tank to facilitate visual observations of the condensation-melting process during experiments. In addition, a valve is placed at the bottom of the tank for draining the contents of the tank. To boil the test liquid, three cylindrical heating elements each with a rating of 4.5 kW at 220 V are attached to one of the walls of the tank. The tank is covered with an aluminum lid which has a 15-cm dia opening in it. The melting surfaces are exposed to vapor exiting from the opening.

The structure fabricated to support the vertical surface has a wooden base and two side walls such that the test slab just fits in between these walls. A vapor deflector plate made out of aluminum sheet is placed over the vapor generating tank. The deflector plate directs the vapor towards the melting surface. As the melting progresses and the vertical surface starts to recede, the slab needs to be moved forward so that the melt drips off freely and the melting surface experiences

minimum end effects. This is accomplished by turning a 2.5-cm dia threaded rod held between two nuts rigidly fixed to the wooden base plate.

Experimental Procedure. Prior to each experiment a slab of the desired material was cast. To make these parallelepipeds or slabs, the test solid material was melted and poured into a wooden rectangular mold placed on an aluminum sheet wider than the width of the mold. The molten material was cooled from below by placing pieces of dry ice on the portions of the aluminum sheet extending out of the mold. This was necessary to initiate freezing at the bottom. A freezing front moving up from the bottom helped avoid cracking of the slab and yielded a very smooth external surface. After casting, the slab was placed in a bath of warm water. The temperature of the bath was maintained a few degrees below the melting temperature of the solid. This was done to make sure that almost all the energy liberated during condensation was utilized only in melting of the solid. Meantime the heaters in the tank were switched on to boil the test liquid. The liquid in the vapor generator was kept in a boiling state for about 10 minutes to ensure that neither the liquid nor the tank contained any air. The power to the heaters was adjusted so that the vapor generation rate was several times the rate needed for steady-state condensation on the melting surface. High vapor volume flow rate was used to assure that melting surface did not starve because of lack of vapor. However, the provided flow area was large enough so that vapor velocity over the melting surface was rather small.

Experiments were conducted by positioning the slab in the holder, which was subsequently placed over the lid of the vapor generator. The vapor was deflected towards the solid leading to melting of the surface exposed to vapor. As the melting progressed and the surface receded, the threaded rods was turned fast enough ($\simeq 0.1$ mm/s) to keep the trailing edge of the melting surface at the edge of the wooden base plate. This was important since otherwise the melt would not flow down freely. The experiments were terminated when the end effects or the changes in the shape of the melting surface were seen to begin to influence the melting rate.

After each experiment, the test surface was visually examined. Sometimes the visual observation showed uneven melting near the edges. To exclude the edge effects, the pits near the edges were filled with clay. Knowing the volume of the clay, the mass of the test solid needed to fill the pits in the surface was determined. This mass was then subtracted from the total mass lost by the slab during a particular experiment to determine the net melted mass, Δm, of the solid. Thereafter, the average heat-transfer coefficient $\bar{h}$ was determined as

$$\bar{h} = \frac{\Delta m h_{sf}}{\Delta T_t WL\Delta t} \tag{46}$$

In equation (46), W and L are the width and height of the test surface, and Δt is the duration of the experiment. The overall uncertainty in evaluating the average heat-transfer coefficient from equation (46) is calculated to be ± 11 percent [8].

Results and Discussion

Equations (37) and (38) were integrated numerically using a finite difference scheme for certain values of the thermophysical property ratios and thickness of the melt and condensate layers. The values of θ' either at the inner or the outer edge of the film were used to determine values of numerical constant, γ, in the expression for the Nusselt number. Although the values of the numerical constant, γ, are obtained for a vertical wall with a constant gravitational acceleration in the direction of flow, it is shown in the Appendix that these values of γ are valid even when the

gravitational acceleration varies in the direction of flow. Before going on to simultaneous melting-condensation, it is appropriate to treat the limiting cases of condensation alone $(c_{pm}\Delta T_m/h_{sf} = 0)$ and melting along $(c_{pc}\Delta T_c/h_{fg} = 0)$. Epstein and Cho [7] also analyzed the limiting cases, yet they did not elaborate on the finer differences between melting and condensation.

Condensation or Melting Alone. The values of the numerical constants γ_c and γ_m obtained from the present analysis for melting or condensation alone and those obtained by carrying out an analysis similar to that of Nusselt [1] are plotted in Fig. 3 as a function of $c_{pc}\Delta T_c/h_{fg}$ or $c_{pm}\Delta T_m/h_{sf}$. The plotted values are for heat flux at the wall and at the free surface (superscripts 0 and 1 correspond to wall and free surface, respectively). For very small values of condensation parameter, $c_{pc}\Delta T_c/h_{fg}$, or melt parameter, $c_{pm}\Delta T_m/h_{fg}$, Nusselt's approximation is valid and little difference exists between the values of γ_m and γ_c for melting or condensation. However, for large values of $c_{pc}\Delta T_c/h_{fg}$ or $c_{pm}\Delta T_m/h_{fg}$, the constants γ_c and γ_m start to differ and a distinction must also be made as to whether the heat fluxes used in defining Nusselt numbers are evaluated at the wall or at the free surface.

In the past, for high Prandtl number condensation it has been customary to include the dependence of Nusselt number on condensation parameter in the latent heat of vaporization corrected for sensible heat as [2, 3]

$$h'_{fg} = h_{fg}\left(1 + r_c\frac{c_{pc}\Delta T_c}{h_{fg}}\right) \quad (47)$$

where r_c generally varies with $c_{pc}\Delta T_c/h_{fg}$ [3]. Comparing equations (1) and (40) γ_c and r_c are related through

$$\gamma_c = \left(1 + r_c\frac{c_{pc}\Delta T_c}{h_{fg}}\right)^{1/4} \quad (48)$$

While it is always possible to replace γ_c by r_c using equation (48), physically r_c should always be positive and should lie between 0 and 1 since no film could be cooled below wall temperature during condensation or could be heated beyond free surface temperature during melting.

From Fig. 3, it is seen that the value of r_c will be positive if condensation heat flux is evaluated at the wall but will be negative if the heat flux is evaluated at the outer edge of the condensate layer. Evidently it will not be appropriate to use negative value of r_c in equation (47). Similarly the constant, γ_m^1, for melting heat transfer at the free surface of the melt layer corresponds to values of r_m^1 (in an equation similar to equation (47)) that are greater than 1. Use of such values to correct latent heat of fusion for sensible heat will be unrealistic.

The reason for this abnormal behavior of the constant, r, is that the constant accounts for both sensible heat carried away by the condensate or melt and the crossflow of the condensate or melt into the film. The role of the crossflow is clearly seen when the values of r_c^0 and r_m^1 are compared in the limit as $c_{pc}\Delta T_c/h_{fg}$ or $c_{pm}\Delta T/h_{sf} \rightarrow 0$. In Fig. 3, the limiting value of γ_c^0 corresponds to the well known constant $r_c^0 = 0.68$, while the limiting value of γ_m^1 is 1.3. This difference in the values of r_c^0 and r_m^1 results from the fact that in condensation the condensate enters the film at the free surface where velocity in the direction of flow is maximum. In melting, the melt enters the film at the wall where velocity in the direction of flow is zero. To avoid these anomalies arising out of use of r as a correction parameter to latent heat of vaporization or fusion, and possible dependence of r on $c_{pc}\Delta T_c/h_{fg}$ or $c_{pm}\Delta T_m/h_{sf}$, it is proposed that a single constant, γ, be used to account for corrections due to sensible heat and crossflow.

Simultaneous Melting-Condensation. Before studying the heat-transfer results of the present investigations for
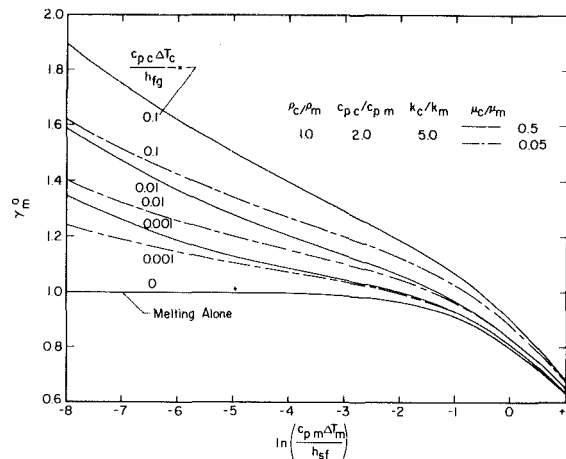

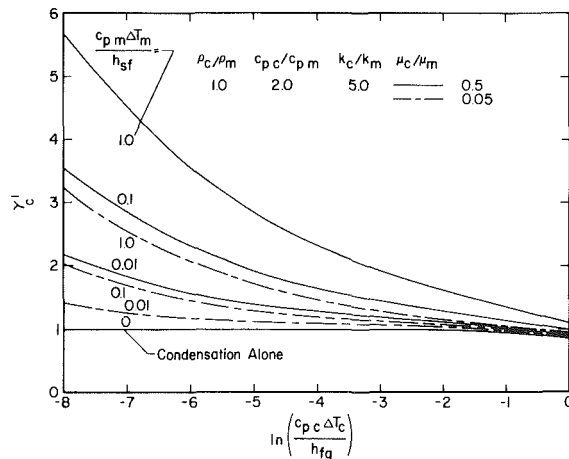**Fig. 4 Dependence of the coefficient γ_m^0 on melt and condensate parameters**

Fig. 5 Dependence of the coefficient γ_c^1 on condensate and melt parameters

simultaneous melting-condensation of two components, a comparison of the present results was made with those of Tien and Yen [6] and Epstein and Cho [7] for a one-component system and Epstein and Cho [7] for a two-component system. It was found that the values of γ_t^0 obtained form the present analysis matched exactly with the similarity solution of Tien and Yen. This was expected since for one-component systems the approach used in this work reduces to that of reference [6]. The integral solution of Epstein and Cho tended to predict a slightly higher rate of heat transfer at the melting surface. For the two-component system studied in reference [7], the heat-transfer results of Epstein and Cho tended to be as much as 20 percent lower than those obtained from the present analysis. Slight underprediction compared to the present high Prandtl number results is expected since the Prandtl numbers of the two components considered in [7] were 4. However, the more probable cause of the difference in the two results is believed to be the use in [7] of specific profiles for temperature and velocity in the melt and condensate films, since the results of exact solutions obtained by Taghavi-Tafreshi [8] for the two-component case ($Pr_m = Pr_c = 4$) studied by Epstein and Cho differ by less than 1 percent from the present high Prandtl number results.

The Nusselt numbers defined in equations (39), (40), and (41) contain the individual thermophysical properties of the melt and the condensate. The ratio of the thermophysical properties of the melt and condensate along with the parameters $c_{pm}\Delta T_t/h_{sf}$ and $c_{pc}\Delta T/h_{fg}$ determine the magnitude of the interaction of one layer on the other. A survey of the thermophysical properties of ordinary high

Table 1 Percentage change in the values of γ_m^0 and γ_c^1 with variations in the ratios of densities, specific heats, and thermal conductivities of melt and condensate from those for the base case[5]

$\dfrac{c_{pc}\Delta T_c}{h_{fg}}$	$\ln\left(\dfrac{c_{pm}\Delta T_m}{h_{sf}}\right)$	Percentage change in γ_m^0 from base value						Percentage change in γ_c^1 from base value					
		ρ_c/ρ_m		c_{pc}/c_{pm}		k_c/k_m		ρ_c/ρ_m		c_{cp}/c_{pm}		k_c/k_m	
		1/2	2	1	5	1	10	1/2	1	1	5	1	10
0.001	+1	−1	+1	<+1	<−1	<−1	<+1	<−1	+1	−15	+25	+48	−15
	−3	−2	+2	+2	−2	−3	+2	−2	+3	−12	+21	+40	−12
	−8	−6	+7	+5	−6	−10	+5	−3	+3	−4	+7	+15	−4
0.01	+1	−2	+2	+1	−1	−2	+1	−1	+2	−14	+23	+45	−14
	−3	−3	+4	+4	−4	−6	+4	−3	+4	−9	+15	+30	−9
	−8	−8	+9	+5	−6	−11	−5	−2	+2	−2	+3	+7	−2
0.1	+1	−3	+3	+3	−2	−4	+3	−3	+4	−11	+18	+36	−11
	−3	−6	+7	+5	−5	−9	+5	−3	+4	−37	+8	+17	−5
	−8	−8	+9	+5	−7	+11	+5	−2	+2	−2	+4	+7	−2

[5]In the case $\rho_c/\rho_m = 1.0$, $c_{pc}/c_{pm} = 2.0$, $k_c/k_m = 5.0$, $\mu_c/\mu_m = 0.5$
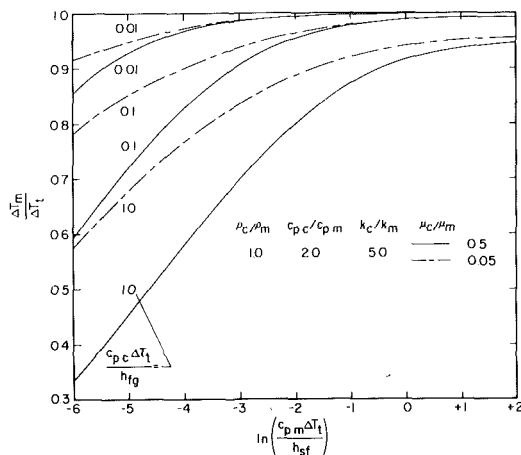

Fig. 6 Dependence of temperature drop across melt layer on $c_{pm}\,\Delta T_t/h_{sf}$ for different values of $c_{pc}\,\Delta T_t/h_{fg}$ and μ_c/μ_m

Fig. 7 Dependence of temperature drop across melt layer on $c_{pm}\,\Delta T_t/h_{sf}$ for different values of $c_{pc}\,\Delta T_t/h_{fg}$ and k_c/k_m

Prandtl number liquids indicates that the ratio of densities and specific heats do not vary significantly. Preliminary numerical computation also showed that the values of γ were less sensitive to ratios of densities and specific heats. Thus, while plotting the numerical results, the ratio of densities and specific heats of condensate and melt were kept fixed at 1 and 2, respectively. The ratio of either viscosities or thermal conductivities or both were varied depending on the magnitude of change in γ with these variations. To enhance the usefulness of the present study to a large variety of liquids, the deviations in γ caused by changes in the base parameters (parameters kept fixed while plotting the results) are also tabulated. This approach avoids unnecessary details and computations without compromising the physical insight to the problem.

The numerical constant γ_m^0 of the Nusselt number for the melt layer is plotted in Fig. 4 as a function of the melt layer parameter $c_{pm}\Delta T_m/h_{sf}$ for different values of $c_{pc}\Delta T_c/h_{fg}$. It should be mentioned that the temperature differences used in Fig. 4 are those across the melt and condensate layers and not the total temperature difference between the vapor and the melting wall. The evaluation of these temperature differences requires a priori knowledge of the interface temperature. It is noted that reduction in $c_{pm}\Delta T_m/h_{sf}$ or thinning of the melt layer improves wall heat transfer. The presence of a condensate layer also enhances the rate of heat transfer to the wall. This enhancement in melting heat transfer is caused by the traction of the condensate film on the melt layer. The thicker and more viscous the condensate layer, the larger is the traction, hence higher is the melting heat transfer. The effect of thickness and viscosity of the condensate layer is
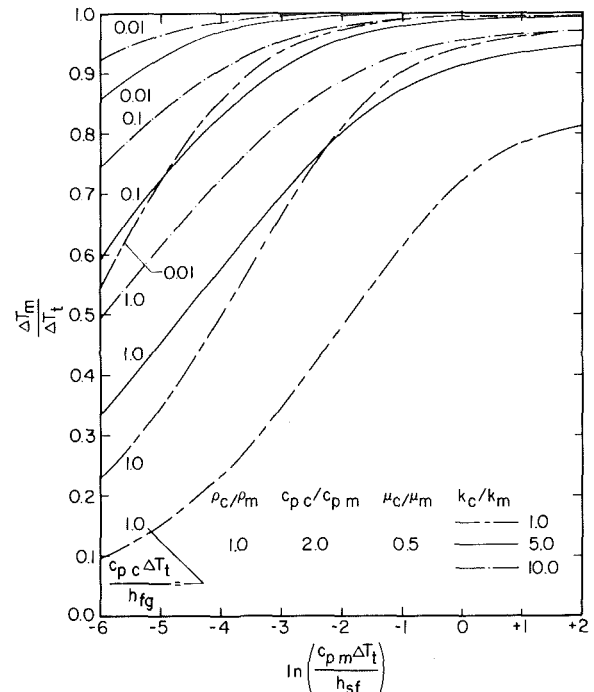
more pronounced as the melt layer becomes thin. It is interesting to note that as $h_{fg} \rightarrow \infty$ the results for simultaneous melting-condensation tend to approach those for simple melting.

Figure 5 shows the dependence of $c_{pc}\Delta T_c/h_{fg}$ on γ_c^1, the numerical constant for the Nusselt number based on the heat flux at the free surface of the condensate layer. The effect of melt layer on condensate layer is similar to the effect of condensate layer on melt layer seen in Fig. 4. Presence of melt layer enhances condensation heat transfer. The thicker the melt layer, the higher is the condensation heat transfer. Increased melt viscosity results in lower velocity at the interface between melt and condensate layers and in turn reduced condensation het transfer. In the limit as $h_{sf} \rightarrow \infty$, or the melt layer thickness goes to zero, the results of simultaneous melting-condensation process go to those for simple condensation.

The deviations in the values of γ_m^0 and γ_c^1, with change in the ratio of densities, specific heats, and thermal conductivities of condensate and melt from the base values plotted in Figs. 4 and 5, are listed in Table 1. The magnitude of the deviations in the base values is noted to depend on the

Table 2 Percentage change in the values of $\Delta T_m/\Delta T_t$ and γ_t^0 with variations in the ratios of densities and specific heats from those for the base case[6]

$\dfrac{c_{pc}\Delta T_t}{h_{fg}}$	$\ln\left(\dfrac{c_{pm}\Delta T_t}{h_{sf}}\right)$	Percentage change in $\Delta T_m/\Delta T_t$ from base value				Percentage change in γ_t^0 from base value			
		ρ_c/ρ_m		c_{pc}/c_{pm}		ρ_c/ρ_m		c_{pc}/c_{pm}	
		1/2	2	1	5	1/2	2	1	5
0.01	+2	<-1	$<+1$	<-1	$<+1$	<-1	$<+1$	$<+1$	<-1
	-2	-1	$<+1$	-1	$<+1$	<-1	$<+1$	$+1$	<-1
	-6	-10	$+7$	-8	$+8$	-9	$+7$	$+1$	-3
0.1	+2	-1	$<+1$	-1	$<+1$	<-1	$<+1$	$<+1$	<-1
	-2	-4	$+2$	-3	$+3$	-3	$+2$	$+2$	-2
	-6	-18	$+17$	-16	$+20$	-18	$+19$	-5	$+3$
1.0	+2	-4	$+3$	-4	$+3$	-1	$+2$	$+3$	-1
	-2	-11	$+9$	-9	$+10$	-11	$+9$	$<+1$	-2
	-6	-23	$+25$	-22	$+33$	-23	$+28$	-9	$+11$

[6]In the base case $\rho_c/\rho_m = 1.0$, $c_{pc}/c_{pm} = 2.0$, $k_c/k_m = 5.0$, $\mu_c/\mu_m = 0.5$
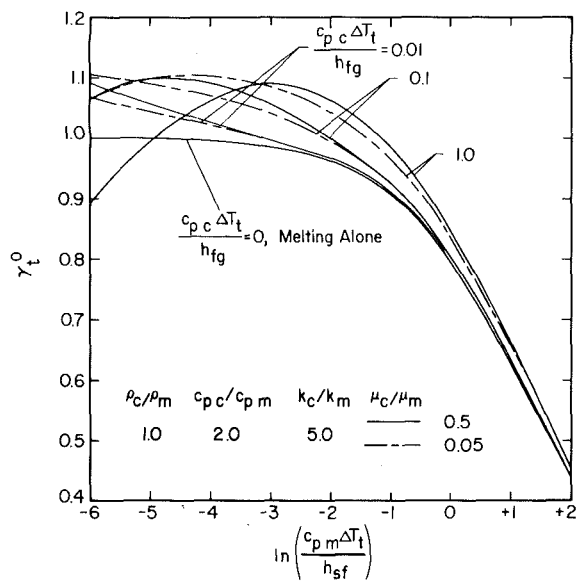

Fig. 8 Dependence of the coefficient γ_t^0 on melt and condensate parameters for different values of μ_c/μ_m
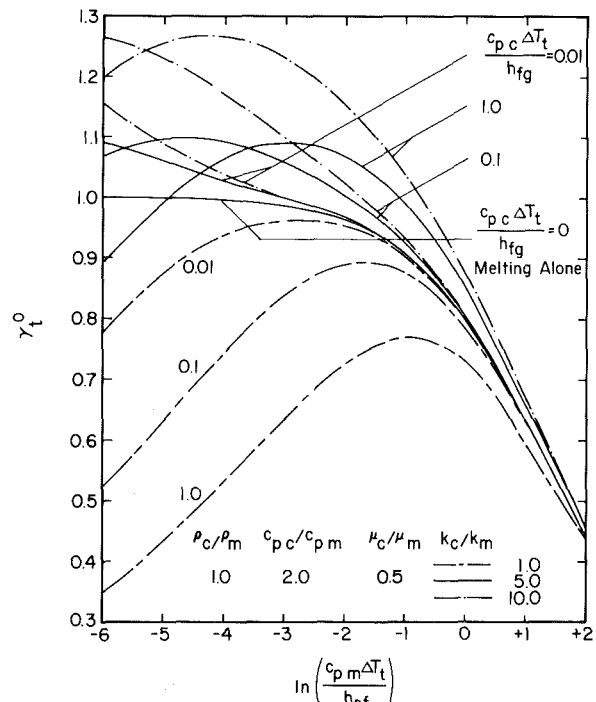

Fig. 9 Dependence of the coefficient γ_t^0 on melt and condensate parameters for different values of k_c/k_m

relative values of the melt and condensate layer parameters $c_{pm}\Delta T_m/h_{sf}$ and $c_{pc}\Delta T_c/h_{fg}$. For very thin condensate and relatively thicker melt layers the effect of ratio of specific heats and thermal conductivites on γ_c^1 is more pronounced. With fixed $c_{pc}\Delta T_c/h_{fg}$ and $c_{pm}\Delta T_m/h_{sf}$, a reduction in specific heat of the melt means a corresponding increase in the temperature difference across the melt layer. Increased temperature difference across the melt layer results in higher heat fluxes at the melt-condensate interface and at the free surface. Hence it yields a higher value of γ_c^1. Similarly increased thermal conductivity of the melt results in a higher value of γ_c^1. The variation in the density ratio has a relatively small effect on γ_c^1 and γ_m^0, though increased condensate density increases both γ_c^1 and γ_m^0. It should be mentioned again that the deviations in the values of γ_m^0 and γ_c^1 listed in Table 1 reflect the interaction of the two layers, as the individual properties of the melt and condensate are already included in the Nusselt numbers for the melt and condensate layers.

The ratio of the temperature difference across the melt layer to the total temperature difference across the melt and condensate layers is plotted in Fig. 6 as a function of $c_{pm}\Delta T_t/h_{sf}$. In Fig. 6, the ratio of condensate to melt density, specific heat, and thermal conductivity is kept the same while a tenfold variation in the ratio of viscosities is considered. The temperature difference across the melt layer increases with

$c_{pm}\Delta T_t/h_{sf}$, or thickness of the melt layer. The effect of the presence of condensate layer is to decrease the temperature difference across the melt layer. The thicker the condensate layer the smaller is the temperature difference across the melt layer. For very small values of $c_{pm}\Delta T_t/h_{sf}$, or very thin melt layers, the magnitude of the ratio of viscosities has a significant effect on the temperature difference across the melt layer. Increased viscosity of the melt results in a larger temperature difference across the melt layer.

Figure 7 shows the effect of variation of ratio of thermal conductivities on the temperature difference across the melt layer. For very low values of $c_{pm}\Delta T_t/h_{sf}$ and relatively larger values of $c_{pc}\Delta T_t/h_{fg}$, the temperature difference across the melt layer is very sensitive to the magnitude of the ratio of thermal conductivities. The larger the thermal conductivity of the melt, the smaller is the temperature difference across the melt layer. It is interesting to note that as the melt layer thickness becomes very large, the temperature difference across the melt layer reaches an asymptotic value, which is less than the total temperature difference across the two layers. This suggests that the condensate layer resistance does not vanish as the melt layer becomes very thick.

Table 3 Comparison of the predicted and observed values of the coefficient γ_t^0

Melt/condensate	Surface length L [m]	Duration of experiment t [sec]	Prediction $\Delta T_m/\Delta T_t$	Prediction γ_t^0	Data γ_t^0	% Error
Naphthalene/water	0.080	112.8			0.92	− 3
	0.080	93.6	0.990	0.95	0.78	−17
	0.078	99.5			0.88	− 7
Biphenyl/water	0.085	66.0			0.92	+ 4
	0.079	79.2	0.991	0.89	1.08	+22
Stearic acid/water	0.077	63.6			1.08	+15
	0.069	88.8	0.985	0.92	0.92	< − 1
	0.087	94.5			0.91	− 1
	0.087	75.8			1.11	+20

The temperature difference across the melt layer is needed to assure that in a given application, the temperature of the interface will be below the boiling temperature of the melt and above the freezing temperature of the condensate. For example, consider condensation of steam at 1 atmosphere pressure on a vertical wall of frozen methanol. From Figs. 6 and 7, the interface temperature for this combination, is evaluated to be 90°C. This temperature is about 15°C above the boiling temperature of methanol. Similarly if naphthalene vapor at 1 atmosphere pressure condenses on ice, the interface temperature will be 70°C. This temperature is about 10°C below the freezing temperature of naphthalene. Formation of vapor bubbles or crust at the interface will invalidate the analysis such as presented in this work.

The constant γ_t^0 of the melt layer Nusselt number based on the total temperature difference is plotted in Figs. 8 and 9. In these figures, the ratios of viscosities and thermal conductivities are varied parametrically while ratios of other thermophysical properties are kept constant. From Fig. 8, it is seen that in the range of parameters considered the variations in the ratio of viscosity does not have a significant effect on γ_t^0. It is interesting to note from Fig. 8 that depending on the magnitude of $c_{pc}\Delta T_t/h_{fg}$ and $c_{pm}\Delta T_t/h_{sf}$, values of γ_t^0 greater or smaller than simple melting can occur. Higher values imply an improvement in the melting heat transfer due to traction of the condensate layer. However, as the melt layer becomes thin $(c_{pm}\Delta T_t/h_{sf} \rightarrow 0)$, the additional thermal resistance of the condensate layer dominates any improvement in heat transfer and values of γ_t^0 start to drop below those for melting alone. For a given value of $c_{pc}\Delta T_t/h_{fg}$ and the base parameters, maximum value of γ_t^0 occurs at a unique values of $c_{pm}\Delta T_t/h_{sf}$.

Figure 9 shows the effect of variation of ratio of thermal conductivities on γ_t^0. In comparison to Fig. 8, the ratio of thermal conductivities is seen to have a much stronger influence than the ratio of viscosities. For relatively thicker melt layers, depending on the magnitude of the ratio of thermal conductivities, values of γ_t^0 higher or lower than melting alone can occur. Higher thermal conductivity of melt yields lower values of γ_t^0. This behavior is similar to the behavior of the temperature difference across the melt layer. For thinner melt layers the values of γ_t^0 depends both on the ratio of thermal conductivity and thickness of the condensate layer. The maximum value of γ_t^0 and the value of $c_{pm}\Delta T_t/h_{fg}$ at which this maxima occurs depends both on the ratio of thermal conductivities and $c_{pc}\Delta T_t/h_{fg}$. Thinner layers of larger thermal conductivity condensate yield higher values of γ_t^0. The deviations in the values of γ_t^0, due to changes in the base values of ρ_c/ρ_m and c_{pc}/c_{pm} used in Figs. 5–8, are given in Table 2. Table 2 shows that for the large range of values of $c_{pm}\Delta T_t/h_{sf}$ and $c_{pc}\Delta T_t/h_{fg}$ considered here, the changes in γ_t^0 are limited to about ±30 percent. For moderate values of the melt and condensate layer parameters, the deviation in γ_t^0

are only a few percent of the values corresponding to the base parameters.

The deviations in the values of γ_m^0, γ_c^1, $\Delta T_m/\Delta T_t$ and γ_t^0, listed in Tables 1 and 2 show that the condensate to melt density ratio has a minimal effect on the results. This suggests that present results could have easily been obtained in terms of three property ratios excluding density ratio. Such a conclusion could not be drawn had the analysis been carried out in terms of parameters R_1, R_2 and R_3.

Several experiments were conducted by condensing saturated steam at 1 atmosphere pressure on one of the vertical faces of slabs made of naphthalene, biphenyl, and stearic acid. The thermophysical properties of these materials are listed in reference [8]. The vertical surfaces were generally 8 cm high and 12 cm wide. The experiments lasted between 1 and 2 minutes. The duration of the experiments was chosen such that the end effects remained small and no appreciable change in the shape of the surface occurred. This time period, however, was much longer than the time needed for the melt and condensate layers to attain their steady states. At present no study on transient melting-condensation of two components exists in the literature.

The transient times needed by the melting and condensation processes to reach steady state have been studied by Contreras and Thorsen [9] for a one-component system. For steam condensing on a 8 cm high slab of ice, their analysis [9] yields the steady-state time to be less than 1 s. The approximate times needed by the melt and condensate layers to reach steady state were also calculated by using the analysis of Sparrow and Siegel [10] for transient condensation on a vertical wall. For the melt and condensate combinations used in the present experiments, the longest times for the layers to reach steady state are found to be less than 6 s.

Visual observations of the condensation-melting process showed that vapor condensed in the form of a nearly continuous film and both melt and condensate films flowed downwards due to gravitational acceleration. Water film was seen to be free of any ripples. The maximum Reynolds number for the melt and the condensate films is calculated to be less than 60, thus both films are expected to be laminar. On post-experiment examination, the vertical surface was found to be generally flat with upper horizontal edge slightly contoured and some erosion near the vertical edges. The contouring of the upper horizontal edge was caused by faster melting at the leading edge while erosion at the vertical edges resulted either from the nature of the local vapor flow pattern or the heat transfer from the holder to the faces of the slab touching the holder.

The experimental values of γ_t^0, determined by comparing the average heat-transfer coefficients given by equations (42) and (46), are listed in Table 3. In this table the values of γ_t^0 obtained from the high Prandtl number analysis are included. The values of γ_t^0 were also calculated [8] by solving the full

equations (14) and (20) using the exact Prandtl numbers of the melt and the condensate. These values were found to be within 1/2 percent of the limiting results listed in Table 3. It is noted that the observed values of γ_t^0 lie within 22 percent of the predictions. This agreement seems quite satisfactory since uncertainty in the experimental measurements of $\bar{h}$ can be as high as ±11 percent. The uncertainty in the thermophysical properties of naphthalene, biphenyl, and stearic acid can cause as much as ±8 percent error in the experimental values of γ^0_t. Although the duration of the experiments was much longer than the steady-state times and efforts were made to limit the uncertainties due to end effects, yet the contributions of these sources may have also been reflected in the experimental results.

Conclusions

1 Similar solutions to full boundary layer equations governing simultaneous melting-condensation of a two-component system can be obtained.

2 The analytical results of simultaneous melting-condensation on vertical walls show that presence of melt or condensate layer tends to enhance the rate of heat transfer associated with either of the layers. This enhancement in heat transfer is caused by traction of one layer on another.

3 For a fixed condensate parameter, $c_{pc}\Delta T_t/h_{fg}$, the temperature drop across the melt layer increases with increase in melt parameter $c_{pm}\Delta T_t/h_{sf}$ and with increase in ratios of viscosities and thermal conductivities of condensate and melt.

4 The ratio of densities, specific heats, viscosities, and thermal conductivities of the condensate and melt layer are found to affect the values of γ_m^0, γ_c^1, $\Delta T_m/\Delta T_t$ and γ_t^0. In the range of parameters considered, the ratio of densities is found to have the least affect.

5 The experiments conducted by condensing steam at 1 atmosphere pressure on vertical surfaces of slabs made of naphthalene, biphenyl, and stearic acid show that observed melting rates compare within ±20 percent of the predicted values.

6 The vertical wall high Prandtl number results can be directly applied to surfaces having variable gravity in the direction of flow when g_e is replaced by g_{eff}.

References

1 Nusselt, W., "Die Oberflachenkondensation des Wasserdampfes," *Zeitschrift des Vereines deutcher Ingenieure*, Vol. 60, 1916, pp. 541–569.

2 Rohsenow, W. M., "Heat Transfer and Temperature Distribution in Laminar Film Condensation," ASME JOURNAL OF HEAT TRANSFER, Vol. 78, 1956, pp. 1645–1648.

3 Sparrow, E. M. and Gregg, J. L., "A Boundary-Layer Treatment of Laminar-Film Condensation," ASME JOURNAL OF HEAT TRANSFER, Vol. 81, 1959, pp. 13–18.

4 Dhir, V. K., and Lienhard, J. H., "Laminar Film Condensation on Plane and Axisymmetric Bodies in Nonuniform Gravity," ASME JOURNAL OF HEAT TRANSFER, Vol. 91, 1971, pp. 97–100.

5 Dhir, V. K., and Lienhard, J. H., "Similar Solutions for Film Condensation with Variable Gravity or Body Shape," ASME JOURNAL OF HEAT TRANSFER, Vol. 95, 1973, pp. 483–486.

6 Tien, C. L. and Yen, Y. C., "Condensation-Melting Heat Transfer," *Chem. Engr. Prog. Symp. Ser.*, Vol. 67, No. 113, 1971, pp. 1–9.

7 Epstein, M. and Cho, D. H., "Laminar Film Condensation on a Vertical Melting Surface," ASME JOURNAL OF HEAT TRANSFER, Vol. 98, 1976, pp. 108–113.

8 Taghavi-Tafreshi, K., "Condensation of Saturated Vapor on Melting Surfaces," Ph.D. dissertation, UCLA, 1982.

9 Contreras, W. and Thorsen, R. S., "Transient Melting of a Solid Heated by a Condensing Saturated Vapor—Cast 1. Negligible Interface Curvature," ASME JOURNAL OF HEAT TRANSFER, Vol. 97, 1975, pp. 570–757.

10 Sparrow, E. M. and Siegel, R., "Transient Film Condensation," ASME JOURNAL OF HEAT TRANSFER, Vol. 81, 1959, pp. 120–121.

APPENDIX

Extension of Vertical Wall Analysis to Variable Gravity Surfaces

The analysis for simultaneous melting-condensation on a vertical wall can easily be extended to surfaces on which the gravitational acceleration varies in the direction of flow. The governing equations and boundary conditions for the melt and condensate are the same except that now the gravitational acceleration, g_e, is replaced by $g(x)$. Using an approach resembling that used by Dhir and Lienhard [5] to study laminar film condensation on surfaces admitting similar solution, the similarity parameters for melt and condensate layers are written as

$$\eta_m^* = c_m y / x^{*\,1/4} \tag{A1}$$

$$F_m^*(\eta_m^*) = \psi_m g_e / 4\alpha_m c_m g(x) x^{*\,3/4} \tag{A2}$$

$$\eta_c^* = c_c \, (y - \delta_m) / x^{*\,1/4} \tag{A3}$$

$$F_c^*(\eta_c^*) = \psi_c g_e / 4\alpha_c c_c g(x) x^{*\,3/4} \tag{A4}$$

where * denotes that the parameters have been modified for the general case of a variable gravity surface.

With new transformations, the governing equations reduce to

$$F_i^{*\,'''} + \frac{1}{\mathrm{Pr}_i}[AF_i^* F_i^{*\,''} + B(F_i^{*\,'})^2] + 1 = 0 \quad i=m,c \tag{A5}$$

$$\theta_i^{*\,''} + AF_i^* \theta_i^{*\,'} = 0 \qquad\qquad i=m,c \tag{A6}$$

The relations based on energy balance for the melt and condensate layers become

$$\frac{c_{pm}\Delta T_m}{h_{sf}} = -A \frac{F_m^*(0)}{\theta_m^{*\,'}(0)} \ \text{and} \ \frac{c_{pc}\Delta T_c}{h_{fg}} = A \frac{F_c^*(\eta_{\delta c}^*)}{\theta_c^{*\,'}(\eta_{\delta c}^*)} \tag{A7}$$

In equations (A5–A7) A and B are defined as

$$A = \frac{4x^{*\,1/4}}{g_e} \frac{d}{dx}(x^{*\,3/4}g(x)) \ \text{and} \ B = \frac{x^{*\,1/2}}{g_e} \frac{d}{dx}(x^{*\,1/2}g(x)) \tag{A8}$$

To have a similar solution, A and B have to be independent of x^*. However, for the limiting cases of high Prandtl number liquids, the term involving constant B does not appear in the analysis. Thus only A need be set equal to a constant. Integration of the relation for A yields

$$x^* = \frac{g_e A}{3} \frac{\int_0^x g(x)^{1/3} dx}{g(x)^{4/3}} \tag{A9}$$

Here without loss of generality, the constant A is chosen to be 3 so that variable gravity formulation reduces to a vertical wall case when $g(x) = g_e$.

It is noted that equations (A5), (A6) and (A7) in the new variables are similar to equations (14), (15), (20), (21), (30), and (32). The boundary and interfacial conditions for equations (A5) and (A6) are the same as given by equations (22–24). Thus the solutions obtained earlier are also applicable to the equations (A5–A7). The local Nusselt number based on heat-transfer coefficient at the melting surface can be written in a fashion similar to equation (41) as

$$\mathrm{Nu}_t^0 = \gamma_t^0 \left[\frac{(\rho_m - \rho_v)gh_{sf}x^4}{4\nu_m k_m \Delta T_t x^*}\right]^{1/4} \tag{A10}$$

where γ_t^0 has the same values as given in the section on Results and Discussion. Interestingly at this stage, an effective gravity as proposed by Dhir and Lienhard [4] for condensation alone could be defined such that equation (A10) is rewritten as

$$\mathrm{Nu}_t^0 = \gamma_t^0 \left[\frac{(\rho_m - \rho_v)g_{eff}h_{sf}x^3}{4\nu_m k_m \Delta T_t}\right]^{1/4} \tag{A11}$$

where

$$g_{eff} = \frac{g(x)^{4/3}x}{\int_0^x g(x)^{1/3} dx} \tag{A12}$$

B. M. Howe

Institute for Hydromechanics,
University of Karlsruhe,
West Germany

A. J. Chambers

Department of Mechanical Engineering,
University of Newcastle, N.S.W.,
Australia
Mem. ASME

S. P. Klotz

T. K. Cheung

R. L. Street
Mem. ASME

Department of Civil Engineering,
Stanford University,
Calif. 94305

Comparison of Profiles and Fluxes of Heat and Momentum Above and Below an Air-Water Interface

The velocity and temperature fields on both sides of an air-water interface were examined experimentally in order to understand better the physical processes of momentum and heat transfer through the surface layers about the interface. An examination of temperature and velocity profiles plotted in "law-of-the-wall" coordinates leads to the conclusion that, both in the air and in the water, the mechanism of momentum transfer is affected by surface roughness changes, but the mechanism of heat transfer is not. In the water surface layer the velocity fluctuations due to the wave-related motions are of the same order as the purely turbulent motions. The turbulent components closely resemble those found in boundary layers over solid walls. The measured total energy flux from the interface agrees well with the measured single-phase, vertical heat transport through the water surface layer.

Introduction

The velocity and temperature fields on both sides of an air-water interface have been examined experimentally in order to understand better the physical processes related to momentum and heat transfer through a water surface layer and a mobile boundary. These data will be ultimately used to calibrate a numerical model which couples the air and water boundary layers across the interface.

Experimental Equipment and Measurements

Instantaneous measurements of the horizontal velocity, u, the vertical velocity, v, the temperature, θ, and the wave height, η, were made beneath the air-water interface in the Stanford Wind, Water-Wave Research Facility. They were obtained using, respectively, a laser Doppler anemometer (LDA), a fast response (5 Hz) thermistor, and a capacitance-type wave height gage. A traversing Pitot-static tube and thermistor were referenced against free-stream probes to obtain velocity and temperature profiles in the air. Free-stream humidity was monitored by means of wet and dry-bulb thermistor thermometers. The water surface temperature was measured with an infrared radiometer (PRT-5).

The Stanford Wind, Water-Wave Research Facility [1–3] is about 35 m long; the test section is approximately 20 m long, 0.9 m wide and 1.93 m high. The channel is filled with water to a depth of about 1 m, leaving a 1 m deep air flow section. Air flow is produced by drawing air through the test section

with a fan at the downstream end of the channel. Honeycombs, a series of turning vanes in the inlet, a set of filters, and several small-mesh screens straighten and condition the air flow. In the water a "beach" is used at the downstream end of the channel to minimize wave reflections into the test section. The water in this facility is heated from below by electric heating cables to establish an appropriate water-air temperature difference for each experimental run. However, the heaters must be turned off during the runs; otherwise the heater-induced buoyant convection would dominate the water boundary layer. As a consequence, since the water is warmer than the air, the water body cools during an experimental run.

The basic experimental setup and procedure was outlined in Howe et al. [1], in which preliminary water measurements at a wind speed of 3 m/s are reported. For the measurements reported herein, profiles consisting of a nominal 20 points (with 10 min of data per point) were made both in the air and the water. The wind speeds U_∞ were between 1.5 and 15.5 m/s, and the nominal bulk-water/free-stream-air-temperature difference was 8°C. The measuring station was 13 m from the air inlet.

There were specific objectives for each data run at a given wind speed; accordingly, not all instruments were used in each run. For example, in one case 10 data runs were made in a group, with two runs made at each of 5 wind speeds (1.6 to 13.1 m/s). The objective was to establish the repeatability of the measurements and to document the velocity and temperature profiles in the water; hence, no humidity data were taken. The velocity and temperature profile data were used from this data set, while other runs were made to focus on the

Copyright © 1982 by ASME

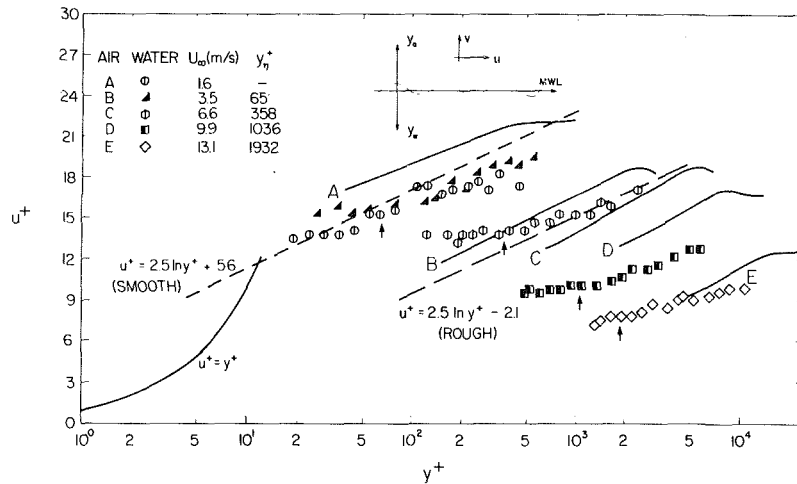**Transactions of the ASME**

Fig. 1 Water and air velocity profiles in u^+, y^+ coordinates (y_η^+ values for each windspeed are shown by vertical arrows)

fluxes, and, in these cases, the free-stream humidity was measured so Stanton numbers could be computed.

The radiometer was calibrated in place after the method of Miller and Street [2]. Subsequent data analysis has indicated that the PRT-5 radiometer gave inconsistent results for $U_\infty = 9.9$ m/s. This is not significant for most results deduced herein. However, the law-of-the-wall temperature profiles require use of θ_s, the water-air interface temperature. Accordingly, as outlined below, we evaluated the variance in θ_s and developed a rational procedure to account for time-dependent trends in the data, reduce the impact of inherent uncertainties (see Appendix B where uncertainty estimates are given), and correct the 9.9 m/s data base.

Experimental Results

In what follows, u_s is the surface drift current, q is specific humidity in the air, and the subscripts a, w, s, ∞, and B refer, respectively, to air, water, the interface, the air free-stream, and the bulk water. In addition, u_* is the friction velocity, θ_* is the friction temperature, and η is the free surface displacement.

In Fig. 1, mean profiles of velocity in both the air and the water are plotted in "law-of-the-wall" coordinates (u^+ and y^+) for a range of wind speeds. As indicated on the insert, the coordinate y is the distance from the mean water level (MWL) into the air or the water, as appropriate. In the air, the appropriate normalizing quantities are u_{*_a} and ν_a, while for the water we use u_{*_w} and ν_w. To make the air and water plots comparable then, $u_a^+ = (\bar{u}_a - u_s)/u_{*_a}$ but $u_w^+ = (u_s - \bar{u}_w)/u_{*_w}$ (thus, both u^+ values approach zero as $y^+ \to 0$). Of course, $y_a^+ = u_{*_a} y_a/\nu_a$ and $y_w^+ = u_{*_w} y_w/\nu_w$. These data are from the 10 data runs mentioned above, in which two runs were made at each of 5 wind speeds. For clarity, only one profile is shown for each speed, and the air data are shown as a line because the air profile behavior is well known (see [3]). For the water data, we show actual data points. For the air profiles, u_* was determined using the profile technique ($\kappa = 0.40$), whereas for the water data, u_{*_w} was determined by a linear fit (with depth) of the direct measurements of the turbulent shear stress (discussed below) and extrapolation of the trend line to the interface. This procedure seemed to be the most consistent means of determining the interfacial stress and hence u_{*_w}. However, determination of u_{*_w} from u_{*_a} by stress continuity or from the single largest $\overline{u'v'}$ value in the direct measurement profile yields comparable results so the choice of method is not crucial. Also shown are the computed values of the waterwave boundary layer thickness, y_η^+, as

---

Nomenclature

c_p = specific heat
Q = a "heat" flux
q_* = friction humidity
St = a Stanton number $[= Q/\rho_w c_{p_w} U_\infty (\bar{\theta}_B - \bar{\theta}_\infty)]$
$S_{\eta\eta}$ = wave power spectrum
U_∞ = free stream air speed
u = horizontal velocity
u^+ = $(\bar{u}_a - u_s)/u_{*_a}$ or $(u_s - \bar{u}_w)/u_{*_w}$

u_* = friction velocity $[= (-\overline{u'v'})^{1/2}, (\tau_s/\rho)^{1/2}]$
v = vertical velocity
y = vertical coordinate measured as a distance away from the mean water level (y_a in the air; y_w in the water)
y^+ = $u*y/\nu$
y_η = depth such that

$$\left(\int_0^{10} S_{\eta\eta}(f) e^{-2(2\pi f)^2 y_\eta/g} \, df \right) \Big/$$
$$\left(\int_0^{10} S_{\eta\eta}(f) \, df \right) = e^{-2}$$

θ = temperature

θ^+ = $(\bar{\theta}_w - \theta_s)/\theta_{*_w}$ or $(\bar{\theta}_a - \theta_s)/\theta_{*_a}$
η = wave height
θ_* = friction temperature $Q/\rho c_p u_* [= (\overline{v'\theta'})/u_*]$
κ = von Karman constant (0.40)
ρ = density
ν = kinematic viscosity

Superscripts

$^-$ = time average
$'$ = turbulent component
$^\sim$ = wave component

Subscripts

a = air
B = bulk water
L = latent
R = radiative
S = sensible
s = surface
T = total
w = water
∞ = free stream air
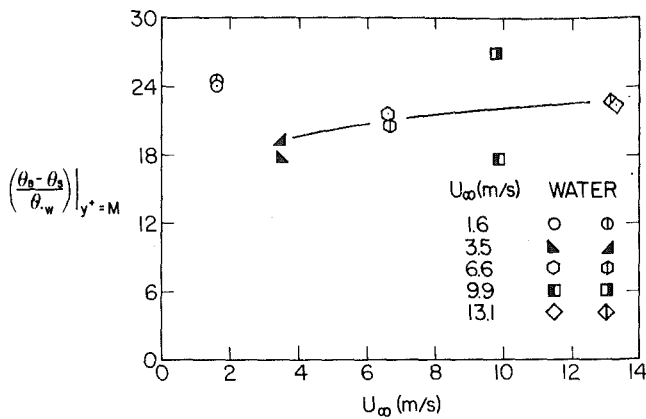
Fig. 2 Inverse Stanton number in water versus wind speed

U_∞(m/s)	WATER	
1.6	⊖	⊕
3.5	◤	◢
6.6	⊖	⊕
9.9	◼	◻
13.1	◇	◈

Fig. 3 Water and air temperature profiles in θ^+, y^+ coordinates (symbols same as in Fig. 1)

defined by Bye [4]. Here $y_\eta^+ = u_{*w} y_\eta / \nu_w$, where y_η is the depth at which wave-associated fluctuations are reduced to e^{-1} times their mean water-level values and is computed as indicated in the nomenclature from the water wave power spectrum $S_{\eta\eta}$.

In Fig. 1, the slopes of the water velocity profiles are generally less than those in the air. Of particular interest is the apparent change in slope at the level of y_η^+ which occurs at all but the highest and lowest wind speeds. The wave effects are, of course, most pronounced for $y^+ < y_\eta^+$, and wave-induced mixing (as evidenced by an augmented eddy viscosity, see Csanady [5]) may well be responsible for the smaller velocity gradients. At the highest wind speed, wave breaking, as seen by heavy white capping, changes the near surface regime, and pronounced flattening of the profile is not evident. The relative interfacial roughness, as seen by the respective flows, is indicated by the vertical placement of the profiles on the plot. At the lowest wind speed (1.6 m/s) there are virtually no waves and the air profile seems to exhibit the "supersmooth" behavior discussed by Csanady [6]; the water profile does not.

The inherent uncertainty ($\pm$ 0.1°C) in the radiometer-measured surface temperature θ_s causes significant scatter in plots in which water temperatures (determined by separate thermistor measurements) are differenced with θ_s because $\theta_w - \theta_s$ is always small. The air results are not significantly affected, because $\theta_B - \theta_s < 1$°C while $\theta_s - \theta_\infty \simeq 8$°C. This effect was noticed because plots of $\theta_B - \theta_w$ show no significant variances compared to $\theta_w - \theta_s$ plots.

As noted above, the water temperature decreases during an experimental run, leading to a trend such that $\theta_B - \theta_\infty$ decreases with time. The decrease is more rapid at high wind speeds; however, the heat, mass, or momentum transport coefficients remain constant because U_∞ is held constant, and the rate of change of $\theta_B - \theta_\infty$ is such that the flow is essentially always in equilibrium. On the other hand, the magnitudes of the actual heat and mass transports do change; hence, profile and flux comparisons should account for this.

Our correction procedure for the water data (the above effects are not significant in the air for the reason that temperature differences are large) is as follows:

(a) The heat flux $\overline{v'\theta'}$ is taken to be the maximum value measured in the profile, and the depth of this measurement is noted as $y_w^+ = M$. Then $\theta_{*w} = \overline{v'\theta'}/u_{*w}$.

(b) The dimensionless number $(\theta_B - \theta_s)/\theta_{*w}$ is plotted as a function of depth (essentially time because data were taken at sequentially increasing values of y_w) for each wind speed. Because the system time constant is very large (the total $\theta_B - \theta_s$ change occurs over several hours), the radiometer-induced scatter is removed by fitting a linear curve to the data and a "run or standard" inverse Stanton number $[(\theta_B - \theta_s)/\theta_{*w}]$ is determined from the curve at $y^+ = M$.
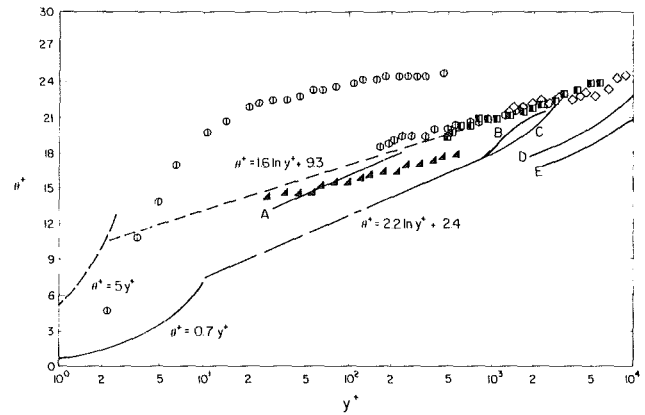
(c) Finally, the time trend of heat transfer is removed by determining θ_w^+ as the product of a shape function and the "standard" inverse Stanton number for each run, viz.

$$\theta_w^+ = \frac{\theta_w(y) - \theta_s}{\theta_B - \theta_s} \left(\left[\frac{\theta_B - \theta_s}{\theta_{*w}} \right]_{at\ y^+ = M} \right)$$

where θ_s and θ_B are those values determined at the time $\theta(y)$ was obtained.

Following step b above, Fig. 2 was plotted for all 10 data sets mentioned above. For all wind speeds except $U_\infty = 9.9$ m/s, the results of the two separate experiments are consistent and form a clear pattern. Accordingly, in Fig. 2,

(a) The dip at 3.5 m/s and the high values at 1.6 m/s are consistent with a change in surface conditions. Indeed, retrospective analysis of the air-flux measurements of McIntosh et al. [7] revealed precisely equivalent results for heat transfer in the air.

(b) The radiometer-induced errors at 9.9 m/s can be corrected either by taking the average of the two results or by using the trend value indicated by the solid curve (the result is the same!).

Figure 3 shows then the air and water temperature profiles in law-of-the wall coordinates. As McIntosh et al. [7] and Street et al. [3] reported, for $U_\infty > 2$ m/s, the air profiles cluster about the single correlation $\theta^+ = 2.2 \ln y^+ + 2.4$ and do not show significant effects of the increasing roughness with wind speed that the velocity profiles do. Surprisingly, the same is true for the water temperature profiles. The low speed case lies significantly above the rest of the data which fall on the correlation $\theta^+ = 1.6 \ln y^+ + 9.3$.

The slope of the water profiles indicates a turbulent Prandtl number of 0.63. This is in close agreement with 0.67 found by Ueda et al. [8] for open channel flow. The water profiles lie above the air profiles as expected because of Prandtl number dependence (see for instance Kader and Yaglom [9]). The profiles for the lowest wind speed case shift upwards and have intercepts comparable with those given by Kader and Yaglom [9] for smooth walls. Measurements in the water thermal sublayer agree roughly with $\theta^+ = \text{Pr}\,y^+$.

Representative normalized plots of the root-mean-square intensities of the velocity fluctuations in the water are contained in Figs. 4 and 5. (Again for clarity, here and in the following Figs. 6–9, only one of each of the pairs of data sets referred to above are plotted since the results are essentially identical.) Because we sought to examine water-wave effects, the vertical scale of the plots is the normalized depth, y/y_η. Wave-induced ($\tilde{u}$, $\tilde{v}$) and turbulent (u', v') components were separated by spectral means (see Appendix A1). Significantly, the wave-separation technique effectively collapses the

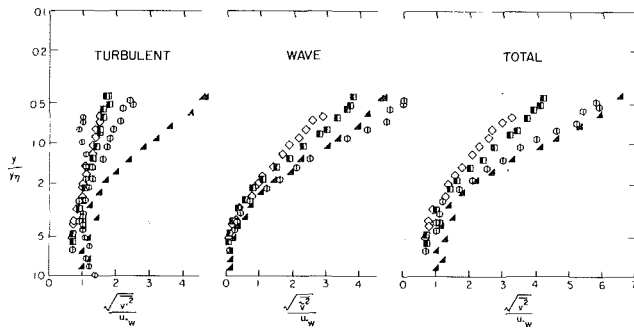$$(\overline{\tilde{u}^2})^{1/2} \text{ and } (\overline{\tilde{v}^2})^{1/2}$$

Fig. 4 Normalized root-mean-square vertical water velocity (symbols same as in Fig. 1)
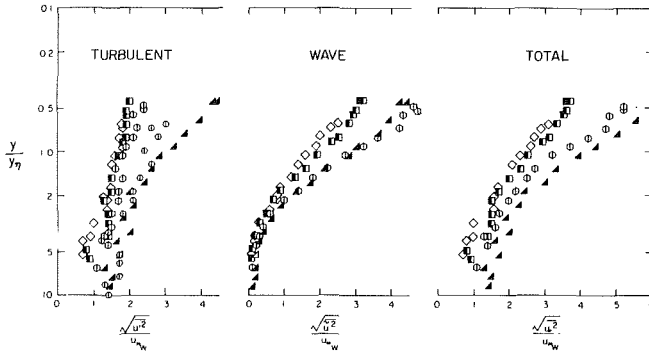

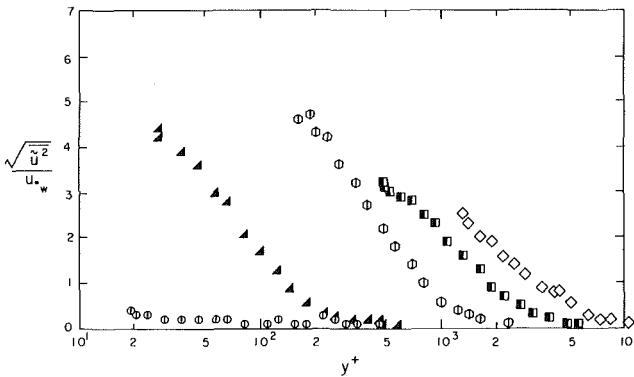**Fig. 5 Normalized root-mean-square horizontal water velocity (symbols same as in Fig. 1)**

Fig. 6 Normalized root-mean-square horizontal, wave-induced velocity component versus y^+ (symbols same as in Fig. 1)

Fig. 7 Normalized root-mean-square turbulent fluctuations of the horizontal velocity versus y^+ (symbols same as in Fig. 1)

Fig. 8 Normalized root-mean-square water temperature (symbols same as in Fig. 1)

profiles. Although there is data scatter, there is no distinct trend with wind speed.

In all cases in which there are waves, for a given wind speed the figures show

$$(\overline{v^2})^{1/2} \gtrsim (\overline{u^2})^{1/2}, (\overline{\tilde{v}^2})^{1/2} \gtrsim (\overline{\tilde{u}^2})^{1/2}$$

and generally

$$(\overline{v'^2})^{1/2} \lesssim (\overline{u'^2})^{1/2}$$

Furthermore, each of the normalized horizontal and vertical components, when plotted versus y/y_η, decreases with increasing wind speed and appears to approach a single curve at the highest wind speeds when the waves become increasingly two-dimensional and when significant white-capping begins to occur.

Except very far from the interface ($y/y_\eta \gtrsim 3$), wave-induced ($\sim$) and purely turbulent ($'$) fluctuations in both the horizontal and vertical at any given wind speed are roughly equal in magnitude. This observation points to the characteristic difference between fetch-limited laboratory flows and field (ocean) studies where the wave-induced components (associated with the dominant wave frequency) are typically much smaller than the purely turbulent components.
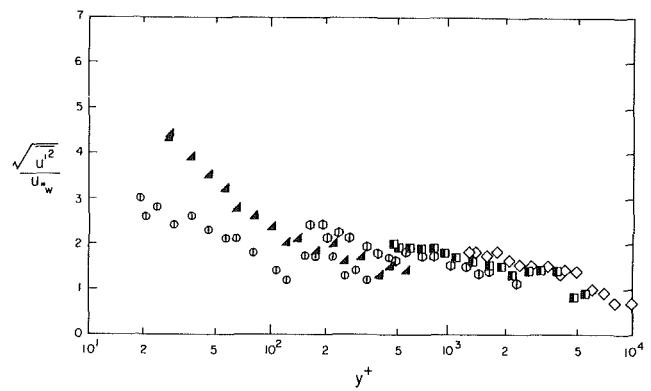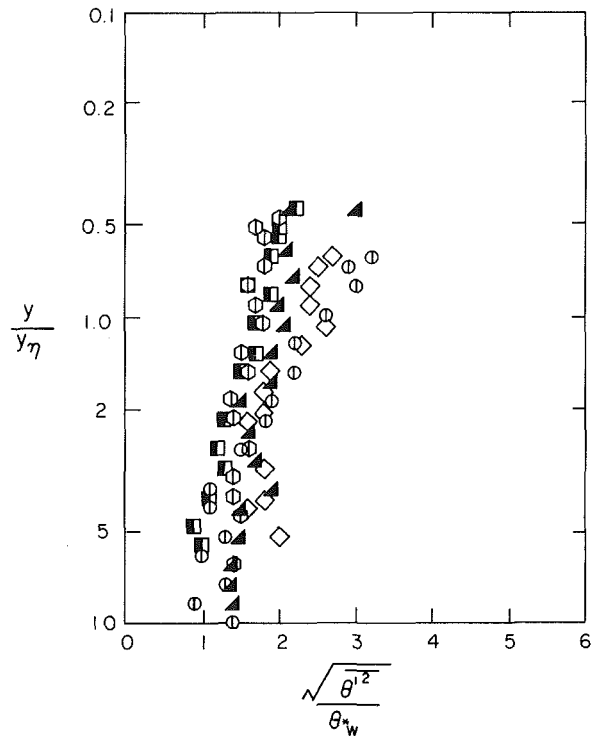
From Figs. 4 and 5 it is also obvious that, at any wind speed for which there are surface water waves, the horizontal and vertical turbulent fluctuations of the velocity are roughly equal

[although generally $(\overline{v'^2})^{1/2} < (\overline{u'^2})^{1/2}$]

at all depths when y_η is used for normalization. In a normal boundary layer over a smooth or rough solid wall,

$$(\overline{v'^2})^{1/2} < (\overline{u'^2})^{1/2}$$

and the ratio

$$(\overline{v'^2})^{1/2}/(\overline{u'^2})^{1/2}$$

decreases as the surface is approached (Hinze [10]). Exactly these trends appear in the present turbulent data for the lowest wind speeds *where the interface is smooth* if the law-of-the-wall coordinate y_w^+ is used in lieu of y/y_η. *When the surface is rough*, the presence of the moving wave forms makes it difficult to approach close enough to the surface with probes to observe if the expected decrease in

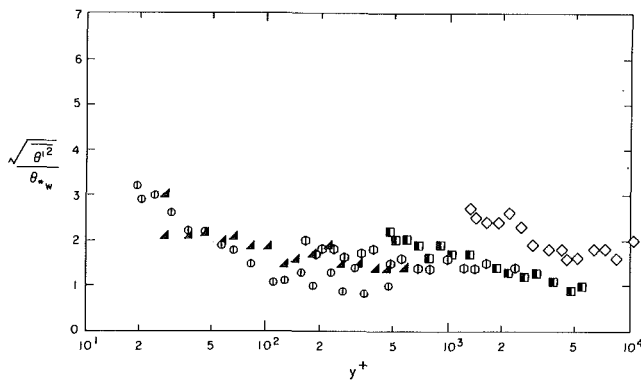$$(\overline{v'^2})^{1/2}/(\overline{u'^2})^{1/2}$$

Fig. 9 Normalized root-mean-square water temperature versus y^+ (symbols same as in Fig. 1)
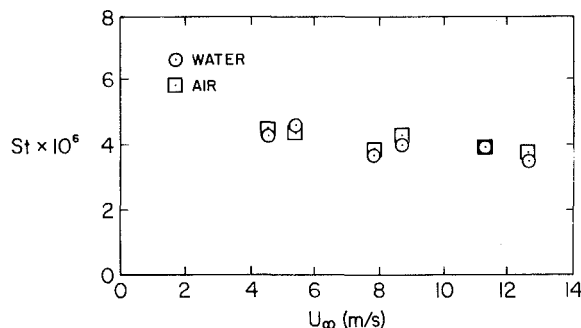

Fig. 10 Comparison of total flux across the interface as measured in the air and in the water

occurs very near the interface. The presence of the surface waves appears, however, to reduce the level of anisotropy in the horizontal and vertical components (the third component was, of course, not measured in our work).

Figures 6 and 7 serve to illustrate the penetration of the wave action with wind speed. As expected, at the lowest wind speed there are essentially no wave-induced fluctuations so

$$(\overline{\tilde{u}^2})^{1/2} << (\overline{u'^2})^{1/2}$$

For $U_\infty = 3.5$ m/s, the fluctuating intensities are about equal at the data points nearest the interface (i.e., for $y_w^+ < 100$). For greater U_∞ values, the maximum

$$(\overline{\tilde{u}^2})^{1/2} \text{ exceeds the maximum } (\overline{u'^2})^{1/2}$$

by a factor of approximately 2. Of course, as y_w^+ increases, the wave-induced quantities decrease very rapidly.

The normalized root-mean-square water temperature fluctuations are plotted in Figs. 8 and 9. There are no obvious trends in the values with wind speed for those cases where waves are measurable. The rapid increase in

$$(\overline{\theta'^2})^{1/2}/\theta_{*_w}$$

with decreasing depth for the 1.6 m/s case reflects typical smooth solid wall boundary layer behavior. As expected, the remaining data for

$$(\overline{\theta'^2})^{1/2}/\theta_{*_w}$$

collapse essentially to a single curve when plotted versus y_w^+ (Fig. 9), which further indicates typical boundary layer behavior within the water surface layer.

The total heat flux into the air is the sum of latent, sensible, and radiative components,

$$Q_{T_a} = Q_L + Q_S + Q_R$$

and should equal the single-phase heat transport, $Q_{T_w} = \rho_w c_{p_w} u_{*_w} \theta_{*_w}$, through the water surface layer. Only those data sets for which mean temperature and mean water-

vapor concentration profiles were measured in the air could be used in these calculations. Q_S and Q_L were calculated using values of θ_{*_a} and q_{*_a} determined from the temperature and water-vapor concentration profiles, respectively; Q_R was estimated at 150 w/m² according to the results of Miller et al. [11]. The results, in the form of a water, heat-transfer Stanton number (based on free-stream wind speed U_∞, and the bulk water/free-stream air temperature difference, $\bar{\theta}_B - \bar{\theta}_\infty$) are given in Fig. 10. The agreement is very good.

Conclusions

The results and conclusions are summarized as follows:

1   Mean velocity and temperature profiles plotted in u^+, y^+ coordinates behave in a similar fashion on both sides of the air-water interface. Velocity profiles show the effects of increasing roughness with wind speed. The temperature profiles for $U_\infty \geq 3$ m/s fall approximately on one correlation (albeit a different one for the air and for the water). This confirms the conclusion of Street et al. [3], viz, that both in the air and in the water, the mechanism of momentum transfer is affected by surface roughness changes, but the mechanism of heat transfer is not (except for waveless surfaces).

2   Total heat flux measurements in the air and the water are in agreement, confirming an ability to predict air and water fluxes from knowledge of only one of them.

3   When viewed in standard boundary-layer wall coordinates, the purely turbulent fluctuations of temperature and velocity behave in a manner generally consistent with flow in boundary layers over solid surfaces.

References

1 Howe, B. M., Chambers, A. J., and Street, R. L., "Heat Transfer at a Mobile Boundary," *Advances in Heat Mass Transfer at Air-Water Interfaces*, ASME, 1978, pp. 1–10.

2 Miller, A. W., Jr., and Street, R. L., "On the Existence of Temperature Waves at a Wavy Air-Water Interface," *Journal of Geophysical Research*, Vol. 83, 1978, pp. 1353–1365.

3 Street, R. L., Wang, C. S., McIntosh, D. A., and Miller, A. W., Jr., "Fluxes Through the Boundary Layers at an Air-Water Interface: Laboratory Studies," *Turbulent Fluxes through Sea Surfaces, Wave Dynamics, and Predictions*, eds. Favre and Hasselmann, 1978, pp. 99–120.

4 Bye, J., "The Wave-Drift Current," *Journal of Marine Research*, Vol. 25, 1967, pp. 95–102.

5 Csanady, G. T., "Turbulent Interface Flows," *Journal of Geophysical Research*, Vol. 83, 1978, pp. 2329–2342.

6 Csanady, G. T., "The 'Roughness' of the Sea Surface in Light Winds," *Journal of Geophysical Research*, Vol. 79, 1974, pp. 2747–2751.

7 McIntosh, D. A., Street, R. L., and Hsu, E. Y., "Turbulent Heat and Momentum Transfer at an Air-Water Interface: The Influence of Surface Conditions," Department of Civil Engineering, T.R. No. 197, Stanford University, 1975.

8 Ueda, H., Moller, R., Komori, S., and Mizushina, T., "Eddy Diffusivity Near the Free Surface of Open Channel Flow," *International Journal of Heat and Mass Transfer*, Vol. 20, 1977, pp. 1127–1136.

9 Kader, B. A., and Yaglom, A. M., "Heat and Mass Transfer Laws for Fully Turbulent Wall Flows," *International Journal of Heat and Mass Transfer*, Vol. 15, 1972, pp. 2329–2351.

10 Hinze, J. O., *Turbulence*, 2nd ed., McGraw-Hill, New York, 1975.

11 Miller, A. W., Jr., Street, R. L., and Hsu, E. Y., "The Structure of the Aqueous Thermal-Sublayer at an Air-Water Interface," Department of Civil Engineering, T.R. No. 195, Stanford University, 1975.

12 Benilov, A. Y., Kousnetsov, O. A., and Panin, G. N., "On the Analysis of Wind Wave-Induced Disturbances in the Atmospheric Turbulent Surface Layer," *Bound.-Layer Met.*, Vol. 6, 1974, pp. 269–285.

APPENDIX A
SPECTRAL WAVE SEPARATION

One can define (as did Benilov et al. [12]) a quantity linearly related to the surface waves as the "wave" component,

$$\tilde{x} = L\eta$$

where L is a linear operator and

$$x = \bar{x} + \tilde{x} + x'$$

where x can be one of the variables u, uv, etc.; $\bar{x}$ is the average value and x' is the turbulent fluctuation. In the frequency domain for the case with two variables,

$$S_{xy}(f) = S_{\tilde{x}\tilde{y}}(f) + S_{x'y'}(f)$$

Here $S_{xy}(f)$ is the cross spectrum of x and y. Computationally

$$S_{\tilde{x}\tilde{y}} = \frac{S_{x\eta}(f) \cdot S^*_{y\eta}(f)}{S_{\eta\eta}(f)}$$

$S_{\eta\eta}(f)$ is the power spectrum of η, the wave height signal. Using this method, one can separate the wave and turbulence components of any quantity of interest. However, turbulent components which are correlated with the wave will be incorporated in and computed as part of the equivalent wave component and non-linear wave terms will show up in the turbulent component.

APPENDIX B
UNCERTAINTY ESTIMATES

An uncertainty analysis was performed and led to the following estimates (at 20:1 odds):

Parameter	Uncertainty	Instrument
Water		
u	± 0.2 mm/s ($U_\infty < 2$ m/s)	LDA
v	± 0.6 mm/s (2 m/s $< U_\infty < 5$ m/s) ± 1.6 mm/s (5 m/s $< U_\infty$)	
θ	$\pm 0.1\,^\circ$C	thermistor or
$\theta_w, y - \theta_B$	$\pm 0.01\,^\circ$C	radiometer- thermistor
	± 0.25 mm	—
u_s	$\pm 10\%$ ($U_\infty < 9$ m/s) $\pm 20\%$ ($U_\infty > 9$ m/s)	paper punchings
η	± 0.3 mm or 2 percent (whichever is larger)	wave height gage
$\overline{u'^2}, \overline{v'^2}, \overline{\theta'^2}$	± 18 percent	—
$\bar{u}^2, \bar{v}^2, \bar{\theta}^2$	± 13 percent	—
$\overline{v'\theta'}$	± 18 percent	—
Air		
$U_\infty, u, u*$	± 0.1 m/s ($U_\infty < 8$ m/s) ± 0.2 m/s (8 m/s $< U_\infty$)	pitot-static tube
θ	$\pm 0.1\,^\circ$C	thermistor

A Study on Limiting Exit Quality of CHF of Forced Convection Boiling in Uniformly Heated Vertical Channels

Y. Katto

Department of Mechanical Engineering,
University of Tokyo,
Hongo, Bunkyo-ku,
Tokyo 113, Japan

This paper presents the results from a phenomenological analysis of limited exit quality X^0_{ex}, that is, the occurrence of critical heat flux at a nearly constant exit quality X^0_{ex} independent of the change of inlet quality under mixed inlet condition. The author's generalized correlation equations of CHF in uniformly heated channels with subcooled inlet condition are employed for this purpose, and the prediction of X^0_{ex} is compared with the existing data of X^0_{ex} satisfactorily. As a basis of the above-mentioned analysis, the applicability of the author's correlation equations to the state near the critical length-to-diameter ratio corresponding to the limiting quality condition is also examined.

Introduction

Postulating an idealized critical heat flux (CHF) curve, such as illustrated in Fig. 1(a), for forced convection boiling in uniformly heated channels, Doroschuk et al. [1] advocated that region I related to the first kind (DNB) of CHF while regions II and III related to the second kind (dryout) of CHF. Further, the authors postulated that CHF in region II took place due to dryout of a liquid film in the absence of replenishment from the core of dispersed-annular flow, whereas CHF in region III was connected with deposition-controlled dryout in a dispersed flow. A constant exit quality X^0_{ex} at which CHF was assumed to take place in region II was called boundary steam quality. Then, Doroschuk et al. [2, 3] made experiments for the CHF of water at 49–186 bars in tubes of $d = 8$ mm under both subcooled and mixed inlet condition, and took into account the data of Smolin [4], Sterman and Nekrasov [5], as well as their own data, to present recommended values of X^0_{ex} for water at 10–167 bars [2], or at 49–167 bars [3]. Meanwhile, the Heat and Mass Transfer Section of the Academy of Sciences in the USSR [6, 7] proposed a standard table of $q_c - X_{ex}$ relation for water at 29.5–196 bars in uniformly heated tubes of $d = 8$ mm, in which recommended values of X^0_{ex} for water at 29.5–137 bars were presented. Recently, Morozov [8] made experiments for CHF in tubes of comparatively large diameter ($d = 14.9$–20.7 mm) under mixed inlet conditions to supply new data of X^0_{ex} for water at 49–169 bars.

For CHF in annuli, Bennett et al. [9, 10] performed experimental studies on water boiling in internally heated annuli under mixed inlet conditions, and reported that a rapid fall of CHF, such as illustrated in Fig. 1(b), was observed, and that the same trend was also found in the data of Adorni et al. [11]. In their papers [9, 10], an exit quality X^0_{ex}, or exactly
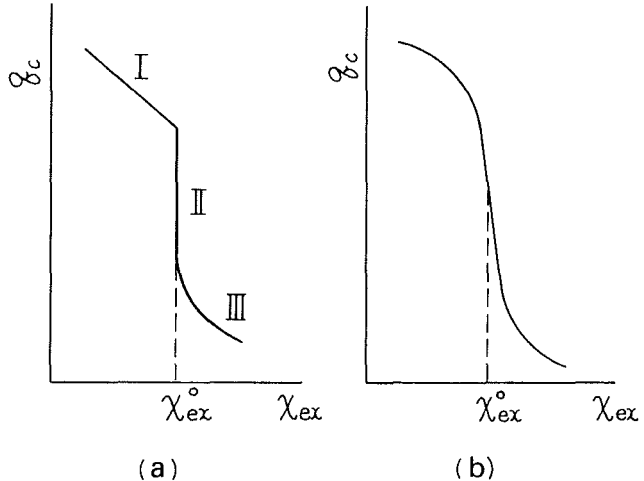
Fig. 1 Critical heat flux q_c versus exit quality X_{ex} for a uniformly heated channel with fixed p, d (or d_{he}) and G

speaking, a narrow range of X_{ex} near X^0_{ex}, where the rapid fall of CHF took place, was called critical steam quality, and the data of X^0_{ex} determined for $d_{he} = 8.52 - 16.9$ mm and $p = 14 - 86$ bar were tabulated. Then, several years later, Moeck [12, 13] made experiments under similar conditions, but with different annular channel dimensions, to give additional data of X^0_{ex}. After the studies for annuli, Bennett et al. [14] also made a study on CHF of water boiling in tubes with a well-defined two-phase inlet, showing results similar to the foregoing for the rapid fall of CHF.

As for fluids other than water, the phenomenon of rapid fall of CHF such as observed by Bennett et al. seems to have appeared in an experiment of Groeneveld [15] for the flow of R-12 in a tube with a mass velocity of 2770 kg/m²s under

Copyright © 1982 by ASME

Table 1 Typical experiments to give X_{ex}^0 under mixed inlet condition

Source	Fluid channel	l' (m)	l'/d or l'/d_{he}	$\dfrac{\rho_v}{\rho_l} \times 100$
Doroschuk et al. [2, 3]	H$_2$O, tube	1.50–3.00	188–375	0.569–20.2
Morozov [8]	H$_2$O, tube	1.71–1.92	86–129	3.21–21.0
Groeneveld [15]	R-12, tube	1.38	177	4.82
Deev et al. [16]	He, tube	0.0489–0.174	30–107	14.4–14.7
Bennett et al. [9, 10]	H$_2$O, annulus	0.737	44–69	0.788–6.34
Adorni et al. [11]	H$_2$O, annulus	0.500	59	4.84
Moeck [12, 13]	H$_2$O, annulus	1.31	147	2.13–4.84

mixed inlet condition. Also, data of X_{ex}^0 were presented by Deev et al. [16] for flow of helium-I in tubes with very low mass velocities of 92-200 kg/m^{2}s under mixed inlet condition.

Among the data sources of X_{ex}^0 mentioned so far, several typical ones are listed in Table 1 with some experimental conditions. For clarity, X_{ex}^0 will be called 'limiting exit quality' or 'limiting quality', after Hewitt [17], in this paper. According to the foregoing studies on X_{ex}^0, the limiting exit quality can be defined as a phenomenon which is observed as a rapidly falling curve of critical heat flux q_c versus exit quality X_{ex} when the experiments are made under mixed inlet condition for fixed p, d and G. Thus, there is an important problem of how the phenomenon of X_{ex}^0 can relate to the CHF with subcooled inlet conditions. This problem is all the more important because it has been postulated in the studies attaching weight to X_{ex}^0 [1-3, 6, 8, 16] that the transition from region I to region II in Fig. 1(a) is due to the change of CHF mechanism from DNB to dryout.

In this paper, therefore, an analysis of the limiting exit quality is attempted employing the generalized equations proposed recently by the author for correlating the CHF data obtained under subcooled inlet conditions.

Analysis of Limiting Exit Quality

CHF correlation equations used. The author's generalized correlations of CHF in tubes [18] has been constructed as follows: for a uniformly heated tube with an inlet subcooling enthalpy $\Delta H_i > 0$, critical heat flux q_c is written as

$$\frac{q_c}{GH_{fg}} = \frac{q_{co}}{GH_{fg}}\left(1 + K\frac{\Delta H_i}{H_{fg}}\right) \qquad (1)$$

First, q_{co}/GH_{fg} is empirically correlated with dimensionless groups of ρ_v/ρ_l, $\sigma\rho_l/G^2l$ and l/d by classifying CHF into four characteristic regimes called L, H, N and HP. Figure 2 illustrates the CHF-regime map for $\rho_v/\rho_l = 0.0484$. Broadly speaking, L, H and N-regimes correspond to dispersed (or annular), spray annular, and froth (or bubbly) flow at the tube exit, respectively, (see [19]), and the HP-regime is the regime which gradually invades the N-regime as ρ_v/ρ_l increases. K on the RHS of equation (1) is derived theoretically from the previous correlation of q_{co}/GH_{fg} by employing the boiling-length concept, except for the N-regime with nonlinear relationship between q_c and ΔH_i (see [21]).
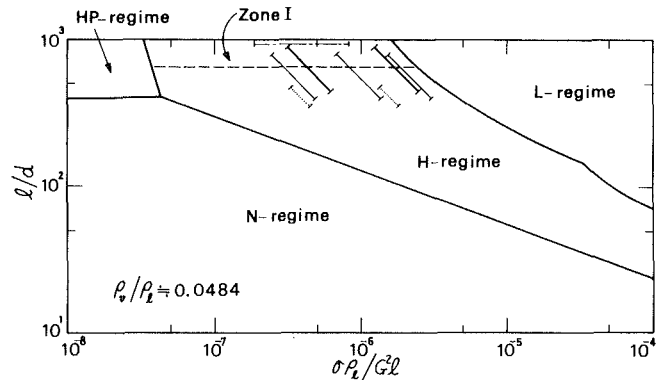

Fig. 2 CHF-regime map: ...., Matzner et al. [34]; ——, Wurtz [36];——, Dell et al. [37], and Hewitt [38]; —·—, Campolunghi et al. [39]

Analysis of X_{ex}^0. For a uniformly heated tube with an inlet subcooling enthalpy ΔH_i, the exit quality X_{ex} is related to the critical heat flux q_c via the heat balance as follows:

$$X_{ex} = \frac{4q_c}{GH_{fg}}\frac{l}{d} - \frac{\Delta H_i}{H_{fg}} \qquad (2)$$

Then, substituting q_c of equation (1) into the RHS of equation (2), it gives

$$X_{ex} = \frac{4q_{co}}{GH_{fg}}\frac{l}{d} + \left(K\frac{4q_{co}}{GH_{fg}}\frac{l}{d} - 1\right)\frac{\Delta H_i}{H_{fg}} \qquad (3)$$

If the term inside the parentheses on the RHS of equation (3) can be kept at zero, that is

$$K\frac{4q_{co}}{GH_{fg}}\frac{l}{d} - 1 = 0 \qquad (4)$$

then the value of X_{ex} is kept at the following constant value X_{ex}^0 independently of ΔH_i:

$$X_{ex}^0 = \frac{4q_{co}}{GH_{fg}}\frac{l}{d} \qquad (5)$$

When the condition of equation (4) is tested by the author's correlation equations of q_{co}/GH_{fg} and K for four characteristic regimes, it is found that equation (4) can be satisfied in the H-regime alone, where q_{co}/GH_{fg} and K read as follows:

Nomenclature

d = I.D. of heated tube
d_{he} = heated equivalent diameter = (4 × flow area)/(heated perimeter)
d_i = I.D. of annulus
d_0 = O.D. of annulus
G = mass velocity
H_{fg} = latent heat of evaporation
ΔH_i = inlet subcooling enthalpy

K = parameter for the effect of ΔH_i on q_c
l = length of heated section for $\Delta H_i > 0$
l' = length of heated section for $\Delta H_i < 0$
p = absolute pressure
q_c = critical heat flux
q_{co} = basic critical heat flux (q_c for $\Delta H_i = 0$)

ρ_l = density of liquid
ρ_v = density of vapor
σ = surface tension
X_{ex} = exit quality at critical heat flux condition
X_{ex}^0 = limiting exit quality
X_{in} = inlet quality $= -\Delta H_i/H_{fg} \leq 0$
X_{in}' = inlet quality $= -\Delta H_i/H_{fg} > 0$

$$\frac{q_{co}}{GH_{fg}} = 0.10 \left(\frac{\rho_v}{\rho_l}\right)^{0.133} \left(\frac{\sigma\rho_l}{G^2 l}\right)^{1/3} \frac{1}{1+0.0031 l/d} \qquad (6)$$

and

$$K = \frac{5}{6} \frac{0.0124 + d/l}{(\rho_v/\rho_l)^{0.133}(\sigma\rho_l/G^2 l)^{1/3}} \qquad (7)$$

Equation (6) is an empirical equation capable of outlining the characteristics of existing q_{co} data for many different fluids (see [20]), and equation (7) derived from equation (6) agrees fairly well with the trend of the experimental data of K (see Fig. 4 of [21]). As mentioned before, CHF in the H-regime is presumed to be associated with spray annular flow where replenishment of liquid film from the core flow is weak. On this point, it is of interest to add that equation (6) has a similarity in form to the correlation equation of CHF on a downward-facing flat surface cooled by a liquid film flow, where the droplet deposition on the liquid film can hardly occur (cf.[22]).

For q_{co} and K of equations (6) and (7), the condition of equation (4) is found to be satisfied at

$$\frac{l}{d} = 645 \qquad (8)$$

Then, substituting equation (6) into the RHS of equation (5) and eliminating l by the critical l/d ratio of equation (8), the limiting quality is yielded as follows:

$$X_{ex}^0 = 9.95 \left(\frac{\rho_v}{\rho_l}\right)^{0.133} \left(\frac{\sigma\rho_l}{G^2 d}\right)^{1/3} \qquad (9)$$

Possible mechanism of X_{ex}^0 observed under mixed inlet condition. Few measurements of CHF in the H-regime have been made for vertical tubes with an l/d ratio as high as 645 under subcooled inlet condition. This is probably due to various difficulties encountered in experiments. However, it will be assumed at the moment that the mode of CHF in the H-regime can extend up to $l/d = 645$ (which will be examined in the final section of this paper) when the axial variation of quality X for the state of limiting quality is represented in Fig. 3. Then, let's imagine a case where the tube of Fig. 3 is cut down to a length l', and a two-phase flow of quality X_{in}' is fed to the bottom end, under conditions of fixed p, d and G. It has been previously mentioned that CHF in the H-regime takes place with a spray annular flow pattern, and Whalley et al. [23] have suggested that this type of CHF is relatively insensitive to inlet behavior. If so, and if the l'/d ratio is sufficiently high (say $l'/d>50$ out of regard for actual examples of l'/d shown in Table 1) to repress the inlet disturbance, then there is a possibility of observing a constant value of exit quality (as predicted by equation (9)) independent of the change of l' and X_{in}' for fixed p, d and G.

Flow conditions to generate X_{ex}^0. As is seen in Fig. 2, the H-regime, where equation (9) applies, borders the L, N and HP-regimes, and these three boundaries have been given by equations (13), (14) and (21) of a previous study [18]. Therefore, substituting the condition of equation (8), that is $l/d = 645$, into these three equations, determines the boundaries of the region of applicability of equation (9) as follows:

$$\frac{\sigma\rho_l}{G^2 d} = 645 \left[\frac{0.0158}{(\rho_v/\rho_l)^{0.133}}\right]^{3.45} \qquad (10)$$

$$\frac{\sigma\rho_l}{G^2 d} = 2.05 \times 10^{-5} \qquad (11)$$

$$\frac{\rho_v}{\rho_l} = 0.308 \left[\left(\frac{\sigma\rho_l}{G^2 d}\right)^{0.160} + 12.3 \left(\frac{\sigma\rho_l}{G^2 d}\right)^{0.393}\right]^{2.14} \qquad (12)$$

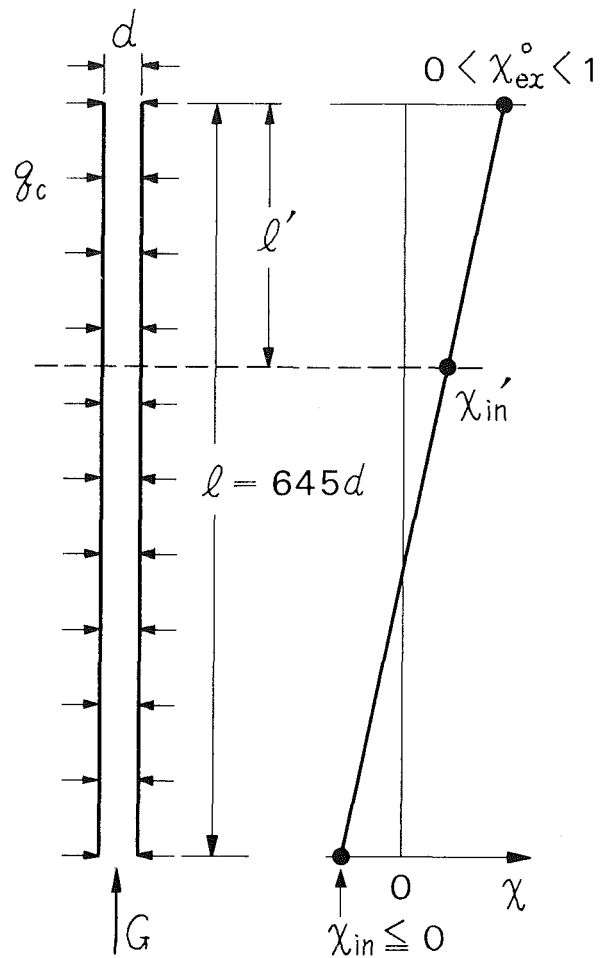The bounding lines given by equations (10–12) are shown by broken lines in Fig. 4.

Fig. 3 Axial variation of quality X for a uniformly heated tube of the critical l/d ratio under subcooled inlet condition

Limiting Quality for Tubes under Mixed Inlet Condition

Experimental range displaying X_{ex}^0. Experimental conditions under which the X_{ex}^0 data were obtained are shown in Fig. 4 by horizontal lines for water, by an open circle for R-12, and by three solid circles for helium-I. Two symbols of x in Fig. 4 represent the conditions of displaying the no-limiting-quality phenomenon in the experiments of Deev et al. [16]. From Fig. 4, therefore, it may be concluded that measured X_{ex}^0 appears virtually in the region predicted for generating X_{ex}^0. As for the protrusion, in the experiments, of water into the HP-regime found for $\sigma\rho_l/G^2 d < 10^{-4}$ in Fig. 4, it may be of interest to point out that the X_{ex}^0 in the range of $\sigma\rho_l/G^2 d < 10^{-4}$ has been eliminated from the USSR standard table of CHF, as will be shown later in Fig. 5(c).

Comparison between predicted and experimental X_{ex}^0 for water. The prediction of X_{ex}^0 by equation (9) is compared with the experimental X_{ex}^0 obtained for water by Doroschuk et al. [5], Morozov [8], and USSR Academy of Sciences [6] in Fig. 5(a), 5(b) and 5(c), respectively. The number of data points, and the deviation of data about the predicted value, are listed in Table 2. Although a certain degree of deviation exists, it is noticed in Fig. 5 that the trend of data is nearly in accord with the prediction, suggesting the significance of the present analysis of X_{ex}^0. Fig. 5(c) is somewhat inferior to Fig. 5(a) for the agreement between prediction and data, but it may be rather natural if it is supposed that the recommended values of X_{ex}^0 shown in Fig. 5(c) were determined on the safety
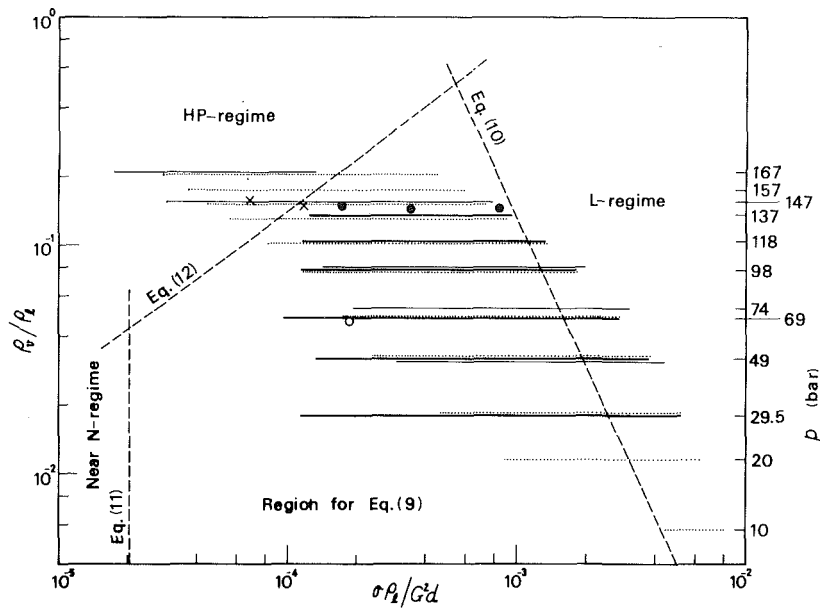
Fig. 4 Comparison between predicted and experimental condition to give X^O_{ex} for tubes (p represents the pressure of water): ...., Doroschuk et al. [2]; ———, Morozov [8]; ———, USSR Academy of Sciences [6], o Groeneveld [15], ● Deev et al. [16] (x: no appearance of X^O_{ex} in [16])
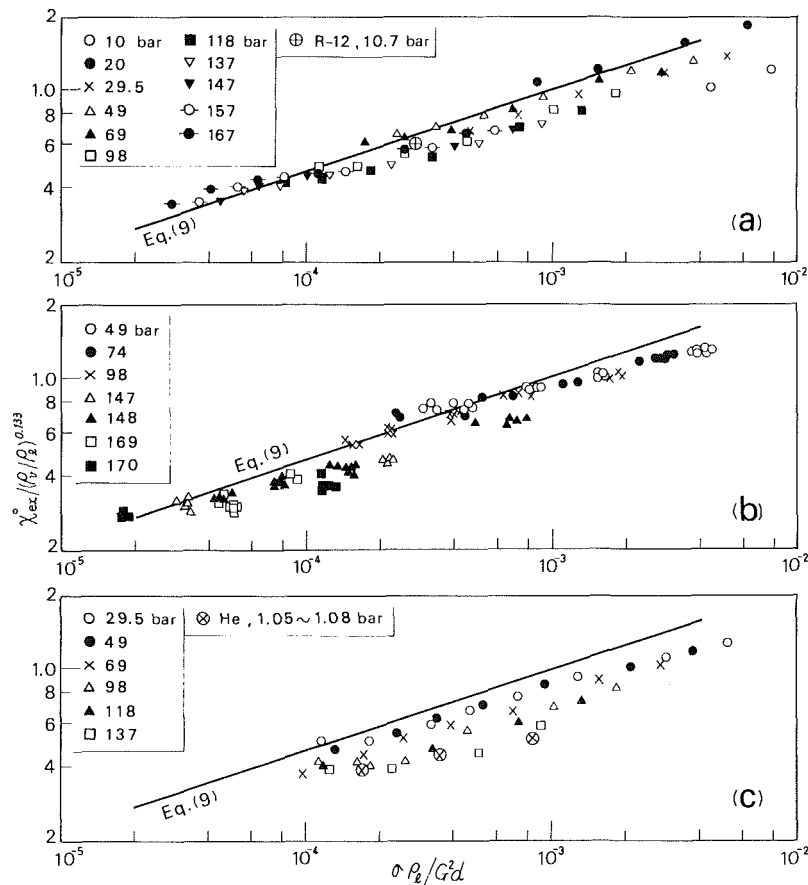

Fig. 5 Comparison between predicted and measured X^O_{ex} for tubes under mixed inlet condition: (a) Doroschuk et al. [2] for water, and Groeneveld [15] for R-12; (b) Morozov [8] for water; and (c) USSR Academy of Sciences [6] for water, and Deev et al. [16] for helium-I.

side in the process of preparing the USSR standard table of CHF for water.

X^0_{ex} **for R-12 and helium-I.** The experiment of Groeneveld [15] for flow of R-12 in a 7.8-mm dia tube with $G = 2770$ kg/m^{2}s gives the data of $X^0_{ex} = 0.4$, showing a good agreement with equation (9) in Fig. 5(a). The X^0_{ex} data obtained by Deev et al. [16] for flow of helium-I in 1.63-mm dia tubes with $G = 92 - 200$ kg/m^{2}s are compared with equation (9) in Fig. 5(c). For unknown reasons, these helium data lie somewhat

below the prediction. But it must be noted that the magnitude of mass velocity G is extraordinarily low for helium and there is the possibility that the data suffers from the effects of the unexpected phenomena due to mixed inlet conditions.

Limiting Quality for Internally Heated Annuli Under Mixed Inlet Condition

Analysis of X_{ex}^0. For annuli with uniform inside heating, the author has proposed the following generalized correlation of q_{co} in H-regime [24]:

$$\frac{q_{co}}{GH_{fg}} = 0.12 \left(\frac{\rho_v}{\rho_l}\right)^{0.133} \left(\frac{\sigma\rho_l}{G^2 l}\right)^{1/3} \frac{1}{1 + 0.0081 \, l/d_{he}} \qquad (13)$$

where d_{he} is the heated equivalent diameter, and is given as $d_{he} = (d_0^2 - d_i^2)/d_i$ in the present case. Heat balance equation (2) holds if d is replaced by d_{he}, and K on the RHS of equation (1) can be derived theoretically from q_{co}/GH_{fg} of equation (13) in the same way as in the case of tubes to give

$$K = \frac{25}{36} \frac{0.0324 + d_{he}/l}{(\rho_v/\rho_l)^{0.133}(\sigma\rho_l/G^2 l)^{1/3}} \qquad (14a)$$

In Fig. 6, the prediction of equation (14a) is compared with the data of K obtained from the experimental results of Janssen and Kervinen [25] for water, of Moeck et al. [26] for water, of Barnett [27, 28] for water, of Stevens et al. [29] for R-12, of Little [30] for water, and of Ahmad and Groeneveld [31] for R-12. The data show a considerable scatter, but its effects on q_c are not necessarily great because the magnitude of $\Delta H_i/H_{fg}$ on the RHS of equation (1) is usually not large. According to Fig. 6, the data are statistically a little lower than the prediction of equation (14). The cause is not yet known, but quite the same trend has also been observed for CHF in rectangular channels [32]. Therefore, a slight adjustment will be made for the prediction of K from the solid line of equation (14) to the broken line in Fig. 6, that is

$$K = 0.9 \times \frac{25}{36} \frac{0.0324 + d_{he}/l}{(\rho_v/\rho_l)^{0.133}(\sigma\rho_l/G^2 l)^{1/3}} \qquad (14b)$$

Table 2 Number of data points and deviation about predicted value for X_{ex}^0

		No. of data points	R.M.S. deviation %	Mean deviation[1] %
Fig. 5(a)	H_2O	59	14.5	− 8.2
"	R-12	1	6.8	− 6.8
Fig. 5(b)	H_2O	158	16.0	−11.7
Fig. 5(c)	H_2O	37	23.2	−20.9
"	He	3	37.4	−36.9
Fig. 7(b)	H_2O	22	19.5	+15.5

[1] Simple average of deviations with sign

Then, equations (13) and (14b) give the following critical l/d_{he} ratio and limiting quality X_{ex}^0 in the same way as in the case of tubes:

$$\frac{l}{d_{he}} = 432 \qquad (15)$$

$$X_{ex}^0 = 6.10 \left(\frac{\rho_v}{\rho_l}\right)^{0.133} \left(\frac{\sigma\rho_l}{G^2 d_{he}}\right)^{1/3} \qquad (16)$$

Flow conditions to generate X_{ex}^0. For internally heated annuli, the boundaries of the H-regime still remain somewhat vague or undecided because of the deficiency of CHF data in L and HP-regimes (cf. [33]). Apart from this problem, however, equations (11) and (12) of a previous study [24] give the following boundary equations:

$$\frac{\sigma\rho_l}{G^2 d_{he}} = 432 \left[\frac{0.0217}{(\rho_v/\rho_l)^{0.133}}\right]^{3.45} \qquad (17)$$

$$\frac{\sigma\rho_l}{G^2 d_{he}} = 3.12 \times 10^{-5} \qquad (18)$$

The above two equations correspond to equations (10) and (11) respectively. No equation corresponding to equation (12) can be given at present.

Comparison with experimental data. Fig. 7(a) shows the region decided by equations (17) and (18). Also shown in Fig. 7(a) are the experimental conditions under which the data of X_{ex}^0 were obtained by Bennett et al. (see Table III of [9] and Tables VII, VIII and IX of [10]) and by Moeck (see Fig. 8.2 of [12] or Fig. 2 of [13]). In addition, two symbols of x in Fig. 7(a) represent the conditions under which X_{ex}^0 cannot be determined at all in the experiments of Bennett et al. [see Fig. 6 of [9] and Fig. 1 of [10]), and two symbols of x? show the conditions under which the fall of CHF is not sharp enough to determine X_{ex}^0 definitely in the experiments of Moeck. The circumstances of Fig. 7(a) may be regarded as nearly the same as those of Fig. 4 for tubes.

Next, the prediction of equation (16) for X_{ex}^0 is compared with the experimental data of [9–13] in Fig. 7(b), and the deviation of data is shown in Table 2. The agreement between predicted and experimental X_{ex}^0 is fairly good.

On the Limiting Character of CHF in H-regime under Subcooled Inlet Conditions

As mentioned before, few experiments of CHF in the H-regime have been made under subcooled inlet conditions for the channels of very high l/d or l/d_{he} ratios. However, as the basis of the present analysis, it is indispensable to check the author's CHF correlation equations against those experimental data up to the critical length-to-diameter ratio.
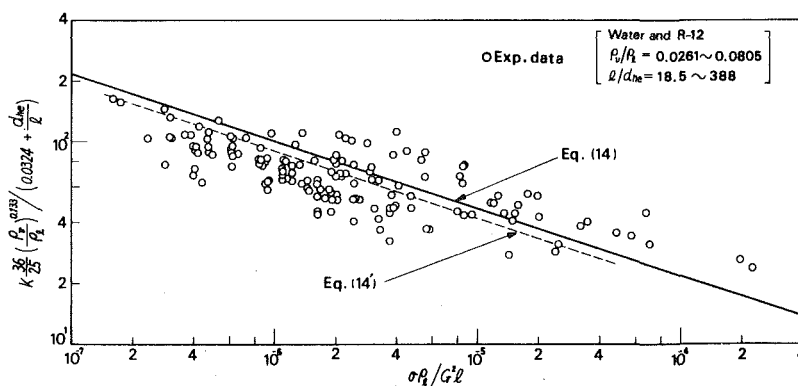

Fig. 6 Comparison between predicted and experimental K

Table 3 Experiments of CHF in H-regime under subcooled inlet condition

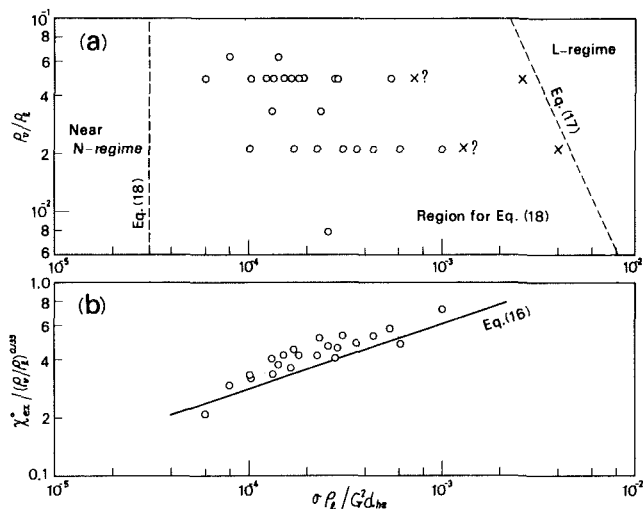| Source	Fluid-channel	Max. l (m)	Max. l/d or l/d_{he}	$\dfrac{\rho_v}{\rho_l} \times 100$
Matzner et al. [34]	H_2O, tube	4.88	480	4.84
Merilo-Ahmad [35]	R-12, tube	3.05	576	4.82
Würtz [36]	H_2O, tube	8.00	800	4.92
Hewitt [37, 38]	H_2O, tube	5.51	893	4.84
Campolunghi et al. [39]	H_2O, tube	11.2 only	983 only	2.82– 17.6
Little [30]	H_2O, annulus	4.57	388	4.84

Fig. 7 Experimental data of X_{ex}^o for internally heated annuli under mixed inlet condition (Bennett et al. [9, 10], Adorni et al. [11], and Moeck [12]): (a) comparison between predicted and experimental condition to give X_{ex}^o (x and x?: no appearance of X_{ex}^o); and (b) comparison between predicted and measured X_{ex}^o.

Vertical tubes. To the author's knowledge, Matzner et al. [34] performed experiments for water flow in vertical tubes up to $l/d = 480$ under subcooled inlet conditions, Merilo and Ahmad [35] for R-12 up to $l/d = 576$, Würtz [36] for water up to $l/d = 800$, Hewitt et al. [37, 38] for water up to $l/d = 893$, and Campolunghi et al. [39] for water at $l/d = 938$. Conditions of l and ρ_v/ρ_l employed in these previous experiments are listed in Table 3. According to Matzner et al. [34] and Merilo [40], CHF for comparatively high l/d and ρ_v/ρ_l seems to have a possibility of suffering from anomalous phenomena such as upstream CHF or slow CHF at very high mass velocities. Therefore, CHF data for $G > 4000$ kg/m²s are now discarded, and the experimental conditions for $\rho_v/\rho_l \doteqdot 0.0484$ are shown in Fig. 2 through short lines corresponding to references [34 and 36–39], for which the limiting condition of $l/d = 645$ is represented by a horizontal broken line.

Thus the data of Würtz [36] and those of Hewitt et al. [37, 38] will be compared with the prediction of equations (1), (2), (6) and (7) for CHF, but both data are similar in character so that the former alone is shown in Fig. 8, where the values of X_{ex}^0 given by equation (9) are also indicated by directed lines.

Internally heated vertical annuli. Little [30] performed experiments of water flow in vertical annuli under subcooled inlet conditions up to $l/d_{he} = 388$ (see Table 3 for experimental conditions). His data given in Appendices I and II of [30] are compared with the prediction of $q_c - X_{ex}$ by equations (1), (2), (13) and (14b) in Fig. 9, where directed lines indicate the limiting qualities predicted by equation (16). Characteristic features of CHF observed in Fig. 9 are similar to those observed in the case of vertical tubes.

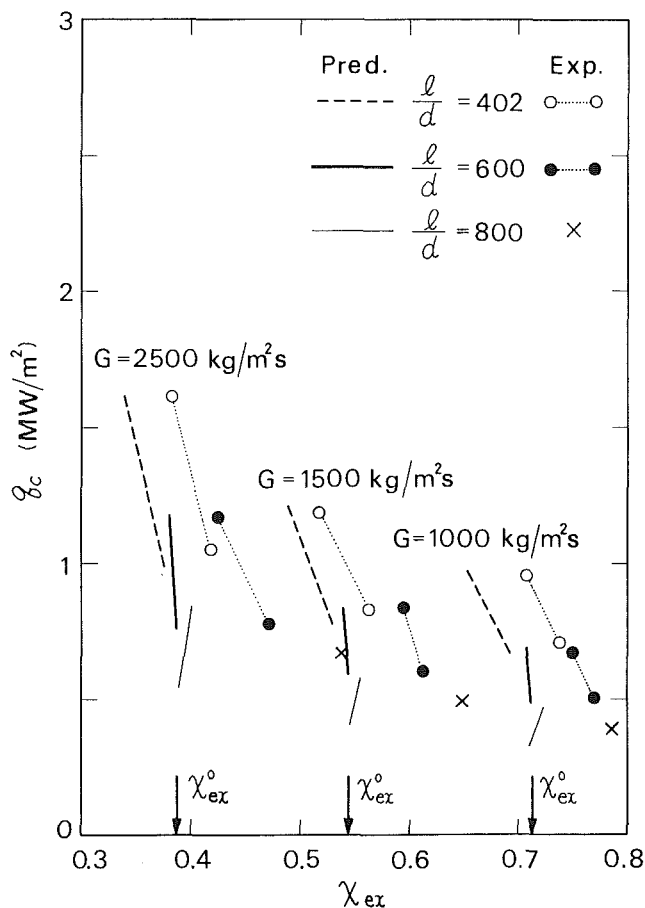**Discussion.** (a) It is noted from Figs. 8 and 9 that if the

Fig. 8 Comparison between predicted and measured q_c for tubes under subcooled inlet condition: Water, $p = 70$ bars, $d = 10.0$ mm (Würtz [36])

value of l/d or l/d_{he} is restricted to the range less than the critical value ($l/d = 645$ and $l/d_{he} = 432$), the agreement of trend between the data and prediction of $q_c - X_{ex}$ relation is good. Therefore, the use of equations (6) and (7) for tubes, or equations (13) and (14b) for annuli, is regarded as justifiable for deriving an approximate prediction of X_{ex}^0.

(b) As has been mentioned in the Introduction, it is postulated in many studies on X_{ex}^0 that the difference in the trend of $q_c - X_{ex}$ relationship between region I and region II in Fig. 1(a) is due to the change of CHF mechanism between DNB and dryout. However, the analysis of this paper suggests that the occurrence of region II (the limiting quality) is possible without a change of CHF mechanism, because the limiting quality takes place simply as a result of the character of $q_c - X_{ex}$ curve in the H-regime associated with spray annular flow (cf. [41]).

(c) As is noticed in Fig. 8, the rapid fall of q_c takes the form of Fig. 1(b) instead of Fig. 1(a) under subcooled inlet conditions. Accordingly, experimental values of X_{ex}^0 cannot be easily or definitely determined. In addition, the extremely

high value of l/d, near which the limiting quality takes place, is beyond the range of ordinary length-to-diameter ratios employed under subcooled inlet conditions of practical importance. Therefore, there seem few chances for the practical application of the limiting quality concept.

(d) According to Fig. 8, shortly before l/d exceeds 645 and during a heavy increase in l/d, experimental data begin to depart from the predicted trend, showing an entry into a special regime, where the author's correlation equations ((6) and (7)) of commonly observed CHF are no longer applicable. This regime is presumed to agree with the regime which was classified before as "zone I" by Hewitt [37, 38, 42, 43], and it claims that the region located above the horizontal broken line in Fig. 2 must be discriminated from other regimes. It may be of interest to note from Fig. 2 that the data of Campolunghi et al. fro $\rho_v/\rho_l = 0.0484$ belong to "zone I" completely.

(e) Recently, studies on the theoretical prediction of CHF on the assumption of liquid film dryout in an annular two-phase flow were advanced by Whalley et al. [23], Würtz [36], Levy et al. [44], and some others. It should be mentioned here that Würtz's prediction are fairly well in accord with his own experimental data of water at 70 bars ($\Delta T_{sub} = 10°C$, $G = 500 - 3000$ kg/m²s, $l/d = 202, 402, 600$ and 800), including the data shown in Fig. 8. Meanwhile, the analysis of Levy et al. with a three-region flow pattern model, shows good agreement with Würtz's data for $G = 2000$ kg/m²s and $l/d = 202-800$ and elucidates the difference of CHF mechanism between the region of rapidly falling q_c and the succeeding region with much higher X_{ex}^0.

Acknowledgment

Fig. 9 Comparison between predicted and measured q_c for internally heated annuli under subcooled inlet condition: Water, $p = 69$ bars, $d_{he} = 11.8$ mm (Little [30])

References

1 Doroschuk, V. K., Lantzman, F. P., and Levitan, L. L., "A Peculiar Type of Burnout in Evaporative Tubes," *Heat Transfer, 1970*, Vol. 6, B6.1. Elsevier, Amsterdam.

2 Doroschuk, V. E., Levitan, L. L., and Lantzman, F. P., "Investigations into Burnout in Uniformly Heated Tubes," ASME-Paper No. 75-WA/HT-22, 1975.

3 Levitan, L. L., and Lantzman, F. P., "Investigating Burnout with Flow of a Steam-Water Mixture in a Round Tube," *Thermal Engineering*, Vol. 22, No. 1, 1975, pp. 102-105.

4 Smolin, V. N., "Boiling Heat Transfer Crisis in Tubes with Dispersed Annular Flow of Steam-Water Mixtures," *Heat Transfer, 1970*, Vol. VI, B6.8. Elsevier, Amsterdam.

5 Sterman, L. S., and Nekrasov, A. V., "Studies of Burnout Heat Fluxes with Water Boiling in Tubes," *Heat Transfer, 1970*, Vol. VI, B6.9. Elsevier, Amsterdam.

6 Scientific Council of the U.S.S.R., Academy of Sciences, Recommendations on Calculating Burnout When Boiling Water in Uniformly Heated Round Tubes," BTD OKB IVTAN, Moscow, 1975.

7 Heat and Mass Transfer Section, Scientific Council, Academy of Sciences, U.S.S.R., "Tabular Data for Calculating Burnout when Boiling Water in Uniformly Heated Round Tubes," *Thermal Engineering*, Vol. 23, No. 9, 1977, pp. 77-79.

8 Morozov, V. G., "Investigation of Limiting Vapor Qualities in the Second Boiling Crisis," *Heat Transfer-Soviet Research*, Vol. 10, No. 2, 1977, pp. 58-69.

9 Bennett, A. W., Collier, G. J., and Lacey, P. M. C., "Heat Transfer to Mixtures of High Pressure Steam and Water in an Annulus—Part II. The Effect of Steam Quality and Mass Velocity on the Burn-Out Heat Flux for an Internally Heated Unit at 1000 p.s.i.a.," UKAEA, AERE-R 3804, 1961.

10 Bennett, A. W., Collier, J. G., and Lacey, P. M. C., "Heat Transfer to Mixtures of High Pressure Steam and Water in an Annulus—Part III. The Effect of System Pressure on the Burn-Out Heat Flux for an Internally Heated Unit," UKAEA, AERE-R 3934, 1963.

11 Adorni, N., Bertoletti, S., Lesage, J., Lombardi, C., Peterlongo, G., Goldani, G., Weckerman, F. J., and Zavatharelli, R., "Results of Wet Steam Cooling Experiments: Pressure Drop, Heat Transfer and Burnout Measurements in Annular Tubes with Internal and Bilateral Heating," CISE Report R-31, 1961.
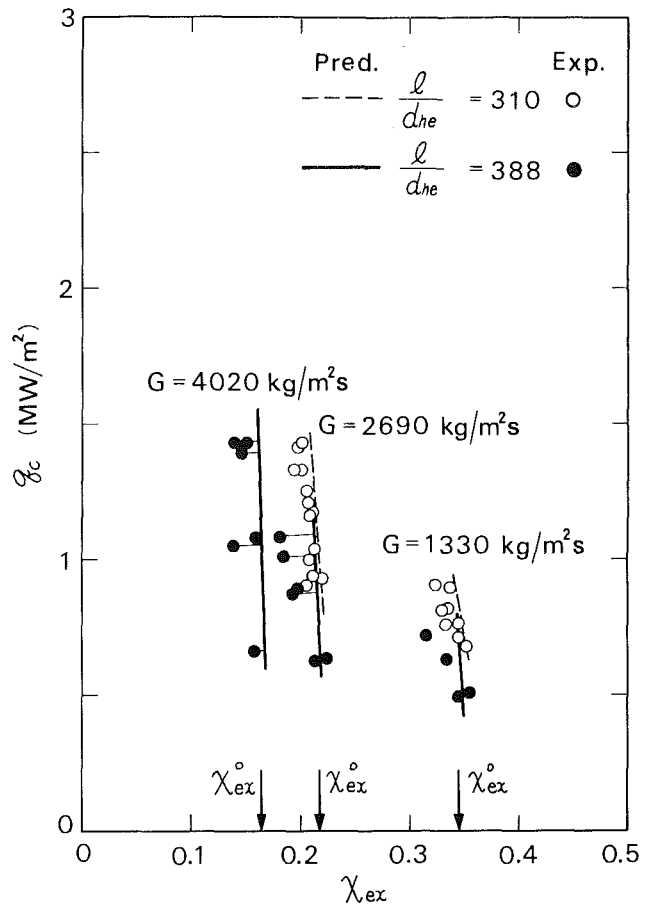
12 Moeck, E. O., "Annular-Dispersed Two-Phase Flow and Critical Heat Flux," Atomic Energy of Canada Ltd., AECL-3656, 1970.

13 Moeck, E. O., and Stachiewicz, J. W., "Liquid Film Behavior in Annular Dispersed Flow at Critical Heat Flux," *Heat Transfer, 1970*, Vol. 6, B6.7., Elsevier, Amsterdam.

14 Bennett, A. W., Hewitt, G. F., Kearsey, H. A., and Keeys, R. K. F., "Experiments on Burnout in a Uniformly Heated Round Tube at 1000 p.s.i.a. with Steam-Water Mixtures at the Tube Inlet," UKAEA, AERE-R 5072, 1965.

15 Groeneveld, D. C., "The Occurence of Upstream Dryout in Uniformly Heated Channels," *Heat Transfer, 1974*, Vol. 4, JSME, Tokyo, pp. 265-269.

16 Deev, V. I., Petrovichev, V. I., Pridantsev, A. I., Gordeev, Yu. V., Arkhipov, V. V., and Parygin, V. V., "Hydraulic Resistance and Burnout with Helium Boiling in Tubes," *Thermal Engineering*, Vol. 26, No. 1, 1979, pp. 45-47.

17 Hewitt, G. F., "Critical Heat Flux in Flow Boiling," *Heat Transfer, 1978*, Vol. 6, Hemisphere, Washington, pp. 143-171.

18 Katto, Y., "Critical Heat Flux of Forced Convection Boiling in Uniformly Heated Vertical Tubes (Correlation of CHF in HP-regime and Determination of CHF-regime Map)," *International Journal of Heat and Mass Transfer*, Vol. 23, 1980, pp. 1573-1580.

19 Katto, Y., "On the Relation between Critical Heat Flux and Outlet Flow Pattern of Forced Convection Boiling in Uniformly Heated Vertical Tubes," *International Journal of Heat and Mass Transfer*, Vol. 24, 1981, pp. 541-544.

20 Katto, Y., "General Features of CHF of Forced Convection Boiling in Uniformly Heated Vertical Tubes with Zero Inlet Subcooling," *International Journal of Heat and Mass Transfer*, Vol. 23, 1980, pp. 493-504.

21 Katto, Y., "An Analysis of the Effect of Inlet Subcooling on Critical Heat Flux of Forced Convection Boiling in Vertical Uniformly Heated Tubes," *International Journal of Heat and Mass Transfer*, Vol. 22, 1979, pp. 1567-1575.

22 Katto, Y., "Toward the Systematic Understanding of CHF of Forced Convection Boiling (Case of Uniformly Heated Round Tubes)," *Heat Transfer in Energy Problems*, Japan-U.S. Heat Transfer Joint Seminar Tokyo, 1980, pp. 53-60. To be published by Hemisphere, Washington.

23 Whalley, P. B., Hutchinson, P., and Hewitt, G. F., "The Calculation of Critical Heat Flux in Forced Convection Boiling," *Heat Transfer, 1974*, Vol. 4, JSME, Tokyo, pp. 290-294.

24 Katto, Y., "Generalized Correlation of Critical Heat Flux for the Forced Convection Boiling in Vertical Uniformly Heated Annuli," *International Journal of Heat and Mass Transfer*, Vol. 22, 1979, pp. 575-584.

25 Janssen, E. M., and Kervinen, J. A., "Burnout Conditions for Single Rod in Annular Geometry," GEAP-3899, 1963.

26 Moeck, E. O., Matzner, B., and Yuill, G. K., "Critical Heat Flux in Internally Heated Annuli of Large Diameter Cooled by Boiling Water at 1000 psia," *Proceedings of the Third International Heat Transfer Conference*, AIChE, Vol. 3, 1966, pp. 86–95.

27 Barnett, P. G., "A Correlation of Burnout Data for Uniformly Heated Annuli and its Use for Predicting Burnout in Uniformly Heated Rod Bundles," UKAEA, AEEW-R 558, 1968.

28 Barnett, P. G., "A Comparison of the Accuracy of Some Correlations for Annuli and Rod Bundles," UKAEA, AEEW-R 558, 1968.

29 Stevens, G. F., Wood, R. W., and Pryzbyski, J., "An Investigation into the Effect of a Cosine Axial Heat Flux Distribution on Burnout in a 12ft Long Annulus Using Freon-12," UKAEA, AEEW-R 609, 1968.

30 Little, R. B., "Dryout Tests on an Internally Heated Annulus with Variation of Axial Heat Flux Distribution," UKAEA, AEEW-R 578, 1970.

31 Ahmad, S. Y., and Groeneveld, D. C., "Fluid Modeling of Critical Heat Flux in Uniformly Heated Annuli," Atomic Energy of Canada Ltd., AECL-4070, 1972.

32 Katto, Y., "General Features of CHF of Forced Convection Boiling in Uniformly Heated Rectangular Channels," *International Journal of Heat and Mass Transfer*, Vol. 24, 1981, pp. 1413–1419.

33 Katto, Y., "General Features of CHF of Forced Convection Boiling in Vertical Concentric Annuli with a Uniformly Heated Rod and Zero Inlet Subcooling," *International Journal of Heat and Mass Transfer*, Vol. 24, 1981, pp. 109–116.

34 Matzner, B., Casterline, J. E., Moeck, E. O., and Wikhammer, G. A., "Critical Heat Flux in Long Tubes at 1000 psi with and without Swirl Promoters," ASME-Paper No. 65-WA/HT-30, 1965.

35 Merilo, M., and Ahmad, S. Y., "Experimental Study of CHF in Vertical and Horizontal Tubes Cooled by Freon-12," *International Journal of Multiphase Flow*, Vol. 5, 1979, pp. 463–478.

36 Würtz, J., "An Experimental and Theoretical Investigation of Annular Steam-Water Flow in Tubes and Annuli at 30 to 90 bar," Risφ National Laboratory, Risφ Report No. 372, 1978.

37 Dell, F. R., Hewitt, G. F., Keeys, R. K. F., and Stinchcombe, R. A., "Burnout Heat Flux Measurements in a Long Tube," UKAEA, AERE-R 2216, 1969.

38 Hewitt, G. F., "Experimental Studies on the Mechanism of Burnout in Heat Transfer to Steam-Water Mixtures," *Heat Transfer, 1970*, Vol. 6, B6.6., Elsevier, Amsterdam.

39 Campolunghi, F., Cumo, M., Ferrari, G., Leo, R., and Vaccaro, G., "Burn-Out Power in Once-Through Tubular Steam Generators," *Heat Transfer, 1974*, Vol. 4, JSME, Tokyo, pp. 280–284.

40 Merilo, M., "Critical Heat Flux Experiments in a Vertical and Horizontal Tube with Both Freon-12 and Water as Coolant," *Nuclear Engineering Design*, Vol. 44, 1977, pp. 1–16.

14 Katto, Y., "On the Heat-Flux/Exit-Quality Type Correlation of CHF of Forced Convection Boiling in Uniformly Heated Vertical Tubes," *International Journal of Heat and Mass Transfer*, Vol. 24, 1981, pp. 533–539.

42 Bennett, A. W., Hewitt, G. F., Kearsey, H. A., Keeys, R. K. F., and Pulling, D. J., "Studies of Burnout in Boiling Heat Transfer," *Transaction of Institution of Chemical Engineers*, Vol. 45, 1967, pp. T319–T333.

43 Hewitt, G. F., "Mechanism of Burnout," in *Two-Phase Flow and Heat Transfer*, edited by D. Butterworth, and G. F. Hewitt, Oxford University Press, Oxford, 1977, pp. 279–294.

44 Levy, S. Healzer, J. M., and Abdollahian, D. "Prediction of Critical Heat Flux for Annular Flow in Vertical Pipes," EPRI NP-1619, 1980.

Forced-Convective Post-CHF Heat Transfer and Quenching[1]

R. A. Nelson

Associate Mem. ASME
EG&G Idaho, Inc.,
Idaho Falls, Idaho 83415

Mechanisms in the postcritical heat flux region that provide understanding and qualitative prediction capability for several current force-convective heat-transfer problems are discussed. In the area of nuclear reactor safety, the mechanisms are important in the prediction of fuel rod cooldown and quenches for the reflood phase, blowdown phase, and possibly some operational transients with dryout. Results using the mechanisms to investigate forced-convective quenching are presented. Data reduction of quenching experiments is discussed, and the way in which the quenching transient may affect the results of different types of quenching experiments is investigated. This investigation provides an explanation of how minimum wall superheats greater than the homogeneous nucleation temperature result, as well as how these may be either hydrodynamically or thermodynamically controlled.

1 Introduction

This article qualitatively describes heat transfer mechanisms in the postcritical heat flux (post-CHF) region that provide understanding and predictive capability for several current, forced-convective heat-transfer problems. Principal application of this investigation is to quenching phenomena. These mechanisms are particularly important to nuclear reactor safety. The heat-transfer mechanisms initiate rod temperature turnaround and quenching during the reflood phase of either a hypothetical loss-of-coolant accident (LOCA) in a pressurized water reactor (PWR), or experiments in the small-scale, nonnuclear FLECHT and Semiscale facilities. The mechanisms are also important to the blowdown phase of a LOCA, as shown by the recent loss-of-fluid test (LOFT) experiments L2-2 and L2-3 [1, 2] (200 percent cold leg break transients), where core quenching occurred in the early part of the blowdown phase at high (6.9 MPa) pressures. The mechanisms may also be important to certain PWR operational transients, where the reactor may operate in the post-CHF regime for short periods of time. In order to limit maximum cladding temperatures or prevent cladding deformation, accurate prediction of the post-CHF heat transfer and core quench during these transients is of prime importance.

Section 2 provides a brief review of the heat transfer surface technique, associated definitions, and a review of how surface quenching is calculated by current computer codes. The results presented by Grush et al. [1], which predicted the quenches in LOFT experiment L2-3, are used as an example.

Section 3 discusses the mechanisms in the post-CHF region that produce quenching. These mechanisms were observed in low-pressure data and were postulated to also exist at high pressures [2]. Recent data now support this high-pressure effect. The changes in the heat transfer surface resulting from incorporating these mechanisms are discussed.

Finally, results using the new heat-transfer surface to investigate forced-convective quenching are presented in section 4. Reduction of quenching experiment data is discussed, and the effects the quenching transient may have on the results of different types of quenching experiments are investigated.

2 The Heat-Transfer Surface Technique

The heat-transfer surface technique was originally developed for RELAP4/MOD6 [3] and was initially presented at a Heat Transfer Workshop [4] sponsored by the U.S. Nuclear Regulatory Commission (NRC). Simultaneously, the technique was independently proposed by Collier [5]. Results utilizing this concept have been presented by Nelson and Sullivan [6, 7], and Bjornard and Griffith [8, 9]. This section discusses the heat-transfer surface concept and definitions pertinent to quenching and provides an understanding of how thermal-hydraulic computer codes currently predict quenching.

2.1 Heat-Transfer Surface Concept and Definitions. The function $z = f(x, y)$ may be viewed as a surface when z is plotted as a function of x and y. The insight gained from this visual approach can be quite helpful, particularly when a number of functions $z_1, z_2, \ldots, z_N$ must be combined to cover a wide range for the independent variables x and y.

This mathematical concept of a surface has been termed "the heat-transfer surface" when the functions $z_1, z_2, \ldots, z_N$ are heat-transfer correlations and the correlations are considered as functions of n variables. Thus, the heat flux defined by a number of different correlations is viewed as a function of wall superheat, quality, pressure, mass flux, etc.:

$$q = q(\Delta T_{sat}, X, P, G, \ldots). \tag{1}$$

A family of heat-transfer correlations used to build a surface is discussed in reference [10].

Within this article, the heat-transfer surface represents the total wall heat flux being convected into the fluid from a given point on the wall, and the quality is defined on an energy basis. Thus, for example, forced convection to subcooled

Copyright © 1982 by ASME

liquid is represented when the quality is less than zero. Also, thermodynamic equilibrium is assumed here for convenience. Thermodynamic nonequilibrium or individual liquid and vapor components from the wall could be included; however, they add complexity to the discussion, while not changing the basic results.

The heat transfer surface is composed of two families of curves. One family is the family of "boiling curves." As shown in Fig. 1, a boiling curve shows the dependence of heat flux upon wall superheat with all other variables held constant. The other family of curves is termed the "isothermal curves." An isothermal curve shows heat flux as a function of quality for a given wall superheat on the heat transfer surface.

Figure 2 constructs a heat-transfer surface from these two families of curves with all other variables held constant. To aid the visualization, different areas on the heat-transfer surface are denoted in terms of classical boiling regimes such as single-phase liquid heat transfer, nucleate boiling, transition boiling, film boiling, and single-phase vapor heat transfer. The slope of the heat-transfer surface with respect to wall temperature, $\partial q/\partial T_w$, is positive in all the boiling regimes, except for the transition boiling region.

In order to relate the heat-transfer surface approach to the "classical pool boiling curve," as originally proposed by Nukiyama [11], assume Fig. 2 can represent a pool boiling situation. The pool boiling curve can now be shown on the heat-transfer surface. For this classical pool boiling curve, the "quality" used is the "time average quality at a point on the wall" and is changing as the wall temperature changes. In reality, for the pool boiling situation, there is only a narrow range of qualities, if not just one, for any given wall temperature, so that a full heat-transfer surface as just assumed does not exist. Thus, a unique (or nearly unique) classical pool boiling curve exists for a given wall material, wall finish or condition, pressure, and geometry. For forced-convective heat transfer, a unique classical boiling curve does not exist as it does for pool boiling. Instead, the heat-transfer surface may be transversed in an infinite number of ways as determined by the coupled response of the wall and the hydraulics. One aspect of this nonunique nature of forced-convective classical boiling curves is fully discussed in section 4.1.

It is now important to define terms which are used herein during the discussion of quenching. These definitions are presented with respect to a typical boiling curve, as shown in Fig. 1. A cooldown of the wall occurs when the wall temperature decreases. This wall cooldown can take place at any point on the boiling curve as long as the energy being convected out of the wall is greater than the energy being conducted through the material to the wall's surface.

The rewet of a point on the wall is defined as having occurred when a point covered by vapor is once again contacted by liquid. This definition relates then to a microscopic view of the heat transfer at a point on the wall and contains no statement as to the average wall temperature at which rewetting occurs. Thus, as observed by Bradfield [12], transient rewetting of a point may occur in the film boiling region for average wall superheats greater than ΔT_{min}.
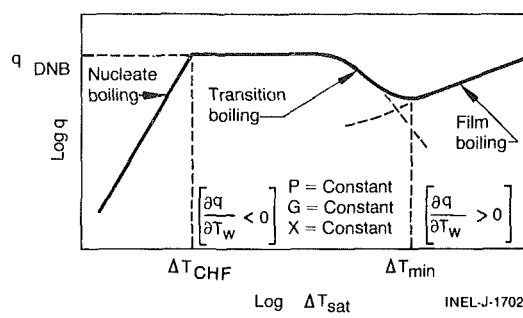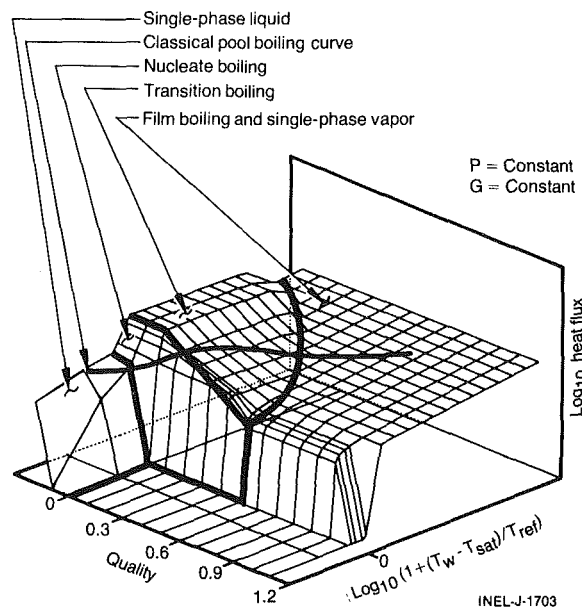

Fig. 1 Boiling curve

Fig. 2 Heat-transfer surface and regimes

A return to nucleate boiling (RNB) occurs when the cooldown is sufficient to reach the nucleate boiling region (indicated in Fig. 1). This return may be initiated from either the transition boiling region or the film boiling region, depending upon the wall temperature. This process will also be termed a quench and is used interchangeably with RNB. Quenching and RNB relate to the average wall temperature and average wall heat flux and represent then the macroscopic nature of quenching.

2.2 Current Predictions of Quenching. Current predictions of quenching can be divided into two major cases. The first case is the prediction of those experiments where quenching is controlled by conduction as a result of poor precursory cooling downstream of the quenching front. While work remains to be done on this case, it has been extensively studied and an excellent review of this work is provided by Elias and Yadigaroglu [13].

──────── Nomenclature ────────

					Subscripts		
			X	= quality	CHF	=	critical heat flux
			α	= void fraction	DNB	=	departure from nucleate
G	=	mass flux	α_c	= void fraction where			boiling
k	=	thermal conductivity		$\Delta T_{CHF} = 0$	HN	=	homogeneous nucleation
P	=	pressure	ΔT_{sat}	$= T_w - T_{sat}$ = wall superheat	L	=	liquid
q	=	heat flux	ΔT_{min}	= minimum wall superheat	ref	=	reference
t	=	time	ΔT_{CHF}	= wall superheat at CHF	sat	=	saturation
T	=	temperature			w	=	wall

The second case, the case concentrated upon here, is the prediction of those experiments where precursory cooling is sufficient to cause cooling downstream of the conduction propagating quenching front. For this case, two axial locations are considered as an artificial means of envisioning the separation of conductive and convective effects. The first location is a point immediately downstream of the conduction propagating quenching front. With sufficient precursory cooling at this downstream point, the speed of the quenching front is increased [14]. Thus, the quenching of this downstream point is influenced by both the quenching front and convection, and the quench front will be termed a "conduction-convective propagating quench front." The second location is far downstream of the conduction-convection quenching front. If precursory cooling is sufficient, a "spontaneous" convective quench may occur at this point prior to the arrival of the conduction-convection quenching front. For the moment, axial conduction as this point quenches is neglected, concentrating instead upon why quenching begins in order to understand how forced-convective heat transfer influences this quench. It is the second location upon which most of the discussion is concentrated in sections 3 and 4. The integration of the effects of axial conduction upon this point is equivalent then to considering the first point and is briefly discussed in section 4.1.

In order to investigate how forced-convective heat-transfer influences the calculation of quenches, the results from the LOFT experiment L2–3 [1, 2] are used briefly as an example. With a fuel rod quenching rate of approximately 1.5 m/s within the core, conduction-controlled quenching cannot be the controlling factor in experiment L2–3. Thus, it must fall into the second case of problems. As discussed by Grush et al. [1], quenching in experiment L2–3 is produced by a two-phase, low-quality fluid front (density wave) propagating through the core. How codes currently predict the quench is best understood by first denoting the relative maxima and minima of the heat-transfer surface shown in Fig. 2. The loci of these points are projected down onto the quality-wall superheat plane and denoted as ΔT_{CHF} and ΔT_{min}, as shown in Fig. 3. Quenching is currently calculated by the density wave (quality decrease) reestablishing transition boiling $(\partial q/\partial T_w < 0)$. This change is shown by a typical quenching path (point A to D) on Fig. 3.

Two factors produce the resulting quench denoted in Fig. 3: first, the increased flow ahead of the density wave causes a cooldown (point A to B) due to the classical Reynold's number effect in forced-convective film boiling; second, once transition boiling is reestablished at point B, a quench is guaranteed, without an increase in either internal heat or quality, because a decrease in wall superheat produces an increase in heat flux resulting in an increased cooldown rate. In order to successfully predict the quench for experiment L2–3, the codes have had to move the ΔT_{min} loci out (increase ΔT_{min}), so that the quality decrease produced by the density wave crosses the ΔT_{min} line.

3 Convective Post-CHF Heat Transfer and Quenching

Section 2.2 discussed how current computer codes typically predict quenching. This technique of calculating quenches (locating the ΔT_{min} loci) is not unique to the example presented from experiment L2–3. Similar procedures have been used in reflood calculations [3, 15]. It is the purpose of this section to study the post-CHF region and determine how convective quenching is really produced. This section investigates that point experiencing spontaneous quench far downstream of the conduction-convection quench front, as identified in section 2.2, and does not involve axial conduction effects initially.
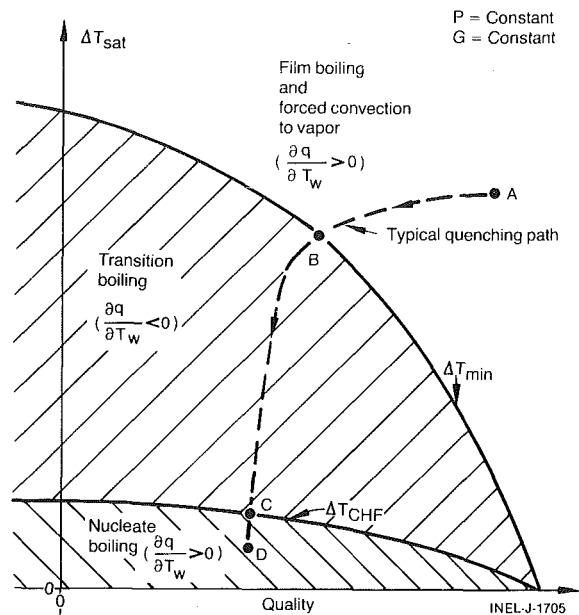
3.1 Low-Flow, Low-Void Film Boiling. The initial step in

Fig. 3 Loci of current maxima and minima of heat flux with respect to quality and superheat
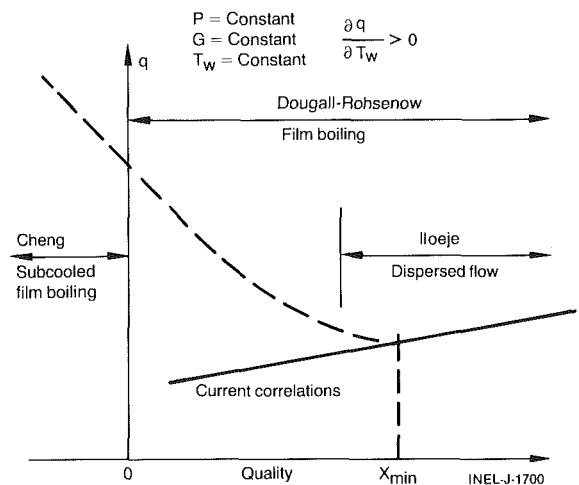
Fig. 4 Synthesized low quality effect on film boiling

determining how convective quenches are produced is to realize that the heat-transfer mechanisms that occur during the low-flow, low-void, post-CHF region, where quenching generally occurs, are not well understood. Recalling the isothermal family of curves that constitute the heat-transfer surface, as shown in Fig. 2, an isothermal line in the film boiling region $(\partial q/\partial T_w > 0)$ for typical current film boiling correlations [16, 17] is shown as the solid line in Fig. 4. The heat flux decreases as the quality decreases. The dashed line in Fig. 4 represents a low-pressure, low-quality effect in the film boiling regime originally synthesized from the work of Iloeje et al. [18], Dougall and Rohsenow [16], and Cheng et al. [19]. Current correlations do not have this synthesized characteristic because the data used for their development in the low-flow regime are primarily high-quality data.

Consider references [16], [18], and [19] and the quality regions they cover. Iloeje's three-step analytical model [18] for dispersed flow shows an X_{min}, as noted in Fig. 4, to exist in the low-flow regime. The increase in film boiling heat flux for decreasing quality is produced in the model by those drops which enter the thermal boundary layer (TBL), but do not contact the wall. This increase in heat flux becomes more pronounced as more drops are available to enter the TBL. As

quality continues to decrease, Dougall and Rohsenow [16] observed experimentally a continuing increase in the heat flux. This increase was attributed to the heat transfer in the inverted annular flow regime. Cheng et al. [19] studied experimentally the effects of subcooling on the boiling curves and found an increase in heat flux as the subcooling was increased.

Recent low-pressure data taken by Barnard et al. [20] and Fung et al. [21] support the synthesized low-quality effect in the low-flow film boiling region. Typical results from Barnard et al. are shown in Fig. 5. Both studies show these effects to be in the film boiling region, since the $\partial q/\partial T_w > 0$, and are not the result of entering the transition boiling region ($\partial q/\partial T_w < 0$) due to a quality change, as typically shown in Fig. 3. It is this low-quality effect in the low-flow film boiling region that initiates low-pressure convection quenches. An example of this type of quenching is seen at the top of the core in the FLECHT forced feed experiments [22]. Once the top of the rod experiences the convective quench, the upper quench front propagates down by conduction-convection to meet the conduction-convection front propagating up from the bottom.

High-pressure data supporting this low-quality effect was obtained by Polomik et al. [23] and utilized by Groeneveld [17] in the development of his film boiling correlation. However, the low-quality effect does not appear in the correlation due to the dominate quantity of high-quality data at low flows. More recent high-pressure data (up to 9 MPa) obtained by Groeneveld et al. [24], further support the low-quality effect. Just as in the low-pressure convection quenches, the same basic low-quality effect should initiate convective quenches at high pressure. LOFT experiment L2-3 provides an example of the influence of this type of convective-initiated quenching.

3.2 Wall Temperature for the Onset of Stable Film Boiling.

The preceding section discussed film boiling characteristics that initiate convective high-temperature, low-quality, and low-flow quenches. While liquid may contact (rewet) the wall for high temperatures in the film boiling region from a microscopic transient viewpoint, as previously noted, the question arises as to the wall temperature when this contact becomes significant from the macroscopic viewpoint and affects the heat transfer. Mathematically this translates into the question of what is the minimum wall superheat as defined by Fig. 1 or when is $\partial q/\partial T_w \equiv 0$? This section addresses that question. As is discussed in detail in section 4.1, the methods used in the reduction of much of the current, forced-convection data makes the direct answering of this question difficult. Thus, while more complex models can be constructed to address this question, only a simple model is proposed until sufficient properly analyzed data are obtained.

Much work has been done in determining how and when significant liquid contact begins. For reviews of the general work in this area, those by Comeau [25] and Fung [26] are useful. To more clearly define our question, recent publications by Gunnerson and Cronenburg [27] and Yao and Henry [28] prove quite useful. Gunnerson and Cronenburg present a generic approach to specifying the onset of stable film boiling, and indicate the wall temperature is bounded by the expression

$$T_{sat} < T_i < T_{max,s} \tag{2}$$

where

$$T_i = \frac{T_w (k/\sqrt{\alpha})_w + T_L (k/\sqrt{\alpha})_L}{(k/\sqrt{\alpha})_w + (k/\sqrt{\alpha})_L} \tag{3}$$

is the interfacial temperature as defined by Carslaw and Jaeger [29], and $T_{max,s}$ is the maximum liquid metastable superheat. Yao and Henry's [28] work emphasizes the effects
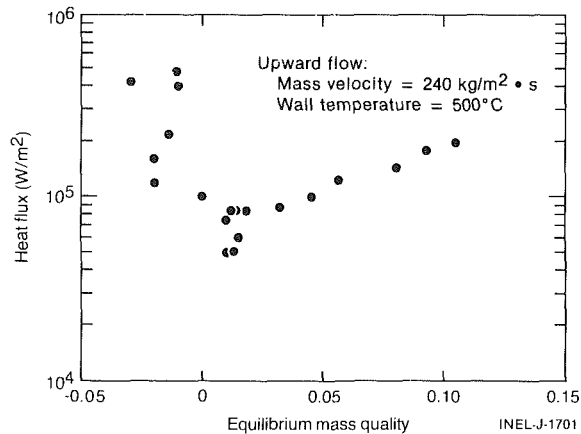

Fig. 5 Post-dryout data from reference [20]

of pressure and materials upon two fluids, one of which is water. Their results indicate that, for pool boiling on a horizontal surface, the minimum film boiling point is determined by the mechanism that is stable to the lowest wall temperature of either the Taylor instability mechanism or the spontaneous nucleation mechanism. For water, the hydrodynamic instability can be assumed to control at pressures less than 1.5 MPa, and the homogeneous nucleation temperature limit is used at higher pressures [28]. For the case of vertical boiling, the Helmhotz instability should replace the Taylor instability. However, due to the uncertainties in the effects of flows upon this instability limit and the fact that there is little practical difference between the homogeneous nucleation temperature (T_{HN}) and $T_{max,s}$, the homogeneous nucleation temperature limit, for simplicity, is assumed to apply for all pressures. Thus, the wall temperature at which stable film boiling begins is assumed to result from the interfacial temperature equaling the homogeneous nucleation temperature and is given by

$$T_{w,HN} = \frac{T_{HN}[(k/\sqrt{\alpha})_w + (k/\sqrt{\alpha})_L] - T_L (k/\sqrt{\alpha})_L}{(k/\sqrt{\alpha})_w} \tag{4}$$

With respect to the wall superheat, this wall temperature for the onset of stable film boiling is denoted as $\Delta T_{HN} = T_{w,HN} - T_{sat}$. The assumption that the wall superheat defined by ΔT_{HN} indicates the onset of film boiling is utilized for all qualities at a given pressure. In the subcooled region ($X < 0$), this assumption is only justified for minimal subcooling since a temperature distribution will exist in the inverted annular flow regime for the post-CHF region. In the two-phase regime or with minimal subcooling as the vapor film on the wall is approached through the fluid, the liquid temperature will approach or reach the saturation condition. Thus, T_L in equation (4) can be replaced by T_{sat}. Low-pressure, subcooled, forced-convective results presented by Cheng et al. [19] support this assumption as a first approximation. For higher subcooling ($T_{sat} - T_L \geq 287\ K$) the bulk temperature of the fluid can be used for T_L in the model; however, the data show additional work is needed.

3.3 Effects on the Heat-Transfer Surface.

The effects on the heat-transfer surface due to changes in the film boiling region are now considered. This can be most easily done in terms of the relative maxima and minima for the new heat transfer surface, as shown in Fig. 6. Figure 6 replaces the original single minimum, ΔT_{min}, of Fig. 3 with two relative minima, X_{min} and ΔT_{HN}.

The X_{min} loci are those minimum heat flux points determined from isothermal curves, presented typically in Fig. 4, as the wall temperature is parametrically varied. The curve denotes when $\partial q/\partial X$ changes sign and is controlled primarily

by the hydraulic conditions adjacent to the wall. The ΔT_{HN} loci represents the wall temperature below which liquid may contact the wall generally (macroscopically) and separates transition boiling $(\partial T_w < 0)$ and film boiling $(\partial_q / \partial T_w > 0)$. This line is controlled primarily by wall material properties, wall finish, and thermodynamic effects.

4 The Effects of Convective Heat Transfer Upon Quenching Experiments

This section addresses the question of how the phenomena discussed in section 3 will influence forced-convective post-CHF data reduction and quenching experiments. As noted in section 2.2, this discussion is limited to that class of experiments where precursory cooling downstream of the conduction-convection propagating quench front causes cooldown.

The current literature on ΔT_{min} and transition boiling for forced convection provides, at best, a very confusing picture. The primary contributing factors in this confusion are believed to be (a) that the data reduction procedure may produce results dependent upon the quenching transient, (b) that different types of experiments have been used, and (c) the effect of axial conduction upon ΔT_{min}, which has undergone much discussion in the literature.

To understand how the data reduction procedure and the quenching transient influenced the results obtained for different experiments, two general types of experiments are discussed. Axial conduction is then factored into the discussion conceptually after the effects of the two factors are understood. The first type of experiment considered is forced-convective quenching experiments with long tubes and/or bundles. The second is forced-convective quenching experiments using short test sections with high thermal inertia.

4.1 Tubes and Bundle Quenching Experiments. Two types of data reduction procedures for a point far downstream of the quench front are considered. The first is that procedure implied by the "classical pool boiling curve" approach where heat flux is considered a function of wall superheat, neglecting the effects of other changing variables. The second is that procedure inherent within the heat-transfer surface approach where the boiling curve represents the heat flux as a function of wall superheat, with all other variables held constant. For either case, the heat flux is assumed to be obtained from a one-dimensional (radial) inverse-conduction calculation using thermocouple measurements at the elevation of interest. If the thermocouple is located on the wall, its measurement yields T_w directly; otherwise the inverse calculation must also yield this quantity.

The "classical pool boiling curve" approach to data reduction assumes that heat flux is only a function of wall superheat. Writing heat flux in functional form for this consideration, the slope of the classical boiling curve is given by the total derivative of heat flux with respect to wall superheat, $dq/d(\Delta T_{sat})$. Using equation (1) and the chain rule, $[dq/d(\Delta T_{sat})]$ is given for the quenching transient by

$$\frac{dq}{d(\Delta T_{sat})} = \frac{\partial q}{\partial(\Delta T_{sat})}$$

$$+ \left(\frac{\partial q}{\partial X} \frac{dX}{dt} + \frac{\partial q}{\partial G} \frac{dG}{dt} + \frac{\partial q}{\partial P} \frac{dP}{dt} \right) \Big/ \frac{d(\Delta T_{sat})}{dt} \quad (5)$$

where t is time. Equation (5) indicates how different factors will affect the "classical boiling curve" when q is plotted against ΔT_{sat} for given times in the quenching transient. Thus, the classical boiling curve for quenching experiments with tubes and bundles is a complex relationship of the heat transfer surface $[\partial q/\partial(\Delta T_{sat}), \partial q/\partial X, \ldots]$, the hydraulic
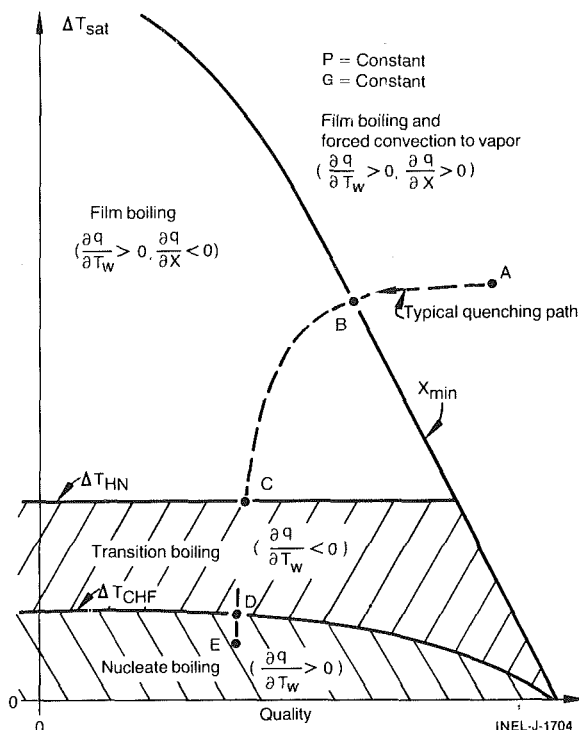

Fig. 6 Loci of maxima and minima of heat flux with respect to quality and wall superheat showing effect of new mechanisms

transient $(dX/dt, dP/dt, \ldots)$, and the one-dimensional (radial) conduction-convection transient of the wall $[d(\Delta T_{sat})/dt]$.

A special case of the general quenching experiments on tubes and bundles exists in those experiments that are run at constant pressure and inlet mass flux. For this case,

$$\frac{dP}{dt} = \frac{dG}{dt} \approx 0 \quad (6)$$

so that equation (5) reduces to

$$\frac{dq}{d\Delta T_{sat}} = \frac{\partial q}{\partial \Delta T_{sat}} + \frac{\partial q}{\partial X} \frac{dX}{dt} \Big/ \frac{d(\Delta T_{sat})}{dt} \quad (7)$$

This classical data reduction procedure yields a minimum wall superheat found from $dq/d(\Delta T_{sat}) \equiv 0$, and a transition boiling region where $dq/d(\Delta T_{sat}) < 0$. From equation (7), it is observed that both the ΔT_{min} and transition boiling are dependent on the experimental transient. Transition boiling will thus appear to occur when, for example,

$$\frac{dX}{dt} < - \left[\frac{\dfrac{\partial q}{\partial(\Delta T_{sat})}}{\dfrac{\partial q}{\partial X}} \cdot \frac{d(\Delta T_{sat})}{dt} \right] \quad (8)$$

Equation (8) can now be interpreted in terms of the new low-flow, low-void film boiling effect for a typical quenching path, as shown in Fig. 6. Quality is decreasing as the conduction-convection quench front progresses toward the point being considered. After X_{min} is crossed, the following relationships exist:

$$\frac{\partial q}{\partial(\Delta T_{sat})} > 0, \frac{\partial q}{\partial X} < 0, \frac{d(\Delta T_{sat})}{dt} < 0 \quad (9)$$

so that transition boiling appears to occur when dX/dt is decreasing at a sufficient rate. The apparent ΔT_{min} resulting from this interpretation, when equation (8) is satisfied, is greater than ΔT_{HN} and, as shown, depends upon the experimental transient.

Another interesting result from this analysis is that the ΔT_{min} obtained from a quenching experiment, where equation (8) is satisfied, will appear to be hydraulically controlled. However, when the transient does not satisfy equation (8), that is, does not decrease the quality fast enough, the resulting ΔT_{min} will be ΔT_{HN} and the minimum will appear to be thermodynamically controlled. Similar results are obtained for the more general quenching experiment, indicated by equation (5); only the relationships are more complex.

The heat-transfer surface approach to data reduction to determine boiling curves yields only the heat-transfer surface characteristic with respect to wall superheat, that is, $\partial q/\partial(\Delta T_{sat})|_{X, G, P = constant}$. This characteristic must be obtained from the experiment by a transient analysis of the hydraulic conditions as a function of axial position, z, so that $X = X(z, t)$, $G = G(z, t)$, and $P = P(z, t)$. Only in this manner can the values of heat flux and wall temperature be selected for constant values of X, G, and P. This analysis may require the use of a number of experimental runs in order to properly span the desired wall temperature range. If other characteristics of the heat transfer surface are desired, a similar procedure must be used. For example, the isothermal curves are obtained from $\partial q/\partial X|_{T_w, G, P = constant}$. In this manner, the experimentor can determine which parameters are necessary in the correlation of heat flux, since the partial derivatives of flux with respect to unimportant parameters will tend to be zero. The heat transfer surface procedure will ensure the proper separation of the variables. It is the improper separation of variables resulting from the classical approach, particularly quality and wall temperature, which has led to the confusion associated with ΔT_{min} and transition boiling for forced-convective heat transfer.

With this understanding of how the data reduction procedures influence the convective heat flux correlations obtained from the quenching of tubes or bundles for a point far downstream of the quenching front, the effect of axial conduction can be integrated into our thinking. Originally the term $d(\Delta T_{sat})/dt$ in equation (5) was discussed in terms of a one-dimensional conduction solution. However, this limitation to one-dimension was not required by equation (5). The limitation arises due to the problem caused by multidimensional conduction when the heat flux must be found from the wall thermocouples through an inverse-conduction solution. Without proper accounting of multidimension conduction, erroneous convective heat fluxes are found. For example, not including axial conduction in the data reduction when a quench front is near causes the ΔT_{min} to appear higher than it really is. For details of the mechanics of how axial conduction and convection combine to affect the results of quench front propagation, the work of Elias et al. [14] can be studied; however, their work does not include two-dimensional (radial and axial) conduction effects nor the low-flow, low-void film boiling effect within its convection model.

This integration of multidimensional conduction into the picture yields then a picture which applies to either of the two axial locations defined in section 2.2. Usually, the point located immediately downstream of the quenching front is the location that provides the majority of the data with respect to transition boiling, or the ΔT_{min}, when quenching of a tube or bundle is studied. Unfortunately, this is also the point where axial conduction and the rate of change of the hydraulic transient are at their maximum, making analysis of this type of experiment very difficult.

4.2 Short Test Sections of High Thermal Inertia. As developed by Cheng et al. [19], the short test section with high thermal inertia, proper prevention of axial conduction out the ends, and the use of guard heaters to keep the quench front stationary outside the test section, provides the advantage that it quenches due to its shortness with "constant" hydraulic

conditions defined by the inlet conditions and without axial conduction effects. Thus, the change in the hydraulic conditions over the short test section can be neglected,

$$\frac{dP}{dt} = \frac{dG}{dt} = \frac{dX}{dt} \simeq 0 \qquad (10)$$

so that equation (5) yields

$$\frac{dq}{d(\Delta T_{sat})} \simeq \frac{\partial q}{\partial(\Delta T_{sat})} \qquad (11)$$

for the experiment. The high thermal inertia prolongs the quenching period such that sufficient data can be acquired during the true transition boiling period, $\partial q/\partial T_w < 0$.

Equation (11) indicates that the results obtained from this type of experiment will be the same for either of the data reduction procedures discussed in section 4.1. This is an advantage, since the results from this type of experiment provide boiling curves that immediately separate the variables properly. The problem, if it can be termed that, created by this type of experiment has been that its results, $\Delta T_{min} \equiv \Delta T_{HN}$, often disagreed with tube results analyzed according to equations (5) or (7), and confusion has arisen. Equation (11) also indicates why the results of Cheng et al. were cited as indicating that ΔT_{HN} was a good first approximation for defining the onset of film boiling in section 3.2.

5 Conclusions

The heat transfer surface technique has been used to study how quenching of forced-convective water systems occurs. This understanding is particularly important to both the blowdown and reflood phases of experiments associated with nuclear reactor safety. A low-flow, low-void film boiling effect has been found in data which is believed to initiate cooldowns from high film boiling wall temperatures. This effect has been masked in the past by the vast amount of data in low-void, high flow and high-void, low-flow regimes. The effect is believed to have given rise to the current confusion associated with forced-convective ΔT_{min} and transition boiling. This effect may also give rise to the apparent post-CHF dependence upon "distance from the quench front" when thermodynamic nonequilibrium between the phases is also included. If the cooldown continues, film boiling destabilization is defined as occurring when the interfacial temperature equals the homogeneous nucleation temperature.

Integration of these effects into the heat-transfer surface provided a means of further study of how the new post-CHF heat transfer model affected data reduction of different quenching experiments. For the quenching of tubes or bundles, both axial conduction and low-flow, low-void film boiling convective heat transfer confuse the quenching issue. It was shown that, without proper separation of the variables, apparent values of ΔT_{min} result which are dependent upon the particular quenching transient of the experiment. Thus, values of ΔT_{min} greater than ΔT_{HN} result. Also, both hydraulically controlled and thermodynamically controlled ΔT_{min} values result, depending upon the transient. From these results, it is concluded that extreme care must be exercised in the reduction of data from quenching tubes and/or bundles. For the quenching of short test sections of high thermal inertia, the data reduction was found to be far more straightforward from a convective viewpoint. Care must be exercised, however, in terms of (a) either preventing experimentally or analyzing properly the effects of axial conduction and (b) providing guard heaters to keep the quench front outside the test section in order to provide constant hydraulic conditions during the quench.

References

1 Grush, W. H., et al., "Results and Predictions of Scaled, Nuclear Large Break Loss-of-Coolant Experiments," ASME Paper 80-WA/HT-49, ASME 1980 Winter Annual Meeting, Chicago, Ill., Nov. 16-21, 1980.

2 Nelson, R. A., "Forced Convective Post-CHF Heat Transfer and Quenching,"ASME Paper 80-WA/HT-69, ASME 1980 Winter Annual Meeting, Chicago, Ill., Nov., 16-21, 1980.

3 "RELAP4/MOD6—A Computer Program for Transient Thermal-Hydraulic Analysis of Nuclear Reactors and Related Systems, User's Manual," CDAP-TR-003, May 1978, EG&G Idaho, Inc., Idaho Falls, Idaho (available from the U.S. Nuclear Regulatory Commission Public Document Room in Washington, D.C.).

4 Nelson, R. A., "The Heat-Transfer Surface Technique," *LOCA Heat Transfer Workshop*, Idaho Falls, Idaho, July 21-22, 1975.

5 Collier, J. G., "Two-Phase Flow and Heat Transfer in Water Cooled Nuclear Reactors," Lecture Series Presented at Dartmouth College, Hanover, New Hampshire, Aug. 4-8, 1975.

6 Nelson, R. A., and Sullivan, L. H., "RELAP4/MOD6 Reflood Heat Transfer and Data Comparison," *CSNI Specialists Meeting on Transient Two-Phase Flow*, Paris, France, June 1978.

7 Nelson, R. A., and Sullivan, L. H., "Blowdown Heat Transfer Surface in RELAP4/MOD6 and Data Comparison," *ENS/ANS International Topical Meeting on Nuclear Power Reactor Safety*, Vol. 2, Brussels, Belgium, Oct. 1978, pp. 1719-1728.

8 Bjornard, T. A., "Blowdown Heat Transfer In a Pressurized Water Reactor," Ph.D. thesis, M.I.T., Aug. 1977.

9 Bjornard, T. A., and Griffith, P., "PWR Blowdown Heat Transfer," *ASME Symposium on the Thermal and Hydraulic Aspects of Nuclear Safety*, Nov. 27-Dec. 2, 1977, Vol. 1, pp. 17-39.

10 Ransom, V. H., et al., "RELAP5/MOD1 Code Manual Volume 1: System Models and Numerical Methods," NUREG/CR-1826, EGG-2070 Revision 1, Mar. 1981.

11 Nukiyama, I., "Maximum and Minimum Values of Heat Transmitted from a Metal to Boiling Water Under Atmospheric Pressure," *Journal of the Society of Mechanical Engineers Japan*, Vol. 37, 1934.

12 Bradfield, W. S., "Liquid-Solid Contact in Stable Film Boiling," ITEC Fundamentals, Vol 5, May 1966, pp. 200-204.

13 Elias, E. and Yadigaroglu, G., "The Reflooding Phase of the LOCA in PWRs. Part II: Rewetting and Liquid Entrainment," *Nuclear Safety*, Vol. 19, No. 2, Mar.-Apr. 1978, pp. 160-175.

14 Elias, E., Arrieta, L., and Yadigaroglu, G., "An Improved Model for the Rewetting of a Hot Fuel Rod," *Transactions of the American Nuclear Society*, Vol. 24, 1976, pp. 299-300.

15 Kirchner, W. L., "Reflood Heat Transfer in a Light-Water Reactor," Ph.D. thesis, M.I.T., Jan. 1976; also *NAC Report*, Vols. 1 and 2, NUREG-0106, 1976.

16 Dougall, R. S., and Rohsenow, W. M., "Film Boiling in the Inside of Vertical Tubes with Upward Flow of the Fluid at Low Qualities," M.I.T. Technical Report 9079-26, 1963.

17 Groeneveld, D. C., "An Investigation Of Heat Transfer In The Liquid Deficient Regime," AECL-3281, Dec. 1969.

18 Iloeje, O. C., Rohsenow, W. M., and Griffith, P., "Three-Step Model of Dispersed Flow Heat Transfer (Post-CHF Vertical Flow)," ASME Paper 75-WA/HT-1, 1975.

19 Cheng, S. C., Ny, W. W. L., and Heng, K. T., "Measurements of Boiling Curves of Subcooled Water under Forced Convective Conditions," *International Journal of Heat Mass Transfer*, Vol. 21, 1978, pp. 1385-1392.

20 Barnard, D. A., Glastonbury, A. G., and Ward, J. A., "The Measurement of Post-Dryout Heat Transfer at Low Pressure and Low Mass Quality under Steady State Conditions," *Proceedings of the European Two-Phase Flow Group Meeting, Joint Research Center*, ISPRA, June 1979.

21 Fung, K. K., Gardiner, S. R. M., and Groeneveld, D. C., "Subcooled and Low Quality Flow Film Boiling of Water at Atmospheric Pressure," a paper accepted for publication in *Nuclear Engineering and Design*.

22 Rosal, E. R., et al., "FLECHT Low Flooding Rate Cosine Test Series Data Report," WCAP-8651, Dec. 1975, Westinghouse Electric Corporation.

23 Polomik, E. E., et al., "Heat Transfer Coefficients with Annular Flow During Once-Through Boiling of Water to 100 Percent Quality at 800, 1100 and 1400 psi," GEAP-3703, 1961.

24 Groeneveld, D. C., et al., "Calk River Progress In Updating Best-Estimate Heat Transfer Correlations," *Best-Estimate Heat Transfer Workshop*, Washington, D. C., Jan. 28-29, 1981.

25 Comeau, J. G., "A Review of the Liedenfrost Phenomenon," Master of Mechanical Engineers Report, University of Ottawa, 1979.

26 Fung, K. K., "Post-CHF Heat Transfer during Steady-State and Transient Conditions," NUREG/CR-0195, ANL-78-55, June 1978.

27 Gunnerson, F. S., and Cronenburg, A. W., "On the Thermodynamic Superheat Limit for Liquid Metals and Its Relation to the Liedenfrost Temperature," JOURNAL OF HEAT TRANSFER, Vol. 100, Nov. 1978, pp. 734-737.

28 Yao, S. C., Henry, R. E., "An Investigation of the Minimum Film Boiling Temperature on Horizontal Surfaces," JOURNAL OF HEAT TRANSFER, Vol. 100, May 1978, pp. 260-267.

29 Carslaw, H., and Jaeger, J., *Conduction of Heat in Solids*, 2nd ed., Clarendon Press, Oxford, 1959.

C. P. Bankston
Technical Staff.
Assoc. Mem. ASME

L. H. Back
Technical Group Leader.
Mem. ASME

Energy and Materials Research Section,
Jet Propulsion Laboratory,
California Institute of Technology,
Pasadena, Calif. 91109

Heat Transfer From Combustion Gases to a Single Row of Closely Spaced Tubes in a Swirl Crossflow Stirling Engine Heater[1]

This paper describes an experimental program to determine the heat-transfer characteristics of a combustor and heat-exchanger system in a hybrid solar receiver which utilizes a Stirling engine. The system consists of a swirl combustor with a crossflow heat exchanger composed of a single row of 48 closely spaced curved tubes. In the present study, heat-transfer characteristics of the combustor/heat-exchanger system without a Stirling engine have been studied over a range of operating conditions and output levels using water as the working fluid. Non-dimensional heat-transfer coefficients based on total heat transfer have been obtained and are compared with available literature data. The results show significantly enhanced heat transfer for the present geometry and test conditions. Also, heat transfer along the length of the tubes is found to vary, the effect depending upon test condition.

Introduction

The development of point focusing solar receivers for electric power generation has resulted in concepts for hybrid fossil fuel operation in order to generate power under varying solar insolation levels. One of these concepts is the Dish Stirling Solar Receiver (DSSR) [1] presently being developed under a Department of Energy program. Not unexpectedly, the geometric requirements of a point focusing receiver and thermal requirements of the Stirling engine present unique problems requiring novel combustion and heat exchanger design integration.

The purpose of the DSSR program is to demonstrate the technology for a nonheat pipe Dish Stirling Solar Receiver with fossil fuel augmentation [1]. This would allow a P-40 United Stirling engine to be operated at constant power and speed under varying solar insolation levels. A diagram of the receiver system is provided in Fig. 1. The DSSR is designed to operate on a point focusing solar concentrator at a solar input of 76.5 kW_t. Maximum fossil fuel combustor input would be 67 kW_t with a 10:1 combustor turndown ratio required. The receiver is designed to operate in the hybrid (combustion) mode at all times; where combustor heat input will be at the maximum for zero solar input and the minimum (~ 10 percent max) at maximum solar input. Solar energy is transferred to the cylinder side of the 48 Stirling heater tubes which are embedded in the receiver body; energy is transferred to the regenerator side of the heater tubes by combustion gases provided by eight burner jets located circumferentially behind the receiver body. Thermal energy thus transferred is con-

verted to shaft power by the Stirling engine, and thence to electricity by a generator.

In order to evaluate the operational and heat-transfer characteristics of the proposed DSSR Combustor design prior to the fabrication of a prototype, a Combustor Test Program was conducted by the Jet Propulsion Laboratory and Fairchild Stratos Division. This paper presents the results of one aspect of that test program. Specifically, detailed heat-transfer measurements are reported for the combustor/heat-exchanger system characterized by a single row of closely spaced tubes in a swirling crossflow. For other aspects of the DSSR combustor test program, the reader is referred to reference [2].

DSSR Combustor and Heat Exchanger. The combustor is designed to deliver up to 67 kW_t to the Stirling engine utilizing natural gas as the fuel. The eight burner jets are located circumferentially around the heat-exchanger bank (Fig. 2). The jets fire tangentially into the annulus behind the heater bank at a maximum outlet velocity of approximately 30 m/s (100 ft/s). THey are designed to operate at 10 percent excess stoichiometric air at total flow rates up to 60 g/s (air + fuel). The air is preheated to 1030 K by a recuperator which would provide combustion gas temperatures of 2250 K assuming 20 percent flame losses. A burner detail is shown in Fig. 3.

The heat exchanger bank consists of 48 1.30 cm (0.512 in.) o.d. tubes with transverse pitchs of 1.41 cm (0.555 in.). The tube bank forms the frustrum of a cone with the smaller diameter of 27.9 cm (11 in.) and larger diameter of 40.6 cm (16 in.). The tubes swirl (or curve) through an arc of approximately 60 deg from minimum to maximum diameter such that the gap between tubes remains constant at 1.1 mm
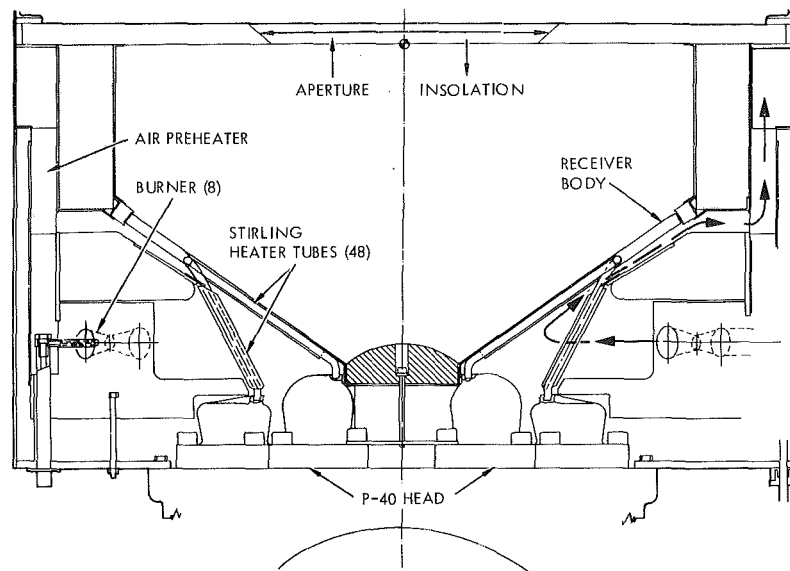

Fig. 1 Dish Stirling Solar Receiver

(0.043 in.) over the surface of the tube bank. A photograph of the tube bank utilized in the combustor test program is presented in Fig. 4; and a diagram showing relative tube diameter and spacing is given in Fig. 5. For the present application, Stirling engine tube-wall and working fluid (helium) operating temperatures will be approximately 1300 K. Thus for combustion gas temperatures of 2250 K, an average gas-to-tube heat-transfer coefficient of approximately 220 W/m²K (39 Btu/hr·ft²·°F) is required to transfer 67 kW$_t$ to the working fluid.

Fuel ignition is initially achieved utilizing spark igniters at the outlet of two of the jets. These igniters are also sensors whereby the fuel flow is automatically shut off if the flame extinguishes. Thus, for given combustion thermal requirements, metered air and fuel flows are supplied to the burner jets, premixed in the jet nozzle, and combusted (see the arrows in Fig. 1). The combustion gases enter the annular region, swirl around the tube bank, pass over the tubes and through the tube gaps; heat transfer to the Stirling working fluid (helium) being the result. Once past the tube bank, the combustion gases will transfer some additional heat to the

receiver body and then flow out through the gap behind the receiver body and enter the air preheater. The final products are exhausted to atmosphere at approximately 650 K.

Design Background. The combustor and heat exchanger system design utilized in the DSSR is based on the geometric configuration, total working fluid volume and thermal input requirements of the United Stirling P-40 engine. The eight burner combustor was designed to provide uniform combustion gases with a large swirl component; where estimates of flow characteristics for design purposes have been made utilizing potential flow theory. The flow field was assumed to be a sink superimposed upon a vortex for which the velocity potential and stream function for the irrotational, two-dimensional flow are:

$$\phi = -\frac{\dot{V}}{2\pi l}\ln r + \Gamma\theta/2\pi, \text{ and} \tag{1a}$$

$$\psi = -\frac{\dot{V}\theta}{2\pi l} - \frac{\Gamma}{2\pi}\ln r \tag{1b}$$

_____ **Nomenclature** _____

A_f = frontal area of the tube bank, m²

d = outside tube diameter, m

G_{max} = mass flow rate per-unit-area in the minimum free flow area between tubes, kg/m²s

$\bar{h}$ = local average heat-transfer coefficient along the tube length based on $(T_c - T_{s_n})$, W/m²K

$\bar{H}$ = average gas side heat-transfer coefficient to heater tubes based on $(T_c - \bar{T}_s)$, W/m²K

k_f = gas film thermal conductivity, W/mK

l = combustion chamber height, m

$\dot{m}$ = total mass flow rate, kg/s

Nu = Nusselt number, $\bar{H}d/k_f$, dimensionless

Pr = gas film Prandtl number, dimensionless

$\dot{Q}_W$ = total heat-transfer rate to water flow through tubes, W

r = radius of combustion chamber cross-section, m

Re_{max} = Reynolds number based on maximum velocity in the minimum free flow area between tubes and tube outside diameter, $G_{max}d/\mu_f$, dimensionless

s = transverse center-to-center tube spacing (pitch), m

T_A = temperature of preheated combustion air, K

T_c = combustion gas temperature, K

T_p = flue gas temperature, K

T_{s_n} = local tube wall temperature at the nth location along the tube length, K

$\bar{T}_s$ = average tube wall temperature, K

v_r = radial velocity component, m/s

v_θ = tangential velocity component, m/s

$\dot{V}$ = volumetric flow rate, m³/s

β = angle between the flow and radial directions, rad

Γ = vortex strength, m²/s

θ = turning angle in polar coordinates, rad

μ_f = gas film viscosity, Pa·s

ϕ = velocity potential

ψ = stream function
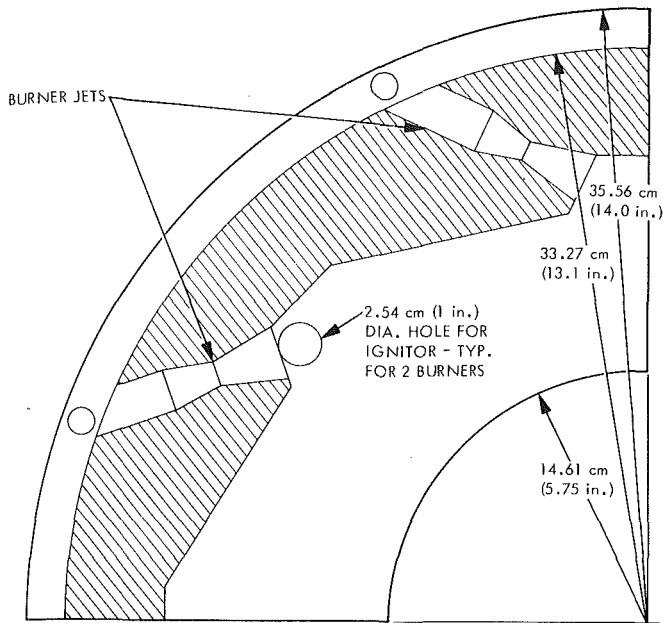
Fig. 2 Combustor quadrant cross section (plan view)

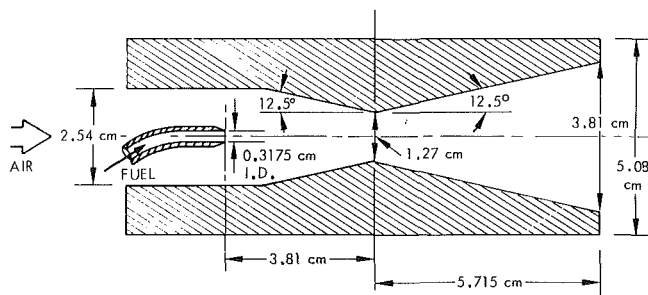Fig. 4 Combustor test rig heat-exchanger tube bank

Fig. 3 Burner detail

The resulting streamlines are spiral, and the tangent of the angle (β) between the flow and radial directions is:

$$\tan\beta = \frac{v_\theta}{v_r} = \frac{\Gamma}{V/l} \qquad (2)$$

For the present configuration, the vortex strength (Γ) was evaluated by using the burner outlet jet velocity. To obtain a conservative estimate, Γ was then reduced by approximately one-half to account for the finite number of jets and friction losses. The resulting swirl angle (β) is 76 deg, and if the vortex strength were again reduced by one-half, the resulting $\beta = 64$ deg. Thus, the estimated swirl angle of incidence upstream of the tube bank is large as indicated in Fig. 5; and β is relatively insensitive to the assumed vortex strength (Γ). Also, if the streamlines are determined from equation (1b), it can be shown that the flow traverses approximately one-fourth (90 deg) of the combustor circumference prior to entering the tube bank. This should allow adequate mixing of the combustion products for uniform heat transfer to the tube bank.

The DSSR heat exchanger consists of a single row of closely spaced curved tubes in a swirling crossflow as described previously. It is thus a special case of the general category of tubular heat exchangers in crossflow. This category of heat exchangers is widely used in industry and experimental data are available for a range of conditions and configurations. A review of such data is provided by McAdams [3], and later data are provided by Kays and London [4], and Zukauskas [5]. In general, data have been obtained for banks of straight tubes containing several rows that are perpendicular to the direction of crossflow. Local and average convective heat-transfer coefficients are determined for different transverse
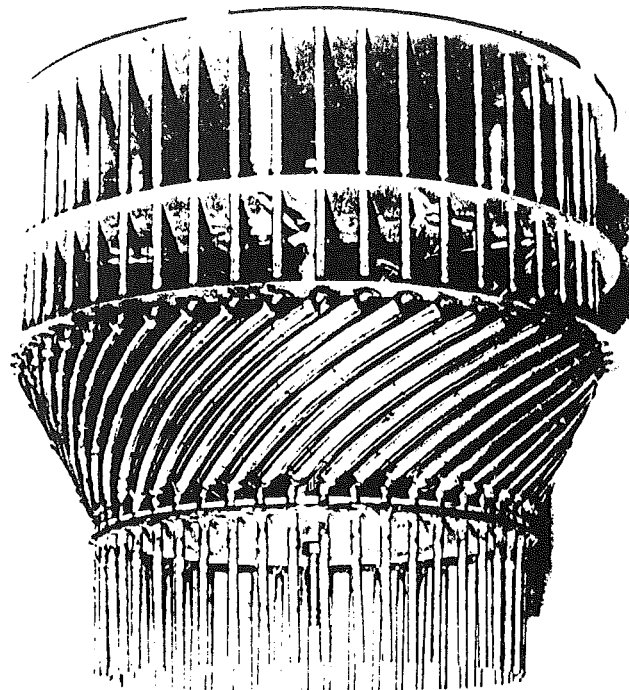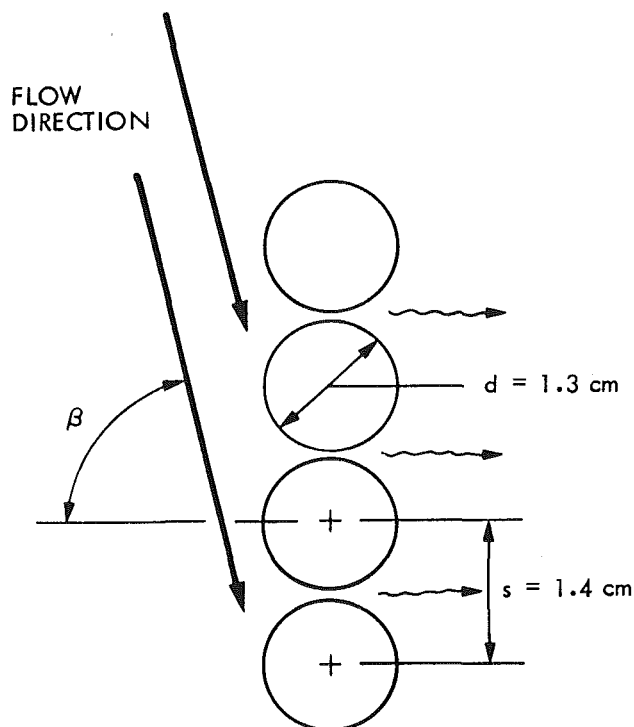

Fig. 5 Tube and flow configuration

and longitudinal tube spacings. The results are usually correlated with a Reynolds number referenced to tube or hydraulic diameter and flow velocity in the minimum [3-5] or average [6, 7] free cross-sectional area. For small spanwise spacing ($s/d < 1.25$), empirically determined reference velocities have also been suggested [6].

For single rows of tubes, a limited amount of data are available, the work of Ward and Jewad [6] being an important exception. They reported measurements of heat transfer to a flowing air stream from a single electrically heated tube in a row of closely spaced tubes. The tubes were
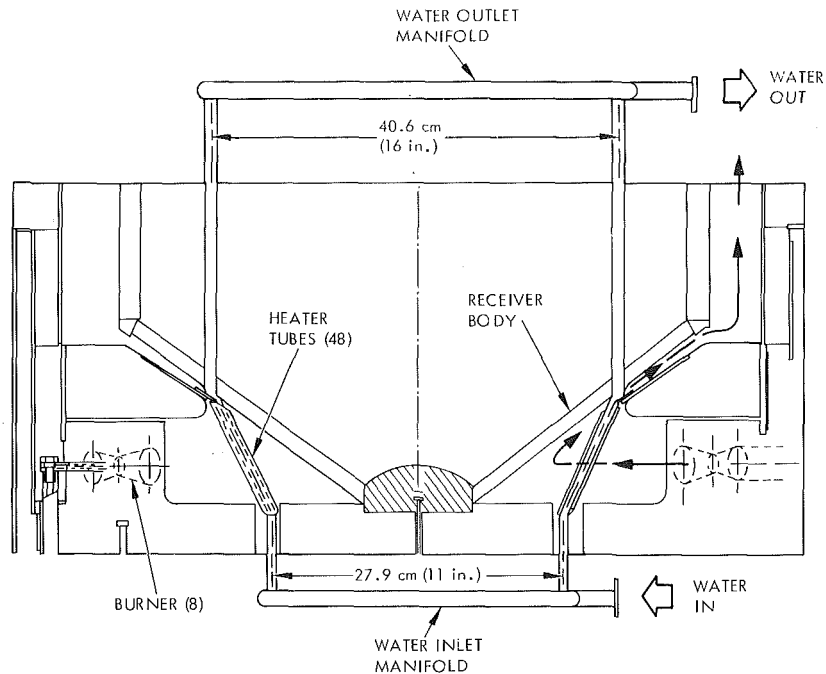
Fig. 6 DSSR combustor test rig

straight and aligned perpendicular to the flow, where average and local heat-transfer coefficients are presented for a range of transverse tube spacings ($1.083 \leqslant s/d \leqslant 1.377$). Average Nusselt numbers are correlated with Reynolds numbers based upon velocity in the average free cross-sectional area. For the smallest tube spacings ($s/d < 1.176$), an empirically determined reference velocity is employed. The data span a range of Reynolds numbers from approximately 10^3 to 2×10^4. However, these data do not cover the Reynolds number range of interest in this investigation and no data are available in the literature for the complex flow geometries studied in this program. Also, previous investigations have usually been conducted with gas-to-tube wall ΔT's of 10-20 K, while in the present application corresponding ΔT's are of the order of 1000 K.

In view of the previously mentioned information gaps, the DSSR heat-exchanger performance required detailed experimental evaluation and analysis before a prototype could be fabricated. This paper describes the experimental program designed to meet these needs, as well as provide new information on high temperature heat transfer in complex combustion systems.

Experimental Setup. The combustor test program was conducted utilizing the modified DSSR design shown in Fig. 6 without the Stirling engine. The test rig combustor utilizing natural gas and combustion gas heat-exchanger configuration is identical to the actual DSSR design. The heat-transfer fluid utilized in the test program is water which enters the inlet manifold and flows through the 48 heat-exchanger tubes. The tubes extend through a blank receiver body to the outlet manifold where the water flows out. The combustor body is fabricated from a refractory material and the heat-exchanger tubes from 310 stainless steel; the tube wall thickness is 0.47 cm (0.184 in.). The gap between tubes was precisely maintained by spacer wires wrapped around alternate tubes as shown in Fig. 4. Combustion air was supplied by a compressed air system and was preheated electrically upstream of the burner jets. The combustion products were exhausted directly to atmosphere, as no recuperator was incorporated in the test rig. Also, the water utilized as the heat-transfer fluid was preheated to prevent condensation of water vapor from the combustion products on the tube walls.

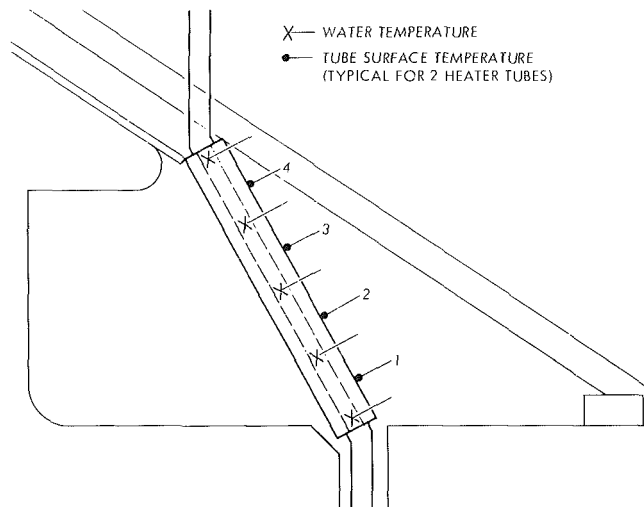Temperature measurements used in heat-transfer

Fig. 7 DSSR combustor heater tube instrumentation

calculations include: inlet and outlet manifold water temperatures, local water temperatures in the tubes, local tube surface temperatures, combustion gas temperatures, and exhaust product gas temperature. The local water and tube wall temperatures were measured along two tubes as shown in Fig. 7, where one tube was located midway between burners and the second located nine tubes in a counterclockwise direction away from the first. The tube surface thermocouples were spot welded to the tube surface to ensure good contact with the surface. These thermocouples thus measured the actual tube surface temperature and were not subject to radiation effects. Supplemental water temperatures were measured at the inlet and outlet of two tubes located 180 deg away from the primary (instrumented) tubes. Flame temperatures were measured at two positions in the combustor. Also, receiver body surface temperatures were monitored to insure integrity of the materials. Chromel-Alumel (type K) thermocouples were utilized for temperature measurements, except for combustion gas (flame) temperatures where Platinum versus Platinum-10 percent Rhodium (type R) thermocouples were used.

Table 1 DSSR Combustor Experimental Conditions

Operating level %*	T_A K	Excess stoichiometric air %	$\dot{Q}_W$ kW	$\bar{H}$ $\dfrac{W}{m^2 K}$	T_c K	T_p K	$\tilde{T}_s$ K
13.0	1035	11.75	18.7	51.0	1520	530	360
30.4	1035	11.75	36.6	91.2	1710	690	450
40.8	1035	11.0	45.9	114.0	1760	740	490
50.4	975	11.75	51.9	128.0	1810	740	530
10.0	810	11.75	18.5	51.4	1480	500	360
20.1	810	11.75	25.1	65.9	1590	580	390
30.0	810	11.75	35.6	90.7	1680	660	440
40.0	810	11.5	45.5	113.0	1760	740	490
50.4	810	11.75	46.9	119.0	1750	740	500
63.0	810	11.0	57.4	142.0	1820	800	540
71.6	810	11.75	66.0	162.0	1860	860	580
82.5	810	13.0	73.3	181.0	1890	930	610
92.0	755	11.5	78.5	198.0	1910	960	660

*Percent of predicted fuel input required with 10 percent excess air preheated to 1035 K for 67 kW$_t$ input to Stirling engine. Fuel plus air mass flow rate at 100 percent = 55.5 g/s.

Product (exhaust) gas compositions were monitored continuously to insure that correct air/fuel ratios were maintained and complete combustion occurred. These measurements consisted of: (a) oxygen concentration, and (b) percent combustibles equivalent to a mixture of equal parts hydrogen and carbon monoxide. At the measured flame temperatures, dissociation of the combustion products was estimated to be negligible.

Results and Discussion

A summary of experimental conditions and combustor performance is presented in Table 1. Heat-transfer data are then presented in nondimensional form in Figs. 8 and 9. Average gas side heat-transfer coefficients, $\bar{H}$, were calculated based on total heat transfer to the tube bank, total tube bank surface area of 0.318 m², and temperature difference, $T_c - \bar{T}_s$. Gas temperatures, T_c, were taken to be the average of the two combustion gas thermocouples. Characteristic tube surface temperatures $\bar{T}_s$ were taken to be an average of the local measurements (Fig. 7). This temperature $\bar{T}_s$ varied from the (extrapolated) temperature at the midpoint of the tube by less than approximately 15 K. To calculate the average heat-transfer coefficients along the length of the tube, h, local water temperature differences and tube surface temperatures were utilized as indicated in Fig. 7. The data for each point along the length of the tube in Fig. 9 represent an average of measurements from the four instrumented tubes in the heat exchanger. The tube surface and water temperatures utilized in these calculations are tabulated in reference [2]. Uncertainty in the resulting Nusselt number data based on the average gas side heat-transfer coefficient was estimated by the technique described by Hetenyi [8]. The probable error is within ±8 percent at the highest firing rates and ±12 percent at the lower firing rates.

During the experiments, outlet bulk-water temperatures were maintained below the saturation temperatures, even at the highest heat-transfer rate, so that the energy transferred to the water increased its measurable sensible heat. At firing rates of 40 percent and higher, average tube wall inner-surface temperatures, determined from the heat conduction equation by using the measured tube wall outer surface temperatures and the total heat transfer to each tube, were above the saturation temperature of water. Undoubtedly some surface boiling occurred, but subsequent condensation took place because of the significant amount of water subcooling. Good mixing occurred in the straight tubes and manifold section (Fig. 6) between the heater tubes outlets and the location in the manifold outlet where water temperatures were measured. Because of the presence of the thermocouples in the water
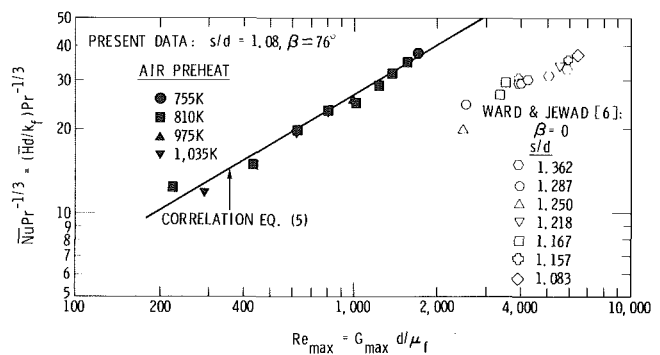

Fig. 8 Average gas side heat-transfer coefficients

flow, mixing was also improved in the flow through those heater tubes which were instrumented with water thermocouples, and for which semilocal gas side heat-transfer coefficients were determined. Also, the conduction loss along the tubes was negligible.

Due to the complex geometry of the flow downstream of the heater tubes, a meaningful mixed-mean downstream gas temperature could not be obtained. Also, final exhaust gas temperatures could not be used for heat balances due to heat losses to the surrounds as the exhaust gases flowed from the region downstream of the tubes to the exhaust outlet. Thus, no gas side heat balances could be obtained for comparison with water side heat transfer. However, the authors believe that the measurement of the increase in bulk-water sensible heat provides an accurate measure of the heat transfer as described. This is supported by the local heat-transfer data which is consistent with the data based on the total heat transferred to the water, as presented later in this section.

In the present data, Reynolds number is based on the maximum velocity in the minimum free flow area between tubes and is calculated using the definitions:

$$Re_{max} = \frac{(G_{max})d}{\mu_f} \qquad (3)$$

and

$$G_{max} = \frac{\dot{m}}{A_f} \frac{s}{(s-d)} \qquad (4)$$

where $\dot{m}$ is the total mass flow rate, and A_f is the frontal area of the tube bank. Film temperatures for Reynolds and Nusselt numbers were taken to be the midpoint between the combustion gas and tube surface temperatures, and transport properties for nitrogen were used. Regarding transport properties, the viscosity of the actual gas mixture was

estimated by the technique of Andrussow [9] and variations from the viscosity of pure nitrogen were found to be less than 5 percent for the temperature range of interest. Also, the heat-transfer coefficients reported here include a radiation component. However, estimates of the contribution of radiation from the refractory to the tube bank have been carried out and the results show that radiation contributes less than 5 percent of the heat transfer at the highest firing rates and up to 10 percent of the heat transfer at the lowest firing rates. Radiation from the combustion gases to the tube bank was estimated to be negligible in comparison.

Figure 8 presents heat-transfer data for the four air preheat conditions and the range of Reynolds numbers (firing rates) studied. The data are well correlated by the relation

$$\overline{Nu} = 0.42\,(Re_{max})^{0.6}Pr^{1/3} \qquad (5)$$

which is indicated by the solid line on the figure. Also shown are data from Ward and Jewad [6] for a range of tube spacings. Note that the Ward and Jewad data were correlated using a reference velocity based on the average free cross-sectional area [7]. Their data have been plotted here using the Reynolds number defined by equation (3) with the result being a near overlap of the two sets of data at the higher Reynolds numbers. As indicated, the present data show significantly enhanced heat-transfer characteristics for the DSSR heat-exchanger tube bank when compared to the trend of the data for a perpendicular row of straight tubes, i.e., $\beta = 0$. While part of this enhancement is due to radiation, the majority is presumed due to the large swirl component in the flow which leads to the complex flow pattern incident on the tube bank. In this situation, the superimposed tangential velocity component may act to substantially increase local heat-transfer coefficients on the front side of the tubes, thereby

increasing the average gas side heat transfer coefficient $(\bar{H})$. The tubes were also inclined to the flow transversely (Fig. 7) and curved (Fig. 4), so that the flow field around the tubes was undoubtedly very complex.

It is possible that the measured enhancement may have also been due to other differences between the two experiments.
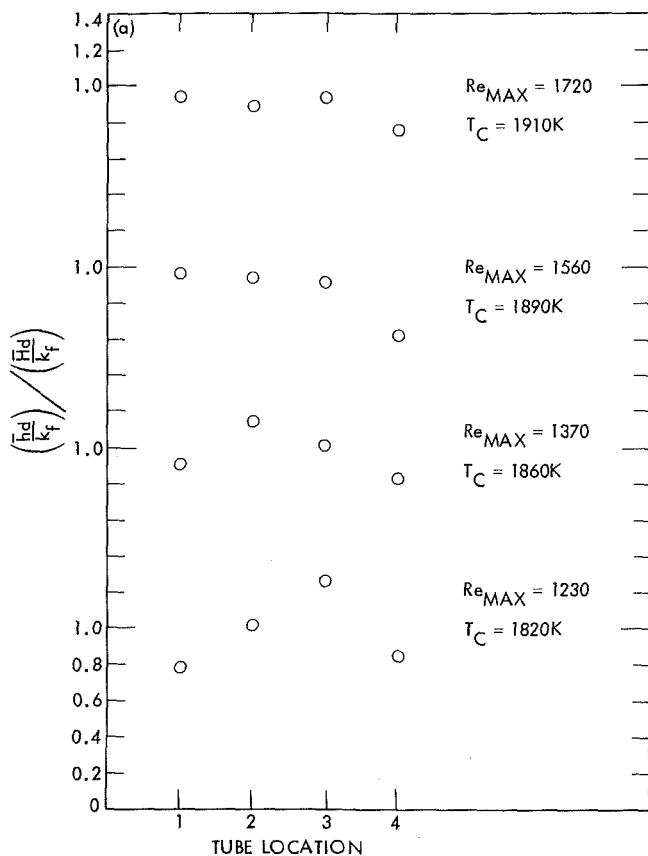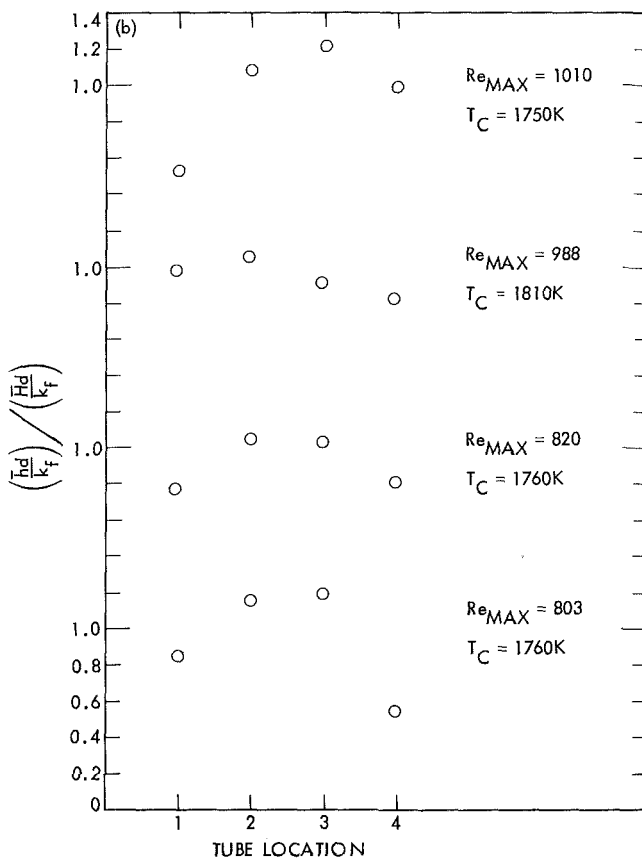

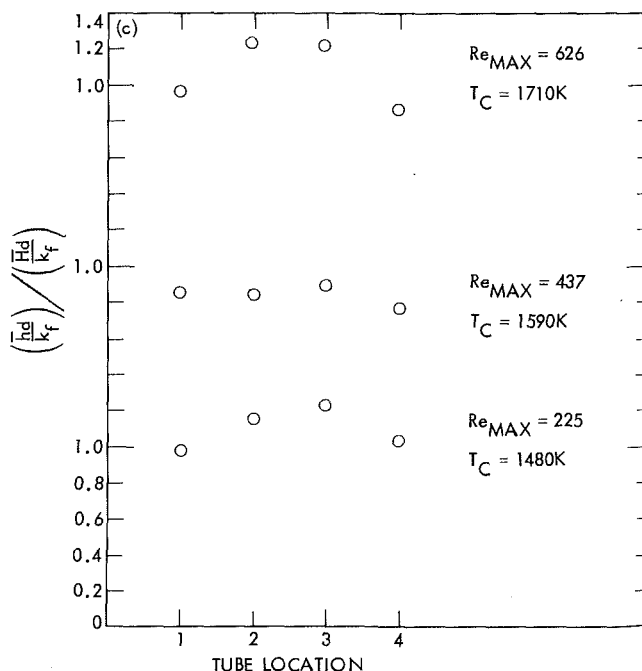Fig. 9(b) Re_max = 803-1010

Fig. 9(a) Re_max = 1230-1720

Fig. 9(c) Re_max = 225-626

Fig. 9 Heat-transfer coefficients along the tube length

Different turbulence intensities would have some effect, however, the complexity of the flow and severity of the environment prevented the measurement of turbulence for comparison with Ward and Jewad's measured value of 0.8 percent. Also, Ward and Jewad used low temperature heating of the gas in contrast to high temperature cooling; they used a *single* heated cylinder while all of the tubes in the present study were active and the tube surface thermal boundary conditions were not the same. However, little can be said of a definitive nature regarding such effects, and it is unlikely that they would account for the magnitude of the observed enhancement in heat transfer.

Figure 9 shows the variation of heat transfer coefficients along the tube length normalized by the average gas side heat-transfer coefficient ($\bar{H}$) and for a range of Reynolds numbers. In general, the data show some variations along the length of the tube where the profile exhibiting a peak near the middle was observed most frequently. By referring to Figs. 7 and 8, the variation of $\bar{h}$ along the tube length can also be interpreted as a variation in local Reynolds number. Thus, these data give an indication of local mass flux nonuniformity along the tube length. This is probably due to flow turning effects near the ends of the tubes at the upper and lower surfaces of the combustor.

Finally, utilizing the data in Fig. 8, combustor performance for the actual operating conditions of the Stirling engine can be estimated. Operating at the design 100 percent (maximum) firing rate with P-40 engine tube wall temperatures of approximately 1300K; and assuming combustion gas temperatures of 2150K, the resulting heat-transfer coefficient ($\bar{H}$) would be 248 W/m^{2}K (44 Btu/hr·ft^2·°F) and total energy transfer would be approximately 67 kW$_t$. Thus it appears that design specifications can be met with the present DSSR combustor/heat exchanger configuration.

Conclusions

An experimental program to investigate the heat-transfer characteristics of a combustor and heat exchanger system design for a hybrid solar receiver (DSSR) has been conducted. The design is characterized by a single row of closely spaced curved tubes in a swirling crossflow of high temperature combustion gases. Average gas side heat-transfer coefficients and semilocal heat-transfer coefficients along the lengths of the tubes were obtained. The results show significantly enhanced heat-transfer characteristics for the DSSR heat exchanger when compared to similar data for closely spaced tubes perpendicular to crossflow. Also, some variation in heat transfer along the tubes was observed presumably due to flow nonuniformity. These data provide new information on heat transfer to tubes in crossflow that can be achieved in a high temperature combustion system when complex geometries such as the one described here are utilized. Finally, it was concluded that the present DSSR combustor/heat exchanger meets design specifications such that prototype fabrication could proceed.

References

1 Haglund, R. and Tatge, R. "Dish Stirling Solar Receiver (DSSR)," *3rd Semi-Annual Advanced Technology Meeting: A Review of Advanced Solar Thermal Power Systems (Meeting Abstracts)*, Long Beach, Calif., U.S. Department of Energy, June 1979, pp. 20–28.

2 Bankston, C. P. and Back, L. H., "DSSR Combustor Test Program," Jet Propulsion Laboratory Publication No. 81-23, California Institute of Technology, Pasadena, Calif., Aug. 15, 1981.

3 McAdams, W. H., *Heat Transmission*, 3rd ed., McGraw-Hill, New York, 1954, pp. 258–276.

4 Kays, W. M. and London, A. L., *Compact Heat Exchangers*, 2nd ed., McGraw-Hill, New York, Ch. 7 and 10, 1964.

5 Zukauskas, A., "Heat Transfer from Tubes in Crossflow", in *Advances in Heat Transfer*, Vol. 8, edited by J. P. Hartnett and T. F. Irvine, Jr., Academic Press, New York, 1972, pp. 93–160.

6 Ward, J. and Jewad, M. A., "Local and Average Heat Transfer Associated with a Single Row of Closely-Spaced Tubes in Crossflow," *Heat Transfer 1978*, Vol. 4, Hemisphere Publishing Corporation, New York, 1978, pp. 273–278.

7 Perkins, H. C., Jr. and Leppert, G., "Forced Convection Heat Transfer From a Uniformly Heated Cylinder," JOURNAL OF HEAT TRANSFER, Vol. 84, 1962, pp. 257–263.

8 Hetenyi, M., "The Precision of Measurements", in *Handbook of Experimental Stress Analysis*, edited by M. Hetenyi, John Wiley and Sons, Inc., New York, 1950, pp. 1046–1060.

9 Andrussow, L., "Diffusion, Viscosity and Conductivity of Gases," in *Progress in International Research on Thermodynamic and Transport Properties*, edited by J. F. Masi and D. H. Tsai, Academic Press, New York, 1962, pp. 279–287.

Transient Heat-Flux Measurements in the Combustion Chamber of a Spark-Ignition Engine

A. C. Alkidas
Mem. ASME

J. P. Myers
Mem. ASME

Engine Research Department,
General Motors Research Laboratories,
Warren, Mich. 48090

Heat-flux measurements were obtained at several locations on the cylinder head and liner of a four-stroke, single-cylinder, spark-ignition engine. The variations of heat transfer with air-fuel ratio and volumetric efficiency were investigated. The magnitude of the heat flux was found to be highest at near-stoichiometric composition, whereas at either leaner or richer composition the heat flux decreased. An increase in volumetric efficiency from 40 to 60 percent resulted in an increase in peak heat flux of about 30 percent. The largest cycle-to-cycle variation in the measured heat flux occurred at the time of the initial high rate of heat flux. This is related to the cycle-to-cycle variation of flame propagation in the combustion chamber. Finally, the calculated amount of heat transferred to the walls of the combustion chamber during the closed portion of the engine cycle (intake valve closing to exhaust valve opening) agreed with the corresponding values obtained from the heat-flux measurements.

Introduction

The process of transient heat transfer in the combustion chamber of spark-ignition engines has not been adequately studied experimentally, although its importance in combustion simulations and analyses is well recognized [1, 2].

Past studies of transient heat transfer in spark-ignition engines include those of Overbye et al. [3], Oguri [4], and Alkidas [5]. Overbye et al. [3] measured the heat flux at several positions on the cylinder head of a CFR engine. Tests were performed at near-stoichiometric air-fuel ratio and an engine speed of 830 r/min. The effects of intake manifold pressure (supercharging), turbulence, and wall deposits on surface heat flux were investigated. Oguri [4] measured the transient heat flux at one position on the piston of a spark-ignition engine. The only operational parameter of the engine that was varied was load. Recently Alkidas [5] measured the transient heat flux at four locations on the cylinder head of a spark-ignition engine. The influence of engine speed and spark timing on the heat flux was examined. This study showed that the initial rate of increase of the heat flux at each position of measurement correlated with the calculated time of flame arrival. In addition, it was found that the measured heat flux varied considerably with position of measurement.

The presently available experimental data on transient heat-transfer processes in spark-ignition engines is limited. The objective of this investigation was to complement the earlier study [5] by investigating the influence of air-fuel ratio and volumetric efficiency (load) on heat transfer in the combustion chamber of a spark-ignition engine.

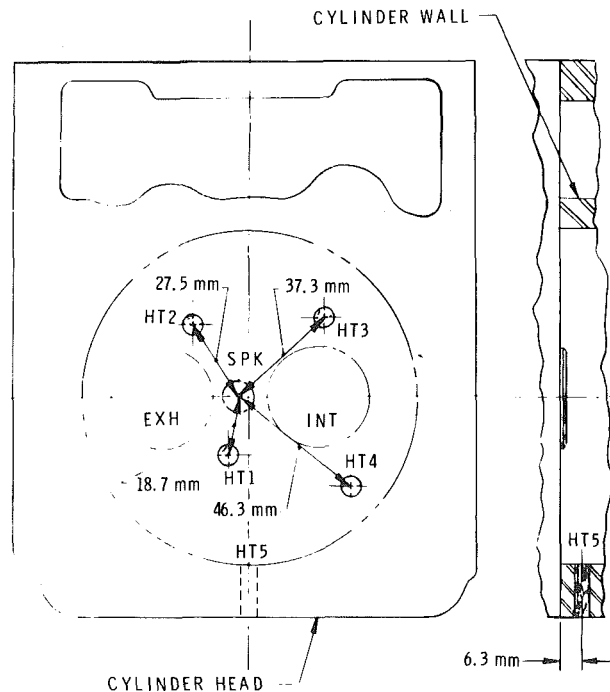It is a usual practice in heat-transfer studies in engines to

Fig. 1 Location of heat flux probes

base the heat-flux calculations on surface temperature measurements averaged over a large number of cycles. In this study the cycle-to-cycle variation of measured surface temperature histories and the resultant cycle-to-cycle variations of the heat flux have also been examined.

Copyright © 1982 by ASME

Apparatus and Procedure

Engine. The engine was a four-stroke, 6.5-L, V-8, spark-ignition engine modified for operation on one cylinder. The combustion chamber was disk-shaped with a centrally located spark plug. The intake port was a production design and had low swirl. The principal geometric characteristics of the engine are shown in Table 1.

Table 1 Engine Description

Displacement (L)	0.82
Bore (mm)	104.7
Stroke (mm)	95.3
Compression ratio	8.56
Inlet valve opening (*CA*)	30 *BTDC*
Inlet valve closing (*CA*)	63 *ABDC*
Exhaust valve opening (*CA*)	77 *BBDC*
Exhaust valve closing (*CA*)	50 *ATDC*

Heat-Flux Probes. Figure 1 shows the locations of the five heat-flux probes. Four of the probes were installed on the cylinder head. The distances from the spark plug to these probes, HT1, HT2, HT3 and HT4, are 18.7, 27.5, 37.3 and 46.3 mm, respectively. THe fifth heat-flux probe, designated HT5, was located on the thrust side of the cylinder and 6.3 mm below the surface of the head.

These heat-flux probes were made from commercially available surface thermocouples that have a response time of the order of 10 μs. Each probe utilized a second reference thermocouple ("in-depth" thermocouple) at a known distance (δ) from the tip of the probe (surface thermocouple) to measure the steady-state component of the heat flux.

The design of the heat-flux probes used on the cylinder head is shown in Fig. 2. A detailed description is given in reference [5]. The heat-flux probe used on the cylinder wall, HT5, was adapted from a Bendersky-type surface thermocouple [6] frequently used in heat-transfer studies in engines [3, 7, 8].

Measurements and Analyses. At each operating condition of the engine, after the engine was completely warmed and operating at steady state, the temporal variations of pressure and surface temperature at 4 locations in the combustion chamber (3 on the cylinder head and 1 on the cylinder wall)[1] were recorded for 198 consecutive cycles. From the transient surface temperature measurements at each location and the corresponding steady-state "in-depth" thermocouple measurement at the location, the variation of heat flux during the engine cycle at each location was calculated. The

---

[1] Due to speed limitations of the data acquisition system, only four surface-temperature measurements could be recorded simultaneously.
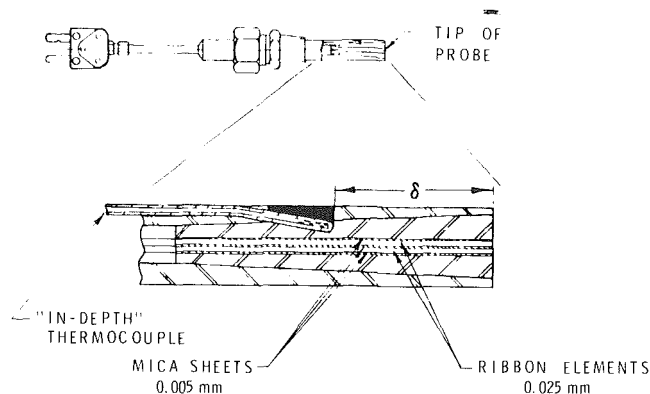

Fig. 2   Design of heat-flux probe used on the cylinder head

Table 2   Test Parameters

Air-fuel ratio	11.5-18
Volumetric efficiency[2] (percent)	30-60
Speed (r/min)	1500
Spark timing	MBT
Intake air temperature (K)	306
Coolant temperature (K)	357
Oil temperature (K)	364

technique of calculating the heat flux from surface temperature measurements is well documented [3, 8]. Very briefly, the measured surface temperature during an engine cycle is represented by a Fourier series. The heat flux is then calculated from the known solution of the one-dimensional, unsteady, heat-conduction equation with a periodic surface-temperature boundary condition. Errors associated with the measurement of heat flux are discussed in the Appendix.

In general, the heat flux was derived from surface-temperature data averaged over a large number of consecutive cycles (in this case 198 cycles). This is the usual practice in heat-transfer studies in engines. However, in order to examine the cycle-to-cycle variations of the heat flux, calculations based on surface-temperature data during individual cycles were also performed.

Test Conditions. Propane was used as the engine fuel. The stoichiometric air-fuel ratio is 15.58. The operating parameters of the engine varied and were air-fuel ratio, volumetric efficiency and engine speed. In all tests the spark timing was kept at minimum advance for best torque (*MBT*). The baseline condition was: engine speed = 1500 r/min, air-fuel ratio = 18, and volumetric efficiency = 40 percent. The controlled engine parameters and their values are listed in Table 2.

---

[2] Defined as the ratio of actual mass of air supplied to the cylinder per cycle to the theoretical mass of air necessary to fill the displacement volume at 288 K and 101 kPa.

———————— **Nomenclature** ————————

$A(\theta)$ = surface area of the combustion chamber at θ, m^2
A_{CL} = surface area of the combustion chamber at TDC, m^2
ABDC = after bottom dead center
ATDC = after top dead center
A/F = air-fuel ratio
BBDC = before bottom dead center
BTDC = before top dead center
c = specific heat of probe material, J/kgK
CA = crank angle, deg
D = cylinder bore diameter, m
K = thermal conductivity of probe material, W/mK

L = connecting rod length, m
m_b = burned mass of fuel, kg
MBT = minimum advance for best torque
P = cylinder pressure, Pa
P_{MAX} = peak gas pressure, kPa
$q(\theta)$ = surface heat flux at θ, W/m^2
Q_{12} = heat transfer to the combustion chamber surface, W
R = crank radius, m
T_{MAX} = peak gas temperature, K
TDC = top dead center
$U_1 U_2$ = gas internal energy, W

V = combustion chamber volume, m^3
VE = volumetric efficiency (defined in Table 2), percent
W_{12} = work done, W
ΔH = heat of combustion per unit mass of fuel, W/kg
λ = ratio of crank radius to connecting rod length
θ = crank angle, rad
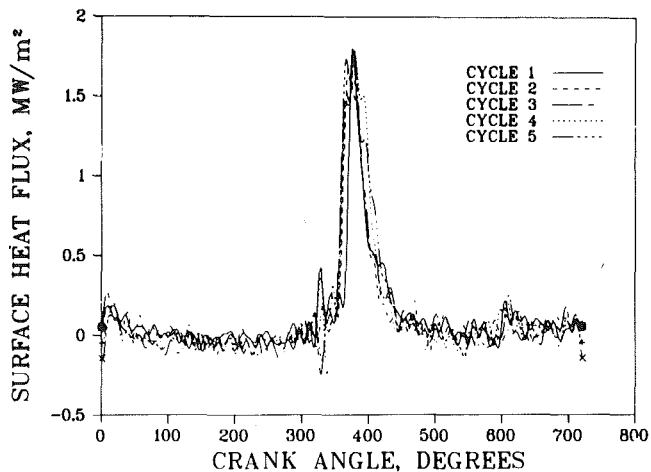ρ = density of probe material, kg/m^3

Fig. 3 Heat-flux histories of five consecutive cycles at location HT1 (baseline condition)

Fig. 5 Surface-temperature histories near *TDC* for five consecutive cycles and the 198-cycle average at location HT1 (baseline condition)

Fig. 4 Heat-flux histories near *TDC* for five consecutive cycles and the 198-cycle average at location HT1 (baseline condition)

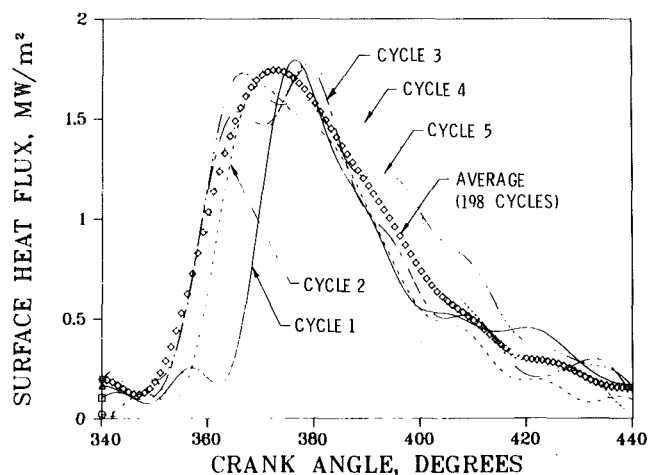**Fig. 6** Surface-temperature histories near *TDC* for five consecutive cycles and the 198-cycle average at location HT5 (baseline condition)

Results and Discussion

Cycle-to-Cycle Variations. Figure 3 shows the heat-flux histories of 5 consecutive cycles measured at position HT1. It is evident that there is considerable cycle-to-cycle variation of the heat flux. To demonstrate clearly the magnitude of this variation, Fig. 4 shows the above measurements in the region of the compression and expansion strokes near *TDC*. This is the region of most interest in heat-transfer studies because of the high heat-transfer rates caused by the combustion process. On the same figure, heat-flux data derived from surface-temperature measurements averaged over 198 cycles are superimposed. Comparison of the heat-flux histories at each engine cycle shows that the largest cycle-to-cycle variation occurs at the time of the initial high rate of increase of the heat flux. The cycle-to-cycle variation of the peak heat flux is relatively small, as is the variation of the heat flux after peak heat flux.

The initial high rate of increase of the heat flux is caused by the arrival of the flame at the location of measurement. Thus it may be concluded that the cycle-to-cycle variation of the heat flux is primarily[3] caused by the cycle-to-cycle variation of flame propagation. This, in turn, is believed to be due to mixture velocity variations that exist in the cylinder near the spark plug at the time of ignition [10].

Figures 5 and 6 show the temporal variations of surface

temperature for five consecutive cycles at combustion chamber locations HT1 and HT5, respectively. The surface-temperature data of Fig. 5 were utilized to obtain the heat-flux variations shown in Fig. 4. On these figures the corresponding values of the surface temperature averaged over 198 cycles were superimposed. The test conditions associated with these figures were engine speed = 150 r/min, air-fuel ratio = 18, and volumetric efficiency = 40 percent.

Comparing Figs. 5 and 6, it appears that the cycle-to-cycle variation of the time of the initial high rate of increase of the surface temperature increases with increasing distance from the spark plug to the location of measurement. The largest cycle-to-cycle variation is at HT5 and the smallest is at HT1. This is in agreement with Curry [11]. He found, using ionization gaps, that the cycle-to-cycle variation of the flame propagation increases with the distance from the spark plug.

Influence of Volumetric Efficiency and Air-Fuel Ratio. In this and subsequent sections the term "heat flux" is defined as the heat flux calculated from surface-temperature measurements averaged over 198 consecutive cycles.

Figure 7 shows the temporal variations of the heat flux during the engine cycle at locations HT1 and HT2 on the cylinder head and at location HT5 on the cylinder liner. The test conditions correspond to the baseline conditions, i.e., engine speed = 1500 r/min, air-fuel ratio = 18, and volumetric efficiency = 40 percent.

As expected, the initial high rate of increase of the heat flux, which as discussed earlier is associated with the arrival

---

[3] Significant cycle-to-cycle variations of heat flux were observed in a motored engine [9], which indicates that combustion is not the only source of these variations.
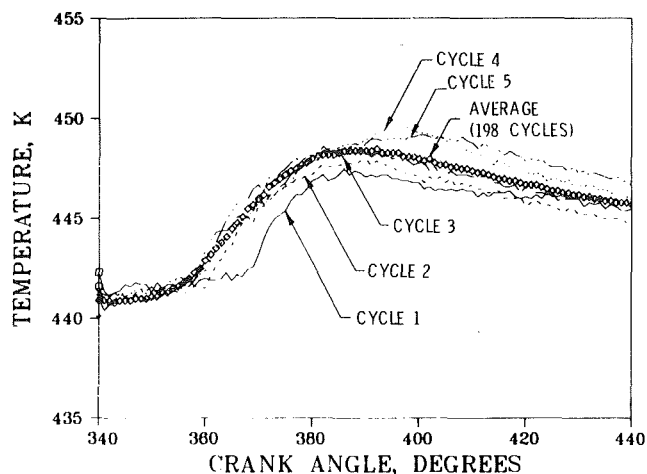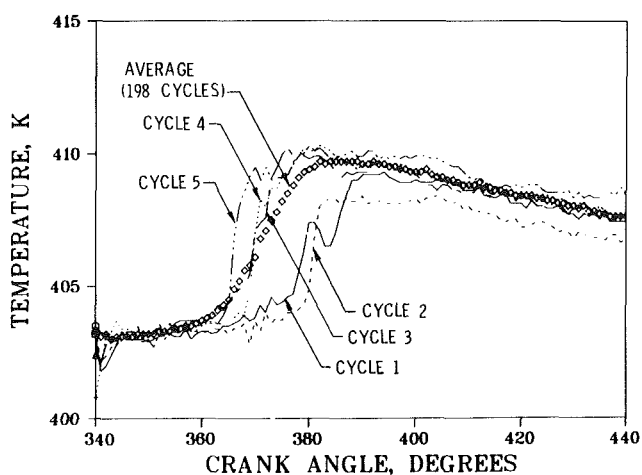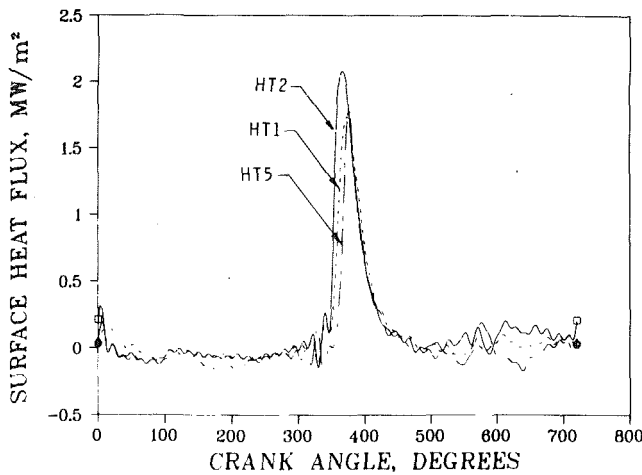
Fig. 7 Heat-flux histories for three different locations: HT1, HT2, and HT5 (baseline condition)

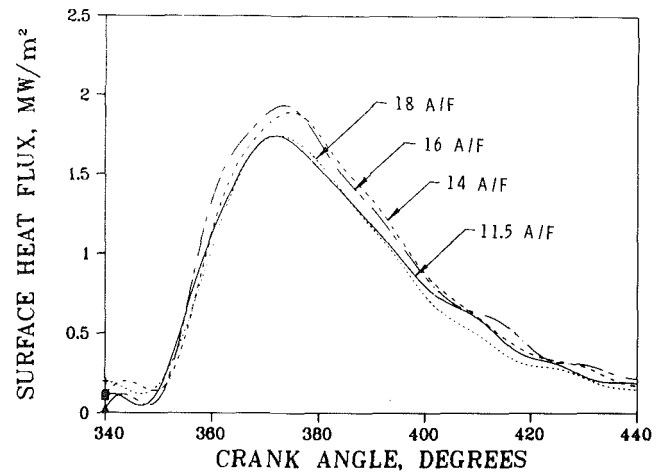Fig. 8 Effect of volumetric efficiency on heat-flux history at location HT1 (N = 1500 r/min, A/F = 18, MBT)

Fig. 9 Effect of air-fuel ratio on heat-flux history at location HT1 (N = 1500 r/min, volumetric efficiency = 40 percent, MBT)

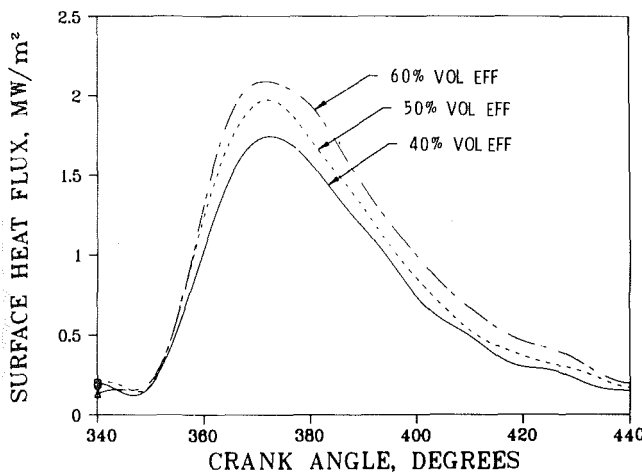**Table 3 Variations of Peak Pressure and Temperature with Air-Fuel Ratio and Volumetric Efficiency**

Engine speed = 1500 r/min
Spark setting: MBT

A/F	VE (%)	P_{MAX} (kPa)	T_{MAX} (K)
11.5	40	2574	2363
14	40	2648	2563
16	40	2543	2552
18	40	2363	2495
18	50	2925	2500
18	60	3581	2531

of the flame at the position of measurement, occurs later in the cycle for location HT5 than HT1 and HT2. Furthermore, the magnitude of the peak heat flux varies with the position of measurement. Spatial variations of the heat flux on the combustion chamber of reciprocating engines have also been observed by Overbye et al. [3] and Alkidas [5] in spark-ignition engines, and by Annand and Ma [12], LeFeuvre et al. [7], and Whitehouse [13] in diesel engines.

The effect of volumetric efficiency on the heat-flux histories at location HT1 on the cylinder head is shown in Fig. 8. The heat flux increases with increasing volumetric efficiency. The effect of volumetric efficiency on the heat flux is more pronounced at "near peak heat flux" conditions. An increase in volumetric efficiency from 40 to 60 percent resulted in increases in the peak heat flux of 19 percent. Similar trends were also observed for other measurement locations. At location HT5, the corresponding increase in peak heat flux with volumetric efficiency was of the order of 30 percent. The increase in the heat flux with increasing volumetric efficiency is primarily attributed to the increase of the convective heat-transfer coefficient because of the resulting increase in gas density with volumetric efficiency.

The influence of air-fuel ratio on the heat-flux history at location HT1 is shown in Fig. 9. Over the relatively wide range of air-fuel ratios studied, the heat-flux history is not strongly influenced by air-fuel ratio. It appears, however, that the peak heat flux is highest at near-stoichiometric composition, whereas at either leaner or richer compositions the peak heat flux decreases. This behavior is caused by the

similar variation of the burned-gas temperature with air-fuel ratio. If dissociation were not present, the highest burned gas temperature would occur at the stoichiometric mixture composition, whereas at either richer or leaner mixture composition the excess fuel or oxidant, whichever may be the case, reduces this temperature. Due to the presence of dissociation, however, and the influence of the specific heats of burned-gas species, the highest burned-gas temperature occurs on the rich side at near-stoichiometric composition.

Table 3 shows the variations of peak pressure and temperature with air-fuel ratio and volumetric efficiency. The peak temperatures were computed from a two-zone thermodynamic heat release analysis [14] that requires engine cylinder-pressure data as input. In agreement with the above discussion, Table 3 shows that the peak temperature varies considerably with air-fuel ratio; in contrast, volumetric efficiency has comparatively little effect on the peak temperature.

Net Heat Loss During Closed Portion of the Cycle. The amount of heat transferred to the combustion-chamber walls during the closed portion of the engine cycle (net heat loss) can be calculated [15, 16] by applying the integrated form of the first law of thermodynamics at the two end states, namely the closng of the inlet valve (state 1) and the opening of the exhaust valve (state 2). Assuming leakage is negligible, the amount of heat transferred to the walls during this interval is given by:

$$Q_{12} = W_{12} + U_2 - U_1 - m_b \, \Delta H \tag{1}$$

ΔH is the heat of combustion per unit mass of fuel, and m_b is the burned mass of fuel. U_1 and U_2 represent the internal energy of the mixture at the two end points. The work done, W_{12}, is obtained from experimental p $-$ t data by evaluating the integral

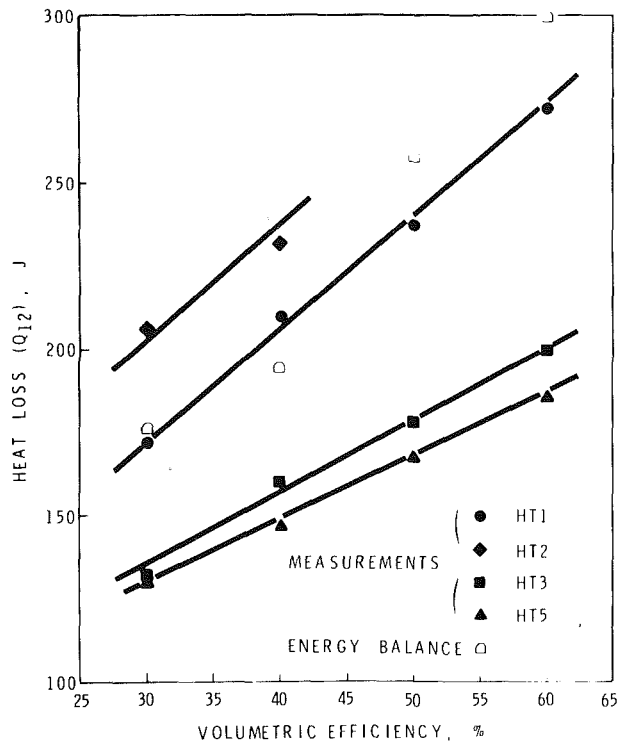$$W_{12} = \int_1^2 p \, dV \tag{2}$$

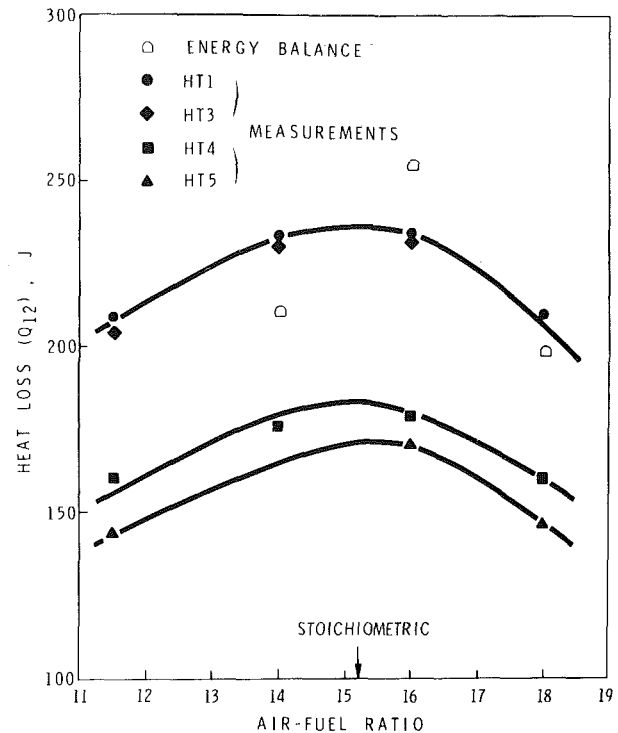Fig. 10 Effect of volumetric efficiency on net heat loss

Fig. 11 Effect of air-fuel ratio on net heat loss

The calculation of Q_{12} from equation (1) is straightforward provided that the amount of fuel burned is known. In practice, this is estimated from the mass of fuel-per-cycle present in the combustion chamber and exhaust gas analysis data.

If it is assumed, inaccurately, that the heat flux is uniform over the whole surface area of the combustion chamber, then the amount of heat transferred to the walls during the closed portion of the cycle can be evaluated from local transient heat-flux measurements. This heat is given by

$$Q_{12} = \int_1^2 q(\theta)A(\theta)d\theta \qquad (3)$$

where $q(\theta)$ is the magnitude of the heat flux at crankangle θ. The surface area of the combustion chamber $A(\theta)$ is given by

$$A(\theta) = A_{CL} + \pi DR[1 - \cos\theta + \frac{1}{\lambda}(1 - \sqrt{1 - \lambda^2 \, som^2 \theta})] \qquad (4)$$

where

$$\lambda = \frac{R}{L}$$

A_{CL} is the surface area of the combustion chamber at TDC, D is the bore diameter of the cylinder, R is the crank radius and L is the length of the connecting rod.

Figures 10 and 11 show net heat losses estimated from heat-flux measurements at different locations on the combustion chamber as functions of volumetric efficiency and air-fuel ratio, respectively. On these plots, the corresponding values derived from application of the first law of thermodynamics (labeled "energy balance") were superimposed.

Both figures demonstrate effectively the considerable spatial variation in heat flux that exists in the combustion chamber of a spark-ignition engine. The magnitudes of the heat losses computed from measurements at locations on the cylinder head near the center of symmetry of the cylinder, i.e., HT1, HT2, and HT3, are higher than the corresponding values computed from locations further away from the spark plug such as HT4 and HT5. This is because a location near the

centrally-located spark-plug is in contact with the high temperature burned gases longer than a location further away from the spark plug. In addition, the burned gas near the spark-plug achieves higher temperatures than that further away from the spark plug because it undergoes compression with each successive element that burns [17, 18].

The net heat losses increase linearly with volumetric efficiency. On the other hand, as in the peak heat-flux measurements, the variation of the heat losses with air-fuel ratio exhibits a maximum at near-stoichiometric compositions. A similar trend has also been observed on the variation of heat rejection to the coolant with air-fuel ratio [19].

As shown in Figs. 10 and 11, the "area-averaged" heat losses computed from an energy balance are in reasonable agreement with the corresponding values derived from the local heat-flux measurements. Overall, the agreement is better when the heat losses are computed from measurements obtained at locations near the center of symmetry of the cylinder. The agreement between the two methods provides a degree of confidence in the heat-flux measurements. It must be noted, however, that the energy balance method is by no means error-free.

A sensitivity analysis of this method showed that the input parameters most critical to the accuracy of the calculations are the mass of fuel burned and the phasing of the pressure data with cylinder volume. For example, it was estimated that a 1.5 percent error in the mass of fuel burned produced a 5 percent error in the computed value of the heat loss. On the other hand, one CA change in the pressure phasing produced a 12 percent error. It was estimated that the maximum absolute error in the calculated heat loss should be less than 10 percent.

Conclusions

Based on tests performed on a single-cylinder, disk-chambered engine that was propane fueled and always operated at MBT spark advance, the following conclusions were reached:

1 The local transient heat flux was found not to be affected strongly by variations of the air-fuel ratio at constant conditions of engine speed and volumetric efficiency. The peak heat fluxes reached a maximum near-stoichiometric mixture composition, whereas at leaner or richer mixture compositions the heat flux decreased. This trend was caused by the burned-gas temperature, which exhibits a similar variation with air-fuel ratio.

2 An increase in volumetric efficiency from 40 to 60 percent resulted in an increase in peak heat flux of about 30 percent. This increase is primarily attributed to the increase of the convective heat-transfer coefficient because of the increase in gas density with volumetric efficiency.

3 The calculated amount of heat transferred to the walls of the combustion chamber during the closed portion of the cycle using the first law of thermodynamics (Global-Q Method) agreed well with the corresponding values obtained from the transient heat-flux measurements.

4 Significant cycle-to-cycle variations in the surface-temperature history, and consequently in the heat-flux history, were observed at each location of measurement. These cycle-to-cycle variations were primarily associated with corresponding variations of the propagation of the flame through the combustion chamber.

References

1 Krieger, R. B., "Applications of Engine Combustion Models — An Introductory Overview," *Combustion Modeling in Reciprocating Engines,* Edited by J. N. Mattavi and C. A. Amann, Plenum Press, 1980, pp. 485–507.

2 Blumberg, P. N., Lavoie, G. A., and Tabaczynski, R. J., "Phenomenological Models for Reciprocating Internal Combustion Engines," *Prog. Energy Combust. Sci.,* Vol. 5, 1979, pp. 123–167.

3 Overbye, V. D., Bennethum, J. E., Uyehara, O. A., and Myers, P. S., "Unsteady Heat Transfer in Engines," *SAE Transactions,* Vol. 69, 1961, pp. 461–494.

4 Oguri, T., "On the Coefficient of Heat Transfer between Gases and Cylinder Walls of the Spark-Ignition Engine," *Bulletin of JSME,* Vol. 3, No. 11, 1960, pp. 363–369.

5 Alkidas, A. C., "Heat Transfer Characteristics of a Spark-Ignition Engine," ASME *Journal of Heat Transfer,* Vol. 102, No. 2, 1980, pp. 189–193.

6 Bendersky, D., "A Special Thermocouple for Measuring Transient Temperatures," ASME *Mechanical Engineering,* Vol. 75, No. 2, 1953, pp. 117–121.

7 LeFeuvre, T., Myers, P. S., and Uyehara, O. A., "Experimental Instantaneous Heat Fluxes in a Diesel Engine and Their Correlation," SAE Paper No. 690464, 1969.

8 Wendland, D. W., "The Effect of Periodic Pressure and Temperature Fluctuations on Unsteady Heat Transfer in a Closed System," NASA Report CR-72323, March 1968.

9 Annand, W. J. D. and Pinford, D., "Heat Transfer in the Cylinder of a Motored Reciprocating Engine," SAE Paper No. 800457, 1980.

10 Patterson, D. J., "Cylinder Pressure Variations, A Fundamental Combustion Problem," SAE Paper No. 660129, 1966.

11 Curry, S., "A Three Dimensional Study of Flame Propagation in a Spark Ignition Engine," *SAE Transactions,* Vol. 71, 1963, pp. 628–650.

12 Annand, W. J. D. and Ma, T. H., "Instantaneous Heat Transfer Rates to the Cylinder Head Surface of a Small Compression-Ignition Engine," *Proceedings of the Institution of Mechanical Engineers,* Vol. 185, 1971-1972, pp. 976–987.

13 Whitehouse, N. D., "Heat Transfer in a Quiescent Chamber Diesel Engine," *Proceedings of the Institution of Mechanical Engineers,* Vol. 185, 1971-1972, pp. 963–975.

14 Krieger, R. B. and Borman, G. L., "The Computation of Apparent Heat Release for Internal Combustion Engines," ASME Paper No. 66-WA/DGP-4, 1966.

15 Samaga, B. S., "Assessment of a Heat Transfer Formulation for Reciprocating Combustion Engines," *Indian Journal of Technology,* Vol. 13, 1975, pp. 484–487.

16 Young, M. B. and Lienesch, J. H., "An Engine Diagnostic Package (EDPAC) - Software for Analyzing Cylinder Pressure-Time Data," SAE Paper No. 780967, 1978.

17 Muzio, L. J., Starkman, E. S., and Caretto, L. S., "The Effect of Temperature Variations in the Engine Combustion Chamber on Formation and Emission of Nitrogen Oxides," *SAE Transactions,* Vol. 80, 1971, pp. 652–662.

18 Garforth, A. M. and Rallis, C. J., "Gas Movement During Flame Propagation in a Constant Volume Bomb," *Acta Astronautica,* Vol. 3, 1976, pp. 879–888.

19 Taylor, C. F., *The Internal Combustion Engine in Theory and Practice,* Vol. 1, Ch. 8, The MIT Press, 1977, pp. 294–295.

20 Bennethum, J. E., "Heat Transfer and Combustion-Chamber Deposits in a Spark Ignition Engine," PhD thesis, University of Wisconsin, 1959.

APPENDIX

Errors Associated With the Measurement of Heat Flux

The principal assumption used to calculate surface heat flux from temperature measurements is that the heat flow through the walls of the combustion chamber is one-dimensional. To enhance the one-dimensional character of the heat transfer, the probes were manufactured from the same material used in making the cylinder head, and were installed with a circumferential air gap.

A source of significant error in the heat flux measurements is the accumulation of surface deposits on the probe. This accumulation reduces the amplitude of the measured surface temperature variation and hence the heat flux [20]. The amounts of deposits depend primarily on the fuel and the test time. The present tests were performed with propane fuel which produces very little deposits. In addition, the tests were carefully planned to minimize the amount of test time.

The uncertainty of thermal properties of the probe material is another source of error. The transient component of the heat flux is proportional to $(K\rho c)^{1/2}$. A 10 percent error in any one of the three properties produces only a 5 percent error in the transient component of heat flux. The specific heat (c) and density (ρ) of the probe material were obtained from the literature, whereas the thermal conductifity (K) was measured by exposing the probes to a known heat flux.

Finally, the accuracy of the heat flux measurement depends also on the number of harmonics used to represent the experimental surface temperature variation. In general, increasing the number of harmonics increased the accuracy. In a typical case, increasing the number of harmonics from 50 to 100 decreased the peak heat flux by only 2 percent.

H. Lee

R. O. Buckius
Assoc. Mem. ASME

Department of Mechanical and
Industrial Engineering,
University of Illinois at Urbana-Champaign,
Urbana, Il 61801

Scaling Anisotropic Scattering in Radiation Heat Transfer for a Planar Medium

Radiation heat transfer in a planar participating medium which scatters anisotropically is scaled to an isotropically scattering medium. Only isotropic scattering problems need to be solved with a scaled optical depth and albedo. The scaling is derived from approximate solution methods to the equation of transfer. From the P-1 approximation, the two-flux method, and the modified linear anisotropic scattering model, three scalings are derived. The scaling that gives the best results when comparing the scaled solutions to exact solutions is the one derived from the P-1 approximation.

1 Introduction

Recent investigations in radiation heat transfer have considered solutions to energy transport in participating media which scatter anisotropically. Exact solutions for the general form of the transport equation are difficult to obtain due to the integro-differential nature of the equation of transfer, complexities introduced by geometry, and the angular details required for anisotropic scattering. Many physical problems are well-approximated by a plane parallel medium which greatly reduces the effort involved. The complexity is further reduced if the scattering is considered to be isotropic which assumes that the scattering constituents redistribute energy in each direction with equal probability.

The angular distribution of radiation by the scattering particles is described by the phase function. The general phase function is expanded into an infinite series of weighted Legendre polynomials of increasing order to describe anisotropic scattering. Problems with anisotropic scattering are solved by using a truncated series of the phase function expansion. Even with this simplification, the effort required to include the angular information of anisotropic scattering is prohibitive in many applications, particularly when dealing with other forms of energy transport coupled with radiation.

Exact calculations of radiation heat transfer in planar participating media characterized by scattering albedos and phase functions describing anisotropic scattering have been presented [1–5]. Modest and Azad [1] have presented the average incident radiation and the heat flux distributions within isothermal media and media in radiative equilibrium. The number of terms needed for the predominantly forward scattering phase functions ranged from 26 to 36, which resulted in sets of 26 to 36 simultaneous integral equations to be solved numerically. Sutton and Özisik [2] have calculated reflectances and transmittances for both a forward (eleven-term phase function) and backward (six-term phase function)

anisotropic scattering media with reflecting boundaries. Eleven-term Legendre polynomial solutions are presented which involve solving sets of twelve coupled ordinary differential equations. Orchard [3] gave reflectance values of optically thick media for conservative scattering and a three-term phase function. Orchard obtained exact solutions by numerically integrating the integro-differential equations for the auxiliary functions defined by Chandrasekhar. Linear anisotropic scattering, a two-term spherical harmonics expression, has also been considered [4, 5]. These results clearly indicate the computational difficulties encountered for anisotropic problems. For the special case of isotropic scattering, the problem becomes easier to solve and much of the earlier investigations have concentrated on this area [6].

The objective of this work is to scale anisotropic scattering problems to isotropic scattering problems. The techniques already available for solving isotropic scattering problems are then applied directly to solve the more complicated anisotropic problem. The scaling method is applied to heat transfer calculations for which it is more important to calculate the energy transfer involved in an anisotropic scattering problem than it is to show all the angular details of scattering. Therefore, only the radiative heat flux and average incident intensity are considered.

2 Scaling

Any problem which is described by the same set of normalized governing equations and conditions belongs to the same class of problems. The mathematical solution of the nondimensionalized variables is identical if the form of the equations and the values of the dimensionless parameters are the same. Scaling is the process by which two problems that are not in the same class of problems are made to belong to the same class by suitable transformation of variables. If the form of the normalized governing equations for the two problems are already the same, only the parameters need to be properly scaled. In certain cases, anisotropic scattering

---

problems can be scaled to isotropic scattering problems by adjusting the dimensionless parameters of the problem.

Consider a plane parallel medium which absorbs, emits, and scatters radiant energy. The intensity of radiation in the medium is assumed to vary only in the x-spacial direction. In terms of the dimensionless optical depth, the limits of the medium are $\kappa = 0$ to $\kappa = \kappa_0$. Azimuthal symmetry is assumed and θ is the angle from the positive x-direction ($\mu = \cos\theta$). The radiant intensity in the medium is given by the equation of transfer as

$$\mu \frac{\partial I(\kappa,\mu)}{\partial \kappa} + I(\kappa,\mu) = S(\kappa,\mu)$$

$$= (1-\omega)I_b(T) + \frac{\omega}{2}\int_{-1}^{1} P(\mu,\mu')I(\kappa,\mu')d\mu' \qquad (1a)$$

where $I(\kappa,\mu)$ is the intensity and $S(\kappa,\mu)$ is the source function. The phase function is expanded into a series using Legendre polynomials of order n as

$$P(\mu,\mu') = \sum_{n=0}^{\infty} a_n P_n(\mu)P_n(\mu'), \quad a_0 = 1 \qquad (1b)$$

where the coefficients a_n are calculated from Mie theory. The intensity at the $\kappa = 0$ is denoted by I_0 and the boundary at $\kappa = \kappa_0$ does not contribute.

The governing equation and the boundary conditions contain all the information that is known about the problem. The complete set of dimensionless parameters is obtained by introducing the nondimensional variables defined by $I^* = I/I_0$, $\kappa^* = \kappa/\kappa_0$ and $I_b^* = I_b/I_0$. The resulting governing equation is divided by one of the dimensionless parameters. The normalized governing equation is

$$\frac{dI^*(\kappa^*,\mu)}{d\kappa^*} + \frac{\kappa_0}{\mu}I^*(\kappa^*,\mu) = \frac{(1-\omega)\kappa_0}{\mu}I_b^* + \frac{\omega\kappa_0}{2\mu}$$

$$\cdot \int_{-1}^{1} I^*(\kappa^*,\mu')P(\mu,\mu')d\mu' \qquad (2)$$

Since the boundary conditions do not introduce any scaling groups, the dimensionless parameters which determine the solution are

$$\kappa_0/\mu, [(1-\omega)\kappa_0]/\mu, \text{ and } P(\mu,\mu')$$

An anisotropic scattering problem can be scaled to isotropic if

$$[(1-\omega)\kappa_0]/\mu|_a = [(1-\omega)\kappa_0]/\mu|_i, \kappa_0/\mu|_a = \kappa_0/\mu|_i$$

$$\text{and } P(\mu,\mu') = 1.0$$

Because of the angular information required to perform the scaling, this scaling is only useful for very special cases.

There have been numerous attempts at scaling the equation of transfer. McKellar and Box [7][1] present an excellent review and clarification of previous works on scaling in terms of an infinite set of scaling transformations in optical depth and the phase function. This scaling concept was also considered by Inönü [8] in neutron transport applications. McKellar and Box show that the works by Joseph, Wiscombe, and Weinman [9], Wiscombe [10], and Potter [11], which employ delta function approximations for the forward peak, can be interpreted from the set of scaling transformations. Inönü [12] also presented a theorem which proved that it is possible to scale a problem with an arbitrary phase function $P(\theta)$, plus a δ-distribution in the forward or backward direction to a problem containing just the phase function $P(\theta)$. The transformation proposed by Inönü [12] scales an isotropic plus δ-distribution in the forward direction to isotropic. The scaling of the backward direction requires a modification of the scaled boundary conditions. Sobolev [13] also presents a set of similarity relations which reduce a forward delta function plus isotropic phase function to isotropic. The scaling proposed by van de Hulst and Grossman [14], which was studied by Hansen [15], is derived from an eigenvalue approach for an optically thick medium and can be understood from the approach of McKellar and Box.

When the phase function is expanded as in equation (1b), the transformations presented by McKellar and Box scale a linear anisotropic phase function to isotropic. The approach taken here is to look at approximate solutions to the equation of transfer for general anisotropic scattering. Approximate scaling is obtained from approximate solutions which have been developed to reduce the governing equations to differential equations. These resulting equations are then normalized and the dimensionless parameters obtained. The first-order spherical harmonics (P-1) approximation and the two-flux method are used to generate the governing equations.

2.1 Scaling from the P-1 Approximation. The spherical harmonics method assumes a form for the solution of the equation of transfer but does not make any assumptions about the physical nature of intensity. Exact solutions are obtained by solving a coupled set of equations for all the moments and then calculating the intensity. The number of coupled equations considered depends upon the accuracy required. The P-N approximation requires the solution to $N+1$ equations with the highest order derivative neglected. The $q(\kappa)$ and $G(\kappa)$ are obtained by the P-1 approximation.

---

[1] Professor A. C. Cogley, University of Illinois at Chicago Circle, brought this recently published work to the attention of the authors after the completion of this paper.

————— **Nomenclature** —————

a_n = coefficients of phase function
b = backward fraction of the scattered energy
$<\cos\theta>$ = asymmetry factor
f = forward fraction of the scattered energy
$G(\kappa)$ = average incident radiation
I = intensity
m = ratio of incident radiation to radiative heat flux
P_n = Legendre polynomials of order n
$P(\mu,\mu')$ = phase function

$q(\kappa)$ = radiation heat flux
q_0 = surface radiosity at $\kappa = 0$
S = source function
T = temperature
δ = Dirac delta function
κ = optical depth
μ = $\cos\theta$
Θ = angle between incoming and outgoing direction
θ = angle from x-direction
ρ = reflectance
σ = Stefan-Boltzmann constant
τ = transmittance
ω = scattering albedo

Superscripts

$*$ = nondimensional variable
$+$ = forward direction
$-$ = backward direction
$'$ = integration variable, incoming direction

Subscripts

a = anisotropic scattering
b = blackbody
i = isotropic scattering
m = modified
0 = condition at boundary

The governing differential equations for the P-1 approximation are

$$\{[dq(\kappa)]/d\kappa\} + (1-\omega)G(\kappa) = 4\pi(1-\omega)I_b(T) \qquad (3a)$$

$$\{[dG(\kappa)]/d\kappa\} + 3[1 - \omega(a_1/3)]q(\kappa) = 0 \qquad (3b)$$

These equations combine to yield a single ordinary differential equation for the heat flux which is

$$\{[d^2 q(\kappa)]/d\kappa^2\} - 3(1-\omega)[1-\omega(a_1/3)]q(\kappa)$$
$$= 4\pi(1-\omega)(dI_b/d\kappa) \qquad (4)$$

The governing equation is normalized by introducing $q^* = q/q_0$, $\kappa^* = \kappa/\kappa_0$, and $I_b^* = [I_b/(q_0/\pi)]$ where q_0 is the radiosity at the boundary $\kappa = 0$. The normalized governing equation is

$$\frac{d^2 q^*}{d\kappa^{*2}} \{3(1-\omega)[1-\omega(a_1/3)]\kappa_0^2\}q^*$$

$$= [4(1-\omega)\kappa_0]\frac{dI^*_b}{d\kappa^*} \qquad (5)$$

The boundary conditions are converted to Marshak boundary conditions suitable for P-1 approximation (see Ozisik [16] for details) and normalized as above. The boundary conditions do not contribute any new parameters into the problem. Thus, the dimensionless parameters that determine the solution are

$$(1-\omega)\kappa_0 \text{ and } [1-\omega(a_1/3)]\kappa_0.$$

It is possible to scale anisotropic scattering to isotropic problems with the complete set of dimensionless parameters. Scaling is achieved by requiring

$$(1-\omega)\kappa_0|_a = (1-\omega)\kappa_0|_i$$
$$\text{and } [1-\omega(a_1/3)]\kappa_0|_a = [1-\omega(a_1/3)]\kappa_0|_i$$

Although a_1 is only one of the coefficients in the phase function expansion, $a_1/3$ is representative of the complete series. Irvine [17] defines the asymmetry factor for anisotropic scattering as

$$<\cos\theta> = 1/2\int_{-1}^{1} P(\Theta)\cos\Theta\, d(\cos\Theta) \qquad (6)$$

where Θ is the angle between the incoming and the out-scattered intensity. When $P(\Theta)$ is expanded into a series of Legendre polynomials (equation (1b)), the orthogonality of Legendre polynomials reduces $<\cos\theta>$ to simply $a_1/3$. Thus, any general anisotropic scattering problem is scaled to an isotropic problem in the P-1 approximation by

$$\kappa_{0i} = (1-\omega_a <\cos\theta>)\kappa_{0a} \qquad (7a)$$

$$\omega_i = [\omega_a(1 - <\cos\theta>)]/[1-\omega_a <\cos\theta>] \qquad (7b)$$

For conservative scattering, the above scaling is identical to the scaling proposed by van de Hulst and Grossman [14] for the consideration of the reflection.

2.2 Scaling from the Two-Flux Method. The equation of transfer can also be reduced to differential equations when assumptions about the angular nature of the intensity are made. The resulting equations are easier to solve but again only an approximate solution is obtained. The two-flux method assumes that the radiation scattered in all directions is lumped into two directions. The fraction of energy scattered in the forward hemisphere and the backward hemisphere are given by

$$f = (1/2)\int_0^1 P(\mu,\mu')d\mu' \qquad (8a)$$

and

$$b = (1/2)\int_{-1}^0 P(\mu,\mu')d\mu' \qquad (8b)$$

respectively. After decomposing the intensity into positive and negative directions, the governing equations for the two-flux method are

$$\frac{dq^+(\kappa)}{d\kappa} = -m_+(1-\omega f)q^+(\kappa) + m_- b\omega q^-(\kappa) + 2\pi(1-\omega)I_b(T) \qquad (9a)$$

$$\frac{-dq^-(\kappa)}{d\kappa} = -m_-(1-\omega f)q^-(\kappa)$$

$$+ m_+ b\omega q^+(\kappa) + 2\pi(1-\omega)I_b(T) \qquad (9b)$$

The m_+ and m_- are set equal to $m = 3^{1/2}$, as is suggested by Traugott and Wang [18], to satisfy the optically thick limit. The boundary conditions are written in terms of the heat flux as $q^+(\kappa)|_{\kappa=0} = q_0$ and $q^-(\kappa)|_{\kappa=\kappa_0} = 0$. Equations (9a) and (9b) are combined to yield second-order differential equations for q^- and q^+. The governing expression is

$$\frac{d^2 q^\pm}{d\kappa^2} + [m^2 b^2 \omega^2 - m^2(1-\omega f)^2]q^\pm = 2\pi(1-\omega)$$

$$\cdot [(dI_b/d\kappa) - (mb\omega + m(1-\omega f))I_b] \qquad (10)$$

The governing equation is normalized as in the previous section which results in

$$\frac{d^2 q^{\pm *}}{d\kappa^{*2}} + \kappa_0^2[m^2 b^2 \omega^2 - m^2(1-\omega f)^2]q^{\pm *}$$

$$= 2(1-\omega)\kappa_0\left[\frac{dI_b^*}{d\kappa^*} - (mb\omega + m(1-\omega f))\kappa_0 I_b^*\right] \qquad (11)$$

Again, the normalized boundary conditions do not add new parameters. The dimensionless parameters of the two-flux method reduce to $\kappa_0(1-\omega)$ and $\kappa_0[1-\omega(2f-1)]$ after some algebraic manipulations. Scaling is achieved by requiring $\kappa_0(1-\omega)|_a = \kappa_0(1-\omega)|_i$ and $\kappa_0[1-\omega(2f-1)]|_a = \kappa_0[1-\omega(2f-1)]|_i$. If the asymmetry factor of the previous scaling is replaced by $(2f-1)$, then the transformation of variables for the two-flux scaling has the same form as given in equations (7a) and (7b).

2.3 Scaling by Modifying the Linear Anisotropic Scattering Model. The scaling obtained from the P-1 approximation was

$$(1-\omega)\kappa_0|_a = (1-\omega)\kappa_0|_i \text{ and}$$
$$[1-\omega(a_1/3)]\kappa_0|_a = [1-\omega(a_1/3)]\kappa_0|_i$$

where the complete phase function expansion was included into $a_1/3$ by using the definition of the asymmetry factor. The above requirement scales linear anisotropic scattering exactly since the phase function is given by

$$P(\mu,\mu') = 1 + a_1\mu\,\mu' \qquad (12)$$

The higher-order scattering terms can also be included directly into the scaling by modifying a_1. Substituting equation (12) into equation (8a), and using the expression for f given by Clark, Chen, and Churchill [19], yields [20]

$$a_{1m} = 2\sum_{n=0}^{\infty} \frac{(-1)^n a_{2n+1}(2n)!}{2^{(2n+1)}(n!)[(n+1)!]} \qquad (13)$$

If the asymmetry factor in the P-1 scaling is replaced by $a_{1m}/3$, then equations (7a) and (7b) are used to scale an arbitrary anisotropic scattering to an isotropic problem.

3 Results and Discussion

Once an anisotropic scattering problem is scaled to an isotropic problem, it remains to solve the resulting isotropic problem. The successive substitution method is employed to obtain the isotropic solutions. All numerical integrations are done using a Gaussian quadrature of order 40 with error

Table 1 Phase functions

			$<\cos\theta>$			
Phase function	No. of terms	Description	$a_1/3$	$2f-1$	$a_{1m}/3$	Reference
F1	26	highly forward	0.8189	0.8489	0.5659	Modest and Azad [1]
F2	27	highly forward	0.9273	0.9723	0.6999	Sutton and Ozisik [2]
F3	36	forward	0.7693	0.8414	0.5609	Modest and Azad [1]
F4	34	forward with small backward lobe	0.4856	0.5728	0.3819	Modest and Azad [1]
F5	3	forward	0.5000	0.7500	0.5000	Orchard [3]
F6	2	linear anisotropic, forward	0.333	0.5000	0.333	Buckius and Tseng [5]
B1	6	backward	-0.1884	-0.2933	-0.1955	Sutton and Ozisik [2]
B2	4	backward with forward lobe	0.333	0.5938	0.3958	Modest and Azad (unpublished results)
B3	2	linear anisotropic, backward	-0.333	-0.5000	-0.333	Buckius and Tseng [5]

Table 2 Coefficients for phase function expansion

a_n/ Phase function	F1	F2	F3	F4	F5	F6	B1	B2	B3
a_0	1.0	1.0	1.0	1.0	1.0	1.0	1.0	1.0	1.0
a_1	2.45677	2.78197	2.30790	1.45687	1.5	1.0	-0.56524	1.0	-1.0
a_2	3.84181	4.25856	3.23995	2.15059	0.5		0.29783	1.0	
a_3	5.00553	5.38653	3.79936	1.85048			0.08571	-0.75	
a_4	5.96331	6.19015	4.03230	2.35120			0.01003		
a_5	6.72161	6.74492	4.01175	1.85811			0.00063		
a_6	7.28629	7.06711	3.81199	2.16895					
a_7	7.66244	7.20999	3.49134	1.58175					
a_8	7.85767	7.20063	3.10532	1.75408					
a_9	7.88060	7.03629	2.69153	1.21806					
a_{10}	7.73731	6.76587	2.28376	1.33574					
a_{11}	7.44517	6.35881	1.89851	0.890579					
a_{12}	7.00558	5.83351	1.55180	0.932577					
a_{13}	6.44908	5.22997	1.24622	0.585578					
a_{14}	5.77136	4.47918	0.986923	0.554820					
a_{15}	5.01092	3.69000	0.769385	0.338866					
a_{16}	4.19407	2.81577	0.592926	0.340838					
a_{17}	3.30067	1.92305	0.450530	0.185501					
a_{18}	2.43442	1.11502	0.340380	0.182498					
a_{19}	1.67637	0.50766	0.254852	0.111208					
a_{20}	1.03522	0.20927	0.189456	0.100875					
a_{21}	0.546797	0.07138	0.140870	0.0608943					
a_{22}	0.241290	0.02090	0.104504	0.0587712					
a_{23}	0.0887443	0.00535	0.0777386	0.0362599					
a_{24}	0.0275242	0.00120	0.0575404	0.0314965					
a_{25}	0.00729357	0.00024	0.0427188	0.0221769					
a_{26}		0.00004	0.0313215	0.0177937					
a_{27}			0.0229587	0.00953461					
a_{28}			0.0165931	0.0105159					
a_{29}			0.0119847	0.00504125					
a_{30}			0.00851234	0.00468271					
a_{31}			0.00603327	0.00244863					
a_{32}			0.00418646	0.00211119					
a_{33}			0.00288973	0.00108605					
a_{34}			0.00193843						
a_{35}			0.00126717						

estimate parameters [21]. The computations were verified against results published by Crosbie [6] for isotropic scattering.

From the P-1 approximation, the scaling proposed (equation (7)) is

$$\kappa_{0i} = (1 - \omega_a <\cos\theta>)\kappa_{0a} \quad \text{and} \quad \omega_i = \frac{\omega_a(1 - <\cos\theta>)}{1 - \omega_a <\cos\theta>}$$

where $<\cos\theta> = a_1/3$. The scaling from the two-flux method replaces $<\cos\theta>$ with $2f-1$ and replacing $<\cos\theta>$ with $a_{1m}/3$ further modifies the scaling. The different scalings will be referred to as the $a_1/3$ scaling, the $a_{1m}/3$ scaling, and the $2f-1$ scaling. The scaled solutions are compared with the exact solutions of the anisotropic problem. The phase functions scaled are given in Table 1. Figure 1 is a polar plot of all the phase functions given in Table 1, except for linear anisotropic scattering. Table 2 contains a listing of the coefficients of the Legendre polynomial expansion of the phase functions. The results of scaling are compared for three cases: (a) isothermal emission with zero boundary temperatures, (b) cold medium with boundary incidence at $\kappa = 0$, and (c) radiative equilibrium.

The distributions of the heat flux and the incident radiation are compared in Fig. 2 for the isothermal emission case. Fig. 2(a) presents the results for a small optical depth, and Fig. 2(b) shows the results for a large optical depth. Figure 2(a) indicates that all three scalings compare well with the exact solutions for heat flux at small optical depths. At large optical depths, for best scaling for heat flux is achieved by the $a_1/3$ scaling while the $a_{1m}/3$ scaling is noticeably poor. The average incident radiation is generally well scaled. The error in the $G(\kappa)$ scaling presented in Fig. 2(a) is amplified by the ordinate scale chosen. At large optical depths, $a_{1m}/3$ scaling is the only poor result for $G(\kappa)$ while at small optical depths, $a_{1m}/3$
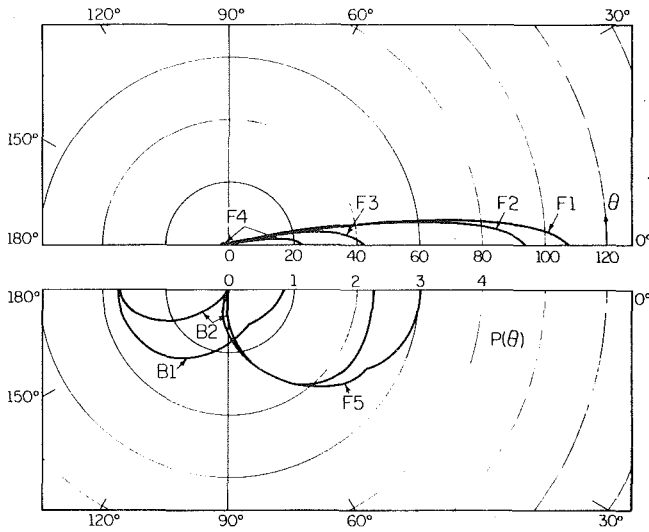
Fig. 1   Phase functions (see Table 1 for Description)

scaling is the best scaling. Consistently good scaling is given by the $a_1/3$ and the $2f-1$ scalings, although the $a_1/3$ scaling is slightly better, which is indicated by the numerical values.

Boundary incidence results are presented in Figs. 3–6. Figures 3(a) and 3(b) present the internal distributions of the heat flux and the average incident radiation profiles for linear anisotropic phase functions, various optical depths and various scattering albedos. In general, the backward scattering problem is scaled more accurately and the $a_1/3$ and $a_{1m}/3$ scalings are the most accurate.

Results for the solutions at the boundaries of the medium for the boundary incidence case are presented in Figs. 4 and 5. The reflectance is defined as

$$\rho = \frac{q^-(0)}{q_0} \tag{14}$$

and the transmittance is

$$\tau = \frac{q^+(\kappa_0) - q^-(\kappa_0)}{q_0} = \frac{q(\kappa_0)}{q_0} \tag{15}$$

Figures 4(a) and 4(b) present the reflectance and the transmittance of a backward scattering phase function. Two
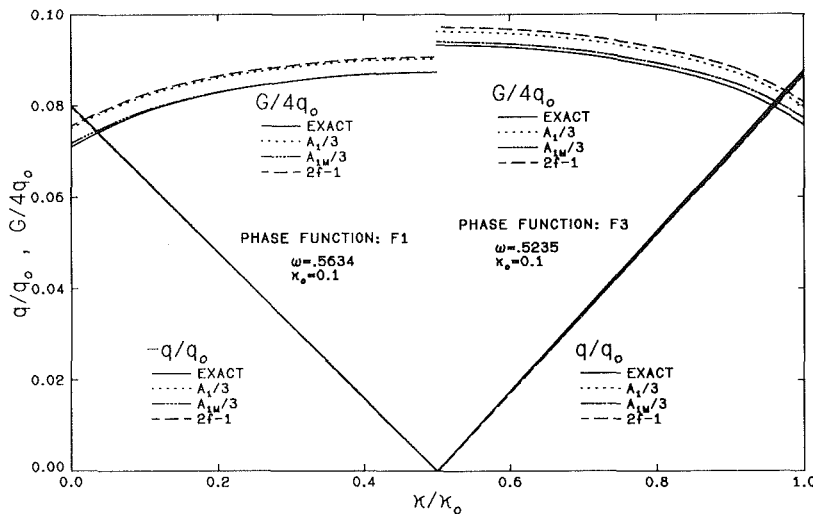
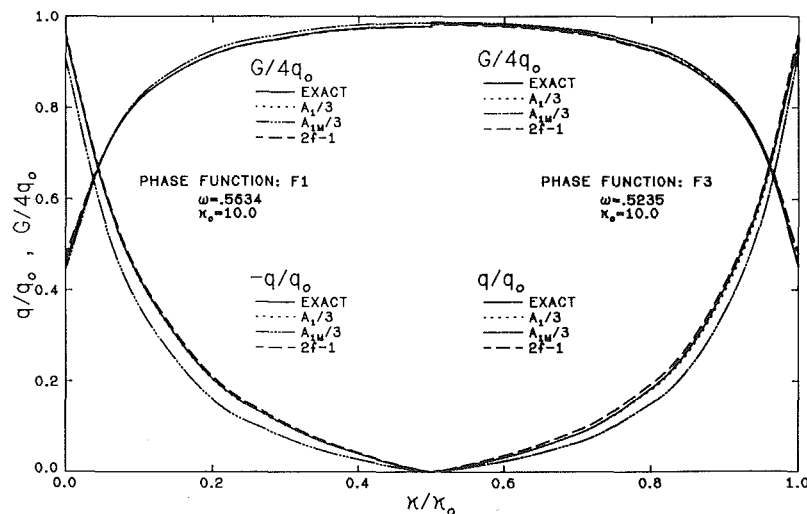Fig. 2(a)   Heat flux and incident radiation versus optical depth: isothermal emission

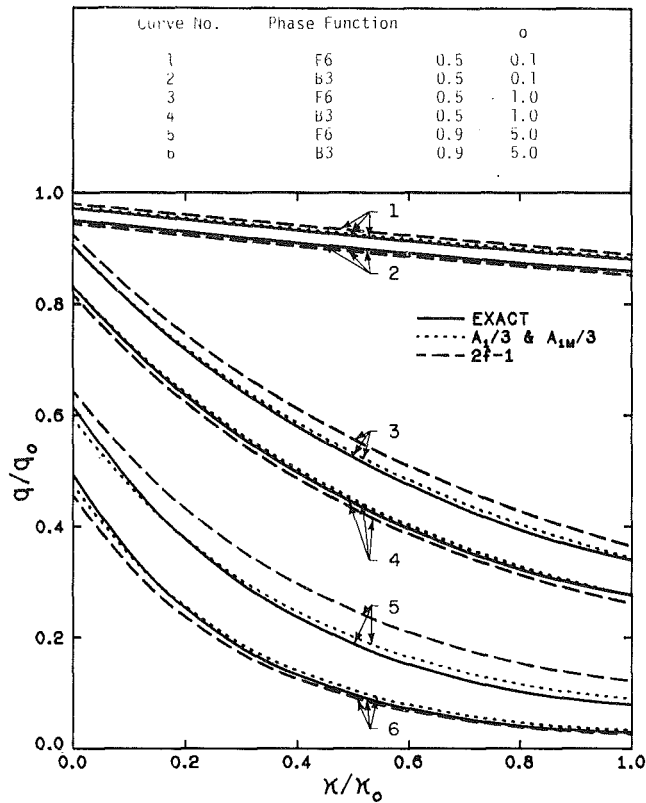Fig. 2(b)   Heat flux and incident radiation versus optical depth: isothermal emission

Curve No.	Phase Function		o
1	F6	0.5	0.1
2	B3	0.5	0.1
3	F6	0.5	1.0
4	B3	0.5	1.0
5	F6	0.9	5.0
6	B3	0.9	5.0

Fig. 3(a) Heat flux versus optical depth: boundary incidence

Curve No.	Phase Function		o
1	F6	0.5	0.1
2	B3	0.5	0.1
3	F6	0.5	1.0
4	B3	0.5	1.0
5	F6	0.9	5.0
6	B3	0.9	5.0
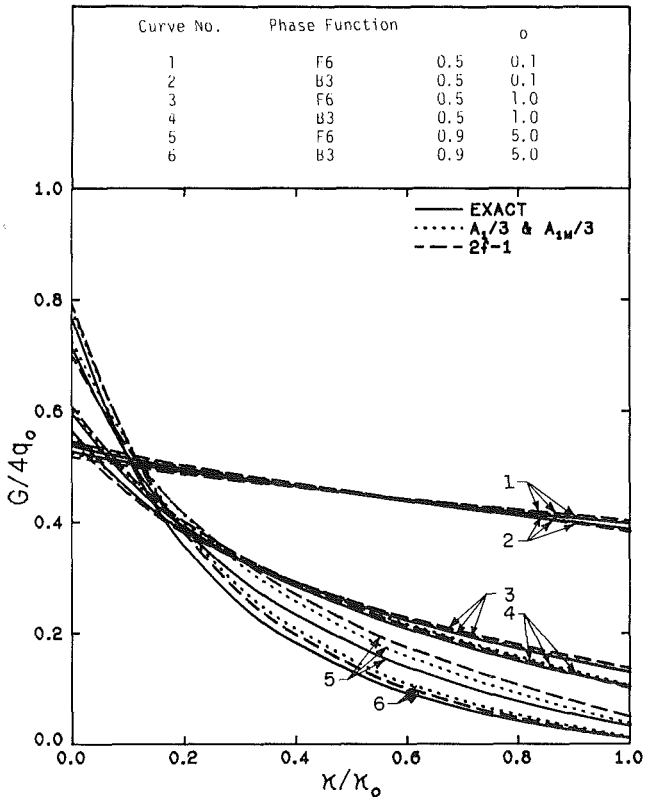
Fig. 3(b) Incident radiation versus optical depth: boundary incidence

optical depths are studied and the same conclusions are drawn from both the studies. The $a_1/3$ and the $a_{1m}/3$ scalings scale well and the $2f-1$ scaling is consistently poor for the range of scattering albedos presented. Figures 5(a) and 5(b) present the reflectance and the transmittance for a highly forward
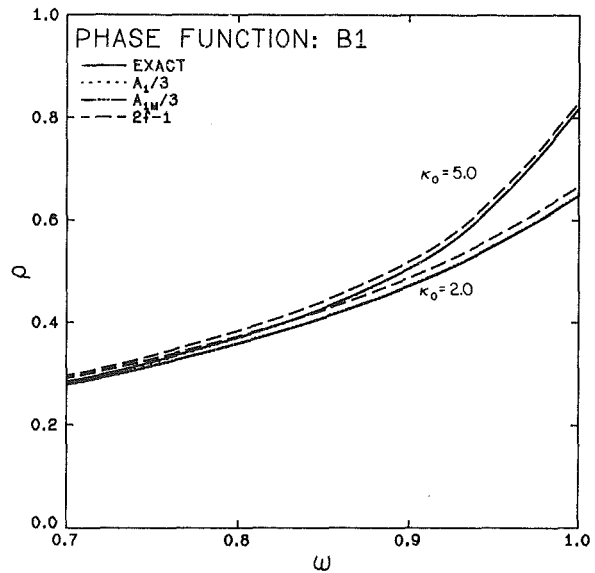
Fig. 4(a) Reflectance versus scattering albedo: boundary incidence
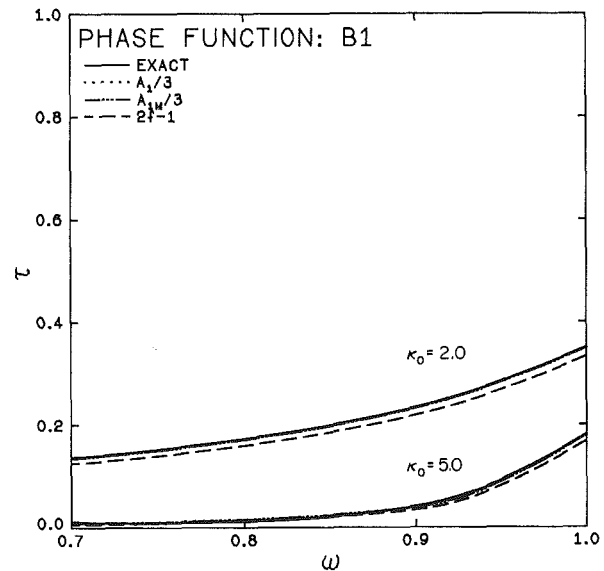
Fig. 4(b) Transmittance versus scattering albedo: boundary incidence

anisotropic phase function at two optical depths. There is a slightly larger error in scaling as the albedo approaches 1.0. The $a_1/3$ scaling is again the most accurate and the error in the $a_{1m}/3$ and the $2f-1$ scalings is large. The reason for the larger than expected error is due to the fact that the exact solutions [2] were computed using a truncated series for the phase function which did not yield a realistic $<\cos \theta>$. Therefore, the full series of 28 terms was used to compute the factors $a_{1m}/3$ and $2f-1$. The scaling using either $a_{1m}/3$ or $2f-1$ no longer scaled the same phase function as that used for the exact solution.

Figure 6 shows the reflectance versus total optical depth for the boundary incidence problem. Exact solutions for a conservatively scattering medium that scatters in the forward direction are compared. The $a_1/3$ and $a_{1m}/3$ scalings compare exactly, except at the smallest optical depth. The $2f-1$ scaling shows a large error for all the optical depths presented. Transmittance results are not presented because for a pure scattering problem, $\tau = 1 - \rho$.

Radiative equilibrium results are presented in Fig. 7 and Table 3. Figure 7 shows the temperature profile comparisons
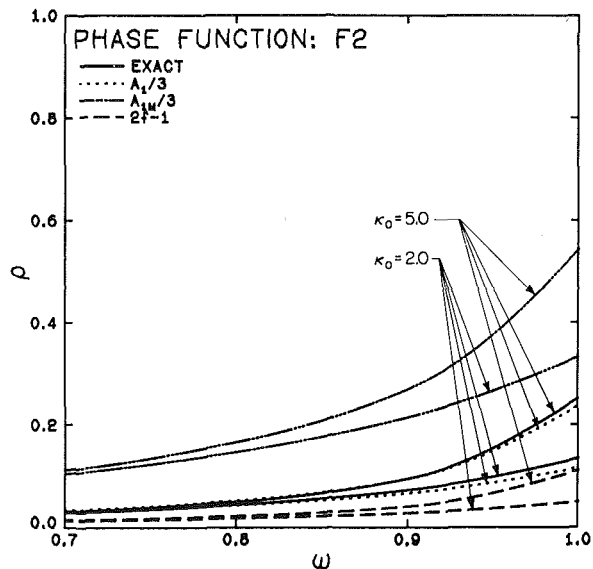
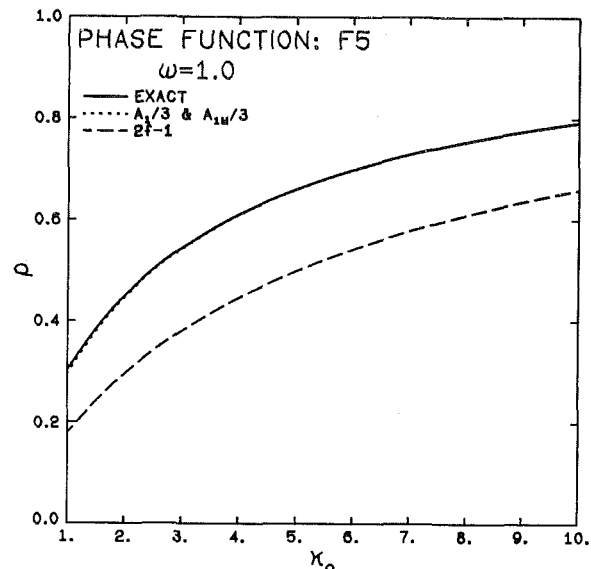Fig. 5(a)   Reflectance versus scattering albedo: boundary incidence

Fig. 6   Reflectance versus total optical depth: boundary incidence
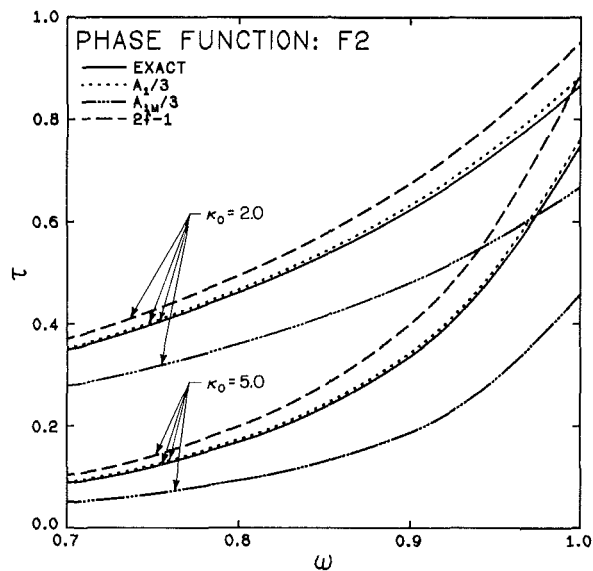

Fig. 5(b)   Transmittance versus scattering albedo: boundary incidence
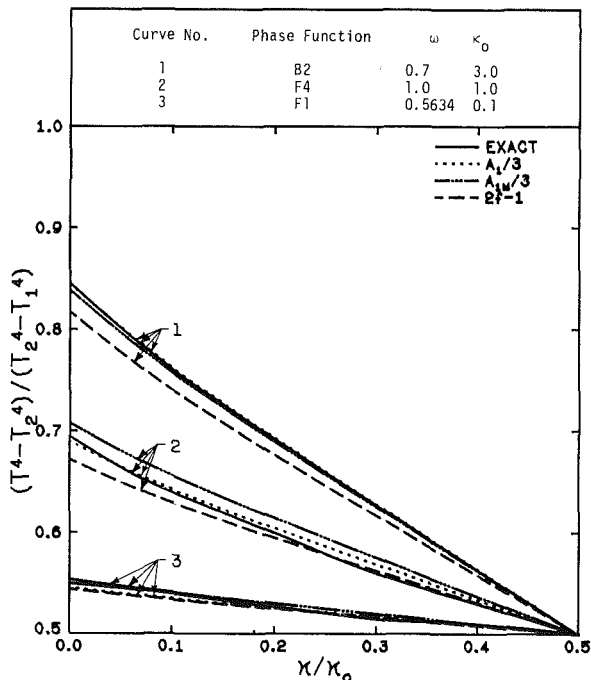

Fig. 7   Temperature profile for radiative equilibrium

for various phase functions, albedos, and optical depths. Small optical depth solutions are well scaled by all 3 scalings. The best scaling for all the cases shown is $a_1/3$. Table 3 shows the result of heat-flux scaling for the same problem and, again, the best scaling for the heat flux is $a_1/3$.

Comparisons have been presented for the heat flux and average incident intensity distributions throughout isothermal and non-isothermal media. The reflectance and transmittance have also been studied. The $a_1/3$ scaling works well in all these cases and also in those cases studied but not presented. The $a_{1m}/3$ scaling is accurate in some cases but in general has the same problems as the $2f-1$ scaling. The $2f-1$ scaling is consistently in error. Figure 6 indicates the nature and the maximum magnitude of the errors observed. The problem appears to be in the value assigned to m in the scaling requirement for the two-flux method presented in Section 2.2. The value of $m_+ = m_- = 3^{1/2}$ matches the optically thick limit for isotropic scattering but the performance of the $2f-1$ scaling suggests that a different constant for anisotropic scattering might be required.

Table 3   Heat flux for radiative equilibrium

Phase function	Optical depth	Scattering albedo	$q/\sigma(T_1^4 - T_2^4)$			
			exact	$a_1/3$	$a_{1m}/3$	$2f-1$
B2	3.0	0.7	0.3584	0.3586	0.3716	0.4206
F1	0.1	0.5634	0.98	0.9516	0.9401	0.9530
F4	1.0	1.0	0.696	0.6986	0.6611	0.7340

4   Conclusions

Radiative heat transfer in a planar participating medium which scatters anisotropically is scaled to the problem in an isotropically scattering medium. Both internal distributions and external exiting energies have been studied. The exact anisotropic scattering solutions which required the solution of up to 36 coupled integral equations are reproduced accurately by the solution of two coupled integral equations for the scaled isotropic problem. Comparing the three cases studied

for this investigation (isothermal emission, boundary incidence, and radiative equilibrium) with exact solutions indicates that the $a_1/3$ scaling derived from the $P-1$ approximation yields very accurate results for all cases. The $a_{1m}/3$ scales well for only a few problems and the $2f-1$ scaling works well for the emission problem but is poor for the boundary problem. Therefore, the $a_1/3$ scaling is the scaling which is the most generally applicable.

Acknowledgment

References

1 Modest, M. F. and Azad, F. H., "The Influence and Treatment of Mie-Anisotropic Scattering in Radiative Heat Transfer," ASME, JOURNAL OF HEAT TRANSFER, Vol. 102, 1980, pp. 92–98.

2 Sutton, W. H. and Özisik, M. N., "An Iterative Solution for Anisotropic Radiative Transfer in a Slab," ASME, JOURNAL OF HEAT TRANSFER, Vol. 101, 1979, pp. 695–698.

3 Orchard, S. E., "Reflection and Transmission of Light by Thick Atmospheres of Pure Scatterers with a Phase Function: $1 + \bar{\omega}_1 P_1(\cos\theta) + \bar{\omega}_2 P_2(\cos\theta)$," Astrophysical Journal, Vol. 149, 1967, pp. 665–674.

4 Dayan, A. and Tien, C. L., "Radiative Transfer with Anisotropic Scattering in an Isothermal Slab," J. Quant. Spectrosc. Radiat. Transfer, Vol. 16, 1976, pp. 113–125.

5 Buckius, R. O. and Tseng, M. M., "Radiative Heat Transfer in a Planar Medium with Anisotropic Scattering and Directional Boundaries," J. Quant. Spectrosc. Radiat. Transfer, Vol. 20, 1978, pp. 385–402.

6 Crosbie, A. L., "Apparent Radiative Properties of an Isotropically Scattering Medium on a Diffuse Substrate," ASME, JOURNAL OF HEAT TRANSFER, Vol. 101, 1979, pp. 68–75.

7 McKellar, B. H. J. and Box, M. A., "The Scaling Group of the Radiative Transfer Equation," Journal of Atmospheric Sciences, Vol. 38, May 1981, pp. 1063–1068.

8 İnönü, E., "Scaling and Time Reversal for the Linear Monoenergetic Boltzmann Equation," Topics in Mathematical Physics, edited by H. Odabasi and Ö. Akyuz, Colorado Associated University Press, 1977, pp. 113–127.

9 Joseph, J. H., Wiscombe, W. J., and Weinman, J. A., "The Delta-Eddington Approximation for Radiative Flux Transfer," Journal of Atmospheric Sciences, Vol. 33, 1976, pp. 2452–2459.

10 Wiscombe, W. J., "The Delta-M Method: Rapid Yet Accurate Radiative Flux Calculations for Strongly Asymmetric Phase Functions," Journal of Atmospheric Sciences, Vol. 34, 1977, pp. 1408–1422.

11 Potter, J. F., "The Delta Function Approximation in Radiative Transfer Theory," Journal of Atmospheric Sciences, Vol. 27, 1970, pp. 943–949.

12 İnönü, E., "A Theorem on Anisotropic Scattering," Transport Theory and Statistical Physics, Vol. 3, 1973, pp. 137–146.

13 Sobolev, V. V., Light Scattering in Planetary Atmospheres, Pergamon Press, 1975.

14 van de Hulst, H. C. and Grossman, K., "Multiple Light Scattering in Planetary Atmospheres," The Atmospheres of Venus and Mars, edited by J. Brandt and M. McElroy, Gordon and Breach Science Publishers, New York, 1968.

15 Hansen, J. E., "Absorption-Line Formation in a Scattering Planetary Atmosphere: A Test of van de Hulst's Similarity Relations," The Astrophysical Journal, Vol. 158, Oct. 1969, pp. 337–349.

16 Özisik, M. N., Radiative Transfer and Interactions with Conduction and Convection, John Wiley and Sons, New York, 1973.

17 Irvine, W. M., "The Asymmetry of the Scattering Diagram of a Spherical Particle," B.A.N., Vol. 17, No. 3, 1963, pp. 176–184.

18 Traugott, S. C. and Wang, K. C., "On Differential Methods for Radiant Heat Transfer," International Journal of Heat and Mass Transfer, Vol. 7, 1964, pp. 269–273.

19 Clark, G. C., Chu, C. M., and Churchill, S. W., "Angular Distribution Coefficients for Radiation Scattered by a Spherical Particle," Journal of the Optical Society of America, Vol. 47, No. 1, 1957, pp. 81–84.

20 Tong, T. W. and Tien, C. L., "Resistance-Network Representation of Radiative Heat Transfer with Particulate Scattering," J. Quant. Spectrosc. Radiat. Transfer, Vol. 24, 1980, pp. 491–503.

21 Kronrod, A. A., Nodes and Weights of Quadrative Formulas, Consultants Bureau, New York, 1965.

S. C. Yao

Associate Professor,
Department of Mechanical Engineering,
Carnegie Mellon University,
Pittsburgh, Pa.
Mem. ASME

L. E. Hochreiter

Assoc. Mem. ASME

W. J. Leech

Westinghouse Electric Company,
Pittsburgh, Pa.
Assoc. Mem. ASME

Heat-Transfer Augmentation in Rod Bundles Near Grid Spacers

Heat-transfer augmentation by straight grid spacers in rod bundles is studied for single-phase flow and for post-critical heat flux dispersed flow. The heat transfer effect of swirling grid spacers in single-phase flow is also examined. Governing heat-transfer mechanisms are analyzed, and predictive formulations are established. For single-phase flow, the local heat transfer at a straight spacer and at its upstream or downstream locations are treated separately. The effect of local velocity increasing near swirling spacer is considered. For post critical heat flux (CHF) dispersed flow, the heat transfer by thermal radiation, fin cooling, and vapor convection near the spacer are calculated. The predictions are compared with experimental data with satisfactory agreement.

Introduction

In a rod or tube bundle the relative position of rods or tubes is usually maintained by spacers. Two basically different types of spacers are commonly used for rod bundles having predominantly axial flows. Spiral wires or helical fins are attached to the rods for the entire length of the bundle. This is called the wire wrap spacing design. Grid spacers, honeycomb or egg-crate grids, are arranged on the rods at fixed planes of the bundle. For a bundle with wide rod-to-rod spacing, the grid spacers are usually used. Wire wrap designs are usually used in fast reactor designs while egg crate grids are used in light-water reactors.

The grid spacer, shown in Fig. 1, acts as flow obstruction in the bundle and causes increased pressure drop due to its form drag and skin friction. The pressure drop due to grid spacers has been correlated in references [1-5]. By neglecting the small skin friction effect and using the ratio of blockage area of the grid and the bundle flow area, the correlation proposed by Rehme [1] gives reasonable spacer pressure drop predictions. The loss coefficient of a grid spacer given by Rehme is

$$K = C_V \, \epsilon^2 \qquad (1)$$

where ϵ is the area blockage ratio of the grid spacer in axial flows. The coefficient C_V has a weak dependency on Reynolds number for Reynolds numbers above 10^4: at this Reynolds number range, a constant value of 7 has been recommended by Rehme [1]. However, through the careful comparison with many other sets of experimental data by the authors, we found that a 50 percent higher value of 10.5 appears to be more appropriate.

The grid spacers also tend to increase the local wall heat transfer. The heat-transfer augmentation of grid spacers has been observed in single phase flow [6] and post critical heat flux dispersed flow [7, 8]. However, the understanding of the heat-transfer mechanisms and the ability to predict the heat
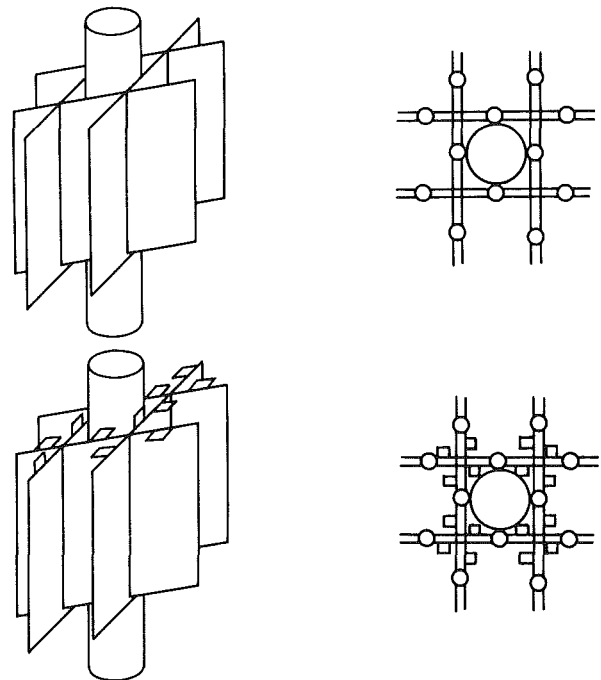
Fig. 1   Typical grid spacers

transfer downstream of the grid spacer are still very limited. The heat-transfer augmentation has been correlated for single phase flow immediately at the location of grid spacer [6], but the heat transfer at the downstream and upstream locations of the grid spacer has not been considered.

In addition to simple egg-crate spacer grids, grids with swirling vanes have been used to improve the flow mixing in rod bundles. Such a spacer is shown in Fig. 1(b). Rod bundles which use swirl vanes or mixing vane spacers have also been observed to have a higher critical heat flux than like bundles with simple egg crate spacers.

The effect of grid spacers on heat transfer in the post-

Table 1 Data Used in Comparison With Equation (4)

Symbol	Author	Type of grid reported in reference		Re × 10⁻⁴	ϵ	Calculated $\dfrac{Nu}{Nu_0^{-1}}$ $= 5.55\,\epsilon^2$	Prediction equation (4)
▣	Rehme	B.3		12.7	0.348	0.672	— · —
△	Velcek	6 cm		15.5	0.289	0.463	——————
●	Kidd	4.3		5	0.245	0.333	– – – –
□	Krett	C		9.5	0.303	0.509	– · – · – –
▲	Velcek	5 mm		12.5	0.237	0.311	— · · —
○	Hudina	Ib. smooth		1.5 ~ 5	0.156	0.135	· · · · · ·

critical heat-flux (CHF) heat-transfer regime has not been studied in detail. Several different heat transfer mechanisms can be acting in this heat transfer regime. The one reported study [8] considered some but not all of the heat transfer mechanisms.

The objective of this paper is to identify the essential mechanisms which influence the heat transfer near various kinds of grid spacers at different flow conditions. Models are developed and predictive methods are proposed. The proposed methods are then compared with the available experimental data.

Single Phase Flow – Straight Egg-Crate Spacer Grids

Since the spacer has a finite thickness it partially blocks the flow passage. The flow at the immediate upstream of the spacer will be accelerated. This acceleration increases the local velocity gradient and temperature gradient at the wall, which augments the local heat transfer. The affected length is limited and can be related to the non-dimensional distance, x/D, upstream of the spacer as the primary variable.

At the grid spacer, the spacer performs as a flow obstruction in the bundle. The velocity and thermal fields will be greatly affected by the presence of the spacer. In addition, the rod bundle may be cooled locally by thermal radiation to the spacer and by fin cooling at the locations where the grid contacts occur. In single phase flow where the flow channels are relatively narrow the mean fluid temperature is generally not much lower than the rod bundle temperature. The spacer will also be at the local fluid temperature in the rod bundle. When the absolute value of the temperature are low ($< 500°C$) the radiative heat transfer between the rod and

spacer will be negligible and the spacer fin cooling effects will also be insignificant. This simplification may not be true for post CHF dispersed flow conditions where the absolute value of the temperatures are much higher and the spacer can be wetted by entrained droplets.

The thermal hydraulic behavior of fluids at the grid spacer is hard to analyze in detail due to the complex geometry. However, the analogy between heat and momentum transfer in turbulent flow may provide information on the determination of the heat transfer near spacers. The ratio of pressure drops in the channel with and without the spacer is

$$\left(\frac{\Delta p}{\Delta p_0}\right)_{sp} = \frac{f + K\dfrac{D}{L}}{f} = 1 + \left(\frac{D}{fL}\right)K \qquad (2)$$

where both the effects of skin friction and contraction-expansion loss are considered. The loss coefficient K can be presented in terms of blockage ratio from equation (1).

It is well known that analogy exists between the frictional pressure drop and the wall heat transfer. Right behind the blockage, the flow deaccelerates and turbulent wakes are generated. The wakes agitate the wall boundary layer and enhance the heat transfer from wall. For simplicity, it may be assumed that the wake induced heat transfer augmentation is linearly dependent upon the blockage induced pressure drop. Following this, the overall heat transfer augmentation due to the spacer will be in a similar form of the pressure drop ratio due to the spacer, which is shown in equation (2). Using equation (1) in equation (2), Marek and Rehme [6] correlated pressure drop data and assumed that the analogy theory applied such that the heat-transfer augmentation at grid spacers on smooth rods in single-phase flow has the form

_____ **Nomenclature** _____

A = the fraction of area of the vanes to the flow cross-section, viewing from upstream.

C_V = a coefficient, used in equation (1)

D = hydraulic diameter of flow channel

f = friction factor of bare flow channel

F_{ws} = view factor from wall to spacer considering gray body effect

K = loss coefficient of grid spacer

L = length of the channel between spacers

Nu = local Nusselt Number at the wall with the spacer installed

Nu_0 = local Nusselt Number at the wall without the spacer installed

Δp = pressure drop across the spacer

Δp_0 = pressure drop without the spacer

q = local wall heat flux

Tw = the temperature of the wall

Ts = the saturation temperature of the fluid

V = local mean velocity of the fluid

V_z = the axial component of local mean velocity

V_ϕ = the circumferential component of local mean velocity

$V_{\phi 0}$ = the circumferential component of mean velocity at downstream end of swirling spacer

x = the axial distance from the downstream end of spacer

Greek Symbols

β = fraction of the total wall area seen by the spacer

σ = Stefan-Boltzman Constant for Radiation

ϵ = the blockage ratio of spacer to flow channel when viewing from upstream

Φ = the angle of swirling vane with respect to axial direction

Subscripts

1ϕ = of the grid spacer at single phase flow

2ϕ = dispersed flow at post CHF

fin = fin cooling

sp = for straight grid spacer

rad = thermal radiation

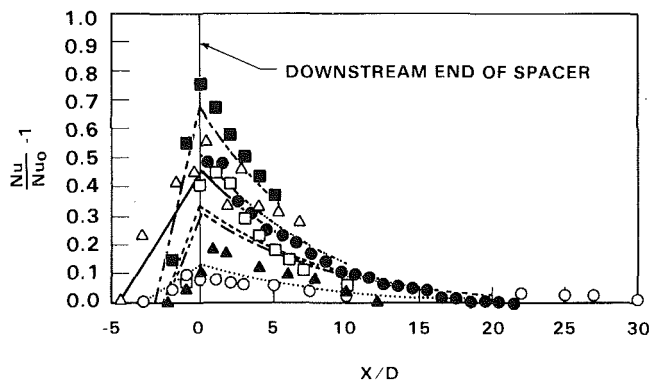sw = of swirling grid spacer

w = wall

Fig. 2 Heat transfer near straight spacers at single phase flow

$$\left(\frac{Nu}{Nu_0}\right)_{sp} = 1 + 5.55 \, \epsilon^2 \tag{3}$$

In the grid spacer region, the fluid is mixed by the spacer structure. The velocity and temperature distributions of the fluid become more uniform. After the fluid leaves the spacer, the hydrodynamic and thermal boundary layers begin to reestablish their fully developed profiles. This boundary layer phenomena is similar to the entry length effect of turbulent tube flow. The augmentation of heat transfer has been observed to be a function of the nondimensional distance x/D at downstream of the spacers. The spacer also induces wakes and secondary flows in the flow stream which increases the subchannel mixing and helps to retard the reformation of the hydrodynamic and thermal boundary layers. The wake and mixing effect will decay along the downstream of the grid spacer.

Experimental data are available for heat-transfer augmentation of various grid spacers in tubes or bundles for single phase flow [6, 9, 10, 11, 12]. The selected data sets are listed in Table 1 with the calculated blockage ratio, ϵ, and its local Nusselt number at the location of spacer grid evaluated from equation (3).

Upstream of the spacer, the data show that the heat transfer is affected over a distance 2 x/D. The augmentation of heat transfer can be approximated as linear in this range from the steady value to the higher heat transfer value within the spacer region. In general, the augmentation of heat transfer in this region varies monotonically. The exact functional form of the variation would depend upon the detail geometry of individual grid.

Downstream of the spacer, the data indicate that the heat-transfer augmentation decays with x/D exponentially. Based on this data, the heat-transfer correlation downstream of straight spacers in a smooth rod bundle with single-phase flow is

$$\left(\frac{Nu}{Nu_0}\right)_{sp} = 1 + 5.55 \, \epsilon^2 \, e^{-0.13(x/D)} \tag{4}$$

for Reynolds number higher than 10^4.

When x/D equals zero, equation (4) gives the heat-transfer coefficient at the spacer. Linear interpolation between this value and unity can be made in the range of 2 x/D upstream of spacer to estimate the upstream effects.

Equation (4) is compared with the data in Fig. 2 as a function of axial location, x/D. In Fig. 2, the grid effect starts at $x/D = -5$ to -2. This is due to the different length of grid spacers considered in the data set. The heat-transfer augmentation downstream of the spacers is generally well predicted by equation (4) while the maximum augmentation at the spacer location is not predicted as well. The deviation is most likely due to the use of a simple analogy approach as given in reference [6].
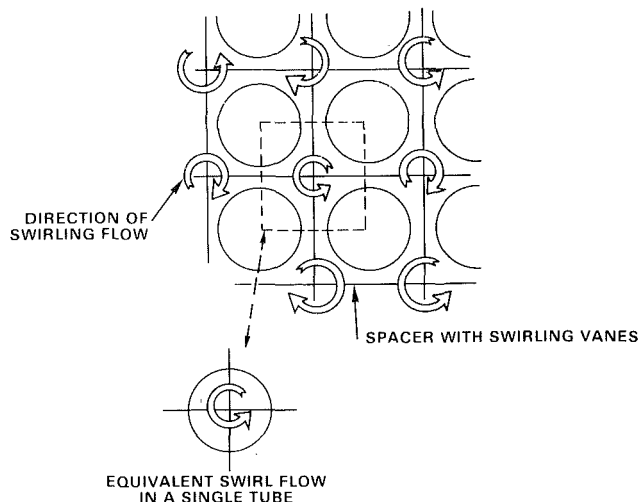

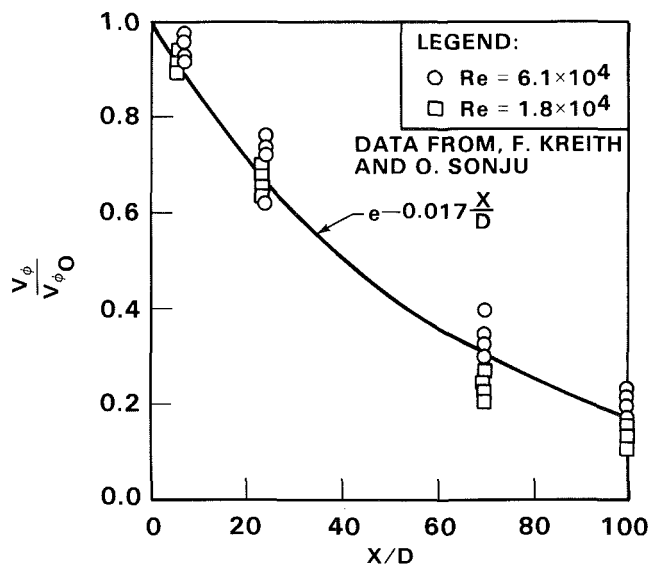Fig. 3 The similarity of swirling bundle and tube

Fig. 4 Decay of swirling flow

Single Phase Flow – Egg-Crate Spacer Grids With Swirling Vanes

Some of the grid spacer designs contain swirling vanes, which are able to strip off the bubble layer near the wall of heating rods at boiling conditions such that the critical heat flux may be increased [19]. For single phase flow situations, the vanes will cause the fluid to swirl, and additional heat transfer from the rods can be obtained by increased velocities and fluid mixing.

In a rod bundle, the pattern of flow swirling is usually designed so that the swirling at adjacent subchannels do not cancel each other as illustrated in Fig. 3. Crossflow mixing patterns can be established by different swirl vane arrangements. Since rod bundle data with spacer grids which have swirling vanes are not available, a simple method of examining thermal hydraulic behavior of a swirling flow in a bundle is to examine the behavior of a swirling flow in a tube.

The heat-transfer augmentation in a circular tube with the gas swirled by twisted ribbon has been studied thoroughly by Thorsen and Landis [13]. The increases of heat transfer is due to the increasing of local gas velocity, the buoyancy induced by centrifugal force, and the variation of fluid properties. The swirling flow induces centrifugal force. With variable density of the fluid in the tube, the hot-and-lighter fluid at the wall
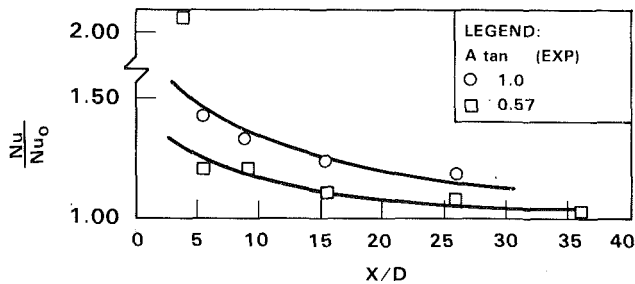
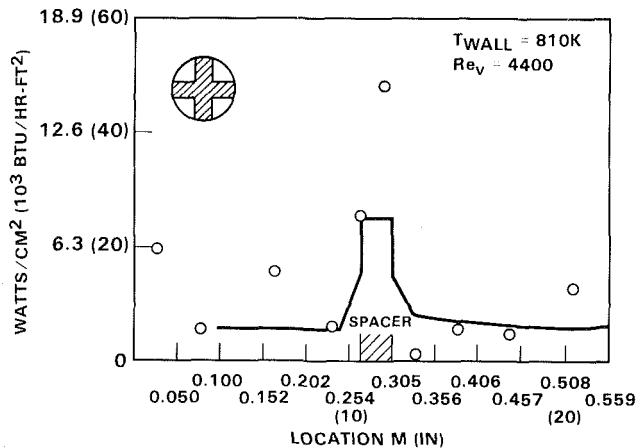Fig. 5   Heat-transfer augmentation with swirl generator at tube inlet

Fig. 6   Comparison of prediction and data [8] for post-CHF droplet flow (run 1)

Fig. 7   Comparison of predication and data [8] for post-CHF droplet flow (run 4)

will experience the buoyancy force and move toward the center of tube. Considering single-phase heat transfer in channels with small hydraulic diameters, the difference between wall temperature and the local bulk mean temperature of fluid will usually be small. Therefore, the radial variation of properties and the centrifugal force induced radial buoyancy will become insignificant.

Downstream of the swirling spacer, however, the local velocity at the wall is increased due to the imposed circumferential motion of the swirling flow. The magnitude of the circumferential velocity in the spacer can be related to the geometry of the swirling vanes as

$$V_{\phi 0} = V_z A \tan \phi \qquad (5)$$

where V_z is the axial component of the fluid velocity, A is the fraction of the projected area of the vanes to the flow cross-section when viewing from upstream, and ϕ is the angle of the vane with respect to the axial direction. It is generally believed that this equation would be more reliable if the angle ϕ is limited to less than 45 degrees. Considering the vector summation, the local mean velocity of the fluid becomes

$$V = V_z (1 + A^2 \tan^2 \phi)^{1/2} \qquad (6)$$

Equation (6) is used for the flow in a tube with an axially twisted ribbon over the full length of the tube. For the flow in a rod bundle with swirling grid spacers, the swirl flow generated by the spacer decays downstream of the grid. The decay of swirl flow in a tube has been studied by Kreith and Sonju [14]. Their data are plotted in Fig. 4, showing the exponential decay along the stream. The weak dependency on the Reynolds number can be neglected for simplicity. Finally, the decay of swirl flow can be represented by simple correlation

$$V_\phi = V_{\phi 0} e^{-0.017 (x/D)} \qquad (7)$$

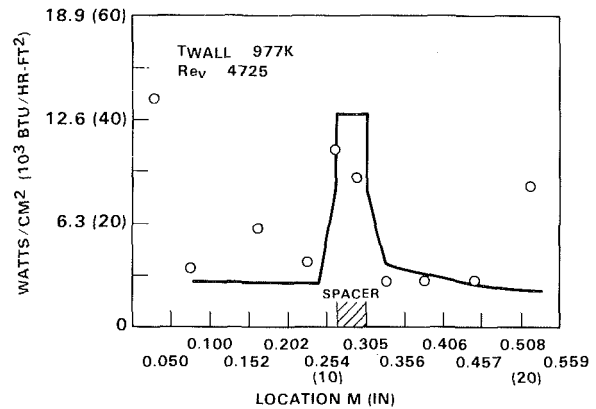The variation of local velocity affects the local heat transfer. Considering the relationship of velocity and Nusselt

number in Dittus-Boelter type equation for forced turbulent tube flow, then

$$\text{Nu} \sim V^{0.8} \qquad (8)$$

Modifying equation (6) by equation (7), then substituting into equation (8), the heat-transfer augmentation due to decaying flow swirling becomes

$$\left(\frac{\text{Nu}}{\text{Nu}_0} \right)_{sw} = [1 + A^2 \tan^2 \phi \, e^{-0.034 (x/D)}]^{0.4} \qquad (9)$$

In addition to the swirling effect, the heat-transfer augmentation is also affected by the boundary layer growth as described in the analysis of straight grid spacers without mixing vanes. Assuming these two mechanisms are not coupled, the overall heat-transfer augmentation due to a grid spacer (straight or swirling) can be established in a general form by multiplying equations (4) and (9) to get

$$\left(\frac{\text{Nu}}{\text{Nu}_0} \right)_{1\phi} = [1 + 5.55 \, \epsilon^2 e^{-0.13(x/D)}]$$

$$[1 + A^2 \tan^2 \phi e^{-0.034 (x/D)}] \qquad (10)$$

for the downstream region for single-phase flow. Here the blockage ratio ϵ includes both the grid and the vane. This equation (10) will be valid if the vane angle ϕ is less than, say, 45 deg.

For the swirling spacer in rod bundle for single-phase flow, there is no published heat-transfer data available for comparison with equation (10). Nevertheless, experimental data were reported by Migay and Goluber [15] for heat transfer augmentation in a tube with swirl generator at the inlet. The data are plotted in Fig. 5 for inlet $V_{\phi 0}/V_z$ equals to 1.0 and 0.57, respectively. The data were fitted nicely by equation (10), as shown in Fig. 5, where the blockage ratio of the swirl generator is selected to be 0.328. This value was not reported in reference [15] and was selected to make equation (10) fit the data. It is observed that the first data point in this figure cannot be predicted. The extreme high heat transfer at the tube inlet could be a result of the jetting of the flow from the blades of the swirl generator in tests.

Definitely, the comparison of the present analysis with the data of swirl generator [15] contains some degree of uncertainty. In view of this discrepancy, experimental data of swirling spacers in rod bundles is needed to substantiate our understanding of this problem.

Post-CHF Droplet Flow – Straight Egg-Crate Spacer Grids

Comparably little is known about the heat transfer near spacer grids for post critical heat-flux droplet flow. The heat-

transfer mechanisms are not clearly identified, and experimental data with detailed information are scarce. Nevertheless, many integral tests indicated that the rod bundle heat transfer is augmented near the spacer in post-CHF droplet flow [7].

Several mechanisms may contribute to the enhancement of post-CHF, spacer-grid heat transfer. Droplets may hit on the front end of the spacer and splash into fine dispersed droplets. This further dispersion of the liquid phase enhances the heat transfer from the wall to the vapor because the increased heat sink effect of the droplets reduce the vapor superheat. The detailed accounting of the heat sink effects to wall heat transfer has been demonstrated by Yao [16] for turbulent tube flow. However, this calculation requires detailed information on the droplet flow (e.g., droplet size) which is usually not reported adequately in many experiments. In addition, the splashed droplets may bounce to the hot wall and cause direct contact heat transfer to the wall. The contact heat transfer has been studied by McCarthy [17] and Iloeje [18] and found to be generally small in magnitude for large wall superheats, but it increases as wall superheat decreases.

The grid spacer itself is very likely to be wetted due to the droplet cooling, and its temperature is kept close to the saturation temperature of the fluid by continuous droplet impingement. As a result, the spacer becomes an effective heat sink for thermal radiation from the rod bundle. If the spacer contacts directly with the rods, the spacer also performs as a cooling fin to the hot rods. In addition to all of these mechanisms, the presence of the spacer may augment the heat transfer in a similar manner as it does in the single-phase flow described previously in this paper.

Due to the lack of knowledge on some complicated phenomena (e.g., the splashing mechanism), it is decided to include only those mechanisms which are presently calculable into our heat-transfer model. In the present analysis, only the effects of thermal radiation, fin cooling, and disturbance of vapor flow due to grid spacers are considered. As a result, the present analysis will only serve as an estimation of the lower bound of the heat-transfer augmentation in post-CHF droplet flow.

The thermal radiation in the region of grid spacer has been examined in the thesis by Cluss [8]. Gray-body radiation with no absorbing media was assumed, and the wall heat flux is given as

$$q_{w,\text{rad}} = \beta F_{ws} \, \sigma (T_w^4 - T_s^4) \tag{11}$$

where the β is the fraction of wall area seen by the spacer to the total area of wall, at the spacer region. The spacer temperature is assumed at the saturation temperature of the fluid. The rod bundle wall upstream or downstream of the grid spacer may also see the spacer as a heat sink. Considering rod bundle as a tube and the spacer as a disk which blocks the tube completely, the view factor from a ring on the tube to the disk can be calculated as a function of the tube axial distance. It appears that at the distance $2D$ away from the spacer, the view factor from wall to spacer is very small and thermal radiation exchange will be negligible. The radiative heat loss from the rod bundle wall can be linearly interpolated between the ends of spacer to the locations at $2D$ away, where the radiative heat loss to the spacer is assumed to be 0.

When contact occurs between the spacer and the rods in the bundle, fin cooling of the rods should also be considered. For post-CHF droplet flow the grid spacer may be quenched by the impinging droplets and will be at the saturation temperature of the entrained liquid flow. As a conservative estimation, the heat-transfer coefficient on the fin is assumed to be the same as that at the post-CHF hot wall. With this, the effect of fin cooling to the wall at the location of grid spacer can be evaluated in a conventional manner.

For very small droplets, the dispersed two-phase flow can be considered as nearly homogeneous. Assuming that the heat and momentum transfer analogy still exist for this homogeneous flow, equation (4) for single-phase flow heat-transfer augmentation at the grid spacer and downstream, can be used.

All the three mechanisms, radiation, fin cooling, and vapor flow disturbance with entrained droplets contribute to the heat transfer augmentation from the wall in post-CHF, heat-transfer situations. Assuming they are not coupled, the total heat flux will be the summation of these three.

$$q_w = q_{w,\text{rad}} + q_{w,\text{fin}} + q_{w,2\phi} \tag{12}$$

where each component can be evaluated as stated previously.

Although many rod bundle experiments have been performed at post-CHF dispersed flow with grid spacers in the flow channel, most of them do not report experimental information with detail for comparison with the above analytical predictions. The test data of Cluss [8] for reflood and quenching of a vertical tube, however, can be used for comparison. In this experiment, the constant wall temperature is maintained by adjusting the individual power to various copper blocks which are clamped axially along the tube. Due to different power requirement, each copper block may have a different temperature while maintaining the same tube wall temperature. Therefore, axial conduction between copper blocks gives significant data scattering, especially at the location near the spacer. Comparisons of Cluss's data and the prediction of using the model given by equation (12) are shown in Fig. 6 and 7 for wall temperatures at 810K and 977K, respectively. The cross-section of the spacer is shown in Fig. 6. Comparison starts at 0.10m from the inlet to exclude the tube entrance effect. The effect of radiative cooling extends to distance $2D$ up and downstream of the spacer. The effect of fin cooling is localized at the spacer. The convective heat-transfer components affects the downstream tube wall.

Even with the scattering of the data, the comparison appears to be reasonable. In the present calculation, at the spacer location the vapor convection and fin cooling represents 35 to 40 percent of the total heat transfer, respectively, while thermal radiation represents 30 to 20 percent. It is important to recall that several other mechanisms have not been considered in this analysis. Considering the strong heat-transfer augmentation at the grid spacer as indicated in Figs. 6 and 7, we may conclude that the location near the grid spacer will be quenched or wetted easier than other locations in the bundle at post-CHF conditions. Therefore, the result of the present analysis should be considered as a first-order estimation of the heat-transfer augmentation in post-CHF dispersed flow.

Conclusion

The presence of grid spacers generally augment the heat transfer at its surroundings. With the present analysis, a model which represents the different heat-transfer mechanisms is proposed for heat-transfer augmentation for straight and swirling grid spacers in single-phase and post-CHF dispersed flow. The corresponding equations (4), (10) and (12) can be used for heat transfer predictions of these cases. While insufficient experimental data exists for verification of this model, it can be used as a guide for understanding heat transfer at and downstream of grid spacers.

References

1 Rehme, K., "Pressure Drop Correlations for Fuel Element Spacers," *Nuclear Technology*, Vol. 17, 1973, pp. 15–23.

2 Rehme, K., "Pressure Drop of Spacer Grids in Smooth and Roughened Rod Bundles," *Nuclear Technology*, Vol. 31, 1977, pp. 314–317.

3 Idel'chik, I. E., *Handbook of Hydraulic Resistance*, AEC-tr-6630, 1966.

4 De Stordeur, A. N., "Drag Coefficients for Fuel-Element Spacers," *Nucleonics*, Vol. 19, No. 6, 1961, pp. 74–79.

5 de Paz, J. F., "Pressure Drop and Volume Fraction of Grid and Wire Spaced Subassemblies," ANL-AFP-13, 1975.

6 Marek, J. and Rehme, K., "Heat Transfer in Smooth and Roughened Rod Bundles near Spacer Grids," *Fluid Flow and Heat Transfer over Rod or Tube Bundles*, Edited by S. Yao and P. Pfund, ASME, 1979, p. 163–170.

7 Conway, C. E., et. al., "PWR FLECHT Separate Effects and Systems Effects Test (SEASET) Program Plan," NRC/EPRI/Westinghouse Report No. 1, 1977.

8 Cluss, E. M., Junior, "Post Critical Heat Flux Heat Transfer in a Vertical Tube Including Spacer Grid Effects," MIT. S. B. thesis, June, 1978.

9 Vlcek, J. and Weber, P., "The Experimental Investigation of a Local (spot) Heat Transfer Coefficient in the Fuel Spacer Area," Australian Atomic Energy Commission Research Establishment, LIB/TRANS 250, Feb. 1970.

10 Kidd, G. J. and Hoffman, H. W., "The Temperature Structure and Heat Transfer Characteristics of an Electrically Heated Model of a Seven-Rod Cluster Fuel Element," ASME paper 68-WA/HT-33.

11 Krett, V. and Majer, J., "Temperature Fluid Measurement in the Region of Spacing Elements," Report ZJE-114, Skoda Works Nuclear Power Construction Dept., Information Centre Plzen-Czechoslovakia, 1971.

12 Hudina, M. and Nothigen, H., "Experiment Study of Local Heat Transfer under and near Grid Spacers Developed for GCFR," Report TM-IN-526, Swiss Federal Institute for Reactor Research Wirenlingen, 1973 or *2nd NEA-GCFR Specialist Meeting on Heat Transfer*, 1972.

13 Thorsen, R. and Landis, F., "Friction and Heat Transfer Characters in Turbulent Swirl Flow Subjected to Large Transverse Temperature Gradients," ASME, *Journal of Heat Transfer*, 1968, pp. 87–97.

14 Kreith, F. and Sonju, O., "The Decay of a Turbulent Swirl in a Pipe," *Journal of Fluid Mechanics*, Vol. 22, Part 2, 1965, pp. 257–271.

15 Migay, V. and Golubev, L., "Friction and Heat Transfer in Turbulent Swirl Flow with Variable Swirl Generator in a Pipe," *Heat Transfer—Soviet Research*, Vol. 2, No. 3, 1970, pp. 68–73.

16 Yao, S. C. and Rane, A., "Numerical Study of Turbulent Droplet Flow Heat Transfer," *International Journal of Heat and Mass Transfer*, Vol. 24, No. 5, pp. 785–792, 1981.

17 Kendall, G. E., "Heat Transfer to Impacting Drops and Post Critical Heat Flux Dispersed Flow," Ph. D. thesis, MIT, 1978.

18 Iloeje, O. C., Plummer, D. N., Rohsenow, W. M., and Griffith, P., "A Study of Wall Reset and Heat Transfer in Dispersed Vertical Flow," MIT Report No. 72718-92, 1974.

19 Tong, L. S. and J. Weisman, *Thermal Analysis of Pressurized Water Reactors*, 2nd ed., American Nuclear Society, 1979, p. 285.

Turbulent Heat Transfer in a Symmetrically or Asymmetrically Heated Flat Rectangular Duct With Flow Separation at Inlet

E. M. Sparrow
Fellow ASME

N. Cur
Department of Mechanical Engineering,
University of Minnesota,
Minneapolis, Minn. 55455

Heat transfer experiments were performed for a high-aspect-ratio (~18) rectangular duct having a sharp-edged inlet, with air being drawn into the inlet from a large upstream space. The experiments encompassed data runs where both of the principal walls of the duct were isothermal (at the same temperature) and other runs where one wall was isothermal while the other was adiabatic. Local heat transfer coefficients were determined for all runs. It was found that flow separation at the duct inlet played a decisive role in shaping the axial distribution of the heat transfer coefficient in the thermal entrance region. Of particular note is a high heat transfer peak at the point of flow reattachment. The peak is situated at an axial station less than one hydraulic diameter from the inlet and moves upstream with increasing Reynolds number. The heat transfer coefficients for symmetric and asymmetric heating are identical in the initial portion of the thermal entrance region. Deviations occur farther downstream but do not exceed more than about 7 percent. The entrance length for asymmetric heating is significantly greater than that for symmetric heating.

Introduction

It is noteworthy that numerous important issues remain unsettled with regard to turbulent, forced-convection heat transfer in flat rectangular ducts. One such issue is the effect of the duct inlet configuration in shaping the velocity field which, in turn, influences the heat transfer at the duct walls. From the standpoint of analysis, consideration has been restricted to either of two types of velocity distributions at the duct cross section where heat transfer begins. For one of these, the velocity distribution is already fully developed at the onset of heating, so that the heat transfer problem is solved with the velocity as a fixed input. The other traditional case is that in which the velocity is assumed uniform across the section where heating is initiated, so that there is simultaneous development of the velocity and temperature fields in the duct. Indeed, owing to the frequent use of the uniform inlet-velocity model in analysis, the simultaneous development of the velocity and temperature fields has been linked more or less exclusively with such a uniform inlet flow. The restrictive nature of such an association will soon become apparent.

With regard to experiments involving rectangular ducts, a search of the literature revealed a paucity of work on simultaneously developing velocity and temperature fields. Furthermore, in the available experiments, the inlet velocity conditions were generally not well defined. Thus, in the oft-quoted work of Byrne, Hatton, and Marriott [1], there is some upstream hydrodynamic development (as pointed out in

[2]) due to the presence of a contoured, converging entrance mouthpiece. The geometry of the mouthpiece is, however, highly specific to the apparatus of [1], as is the degree of upstream development. Tan and Charters [3] devoted three sentences to the description of their experimental apparatus, and no information is provided about the velocity conditions at the inlet. A paper by Sukomel and co-workers [4] reported entrance region heat transfer coefficients for simultaneously developing velocity and temperature fields, and only by innuendo was it revealed that a sharp-edged inlet was not employed. The presence of a laminar region in the upstream portion of the duct at Reynolds numbers as high as 50,000, as inferred from the plotted heat transfer coefficents, suggested the use of a well-designed inlet contraction. None among [1], [3], and [4] report any evidence or effects of flow separation at the inlet, as would occur, for example, if the inlet were sharp edged.

One of the foci of the present experimental study is to provide local results for turbulent heat transfer in a flat, rectangular duct where the simultaneous development of the velocity and temperature fields stems from a well-defined and reproducible inlet configuration. The duct is shown in a schematic side view in the main portion of Fig. 1. As seen there, the flow is drawn from a large upstream space and passes through a sharp-edged inlet as it enters the duct. The upstream edges of the duct walls are flush with the front face of a baffle plate. The baffle dimensions are very large compared with the duct cross-sectional dimensions so that, from the standpoint of the fluid flow, it perceives the duct inlet as an aperture in an infinite wall.

The just-described duct inlet configuration is well-defined, reproducible, and simple, yet, as will be demonstrated later, it does not provide a correspondingly simple inlet velocity distribution. Rather, in the neighborhood of the inlet, zones of flow separation are situated adjacent to the respective walls of the duct. The presence of these separated regions is the decisive factor in the thermal development of the flow, as is documented by the present data. Since flow separation is neglected in the published analyses of the turbulent thermal entrance region, the analyses are not applicable to the case of the sharp-edged inlet. Furthermore, as noted previously, experimental results also appear to be lacking for this case.

In addition to the just-discussed issue of the duct inlet configuration, a second focus of the paper is the effect of the thermal boundary conditions at the duct walls on the heat transfer results. Experiments are performed both for symmetric and asymmetric heat transfer conditions. In the first case, the two principal walls of the duct are maintained at the same uniform temperature, while in the second case one principal wall is at a uniform temperature and the second principal wall is adiabatic. For both cases, heat transfer results are obtained for both the thermal entrance region and the fully developed region.

With respect to the literature, the results corresponding to these boundary conditions are novel in two respects. First, rectangular-duct experiments have not been heretofore reported for the uniform wall-temperature boundary condition, neither for the symmetric case nor the asymmetric case. Second, experimental results encompassing both the thermal entrance and fully developed regions are not available for both the symmetric and asymmetric cases, neither for the uniform wall temperature nor uniform heat flux boundary conditions.

To provide perspective for the foregoing paragraph, the relevant literature will be briefly reviewed. For the uniform heat flux boundary condition, entrance region and fully developed heat transfer coefficients were measured in [1] and [3] for asymmetric heating, but not for symmetric heating. Other asymmetric heat/mass transfer experiments were performed in [5] and [6], respectively, in a two-fluid heat exchanger and for the evaporation of water. On the other hand, experimental results for both symmetric and asymmetric heating with uniform heat flux were determined in [7] and [8], but only for the thermally developed regime.

Some comparisons between the heat transfer results for symmetric and asymmetric heating have been made on the basis of analytical/numerical solutions, but only for hydrodynamically developed flow. Axial Nusselt number distributions were computed in [9] which showed that differences between symmetric and asymmetric heating manifested themselves primarily in the thermally developed regime. These differences diminished with increasing Prandtl number.

As seen at the lower right of Fig. 1, the aspect ratio W/H of the duct cross section is large-equal to 18.3. This large
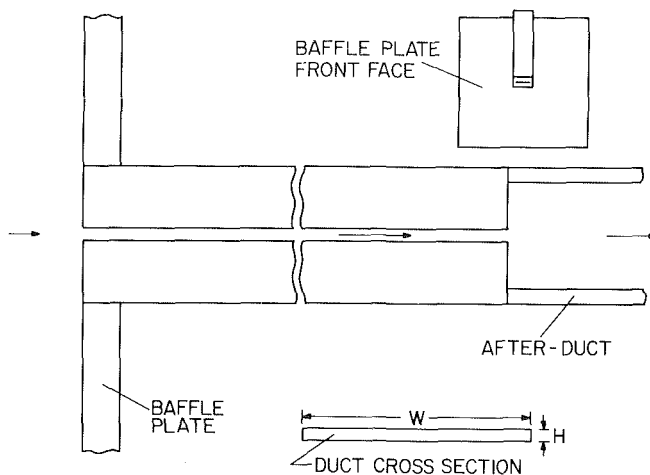

Fig. 1 Schematic side view of the apparatus (main diagram) and related apparatus details (insets)

aspect ratio was chosen so that the duct would closely approximate a parallel-plate channel. Air was the working fluid for the experiments. The details of the duct and related apparatus and instrumentation will now be presented.

The Experiments

The heat transfer results to be reported here were obtained by mass transfer measurements and by the subsequent application of the analogy between heat and mass transfer. The mass transfer measurements were performed utilizing the naphthalene sublimation technique. This technique has been employed for a wide variety of fluid flows, both turbulent and laminar. Its validity has been firmly established both on a first-principles basis [10] and by comparisons with experimental correlations and analytical predictions for heat transfer. The apparatus used in the naphthalene sublimitation experiments will now be described.

Experimental apparatus. The description of the apparatus will begin by elaborating Fig. 1. The main components include: (a) a flat rectangular duct which serves as the test section, (b) a baffle plate at the upstream end of the test section, and (c) an after-duct which receives the discharge from the test section. Air is drawn into the test section from the laboratory room. After traversing the length of the test section, the air passes into the after-duct. The function of the after-duct is to provide a transition from the highly flattened rectangular cross section of the test section to the circular piping of the downstream air-handling system. The dimensions of the after-duct were chosen with a view to avoiding disturbances of the flow in the downstream portion of the test section. Upon exiting the after-duct, the flow passes through a flowmeter (either of two rotameters, depending on the flow rate), a control valve, and a blower. The blower is situated in a service corridor outside the laboratory, and its

--- Nomenclature ---

D_h = hydraulic diameter, equation (7)

$\mathcal{D}$ = naphthalene-air diffusion coefficient

H = duct height, Fig. 1 (inset)

K = mass transfer coefficients, equations (5) and (9)

$\dot{M}$ = rate of mass transfer per unit length

$\dot{m}$ = local rate of mass transfer per unit area

$\dot{m}_u$ = spanwise uniform value of $\dot{m}$

P = duct perimeter

$\dot{Q}$ = volume flow rate in duct

Re = Reynolds number, $4\dot{w}/\mu P$

Sc = Schmidt number

Sh = Sherwood number at axial station x

Sh_{fd} = fully-developed Sherwood number

Sh_{xy} = point Sherwood number

W = duct width, Fig. 1 (inset)

$\dot{w}$ = rate of airflow in duct

x = streamwise coordinate

y = spanwise coordinate

δ = sublimation depth

μ = viscosity

ρ_s = density of solid naphthalene

ρ_{nb} = bulk density of naphthalene vapor

ρ_{nw} = density of naphthalene vapor at wall

τ = duration time of data run

discharge (which contains naphthalene vapor) is vented outside the building.

The test-section duct consists of two principal walls (the upper and lower walls of the channel pictured in Fig. 1) and two short side walls which are, in effect, spacers which separate the principal walls. Each principal wall was fabricated from an aluminum block, with overall dimensions 20.32 × 10.74 × 2.22 cm (length × width × height). All told, a total of three such blocks were fabricated to accommodate the desired boundary conditions. An adiabatic boundary in a heat transfer problem corresponds, in terms of the naphthalene sublimation technique, to a surface made of a material other than naphthalene, thereby ensuring the absence of mass transfer at that surface. One of the three aluminum blocks was used to model the adiabatic boundary condition. The face of the block that was chosen to serve as the bounding surface of the duct flow was painstakingly polished to a high degree of smoothness, and an array of pressure taps was installed along the length of the block to monitor the axial variation of the pressure in the airflow.

The other two blocks were carefully machined so that each could participate in a casting process which would produce a smooth, solid napthalene surface for bounding the airflow in the duct. These blocks were machined in an identical manner. With the aid of a milling machine, metal was cored out of the interior, leaving a frame-like structure which surrounds an empty space. By a casting process to be described later, the space is filled by solid naphthalene, as shown in Fig. 2. As seen in the figure, the exposed napthalene surface is co-planar with the frame.

The width of the frame along the sides and at the downstream end of the napthalene surface is 1.27 cm. At the upstream end, the frame was made as narrow as possible so that mass transfer would be initiated as close as possible to the duct inlet cross section. Based on considerations of strength and dimensional uniformity, the upstream-end frame was made equal to 0.050 cm. Additional strength was achieved by beveling the metal to greater thickness beneath the exposed surface of the naphthalene. Furthermore, the entire frame structure was strengthened and stiffened by integral ribs internal to the frame for which provision had been made during the milling operations. The framed naphthalene surface was 19 cm long (i.e., in the streamwise direction) and 8.13 cm wide (transverse to the flow direction).

The duct side walls rested on the frame and served as spacers between the principal walls of the duct. They were made of flat brass bars, 20.32 cm long and 1.27 cm wide, thereby matching both the length and the width of the frame. The thickness of the bars was chosen to yield a duct cross-sectional aspect ratio (width/height) of about 18, and the final finished thickness of the bars was measured to be 0.445 cm.

The assembly of the duct, which was performed prior to each data run, was facilitated by locating pins which ensured that alignment was maintained during the stacking of the side walls on the lower plate and the subsequent stacking of the upper plate on the side walls. Once assembled, the duct was held together by screws.

Two versions of the duct were employed. For symmetric heat transfer, the surface of each principal wall which interfaced with the airflow was of naphthalene. For the unsymmetric heat transfer situation, the lower bounding surface of the airflow channel was of naphthalene while the upper bounding surface was the polished face of the aforementioned solid aluminum block.

The baffle plate, which participates in defining the inlet fluid-flow configuration, is shown in side view in the main portion of Fig. 1 and in front-face view in the inset at the upper right of the figure. It is a 66 × 66 cm square, made of 1.27-cm thick aluminum, and is pierced by an opening which accommodates the cross-sectional dimensions of the rectangular duct. As indicated in the inset, the width of the opening was made to precisely fit the width of the duct. The height of the opening is adjustable (by means of a movable panel), so that a precise matching of the heights of the opening and the duct was also achieved. The rear face of the baffle was equipped with a platform which served to support the duct.

The after-duct was fabricated so that its external dimensions precisely matched the external dimensions of the test-section duct. This matchup of dimensions was highly advantageous during the sealing operations at the duct-duct interface. The sealing was accomplished by a highly adhesive, strong, compliant tape which was augmented by silicone rubber sealant. Rigorous tests were performed to verify the absence of leaks. The after-duct is 68.6 cm long, with a flow cross section of 9.40 × 3.65 cm.

As was mentioned earlier, the naphthalene test surfaces were prepared by a casting process. A two-part mold was used, one part of which is the hollowed-out aluminum block which houses the test surface and the other part of which is a highly polished stainless steel plate. For the casting, the surface of the block which frames the test surface is placed face down on the stainless steel plate. Then, molten naphthalene is poured into the hollow space through the open back of the block. Upon solidification of the naphthalene, the mold parts are separated. The separation exposes the naphthalene surface which had solidified against the polished plate. The smoothness of the naphthalene surface is comparable to that of the plate against which it was cast.

The naphthalene exposed by the open back of the aluminum block was covered by highly adhesive tape, with additional sealing being provided by silicone rubber.

Instrumentation and experimentation procedure. Measurements of the contour of the naphthalene test surfaces, made both before and after a data run, enabled the determination of local mass transfer rates and transfer coefficients. These contour measurements were performed with the test surface situated on a movable coordinate table which provided two directions of accurately controlled horizontal travel. The table was equipped with a guide and pins to facilitate horizontal positioning of the surface, the trueness of the positioning being greatly aided by the rigidity of the metal frame which encompassed the test surface. In addition, clamps affixed to the table were employed to provide a downward force on the frame, thereby assisting in the establishment of a consistent vertical positioning of the test surface.

The surface contours were measured by instrumentation which converts the movement of a sensor tip (similar to the tip of a dial gage) into an electrical signal that can be read and recorded by a digital voltmeter. The instrumentation includes a sensing head which houses a linear variable differential transformer and signal conditioning electronics. The last digit of the voltmeter output corresponds to 10^{-5} in.

The layout of the measurement grid on the naphthalene surface was made so as to obtain a higher concentration of points in regions where the mass transfer rates varied rapidly with position. The most rapid variations occurred immediately downstream of the inlet cross section, and the grid point deployment used to resolve these variations will be evident from the presentation of results.

As a preparatory step prior to each data run, the naphthalene remaining within the hollowed-out block from the preceding run was removed by melting and evaporation. Then, the casting procedure was performed, using fresh (previously unused) reagent grade naphthalene. Once the cast surface(s) had been prepared, they were wrapped in impermeable plastic and placed in an air-tight container situated

in the temperature-controlled laboratory where the experiments were to be performed. A thermal equilibration period of overnight duration was allowed prior to the initiation of the data run.

Each data run, in its entirety, involved a succession of operations. These included: (a) warmup of the air supply, (b) surface contour measurements prior to the test period, (c) assembly of the duct and its interfacing with the after-duct, (d) the test period, (e) disassembly of the duct, and (f) surface contour measurements after the test period. In addition to the data runs for which results are reported, auxiliary runs were made at various fixed Reynolds numbers to explore the effect of the duration of the run. Since the extent to which the naphthalene surface recedes is proportional to the run time, the auxiliary runs were performed to verify that the actual surface recessions encountered did not diminish the accuracy of the results.

Data Reduction

The objective of the data reduction procedure was to determine local mass transfer coefficients and local Sherwood numbers (the Sherwood number is the mass transfer counterpart of the Nusselt number). The starting point of the data reduction is the differencing of the surface contour measurements made before and after the data run. The local value of the difference will be referred to as the sublimation depth $\delta(x,y)$, where x and y are, respectively, the streamwise and spanwise coordinates as pictured in Fig. 2. If ρ_s is the density of the solid naphthalene (1.146 gm/cm^3) and τ is the duration time of the run, then the local rate of mass transfer $\dot{m}(x,y)$ per unit surface area is

$$\dot{m}(x,y) = \rho_s \delta(x,y)/\tau \tag{1}$$

In addition to the mass transfer rate, the evaluation of the mass transfer coefficient involves the naphthalene vapor densities in the bulk and at the wall. The bulk density, ρ_{nb}, plays a role analogous to the bulk temperature in the corresponding heat transfer problem. As the air passes through the duct, the sublimation at the wall causes an increase in the naphthalene vapor concentration, so that ρ_{nb} is a function of x.

To find $\rho_{nb}(x)$, a mass balance may be made for a control volume which spans the duct cross section and is contained between axial stations s and $(x+dx)$. Let $\dot{M}(x)dx$ denote the mass of naphthalene vapor added to the flow per unit time between x and $(x+dx)$. Also, let $\dot{Q}$ denote the rate of volume flow passing through the duct cross section; for the present experiments, $\dot{Q}$ is virtually independent of x (less than 1-percent variation relative to the mean value). Then, the mass balance yields

$$\dot{Q}d\rho_{nb} = \dot{M}(x)dx \tag{2}$$

from which there follows, after integration and with $\rho_{nb}=0$ at $x=0$

$$\rho_{nb}(x) = \int_0^x \dot{M}(x)dx/\dot{Q} \tag{3}$$

The quantity $\dot{M}(x)$ which appears in equation (3) is obtained by integration of $\dot{m}(x,y)$ across the width of the duct at each axial station x at which data are collected. If the subscripts 1 and 2 denote the respective principal walls of the duct, then

$$\dot{M}_1(x) = \int_0^w \dot{m}_1(x,y)dy, \quad \dot{M}_2(x) = \int_0^w \dot{m}_2(x,y)dy \tag{4}$$

and

$$\dot{M}(x) = \dot{M}_1(x) + \dot{M}_2(x) \tag{4a}$$

For the data runs where both principal walls participated in the mass transfer process, the values of $\dot{M}_1(x)$ and $\dot{M}_2(x)$
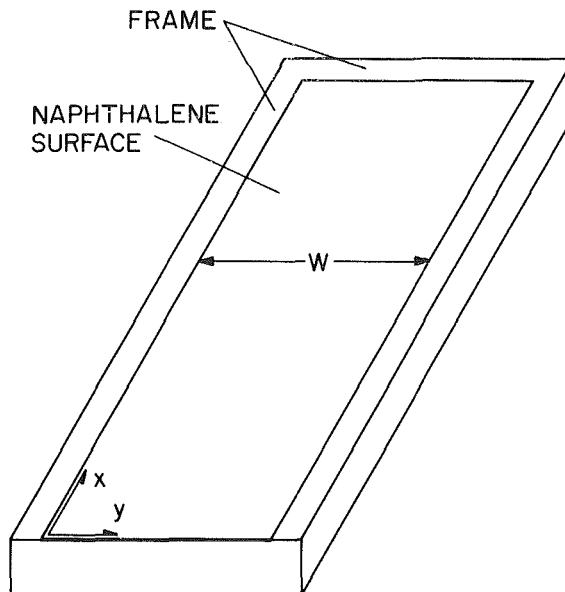

Fig. 2 Naphthalene test surface and its surrounding frame

generally agreed to within a few percent, except at a few stations in the very immediate neighborhood of the inlet in a few of the data runs. As discussed later, some irregularity is to be expected in a region of flow separation. When one of the walls (i.e., the upper wall) was a nonparticipant, then $\dot{M}_2(x) = 0$.

Attention will now be turned to the naphthalene vapor density at either of the participating walls. Earlier measurements had shown that the depression of the surface temperature due to sublimation of naphthalene is negligible. Consequently, the surface temperature can be evaluated at the measured air temperature, provided that proper precautions are taken to ensure that equilibration of the surface has occurred before the beginning of the data run. With the air temperature as input, the naphthalene vapor pressure at the wall, p_{nw}, was determined from the Sogin vapor pressure – temperature relation [11]. Then, the corresponding vapor density, ρ_{nw}, follows from the perfect gas law.

The intent of the research was to determine heat (mass) transfer results characteristic of a parallel-plate channel, and it was that objective which prompted the selection of a large cross-sectional aspect ratio (~ 18). As will be illustrated later, the measured mass transfer rates were essentially uniform across most of the duct width at a fixed axial station x. The minor nonuniformities in the regions of apparent spanwise uniformity were averaged out and, in the case where both of the walls participated, the averaging encompassed both walls. If the uniform mass transfer rate per unit area that is characteristic of each station is denoted by $\dot{m}_u(x)$, then the local mass transfer coefficient for that station is defined as

$$K(x) = \dot{m}_u(x)/\{\rho_{nw} - \rho_{nb}(x)\} \tag{5}$$

The dimensionless counterpart of K is the Sherwood number, which is defined here as

$$Sh = K(x)D_h/\mathfrak{D} \tag{6}$$

where the dependence of Sh on x is not indicated explicitly to simplify the discussion of results, where frequent reference will be made to Sh (Sh(x) is rather cumbersome). The quantity D_h is the hydraulic diameter

$$D_h = 4WH/(2W+2H) \tag{7}$$

in which W and H are illustrated in Fig. 1, and $\mathfrak{D}$ is the naphthalene-air diffusion coefficient.

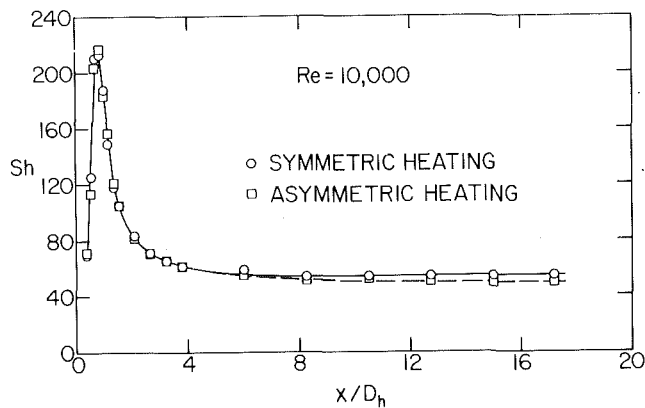With the definition of the Schmidt number, $Sc = \nu/\mathfrak{D}$, equation (6) can be rephrased as

Fig. 3 Distribution of the Sherwood number along the length of the duct for Re = 10,000

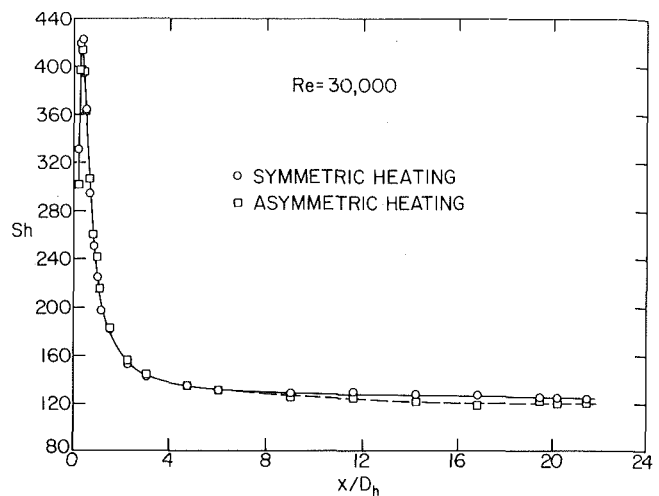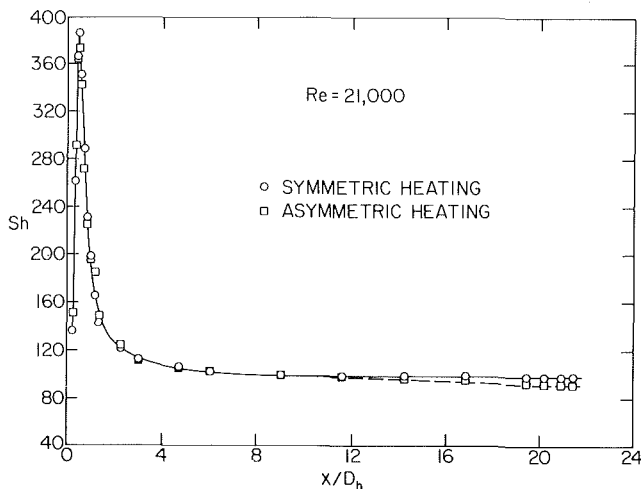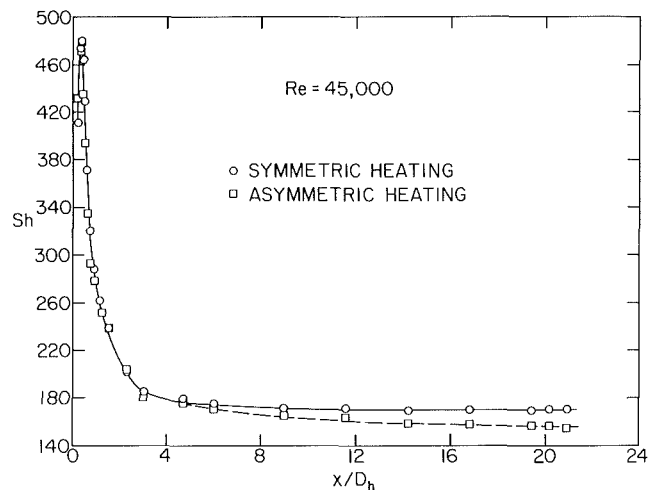Fig. 4 Distribution of the Sherwood number along the length of the duct for Re = 21,000

Fig. 5 Distribution of the Sherwood number along the length of the duct for Re = 30,000

Fig. 6 Distribution of the Sherwood number along the length of the duct for Re = 45,000

$$\text{Sh} = (K(x)D_h/\nu)\text{Sc} \qquad (8)$$

According to [11], $\text{Sc} = 2.5$ for the naphthalene-air system. The kinematic viscosity ν was evaluated for pure air in recognition of the minute amounts of naphthalene vapor that are present. In addition, the density that appears in ν was evaluated at the measured mean test-section pressure.

Illustrative results will also be presented displaying both the spanwise and the streamwise distributions of the mass transfer coefficient. Let $K(x,y)$ denote the point mass transfer coefficient (i.e., at x,y)

$$K(x,y) = \frac{\dot{m}(x,y)}{\rho_{nw} - \rho_{nb}(x)} \qquad (9)$$

with the corresponding point Sherwood number

$$\text{Sh}_{xy} = (K(x,y)D_h/\nu)\text{Sc} \qquad (10)$$

The fluid flow conditions were characterized by the Reynolds number

$$\text{Re} = 4\dot{w}/\mu P \qquad (11)$$

where P is the duct perimeter, $(2W + 2H)$, and $\dot{w}$ is the rate of fluid flow through the duct.

Results and Discussion

In view of the analogy between the two processes, the phrases heat transfer and mass transfer will be used interchangeably during the presentation of results.

The distribution of the heat (mass) transfer coefficient along the length of the duct is presented in Figs. 3–6, respectively, for Reynolds numbers of 10, 21, 30, and 45

thousand. In each figure, the local Sherwood numbers corresponding to a succession of axial stations x are plotted as a function of the dimensionless axial coordinate x/D_h. Results are presented for both symmetric heating (circular data symbols) and for asymmetric heating (square data symbols). For the case of symmetric heating, the boundary condition at both of the principal walls corresponds, via the heat/mass transfer analogy, to the same uniform wall temperature. For asymmetric heating, one of the principal walls is isothermal and participates in the heat transfer process while the other wall is nonparticipating (i.e., adiabatic, in accordance with the analogy).

From an overall examination of Figs. 3–6, a number of trends are in evidence, the most interesting of which is the shape of the Sh versus the x/D_h distribution itself. Starting with a moderate value immediately adjacent to the inlet, the Sherwood number soars upward and reaches a sharp maximum, whereafter it begins to decrease at a rate that is about as rapid as that of the initial increase. The rate of decrease slackens with increasing downstream distance, and the Sherwood number ultimately coasts to a fully developed value.

The novel features of the Sh versus x/D_h distribution are the initial rapid rise of the Sherwood number and the maximum. Indeed, these features have not heretofore been reported in the experimental literature on turbulent heat transfer in rectangular ducts, nor have they been encountered

in analytical/numerical work on the subject. Rather, the information available in the literature shows a steady decrease of the Sherwood number (or Nusselt number) with x/D_h.

From a consideration of the fluid-flow phenomena that occur at a sharp-edged inlet, the results of Figs. 3–6 are readily rationalized. The initial moderate values of the Sherwood number, the rapid rise, the sharp maximum, and the subsequent rapid decline are indicative of the successive processes of flow separation, reattachment, and redevelopment. Indeed, the initial portion of the Sh versus x/D_h curve can be regarded as the characteristic signature of these processes.

Curves showing a similar form have been encountered in other physical situations where the geometry of the system mandates that the flow separate. These include the flow downstream of an orifice in a pipe [12] and the flow downstream of an enlargement step in a duct [13].

The peak of the curve is usually associated with the reattachment of the separated flow. Thus, in the present experiments, reattachment is seen to occur for values of $x/D_h < 1$. At Re = 10,000, the reattachment occurs at $x/D_h \simeq 0.85$. As Re increases, the reattachment point moves upstream toward the inlet; at Re = 45,000, the reattachment is at $x/D_h \simeq 0.4$. As seen in Fig. 6, the very close proximity of the peak to the duct inlet has precluded a complete resolution of the increase in Sh which occurs upstream of the peak.

The aforementioned small values of x/D_h, corresponding to the peak of the Sh versus x/D_h curves, cast light on why the presence of flow separation adjacent to a sharp-edged inlet has not been detected in prior experiments. Those experiments were performed for heat transfer, with inherent difficulties in obtaining sufficiently localized heat transfer and temperature measurements to resolve the peak of the curve. Another factor of equal importance is the difficulty in controlling the thermal boundary conditions in the immediate neighborhood of the inlet.

With regard to analysis/computation, the absence of a peak in the predicted axial distribution of Nu (or Sh) can be traced to the nature of the velocity models selected for the analysis. In general, the models have not taken flow separation into account but, rather, have assumed either a uniform or a fully developed velocity profile at the duct inlet.

The numerical values of Sh at the peak are impressively high, and this is another important characteristic of a reattached separated flow. For example, for the symmetric-heated case, the peak value of Sh is about four times the fully developed value of Re = 10,000. This ratio decreases with the Reynolds number; at Re = 45,000, the peak to fully developed ratio is about 2.8. Thus, the presence of the separation-reattachment process gives rise to much higher entrance region heat transfer coefficients than would be encountered for a conventional thermally and hydrodynamically developing duct flow.

Beyond the peak, the monotonic decrease of Sh with x/D_h resembles that for a conventional duct flow although, as indicated in the foregoing, different numerical values of Sh should prevail as long as the flow remembers the existence of the separated region. In the thermally developed regime, there should be no effects of the upstream history of the flow.

Attention may now be turned to a comparison of the results for the symmetric and asymmetric heating conditions. In this regard, several general observations can be made in Figs. 3–6. First, within the scatter of the data (to be discussed shortly), the Sherwood numbers for the two cases are equal in the initial portion of the thermal entrance region, as is consistent with the development of identical, noninteracting thermal boundary layers on the heated walls. In the downstream portion of the entrance region, the two sets of Sherwood numbers lie on separate lines, with those for asymmetric heating falling below those for symmetric heating. The dif-

ferences between the Sherwood numbers for the two cases are modest, being typically about seven percent in the thermally developed region. The lower Sherwood numbers for the asymmetric case reflect what is, in effect, a thicker thermal boundary layer. As a consequence of this thicker thermal layer, the thermal development requires a greater length of duct for asymmetric heating than for symmetric heating, and this characteristic is in evidence in the figures. If the thermal entrance length is defined as corresponding to a 5 percent approach to the fully developed value, then the entrance lengths for symmetric heating lie in the x/D_h range from 5 to 7, while those for asymmetric heating range from x/D_h of 10 to 13.

The fact that asymmetric heating gives rise to lower heat transfer coefficients than symmetric heating is well established, both by experiment (e.g., [7]) and by analysis (e.g., [9]). The analysis of [9] deals with the same thermal boundary conditions that were employed here but is based on the assumption of a hydrodynamically developed velocity distribution. All of the qualitative relationships between symmetric and asymmetric heating that were observed in Figs. 3–6 are in evidence in the graphical presentation of [9]. In addition, the seven percent deviations in the fully developed Sherwood numbers for the two cases, as cited in an earlier paragraph, appear consistent with the best estimates that can be made by interpolation of information available in [9].

Before leaving Figs. 3–6, it is appropriate to make mention of auxiliary experiments that were undertaken to explore the reproducibility of the data in the separation-reattachment region. It is well known that a separated flow is not a truly steady flow and that the reattachment point tends to wander. In this regard, it is relevant to inquire whether the extent of the surface recession due to sublimation might affect the wandering of the reattachment point and, thereby, the general pattern of fluid flow in the separated region.

For a fixed Reynolds number, data runs of different duration were performed so as to vary the amount of sublimation. These runs revealed only modest differences in the Sherwood numbers in the separation-reattachment region (typically 5 percent and, in the extreme, 10 percent). Indeed, these differences were not unlike those encountered when repeated runs were made at a fixed Reynolds number and a fixed duration time. Such run-to-run differences in the separation-reattachment region are not unexpected, owing to the unsteady nature of the physical processes involved. The outcome of the auxiliary runs lends support to the general accuracy of the data presented in Figs. 3–6, but calls attention to the fact that uncertainty bands (say, 5–10 percent) should be allowed when interpreting data in the separation-reattachment region.

Point Sherwood numbers. Representative results for the point Sherwood number, showing both spanwise and streamwise distributions, are presented in Fig. 7. The specific case to which Fig. 7 corresponds is asymmetric heating and Re = 21,000, but the patterns shown there are also in evidence for the other cases. The figure portrays the distribution of point Sherwood number across the width of the surface at 11 individual axial stations. Most of these stations are situated very near the inlet, since it is in that region that the spanwise variations are primarily confined.

It is seen from Fig. 7 that at the first three stations, there are relatively high values of the Sherwood number adjacent to the side walls, but aside from these the Sherwood number is relatively uniform across the width of the surface. The high sidewall-adjacent values are believed due to the presence of three-dimensional flows caused by fluid entering the duct laterally (i.e., passing over the edge of the side wall). The spanwise variations are much diminished downstream of reattachment, and there is a region where the Sherwood numbers adjacent to the wall are somewhat lower than those

which prevail across most of the duct width. Such lower wall-adjacent values are what would be expected in conventional duct flows. Farther downstream, spanwise uniformity prevails at all measurement points.

From a closer inspection of Fig. 7, it is seen that at all axial stations aside from the first, the Sherwood number is essentially uniform at the six inner measurement points (i.e., the six points away from the side walls). In light of this, the mass transfer rates at these six points were averaged to obtain the $\dot{m}_u(x)$ that appears in equation (5).

Fully developed values. The final item in the presentation of results is the fully developed Sherwood number, and these are plotted logarithmically as a function of the Reynolds number in Fig. 8. The data for symmetric heating and asymmetric heating have been fit with respective least-squares straight lines, with the equations

$$Sh = 0.0500Re^{0.76}, \quad Sh = 0.0464Re^{0.76} \tag{12}$$

These equations are represented by solid lines in Fig. 8. The Sherwood numbers given by the two equations differ by 7.5 percent.

Also shown in Fig. 8 are the venerable Dittus-Boelter equation and the more contemporary Petukhov-Popov equation (equation (48) of [14]). Both of these equations are based on the circular tube, and the Petukhov-Popov equation was originally derived for the uniform wall heat-flux boundary condition. The motivation for considering these equations here is that circular tube results for turbulent flow are often applied to noncircular geometries by replacing the tube diameter with the duct hydraulic diameter D_h; also, the specifics of the thermal boundary conditions (uniform wall temperature versus uniform heat flux) are regarded as a secondary issue in turbulent flow.

In the Reynolds number range of the experiments, the literature equations are in very good agreement with the symmetric heating data, especially the Dittus-Boelter equation, for which the agreement is within 3.5 percent. However, the correlating line of the data (equation (12)) is somewhat less sloped than are the literature equations. All told, considering the differences in geometry and, with regard to Petukhov-Popov, in boundary condition, better agreement could not have been expected.

Concluding Remarks

The present experiments appear to be the first in which the effects of inlet-induced flow separation on turbulent heat transfer in a flat rectangular duct have been detected. The flow separation plays a decisive role in shaping the distribution of the heat transfer coefficient in the thermal entrance region. Of particular note is the presence of a sharp peak in the distribution which occurs at the point of reattachment. The heat transfer coefficient at the peak was found to be as much as four times as large as that in the fully developed regime. The ratio of the peak value to the fully developed value decreased with increasing Reynolds number.

Reattachment of the flow occurred at an axial station situated less than one hydraulic diameter downstream of the inlet. The reattachment point moves upstream as the Reynolds number increases.

The experiments encompassed data runs where both of the principal walls were at the same uniform temperature, and other runs where one wall was isothermal while the other was adiabatic. The results for symmetric and asymmetric heating were identical in the initial portion of the thermal entrance region. Farther downstream, deviations occurred, with the asymmetric-heating results falling below those for symmetrical heating. The maximum deviations, which occur in the thermally developed regime, are only 7.5 percent. The thermal entrance length for asymmetric heating is appreciably
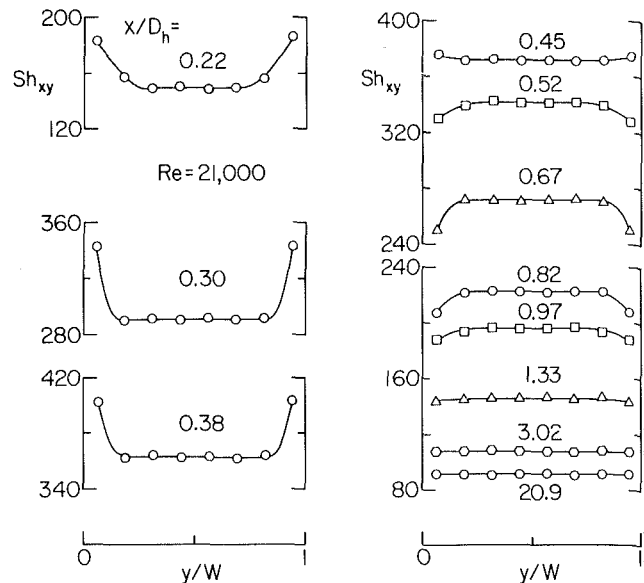

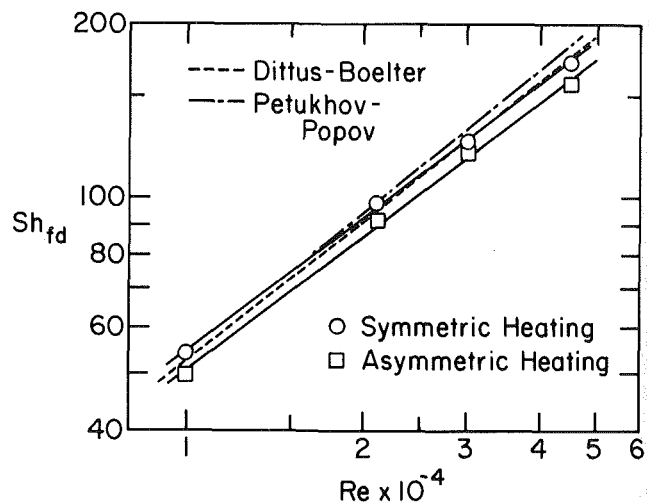Fig. 7 Representative distributions of the point Sherwood number, asymmetric heating, Re = 21,000

Fig. 8 Fully developed Sherwood numbers

longer than that for symmetric heating ($10-13D_h$ for the former versus $5-7D_h$ for the latter).

The fully developed Sherwood numbers for the two heating modes were respectively correlated by least-squares lines having a common power of the Reynolds number (i.e., $Re^{0.76}$). With the hydraulic diameter as characteristic dimension, the results for symmetric heating were in very good agreement with the Dittus-Boelter and Petukhov-Popov equations, both of which are based on the circular tube.

Acknowledgment

References

1 Byrne, J., Hatton, A. P., and Marriott, P. G., "Turbulent Flow and Heat Transfer in the Entrance Region of a Parallel Wall Passage," *Proceedings of the Institution of Mechanical Engineers*, Vol. 184, 1969–1970, pp. 697–710.

2 Emery, A. F. and Gessner, F. B., "The Numerical Prediction of Turbulent Flow and Heat Transfer in the Entrance Region of a Parallel Plate Duct," JOURNAL OF HEAT TRANSFER, Vol. 98, 1976, pp. 594–600.

3 Tan, H. M. and Charters, W. W. S., "Effect of Thermal Entrance Region on Turbulent Forced-Convection Heat Transfer for an Asymmetrically

Heated Rectangular Duct with Uniform Heat Flux," *Solar Energy*, Vol. 12, 1969, pp. 513–516.

4 Sukomel, A. S., Velichko, V. I., Abrosimov, Yu. G., and Gutsev, D. F., "An Investigation of Heat Transfer in the Entry Section of a Rectangular Duct," *Teploenergetika*, Vol. 22, No. 3, 1975, pp. 81–83.

5 Haynes, F. D. and Ashton, G. D., "Turbulent Heat Transfer in Large Aspect Channels," JOURNAL OF HEAT TRANSFER, Vol. 102, 1980, pp. 384–386.

6 Larson, R. I. and Yerazunis, S., "Mass Transfer in Turbulent Flow," *International Journal of Heat and Mass Transfer*, Vol. 16, 1973, pp. 121–128.

7 Sparrow, E. M., Lloyd, J. R., and Hixon, C. W., "Experiments on Turbulent Heat Transfer in an Asymmetrically Heated Rectangular Duct," JOURNAL OF HEAT TRANSFER, Vol. 88, 1966, pp. 170–174.

8 Barrow, H., "An Analytical and Experimental Study of Turbulent Gas Flow Between Two Smooth Parallel Walls with Unequal Heat Flux," *International Journal of Heat and Mass Transfer*, Vol. 5, 1962, pp. 469–487.

9 Sakakibara, M. and Endo, K., "Analysis of Heat Transfer for Turbulent Flow Between Parallel Plates," *International Chemical Engineering*, Vol. 16, 1976, pp. 728–733.

10 Eckert, E. R. G., "Analogies to Heat Transfer Processes," in *Measurements in Heat Transfer*, edited by E. R. G. Eckert and R. J. Goldstein, Hemisphere Publishing, Washington, D. C., 1976.

11 Sogin, H. H., "Sublimation from Disks to Air Streams Flowing Normal to their Surfaces," Trans. ASME, Vol. 80, 1958, pp. 61–71.

12 Krall, K. M. and Sparrow, E. M., "Turbulent Heat Transfer in the Separated, Reattached, and Redevelopment Regions of a Circular Tube," JOURNAL OF HEAT TRANSFER, Vol. 88, 1966, pp. 131–139.

13 Filetti, E. G. and Kays, W. M., "Heat Transfer in Separated, Reattached, and Redevelopment Regions Behind a Double Step at Entrance to a Flat Duct," JOURNAL OF HEAT TRANSFER, Vol. 89, 1967, pp. 163–168.

14 Petukhov, B. S., "Heat Transfer and Friction in Turbulent Pipe Flow with Variable Physical Properties," in *Advances in Heat Transfer*, Vol. 6, 1970, pp. 503–564.

A. Brosh
Department of Aeronautical
Engineering.

D. Degani
Department of Mechanical
Engineering.

Technion-Israel
Institute of Technology,
Haifa, Israel

S. Zalmanovich
School of Engineering,
Tel-Aviv University,
Tel-Aviv,
Ramat-Aviv, Israel

Conjugated Heat Transfer in a Laminar Boundary Layer With Heat Source at the Wall

This work presents the solution of the temperature field in a two-dimensional laminar incompressible flow over a conducting solid plate with a line heat source located at the fluid-solid interface perpendicular to the flow direction. A numerical scheme was used to obtain the temperature profiles as a function of the source strength, and of the properties of the fluid and the solid. The heat conduction and forced convection in the fluid and the heat conduction in the solid were solved for the case of moderate temperature rise, where the assumption of constant properties applies. The model enables the improvement of an instrument for the detection of boundary layer separation. It was found that for the actual parameters of the separation detector, a distance of 4 to 24 mm between the sensors gives an indication of 70 percent of the maximum temperature difference.

Introduction

This work presents a two-dimensional solution of the conjugated heat transfer problem of a flow over a solid wall with a heat source at the interface. This is a mathematical model for the separation detector by Rubesin et al. [1]. The principle of operation of this detector is based on the heat transferred between thin hot wires mounted on the wall of a boundary layer flow. The detector consists of a small styrene plug (plastics with low thermal conductivity) which is embedded in a conducting wall. Three wires are flush mounted in the plug to blend with the contour of the wall. The middle wire serves as a heater and the other two as sensors. Under normal conditions the heat from the middle wire is convected downstream, hence the downstream sensor measures higher temperature than the upstream one. When the boundary layer is separated, the flow direction next to the wall is reversed and the sign of the temperature difference is changed. A string of such detectors mounted on a airfoil can indicate the points of separation and reattachment. The solution of the temperature field generated by the heat source can be used to design detectors with high sensitivity.

To calculate the temperature field in conjugated heat transfer problems, the momentum and energy equations in the two phases have to be solved simultaneously. The matching conditions at the interface are heat flux continuity and equal interface temperatures in the fluid and in the solid.

In this work the case of a low mach number with moderate heat source strength is treated; therefore, the flow is considered incompressible and with constant properties. It is true that for high temperature variations the assumption of constant properties is not valid. However, the actual separation detection gage works at low power input (less than 1 W) and at low temperature variations (the solid plastics material, which is used in the actual gage, melts at about

120°C); therefore, in practice, the assumption of constant properties is valid. Since the wires are fairly long, they may be represented as a line heat source; therefore, the problem can be considered two-dimensional as well. Several different approach were used in the past on the problem of conjugated heat transfer. Most of the previous works deal with continuous-velocity profile and temperature distributions. The flow over a body with continuous distribution of heat sources was solved by Perelman [2]. The compressible flow over a flat plate with no heat source was solved by Luikov et al. [13]. These works are therefore unable to describe properly the vicinity of a line heat source because of the temperature discontinuity in this case. Saukin et al. [4] investigated the temperature field caused by a step in the interface temperature. They presented an approximate solution that can be applied to other interface temperature distributions. This solution is good far from the step, but loses its accuracy near the point of discontinuity, and therefore is not valid for our case.

Sohal [5] calculated the relative importance of various mechanisms of conjugated heat transfer for laminar boundary layer over a flat plate. His results indicate that for small temperature differences, as in our case, the radiation term is negligible compared with conduction and convection terms.

A similar problem has been solved by Zinnes [6], but while Zinnes describes the case of free convection where gravity and density are important, the present case describes a forced convection flow; gravity is neglected and density changes are small.

Mathematical Model and Numerical Approach

The two-dimensional energy equation for incompressible laminar boundary layer flow with constant properties is

$$u \frac{\partial T}{\partial x} + v \frac{\partial T}{\partial y} = \alpha \left(\frac{\partial^2 T}{\partial x^2} + \frac{\partial^2 T}{\partial y^2} \right) + \frac{\mu}{\rho C_p} \left(\frac{\partial u}{\partial y} \right)^2 \quad (1)$$
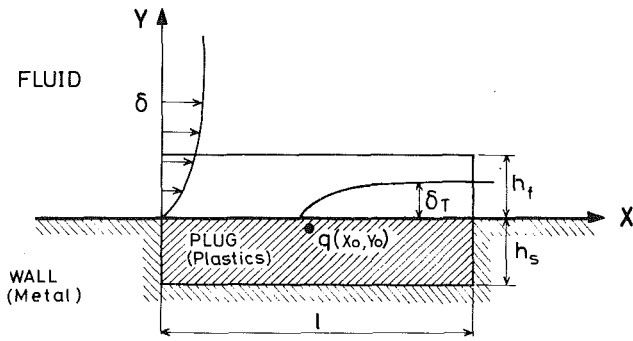
Fig. 1 Schematic flow field and thermal boundary layer caused by heat source q

The conduction term in the direction of the flow is added to the equation to take care of the heat transfer due to possible high temperature gradients near the heat source q (Fig. 1).

The constant properties assumption enables a solution of the momentum equation independently of the temperature field, and then a substitution of the resulting velocity profile into the energy equation. The velocity profile used is the Blausius solution for viscous flow over flat plate with zero pressue gradient (Schlichting [7]).

The energy equation for the solid with line heat source located at $x = x_0 \ y = y_0$ is:

$$k_s \left(\frac{\partial^2 T}{\partial x^2} + \frac{\partial^2 T}{\partial y^2} \right) = -q \delta[(x - x_0); (y - y_0)] \tag{2}$$

The boundary conditions are specified on the boundaries of the computation domain (Fig. 1).

Table 1 Coefficients used in the set of algebraic equations (5).

	A_1	A_2	A_3	A_4	A_5	A_6
Fluid (blausus b.1)	$f_1 + 1$	f_2	f_3	f_4	$1 - f_1$	0
Solid	1	1	-4	1	1	f_5
B.C.(3a)	$-f_1 - 1$	0	$-f_3$	$-f_4$	$f_1 - 1$	$-f_2 T_\infty$
B.C. (3b)	$-f_1 - 1$	$-f_2$	$-f_3$	$-f_4$	0	$(f_1 - 1)T_\infty$
B.C. (3c)	$f_1 + 1$	$f_2 - f_4$	$f_3 + 2f_4$	0	$1 - f_1$	0
B.C. (3d)	1	0	-4	1	1	$-T_\infty$
B.C. (3e)	1	1	-4	0	1	$-T_\infty$
B.C. (3f)	1	1	-4	1	0	$-T_\infty$
Interface	k_S / f_8	$\frac{1}{2}k_8 k_s + \frac{1}{2}f_7 k_f + f_{10}$	$f_{10} - f_9 + f_6 - k_S(f_8 + 1/f_8) - k_f(f_7 + 1/f_7)$	$\frac{1}{2}k_s f_8 + \frac{1}{2}k_f f_7 - f_9$	$k_f / f_7 + f_6$	0

$$f_1 = \frac{\Delta y_f}{2\alpha} V_{ij}$$

$$f_6 = \frac{1}{4}\rho_f Cp_f \Delta y_f (U_{1+\frac{1}{2}j+\frac{1}{2}} - U_{i-\frac{1}{2}j+\frac{1}{2}})$$

$$f_2 = \left(\frac{\Delta y_f}{\Delta x} \right)^2 \frac{\Delta y_f^2}{2\alpha \Delta x} U_{ij}$$

$$f_7 = \frac{\Delta y_f}{\Delta x}$$

$$f_3 = -2\left[\left(\frac{\Delta y_f}{\Delta x} \right)^2 + 1 \right]$$

$$f_8 = \frac{\Delta y_s}{\Delta_x}$$

$$f_4 = \left(\frac{\Delta y_f}{\Delta x} \right)^2 - \frac{\Delta y_f^3}{2\alpha \Delta x} U_{ij}$$

$$f_9 = \frac{1}{16} \rho_f Cp_f \Delta y_f U_{i+\frac{1}{2}j+\frac{1}{2}}$$

$$f_5 = -q\delta[(x - x_0), (y - y_0)]\Delta x^2 / k_s$$

$$f_{10} = \frac{1}{16} \rho_f Cp_f \Delta y_f U_{i-\frac{1}{2}j+\frac{1}{2}}$$

_____ **Nomenclature** _____

$A_1 - A_6$ = coefficients, equation (5)
Cp = heat capacity at constant pressure
i, j = index, integer
k = thermal conductivity
k^* = k_s / k_f
l, h_f, h_s = computation field dimensions
q = source intensity
R_{ex} = Reynolds number
T = temperature
$\bar{T} = \dfrac{T - T_\infty}{T_{w_{max}} - T_\infty}$, normalized temperature
u, v = velocity components
x, y, z = coordinates
y^* = y/h_f, normalized distance from the wall
α = thermal diffusivity
$\delta(x, y)$ = delta function
δ = velocity boundary layer thickness

δ_T = thermal boundary layer thickness
μ = viscosity
ρ = density

Subscripts

f = fluid
0 = source
s = solid
w = wall
∞ = free stream

Superscripts

S = South
W = West
C = Center
E = East
N = North

The boundary conditions for the fluid are:

at $\qquad x=0;\, 0<y<h_f:\quad T=T_\infty$ $\qquad(3a)$

at $\qquad 0<x<1;\, y=h_f:\quad T=T_\infty$ $\qquad(3b)$

at $\qquad x=1;\, 0<y<h_f:\ \dfrac{\partial^2 T}{\partial x^2}=0$ $\qquad(3c)$

The condition 3(b) is valid since the thermal boundary layer is completely contained inside the computation domain, i.e., $h_f>\delta_T$. The thermal boundary layer is thin when the heat-source intensity is small and the velocity boundary layer has already developed some thickness.

In our case this is not a requirement, but if one wants to use the model to simulate a hot wire skin friction gage this requirement becomes important, otherwise the measurement is affected by the flow regime (turbulent or laminar), as ex-

Fig. 2 The numerical grid

plained by Liepman and Skinner [8] (see also Figs. 1 and 2 in reference [1]).

The plastic plug is actually inserted in a metallic airfoil (wall) of high conductivity; therefore, the airfoil temperature is equal to the ambient temperature, and the boundary conditions for the solid are:

at $\qquad x=0;\, 0<y<h_s:\quad T=T_\infty$ $\qquad(3d)$

at $\qquad x=1;\, 0<y<h_s:\quad T=T_\infty$ $\qquad(3e)$

at $\qquad 0<x<1;\, y=h_s:\quad T=T_\infty$ $\qquad(3f)$

The boundary conditions at the interface (matching conditions) are:

$$T_f(x,y=0)=T_s(x,y=0) \qquad(4a)$$

$$k_s\left.\frac{\partial T_s}{\partial y}\right|_{y=0}=k_f\left.\frac{\partial T_f}{\partial y}\right|_{y=0} \qquad(4b)$$

Substitution of central differences for the derivatives of the differential equations (1) and (2) for every grid point in the computation domain results in a linear algebraic equation of the form

$$A_1\,T^S+A_2\,T^W+A_4\,T^E+A_5\,T^N=A_0 \qquad(5)$$

The symbols used in equation (5) are explained in Fig. 2. The coefficients A_1–A_6 are determined according to the region (fluid or solid) and the boundary conditions, and are summarized in Table 1.

The interface matching conditions were derived through heat balance in the vicinity of a point $(i,\, j)$, rather than expressing the boundary condition equations (4) in a finite difference form. This procedure was chosen to gain higher accuracy as suggested by Saitoh [9].
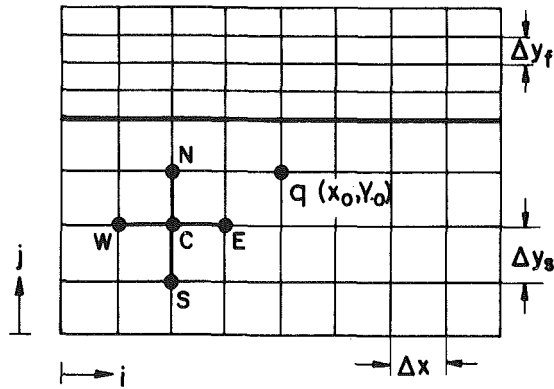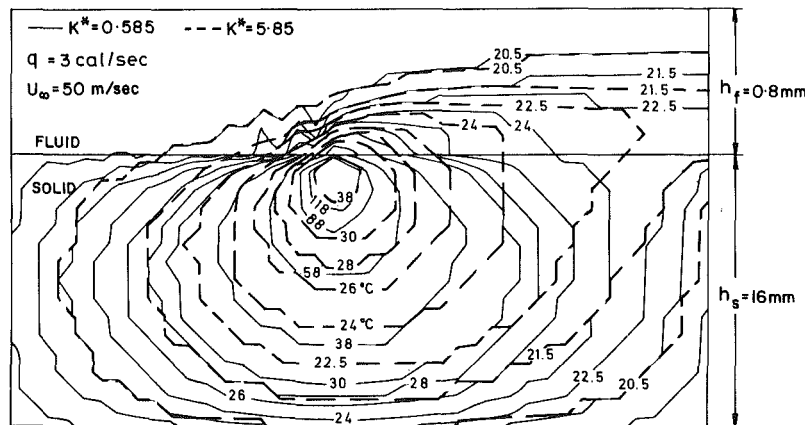

Fig. 3 Temperature contours. The effect of conductivity ratio on the temperature distribution.
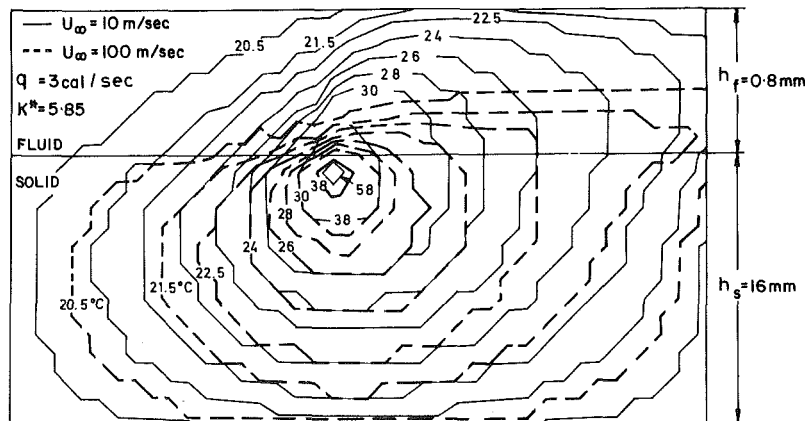

Fig. 4 Temperature contours. The effect of velocity on the temperature distribution.
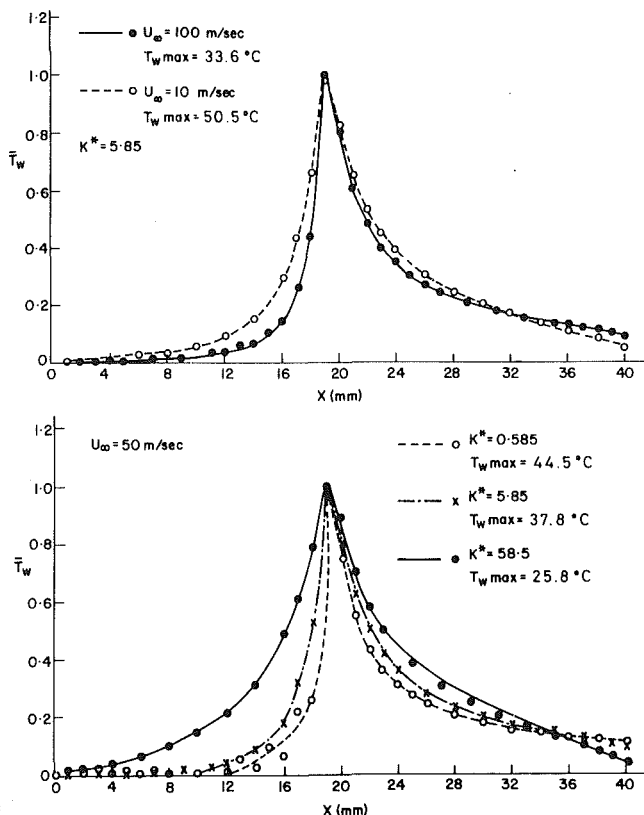
Fig. 5 Normalized interface temperature as a function of (a) velocity and (b) conductivity ratio

Fig. 6 Temperature distribution in the fluid for two velocities

Constant grid size was used in the calculations as follows:

$$\Delta x_i = 10^{-3}\text{m}; i = 1 \ldots 40 \quad \text{(in the axial direction)}$$

$$\Delta y_{s_j} = 10^{-3}\text{m}; j = 1 \ldots 16 \quad \text{(in the solid)}$$

$$\Delta y_{f_j} = 10^{-4}\text{m}; j = 17 \ldots 24 \quad \text{(in the fluid)}$$

Note that $\Delta x_s = \Delta x_f = \Delta y_s$, (see also Table 1).

The set of linear algebraic equations [5] is solved simultaneously for the entire computation domain using the numerical scheme of H. H. King [10], who used a Gaussian elimination procedure to obtain a direct solution to the governing differential equations.

The velocity profile used for the solution is the Blausius profile, with $\text{Re}_x = 5.33 \times 10^4$ for the lowest velocity case. The program was compared with the example presented by Holman [11], which was solved using a relaxation method, and with results of H. H. King [10] for a similar heat transfer problem (without heat source), using a similar numerical method. The disagreements in both cases were less than 1 percent.

The grid density was tested using $\Delta y_f = 0.2 \cdot 10^{-3}\text{m}$ and 8 grid lines, yielding flow field height $h_f = 1.6 \cdot 10^{-3}\text{m}$. The temperature was found to be constant above $y_f = 0.8 \cdot 10^{-3}$. Based on the results of this test we reduced the flow field height to $y_f = 0.8 \cdot 10^{-3}\text{m}$ using the same number of lines (eight) to gain higher grid density. The temperatures were compared and the maximum temperature difference between the two cases was less than 1/2 percent.

Results and Discussion

Typical results of the isothermal lines in the fluid and in the solid are shown in Figs. 3 and 4. The fluid region was magnified 10 times relative to the solid region, in order to show the thermal boundary layer details. The slopes of the temperature contours on the two sides of the interface are an
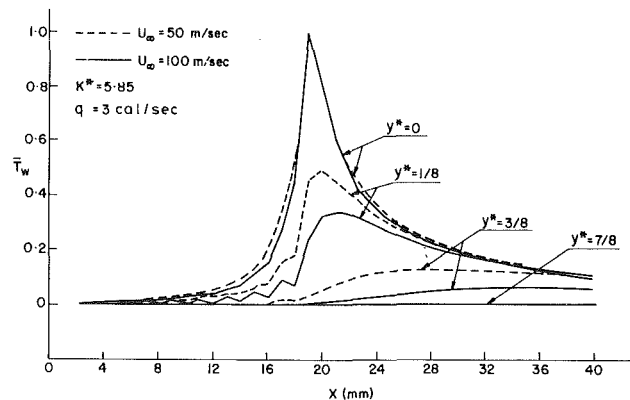
outcome of the simple plotter procedure, which executes first-order interpolation only (note also the discontinuity in the derivatives of the contours).

For constant far-field velocity U, the heat flux through the interface depends mainly on the conductivity ratio $k^* = k_s/k_f$. For the case of source strength $q = 3$ cal/s, fluid velocity $U_\infty = 100$ m/s, and conductivity ratio $k^* = 58.5$, the solid loses 38 percent of the heat through the interface, 7 percent through the upstream boundary, 41 and 14 percent, respectively, through the bottom and the downstream boundary. When k^* is reduced to 5.85 (which is the conductivity ratio of the actual separation detector), the heat transferred through the interface amounts to 81 percent of the heat: 13 percent is lost through the bottom, with 5 and 1 percent, respectively, going through the downstream boundary and the upstream boundary. Further reduction of the solid conductivity ($k^* = 0.585$) yields 91 percent of the source heat through the interface and 7 percent through the downstream boundary; the remaining 2 percents are equally divided between the other two boundaries.

The effect of the conductivity ratio k^* on the temperature distribution is shown in Fig. 3. For low k^*, high-temperature gradients near the source enable the removal of the heat, most of which goes into the fluid. High k^* widens the effective region of the heat source; a bigger part of the heat is lost to the surroundings and less goes into the fluid.

The effect of far-field velocity on the temperature field is shown in Fig. 4. For constant k^*, the thickness of the thermal boundary layer decreases when the velocity increases. More heat is removed by convection, and the solid temperature goes down. An increase of the heat source strength, q, results in higher temperatures, steeper gradients, and higher heat flux. But since the material properties are independent of the temperature (both solid and fluid), there is no influence of the source strength on the shape of the normalized isotherms. This latter result is independent of the fluid velocity or conductivity ratio.

Since the thermal boundary layer generated by the heat source is thin, the temperature profiles should be dependent solely on the velocity gradient at the wall. To verify this point, two velocity distributions were compared; the Blausius profile and a linear profile with the same velocity gradient at the wall. The temperature distributions were found to be identical for these two cases both in the solid and in the fluid.

The effects of the far field velocity U_∞ and of the conductivity ratio k^* on the normalized interface temperature distribution is shown in Fig. 5. A decrease of the flow velocity U_∞ results in an increase of the interface temperature (the maximum temperature in the low velocity case is twice as high as that of the high velocity), and in a lower axial gradient of the interface temperature near the source. The effective source width source width grows in the upsteam as well as downstream directions (Fig. 5(a). A higher conductivity ratio k^*
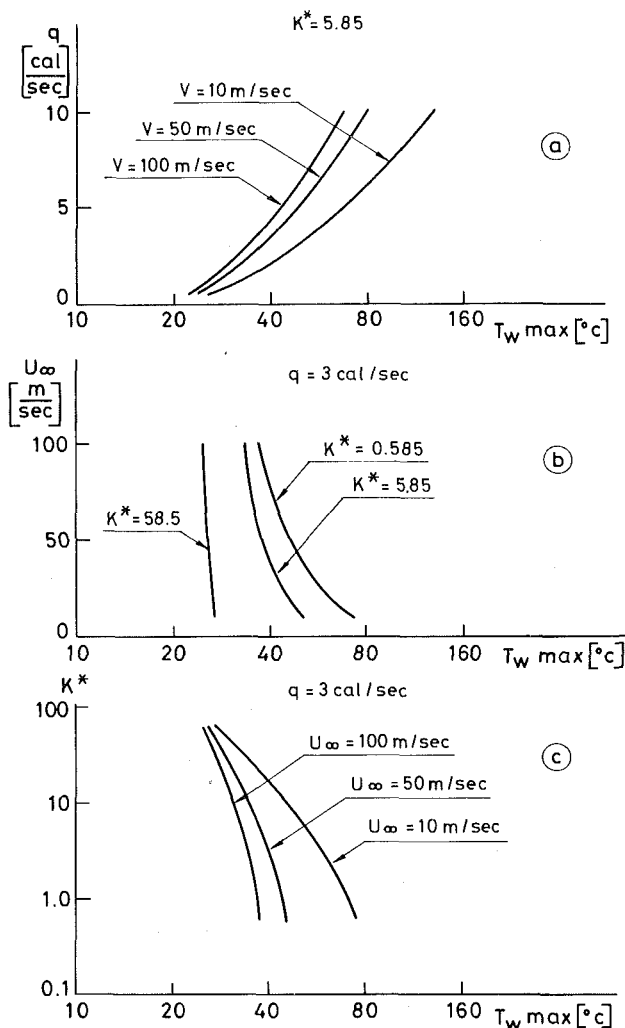
Fig. 7 Maximum interface temperature for various velocities, conductivity ratio, and heat source strength

Fig. 8 The temperature difference between two points of the interface located at equal distance upstream and downstream of the heat source

results in a wider effective source width, and reduced axial temperature gradients, because of the increased effect of conduction in the solid (Fig. 5(b).

The heat convection in the downstream direction causes an asymmetry in the temperature profile; the axial temperature gradient is higher on the upstream side of the heat source. Fig. 6 shows this change of the normalized temperature distribution in the boundary layer

$$\left(\bar{T}(x,y) = \frac{T(x,y) - T_\infty}{T_{w\,max} - T_\infty} \right)$$

as affected by the free stream velocity. $T = 20°C$ in this example. Further downstream ($x > 35$), the fluid temperature is higher than that of the wall as may be seen from Fig. 6, where the line of $y^* = 0$ ($y^* = y/h_f$) crosses the line of $y^* = 1/8$. This phenomenon is more pronounced for cases of high wall conductivity k_s.

The oscillations upstream of the source, which are more distinct at low k^*, are caused by numerical instability. These oscillations are small and can be further reduced by introducing an artificial viscosity. The term "artificial viscosity" refers to adding terms of higher order to the differential equation rather than increasing the fluid viscosity (see, e.g., Steger [12]). The wiggles may be a result of the use of central differences in the differential equation and can be also eliminated using the upwing method for the convection terms (see Roache [13]).

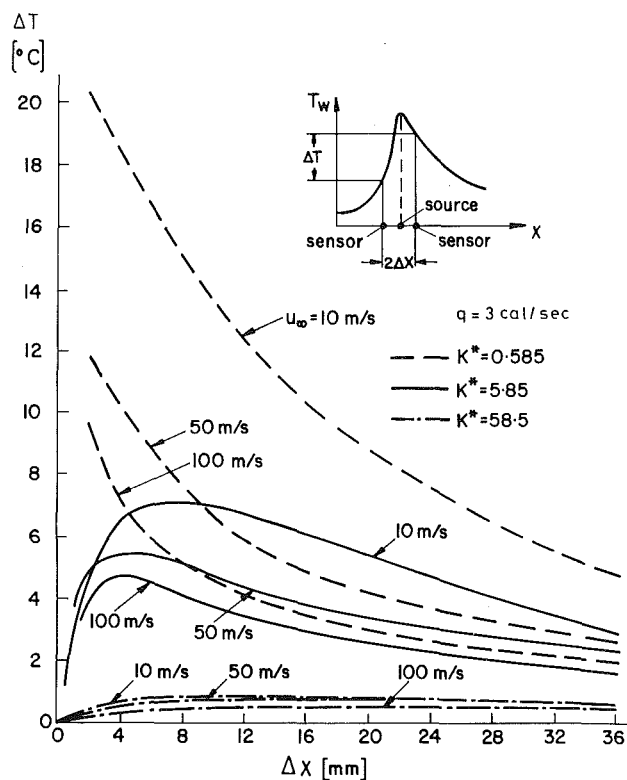At low velocity the part of conduction in the heat-transfer

process grows. It contributes to the symmetry of the temperature profile around the source, and the gradients, especially on the upstream side of the source, decrease. Although our model is not valid for the zero velocity case, where free convection becomes a main factor, an extrapolation of our model to this extreme shows a symmetrical temperature field as expected. Further into the fluid, the point of maximum temperature is convected downstream with increased velocity (see, e.g., $y_f^* = 1/8$ in Fig. 6).

A summary of the effects of the three parameters, source strength, q, velocity, U_∞, and conductivity ratio, k^*, on the interface temperature is presented in Fig. 7. As expected, the peak temperature increases with source strength. A decrease in the velocity results in the same trend when the conductivity ratio is held constant (Fig. 7(a)). The rate of increase of the peak temperature with the reduction of velocity is dependent upon the conductivity ratio. In Fig. 7(b), one can notice that when k^* is higher, the effect of velocity changes on the peak temperature is smaller. Another point evident from Fig. 7(c) is that an increase in the conductivity ratio results in lower peak temperature for the same velocity.

The separation detector measures the temperature difference between the two sensors located on opposite sides of the source. Figure 8 shows this difference calculated for various cases of k^* and U_∞ for the same source strength. In most cases there is a distinct maximum, which shows that there exists an optimum location for measurement purposes. It seems peculiar that larger temperature differences are observed at lower velocities. At zero velocity, there should be no temperature difference physically bacause of symmetry. The rise in the temperature difference for lower velocities results from the fact that this difference is presented in dimensional form. Since all the temperatures in the field rise when the velocity decreases (because less heat is convected away), the temperature difference in the presented range is higher for lower velocity, but a normalized temperature difference (if normalized by using, for example, T_{max}) goes down, and there is no contradiction.

Conclusions

This work presents a solution to the conjugated heat transfer from a line heat source located on the interface between a solid plate and fluid with constant properties in a two-dimensional steady laminar flow.

For thin thermal boundary layer, the heat-transfer rate is determined by the velocity gradient at the wall. A comparison between the Blausius velocity profile and a linear profile and a linear profile with the same wall gradient gives identical temperature distribution. Hence a linear velocity profile can be used to calculate the temperature field for cases with complicated velocity profiles.

The effect of three parameters was investigated: (a) solid to fluid conductivity ratio, (b) upstream velocity, and (c) heat source intensity. An increase in the conductivity ratio spreads the heat over a wider region on both sides of the source and lowers the maximum temperature. An increase in the velocity results in a thinner thermal boundary layer and contributes to the asymmetry of the temperature profiles, making them steeper at the upstream side of the source. Also the maximum temperature is reduced. The source strength does not effect the normalized temperature profiles as long as it is small enough not to invalidate the constant properties assumption.

The purpose of this paper is to supply an efficient and simple tool to test and optimize the separation gage for cases of low speed air flow where the fluid can be considered incompressible. Using this model for the conductivity ratio for the existing separation detector ($k^* = 5.85$), one gets a measureable temperature difference (90 percent of ΔT_{max}) between two sensors located about 5 mm upstream and 5 mm downstream of the line heat source. This result conforms with the basic assumptions of the model, and, therefore, the model can be used to calculate the optimum parameters for design purposes of the instrument in this type of flow.

Acknowledgment

References

1 Rubesin, M. W., Okuno, A. F., Mateer, G. G., and Brosh, A., "A Hot Wire Surface Gage for Skin Friction and Separation Detection Measurements," NASA TMX-62465, July 1975.

2 Perelman, T. L., "On Conjugated Problems of Heat Transfer," *International Journal of Heat and Mass Transfer*, Vol. 3, 1961, pp. 293-303.

3 Luikov, A. V., Aleksashenko, V. A., and Aleksashenko, A. A., "Analytical Method of Solution of Conjugated Problems in Convective Heat Transfer," *International Journal of Heat and Mass Transfer*, Vol. 14, 1971, pp. 1047-1065.

4 Saukin, W. P., Weinbaum, S. and Jiji, L. M., "Thermal Convection in the Vicinity of a Discontinuous Change in Wall Temperature," *The Physics of Fluids*, Vol. 17, No. 8, 1974, pp. 1496-1502.

5 Sohal, M. S. and Howel, J. R., "Determination of Plate Temperature in Case of Combined Conduction, Convection and Radiation Heat Exchange," *International Journal of Heat and Mass Transfer*, Vol. 16, 1973, p. 2055-2066.

6 Zinnes, A. E., "The Coupling of Conduction with Laminar Natural Convection from Vertical Flat Plate with Arbitrary Surface Heating," ASME JOURNAL OF HEAT TRANSFER, Vol. 92, 1970, pp. 528-535.

7 Schliechting, H., *Boundary Layer Theory*, 6th ed., M. G. H., 1968.

8 Liepman, H. W. and Skinner, G. T., "Shearing Stress Measurements by use of a Heated Element," NACA TN 3268, 1954.

9 Saitoh, A., "Numerical Method for 2-D Navier-Stokes Equation by Multi-Point Finite Differences," *International Journal of Numerical Methods in Engineering*, Vol. 2, 1977.

10 Hartley, H. K., "A Poisson Equation Solver for Rectangular or Annular Regions," *International Journal for Num. Math. in Eng.*, Vol. 10, 1976, pp. 799-801.

11 Holman, J. P., *Heat Transfer*, 2nd ed., McGraw-Hill, New York, 1968, p. 65.

12 Steger, J. L., "Implicit Finite Difference Simulation of Flow About Arbitrary Two Dimensional Geometries," *AIAA Journal*, Vol. 16, 1978, pp. 679-686.

13 Roache, P. J., *Computational Fluid Dynamics*, Hemosa Publishers, 1972.

S. M. ElSherbiny
Student Mem. ASME

G. D. Raithby
Mem. ASME

K. G. T. Hollands
Mem. ASME

Department of Mechanical Engineering,
University of Waterloo,
Waterloo, Ontario, Canada N2L 3G1

Heat Transfer by Natural Convection Across Vertical and Inclined Air Layers

Measurements of the heat transfer by natural convection across vertical and inclined air layers are reported. The air layer is bounded by flat isothermal plates at different temperatures and around the edges by a perfectly conducting boundary (i.e., one that takes on a linear temperature distribution between the two plates). Measurements are reported for six aspect ratios between 5 and 110, covering a portion of the range of practical interest for windows, solar collectors, etc. Rayleigh numbers were in the range 10^2 to 2×10^7. The present measurements permitted the role of aspect ratio to be clearly defined. In addition, correlation equations are presented which allow the heat trnasfer across a vertical or inclined air layer to be calculated.

Introduction

A knowledge of the heat transfer by natural convection across vertical and inclined fluid layers is often of interest. Such layers occur, for example, between window glazings, in wall cavities, and between the absorber and cover plates of a solar collector. An active interest in the problem for over 70 years has led to numerous analytical and experimental studies. Despite this activity, the heat transfer can still not be confidently predicted over all the parameter ranges of interest.

Figure 1 shows an inclined air layer, of thickness L, bounded on the sides by flat isothermal plates of different temperatures. The height and width of the plates are H and W, respectively. A dimensional analysis shows that the average Nusselt number, Nu, depends on Rayleigh number, Ra, Prandtl number, Pr, vertical and horizontal aspect ratios $A = H/L$ and $A_H = W/L$, the angle of inclination, ϕ, and on the end-wall boundary conditions. Since the fluid is air, Pr is about constant (0.71). If the end walls have high conductivity relative to air, and if A_H is asymptotically large, the Nusselt number will depend only on Ra, A and ϕ. The ranges of Ra and A of practical interest for wall cavities, windows, and solar collectors are depicted in Fig. 2.

The early experimental studies of this problem were reviewed by Jakob [1] and correlation equations of the form

$$\text{Nu} = c\,\text{Ra}^m / A^n \qquad (1)$$

were proposed for vertical fluid layers. The exponent m was taken as 1/4 and 1/3 below and above Ra = 140,000 respectively, and n had a value of 1/9. DeGraaf and Van Der Held [2] later concluded on the basis of their data that n should be zero. In 1961, Eckert and Carlson [3], from an interferometric study, obtained values of m $\approx$ 0.3 and n = 0.1 in the laminar boundary-layer regime. Four years later, for fluids with Pr > 1, Emery and Chu [4] fitted their data with $m = n = 1/4$, while Dropkin and Sommerscales [5]
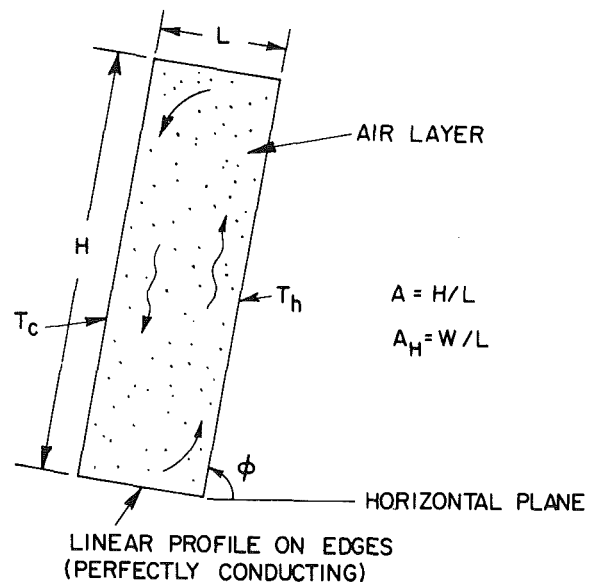
Fig. 1 A sketch of the air layer. W is the plate width normal to plane of paper.

concluded that n should be zero. More recently, Yin et al. [6] presented a correlation equation fitting their data for air with $m = 0.269$ and $n = 0.131$, while Randall et al. [7] correlated their data with $m = 0.29$ but could detect no dependence on A. Schinkel and Hoogendoorn [21] did not attempt to separate out aspect ratio and Rayleigh number effects.

The experimental conditions (i.e., values of Ra and A) for which heat transfer across vertical air layers has been measured, and the specific conditions reported, are indicated in Fig. 2. This plot has two striking features. The first is that the data have been obtained for aspect ratios that cover only the very lowest portion of the region of interest. The second feature is that the data lie in a sloping band. The latter apparent correlation between Ra and A results from the attempts of experimenters to achieve a desired experimental
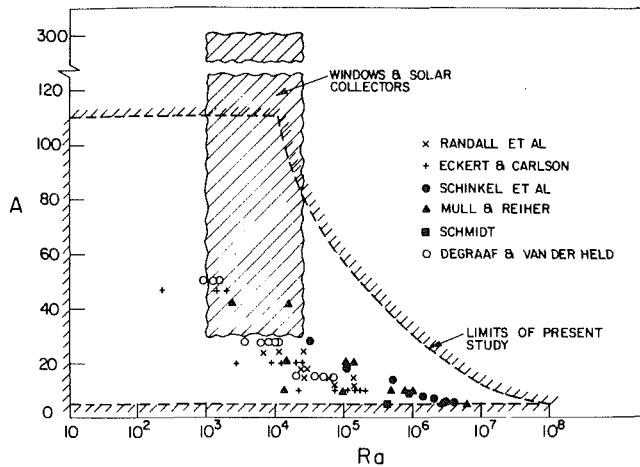
Fig. 2 Previous and present ranges of parameters covered for vertical air layers

(a)

Fig. 3(a) A sketch of the hot plate

(b)

Fig. 3(b) Details of the arrangement of heater plate and heat flux meter in the recess

range of Ra by varying L, which also results in a change in A. It is this dependence of Ra on A that has made it difficult to clearly sort out the separate effects of Ra and A on Nu. An incorrect dependence on A can cause severe errors in Nu when it becomes necessary to extrapolate the design equations to the large values of A that are frequently of practical interest.

Batchelor [8] provided the first analysis for this problem, correctly predicting the existence of various flow regimes. Unlike the experimental studies, the analytical studies that have followed have quite consistently predicted a strong aspect ratio effect (usually $n \approx 0.25$ for $A \geq 5$ in the boundary layer regime). However, the results would be expected to be valid only for low values of Ra, before instabilities have occurred. Also, the high cost of obtaining accurate finite difference solutions has resulted in only a few predictions [9, 10] for aspect ratios larger than 10. The approximate analysis of Raithby et al. [11] covered the entire range of Ra and A and was compared to the data available up to 1975. Good agreement was found in regions where data were available, but the lack of data at high Ra and A prevented assessment of the predictions in the turbulent regime.

The present investigation was undertaken to accurately measure the heat transfer across vertical and inclined air layers over a large range of Ra and A, while varying Ra and A independently. Results are reported for $A = 5, 10, 20, 40, 80$ and 110, for the Ra range shown in Fig. 2. Measurements were undertaken to ensure that the horizontal aspect ratio, A_H, was sufficiently large so as not to appreciably affect the heat transfer results. A linear temperature profile was established between the plates along all edges of the air layer. Equations that accurately correlate the heat transfer data are provided, and the question of the role of A is resolved.

Apparatus

The same experimental method and the same ancillary equipment were used in the present set of experiments as were used in those described earlier [12, 13]. However, the hot and cold copper plates bounding the air layer were replaced by two new ones in order that the heat flux across the air layer could be measured over the full length of hot plate, rather than just over the central region as was the case in the earlier experiments. The earlier technique of measuring the heat flux only in the central region was satisfactory for honeycombs and for air layers tilted slightly from the horizontal, but is inapplicable to vertical and near vertical air layers because of the strong variation in local heat flux that occurs.

Measurement of the heat flux over the full length of the hot plate was accomplished in the present experiments by using three electrically heated "heater plates" imbedded into three recesses machined into the main part of the hot plate, as sketched in plan and cross-section in Fig. 3(a). The heater plates were highly conducting copper so that their surfaces were very nearly isothermal in all the experiments. Each of the

Nomenclature

A = aspect ratio, H/L
A_H = horizontal aspect ratio, W/L
g = acceleration of gravity [m/s²]
H = height of air layer, m (see Fig. 1)
k = thermal conductivity of air at $\bar{T}$, W/m K
L = width of air layer, m (see Fig. 1)
Nu = average Nusselt number for convective heat transfer across the air layer = $qL/k\Delta T$
Pr = Prandtl number of fluid = ν/α
P = pressure, Pa

q = average non-radiative heat flow across air layer, W/m²
Ra = Rayleigh number = $g\beta\Delta T L^3/(\nu\alpha)$
$\bar{T}$ = temperature at which air properties are evaluated = $(T_c + T_h)/2$
T_c = temperature of cold plane, K (see Fig. 1)
T_h = temperature of hot plane, K (see Fig. 1)
ΔT = temperature difference between plates = $T_h - T_c$, K
W = width of air layer, m, in

direction normal to the plane of sketch in Fig. 1
α = thermal diffusivity of air, m²/s
β = thermal expansion coefficient of air, K^{-1}
ν = kinematic viscosity of air, m²/s
ϕ = angle of air layer from horizontal (see Fig. 1)

Subscripts

60 = value at $\phi = 60$ deg
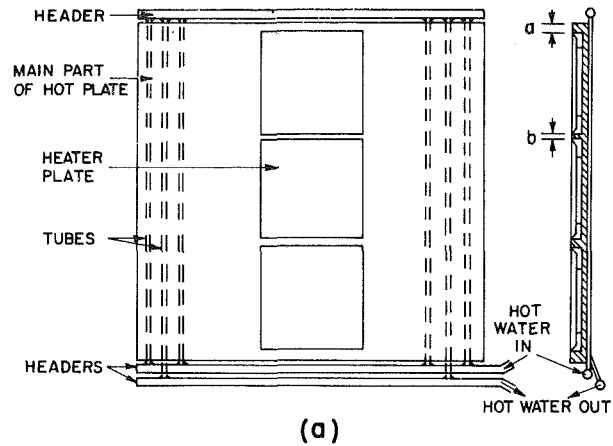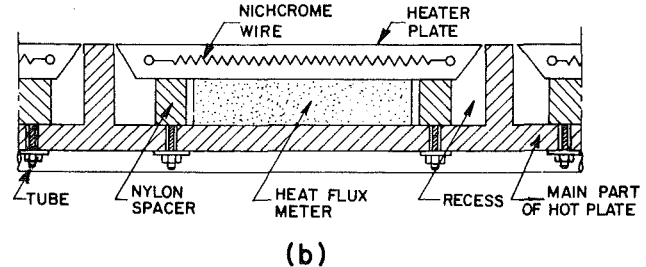90 = value at $\phi = 90$ deg, vertical orientation

three heater plates measured 200 by 200 by 3.1 mm thickness in overall dimensions, and had chamfered edges (see Fig. 3(b)). They were heated by passing a current through an embedded nichrome resistance wire of nominal 10 Ω resistance. Provision was made to accurately measure the electrical heating.

In an arrangement identical to that used for the single heater plate of earlier experiments [12, 13], a heat-flux meter was placed centrally in the recess below each heater plate as shown in Fig. 3(b). These meters, supplied by Technisch Physische Dienst TNO-TH of the Netherlands, were thin disks, 165 mm in dia, and 6 mm in thickness. Made from silicon rubber with an embedded thermopile, their sensitivity was nominally 0.4 mv/(W/m^2), and their thermal resistance 0.02 K/(W/m^2). The total thickness of the main part of the hot plate was 12.7 mm and the recesses were 9.1 mm deep, so that a 3.6 mm thickness of copper remained at the bottom of each recess. Vacuum grease was applied to each side of the heat flux meters before insertion into the recesses to ensure good thermal contact. Tapped nylon spacers and metal screws were used to secure each heater plate to the main part of the hot plate so that it applied a slight pressure to the heat flux meters and so that, at its edges, it was flush with, but not touching, the main part of the hot plate.

The hot and cold plates both measured 635 by 635 by 12.7 mm in overall dimensions. The hot plate was heated, and the cold plate was cooled by two completely separate water streams passing through tubes soldered to the backs of the respective plates and connected to two constant temperature baths whose thermostats were each set at different temperatures. In this way a constant temperature difference was maintained between the plates of about 20°C, depending upon the setting of the thermostats. The high thermal conductivity of copper relative to that of air ensured uniformity of temperature between the tubes, and a manifolding arrangement, shown in Fig. 3(a), whereby the water was made to flow in opposite directions in adjacent tubes, eliminated plate end-to-end temperature variations. Calculations showed that an upper bound on spatial temperature variations within each plate was 0.02 K. The temperature difference between the two plates was measured by 6 thermocouple junctions embedded in each plate and connected in thermopile.

The heat flux meters were calibrated in situ so as to establish the value of the coefficient in the linear relation between the heat flux meter emf and the heat flow between the heater plate and the main part of the hot plate. To make a heat-flux measurement, the individual heater plate currents were first adjusted until each heater plate had a temperature within 0.07 K of the main part of the hot plate, the latter being maintained at constant temperature by the circulating water. Any remaining heat flow between the heater plate and the main part of the hot plate was determined from the emf of the heat-flux meter and this result was added to the electrical heating in the heater plate to obtain the heat transfer into the air layer.

The choice of the heater plate spacing dimensions b in Fig. 3(a) was a compromise. Too large a spacing would detract from the goal of measuring the heat flux over the total surface of the hot plate; too small a spacing would cause undesirable thermal coupling between the two heater plates, and would also produce a low temperature at the tops of the copper strips between the recesses. From analysis, a thickness of b = 6.4 mm was established as meeting all requirements. In calculating the average heat flux for the total plate, the spacers between heater plates were each assigned a heat flux equal to the average of the heat fluxes of the adjacent heater plates, and the spacers at the ends of the plate were each assigned the heat flux of its adjacent heater plate. The average

heat flux was then taken as the area-weighted average of the heat flux of three heater plates and four spacers. Even for the worst case of a local heat flux varying inversely as the fourth root of the distance from the bottom edge, this averaging procedure was calculated to produce an error in Nu no greater than 0.7 percent.

Because of the provision in the ancillary apparatus for taking the pressure in the air layer up to 0.7 MPa [12, 13], it was possible to achieve Rayleigh numbers as high as 10^4 and 4×10^4, using spacings as small as 6 and 8 mm, respectively. Since $A = H/L$, this permitted the study of the high aspect ratios (110 and 80, respectively) which had eluded previous experimenters working with air at atmospheric pressure. Also, the experimental technique of varying the Rayleigh number by varying the pressure while keeping L and H constant, eliminated the hidden correlation between A and Ra discussed in the previous section. The small spacing, L, required for the high aspect ratio experiments demanded that the plates be parallel and flat to a high degree of precision in order to keep errors in measuring L within desired bounds. By stiffening and careful machining, a trueness was established sufficient for L to be measured with an uncertainty of ± 0.1 mm.

A perfectly conducting boundary condition – i.e., a linear temperature rise from cold plate to hot plate – was established at the periphery of the air layer by stretching 0.5 mm thick copper sheet from plate to plate. Calculations indicated that this thickness would produce a departure from temperature linearity of no more than 1 percent, even at the highest Rayleigh number. Good thermal contact was required at the juncture of the copper sheets and the copper plates. Both ends of each sheet were coated with vacuum grease and sandwiched between the end face of the copper plate and a steel bar washer held firmly against the end face by machine screws. In certain experiments the air layer under study was made to cover only one or two (rather than all three) of the heater plates. In this instance, the copper sheet was bent into a channel shape and the flanges were greased and held firmly against the copper plates by steel rods clamped at the two ends.

The radiation component had to be subtracted from the total measured heat transfer to obtain the convective heat transfer. Prior to tests at each aspect ratio, the heat transfer by conduction and radiation was measured by lowering the pressure until Ra fell in the range $10 < \text{Ra} < 700$. The radiation heat transfer was obtained by subtracting the calculated conduction component, and a radiation heat transfer coefficient was derived. Since the temperatures of the plates were held very nearly constant over the entire Ra range, this coefficient permitted radiation to be accurately calculated for each data point. The emissivity of the plates was about 0.06 so that radiation transfer was roughly equal to conduction for $L = 49$ mm and was about 6 percent of conduction for $L = 5.8$ mm.

An error analysis indicated that the major sources of error were in measuring the spacing, L, and in measuring the heat-flux emf. The heat-flux meter signal, observed on a potentiometric recorder, showed low-frequency noise with an indication of a strong harmonic at roughly 3 mHz. These fluctuations appear to be responses to low frequency variability in the flow and did not arise from the controls or instrumentation. High frequency variability could not be detected because of the large thermal mass of the heater plates. For each heat-flux measurement, readings of the heat-flux meter signal were taken automatically at 11-s intervals and averaged over at least 27 min, yielding a minimum of 150 readings over the period in all. A statistical analysis [23], based on time series analysis, was performed to estimate the error bounds on the emf reading; it gave a corresponding error in the heat flux of 0.075 W/m^2. The maximum error in
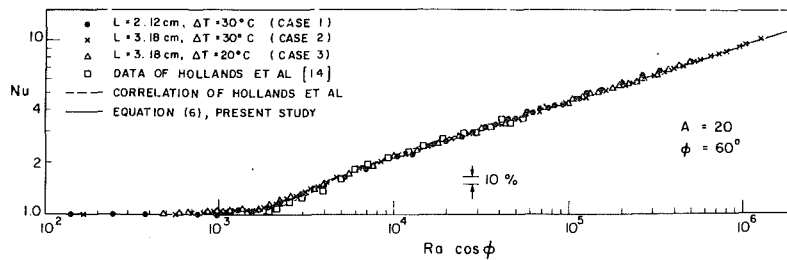
Fig. 4 Measurements of Nu versus Ra for A = 20 and ϕ = 60 deg using different plate spacings, temperature differences, and horizontal aspect ratios. The degree to which the data fall on a single curve indicates the reliability of measurements.
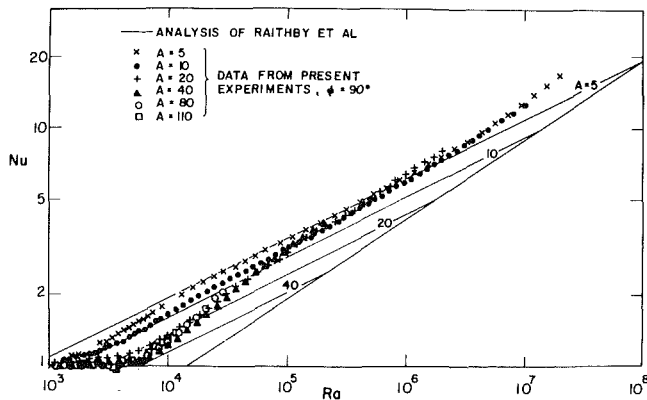

Fig. 5 Present data for vertical air layers

the *convective component* of the heat transfer was then estimated to be twice this, or 0.15 W/m², and the following approximate formulae for the errors in Nu (δNu) and in Ra (δRa) were derived [24]:

$$\delta\text{Nu} \leq [(0.50 + 10L^{-1})(\text{Nu} - 1) + 0.027L] \times 10^{-2} \tag{2}$$

$$\frac{\delta\text{Ra}}{\text{Ra}} \leq \frac{0.3}{L} + 0.0064 + 8 \times 10^{-4} L^{3/2}/\text{Ra}^{1/2} \tag{3}$$

where L is in mm. According to these errors the greatest uncertainties in Nu and Ra in the present experiments were 2.2 percent (for A = 5 and Nu close to unity) and 5.8 percent (for A = 110), respectively.

Experimental Results

Consistency Checks. If Nu indeed depends on Ra alone for a given A and ϕ, it should be possible to reproduce the relationship using different physical plate spacings, L, and temperature differences, ΔT. Figure 4 shows results achieved from three separate tests in which A = 20 and $\phi = 60$ deg was maintained. In case 1 only two heater plates were used, while in cases 2 and 3, all three heaters were used. In all cases, the total width of the layer, W, was maintained so that the horizontal aspect ratio of the layer was 30 in case 1 and 20 in cases 2 and 3. For the three cases, the differences in Nu were less than 3 percent. A comparison with earlier measurements of Hollands et al. [14] on a different apparatus are also shown in Fig. 4. The agreement over the middle Ra range was found to be excellent. The small differences at low Ra result from the fact that the heat transfer in that study [14] was only measured over the central portion of the plates.

With ϕ = 0 deg (horizontal layer heated from below), the critical Rayleigh number was determined from the measurements, using the technique described by Hollands and Konicek [13], to be 1724. This agrees to within about 1 percent with the expected value of 1708.

As mentioned previously, a large enough horizontal aspect ratio was desired to guarantee that the results were independent of A_H. Based on measurements reported in the literature [22], it was expected that $A_H \geq 5$ would be sufficient, especially since the heat transfer was measured only along a strip lying midway between the two edges (Fig. 3(a)). However, a direct experimental check was still desirable. Thus measurements were repeated for a vertical aspect ratio, A, of 5, using respectively one, two, and all three heater plates while maintaining, for all tests, the full width W. The corresponding A_H for these measurements were 15, 7.5 and 5. For $8 \times 10^3 < \text{Ra} < 2 \times 10^5$, the maximum difference between Nu for A_H = 5 and Nu for A_H = 7.5 was about 4.3 percent; the corresponding difference in Nu for A_H = 7.5 and A_H = 15 was smaller (about 3 percent). Outside this Ra range the differences in Nu caused by changes in A_H were negligible. Changing A_H from 20 to 30 was also shown to have no significant effect on Nu (for ϕ = 60 deg) in Fig. 4.

As A_H is increased, the highest value of Ra that can be reached decreases. As a compromise between A_H independence and Ra range, the Nu measurements reported below were obtained using A_H = 7.5, 10, 20, 40, 80 and 110, respectively, for A = 5, 10, 20, 40, 80 and 110.

Data for Vertical Layers. All data obtained for vertical layers have been plotted together in Fig. 5. The data for A = 5 are the first to depart from Nu = 1 with increasing Ra; after an initial transition, these data fall along a line of slope close to 1/4 up to Ra $\approx 2 \times 10^6$, where they rather abruptly depart and follow a slope of about 1/3. For larger values of A, the departure of Nu from unity is delayed to larger Ra. However, beyond $A \approx 40$, little additional change in the point of departure was found. After its departure from unity, the Nu versus Ra curve for A = 10 increased more rapidly with Ra than for A = 5 (slope ≈ 0.28), but also followed a 1/3 slope for Ra $\geq 2 \times 10^6$. For A = 20, the Nu data rise from unity and gradually approach a 1/3 slope, and actually cross over and lie above the data for A = 5 and 10 for large Ra (Ra > 6.3×10^5). For still larger A, the rise from unity is more abrupt, and for A > 40, increasing A caused a slight increase in Nu while the data closely approached the same Nu $\propto$ Ra$^{1/3}$ relation as for A = 20. The complex dependence of the Nu-Ra relation on A revealed in Fig. 5 was, based on previous studies, unexpected and explains why there has been difficulty in reaching agreement on the exponents in equations such as equation (1).

Comparison with Previous Vertical Layer Measurements. Figure 6 presents separate graphs for each value of A, and plots the Nu data obtained from previous studies that had corresponding values of A. Excellent agreement was found with the measurements of Eckert and Carlson [3], and with Randall et al. [7], except for A = 10. With the exception of A = 5, the present measurements are generally higher than those of Mull and Reiher [1].

Data for Inclined Layers. Figure 7 shows the data, for all aspect ratios, for air layers tilted at 60 deg from the horizontal. It is seen that there is a definite effect of A on Nu in the low Ra range (500 < Ra cos (60 deg) < 2×10^4). For Ra
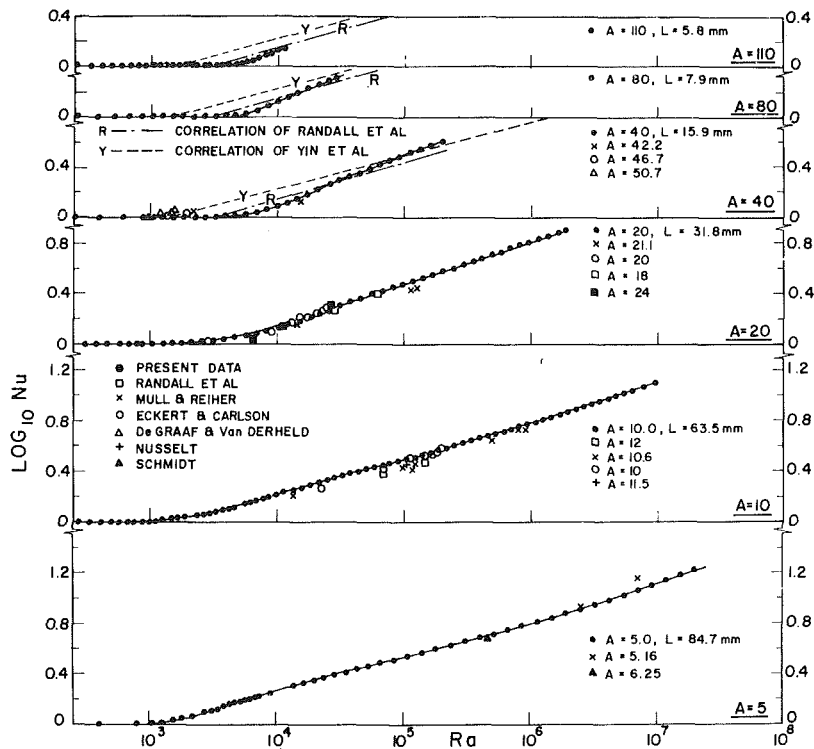
Fig. 6 Comparison of present data with previous measurements and with the correlation equations of Yin et al. and Randall et al. Solid lines represent the present correlations given in the Appendix.
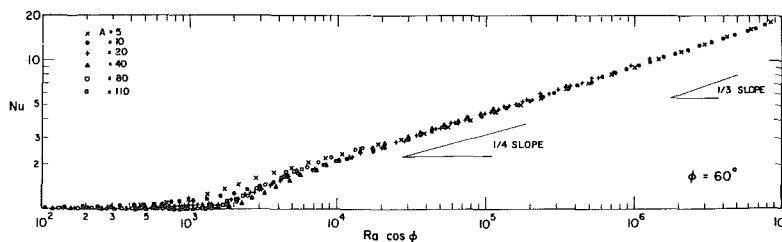

Fig. 7 Present data for tilted air layers, ϕ = 60 deg

$\cos (60 \text{ deg}) > 2 \times 10^4$, no significant effect of A on Nu was observed. For $A \geq 20$, the Ra value at which Nu rises from unity agrees well with the stability criterion $\text{Ra}_c \cos\phi = 1708$.

Angle Dependence of Nu. For given values of Ra and A, the heat transfer across the air layer was measured in increments of ϕ for 0 deg $\leq \phi \leq$ 90 deg. The value of Ra was then changed, and this process was repeated. The data are reported in Fig. 8 for aspect ratios of 5, 10, 20, 40, 80 and 110. In all cases the Nusselt number is about minimum for $\phi = 90$ deg. Only at low Ra (see lower curves for $A = 5$ and $A = 10$) is Nu approximately independent of ϕ for 60 deg $\leq \phi \leq$ 90 deg. These trends agree with the observations of Schinkel and Hoogendoorn [21].

Comparison of Data with Previous Equations

Vertical Layer. The recent correlation equations of Randall et al. [7] and Yin et al. [6] were simple power law equations of the form of equation (1). Equations of this form, with single constant values of m and n, cannot account for the complex interaction of A and Ra on Nu seen in Fig. 5. Applying the correlations of Randall et al. and Yin et al. to the present range of variables results in errors in Nu up to 15 percent and 40 percent, respectively.

The approximate analysis of Raithby et al. [11] resulted in the following equation (for air):

$$\text{Nu} = [1, 0.288(\text{Ra}/A)^{1/4}, 0.041\,\text{Ra}^{1/3}]_{\max} \qquad (4)$$

where the maximum of the three terms for a given Ra and A is to be used. The third term, for fully turbulent flow, was obtained by assuming that the hot and cold plates would, for asymptotically high Ra, each behave as a single vertical plate in a quiescent environment. This "independent-plate hypothesis" was found [11] to yield good agreement with measurement for high Pr, but could not be checked for gases because reliable data were unavailable.

Equation (4) has been plotted in Fig. 5 for the experimental values of A. While the predicted trends are correct, the independent plate hypothesis predicts turbulent heat flow which is too low by about 34 percent for Pr = 0.71; reasonable agreement with the data is restored simply by replacing 0.041 in equation (4) by 0.062. In view of the agreement with previous data for Pr > 1, this comparison was quite surprising and it suggests that there may be a strong mixing across the fluid layer even at $A = 5$. The fact that the value of Nu decreases slightly with A at high Ra could be explained by an attenuation of the mixing at large plate spacings.

Inclined Layer. If it is assumed that longitudinal rolls are formed for $\phi > 0$ deg, Clever [15] showed that, for Pr $\rightarrow \infty$, the separate Ra and ϕ parameters combine in a single new parameter Ra $\cos\phi$. This implies a decrease of Nu with increasing ϕ for a fixed Ra. Hollands et al. [14] extended the

proof to include all Pr but showed that the scaling was not experimentally obtained. This problem has now been resolved by Clever et al. [16] and Ruth et al. [17, 18]. The correlation equation developed by Hollands et al. [14], valid for 0 deg $\leq$ $\phi \leq$ 60 deg, for Ra $\leq 10^5$, and for large A, is plotted for comparison with the present data in Fig. 8. The maximum deviation of the data from this equation is about 10 percent. For Ra values beyond the range of validity of this equation, the broken curves in Fig. 8 show that heat transfer rates are underpredicted.

Near the vertical, 60 deg $< \phi \leq$ 90 deg, there are several proposed correlation equations. Ayyaswamy and Catton [19] and Raithby et al. [11] propose that the Nusselt number at ϕ = 90 deg be multiplied by $(\sin \phi)^{1/4}$ to obtain a value for other ϕ values near the vertical. This implies a local maximum in the Nusselt number at the vertical, and also a minimum in the range 0 deg $< \phi <$ 90 deg since Nu in the horizontal orientation (ϕ = 0 deg) exceeds that for the vertical. The data of Arnold et al. [20] verified these extrema but found that for larger Ra and A the minimum becomes much less pronounced; they proposed an alternative simple equation that correlated their data for large Pr well in the range $1 \leq A \leq 12$, $10^3 < $ Ra $\leq 4 \times 10^6$.

The data in Fig. 8 suggest that the minimum disappears completely for large A and large Ra (for Pr = 0.71), and is replaced by a continuous rise in Nu with decreasing ϕ. The previous correlations do not, therefore, represent the data over the present range of variables.

Correlation Equations

Vertical Layers. The dependence of Nu on Ra and A in Fig. 5 contains both gross features and "fine-grain structure." The Appendix contains precise, but complex correlation equations which reproduce the fine-grain structure. The following correlation equation for a vertical layer compromises some accuracy for the sake of simplicity:

$$Nu_1 = 0.0605 \, Ra^{1/3}$$

$$Nu_2 = [1 + \{0.104 Ra^{0.293}/(1 + (6310/Ra)^{1.36})\}^3]^{1/3}$$

$$Nu_3 = 0.242 \, (Ra/A)^{0.272}$$

$$Nu = [Nu_1, Nu_2, Nu_3]_{max} = Nu_{90} \qquad (5)$$

According to the last equation the maximum value of Nu_1, Nu_2 and Nu_3 should be used. The data agree with equation (5) to within 9 percent (maximum deviation) and with a standard deviation of 3.6 percent. Equation (5) is not claimed to be valid beyond the experimental range of measurements (see Figs. 2 or 6).

Inclined Layers. For air layers inclined at 60 deg, the following equation correlates the measurements in Fig. 7 with a maximum deviation of 11.5 percent and a standard deviation of 3.3 percent:

$$Nu_1 = [1 + \{0.0936 Ra^{0.314}/(1 + G)\}^7]^{1/7}$$

$$G = 0.5/[1 + (Ra/3160)^{20.6}]^{0.1}$$

$$Nu_2 = (0.104 + 0.175/A) Ra^{0.283}$$

$$Nu = [Nu_1, Nu_2]_{max} = Nu_{60} \qquad (6)$$

Again, extrapolation of this equation beyond the experimental range of variables is not recommended.

For near vertical layers (60 deg $\leq \phi \leq$ 90 deg), a straight line interpolation between equations (5) and (6) may be used, i.e.,

$$Nu_\phi = [(90 \, deg - \phi)Nu_{60} + (\phi - 60 \, deg)Nu_{90}]/30 \, deg \qquad (7)$$

----- EQ (7), 60° $\leq \phi \leq$ 90° (PRESENT STUDY)
——— HOLLANDS ET AL [14], Ra $< 10^5$, A $\geq$ 20
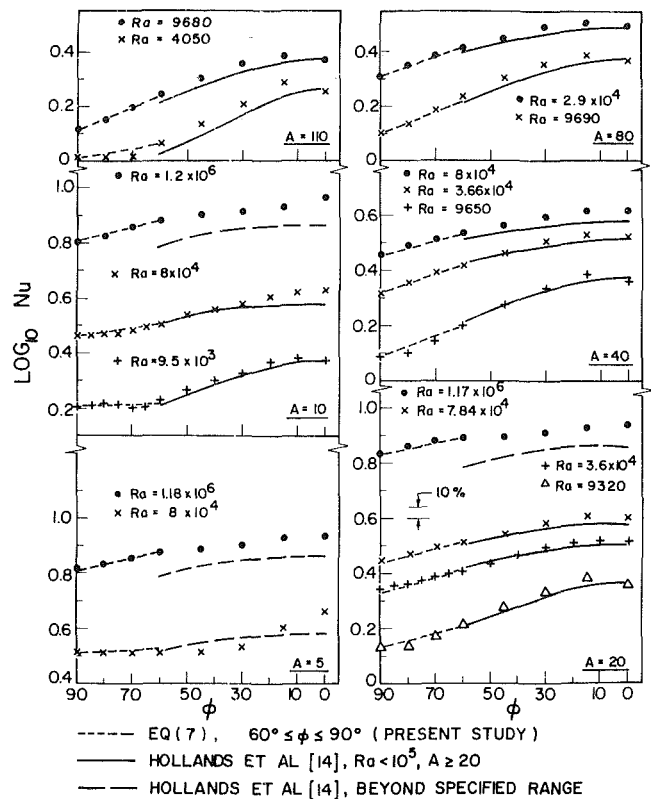— — HOLLANDS ET AL [14], BEYOND SPECIFIED RANGE

Fig. 8 Dependence of Nu on orientation. Data points are from the present study.

Figure 8 shows a plot of equation (7). The maximum deviation from the data for 60 deg $< \phi <$ 90 deg was about 6.5 percent.

Summary

1 Data are presented for heat transfer across air layers for a wide range of parameters. By maintaining a constant aspect ratio while varying the Rayleigh number over a wide range, and repeating this for several aspect ratios, the separate effects of aspect ratio and Rayleigh number on the heat transfer have been determined. The relationship is rather complex.

2 A correlation equation (equation (5)) has been provided from which the convective heat transfer across vertical air layers can be calculated. The maximum discrepancy between this equation and the measurements is about 9 percent, but the agreement is generally well within 3 percent.

3 Correlation equations have also been provided (equations (6)) for a layer tilted 30 deg from the vertical (i.e., ϕ = 60 deg). For 60 deg $< \phi <$ 90 deg, a linear interpolation between the equations for ϕ = 60 deg and ϕ = 90 deg is recommended. Such a procedure agrees with most of the data to within 5 percent, but discrepancies up to 7 percent occur.

References

1 Jakob, M., *Heat Transfer*, Vol. 1, Wiley, New York, 1967, pp. 536–539.
2 DeGraaf, J. G. A., and Van Der Held, E. F. M., "The Relation Between the Heat Transfer and Convection Phenomena in Enclosed Plane Air Layers," *Applied Science Research*, Vol. 3, 1953, pp. 393–409.

3 Eckert, E. R. G., and Carlson, W. O., "Natural Convection in an Air Layer Enclosed Between Two Vertical Plates with Different Temperatures," *International Journal of Heat and Mass Transfer,* Vol. 2, 1961, pp. 106–120.

4 Emery, A., and Chu, N. C., "Heat Transfer Across Vertical Layers," JOURNAL OF HEAT TRANSFER, Vol. 87, 1965, pp. 110–116.

5 Dropkin, D., and Somerscales, E., "Heat Transfer by Natural Convection in Liquids Confined by Two Parallel Plates Which Are Inclined at Various Angles with Respect to the Horizontal," JOURNAL OF HEAT TRANSFER, Vol. 87, 1965, pp. 77–84.

6 Yin, S. H., Wung, T. Y., and Chen, K., "Natural Convection in an Air Layer Enclosed Within Rectangular Cavities," *International Journal of Heat and Mass Transfer,* Vol. 21, 1978, pp. 307–315.

7 Randall, K. R., Michell, J. W., and El-Wakil, M. M., "Natural Convection Heat Transfer Characteristics of Flat Plate Enclosures," JOURNAL OF HEAT TRANSFER, Vol. 101, 1979, pp. 120–125.

8 Batchelor, G. K., "Heat Transfer by Free Convection Across a Closed Cavity Between Vertical Boundaries at Different Temperatures," *Quarterly of Applied Mathematics,* Vol. 12, 1954, pp. 209-233.

9 Thomas, R. W., and de Vahl Davis, G., "Natural Convection in Annular and Rectangular Cavities: A Numerical Study," *Proceedings of the 1970 International Heat Transfer Conference,* Paper NC2.4, Paris.

10 Newell, M. E., and Schmidt, F. W., "Heat Transfer by Laminar Natural Convection Within Rectangular Enclosures," JOURNAL OF HEAT TRANSFER, Vol. 92, 1970, pp. 159-165.

11 Raithby, G. D., Hollands, K. G. T., and Unny, T., "Analysis of Heat Transfer by Natural Convection Across Vertical Fluid Layers," JOURNAL OF HEAT TRANSFER, Vol. 99, 1977, pp. 287–293.

12 Hollands, K. G. T., "Natural Convection in Horizontal Thin-Walled Honeycomb Panels," JOURNAL OF HEAT TRANSFER, Vol. 95, 1973, pp. 439-444.

13 Hollands, K. G. T., and Konicek, L., "Experimental Study of the Stability of Differentially Heated Inclined Air Layers," *International Journal of Heat and Mass Transfer,* Vol. 16, 1973, pp. 1467–1476.

14 Hollands, K. G. T., Unny, T. E., Raithby, G. D., and Konicek, L., "Free Convective Heat Transfer Across Inclined Air Layers," JOURNAL OF HEAT TRANSFER, Vol. 98, 1976, pp. 189–193.

15 Clever, R. M., "Finite Amplitude Longitudinal Convection Rolls in an Inclined Layer," JOURNAL OF HEAT TRANSFER, Vol. 95, 1973, pp. 407–408.

16 Clever, R. M., and Busse, F. H., "Instabilities of Longitudinal Convection Rolls in an Inclined Layer," *Journal of Fluid Mechanics,* Vol. 81, 1977, pp. 107–127.

17 Ruth, D. W., Hollands, K. G. T., and Raithby, G. D., "On Free Convection Experiments in Inclined Air Layers Heated from Below," *Journal of Fluid Mechanics,* Vol. 96, 1980, pp. 459–479.

18 Ruth, D. W., Raithby, G. D., and Hollands, K. G. T., "On the Secondary Instability in Inclined Air Layers," *Journal of Fluid Mechanics,* Vol. 96, 1980, pp. 480–491.

19 Ayyaswamy, P., and Catton, I., "The Boundary-Layer Regime for Natural Convection in a Differentially Heated Tilted Rectangular Cavity," JOURNAL OF HEAT TRANSFER, Vol. 95, 1973, pp. 543–545.

20 Arnold, J. N., Catton, I., and Edwards, D. K., "Experimental Investigation of Natural Convection in Inclined Rectangular Regions of Differing Aspect Ratios," JOURNAL OF HEAT TRANSFER, Vol. 98, 1976, pp. 67–71.

21 Schinkel, W. M. M., and Hoogendoorn, C. J., "An Interferometric Study of the Local Heat Transfer by Natural Convection in Inclined Airfilled Enclosures," *Proceedings of the 6th International Heat Transfer Conference,* Paper NC-18, Toronto, 1978.

22 Catton, I., "Natural Convection in Enclosures," *Proceedings of the 6th International Heat Transfer Conference,* Toronto, 1978.

23 Hipel, K. W., "Advances in Box-Jenkins Modeling - 1. Model Construction," *Water Resources Research,* Vol. 13, No. 3, June 1977, pp. 567–575.

24 ElSherbiny, S. M., "Heat Transfer by Natural Convection Across Vertical and Inclined Air Layers," Ph.D. thesis, Department of Mechanical Engineering, University of Waterloo, Waterloo, Canada, 1980.

APPENDIX

Correlation Equations for Vertical Air Layers

The following equations correlate the data for vertical fluid layers to a higher accuracy than equation (5).

$A = 5, \mathrm{Ra} < 10^8$

$$\mathrm{Nu} = \left\{ \left[1 + \left(\frac{0.193 \, \mathrm{Ra}^{1/4}}{1 + (1800/\mathrm{Ra})^{1.289}} \right)^3 \right]^{1/3}, 0.0605 \, \mathrm{Ra}^{1/3} \right\}_{max}$$

(A1)

$A = 10, \mathrm{Ra} < 9.7 \times 10^6$

$$\mathrm{Nu} = \{ [1 + (0.125 \, \mathrm{Ra}^{0.28})^9]^{1/9}, 0.061 \, \mathrm{Ra}^{1/3} \}_{max}$$

(A2)

$A = 20, \mathrm{Ra} < 2 \times 10^6$

$$\mathrm{Nu} = [1 + (0.064 \, \mathrm{Ra}^{1/3})^{6.5}]^{1/6.5}$$

(A3)

$A = 40, \mathrm{Ra} < 2 \times 10^5$

$$\mathrm{Nu} = [1 + (0.0303 \, \mathrm{Ra}^{0.402})^{11}]^{1/11}$$

(A4)

$A = 80, \mathrm{Ra} < 3 \times 10^4$

$$\mathrm{Nu} = [1 + (0.0227 \, \mathrm{Ra}^{0.438})^{18}]^{1/18}$$

(A5)

$A = 110, \mathrm{Ra} < 1.2 \times 10^4$

$$\mathrm{Nu} = [1 + (0.0607 \, \mathrm{Ra}^{1/3})^{18}]^{1/18}$$

(A6)

High Rayleigh Number Laminar Convection in Low Aspect Ratio Enclosures With Adiabatic Horizontal Walls and Differentially Heated Vertical Walls[1]

J. Tichy

Assistant Professor,
Department of Mechanical Engineering,
Rensselaer Polytechnic Institute,
Troy, N.Y. 12181
Mem. ASME

A. Gadgil

Staff Scientist,
Passive Solar Analysis and Design Group,
Lawrence Berkeley Laboratory,
University of California,
Berkeley, Calif. 14720

Laminar flow in shallow horizontal cavities (aspect ratio a << 1) at high Rayleigh numbers (> 10^6) is investigated using an approximate analysis based on first principles, and also with numerical solutions to the full equations. A Prandtl number of approximately one is assumed. It is found that the flow regime at such high values of Ra is characterized by boundary layers lining both vertical as well as horizontal walls of the enclosure, and is qualitatively different from the flow regimes at lower Rayleigh numbers. The internal region of the core (near to the horizontal centerline) exhibits linear velocity and temperature profiles. Typical isotherms and streamlines characteristic of this flow regime are presented, based on the numerical solutions. The velocity and temperature profiles predicted from the approximate analysis are found to compare well with those obtained from the numerically obtained solutions. The Nusselt numbers predicted from the analysis are also in good agreement with the numerical solutions, and with the limited experimental data in the literature. The various physical processes in this type of flow are discussed based on the findings of the analytical and numerical studies.

Introduction

The relative scarcity of published work on natural convection flows in shallow cavities driven by differentially heated end walls has been noted by Ostrach [1]. The first detailed study of this problem appears to be the series of papers by Cormack et al. [2, 3], and Imberger [4] which addresses the problem of viscous dominated flow at large but finite Rayleigh numbers with adiabatic horizontal surfaces in the asymptotic limit of aspect ratio $a \to 0$. Rayleigh number Grashof number Gr are based here on enclosure height, and aspect ratio is the ratio of height to length. Elder [5], Gill [6], and Quon [7] have addressed the problem of flow with developed boundary layers on the differentially heated vertical walls of square or vertical cavities ($a \geq 1$). Bejan and Tien [8] have extended the solution of [2] to higher Rayleigh numbers, or shorter cavities, by matching the boundary layer solution on the vertical end walls to the solution for the fully developed asymptotic flow in the core region away from the end walls. Typical conditions for the Cormack theory are $Ra = 10^5$, $a = 0.01$, while typical conditions for Bejan and Tien are $Ra = 10^7$, $a = 0.05$.

As the Rayleigh number is increased further, greater momentum is imparted to the core flow by the fast moving boundary layers on the vertical end walls. The fully developed, friction-dominated core flow profile gives way to a distinct boundary layer structure lining the horizontal walls in the core. This regime thus qualitatively differs from the flow considered in [2–8]. Flow at these high Rayleigh numbers was first theoretically studied by Shiralkar et al. [9], where they predicted the qualitative behavior of the Nusselt number as a function of the Rayleigh numbers and the aspect ratio and presented new correlations based on numerical simulations. However, to the author's knowledge, there has been no analytical study of the detailed flow profiles arriving in this flow. Experimental results are reported by Al-Hammoud and Bejan [10] for an enclosure with $Ra \simeq 1.6 \times 10^9$, Prandtl number $Pr = 6.3$ and $a = 0.0625$. Ostrach [1] presents dye-streak velocity field results, similar to those suggested here for $Ra = 1.8 \times 10^7$, $a = 0.2$ but $Pr = 1.4 \times 10^3$. Kimura and Bejan [11] experimentally studied the case of a horizontal cylinder at $Ra = 1.8 \times 10^9$ for a diameter-to-length ratio of 0.112, $Pr \cong 5$. Velocity fields similar to those of the present study are exhibited. The authors discussed fundamental differences between the previously known fully developed profiles and those observed. The attempts at numerical simulations of flows at these high Rayleigh numbers ($Ra > > 10^6$) have been plagued with numerical instabilities, and the analytic treatment of this flow regime from first principles has seemed formidable.

This type of flow is of considerable interest to the study of intra and interzonal heat transfer in buildings (mixing of air

within a room and energy flow between rooms). Otherwise detailed computer simulation programs for building heating and cooling loads make very rudimentary assumptions concerning convective heat transfer. Many passive solar heating and cooling techniques rely on free convection flow in enclosures where surfaces are maintained at different temperatures. Certain processes in environmental engineering and geophysics are also governed by flows of this nature — dispersion of pollutants in buildings, buoyancy driven flows in bodies of water, etc.

Two laminar core flow regimes have been identified by prior analytical investigators: (a) a purely conductive regime for Gr→0 at any fixed a by Batchelor [12] and (b) a viscous-dominated core flow for any fixed (but perhaps large) Gr as a→0, due to Cormack, Leal and Imberger [2]. In the latter case, the core length and fluid viscosity both serve to throttle the core flow. Thus, even for a relatively high buoyancy effect (Grashof number) it is required that viscous effects will dominate in a sufficiently long enclosure. The resulting purely horizontal core flow is cubic with respect to the vertical coordinate and antisymmetric about the horizontal mid-plane.

A purpose of this paper is to study the third core flow regime, previously observed by experiment [1, 10, 11], and discussed above. In this case, the core itself consists of horizontal boundary layers on the top and bottom surfaces matched to an outer region (i.e., away from the walls) near the horizontal centerline. The aspect ratio is assumed to be small but the asymptotic limit is for Gr→∞. This core solution is then matched to an end solution which is similar to that of Bejan and Tien [8] but fluid entrainment from the core is now included.

Analysis

In the present analysis, a matching procedure between the core and the end regions is developed along the lines of Cormack et al. [2] and Bejan and Tien [8]. The major dif-
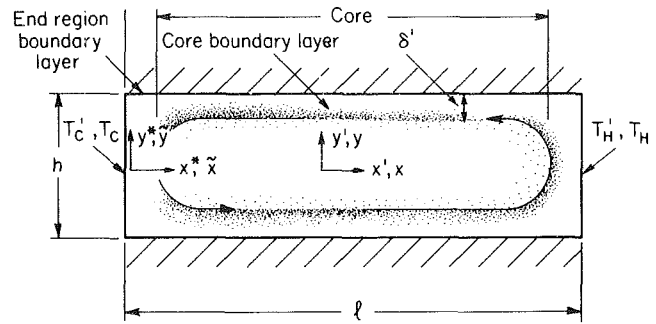

Fig. 1 Schematic of enclosure geometry

ference in this work is that for the flow regime under consideration the core itself consists of a central zone near the horizontal centerline and boundary layers along the adiabatic horizontal walls.

The Core Solution. A Cartesian coordinate system x', y' has its origin at the center of the cavity as shown, hence $-l/2 \leq x' \leq l/2$ and $-h/2 < y' < h/2$. The enclosure is shallow, i.e., the aspect ratio $a = h/l < < 1$. Flow in the core is assumed to be nearly parallel to the x'-axis (see Fig. 1) and the end regions only have influence as matching boundary conditions.

The governing equations are the usual incompressible continuity, momentum and energy equations for steady, two-dimensional, buoyancy-driven flow along with the Boussinesq approximation for density variation. The following dimensionless variables are used:

$$u = \frac{u'h}{\nu}, v = \frac{v'l}{\nu}, x = \frac{x'}{l}, y = \frac{y'}{h},$$

$$T = \frac{T' - \frac{1}{2}(T_H' + T_C')}{T_H' - T_C'} \tag{1}$$

and the governing equations in dimensionless form become:

Nomenclature

a = aspect ratio = h/l

b = real constant, cf. equations (24), (30)

C_u, C_u^*, C_T = constant in core outer solution, see equations (9), (22), (29), (32)

g = gravitational constant

Gr = Grashof number = $\dot{g}\beta(T_H' - T_C')h^3/\nu^2$

h,l = cavity height, length

k = free parameter in end linearization, see equation (19)

K = "constant" of integration, see equation (28)

Nu = Nusselt number, equation (34)

p,q = auxiliary variables, equation (28)

Pr = Prandtl number = ν/α

$Ra (= Gr\,Pr)$ = Rayleigh number

T',T = temperature; dimensionless temperature, equation (1)

u',v' = horizontal, vertical velocities

u,v,U = horizontal, vertical velocities, dimensionless variables for the core flow, equations (1), (14)

U^*, V^* = horizontal, vertical velocities, dimensionless variables for the end region, equation (18)

x',y' = Cartesian coordinates, see Fig. 1

x,y = Cartesian coordinates, dimensionless core region variables, equation 1

x^*, y^* = Cartesian coordinates, dimensionless end region variables, equation (18)

$\tilde{u}, \tilde{v}, \tilde{x}, \tilde{y}$ = Horizontal and vertical velocity, horizontal and vertical coordinate, dimensionless numerical variables, equation (35)

α = thermal diffusivity

β = coefficient of thermal expansion

α, β, γ = auxiliary constants of end region solution, equation (24)

δ = core boundary layer thickness (dimensionless)

η = Dimensionless strained coordinate for core, equation (14)

ν = kinematic viscosity

ρ = fluid density

Subscripts

$0,1$ = perturbation solutions – outer, first

$core, end$ = core, end variables (used when referring to core from end solution, and vice versa)

H,C = hot (right), cold (left) end

Superscripts

$'$ = dimensionless variable

$*$ = end variable

$\tilde{\ }$ = numerical variable

$$\frac{\partial u}{\partial x} + \frac{\partial v}{\partial y} = 0 \qquad (2)$$

$$a\frac{\partial}{\partial y}\left(u\frac{\partial u}{\partial x} + v\frac{\partial u}{\partial y}\right) - a^3\frac{\partial}{\partial x}\left(u\frac{\partial v}{\partial x} + v\frac{\partial v}{\partial y}\right)$$

$$= \frac{\partial}{\partial y}\left(a^2\frac{\partial^2 u}{\partial x^2} + \frac{\partial^2 u}{\partial y^2}\right)$$

$$- a^2\frac{\partial}{\partial x}\left(a^2\frac{\partial^2 v}{\partial x^2} + \frac{\partial^2 v}{\partial y^2}\right) - a\mathrm{Gr}\frac{\partial T}{\partial x} \qquad (3)$$

and

$$a\mathrm{Pr}\left(u\frac{\partial T}{\partial x} + v\frac{\partial T}{\partial Y}\right) = a^2\frac{\partial^2 T}{\partial x^2} + \frac{\partial^2 T}{\partial y^2} \qquad (4)$$

Boundary conditions on u, v and T are

$$y = \pm\frac{1}{2} \qquad u = 0 \quad v = 0 \qquad \frac{\partial T}{\partial y} = 0 \qquad (5a)$$

$$x = +\frac{1}{2} \qquad u = 0 \quad v = 0 \qquad T = \frac{1}{2} \qquad (5b)$$

$$x = -\frac{1}{2} \qquad u = 0 \quad v = 0 \qquad T = -\frac{1}{2} \qquad (5c)$$

Equations (2–5) are valid for both the core and the end solutions. Cross-differentiation has been used to combine the x and y-momentum equations.

Due to the scaling of equation (1), and the assumptions of nearly parallel core flow and $a << 1$, for the core equations (2–4) reduce to:

$$\frac{\partial u}{\partial x} + \frac{\partial v}{\partial y} = 0 \qquad (6)$$

$$\mathrm{Gr}^{-1}a\frac{\partial}{\partial y}\left(u\frac{\partial u}{\partial x} + v\frac{\partial u}{\partial y}\right) = \mathrm{Gr}^{-1}\frac{\partial^3 u}{\partial y^3} - a\frac{\partial T}{\partial x} \qquad (7)$$

$$a\mathrm{Pr}\left(u\frac{\partial T}{\partial x} + v\frac{\partial T}{\partial y}\right) = \frac{\partial^2 T}{\partial y^2}. \qquad (8)$$

For the present study the Grashof number is assumed to be very large relative to 1, say $\mathrm{Gr} \geq 10^6$, thus an expansion in Gr^{-1} is suggested. An outer expansion for the core flow can be obtained by gathering terms 0 (Gr^0), giving

$$u_0 = -C_u y, \qquad (9a)$$
$$T_0 = C_T y, \qquad (9b)$$
$$v_0 = 0, \qquad (9c)$$

where C_u and C_T are (currently unknown) positive constants. Equation (9) is a satisfactory outer-core solution provided it can satisfy the matching boundary conditions at the ends and at the horizontal surfaces.

The inner expansion for the boundary layers on the top surface is now sought, although an analytical solution does not appear to be possible. The most satisfactory approximation as a compromise between mathematical complexity and simulating the physical reality is to assume parallel flow, i.e., $u = u(y)$, $v = 0$ and to use some suitable averaged constant value for the horizontal temperatue gradient. This process gives

$$\mathrm{Gr}^{-1}\frac{d^3 u_1}{dy^3} = a\frac{\overline{\partial T}}{\partial x} \qquad (10)$$

$$-a\mathrm{Pr}u_1\frac{\overline{\partial T}}{\partial x} = \frac{d^2 T_1}{dy^2} \qquad (11)$$

along with the boundary conditions,

$$y = \frac{1}{2} \qquad \frac{\partial T}{\partial y} = 0 \quad u = 0;$$

$$y = \frac{1}{2} - \delta, \, T = C_T\left(\frac{1}{2} - \delta\right), \, u = -C_u(1-\delta);$$

$$\frac{\partial u}{\partial y} = -C_u \qquad (12)$$

The bar superscripts imply averaged value while the dimensionless boundary-layer thickness δ is the location at which the inner and outer-core solutions are matched. An additional condition

$$y = \frac{1}{2} - \delta\frac{\partial T}{\partial y} = C_T \qquad (13)$$

serves to find the value of δ. Equation (12) implies that the thermal and momentum boundary layer thicknesses are identical, i.e., $\mathrm{Pr} \cong 1$.

To obtain the inner solution by standard "strained" coordinate methods, a transformation is required where

$$\eta = \mathrm{Gr}^{1/5}\left(\frac{1}{2} - y\right), \quad U = -\mathrm{Gr}^{-2/5}u_1 \qquad (14)$$

The resulting solutions are as follows for $\frac{1}{2} - \delta < y < \frac{1}{2}$:

$$u = -a\frac{\overline{\partial T}}{\partial x}\mathrm{Gr}\left[\frac{(1/2-y)^3}{6} - \frac{(1/2-y)^2\delta}{3} + \frac{(1/2-y)\delta^2}{6}\right]$$

$$- C_u\mathrm{Gr}^{1/4}\left[\frac{(1/2-y)^2}{\delta} - (1/2-y)\right] \qquad (15)$$

$$- C_u\mathrm{Gr}^{1/4}(1/2-\delta)\left[-\frac{(1/2-y)^2}{\delta^2} + \frac{2(1/2-y)}{\delta}\right]$$

and

$$T = -a\mathrm{Pr}\frac{\overline{\partial T}}{\partial x}\left\{a\frac{\overline{\partial T}}{\partial x}\mathrm{Gr}\left[\frac{(1/2-y)^5}{120} - \frac{(1/2-y)^4\delta}{36}\right.\right.$$

$$\left. + \frac{(1/2-y)^3\delta^2}{36} - \frac{\delta^5}{120}\right]$$

$$+ C_u\mathrm{Gr}^{1/4}\left[\frac{(1/2-y)^4}{12\delta} - \frac{(1/2-y)^3}{6} + \frac{\delta^3}{12}\right] \qquad (16)$$

$$+ C_u\mathrm{Gr}^{1/4}(1/2-\delta)\left[-\frac{(1/2-y)^4}{12\delta^2}\right.$$

$$\left.\left. + \frac{(1/2-y)^3}{3\delta} - \frac{\delta^2}{4}\right]\right\} + C_T(1/2-\delta).$$

From equations (13) and (16) the boundary layer thickness, δ, is found by a simple iterative method. The reader should be warned that the type of simplification of the temperature field used in equations (10) and (11) eliminates any explicit x-dependence of the core temperature and velocity.

The average horizontal temperature gradient in the core boundary layer $\overline{\partial T}/\partial x$ can be related to the vertical temperature gradient $\partial T/\partial y \equiv C_T$:

$$-\frac{\overline{\partial T}}{\partial x}\int_{1/2-\delta}^{1/2}udy = \frac{\partial T}{\partial y}\Big|_{y=1/2-\delta} = C_T \qquad (17)$$

Equation (17) is a balance of overall convection across the boundary layer with conduction across the interface.

The End Solution. The following analysis is concerned with the left (cold) wall, but an entirely analogous procedure can be performed on the right (hot) wall. A new set of dimensionless variables are now to be used for the end solution, in particular a strained coordinate x^*, whose origin is at the left wall:

$$U^* = \mathrm{Gr}^{-1/4} u \quad V^* = v\mathrm{Gr}^{-1/2} a^{-1}$$

$$x^* = \left(x + \frac{1}{2}\right)\mathrm{Gr}^{1/4} a^{-1} \quad y^* = y \tag{18}$$

The convection terms of the momentum and energy equations are linearized in the manner of Gill [6] and Bejan and Tien [8]:

$$U^* \frac{\partial}{\partial x^*} + V^* \frac{\partial}{\partial y^*} \cong k \left(U^*_{\mathrm{core},0} \frac{\partial}{\partial x^*} + V^* \frac{\partial}{\partial y^*} \Big|_{\mathrm{core},0} \right) \tag{19}$$

It is assumed that the core boundary layers are small, hence the "core" variable and operator of equation (19) are determined from the outer core solution (9). The parameter k is a number of the order of $1/2$ to account for the fact that the core variable and operator become identically zero at the wall, analogous to the parameter γ used in reference [8]. Transforming equations (2–4) by (18) and using the linearization (19) yields:

$$\frac{\partial u^*}{\partial x^*} + \frac{\partial V^*}{\partial y^*} = 0, \tag{20a}$$

$$-y^* k C_u \frac{\partial V^*}{\partial x^*} = \frac{\partial^3 V^*}{\partial x^{*3}} + \frac{\partial T}{\partial x^*}, \tag{20b}$$

$$-y^* k C_u \frac{\partial T}{\partial x^*} + k C_T V^* = \frac{1}{\mathrm{Pr}} \frac{\partial^2 T}{\partial x^{*2}} \tag{20c}$$

Note that y^* can be regarded as a parameter in equations (20b) and (20c). The boundary conditions for equations (20b) and (20c) are:

$$\begin{aligned}
x^* &= 0 & V^* &= 0 & T &= -\frac{1}{2} \\
x^* &= \infty & V^* &= V^*_{\mathrm{core},o} = 0 & T &= C_T y^*.
\end{aligned} \tag{21}$$

Additional requirements for the cross-film velocity U^* are:

$$x^* = 0 \quad U^* = 0 \tag{22a}$$

$$x^* = \infty \quad U^* = U^*_{\mathrm{core},0} = -C_u^* y^*, C_u^* = \mathrm{Gr}^{1/4} C_u \tag{22b}$$

Equation (22b) will be regarded as a boundary condition on (20a), while (22a) provides an additional constraint to determine the constant C_u^*.

The variable T can be eliminated from equations (20b) and (20c) to obtain

$$\frac{d^4 V^*}{dx^{*4}} + 4b^4 V^* = y^* \left(-\alpha \frac{d^2 V^*}{dx^{*3}} - \beta \frac{d^2 V^*}{dx^{*2}} \right)$$

$$+ y^{*2} \left(-\gamma \frac{dV^*}{dx^*} \right), \tag{23}$$

with

$$\alpha = k C_u \mathrm{Pr}, \ \beta = k C_u, \ \gamma = k^2 C_u^2 \mathrm{Pr}, \ 4b^4 = k C_T \mathrm{Pr}. \tag{24}$$

For $y^* \to 0$, the Bejan-Tien equation is obtained.

The exact solution of equation (23) involves finding the roots of an arbitrary quartic equation – a difficult task. As a reasonable alternative, a perturbation solution is sought for equation (23) for small y^*, since $|y^*|$ is at most $1/2$, and the core matching is for $y^* \approx 0$. The conventional regular perturbation method applied to equation (23) will lead to "secular" terms which blow up for $x^* \to \infty$, hence the so-called "method of multiple scales" must be used, see Nayfeh [13].

By this procedure, the perturbation solution is:

$$V^* = K e^{-px^*} \sin qx^*, \tag{25}$$

$$T = -y^* C_u V^* - \frac{d^2 V^*}{dx^{*2}} + f(y^*) \tag{26}$$

$$= K e^{-px^*} \left[\left(-y^* \frac{C_u}{2} + q^2 - p^2 \right) \sin qx^* \right.$$

$$\left. + 2pq \cos qx^* \right] + C_T y^*,$$

$$U^* = -\int \frac{\partial V^*}{\partial y^*} dx^* - C_u^* y^* \tag{27}$$

where

$$p(y^*) = b\left[1 + y^* \left(\frac{2\alpha b - \beta}{8b^2} \right) + y^{*2} \left(\frac{8\alpha b \beta - 6\alpha^2 b^2 - \beta^2}{128 b^4} \right) \right]$$

$$q(y^*) = b\left[1 + y^* \frac{\beta}{8b^2} + y^{*2} \left(\frac{6\alpha^2 b^2 - \beta^2}{128 b^4} \right) \right] \tag{28}$$

$$K = -\frac{\dfrac{1}{2} + C_T y^*}{2pq}$$

The condition (22a) $u^* = 0$ at $x^* = 0$ cannot be satisfied at arbitrary y^* from (25–28). Hence the restriction $u^* = 0$ at $x^* = y^* = 0$ is applied which leads to

$$C_T = \frac{1}{4} \mathrm{Pr}^{-5} k^{-1} \tag{29}$$

$$b = \frac{\mathrm{Pr}^{-1}}{2} \tag{30}$$

The Matching Conditions. The constant C_u is determined by matching heat transfer rates across the core and at the wall:

$$\int_{-1/2}^{1/2} \left(-\frac{\overline{\partial T}}{\partial x^*} \right)_{x^*=0} dy^* = \int_{-1/2}^{1/2} U^*_{\mathrm{core},o} T dy^*$$

$$-\frac{b}{2} + 0(y^{*3}) = -\frac{1}{12} C_u^* C_T \tag{31}$$

Several observations are made here which may bear on the accuracy of the result obtained. First, the solution in the end boundary layer is strictly accurate near the centerline ($y^* = 0$), so extending the analysis to the corners ($y^* = \pm \frac{1}{2}$) undoubtedly introduces some error. Second, the heat transfer expression across the core ignores the effect of the core boundary layer. This simplifying assumption is made here to obtain a concise expression for C_u^*. The $0(y^{*3})$ terms are ignored in the end boundary layer heat-transfer expression because the multiple scale analysis was only applied to $0(y^{*2})$.

Substituting for C_T and b, from equations (29) and (30), an expression for C_u^* is obtained:

$$C_u^* = 12\mathrm{Pr}^4 k. \tag{32}$$

Substituting for C_T and C_u^* in the overall core energy balance equation (17), one obtains the following empirical expression for the core boundary layer temperature gradient:

$$\frac{\partial \overline{T}}{\partial x} = \frac{(\mathrm{Pr}^{-17/2} + 36\mathrm{Pr}^{-3/2}\mathrm{Gr}^{-1/4} - a\mathrm{Pr}^{-15/2})^2}{96a} \tag{33}$$

Finally, the overall Nusselt number, Nu, is calculated from the equation

$$\mathrm{Nu} = \frac{-1}{\alpha(T_H' - T_C')} \int_{-h/2}^{h/2} u'$$

$$\left[T' - \frac{1}{2}(T_H' + T_C') \right] dy' = -\mathrm{Pr} \int_{-1/2}^{1/2} u T dy \tag{34}$$

This expression is evaluated by numerical integration of the uT product with the appropriate values for C_T, C_u^* and $\overline{\partial T}/\partial x$.

Numerical Technique

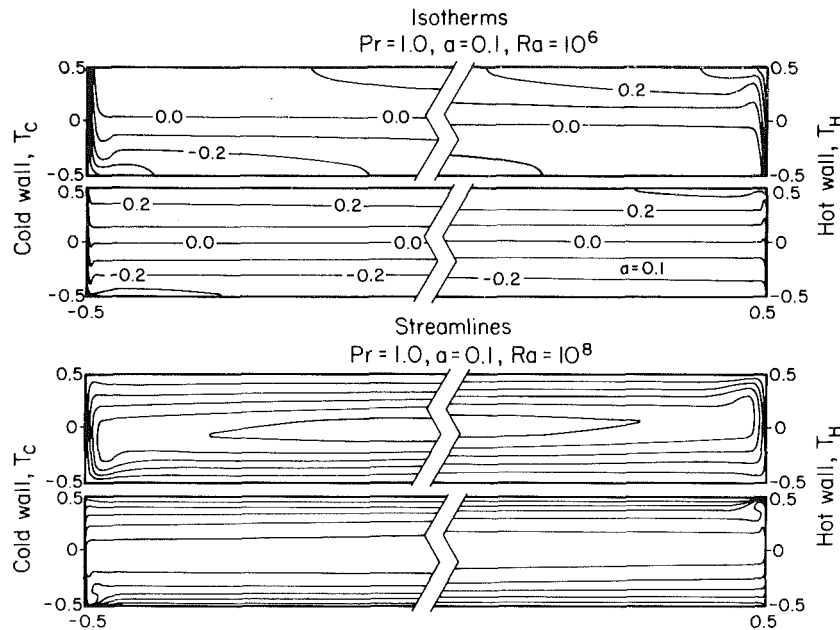The numerical solutions were obtained with a computer

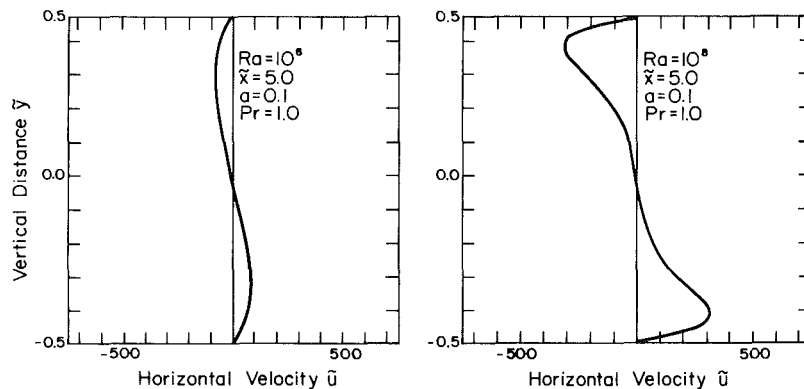Fig. 2 Typical streamlines and isotherms; $Ra = 10^6$, $Ra = 10^8$

Fig. 3 Typical core velocity profiles; $Ra = 10^6$, $Ra = 10^8$

simulation code based on the Patankar-Spalding differencing scheme [14]. This scheme switches between the so-called Central Difference Scheme (CDS) and the Upstream Difference Scheme (UDS), depending on the local magnitude and direction of the fluid velocity at each node. This combines the stability of the UDS with accuracy of the CDS. Due to the capability of the scheme to dynamically change the differencing method used in setting up the matrix of equations for solution, the scheme remains stable throughout the calculation of developing flow in the enclosure starting from fluid at rest. The computer code uses the primitive variables (velocities, temperature, and pressure) and solves the full continuity, momentum, and energy equations along with the Boussinesq approximation.

For interpretation of the numerical results it is useful to define new dimensionless variables:

$$\tilde{u} = u, \ \tilde{v} = va = V^* \mathrm{Gr}^{1/2}, \ \tilde{x} = \frac{x + \dfrac{1}{2}}{a} = x^* Gr^{-1/4}, \ \tilde{y} = y \quad (35)$$

With these variables both pairs $(\tilde{u}, \tilde{v})$ and $(\tilde{x}, \tilde{y})$ have the same measure (i.e., if the velocities of both $\tilde{u}$ and $\tilde{v}$ are one unit, the dimensional physical velocities u' and v' are equal).

The details of the differencing scheme, and the iterative method have been described in references [15] and [16]. Validation of the code by comparison with experiment is also described. Very good correlation was obtained between the numerical results and measured temperature profiles at aspect ratio $a = 0.5$, $Ra \cong 10^9$. In simulating room geometry heat-transfer processes, good correlation was obtained between numerically predicted isotherms and measured isotherms for a more complex three-dimensional geometry with heat flux applied over a portion of one surface.

Typical streamlines and isotherms obtained from numerical solutions are displayed in Fig. 2 for $Ra = 10^6$ and $Ra = 10^8$. In Fig. 3 corresponding core velocity profiles are shown. The lower value of Ra is chosen to exhibit Cormack type viscous dominated flow regime, while the high Ra value was chosen to display typical flow fields for the regime under study, which exhibits a boundary layer structure. These conditions (at $Ra = 10^6$) are not actually those of Cormack where $\partial T / \partial x$ is 0(1) in the core and constant over y. At $Ra = 10^6$, the boundary layer essentially fills the gap, i.e. $\delta \rightarrow \frac{1}{2}$.

Results

Comparison of Analytical and Numerical Results. The horizontal velocity in the core was calculated as a function of enclosure height based on equation (15) and the values for the constants C_u, C_T and $\overline{\partial T} / \partial x$. The boundary layer thickness, δ, was computed from application of equations (13) and (16). The results are compared with the numerically obtained

profiles at the vertical centerline ($\tilde{x} = 1/2a$) for aspect ratios $a = 0.1$ and three different Rayleigh numbers in Fig. 4. The agreement is seen to be good.

The temperature profile as a function of height in the core, obtained by using equation (16), is shown in Fig. 5 compared with the numerical solution at $\tilde{x} = 1/2$, a for aspect ratio $a = 0.1$, and three Rayleigh numbers. The analytic prediction is in good agreement with the numerical solution. The best fit is obtained for the parameter $k = 1/3$.

The numerical results show that for a given aspect ratio, the core profiles change very little with horizontal distance, see Fig. 2. The analytical method assumes there is no change at all other than that implied through the constant $\partial T/\partial x$. Both the analytical and numerical methods show little discernible

change in the profiles at the core midsection when aspect ratio is varied from $a = 0.1$ to $a = 0.2$ (not shown).

A typical profile of the boundary layer on the vertical end wall is examined by considering the case of $a = 0.1$ and $Ra = 3 \times 10^8$.

The analytically predicted velocity profiles at $y^* = \pm 0.179$ are obtained from using equations (24), (25), and (28) with appropriate values for C_u and C_T. The results have been plotted in Fig. 6 together with the numerically obtained velocity profiles. The agreement is excellent.

The temperature profiles at $y^* = \pm 0.132$ are found by using equations (24), (26), and (28). The resulting profiles are compared with the numerically obtained temperature profiles in Fig. 7. Again the agreement is seen to be excellent.
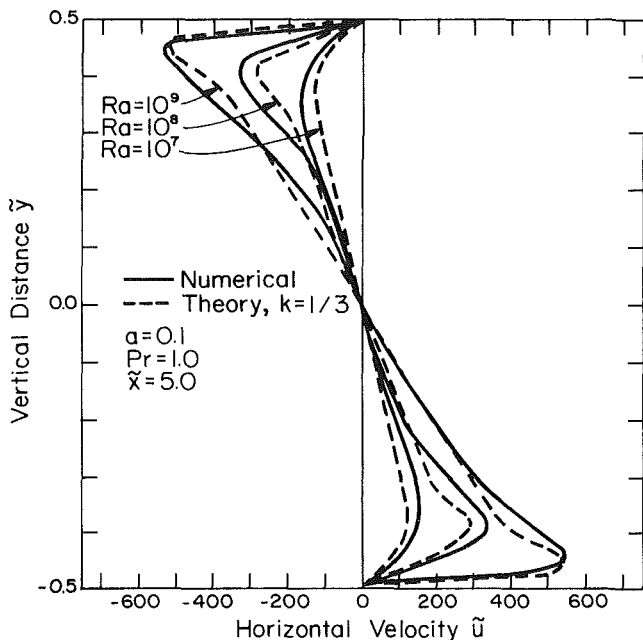

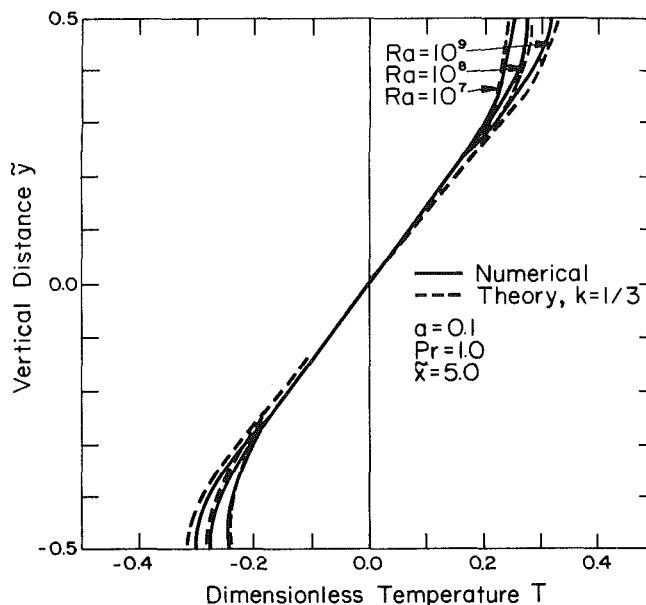Fig. 4 Core horizontal velocity profiles — analytical and numerical results; Ra = 10^7, 10^8, 10^9; $a = 0.1$

Fig. 5 Core temperature profiles — analytical and numerical results; Ra $\simeq 10^7$, 10^8, 10^9; $a = 0.1$
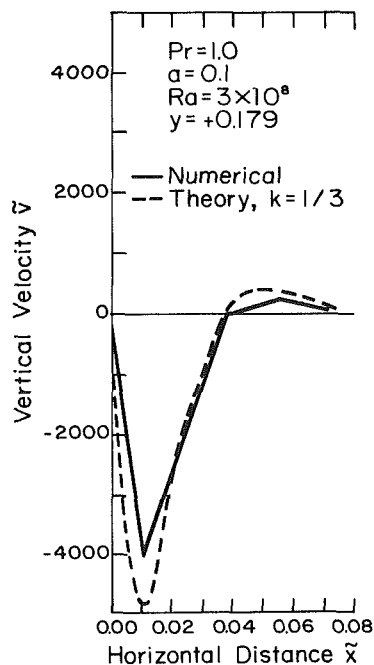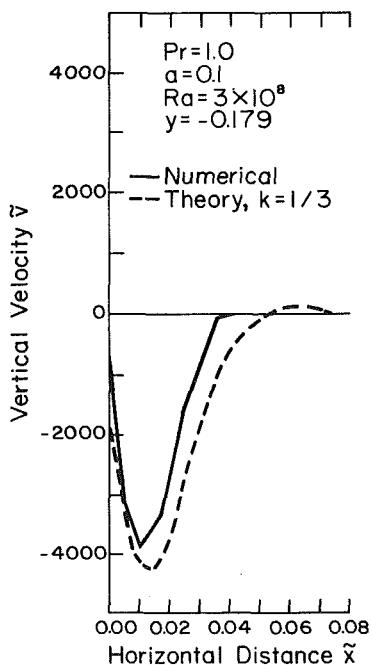

Fig. 6 End vertical velocity profiles — analytical and numerical results; Ra = 3×10^8, $y^* = 0, \pm 0.179$, $a = 0.1$
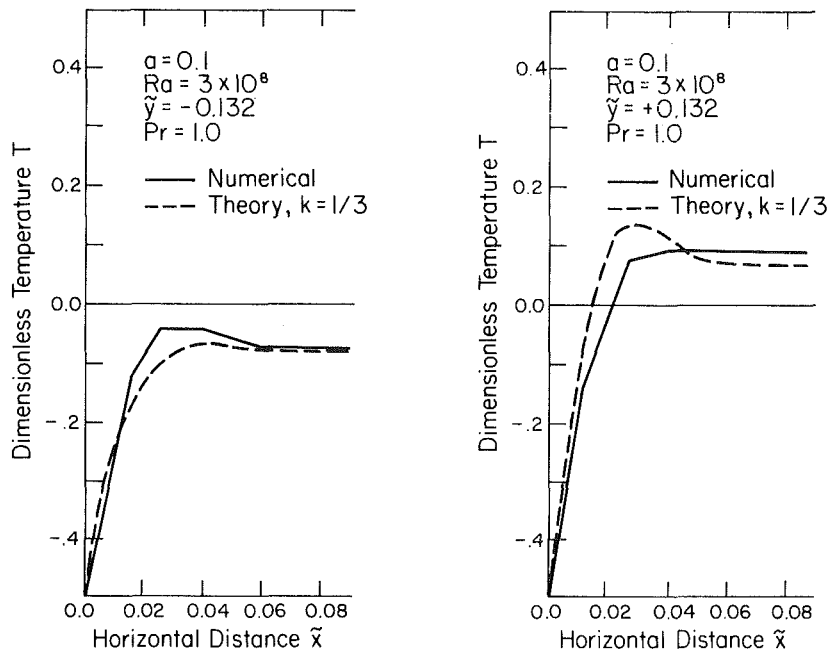
Fig. 7 End temperature profiles—analytical and numerical results; $Ra = 3 \times 10^8$, $y^* = 0, \pm 0.132$, $a = 0.1$
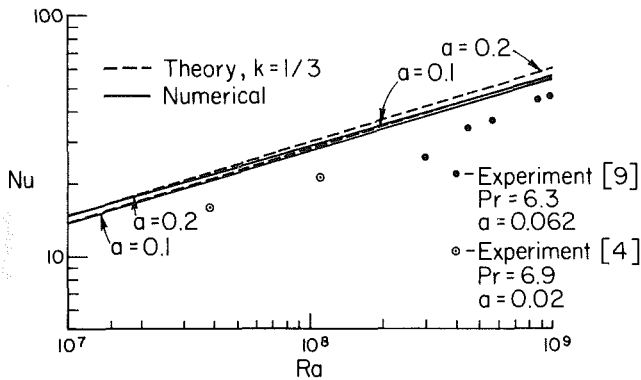

Fig. 8 Nusselt number variation with Rayleigh number—analytical and numerical results, $a = 0.1$, 0.2 (comparison with existing experimental results)

The Nusselt numbers calculated from (34), and also those obtained from the numerical solutions are plotted as a function of Ra for two different aspect ratios in Fig. 8. The analytical predictions are seen to be within 10 percent of the numerically obtained values. Most importantly, they exhibit similar Rayleigh number dependence and sensitivity to aspect ratio a. This seems to indicate that the analysis has correctly grasped the essential physics of this flow regime. Variation of the free parameter k has the effect of shifting the curves up or down, but does not change the Rayleigh number or aspect ratio dependence.

Comparison with Existing Experimental Results. There are very limited experimental data on low aspect ratio horizontal enclosures available in the literature. None are suitable for a direct comparison with the analytical and numerical results presented here.

Ostrach [1] presents dye-streak velocity profiles which look very much like those of Fig. 6. In this case, the aspect ratio and Rayleigh number are comparable, but Ostrach's Prandtl number is much higher, Pr = 1400. Kimura and Bejan [10] also find similar dye-streak velocity profiles; however, their work is for horizontal cylinders. Imberger [4] reports heat-transfer data for $Ra \approx 10^8$ and $a = 0.02$. These results were

originally presented in support of the theory of Cormack et al. [2] for the viscous-dominated core case. Indeed the present theory shows $\delta \approx 1/2$ at these conditions, meaning the boundary layer fills the core cross section. Imberger's data is plotted on Fig. 8 for the reader's interest but correlation with the present core boundary layer theory is not expected.

Only the unpublished work of Al-Hammoud and Bejan [9] seems appropriate for a direct comparison to the present work, with $a = 0.062$, Pr = 6.3 and $3 \times 10^8 < Ra < 1.6 \times 10^9$. These results are also plotted on Fig. 8. The agreement with the present work is only fair. The correlations proposed by Shiralkar et al. [9] are plotted on the same graph and show remarkable agreement with the present theory. Note that the free parameter K was obtained from Fig. 5 and not from the Nu-Ra curve obtained from numerical solutions. Perhaps more disconcerting is the fact that Al-Hammoud and Bejan find a qualitatively different core velocity field with flow reversals between the wall boundary layer jet and the horizontal centerline. The present authors believe this is attributable to heat losses on the horizontal walls, clearly in evidence from the temperature profiles presented. In fact, such reversals have been predicted by the numerical code, when a heat flux is imposed on the horizontal boundaries. A subsequent paper will discuss these results. It appears that more research is needed to resolve this issue.

Concluding Remarks and Discussion

Several points should be discussed regarding the overall accuracy of the analytical methods. First, Nusselt number predictions are strongly sensitive to the constants C_u and C_T. Their actual numerical value affects the Nusselt number roughly according to their product, but does not affect the Nusselt number variation with Rayleigh number or aspect ratio. Recall that the value of the free parameter used is $k = 1/3$ and that k is a number about 1/2 from the theory (see equation (19)). For $k = 1/2$, the analytical method deviates from the numerical by about 35 percent; hence, the figure (35 percent) could be interpreted as the inherent accuracy of the analytical method, without empirical adjustment. Second, the analysis ignores boundary layer development in the core. For this reason the accurate sensitivity to aspect ratio near $a = 0.1$

is fortunate. Particularly in the case of a very long enclosures it would seem that boundary layer thickening across the core would greatly influence overall energy transport.

The physical picture that emerges from the analysis and the numerical solution, in agreement with the conclusions of [9], is as follows:

1 This regime is mainly characterized by boundary layers lining both the vertical end walls as well as the adiabatic horizontal walls.

2 The momentum imparted to the flow in the core by the thin, fast moving boundary layers from the vertical walls plays an important part in the core flow.

3 The boundary layers on the end walls sustain most of the temperature drop in the x-direction, leaving very little horizontal temperature gradient in the mid-core region. Figure 2 shows that the isotherms in the core are very nearly horizontal, with slopes $<<a$.

4 The fluid in the core away from the horizontal walls is predicted to move with a linear velocity profile, although the experiments of Al-Hammoud and Bejan suggest otherwise. The streamlines in the core are very nearly parallel, and the core extends almost the full length of the enclosure.

5 The boundary layers in the core get thinner as the Rayleigh number increases. The lower limit of the range of Ra values for which this flow occurs is given by the Ra at which the upper and lower boundary layers in the core meet, i.e., $\delta \cong 0.5$. The upper limit of Ra is probably determined by the onset of turbulence in the vertical boundary layers on the end walls.

Acknowledgments

References

1 Ostrach, S., "Natural Convection in Low Aspect-Ratio Rectangular Enclosures," *Natural Convection in Enclosures*, 19th National Heat Transfer Conference Proceedings of the ASME Heat Transfer Division, Vol. 8, 1980, pp. 1-10.

2 Cormack, D. E., Leal, L. G., and Imberger, J., "Natural Convection in a Shallow Cavity with Differentially Heated End Walls. Part 1. Asymptotic Theory," ASME *Journal of Fluid Mechanics*, Vol. 65, 1974, pp. 209-229.

3 Cormac, D. E., Leal, L. G., and Seinfeld, J. H., "Natural Convection in a Shallow Cavity with Differentially Heated End Walls. Part 2. Numerical Solutions," ASME *Journal of Fluid Mechanics*, Vol. 65, 1974, pp. 231-246.

4 Imberger, J., "Natural Convection in a Shallow Cavity with Differentially Heated End Walls, Part 3. Experimental Results," ASME *Journal of Fluid Mechanics*, Vol. 65, pp. 247-260, 1974

5 Elder, J. W., "Laminar Free Convection in a Vertical Slot," ASME *Journal of Fluid Mechanics*, Vol. 23, 1965, pp. 77-98.

6 Gill, A. E., "The Boundary-Layer Regime for Convection in a Rectangular Cavity," ASME *Journal of Fluid Mechanics*, Vol. 26, 1966, pp. 515-536.

7 Quon, C., "Free Convection in an Enclosure Revisited," ASME *Journal of Heat Transfer*, Vol. 99, No. 2, 1977, pp. 340-342.

8 Bejan, A. and Tien, C. L., "Laminar Natural Convection Heat Transfer in a Horizontal Cavity with Different End Temperatures," ASME *Journal of Heat Transfer*, Vol. 100, 1978, pp. 641-647.

9 Al-Hammoud and Bejan, A., "Experimental Study of High Rayleigh Number Convection in a Horizontal Cavity with Different End Temperatures," Report CUMER-79-1, Department of Mechanical Engineering, University of Colorado, Boulder, 1979.

10 Shiralkar, G., Tien, C. L., and Gadgil, A., "On High Rayleigh Number Convection in Shallow Horizontal Cavities with Different End Temperatures," to be published in the *International Journal of Heat and Mass Transfer*, Vol. 24, No. 10, 1981, pp. 1621-1629.

11 Kimura, S. and Bejan, A., "Experimental Study of Natural Convection in a Horizontal Cylinder with Different End Temperatures," *International Journal of Heat and Mass Transfer*, Vol. 23, No. 8, 1980, pp. 1117-1126.

12 Batchelor, G. K., "Heat Transfer by Free Convection Across a Closed Cavity between Vertical Boundaries and Different Temperatures," *Quarterly Journal of Applied Mathematics*, Vol. 12, 1963, p. 209.

13 Nayfeh, A., *Perturbation Methods*, Wiley and Sons, New York, 1973, Ch. 6.

14 Spalding, D. B., "A Novel Finite Difference Formulation for Differential Expressions Involving Both First and Second Derivatives," *International Journal of Numerical Methods in Engineering*, Vol. 4, 1972, pp. 541-550.

15 Gadgil, A. J., "On Convective Heat Transfer in Building Energy Analysis," Ph.D. thesis, Department of Physics, University of California, Berkeley, 1979.

16 Bauman, F., Gadgil, A., Kammerud, R., and Greif, R., "Buoyancy-Driven Convection in Rectangular Enclosures: Experimental Results and Numerical Calculations," ASME publication 80-HT-66, presented at 19th National Heat Transfer Conference of ASME, Orlando, also, Lawrence Berkeley Laboratory, Report LBL-10257.

The Effect of Thermal Wall Properties on Natural Convection in Inclined Rectangular Cells

B. A. Meyer[1]

J. W. Mitchell

M. M. El-Wakil

University of Wisconsin,
Madison, Wis.

The effects of cell wall thickness and thermal conductivity on natural convective heat transfer within inclined rectangular cells was studied. The cell walls are thin, and the hot and cold surfaces are isothermal. The two-dimensional natural convection problem was solved using finite difference techniques. The parameters studied were cell aspect ratios (A) of 0.5 and 1, Rayleigh numbers (Ra) up to 10^5, a Prandtl number (Pr) of 0.72 and a tilt angle (ϕ) of 60 deg. These parameters are of interest in solar collectors. The numerical results are substantiated by experimental results. It was found that convection coefficients for cells with adiabatic walls are substantially higher than those for cells with conducting walls. Correlations are given for estimating the convective heat transfer across the cell and the conductive heat transfer across the cell wall. These correlations are compared with available experimental and numerical work of other authors.

Introduction

Heat losses across inclined plates are of interest in many engineering systems and, recently, to designers of solar collectors. Reduction of heat loss from the absorber plate through the cover plate allows smaller collector areas to be used. The range of parameters studied in this paper are of interest in solar collectors.

Natural convection in rectangular enclosures has received increasing attention in recent years. Unny [1], Catton [2], Davis [3], Hart [4], and Hollands et al. [5] reported on the stability of differentially heated enclosures. Hollands [6], Randall et al. [7], Catton et al. [8], Ozoe et al. [9] and Meyer et al. [10, 11], among others, reported the effects of aspect ratio, tilt angle, and Rayleigh and Prandtl numbers on convective heat transfer. In contrast to these studies of convection, there does not appear to have been a definitive study on the effects of cell wall thickness and wall conductivity on the convective and overall rate of heat transfer in cells. Numerical studies in the past generally assumed either that the side walls were adiabatic or that the temperature varied linearly along the cell wall. Koutsoheras [12] presented some limited results showing the effect of wall conductivity at an aspect ratio of 1.

In the present study, the effect of wall conductivity and wall thickness are presented in the form of correlations. Comparison with available experimental and numerical work of other authors is also given.

Analysis

The effect of cell wall thickness and wall conductivity on the convective and overall rate of heat transfer in enclosure
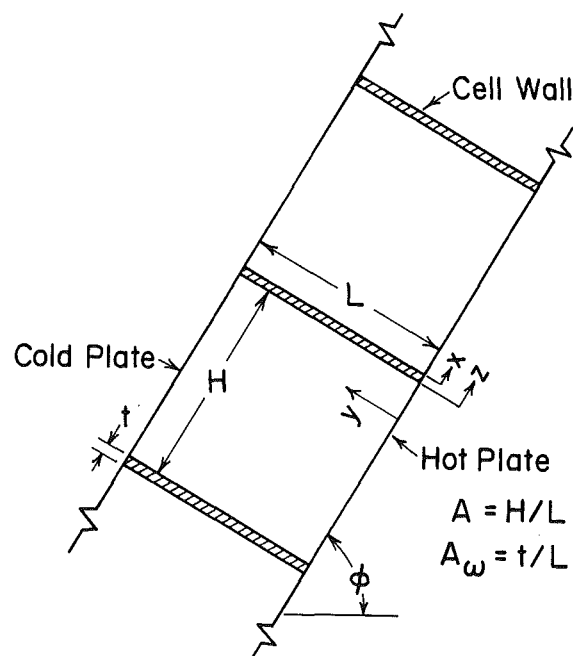
Fig. 1   Test cell geometry

was the subject of this study. The continuity, momentum, and energy equations were solved numerically for the geometry of Fig. 1. With the introduction of the concepts of stream function and vorticity, the steady-state, two-dimensional governing equations and boundary conditions take the following forms.

The energy equation and combined momentum equations for convection within a cell are

$$\frac{\partial(\Theta_f, \psi)}{\partial(X,Y)} = \nabla^2 \Theta_f \qquad (1)$$

$$\frac{1}{\text{Pr}} \frac{\partial(\omega, \psi)}{\partial(X,Y)} = \text{Ra}\left(\cos\phi \frac{\partial\Theta_f}{\partial X} - \sin\phi \frac{\partial\Theta_f}{\partial Y}\right) + \nabla^2\omega \qquad (2)$$

$$\omega + \nabla^2\psi = 0 \qquad (3)$$

where $\quad \partial\psi/\partial Y = V_X; \quad \partial\psi/\partial X = -V_Y$

$$\text{and}\ \frac{\partial(\Theta_f, \psi)}{\partial(X,Y)} = \frac{\partial\Theta_f}{\partial X}\frac{\partial\psi}{\partial Y} - \frac{\partial\Theta_f}{\partial Y}\frac{\partial\psi}{\partial X}$$

The energy equation for conduction within the cell wall is

$$\nabla^2\Theta_w = 0 \qquad (4)$$

The boundary conditions couple the temperature and heat flux in the fluid and the wall. The temperature and velocity boundary conditions are

$$\Theta_f(X,0) = \Theta_w(Z,0) = 1; \quad \Theta_w(A_w, Y) = \Theta_f\ (0, Y)$$

$$\Theta_f(X,1) = \Theta_w(Z,1) = 0; \quad \Theta_w(0,Y) = \Theta_f\ (A,Y)$$

$$V_X = V_Y = \psi = 0 \text{ on all boundaries} \qquad (5)$$

The heat flux boundary conditions are

$$Rk\frac{\partial\Theta_w}{\partial Z}\Big|_{Z=A_w} = \frac{\partial\Theta_f}{\partial X}\Big|_{X=0}; \quad Rk\frac{\partial\Theta_w}{\partial Z}\Big|_{Z=0} = \frac{\partial\Theta_f}{\partial X}\Big|_{X=A} \qquad (6)$$

where $Rk = k_w/k$

The local Nusselt number (Nu) and the average Nusselt number ($\overline{\text{Nu}}$) were evaluated at the hot surface using the following equations.

$$\text{Nu} = -\frac{\partial\Theta}{\partial Y}\Big|_{Y=0}; \quad \overline{\text{Nu}} = -\frac{1}{A}\int_0^A \frac{\partial\Theta}{\partial Y}\Big|_{Y=0} dX$$

The parameter Rk, which equals k_w/k, is the thermal parameter that characterizes the boundary conditions at the cell wall. If the conductivity of the wall is 0, Rk is 0 and equation (6) gives the adiabatic boundary condition of zero temperature gradient in the X direction at the wall. If the conductivity of the wall is infinite, Rk is infinite, which gives a linear temperature profile along the cell wall.

An infinite array of such cells and walls are of interest in solar and other applications. Due to symmetry, it is possible to analyze only one cell and one wall. The temperature and heat flux distribution at the left boundary of the wall are thus matched to the right boundary of the cell. This method therefore neglects end-effects at the end of a finite array of such cells and walls.

The heat transfer results are the main interest in this paper, thus only a brief discussion of the numerical procedure is given. The solution procedure uses a method similar to that used by Schultz [13]. The stream function equation, equation (3), was expressed in finite difference form using a central differences scheme. The energy and momentum equations (equations (1) and (2)) used a windward differencing scheme to maintain diagonal dominance thereby increasing the convergence of the solution. The boundary conditions were all made second-order accurate. The set of equations were successively iterated, using a successive over-relaxation parameter for each equation, until the solutions converged within some given error limit. Once the solutions had initially converged, the windward differencing scheme was replaced by a central differencing scheme, and the equations were again iterated until converging. Replacing the windward differencing scheme by the central difference scheme makes the solution second-order accurate. For more details on the solution procedure see [11].

In numerical solutions of this type, a compromise between accuracy and computer time (expense) must be made. This compromise resulted in using a 21×21 grid system. The effect of grid size on the Nusselt number is shown in Figs. 2(a) and 2(b). Figure 2(a) indicates that the 21×21 grid system underestimates the "exact" Nusselt number by about 2 percent at a Rayleigh number of 10^4. At larger Rayleigh numbers this error is larger.

Local Heat Transfer Results

The numerical solutions yielded temperature distributions

_____ Nomenclature _____

A = H/L cell aspect ratio
A_w = t/L wall aspect ratio
C_1 = constant in equation (7)
C_2 = constant in equation (8)
g = acceleration due to gravity
h = local heat transfer coefficient
$\bar{h}$ = average heat transfer coefficient
H = cell length
k = thermal conductivity of fluid within the cell
k_w = thermal conductivity of the cell wall
L = plate spacing
n_1 = constant in equation (7)
n_2 = constant in equation (8)
N = number of grid points
Nu = hL/k local cell Nusselt number
$\overline{\text{Nu}}$ = $\bar{h}L/k$ average cell Nusselt number
$\overline{\text{Nu}}_L$ = $\bar{h}L/k$ average cell Nusselt number for perfect conducting side walls
$\overline{\text{Nu}}_0$ = Overall average Nusselt number equation (9)
$\overline{\text{Nu}}_w$ = $qL/k_w t\,(T_h - T_c)$ average wall Nusselt number
Pr = ν/α Prandtl number
q = heat transfer in the cell wall from the hot to cold plate per unit depth
R = tk/Lk_w cell coupling group
Ra = $g\beta(T_h - T_c)L^3/\nu\alpha$, Rayleigh number
Rk = k_w/k ratio of wall thermal conductivity to that of the fluid

t = thickness of cell wall
T_c = cold plate temperature
T_f = temperature in cell
T_h = hot plate temperature
T_w = temperature in cell wall
v_x = velocity in x-direction
V_X = $v_x L/\alpha$ dimensionless x velocity
v_y = velocity in y-direction
V_Y = $v_y L/\alpha$ dimensionless y velocity
x = distance measured from the bottom of the cell (see Fig. 1)
X = x/L normalized distance
y = distance measured from hot plate (see Fig. 1)
Y = y/L normalized distance
z = distance measured in wall (see Fig. 1)
Z = z/L normalized distance in cell wall
α = thermal diffusivity
β = coefficient of volumetric expansion
Θ_f = $\dfrac{T_f - T_c}{T_h - T_c}$ dimensionless temperature in cell
Θ_w = $\dfrac{T_w - T_c}{T_h - T_c}$ dimensionless temperature in wall
ν = kinematic viscosity
ϕ = enclosure tilt angle from horizontal
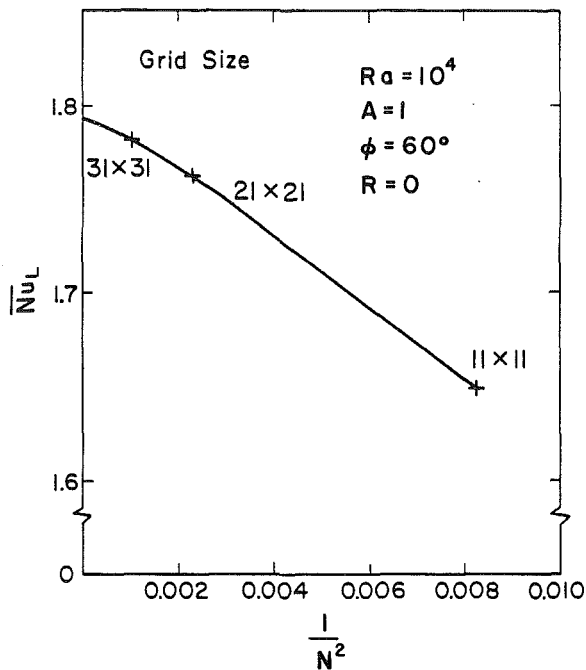ω = vorticity
ψ = stream function

Fig. 2(a) Effect of grid size on finite difference solution of average cell Nusselt number, at $A = 1$, $\phi = 60$ deg, $Ra = 1 \times 10^4$
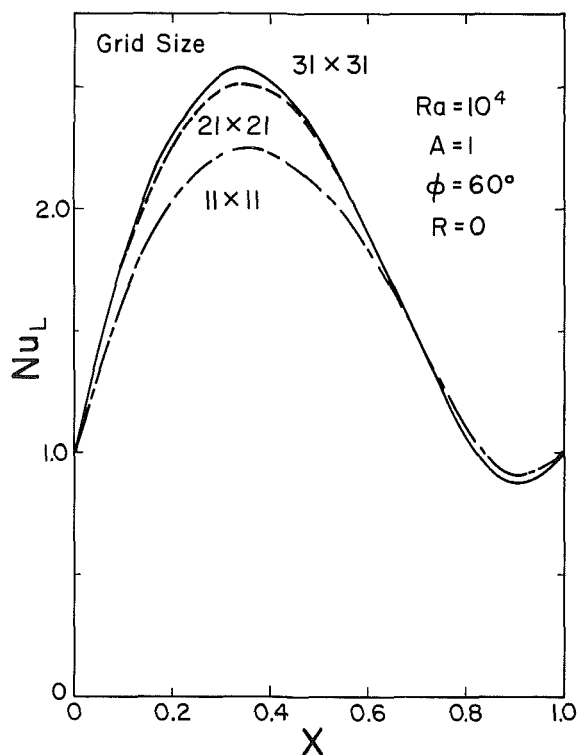

Fig. 2(b) Effect of grid size on finite difference solution for local Nusselt number, at $A = 1$, $\phi = 60$ deg, $Ra = 1 \times 10^4$; the Nusselt number is evaluated at the hot surface.
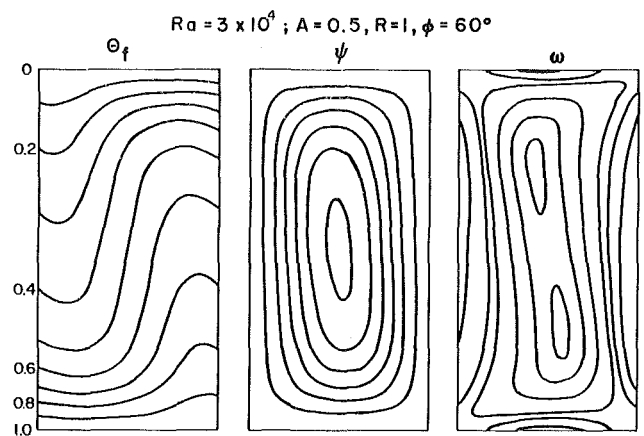

Fig. 3 Finite difference solutions for cell temperature distribution, stream function, and vorticity, at $A = 0.5$, $\phi = 60$ deg, $Ra = 3 \times 10^4$, $R = 1$; the right side is elevated above the left.
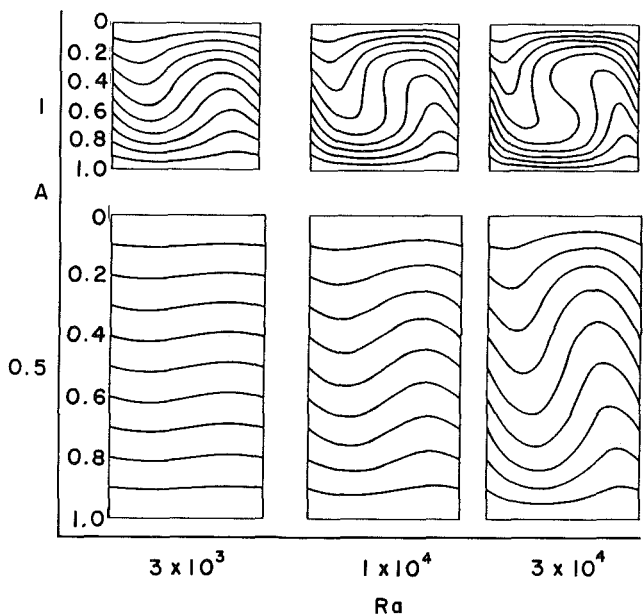

Fig. 4 Effect of Rayleigh number and cell aspect ratio on cell temperature distribution for $R = 0$, $\phi = 60$ deg; the right side is elevated above the left.

in both the cell and cell wall, fluid flow patterns, and local heat-transfer coefficients. Figures 3–5 are plots of the dimensionless temperature (Θ_f), stream function (ψ), and vorticity (ω) for different cell aspect ratios, Rayleigh numbers and cell coupling groups, R. The parameter, R, will be shown later to characterize the wall thermal properties for thin cell walls, and is defined as tk/Lk_w.

The isothermal patterns indicate how the heat flux varies with position along the hot and cold surfaces. Close spacing of isotherms at the wall indicates high rates of heat transfer.

For example, in Fig. 3, the isotherms are closely spaced together near the hot (lower) surface in the left corner of the cell, and farther apart in the right corner. The heat flux therefore decreases along the hot surface from left to right. The temperature, steam function, and vorticity contours indicate the convective flow patterns. The fluid is rotating counterclockwise.

Figures 4 and 5 indicate that there is more convective motion for an aspect ratio of 1 than 0.5. At an aspect ratio of 0.5, heat is transfered nearer the conduction limit. The effect of increasing the Rayleigh number, as shown in Fig. 4, is to increase convective motion.

The effect of the cell coupling group, R, can be substantial. As R increases from zero (highly conducting walls) to infinity (adiabatic walls), both heat transfer and convective motion increase as shown in Fig. 5. Figure 6(a) shows the effect of R on the temperature distribution along the left boundary of the cell. At small values of R, the temperature varies linearly along the spacer. As R increases, the temperature distribution approaches that of an adiabatic wall. Figure 6(b) shows the effect of Rayleigh number on the temperature distribution, along the left boundary of the cell, for an adiabatic wall. The effect of R on the local Nusselt numbers is shown in Fig. 7.
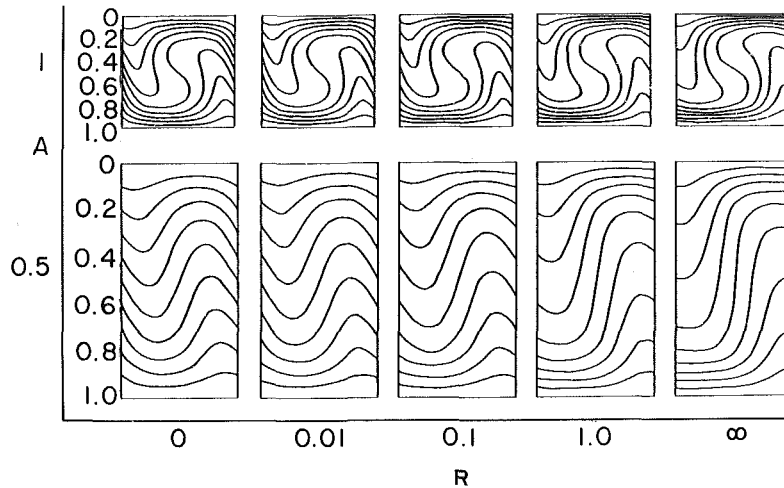
Fig. 5 Effect of cell coupling group R on the cell temperature distribution for Ra $= 3 \times 10^4$, $\phi = 60$ deg; the right side is elevated above the left.
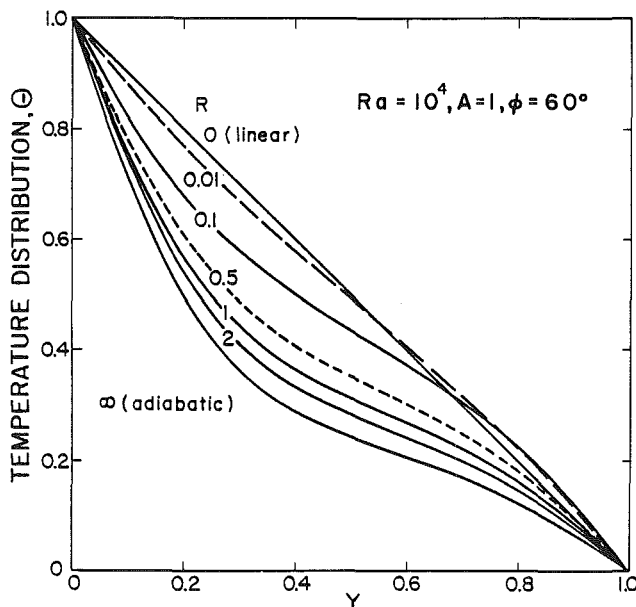

Fig. 6(a) Effect of cell coupling group R on the temperature distribution along the left-hand boundary of the cell for $A = 1$, Ra $= 1 \times 10^4$, $\phi = 60$ deg
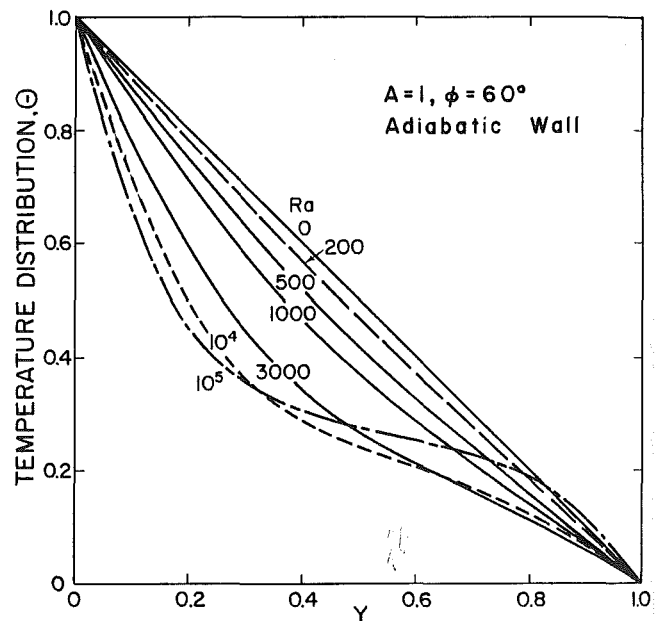

Fig. 6(b) Effect of Rayleigh number on the temperature distribution along the left-hand boundary of the cell for adiabatic walls, $A = 1$, and $\phi = 60$ deg

As R increases, the local Nusselt number increases significantly.

These numerical results are in agreement with a previous experimental study [10] in which the local Nusselt numbers were found to be a strong function of aspect ratio, for aspect ratios less than 10. Study [10] also showed there is enhanced convection for aspect ratios in the range of 1 to 2. As the aspect ratio is decreased from 1, convection is suppressed via viscous effects on the cell wall, which retards the fluid motion. As the aspect ratio increases beyond 2, the flow becomes fully established in the center with relatively lower average Nusselt numbers. The effect of tilt angle was not considered in this study. However, studies by Meyer et al. [10], Koutsoheras [12] and Ozoe et al. [9], show that for tilt angles between 30 and 90 deg, the angle effect on the average Nusselt number is about 5 percent.

Experimentally and numerically determined isotherms and local Nusselt numbers are compared in Figs. 8(a) and 8(b), respectively. The aspect ratio is 1, tilt angle 60 deg, Rayleigh number 10^4, and cell coupling group 0.005. Comparisons for other parameter values show similar agreement.

Average Heat Transfer Results

The normalized equations and boundary conditions (equations 1–6) show that the local and average Nusselt numbers are functions of A_w, A, Pr, Ra, Rk and ϕ. For thin cell walls, it was found that the parameters A_w and Rk could be combined into the parameter R (equal to tk/Lk_w). Physically, this means that for thin cell walls, the temperature gradient in the wall may be approximated by the temperature difference across the wall divided by the wall thickness. Using this, equation (6) can be written as

$$\Theta_w(A_w, Y) - \Theta_w(0, Y) = \frac{A_w}{Rk} \frac{\partial \Theta_f}{\partial X} \bigg|_{X=0}$$

Thus, A_w and Rk combine into the single parameter, R, for thin cell walls. The numerical results indicate that cell walls are thermally thin (within 2 percent) if the wall aspect ratio A_w is less than 0.1.

The average cell Nusselt number was correlated with Rayleigh number and cell coupling group for a tilt angle of 60 deg. The average cell Nusselt number is given by
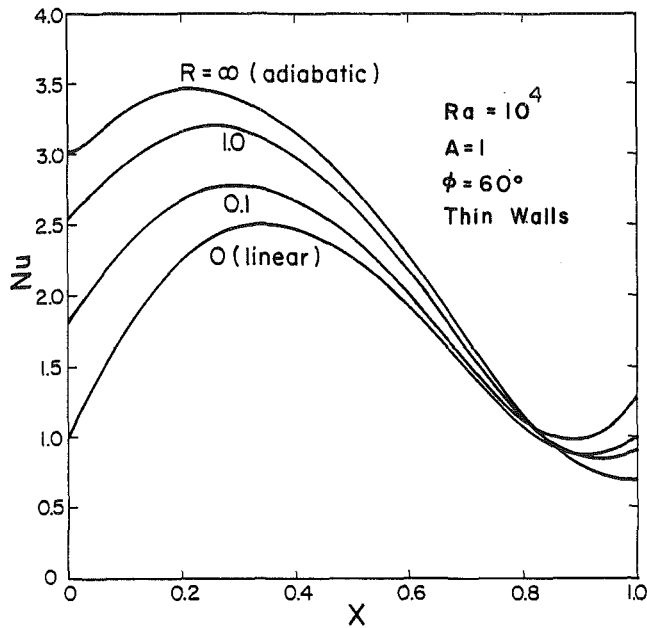
Fig. 7 Effect of cell coupling group on local cell Nusselt numbers $A = 1$, $Ra = 10^4$, $\phi = 60$ deg; the Nusselt number is evaluated at the hot surface.

Fig. 8(a) Comparison between numerical and experimental isothermal patterns for $A = 1$, $\phi = 60$ deg, $R = 0.005$, $Ra = 10^4$; the left side is elevated above the right.
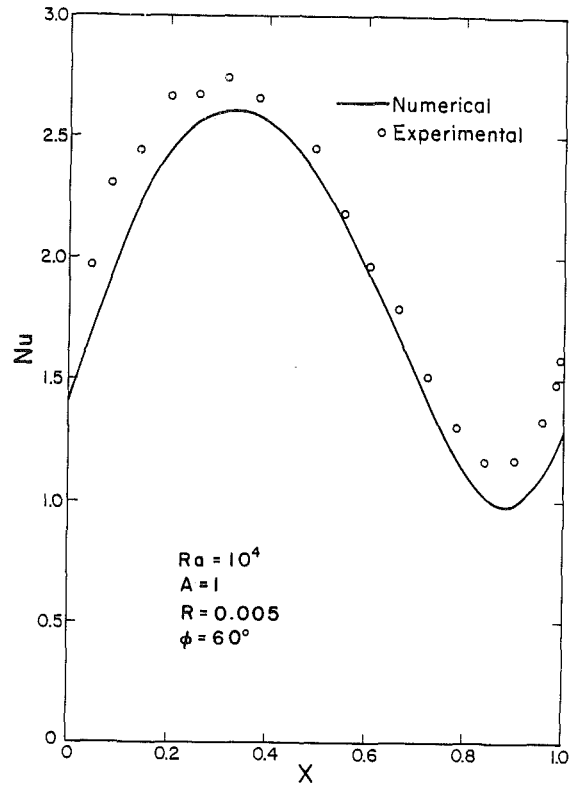

Fig. 8(b) Comparison between numerical and experimental local cell Nusselt numbers $A = 1$, $\phi = 60$ deg, $R = 0.005$, $Ra = 10^4$; the Nusselt number is evaluated at the hot surface.
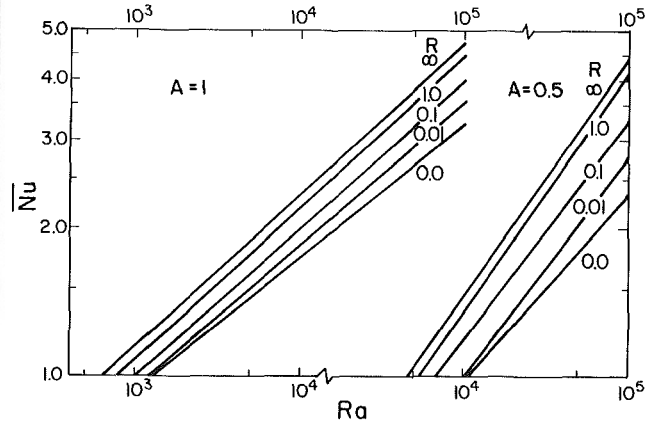
Fig. 9 Average Nusselt number as a function of Rayleigh number

Table 1

$$n_1 = 0.29[1 - 0.069 \exp(-60\,R)]; \text{ for } A = 1$$

$$n_1 = 0.504 - 0.066 \exp(-8.5\,R) - 0.061 \exp(-250\,R); \text{ for } A = 0.5$$

For an aspect ratio of 1		For an aspect ratio of 0.5	
R	C_1	R	C_1
$0 \leq R \leq 0.032$	$0.145 - 0.37\,R$	$0 \leq R \leq 0.1$	$0.0171 - 0.0307\,R$ $+ 0.0133 \exp(-280\,R)$
$0.032 \leq R \leq 0.16$	$0.130 + 0.084\,R$	$0.1 \leq R \leq 0.2$	$0.0155 - 0.0145\,R$
$0.16 \leq R \leq 0.4$	$0.140 + 0.023\,R$	$0.2 \leq R \leq 0.3$ $0.3 \leq R \leq 0.4$	$0.0136 - 0.005\,R$ 0.0121
$0.4 \leq R \leq 1$	$0.146 + 0.0082\,R$	$0.4 \leq R \leq 1$	$0.0116 + 0.0013\,R$
$R \geq 1$	$0.164 - 0.0098/R$	$R > 1$	$0.0138 - 0.001/R$

Table 2

$$n_2 = 0.19 - 0.095[\exp(-23.3\,R) + \exp(-480\,R)]; \text{ for } A = 1$$
$$n_2 = 0.37 - 0.105\exp(-9.8\,R) - 0.265\exp(-280\,R); \text{ for } A = 0.5$$

For an aspect ratio of 1		For an asect ratio of 0.5	
R	C_2	R	C_2
$0 \leq R \leq 0.1$	$0.286 + 0.27 \exp(-35\,R)$ $+ 0.444 \exp(-970\,R)$	$0 \leq R \leq 0.11$	$0.761 \exp(-860\,R)$ $+0.16 \exp(-210\,R)$ $+0.079 \exp(-3.7\,R)$
$0.1 \leq R \leq 0.25$	$0.299 - 0.062\,R$	$0.11 \leq R \leq 0.25$	$0.0618 - 0.079\,R$
$0.25 \leq R \leq 0.5$	0.284	$0.25 \leq R \leq 0.5$	0.0420
$0.5 \leq R \leq 1$	$0.27 + 0.028\,R$	$0.5 \leq R \leq 1$	$0.0397 + 0.0033\,R$
$R \geq 1$	$0.318 - 0.02/R$	$R \geq 1$	$0.0463 - 0.0033/R$

Table 3 Comparison of average cell Nusselt numbers with perfect conducting walls, for $A = 1$ and $\phi = 90$ deg

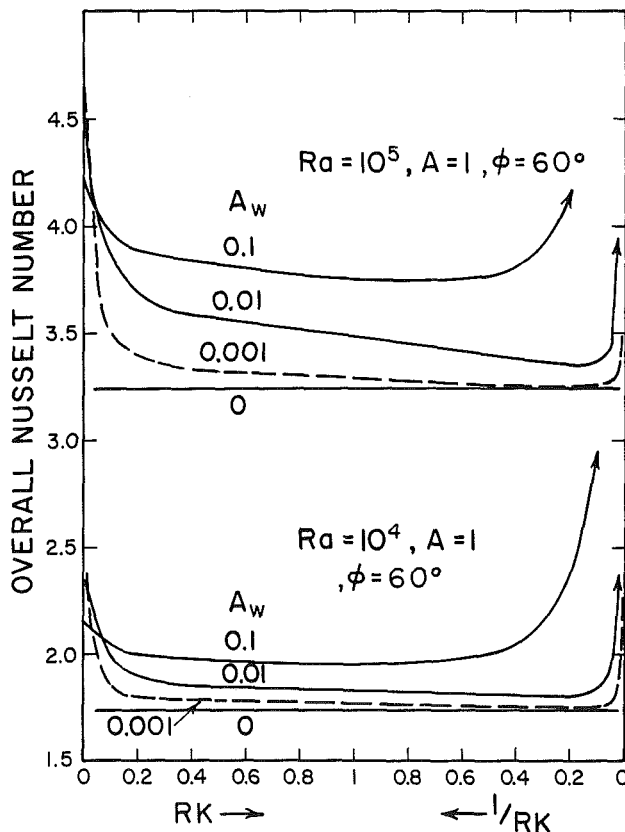| Ra	This study	Schultz [13]	Poots [14]
500	1.015	1.011	1.012
1000	1.050	1.041	1.041
5000	1.408	1.432	1.415
10000	1.709	1.717	1.706
20000	2.072	2.143	–
30000	2.318	2.359	–

Fig. 10 Overall Nusselt number as a function of wall properties

$$\overline{Nu} = C_1 \, Ra^{n_1} \qquad (7)$$

This correlation is restricted to:

$$Ra < 1 \times 10^5; \; A_w \leq 0.1; \; \phi = 60 \text{ deg}, \; \overline{Nu} \geq 1$$

The coefficients C_1 and n_1 are given in Table 1. The correlating equation and the empirically derived constants fit the numerical results within ± 5 percent provided that $\overline{Nu}$ is greater than 1.2. For $\overline{Nu}$ less than 1.2, the numerical results

fit the correlation within ± 8 percent. Equation 7 is plotted in Fig. 9 and shows the effect of aspect ratio, Rayleigh number, and the cell coupling group, R, on the cell Nusselt number. The effect of increasing R is to increase the exponent n_1 and the average cell Nusselt number.

The heat transfer in the cell wall from the hot plate to the cold plate can be represented as a Nusselt number. The average wall Nusselt number was found to fit the following correlation within ± 10 percent.

$$\overline{Nu}_w = C_2 \, Ra^{n_2} \qquad (8)$$

This correlation is restricted to:

$$Ra < 1 \times 10^5; \; A_w \leq 0.1, \; \overline{Nu}_w \geq 1., \; \phi = 60°$$

Values of C_2 and n_2 are tabulated in Table 2. The conduction Nusselt number is unity for both equations (7) and (8).

The total heat transfer (convective plus conductive) is represented by the overall Nusselt number $\overline{Nu}_0$. This represents the sum of the heat flow in the fluid and the cell wall and is given by

$$\overline{Nu}_0 = \frac{\overline{Nu}A + Rk\,A_w\overline{Nu}_w}{A + A_w} \qquad (9)$$

The minimum total heat transfer occurs when the average overall Nusselt number is a minimum. Figure 10 indicates that in order to minimize the total heat transfer A_w should be as small as possible, and the value of Rk should be between 1 and 20 for a cell aspect ratio of 1 and wall aspect ratio of 0.01.

A comparison of average cell Nusselt numbers with other numerical work is presented in Table 3. The agreement is seen to be good.

Summary

A numerical study was used to determine local and average Nusselt numbers for rectangular enclosures with finite walls. The results show the effect of cell wall conductivity, and thickness can be represented by the parameter, R. To minimize the total (convective plus conductive) heat transfer, the cell walls should be as thin as possible and have a value of Rk, which minimizes equation 9. For example, if A_w equals 0.001, 0.01, or 0.1, the total heat transfer can be approximately minimized if Rk is between 0.2 and 100, 1 and 20, or 0.2 and 3, respectively (see Fig. 10).

References

1 Unny, T. E., "Thermal Instability in Differentially Heated Inclined Fluid Layers," ASME *Journal of Applied Mechanics*, Vol. 94E, 1972, pp. 41–46.

2 Catton, I., "The Effect of Insulating Vertical Walls on the Onset of Motion in a Fluid Heated from Below," *International Journal of Heat and Mass Transfer*, Vol. 15, 1972, pp. 667–672.

3 Davis, S. H., "Convection in a Box: Linear Theory," ASME *Journal of Fluid Mechanics*, Vol. 30, 1967, pp. 465–478.

4 Hart, J. E., "Stability of Flow in a Differentially Heated Inclined Box," ASME *Journal of Fluid Mechanics*, Vol. 47, 1971, pp. 547–576.

5 Hollands, K. G. T., and Konicek, L., "Experimental Study of the Stability of Differentially Heated Inclined Air Layers," *International Journal of Heat and Mass Transfer*, Vol. 16, 1973, pp. 1467–1476.

6 Hollands, K. G. T., "Studies of Methods of Reducing Heat Losses from Flat-Plate Solar Collectors," ERDA Annual Progress Report, COO-2597-3, University of Waterloo, Waterloo, Canada, 1977.

7 Randall, K. R., Mitchell, J. W., and El-Wakil, M. M., "Natural Convection Heat Transfer Characteristics of Flat Plate Enclosures," ASME JOURNAL OF HEAT TRANSFER, Vol. 101, 1979, pp. 120–125.

8 Catton, I., Ayyacwamy, P., and Clever, R. M., "Natural Convection Flow in a Finite Rectangular Slot Arbitrarily Oriented with Respect to the Gravity Vector," *International Journal of Heat and Mass Transfer*, Vol. 17, 1974, pp. 173–184.

9 Ozoe, H., Yamamoto, K., Sayama, H., and Churchill, S. W., "Natural Circulation in an Inclined Rectangular Channel Heated on One Side and Cooled on the Other Side," *International Journal of Heat and Mass Transfer*, Vol. 17, 1974, pp. 1209–1217.

10 Meyer, B. A., Mitchell, J. W., and El-Wakil, M. M., "Natural Convection Heat Transfer in Moderate Aspect Ratio Enclosures," ASME JOURNAL OF HEAT TRANSFER, Vol. 101, 1979, pp. 655–659.

11 Meyer, B. A., "An Experimental and Numerical Study of Natural Convective Heat Transfer—In Moderate Aspect Ratio and V-Groove Enclosures," Ph.D. thesis, Mechanical Engineering Department, University of Wisconsin, Madison, 1980.

12 Koutsoheras, W., "Natural Convection Phenomena in Inclined Cells with Finite Walls—A Numerical Solution," Mechanical Engineering Science thesis, The University of Melbourne, Mar. 1976.

13 Schultz, D. H., "Numerical Solution for the Flow of a Fluid in a Heated Closed Cavity," *Quarterly Journal of Mechanics and Applied Mathematics*, Vol. 26, 1973, pp. 173–191.

14 Poots, G., "Heat Transfer by Laminar Free Convection in Enclosed Plane Gas Layers," *Quarterly Journal of Mechanics and Applied Mathematics*, Vol. 11, 1958, pp. 257–273.

S. S. Kwon

Associate Professor,
Department of Mechanical Engineering,
Dong-A University,
Busan, South Korea

T. H. Kuehn

Associate Professor,
Department of Mechanical Engineering and
Engineering Research Institute,
Iowa State University,
Ames, Iowa   50011
Assoc. Mem. ASME

T. S. Lee

Professor and Dean,
College of Engineering,
Seoul National University,
Seoul, South Korea
Mem. ASME

Natural Convection in the Annulus Between Horizontal Circular Cylinders With Three Axial Spacers

Conjugate natural convection heat transfer in an annulus between horizontal isothermal circular cylinders with three equally spaced axial spacers has been studied theoretically and experimentally. A thin-fin approximation was used to model the thermal boundary condition of the spacers in the two-dimensional finite difference numerical computations. Rayleigh number, Prandtl number, diameter ratio, and location and thermal conductivity of the spacers were varied parametrically to determine the variation in flow patterns, temperature distribution and heat transfer. Spacers of low conductivity can decrease the natural convection heat transfer by as much as 20 percent below that for a simple unobstructed annulus. However, radial conduction through spacers of high conductivity overwhelms the natural convection heat transfer between the cylinders. Two diameter ratios were tested experimentally in a Mach-Zehnder interferometer using air at atmospheric pressure with stainless steel spacers between copper cylinders. The numerical and experimental temperature distributions and local convective heat-transfer coefficients show good agreement.

Introduction

Many experimental and theoretical studies have been performed on natural convection in a simple horizontal cylindrical annulus. A review of the literature prior to 1976 is given in [1]. Recent studies have focused on alternate analytical solution techniques [2], improved numerical solution methods [3], eccentric [4, 5] and noncircular [6] geometries, and heat-transfer correlations [7]. Applications include solar collector receiver design [8], compressed-gas-insulated electric power cables [9], a first approximation to modeling fusion reactor blankets [10], and reactor-spent fuel cooling [11].

In most applications, the inner cylinder must be positioned within the outer cylinder by spacers. These may be radial [12, 13], conical [14], or axial [9, 10]. Fluid flow and heat transfer are essentially the same as for a simple annulus when radial or conical spacers are used. However, the use of axial spacers changes the problem to one of flow within annular segments as investigated analytically by Iyican, Bayazitoglu and Witte [15]. In addition, the radial conduction in a spacer and the natural convection in the cavities on each side of it are coupled through the thermal boundary conditions on the surfaces of the spacer. Angular conduction through the spacers couples the natural convection flow in all the cavities of an annulus together. Solutions to conjugate heat transfer by conduction and natural convection are receiving increased attention in the literature because numerical schemes can easily handle the nonlinearities and iterative nature inherent in

such a problem [16, 17, 18]. The present problem involves heat transfer interactions studied in each of the last four references cited above.

Two experimental studies of annuli with axial spacers have appeared in the literature. Grigull and Hauf [19] presented two interferograms of an annulus containing air and three equally spaced balsa wood spacers as an exploratory study on the effect of insulating spacers. Lis [20] conducted an experimental study with SF_6-N_2 gas mixtures and 6 equally spaced axial spacers inclined 30 deg from the radial direction. Mean heat-transfer coefficients were found to be about 20 percent below that for a simple annulus at values of Rayleigh number near Ra $\cong 10^5$ but were nearly identical at higher values, Ra $\cong 10^8$.

The purpose of the present study is to evaluate the coupling between radial and angular conduction through three equally spaced axial spacers and the fluid flow pattern, temperature distribution and heat transfer for laminar natural convection between two horizontal concentric cylinders. A numerical time-independent, finite-difference technique is used to obtain theoretical solutions to the conjugate problem. Experimental results are obtained using atmospheric air with local temperature and convective heat-flux distributions measured in a Mach-Zehnder interferometer. Results are compared with those for a simple annulus from [1].

Numerical Study

The two geometries investigated are shown schematically in Fig. 1. The inner cylinder is located concentrically within the

outer cylinder. The spacers are assumed to be thin and are 120 deg apart. The two geometries will subsequently be referred to as Λ-type and Y-type.

The flow is assumed to be steady, laminar and two-dimensional, with a plane of symmetry passing vertically through the center of the cylinders. The fluid is assumed to be incompressible and to follow the Boussinesq approximation. Radiation is neglected in the computations. The solutions obtained with Pr ≅ 0.7 are valid for gases provided the cylinders and spacers have low emissivities. The numerical solution procedure follows the central-difference, finite-difference technique outlined in [1]. The governing equations (3–11) to (3–13) of reference [1] are solved with the boundary conditions (3–14) to (3–17) of [1] except for changes in boundary conditions as outlined below.

The two cyinders are isothermal, $T_i > T_o$, with nonslip boundary conditions. The spacers are treated as thin fins with negligible angular temperature gradients. The hydrodynamic boundary conditions on the fluid at the surface of a spacer are

$$\psi = u = v = 0, \quad \omega = -\frac{1}{r^2}\frac{\partial^2 \psi}{\partial \theta^2} \qquad (1)$$

The dimensionless thermal boundary condition at a spacer is obtained by writing an energy balance for a one-dimensional fin with different convective coefficients on each side:

$$k_s w \frac{\partial^2 \phi}{\partial r^2} = \frac{1}{r}\left[\left.\frac{\partial \phi}{\partial \theta}\right|_T - \left.\frac{\partial \phi}{\partial \theta}\right|_B\right] \qquad (2)$$

where the subscripts T and B refer to the two sides of the spacer. When the spacer is vertical in the plane of symmetry, the two gradients on the right-hand side are equal in magnitude. First and second derivatives normal to the boundary as given in equations (1) and (2) are approximated with one-sided differencing that is second-order accurate.

The dimensionless temperature at an interior node is computed by

$$\phi_{i,j} = W_i \phi_{i+1,j} + X_i \phi_{i-1,j} + Y_i \phi_{i,j+1} + Z_i \phi_{i,j-} \qquad (3)$$
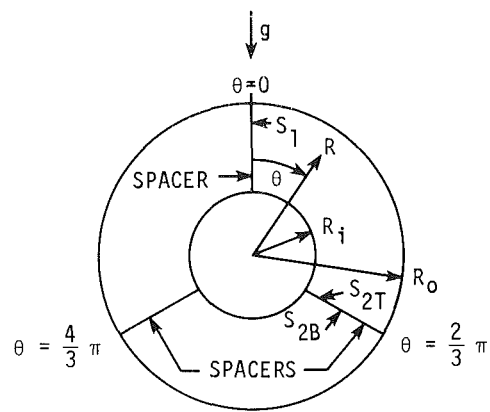
a   Λ TYPE
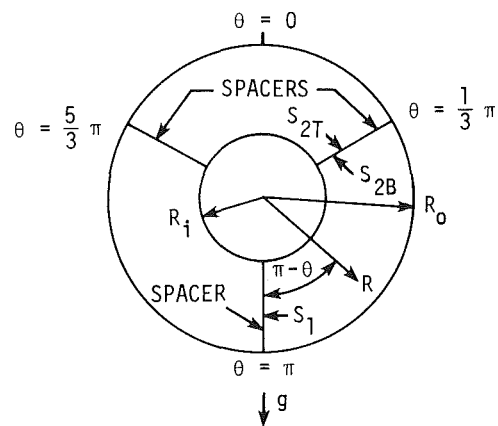
b   Y TYPE

Fig. 1   The two spacer configurations investigated

──────── Nomenclature ────────────────────────

D = cylinder diameter
h = local heat transfer coefficient
h_e = equivalent local heat transfer coefficient for spacer
g = gravitational acceleration
K = thermal conductivity of fluid
K_s = thermal conductivity of spacer
k_s = ratio of spacer to fluid thermal conductivity, K_s/K
L = gap width, $R_o - R_i$
Nu_D = local Nusselt number for cylinder surface, hD/K
Nu_s = local Nusselt number for spacer surface, $h_s L/K$
Pr = Prandtl number, $\vee/\alpha$
q = local heat flux at a solid/fluid interface, $h(T_i - T_o)$
Q = heat flow rate between cylinders, equation 12
R = radius
r = dimensionless radius, R/L
Ra = Rayleigh number, $g\beta L^3 \Delta T/\vee\alpha$

S = surface of spacer, Fig. 1
T = temperature
ΔT = temperature difference between cylinders, $T_i - T_o$
u = dimensionless radial velocity, UL/α
v = dimensionless circumferential velocity, VL/α
W = thickness of spacer
w = spacer thickness to gap-width ratio, W/L
Z = length along cylinder axis

Greek symbols

α = thermal diffusivity
β = thermal expansion coefficient
θ = angular coordinate measured clockwise from upward vertical
$\Delta\theta$ = angular grid spacing near center of cavity, 10 deg
$\Delta\theta_s$ = angular grid spacing near spacer, 2 deg
ϕ = dimensionless temperature, $(T - T_o)/(T_i - T_o)$

$\vee$ = kinematic viscosity
ρ = density
ψ = dimensionless stream function, ψ/α
ω = vorticity

Subscripts

B = bottom surface of inclined spacer
D_i = inner cylinder diameter as reference length
D_o = outer cylinder diameter as reference length
f = fluid
i = inner cylinder or radial grid line
j = circumferential grid line
o = outer cylinder
s = spacer
T = top surface of inclined spacer
1 = vertical spacer
2 = inclined spacer

Superscript

¯ = mean value

where the coefficients for uniform grid spacing in both r and θ directions for second-order, accurate, central differencing become

$$W_i = \left(1 + \frac{\Delta r}{2r_i} - u_{i,j}\frac{\Delta r}{2}\right)\Big/C_i \qquad (4a)$$

$$X_i = \left(1 - \frac{\Delta r}{2r_i} + u_{i,j}\frac{\Delta r}{2}\right)\Big/C_i \qquad (4b)$$

$$U_i = \left(\frac{\epsilon^2}{r_i{}^2} - v_{i,j}\frac{\epsilon\Delta r}{2r_i}\right)\Big/C_i \qquad (4c)$$

$$Z_i = \left(\frac{\epsilon^2}{r_i{}^2} + v_{i,j}\frac{\epsilon\Delta r}{2r_i}\right)\Big/C_i \qquad (4d)$$

with

$$C_i = 2\left(1 + \frac{\epsilon^2}{r_i{}^2}\right), \epsilon = \frac{\Delta r}{\Delta\theta} \text{ or } \frac{\Delta r}{\Delta\theta_s} \qquad (4e)$$

The grid spacing in the angular direction near the surface of each spacer was reduced to $\Delta\theta_s = \Delta\theta/5$ to better resolve the gradients at the fluid-spacer boundary, so the coefficients were changed to

$$Y_i = \left(\frac{5}{3}\frac{\epsilon^2}{r_i{}^2} - v_{i,j}\frac{\epsilon\Delta r}{6r_i}\right)\Big/C_i \qquad (5a)$$

$$Z_i = \left(\frac{25}{3}\frac{\epsilon^2}{r_i{}^2} + 25\,v_{i,j}\frac{\epsilon\Delta r}{6r_i}\right)\Big/C_i \qquad (5b)$$

$$C_i = \left(2 + \frac{10\,\epsilon^2}{r_i{}^2} + 4\,v_{i,j}\frac{\epsilon\Delta r}{r_i}\right) \qquad (5c)$$

when $\theta_j - \theta_{j-1} = \Delta\theta_s, \theta_{j+1} - \theta_j = \Delta\theta$, and

$$Y_i = \left(\frac{25}{3}\frac{\epsilon^2}{r_i{}^2} - 25\,v_{i,j}\frac{\epsilon\Delta r}{6r_i}\right)\Big/C_i \qquad (6a)$$

$$Z_i = \left(\frac{5}{3}\frac{\epsilon^2}{r_i{}^2} + v_{i,j}\frac{\epsilon\Delta r}{6r_i}\right)\Big/C_i \qquad (6b)$$

$$C_i = \left(2 + 10\frac{\epsilon^2}{r_i{}^2} - 4\,v_{i,j}\frac{\epsilon\Delta r}{r_i}\right) \qquad (6c)$$

when $\theta_j - \theta_{j-1} = \Delta\theta, \theta_{j+1} - \theta_j = \Delta\theta_s$. Similar relations were developed for the vorticity and stream function.

The radial grid spacing was uniform with $\Delta r = 0.05$. The angular spacing was uniform at $\Delta\theta = 10$ deg near the center of each cavity segment and at $\Delta\theta_s = 2$ deg within 10 deg on either side of a spacer. The resulting grid is 21×31 with a total of 651 nodes. An indication of the magnitude of truncation errors associated with the finite differencing is given by comparing the total heat transferred at each cylinder. The error between Q_i and Q_o is 0.2 percent for $D_o/D_i = 2$, 1 percent for $D_o/D_i = 3$ and 3 percent for $D_o/D_i = 3.6$ when Ra $\cong 10^4$.

The relaxation factors used in the iterative solution varied from 1.35, 0.5, and 1.2 for ψ, ω and ϕ, respectively, near Ra $= 10^4$ to 0.9, 0.3, and 0.9 near Ra $= 2 \times 10^4$. The stream function usually took longer to converge than the temperature. Therefore, a complete iteration consisted of computing new values for the entire field in the sequence ψ, ω, ψ, ω, ϕ. The solution was considered to be converged when the stream function and temperature both met the following criterion

$$\sqrt{\frac{\Sigma(B^m - B^{m-1})^2}{651}} \leq 10^{-3} \qquad (7)$$

where B is either ψ or ϕ. The calculations were performed on IBM-370 and Facom 230-28S computers using a fortran program. Solution times varied from about 30 min to 1 hr, depending on the relaxation factors and the Rayleigh number. The convergence was checked by comparing the total heat transfer at the inner and outer cylinders, including both the natural convection through the fluid and conduction through the spacers. The Rayleigh number was not large enough to produce any significant stability problems.

The following definitions are used when evaluating the heat transfer.

Nusselt number at a cylinder-fluid surface:

$$\text{Nu}_{D_{i_f}} = \frac{h_i D_i}{K} = -2r_i \frac{\partial\phi}{\partial r}\bigg|_{r=r_i} \qquad (8a)$$

$$\text{Nu}_{D_{o_f}} = \frac{h_o D_o}{K} = -2r_o \frac{\partial\phi}{\partial r}\bigg|_{r=r_o} \qquad (8b)$$

Effective heat transfer coefficient at a cylinder-spacer junction:

$$h_{e_i} = -\frac{K_s}{L}\frac{\partial\phi}{\partial r}\bigg|_{r=r_i}, \quad Q_{s_i} = h_{e_i}WZ(T_i - T_o) \qquad (9a)$$

$$h_{e_o} = -\frac{K_s}{L}\frac{\partial\phi}{\partial r}\bigg|_{r=r_o}, \quad Q_{s_o} = h_{e_o}WZ(T_i - T_o) \qquad (9b)$$

Effective Nusselt number at a cylinder-spacer junction:

$$\text{Nu}_{D_{i_s}} = \frac{h_{e_i}D_i}{K} = -2\,r_i\,k_s\frac{\partial\phi}{\partial r}\bigg|_{r=r_s} \qquad (10a)$$

$$\text{Nu}_{D_{o_s}} = \frac{h_{e_o}D_o}{K} = -2r_o\,k_s\frac{\partial\phi}{\partial r}\bigg|_{r=r_o} \qquad (10b)$$

Nusselt number on the surface of a spacer:

$$\text{Nu}_{s_k} = \frac{h_{s_k}L}{K} = \pm\frac{1}{r}\frac{\partial\phi}{\partial\theta}\bigg|_{\theta=k}, \quad q_k = h_{s_k}(T_i - T_o) \qquad (11)$$

where k indicates the spacer surface location and is equal to 1, $2T$ or $2B$ (see Fig. 1), and the sign is chosen so that the net heat transfer coefficient on the surface of a spacer is positive.

Total heat transfer across the annulus by conduction and convection:

$$Q = \bar{h}_i \pi D_i Z(T_i - T_o),$$

$$\bar{h}_i = \frac{K}{D_i}\left[\overline{\text{Nu}}_{d_{i_f}} + \sum_{\text{spacers}}(\text{Nu}_{D_{i_s}} - \overline{\text{Nu}}_{D_{i_f}})\frac{W}{\pi D_i}\right] \qquad (12a)$$

$$Q = \bar{h}_o \pi D_o Z(T_i - T_o),$$

$$\bar{h}_o = \frac{K}{D_o}\left[\overline{\text{Nu}}_{d_{o_f}} + \sum_{\text{spacers}}(\text{Nu}_{D_{o_s}} - \overline{\text{Nu}}_{D_{o_f}})\frac{W}{\pi D_o}\right] \qquad (12b)$$

Numerical Results

Solutions were obtained for the following range of dimensionless parameters: $9.3 \times 10^3 \leq \text{Ra} \leq 2.8 \times 10^4$, $0.5 \leq \text{Pr} \leq 10.0$, $2.0 \leq D_o/D_i \leq 3.6$, $1.8 \leq k_s \leq 621$, $0.0216 \leq w \leq 0.0703$. A single dimensionless parameter was varied for any set of solutions so that the effect of each one could be ascertained separately. Emphasis was placed on the effect of λ versus Y-geometry and the spacer dimensionless conductivity ratio.

Streamlines and isotherms for two solutions, one with the λ geometry, the other with Y-type, are shown in Figs. 2(a) and 2(b). In all solutions, a single recirculating eddy was found between adjacent spacers or between a vertical line of symmetry and the closest spacer. The direction of rotation is the same for the eddies on the same side of the symmetry plane. This results in different flow directions above and below an inclined spacer but flow in the same direction on both sides of a vertical spacer. The strength of the flow in the lower cavity of the λ-geometry is weaker than the flow in the upper cavity of the Y-geometry. The magnitude of flow
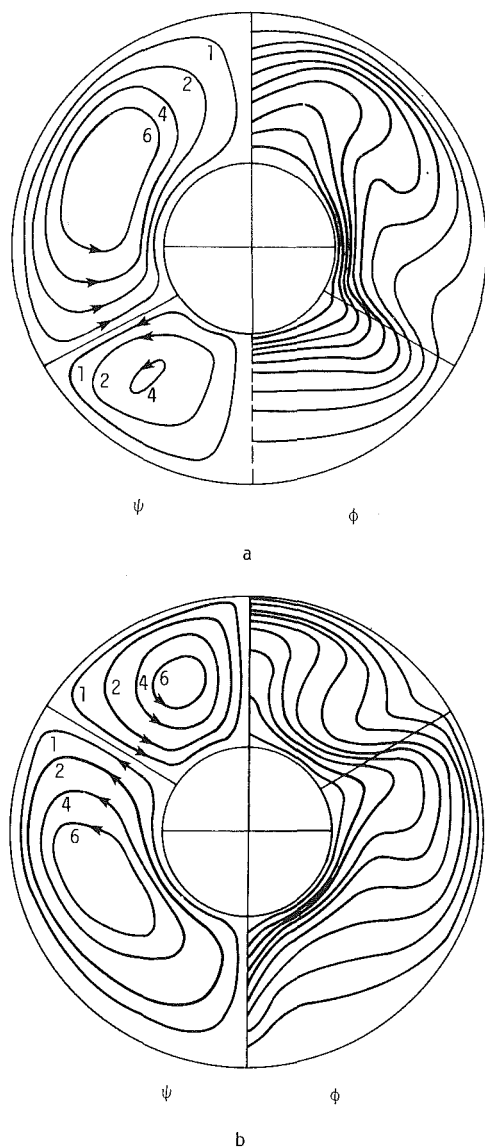
Fig. 2 Streamlines and isotherms at Ra = 10^4, Pr = 0.5, D_o/D_i = 2.6, k_s = 47.6, w = 0.0703 for (a) λ geometry, and (b) Y geometry

recirculation in the large cavities of both geometries is approximately the same. This results in a total recirculation in the λ -geometry that is smaller than the recirculation in the Y-type when all dimensionless parameters are equal. The total heat transfer for the λ -configuration is smaller, which reflects this decreased flow recirculation.

The maximum density of isotherms near the inner cylinder on Fig. 2(a) occurs near θ = 100 deg. This is the region of largest local heat transfer by convection from the inner cylinder and is caused by a region of recirculating flow moving toward the inner cylinder. The maximum density of isotherms near the outer cylinder and the maximum local convective heat flux occur near θ = 30 deg on the outer cylinder, which also is a region of recirculating flow moving toward the cylinder surface. The local isotherm density or heat flux is a maximum near θ = 140 deg on the inner cylinder surface and near θ = 0 deg on the outer cylinder surface for the Y-geometry shown in Fig. 2(b). The shift from maxima at θ = 180 deg on the inner cylinder and θ = 0 deg on the outer cylinder found in simple annuli is caused by the different flow patterns in the partially obstructed annuli.

Various spacer thermal conductivities were evaluated to determine the effect on the flow and heat transfer. These results were obtained using the λ -configuration at Ra = 10^4,
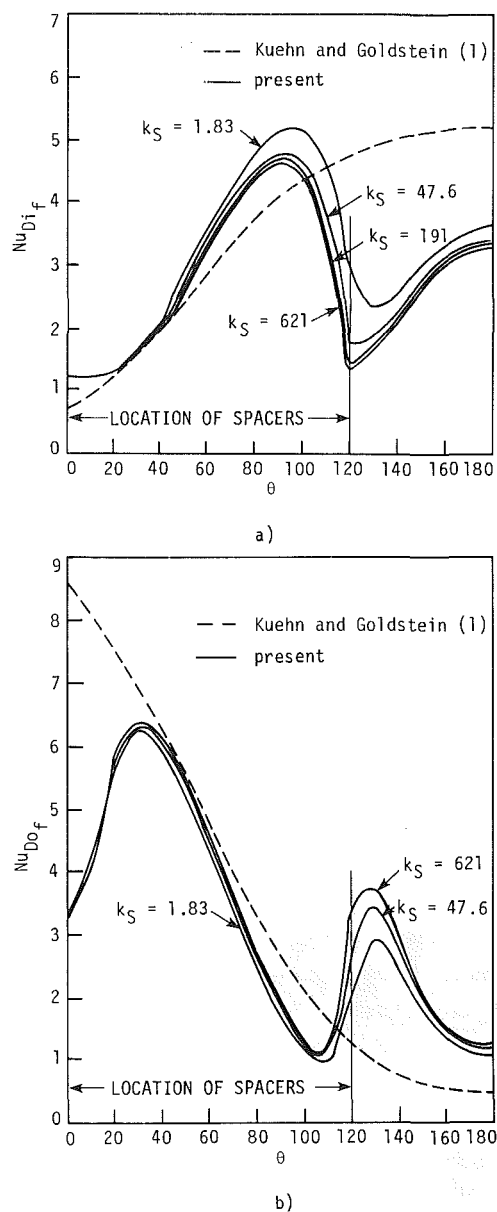

Fig. 3 Effect of spacer thermal conductivity on (a) inner cylinder and (b) outer cylinder local convective heat-transfer coefficients: Ra = 10^4, Pr = 0.7, D_o/D_i = 2.6, w = 0.0352, λ geometry

Pr = 0.708, D_o/D_i = 2.6 and w = 0.0352. The dimensionless conductivity ratios used were k_s = 1.83 (fiber board), 47.6 (ceramic), 191, 381 (40 percent nickel steel), and 621 (chrome-nickel stainless steel) where k_s = K_s/K and K = 0.02624 W/m°C, which is evaluated for air at 300 K. The spacers are modeled as having an infinite conductivity normal to the spacer surface (thin-fin approximation), so the variation in spacer thermal conductivity affects only conduction in the radial direction.

The effect of spacer conductivity on the local convective heat transfer coefficients for the inner and outer cylinders is shown in Figs. 3(a) and 3(b), respectively. The distribution without spacers is shown for comparison. The distributions with and without spacers are considerably different in the lower protion of the annulus, 120 deg < θ < 180 deg, because of the extra flow recirculation eddy as shown in Fig. 2(a). The values in the larger flow loop (θ < 120 deg) are similar to those for a simple annulus except for θ < 30 deg. This deviation is caused by the spacer replacing a zero shear layer with a stationary nonslip surface at the top plane of symmetry.

Journal of Heat Transfer

As $k_s \to 0$, the spacers do not conduct radially, although heat is conducted through the spacers in the angular direction. The results for $k_s = 1.83$ approach this limit. The temperature distribution along the spacers is governed exclusively by the natural convection flow. As $k_s \to \infty$, the radial temperature distribution along the spacers becomes linear and independent of the flow. Values for $k_s > 200$ closely approximate this limit. The local natural convection heat-transfer results for the cylinders shown in Fig. 3 are affected very little by the change in spacer conductivity. The total convective heat transfer is lower than for the simple annulus. The total heat convected from the inner cylinder is less than the total convected to the outer cylinder because of net convection to the fluid from the surfaces of the spacers.

Heat convected between the spacers and the fluid is caused by local differences in temperature, particularly when the spacers have a thermal conductivity quite different from the fluid. The local spacer Nusselt numbers for the three fluid-spacer iterfaces of the λ-geometry are shown in Fig. 4. At the lowest value for k_s, $k_s = 1.83$, the heat transfer to the vertical spacer (S_1) from the fluid is nearly zero because of the symmetry of the flow. The heat transfer above and below the spacer at $\theta = 120$ deg (S_{2T} and S_{2B}) is nearly the same when $k_s = 1.83$ and would be identical when $k_s = 0$. As the spacer conductivity increases, the heat transfer from the fluid to the vertical spacer increases because the adjacent fluid is warmer than the spacer. The heat transfer also increases at the inclined spacer; heat flows from the fluid to the spacer on the bottom, S_{2B}, except when $r < 0.2$, and from the spacer to the fluid on top, S_{2T}. The net heat transferred from the spacers to the fluid is 1.2 percent of the heat convected from the fluid to the outer cylinder when $k_s = 1.83$, and 13 percent when $k_s = 621$.

The total heat transferred between the cylinders is greatly affected by radial conduction through the spacers. For the dimensionless parameters given above, $\overline{Nu}_{D_{i_f}}$ through the fluid is 11 percent less than $\overline{Nu}_{d_i}$ for the simple annulus, and $\overline{Nu}_{D_{i_s}}$ for the spacers is 10 percent less than $\overline{Nu}_{D_i}$ for the unobstructed annulus when $k_s = 1.83$. However, $\overline{Nu}_{D_{i_f}}$ is 23 percent less and $Nu_{D_{i_s}}$ is 590 percent larger when $k_s = 621$.

The effect of Prandtl number on the fluid flow and heat transfer is much the same as for a simple annulus [21]. The local heat transfer coefficients increase slightly in magnitude, but the angular variation does not change appreciably as the Prandtl number varies from 0.5 to 10.0.

A change in Rayleigh number from $Ra = 9.3 \times 10^3$ to $Ra = 2.8 \times 10^4$ does not affect the basic flow pattern or the local heat transfer coefficient distribution. The only significant change is the increase in flow recirculation and total heat transfer as the Rayleigh number increases.

The diameter ratio was varied from 2.0 to 3.6 at $Ra = 10^4$, $Pr = 0.7$, $k_s = 621$, and $0.0216 \leq w \leq 0.0562$. The flow and heat transfer follow the same trends as in the simple annulus [21]. However, the fluid Nusselt number, $\overline{Nu}_{d_{i_f}}$, is 3.6 percent below that for the simple annulus at $D_o/D_i^f = 2.0$, and 15 percent less at $D_o/D_i = 3.6$. This agrees qualitatively with the results of Lis [20] for the smallest Rayleigh numbers investigated.

Experimental Study

A test cell was constructed for use in a Mach-Zehnder interferometer capable of using air at atmospheric pressure. A cross-section of the apparatus with the large inner cylinder in place is shown in Fig. 5. Two inner cylinders were fabricated from copper, each 25 cm long with a wall thickness of 0.3 cm. The outside diameters were 5.05 cm and 6.33 cm for the small
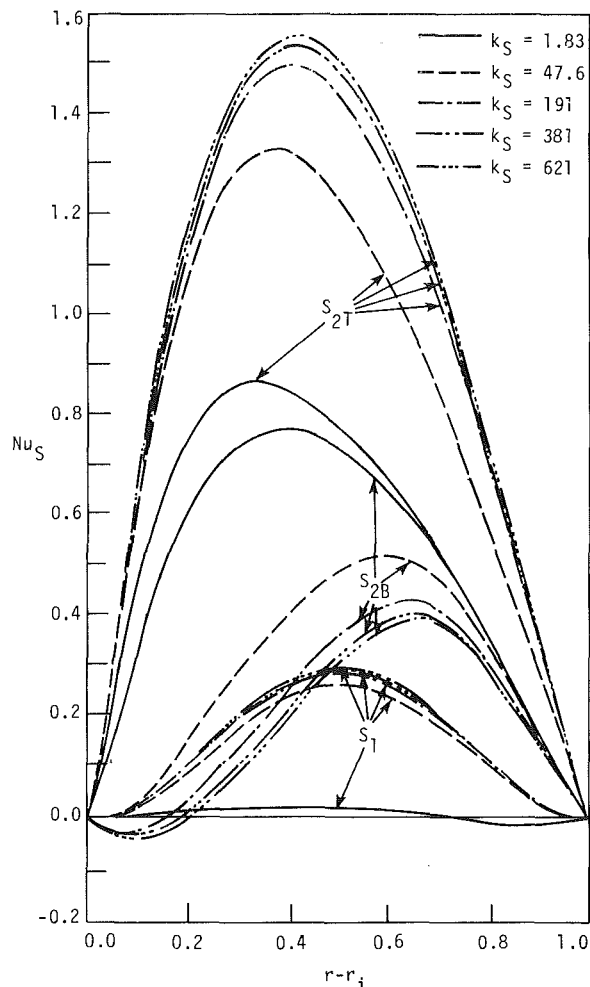

Fig. 4 Influence of spacer thermal conducitivty on local heat-transfer coefficient on spacer surface: Ra = 10^4, Pr = 0.708, D_o/D_i = 2.6, w = 0.0352, λ geometry
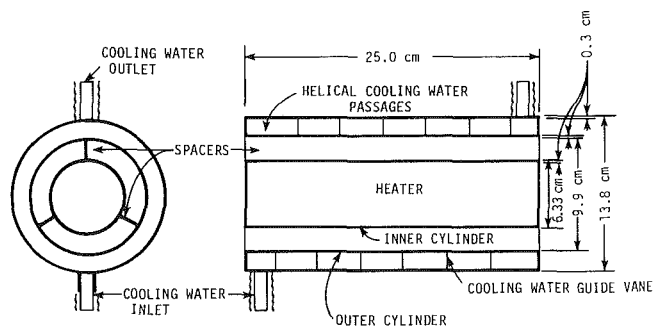

Fig. 5 Schematic cross-section of the experimental test cell with large inner cylinder

and large inner cylinders, respectively. Six chromel constantan thermocouples (four in the midplane spaced 90 deg apart, and one at each end) were positioned within 1 mm of the surface of each cylinder to measure angular and axial temperature variations. An electric resistance heater within each cylinder served as the heat source.

The outer cylinder was also constructed from copper, 25 cm long with an inside diameter of 9.9 cm and a wall thickness of 0.3 cm. Six thermocouples were positioned within 1 mm of the inside surface, similar to those in the inner cylinder. The diameter ratio, using the small inner cylinder, is D_o/D_i = 1.96 (L/D_i = 0.48), and D_o/D_i = 1.56 (L/D_i = 0.28), using the large inner cylinder. The outer surfaces of the inner cylinders and the inner surface of the outer cylinder were
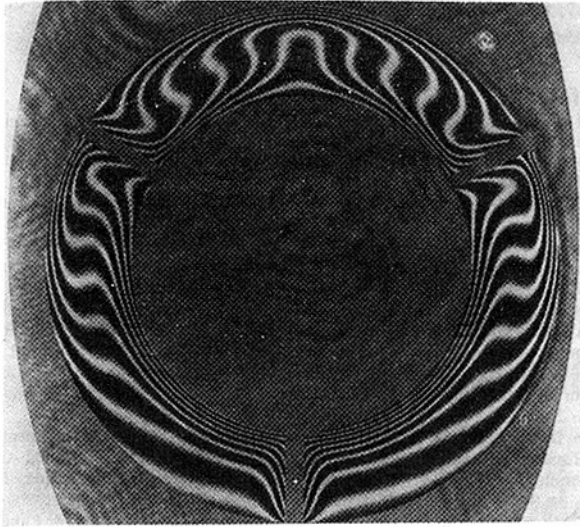
Fig. 6 Interferogram for Y geometry: Ra $= 1.23 \times 10^4$, Pr $= 0.708$, $D_o/D_i = 1.56$, $k_s = 621$, $w = 0.112$
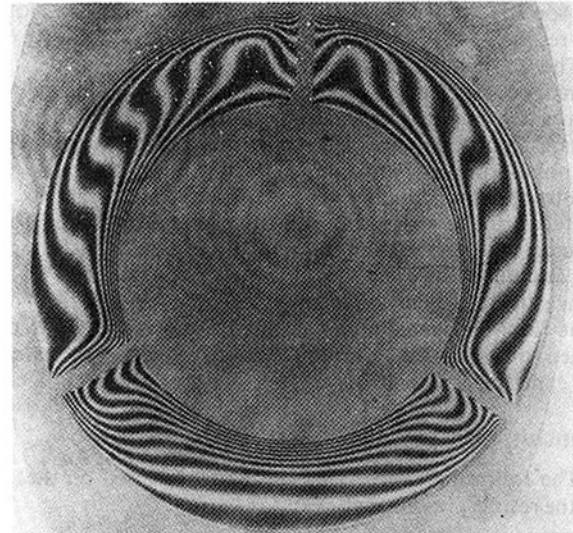

Fig. 7 Interferogram for λ geometry: Ra $= 1.41 \times 10^4$, Pr $= 0.707$, $D_o/D_i = 1.56$, $k_s = 621$, $w = 0.112$

$\Delta\phi = 0.142$ $\Delta\phi = 0.1$

Fig. 8 Comparison of experimental and numerical isotherms for Ra $= 2.48 \times 10^4$, Pr $= 0.708$, $D_o/D_i = 1.96$, $k_s = 621$, $w = 0.082$, Y geometry

polished to minimize radiation heat transport. Three slots spaced 120 deg apart, 25 cm long, 2 mm wide, and 1 mm deep, were machined on the outside surface of each of the inner cylinders and on the inside surface of the outer cylinder. Two sets of spacers were fabricated from stainless-steel plate for the two cylinder combinations. The spacers were 25 cm long, 2 mm wide, and 1.985 cm high for use with the large inner cylinder, and 2.625 cm high for the small inner cylinder. Cooling water was passed around the outer cylinder in helical flow passages, as shown in Fig. 5.

Before each run, the assembled test cell was aligned with the test beam of a Mach-Zehnder interferometer that used a 5 mW He-Ne laser as the light source and that had been leveled previously. The interferometer was then given an infinite fringe setting. Electric power was supplied to the heater using an a-c power supply with a variable transformer. A portable potentiometer of 0.001 mV/div and an X-Y recorder were used for reading the thermocouples. The maximum angular temperature difference in either cylinder was found to be less than 2 percent of the temperature difference between the cylinders ($\Delta T \cong 20°C$). When the cylinders had reached steady temperatures as shown by the X-Y recorder, a photograph of the fringe pattern was made. The fluid properties were evaluated for dry air at the arithmetic mean temperature of the cylinders, approximately 300 K.

Experimental Results

Two interferograms obtained using the large inner cylinder are shown in Figs. 6 and 7. A salient feature is the fringe density near the boundaries, which indicates the relative magnitudes in local heat flux. The heat flux is symmetric on each side of a vertical spacer, but much higher above than below on the inclined spacers, in agreement with the theoretical predictions shown in Fig. 4. The fringe distributions agree qualitatively with the isotherm distributions obtained in the numerical study, which verifies the existence of two flow cells rotating in the same direction in each vertical half of the annulus. The fringes may be considered two-dimensional isotherms, assuming end effects are small and the index of refraction of air is only a function of temperature. The radial temperature distribution along each spacer is nearly linear as predicted by the numerical results for $k_s = 621$. The angular temperature gradients through the spacers are very small, which shows that the one-dimensional temperature distribution assumed in the numerical study is a valid approximation. Heat flows from the fluid to a vertical
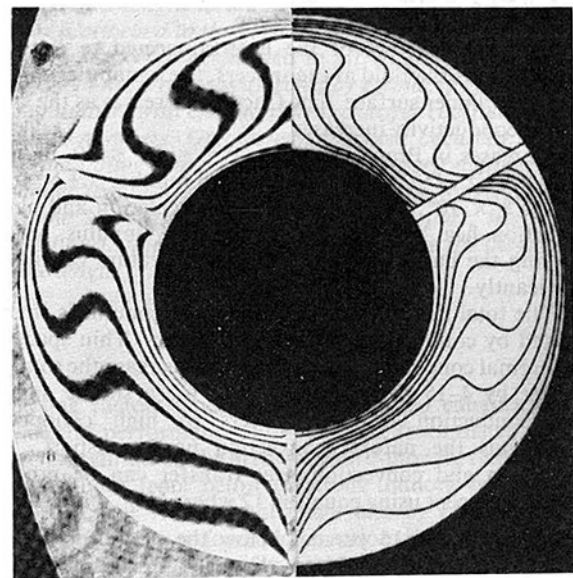
spacer above the inner cylinder and to the underside of an inclined spacer. Heat flows from a spacer to the fluid on the top side of an inclined spacer and from a vertical spacer positioned below the inner cylinder.

The experimental fringes or isotherms can be compared directly to an isothermal plot generated by the numerical program, providing the dimensionless governing parameters are the same for each case. Figure 8 is such a comparison evaluated at Ra $= 2.48 \times 10^4$, Pr $= 0.708$, $D_o/D_i = 1.96$, $k_s = 621$ and $w = 0.082$. The dimensionless temperature difference between the experimental isotherms is 0.142; between the numerical isotherms, it is 0.1. Although this does not provide a one-to-one comparison, the similarity in isotherm contours is evident. A finite-thickness spacer was drawn for the numerical distribution, although the spacer was treated as having zero thickness in the computations. The experimental errors are primarily optical, due to imperfect adjustment of the interferometer and end effects included in the axial beam integration. The errors in the numerical solution arise from the constant property assumption, a finite number of nodes,

the specified convergent limit, and errors that arise in plotting the results.

The experimental and theoretical local convective heat-transfer coefficients agree to within 10 percent. The integrated convective heat transfer at each cylinder surface is difficult to obtain from the interferograms because of the large number of points on the fluid boundary that must be analyzed to resolve the sharp angular changes in convective heat flux. The surfaces of the spacers must be analyzed in addition to the cylinders to obtain the total convective heat transfer across the annulus. However, the optical technique does give actual convective coefficients independent of any thermal radiation heat flux. The maximum radiative heat transfer was computed to be only 2.3 percent of the convective heat transfer for the experimental conditions.

Conclusions

The following conclusions can be formulated on the basis of the results presented above:

1 Natural convection heat transfer in a horizontal annulus with three equally spaced axial spacers is 3–20 percent less than for a simple unobstructed annulus for $Ra \cong 10^4$, $Pr \cong 1.0$, $D_o/D_i \cong 3$ and $w \cong 0.05$. The heat transfer is less for the λ configuration than for the Y type.

2 Up to 13 percent of the heat convected to the outer cylinder enters the fluid at the spacers, the remainder enters at the inner cylinder surface. The fraction increases as the spacer thermal conductivity increases.

3 Increases in Prandtl number, $0.5 \leq Pr \leq 10$, diameter ratio, $2 \leq D_o/D_i \leq 3.6$, and Rayleigh number $9.3 \times 10^3 \leq Ra \leq 2.8 \times 10^4$, all increase flow recirculation and natural convection heat transfer, as in a simple annulus, without changing the basic flow pattern or temperature distribution significantly.

4 The total heat transferred across the annulus is strongly affected by conduction through the spacers. Thin spacers of low thermal conductivity can be used to decrease the total heat transfer by 4–15 percent below that for a simple annulus. Heat conduction through spacers of high conductivity overwhelms the natural convection heat transport. Total conduction and convection heat transfer can be predicted within 10 percent using equation 12 where $Nu_{D_{i_f}}$ is evaluated at between 4 and 15 percent below the value for a simple annulus (increasing for larger diameter ratio) and $Nu_{D_{i_s}}$ is computed for steady one-dimensional heat conduction through the spacers.

Acknowledgment

References

1 Kuehn, T. H., and Goldstein, R. J., "An Experimental and Theoretical Study of Natural Convection in the Annulus Between Horizontal Concentric Cylinders," ASME *Journal of Fluid Mechanics*, Vol. 74, Part 4, 1976, pp. 695–719.

2 Shaughnessy, E. J., Custer, J. R., and Douglass, R. W., "Partial Spectral Expansions for Problems in Thermal Convection," ASME JOURNAL OF HEAT TRANSFER, Vol. 100, 1978, pp. 435–441.

3 Ingham, D. B., "Natural Convection Between Spheres and Cylinders," *Numerical Heat Transfer*, Vol. 4, 1981, pp. 53–68.

4 Kuehn, T. H., and Goldstein, R. J., "An Experimental Study of Natural Convection Heat Transfer in Concentric and Eccentric Horizontal Cylindrical Annuli," ASME JOURNAL OF HEAT TRANSFER, Vol. 100, 1978, pp. 635–640.

5 Projahn, U., Rieger, H., and Beer, H., "Numerical Analysis of Laminar Natural Convection Between Concentric and Eccentric Cylinders," *Numerical Heat Transfer*, Vol. 4, 1981, pp. 131–146.

6 Boyd, R. D., "Steady Natural Convection Heat Transfer Experiments in a Horizontal Annulus for the United States Spent Fuel Shipping Cask Technology Program," Sandia National Laboratories, Albuquerque, New Mexico, SAND80-1057, Apr. 1981.

7 Jischke, M. C., and Farshchi, M., "Boundary Layer Regime for Laminar Free Convection Between Horizontal Circular Cylinders," ASME JOURNAL OF HEAT TRANSFER, Vol. 102, 1980, pp. 228–235.

8 Ratzel, A. C., Hickox, C. E., and Gartling, D. K., "Techniques for Reducing Thermal Conduction and Natural Convection Heat Losses in Annular Receiver Geometries," ASME JOURNAL OF HEAT TRANSFER, Vol. 101, 1979, pp. 108–113.

9 Hitchcock, J. A., and Thelwell, M. J., "The Cooling of Underground EHV Transmission Cables," IEEE Transactions, *Power Apparatus and Systems*, Vol. 87, 1968, pp. 129–134.

10 Gierszewski, P. J., Mikic, B., and Todreas, N. E., "Natural Circulation in Fusion Reactor Blankets," ASME Paper 80-HT-69.

11 Klima, B. B., "LMFBR *Spent Fuel Transport: Single Assembly Heat Transport Test*," Oak Ridge National Laboratory. TM-4936, 1975.

12 Ramsey, J. W., Gupta, B. P., and Knowles, G. R., "Experimental Evaluation of a Cylindrical Parabolic Solar Collector," ASME JOURNAL OF HEAT TRANSFER, Vol. 99, 1977, pp. 163–168.

13 Pedersen, B. O., Doepken, H. C., Jr., and Bolin, P. C., "Development of a Compressed-Gas-Insulated Transmission Line," IEEE Paper 71 TP 193-PWR.

14 Cronin, J. C., Bacvarov, D., Cron, J. C., Katzbeck, J. W., Samm, R. W., and Perry, E. R., "Incorporating Flexibility into a Gas-Insulated Transmission System Designed for Underwater Use," *Proceedings of the IEEE Underground Transmission and Distribution Conference*, 1974, pp. 343–348.

15 Iyican, L., Bayazitoglu, Y., and Witte, L. C., "An Analytical Study of Natural Convective Heat Transfer Within a Trapezoidal Enclosure," ASME JOURNAL OF HEAT TRANSFER, Vol. 102, 1980, pp. 640–647.

16 Anderson, R., and Bejan, A., "Natural Convection on Both Sides of a Vertical Wall Separating Fluids at Different Temperatures," ASME JOURNAL OF HEAT TRANSFER, Vol. 102, 1980, pp. 630–635.

17 Sparrow, E. M., and Prakash, C., "Interaction Between Internal Natural Convection in an Enclosure and an External Natural Convection Boundary-Layer Flow," *Internaitonal Journal of Heat and Mass Transfer*, Vol. 24, 1981, pp. 895–906.

18 Sparrow, E. M., and Acharya, S., "A Natural Convection Fin with a Solution-Determined Nonmonotonically Varying Heat Transfer Coefficient," ASME JOURNAL OF HEAT TRANSFER, Vol. 103, 1981, pp. 218–225.

19 Grigull, U., and Hauf, W., *Proceedings of the Third International Heat Transfer Conference*, Discussion Volume, 1966, pp. 159–160.

20 Lis, J., "Experimental Investigation of Natural Convection Heat Transfer in Simple and Obstructed Horizontal Annuli," *Proceedings of the Third International Heat Transfer Conference*, Vol. 2, 1966, pp. 196–204.

21 Kuehn, T. H., and Goldstein, R. J., "A Parametric Study of Prandtl Number and Diameter Ratio Effects on Natural Convection Heat Transfer in Horizontal Cylindrical Annuli," ASME JOURNAL OF HEAT TRANSFER, Vol. 102, 1980, pp. 768–770.

Heat Transfer by Natural Convection From an Array of Short, Wall-Attached Horizontal Cylinders

E. M. Sparrow

Fellow ASME

D. S. Cook

G. M. Chrysler

Department of Mechanical Engineering,
University of Minnesota,
Minneapolis, Minn. 55455

Per-cylinder natural convection Nusselt numbers were measured for an in-line array of short horizontal cylinders that were affixed to a convectively participating vertical plate. The effect of cylinder length-to-diameter ratio, intercylinder spacing, position at which the cylinder is attached to the vertical plate, and Rayleigh number were investigated. The experiments were performed in air. It was found that the extent to which a given cylinder in the array was affected by cylinders situated below it depended on the Rayleigh number, with enhanced heat transfer coefficients being more likely at higher Rayleigh numbers. Greater enhancement occurred at larger intercylinder spacings. The qualitative characteristics of the Nusselt number results were insensitive to the cylinder length-to-diameter ratio, but the longer cylinders exhibited higher values of the Nusselt number. For the most part, the Nusselt numbers for the wall-attached horizontal cylinders fell below those for the classical horizontal cylinder of infinite length.

Introduction

Whereas the use of fin arrays represents a logical approach to heat-transfer enhancement, there is a paucity of information about the characteristics of fin arrays operating in the natural convection mode. The existent information is, in the main, limited to plate-type fins arranged to form an array of parallel vertical channels ([1–4] are representative of the experimental literature). In such a parallel configuration, the flows in the respective channels do not interact strongly with each other, and, indeed, there may be only a modest convective interaction between the fins and the base surface to which they are attached [4].

Another type of fin array which holds high promise for enhancing natural convection heat transfer is an assemblage of short cylinders (that is, pin fins) attached to a wall which exchanges heat with an adjacent fluid. Such a configuration can give rise to strong natural convection interactions between individual fins as well as between the fins and the wall. In this regard, attention may be focused on a heated vertical plate on whose surface is positioned an array of short horizontal cylinders deployed in a regular pattern (e.g., staggered or in-line). The plate induces an upflowing boundary layer which washes over the cylinders. In turn, each cylinder induces a buoyant upflow, and the rising plume (or wake) may impinge on other cylinders situated at higher elevations. The plumes may also interact with the flat-plate boundary layer.

In the absence of quantitative data, it is difficult to foresee whether the aforementioned interactions will enhance or degrade the heat-transfer performance. There are, in fact,

conflicting factors tending, respectively, to enhance and to degrade this performance. For example, from the standpoint of a given cylinder in the array, upward-moving fluid arriving at the cylinder from below (motions induced by buoyancy imparted to the fluid by the plate and by other cylinders) appears similar to a forced convection flow and, thereby, tends to enhance heat transfer. However, this upward-moving fluid was heated prior to its arrival at the given cylinder (by interaction with the plate and with other cylinders), resulting in a lower cylinder-to-fluid temperature difference and a tendency toward degraded heat transfer.

A search of the literature did not reveal any information about the natural convection heat transfer characteristics of an array of pin fins attached to a heated vertical plate. Furthermore, in view of the highly interactive and complex nature of the flow, as discussed in the foregoing paragraphs, it appears unlikely that available results for simple configurations (e.g., long horizontal cylinders without end effects) would be applicable to a pin-fin array.

As is evident from the foregoing discussion, the present research is concerned with an array of short horizontal cylinders (pin fins) affixed to a vertical plate, with heat being transferred by natural convection from the plate and the cylinders to the adjacent air. Experiments were performed with arrays consisting of either two or three pin fins deployed in an in-line pattern. The experimental work encompassed the variation of four parameters, including the fin length-to-diameter ratio, the interfin spacing, the position at which the fin is attached to the host vertical plate, and the Rayleigh number. Nusselt numbers for the individual pin fins were determined for each of these cases.
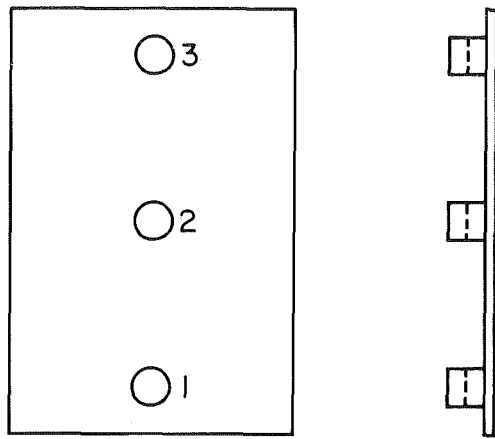
Fig. 1 Schematic view of an array of cylinders affixed to a vertical plate

What with the large number of parameters, the Nusselt numbers will be examined from several standpoints in the presentation of results. One of the key issues to be addressed is the response of the Nusselt number for a given pin fin (i.e., affixed to the plate at a given position) to the presence and positioning of other pin fins. Comparisons made in this connection will demonstrate whether the washing of a given fin by buoyant plumes generated by other fins enhances or degrades its heat transfer performance. The roles played by the interfin spacing and the fin length-to-diameter ratio in enhancing or degrading the heat transfer will be identified.

Another relevant issue to be examined is the row-by-row variations of the Nusselt number. Finally, since each individual pin fin is a short wall-attached horizontal cylinder, a measure of its interactions with the plate and with other fins is afforded by comparisons with literature information for a single end-effect-free horizontal cylinder. Such comparisons are made during the presentation of results.

In [5], experiments were performed involving a single, short horizontal cylinder affixed to a vertical plate. With a view to providing fuller perspective for the present multicylinder results, Nusselt numbers from [5] will be quoted here.

Although much of the prior discussion has been phrased in terms of pin fins, it is clear that the results apply to arrays of cylinders in general, regardless of whether or not they are pin fins.

Experimental Apparatus

A schematic portrayal of the experimental setup is presented in Fig. 1. The right-hand diagram of the figure shows a side view of the vertical plate with all three cylinders in place, whereas the left-hand diagram is a front view in which designations 1, 2, and 3 have been assigned to denote cylinders respectively affixed at the lower, middle, and upper positions on the surface of the host plate.

The apparatus was designed to be operated with either one, two, or three cylinders in place. For one-cylinder operation, the design enabled the cylinder to be affixed at either positions 1, 2, or 3, while for two-cylinder operation, the cylinders could be affixed either at positions 1 and 2, or at positions 1 and 3, or at positions 2 and 3. For either one-cylinder or two-

cylinder operation, the aperture in the plate surface at the unused position(s) (the aperture served to receive the shank of a cylinder) was closed by a specially designed plug which provided precise hydrodynamic and thermal continuity with the remainder of the plate surface. The appartus was also able to accommodate cylinders of different lengths and diameters. For the present experiments, two different cylinder lengths were used, both with the same diameter.

In part, the apparatus employed here was taken over from the single-cylinder studies reported in [5]. The additional cylinders fabricated for the present investigation were modeled after those of the antecedent investigation. In view of this, much of the detailed information presented in [5] about the special procedures employed to obtain results of high accuracy and about fabrication techniques, component dimensions, instrumentation, and operating procedure will not be repeated here. Rather, a broader description of the apparatus will be presented here to enable the general reader to obtain a self-contained view of the research.

The vertical plate was of 1.250-cm (0.492-in.) thick aluminum, with a height of 45.72 cm (18.00 in.) and a width of 30.48 cm (12.00 in.). It was heated by electrical resistance wire affixed to its rear surface, with the wiring pattern selected to give a uniform temperature on the front face. (The measured surface temperatures never deviated from uniformity by more than 1½ percent of the surface-to-fluid temperature difference.) To accommodate the cylinders, 3 holes were machined through the thickness of the plate at the positions shown in Fig. 1. The centers of these apertures were respectively situated 5.08, 22.86, and 40.64 cm (2, 9, and 16 in.) above the leading edge of the plate.

All told, 6 cylinders were fabricated, encompassing 2 sets of 3 cylinders each. Each of the cylinders was machined from a solid block of aluminum. In finished form, each cylinder consisted of a convection section (i.e., the part exposed to the airflow) and a shank which, as already noted, mated with an aperture in the wall of the host vertical plate. Electrical heating of each cylinder was accomplished by means of resistance wire wound around a core and positioned in a cavity that had been machined axially through the shank into the convection section.

For one set of cylinders, to be designated as the shorter cylinders, the length of the exposed portion was 2.000 cm (0.787 in.) and the diameter was 4.000 cm (1.575 in.). The other set of cylinders, the longer cylinders, were 4.000 cm (1.575 in.) in length and 4.000 cm (1.575 in.) in dia.

Both the plate and the cylinders were instrumented with thermocouples. Twelve thermocouples were embedded in the wall of the plate (junctions positioned 0.076 cm (0.030 in.) from the exposed face), and there were 5 thermocouples in each cylinder. Of particular note are the three thermocouples in the shank of each cylinder, installed so as to lie in a common axial plane and at 120 deg circumferential intervals, and a corresponding trio of thermocouples deployed around the circumference of each aperture in the plate. With the cylinder in place in the aperture, there was precise axial and circumferential alignment of the three cylinder-shank thermocouples and the corresponding trio of aperture-adjacent plate thermocouples.

Nomenclature

A = surface area of cylinder
D = cylinder diameter
g = acceleration of gravity
h = cylinder heat transfer coefficient, $Q_c/A(T_w - T_\infty)$
k = thermal conductivity
L = cylinder length

Nu = cylinder Nusselt number, hD/k
Q_c = natural convection heat transfer
Q_{in} = electrical power input
Q_r = radiation heat transfer
Ra = Rayleigh number, $g\beta(T_w - T_\infty)D^3\mathrm{Pr}/\nu^2$

T_r = reference temperature for properties, equation (5)
T_w = cylinder wall temperature
T_∞ = ambient temperature
β = thermal expansion coefficient
ν = kinematic viscosity

This arrangement was employed to eliminate heat conduction between any one (and all) of the cylinders and the plate. Owing to the independent control of the heat inputs to each of the cylinders and to the plate, the emfs of the cylinder-shank thermocouples could be brought into agreement (to within 1 μV) with the emfs of the aperture-adjacent plate thermocouples. To amplify possible cylinder-to-plate temperature differences associated with a non-zero conductive heat flow, a Delrin plastic bushing was used as a liner in each aperture, thereby separating the shank of the cylinder from the metal wall of the aperture. This increased sensitivity of the temperature imbalance to the heat flux facilitated the attainment of the zero conduction condition. As a further defense against conduction, an O-ring prevented direct contact between the plate-adjacent face of the cylinder and the plate surface.

As a consequence of the nulling-out of the plate-cylinder heat conduction, all of the heating power supplied to a given cylinder was dissipated at its exposed surfaces by natural convection and by radiation. The radiation heat transfer was reduced to a very small value (5 to 8 percent of the total power input) by a painstaking surface polishing and lapping procedure which produced a mirror finish which merits being described as "highly polished" from the standpoint of radiation properties. Both the plate and each of the cylinders were finished in this manner. As will be described shortly, the radiation heat transfer for each cylinder was determined by calculation and subtracted from the total power input, thereby yielding the per-cylinder natural convection heat-transfer rate.

In all cases, regardless of whether the array consisted of one, two, or three cylinders, each cylinder was isothermal (to within 1-2 μV) and equal in temperature to that of the other cylinders and the plate. Thus, when viewed as fins, the cylinders had an efficiency of unity. What with the low heat-transfer coefficients that are typical of natural convection in air, a fin efficiency of unity is quite reasonable from the standpoint of practice.

The thermocouple wire and the electrical leads for the heaters and for the heater voltage measurements were all chosen to be of the smallest practical diameter in order to minimize extraneous conduction. As a further precaution, these wires were held by tape against the rear face of the plate (an isothermal surface) as they were led out of the apparatus. In addition to the already mentioned plate and cylinder thermocouples, a trio of vertically deployed thermocouples were employed to measure the ambient air temperature and its possible stratification. All thermocouples were taken from rolls specifically calibrated for these experiments.

The vertical plate was insulated along all its edges and at the rear with styrofoam block insulation, with a thin layer of fiberglass interposed between the rear face of the plate and the styrofoam to provide a compliant surface of contact for the lead wires.

The apparatus was situated in a large isolated room (actually, a room within a room) whose walls, ceiling, and floor were insulated with a 1½ ft thickness of cork. All instrumentation and power supplies were located in a room adjacent to that in which the experiments were conducted.

What with the matching of the temperatures of as many as three cylinders with that of the plate in each data run, the duration of a run often extended over several days.

Data Reduction

The main focus of the data reduction procedure was to determine Nusselt numbers for each of the cylinders of the array along with the corresponding Rayleigh numbers. As already noted, the heat transferred at the exposed surfaces of each cylinder is equal to the electrical power delivered to the

heater embedded in the cylinder. Since both radiation and natural convection are operative,

$$Q_{in} = Q_c + Q_r \qquad (1)$$

where Q_{in}, Q_c, and Q_r, respectively, denote the electrical input, the convective heat transfer, and the radiative heat transfer.

For the case in which there is only a single cylinder attached to the host plate, it is possible to deduce an exact solution for Q_r based on a model which includes diffuse emission and specular reflection at the surfaces of the plate and the cylinder, along with blackbody radiation streaming through the laboratory room. This derivation is described in [5]. For a two or three cylinder array, the analysis for the determination of Q_r becomes much more complex because the radiant interchange between a given cylinder and the plate is partially blocked by the presence of the other cylinders; in addition, the cylinder-to-cylinder angle factor is not available in the literature.

Upon due consideration, it is evident that the departure of the Q_r value for a cylinder in a multi array from that for a single cylinder will be greatest when the cylinder in question is affixed to the plate at position 2 and when cylinders are present both at positions 1 and 3 (see Fig. 1). For this situation, a careful estimate was made of the departures of Q_r from the corresponding single-cylinder Q_r. At each stage of the estimating procedure, it was made certain that very conservative assumptions were employed so that the end result would substantially overstate the differences between the Q_r values for the multicylinder and single-cylinder arrays.

From this, an overstated decrease of 8½ percent in Q_r due to the presence of the other cylinders was calculated. However, as noted earlier, Q_r constitutes only 5 to 8 percent of the input power Q_{in} to the cylinder. Thus, realistically speaking, the true Q_r for any cylinder in the multicylinder array will deviate by less than 1/2 percent of Q_{in} compared to that for a single cylinder, with a corresponding deviation in the convective heat transfer Q_c. This margin of error is quite tolerable, especially when viewed relative to the uncertainty in the value of the surface emissivity ϵ. In view of these considerations, Q_r was evaluated from the formula for the single-cylinder, equation (11) of [5]. For the evaluation, ϵ was taken to be 0.04.

Returning now to equation (1), Q_c can be determined by employing the measured value of Q_{in} and the calculated value of Q_r. The average per-cylinder, heat-transfer coefficient was then evaluated from

$$h = Q_c / A (T_w - T_\infty) \qquad (2)$$

In this equation, A encompasses the areas of both the cylindrical surface and the exposed end face of each cylinder (dia D, length L)

$$A = \pi D L + \pi D^2 / 4 \qquad (3)$$

The quantity T_w is the measured temperature of the cylinder which, as stated earlier, was uniform to 1-2 μV. For the ambient temperature, the value read by a thermocouple situated at the same elevation as the cylinder in question was employed.

For a dimensionless presentation, Nusselt and Rayleigh numbers were elevated from

$$Nu = hD/k, \quad Ra = g\beta(T_w - T_\infty)D^3 Pr/\nu^2 \qquad (4)$$

The thermophysical properties appearing in equation (4) were introduced at a reference temperature T_r recommended by [6]

$$T_r = T_w - 0.38(T_w - T_\infty) \qquad (5)$$

except for β, which was evaluated as $1/T_\infty$. The Nu and Ra from equation (4) are the key quantities for the presentation of results.
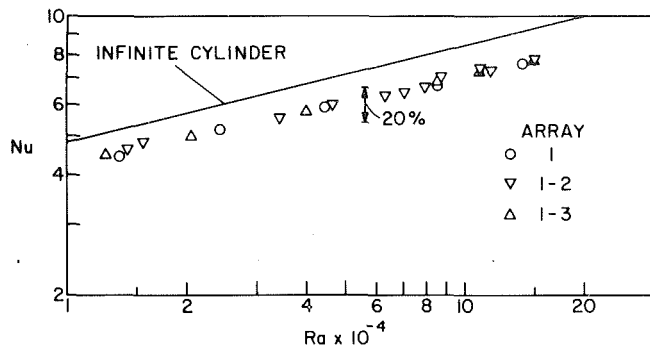
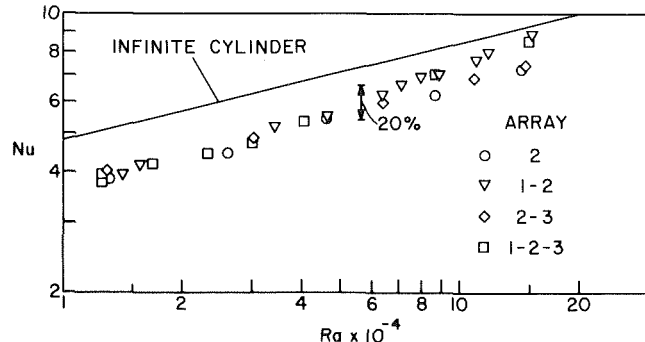Fig. 2 Nusselt numbers for the shorter cylinder situated at position 1

Fig. 3 Nusselt numbers for the shorter cylinder situated at position 2

Fig. 4 Nusselt numbers for the shorter cylinder situated at position 3

Results and Discussion

Format of the presentation. In view of the many participating parameters and of the considerable amount of data that was collected, the results will be presented from several viewpoints. To begin, a fixed cylinder position is selected, either position 1, 2, or 3 (as depicted in Fig. 1). Then, for a cylinder affixed at that position, the Nusselt number is plotted as a function of the Rayleigh number for all the arrays investigated here. Thus, for example, for a cylinder at position 2, results are given for four arrays: 2, 1-2, 2-3, and 1-2-3, where the notation 1-2 denotes an array with cylinders at positions 1 and 2, etc. A presentation of this type is made for the cylinder Nusselt number at each of the positions 1, 2, and 3, as well as for the shorter and longer cylinders.

Next, attention is focused on the two-cylinder arrays, either 1-2, 2-3, or 1-3, and the Nusselt numbers at the upper of the two cylinders are compared. Then, the three-cylinder array 1-2-3 is considered, and comparisons are made of the Nusselt numbers for the successive cylinders (i.e., 1, 2, and 3). Finally, a more global view is taken of the results by plotting all of the shorter-cylinder Nusselt numbers together (i.e., all positions, all arrays), and a similar plot is made for the longer-cylinder Nusselt numbers.

Comparisons will also be made between the present results and those for the classical case of a long horizontal cylinder without end effects. As was noted in [5], there are several available correlations for the horizontal cylinder. That of McAdams [7] dates from 1933 and tends to lie above the others, while the relatively recent correlation of Churchill [8] falls low in the range of Rayleigh numbers investigated here $(1.4 \times 10^4$ to $1.4 \times 10^5)$. The correlations of Morgan [9], Raithby [10], and Fand [11] are nearly coincident in the present Rayleigh number range. That of Morgan is based on a large body of data, much of which is of recent vintage, and is probably the most firmly based of the available correlations. In view of this, the Morgan correlation

$$Nu = 0.480 Ra^{1/4} \qquad (6)$$

will be used here to represent the infinite-cylinder case.

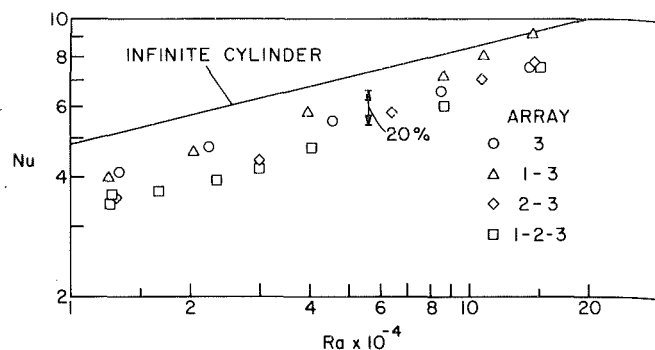According to Morgan, all thermophysical properties ap-

pearing in equation (6), including β, are to be evaluated at the film temperature. For the graphical comparisons to be made here, the Nusselt number results from equation (6) were recast in terms of the present property prescription (equation (5) and $\beta = 1/T_\infty$). However, the property variations that occurred in the experiments were slight, so that the plotted version of equation (6) nearly coincides with equation (6) itself.

Equation (6), recast into the present property prescription, will be plotted in every one of the figures in which the experimental data are to be presented. It will, therefore, serve as a reference line in order to facilitate figure-to-figure comparisons and, in this way, the results appearing in the successive figures will be tied together. In addition, in order to facilitate comparisons among the various cases that are presented in each figure, the vertical distance corresponding to a 20 percent variation in Nusselt number is indicated in all the figures. Since the ordinate scale is logarithmic, the indicated vertical distance represents a 20 percent variation regardless of the magnitude of the Nusselt number.

Position-specific cylinder Nusselt numbers. Attention will first be turned to the Nusselt numbers for the shorter cylinder situated at specific fixed positions, in the presence of various arrays. Figures 2–4 have been prepared in this connection and correspond, respectively, to positions 1, 2, and 3. In each figure, the per-cylinder Nusselt number is plotted as a function of the Rayleigh number. The various arrays of which the cylinder in question is a member are indicated in each figure, and a specific data symbol is used to identify each array.

The results for the shorter cylinder in position 1 are plotted in Fig. 2 (the results for the 1-2-3 array coincide with those for the 1-2 array and are not shown). Inspection of the figure shows that the Nusselt numbers are independent of the nature of the array—that is, the Nusselt numbers at position 1 are the same regardless of whether or not there are cylinders situated above 1. If such cylinders were to have an effect, it would be caused by their possible influence on the plume which rises from the cylinder positioned at 1. Thus, Fig. 2 shows that the inter-cylinder spacing is large enough to preclude such plume modifications. The excellent agreement in evidence among the Nusselt numbers for the various arrays provides strong testimony about the reproducibility of the data.

The fact that the data of Fig. 2 fall below the infinite-cylinder line (from equation (6)) suggests that the presence of the plate tends to degrade the cylinder Nusselt number. As will be documented later, the extent of the degradation is greater for the shorter cylinder than for the longer cylinder.

Figure 3 shows the Nusselt number data for the shorter cylinder at position 2. On the basis of the findings identified during the discussion of Fig. 2, it may be expected that identical results would be in evidence in Fig. 3 for arrays 2 and 2-3 and, in addition, the results for arrays 1-2 and 1-2-3 would also be identical. Within the slight scatter of the data, these expectations are fulfilled.

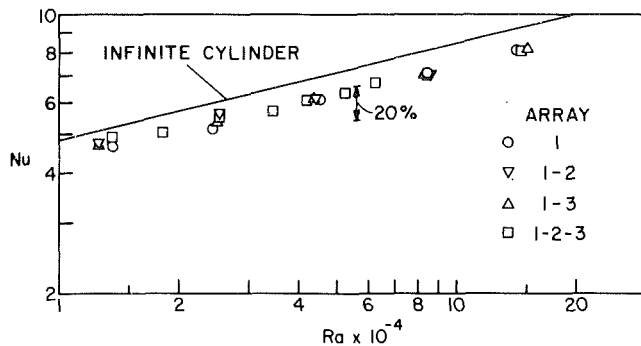In the lower portion of the Rayleigh number range in Fig. 3,

Fig. 5   Nusselt numbers for the longer cylinder situated at position 1

Fig. 6   Nusselt numbers for the longer cylinder situated at position 2

Fig. 7   Nusselt numbers for the longer cylinder situated at position 3

the data for all the arrays generally fall together, indicating that the Nusselt number at position 2 is insensitive to the presence of a cylinder situated at position 1 (i.e., below 2). Furthermore, by using the reference lines (i.e., the infinite cylinder line) which appear in Figs. 2 and 3, it is evident that for this portion of the Ra range, the Nu values at position 2 are somewhat lower than those at position 1.

In the upper part of the Rayleigh number range, the Nusselt numbers for arrays 1-2 and 1-2-3 (arrays with a cylinder situated below position 2) tend to break away from those for arrays 2 and 2-3 (arrays without a cylinder below position 2). This indicates that the plume which impinged from below on the cylinder at 2 tends to enhance its heat transfer.

The enhancement or degradation of cylinder heat transfer due to plate-cylinder and/or cylinder-cylinder natural convection interaction has been mentioned in the preceding paragraphs. Both the plate and the cylinders situated below the cylinder in question give rise to upmoving buoyant streams that impinge on the cylinder. The velocity possessed by the impinging flow tends to enhance the heat transfer. On the other hand, the impinging flow has been preheated owing to its contact with the plate and the other cylinders, and this preheating tends to decrease the heat transfer. This conflict of effects is made more complex because the impinging flow is a mixture of buoyant streams induced by the plate and by the other cylinders. Because of the complexity of the conflict between the enhancing velocity of the impinging flow and its preheating, it is difficult to foresee whether there will be heat transfer enhancement or degradation at a given cylinder.

Various degrees of enhancement or degradation are in evidence in Fig. 4, which pertains to position 3. At the lower Rayleigh numbers, the presence of a cylinder directly below 3 (i.e., at position 2 in arrays 2-3 and 1-2-3) tends to reduce the Nusselt number, while a cylinder situated farther below 3 (i.e., at position 1 in array 1-3) has essentially no effect on the Nusselt number. At higher Rayleigh numbers, on the other hand, enhancement is clearly in evidence for the 1-3 array, while the other multi-cylinder arrays tend to fall in with the single cylinder.

A presentation of results for the longer cylinder, which parallels that of Figs. 2-4 for the shorter cylinder, is made in Figs. 5-7. If each of the corresponding figures are compared, it is seen that all of the trends that have been identified for the shorter cylinders carry over without exception for the longer cylinders. The only notable difference between the two cases is that the Nusselt numbers for the longer cylinder are higher than are those for the shorter cylinder by about 10 percent. As a consequence, the downside deviations of the longer-cylinder results from those for the classical infinite cylinder are smaller than are those for the shorter cylinder.

Certain broad generalizations can be made from study of the data of Figs. 2-7. Compared to the single-cylinder case (represented by the circular data symbols), the presence of a cylinder (or cylinders) below the one in question does not 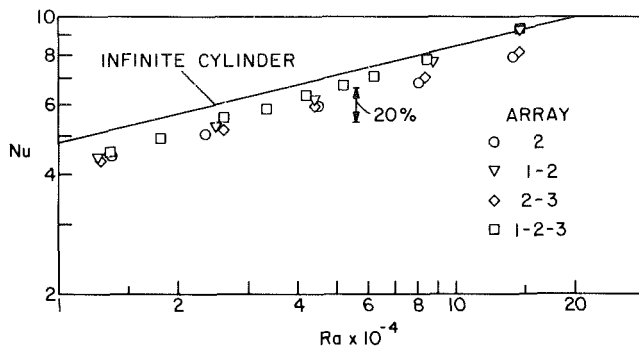enhance the Nusselt number in the lower Rayleigh number range. There may, in fact, be a reduction in the Nusselt number. On the other hand, at the higher Rayleigh numbers, the presence of the lower cylinders does not diminish the Nusselt number and may, in many cases, bring about enhancement. Thus, in broad terms, the single cylinder results provide an upper bound for the multicylinder results at lower Rayleigh numbers and a lower bound at the higher Rayleigh numbers. The extreme deviations of the multicylinder results from those for the single cylinder are about 20 percent. Correlations for the single cylinder are available in [5].
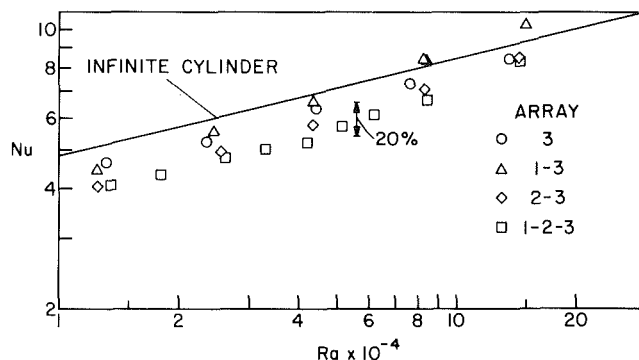
For the intercylinder spacings investigated here, there is no effect of cylinders situated above the cylinder of interest.

For the most part, the Nusselt numbers for the wall-attached horizontal cylinders investigated herein fell below those for the classical infinite horizontal cylinder. The longer the cylinders, the closer are the Nusselt numbers to those for the infinite cylinder.

Array-related characteristics.   It has been established that the lower cylinder of a multicylinder array is not influenced by cylinders situated above it, at least for the intercylinder spacings considered here. Attention will now be focused on the upper cylinder of a two-cylinder array and on its response to various geometrical parameters. Then, the three-cylinder array will be considered and the Nusselt numbers at the successive cylinders in the array compared.

The results for the upper cylinder in various two-cylinder arrays are presented in Fig. 8. The position of the upper cylinder is identified in the legend of the figure, as is the corresponding array. Open symbols are used for the longer cylinders and blackened symbols are used for the shorter cylinders.

The 1-2 and 2-3 arrays are characterized by the same intercylinder spacing, with the distinction between them being that the former is situated lower on the host vertical plate than is the latter. This difference in positioning has a consistent effect on the upper-cylinder Nusselt numbers for the respective arrays – in all cases, the lower the position of the upper cylinder, the higher the Nusselt number. This outcome is probably related to the lesser interference of the plate with the cylinder-to-cylinder interactions when the cylinders are
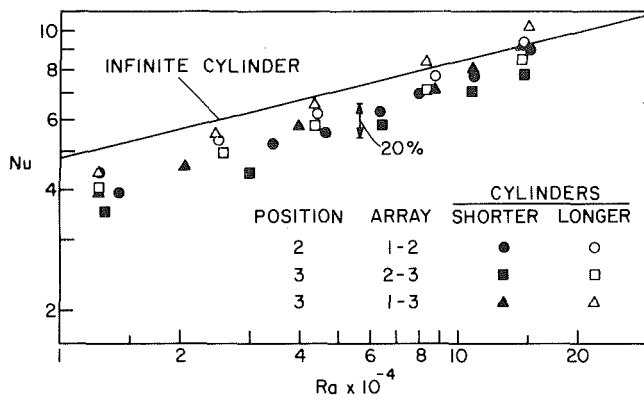
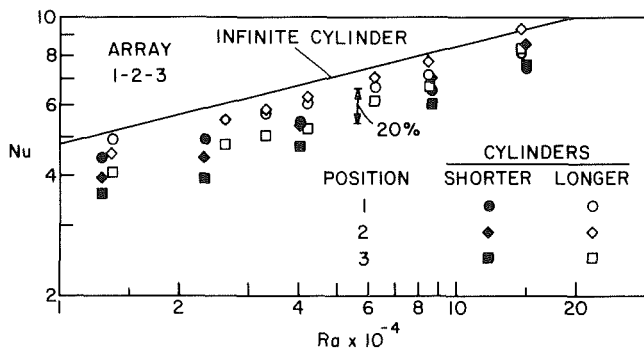Fig. 8 Nusselt numbers at the upper cylinder of a two-cylinder array

Fig. 9 Nusselt numbers at the respective cylinders of a three-cylinder array
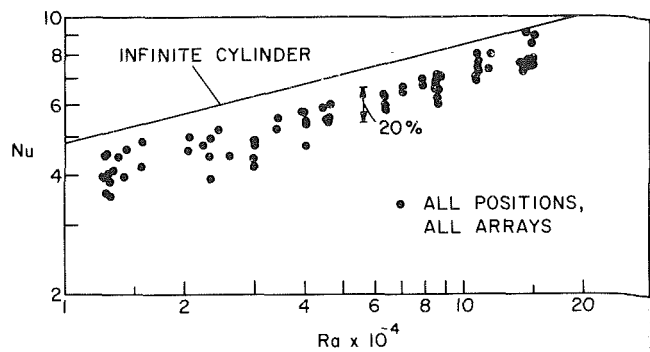

Fig. 10 Nusselt numbers for the shorter cylinders at all positions and for all arrays

Fig. 11 Nusselt numbers for the longer cylinders at all positions and for all arrays

affixed to the lower part of the plate, where the boundary layer is relatively thin. The differences between the upper-cylinder Nusselt numbers for positions 2 and 3 are in the 6–10 percent range.

The effect of intercylinder spacing can be gauged by comparing the Nusselt number results at position 3 for the 2-3 and 1-3 arrays (square and triangle data symbols) and the Nusselt numbers at positions 2 and 3 for the 1-2 and 1-3 arrays (circle and triangle data symbols). In general, it appears that the larger spacing yields higher Nusselt numbers, with a greater enhancement in evidence for the longer cylinders and at higher Rayleigh numbers. The aforementioned two types of comparisons – square versus triangle and circle versus triangle – yield different degrees of enhancement corresponding to the enlarged intercylinder spacing. The general range of enhancement due to enlarged intercylinder spacing is from 0 to 20 percent.

The Nusselt numbers for the successive cylinders in a three-cylinder array are presented in Fig. 9 for both the longer and shorter cylinders (open and blackened symbols). The results for the two different cylinder lengths display remarkably consistent trends. At low Rayleigh numbers, there is a monotonic decrease of the Nusselt number in the streamwise direction, i.e., from 1 to 2 to 3. However, as the Rayleigh number increases, the Nusselt number at position 1 (the lowest position) tends to decrease relative to the others, so that at the highest Rayleigh number it actually falls below that at position 3 (the uppermost position). Thus, at the higher Rayleigh numbers, the second cylinder (position 2) experiences the highest Nusselt number. These trends underscore the complexity of the participating fluid flow and heat transfer processes.

Global presentation of results. The Nusselt number data for the shorter cylinder at all of the three positions and for all of the arrays are brought together in Fig. 10, and a similar presentation for the longer-cylinder Nusselt numbers is made in Fig. 11. The data spread in these figures is not scatter;
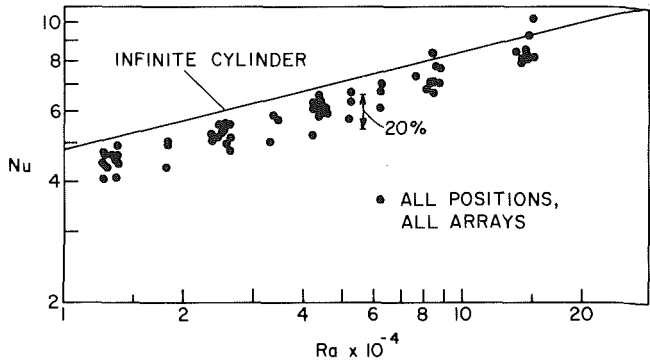
rather, it represents a variation due to differences in the fluid flow and heat transfer processes associated with the position of the cylinder and the presence or absence of other cylinders.

The maximum data spread for the shorter cylinder is about 30 percent, and the spread tends to diminish at higher Rayleigh numbers. A mean line through these data lies about 20 percent below the line for the infinite cylinder, so that equation (6) can be employed for estimating purposes with the constant 0.480 replaced by 0.384. For the longer cylinder, the data spread is about 20 percent, and equation (6), with 0.480 replaced by 0.413, can be used for estimations of the Nusselt number. Overall, the shorter-cylinder Nusselt numbers fall below those for the longer cylinder by 5 to 10 percent.

Concluding Remarks

The experiments reported here have provided basic data about the natural convection heat-transfer coefficients for arrays of short horizontal cylinders (e.g., pin fins) affixed to a vertical plate. The effects of cylinder length-to-diameter ratio, intercylinder spacing, position at which the cylinder is attached to the host vertical plate, and the Rayleigh number were investigated.

Convective interactions among the cylinders were identified by examining the per-cylinder Nusselt number for a single cylinder and for multicylinder arrays. In general, for the intercylinder spacings investigated here, the Nusselt number at a given cylinder was uninfluenced by cylinders situated above it. The extent to which a given cylinder was affected by cylinders situated below it was found to depend on the Rayleigh number. At lower Rayleigh numbers in the investigated range (i.e., $1.4 \times 10^4 \leq Ra \leq 1.4 \times 10^5$), the presence of cylinders situated below that in question gave rise to Nusselt numbers that were less or approximately equal to that of the single cylinder. On the other hand, at higher Rayleigh numbers in the range, the single-cylinder Nusselt number was a lower bound. The extreme deviations of the multicylinder results from those for the single cylinder were about 20 percent.

In a two-cylinder array with a fixed intercylinder spacing, higher upper-cylinder Nusselt numbers were encountered when the array was positioned in the lower reaches of the host plate rather than in the upper reaches of the plate. Larger intercylinder spacings tended to yield higher upper-cylinder Nusselt numbers, especially for longer cylinders and larger Rayleigh numbers.

In a three-cylinder array, the Nusselt numbers for the successive cylinders decreased monotonically in the flow direction in the lower part of the Rayleigh number range. However, at the larger Rayleigh numbers, the highest Nusselt numbers were encountered at the second cylinder.

All of the basic trends were found to be common for both of the investigated cylinder length-to-diameter ratios. In the mean, the shorter-cylinder Nusselt numbers fell about 5 to 10 percent below those of the longer cylinder.

For the most part, the Nusselt numbers for the wall-attached horizontal cylinders investigated here fell below those for the classical horizontal cylinder of infinite length. On the average, the deviations were about 20 percent for the shorter cylinders and about 15 percent for the longer cylinders.

References

1 Starner, K. E., and McManus, H. N., Jr., "An Experimental Investigation of Free Convection from Rectangular Fin Arrays," ASME Journal of Heat Transfer, Vol. 85, 1963, pp. 273–278.

2 Welling, J. R., and Wooldridge, C. B., "Free Convection Heat Transfer Coefficients from Rectangular Vertical Fins," ASME Journal of Heat Transfer, Vol. 87, 1965, pp. 439–444.

3 Chaddock, J. B., "Free Convection Heat Transfer from Vertical Rectangular Fin Arrays," ASHRAE Journal, Vol. 12, August, 1970, pp. 53–60.

4 Sparrow, E. M., and Bahrami, P. A., "Experiments on Natural Convection from Vertical Parallel Plates with Either Open or Closed Edges," ASME Journal of Heat Transfer, Vol. 102, 1980, pp. 221–227.

5 Sparrow, E. M., and Chrysler, G. M., "Natural Convection Heat Transfer Coefficients for a Short Horizontal Cylinder Attached to a Vertical Plate," ASME Journal of Heat Transfer, Vol. 103, No. 3, 1981, pp. 630–637.

6 Sparrow, E. M., and Gregg, J. L., "The Variable Fluid Property Problem in Free Convection," Trans. ASME, Vol. 80, 1958, pp. 878–886.

7 McAdams, W. H., Heat Transmission, 3rd ed., McGraw-Hill, New York, 1954.

8 Churchill, S. W., and Chu, H. H. S., "Correlating Equations for Laminar and Turbulent Free Convection from a Horizontal Cylinder," International Journal of Heat and Mass Transfer, Vol. 18, 1975, pp. 1049–1053.

9 Morgan, V. T., "The Overall Convective Heat Transfer from Smooth Circular Cylinders," in Advances in Heat Transfer, Vol. 11, Academic Press, New York, 1975, pp. 199–264.

10 Raithby, G. D., and Hollands, K. G. T., "Laminar and Turbulent Free Convection from Elliptic Cylinders, with a Vertical Plate and Horizontal Circular Cylinder as Special Cases," ASME Journal of Heat Transfer, Vol. 98, 1976, pp. 72–80.

11 Fand, R. M., Morris, E. W., and Lum, M., "Natural Convection Heat Transfer from Horizontal Cylinders to Air, Water and Silicone Oils for Rayleigh Numbers Between 3×10^2 and 2×10^7," International Journal of Heat and Mass Transfer, Vol. 20, 1977, pp. 1173–1184.

M. Kumari

Research Student.

G. Nath

Professor.

Department of Applied Mathematics,
Indian Institute of Science,
Bangalore 560012, India

Unsteady Mixed Convection Near the Stagnation Point in Three-Dimensional Flow

The combined effect of forced and free convection on the unsteady laminar incompressible boundary-layer flow with mass transfer at the stagnation point of a three-dimensional body with time dependent wall temperature has been studied. Both semisimilar and self-similar solutions have been obtained. The governing equations have been solved numerically using an implicit finite-difference scheme. The results indicate that the buoyancy force strongly affects the skin friction whereas its effect on the heat transfer is comparatively less. However, the heat transfer is significantly changed due to the wall temperature which varies with time, but the skin friction is little affected by it. The mass transfer and Prandtl number affect both the skin friction and heat transfer. The buoyancy force which assists the forced flow causes an overshoot in both the velocity components.

Introduction

The forced or free convection boundary-layer flows over two-dimensional, axisymmetric, and three-dimensional bodies have been extensively studied in the past. Excellent reviews of the pertinent literature for both types of flows are given in [1–3]. It may be remarked that the neglect of buoyancy force effects on forced convective heat transfer may not be justified when the velocity is small and the temperature difference between the surface and the ambient fluid is large. Thus the prediction of the heat-transfer rate under mixed condition is of great practical importance. In spite of its importance, the combined effect of both forced and free convection (i.e., mixed convection) has not been studied as extensively as their individual effects. However, in recent years there has been increasing interest in the mixed convection flows. The mixed convection flows over two-dimensional bodies without pressure gradient (flat plate) under boundary-layer approximations have been studied by Ocsthuizen and Hart [4], Gryzagoridis [5], and Chen et al. [6]. Furthermore, there has been a number of studies [7–11] dealing with two-dimensional and axisymmetric bodies with pressure gradient (cylinders and spheres). Most of the investigations pertain to steady flows. However, a couple of studies of the unsteady flow over two-dimensional bodies have been made. Most of the pertinent literature before 1971 has been reviewed by Gebhert [12]. It may be remarked that the unsteady mixed convection on three-dimensional bodies is of great practical as well as theoretical importance, but it has not been studied so far.

The aim of this paper is to study the combined effect of the unsteady forced and free convection (i.e., mixed convection) flow of an incompressible fluid at a three-dimensional stagnation point with mass transfer when the free stream velocity and wall temperature vary arbitrarily with time. The

resulting semisimilar partial differential equations governing the flow have been solved numerically using an implicit finite-difference scheme [13]. Further, it has been shown that when the free-stream velocity varies inversely as a linear function of time and wall temperature varies inversely as a quadratic function of time, then the self-similar solution of the foregoing problem exists which has also been solved numerically using an implicit finite-difference scheme [13]. The results for both the cases have been compared with the published results.

Governing Equations

We consider the unsteady laminar incompressible boundary-layer flow with mass transfer near the stagnation point of a three-dimensional porous body under the combined effect of forced and free convection. We choose a locally orthogonal set of coordinates $oxyz$ at the body surface in such a way that the origin o coincides with the lower stagnation point and the parametric curves $x =$ constant and $y =$ constant on the surface coincide with the lines of curvatures. Let x and y be the principal (axial) and transverse directions and z the normal direction (perpendicular to the x and y-plane). Let the gravitational field, g, act opposite to the direction of the resultant velocity at the edge of the boundary layer U_e (having components $u_e = ax$, $v_e = by$, $w_e = 0$ in the x, y, and z directions, respectively) in the plane of x and y. We have taken the temperature outside the boundary layer as T_∞ (a constant), and the body at $t = 0$ is maintained at a constant temperature T_{wo}. The buoyancy force then acts in the same direction as the forced flow when $T_{wo} > T_\infty$ and in the opposite direction to the forced flow when $T_{wo} < T_\infty$. The components of the buoyancy force in the x, y, and z directions are

$$g\beta x(T - T_\infty)/L, \quad g\beta cy(T - T_\infty)/L, \quad 0 \qquad (1)$$

The z component of the buoyancy force will be zero as the

direction of g is perpendicular to the z-axis. Here we have assumed that the principal (x) and transverse (y) pressure gradient terms induced by the buoyancy force is very small as compared with the buoyancy force. This assumption is justified provided than $\gamma << \mathrm{Re}_x^{1/2}/\eta_\infty$. For most mixed convection problems, $\mathrm{Re}_x \simeq 10^3 - 10^5$ and $\eta_\infty \simeq 6$. Hence, $\gamma << 80$ deg, which is satisfied in the present case. Since the direction of gravity, g, is perpendicular to the z-axis, its component in the z-direction is zero, and hence it does not introduce any buoyancy-induced pressure gradient in the x and y components of the momentum equations $(2(b)$ and $2(c))$. Furthermore, the fluid properties are assumed to be constant except that the density variations within the fluid are allowed to contributed to the buoyancy forces. The free-stream velocity and surface temperature vary arbitrarily with time and the dissipation terms are considered to be negligible near the stagnation point. The appropriate boundary-layer equations governing the flow can be expressed as

$$u_x + v_y + w_z = 0 \qquad (2a)$$

$$u_t + uu_x + vu_y + wu_z - g\beta x(T-T_\infty)/L = -\rho^{-1}p_x + \nu u_{zz} \qquad (2b)$$

$$v_t + uv_x + vv_y + wv_z - g\beta cy(T-T_\infty)/L = -\rho^{-1}p_y + \nu v_{zz} \qquad (2c)$$

$$T_t + uT_x + vT_y + wT_z = \mathrm{Pr}^{-1}\nu T_{zz} \qquad (2d))$$

where

$$-p_x = (u_e)_t + u_e(u_e)_x, \quad -p_y = (v_e)_t + v_e(v_e)_y \qquad (2e)$$

The relevant initial and boundary conditions are

$$u(x,y,z,0) = u_i(x,y,z); \quad v(x,y,z,0) = v_i(x,y,z)$$

$$w(x,y,z,0) = w_i(x,y,z); \quad T(x,y,z,0) = T_i(x,y,z)$$

$$u(x,y,0,t) = v(x,y,0,t) = 0; \quad w(x,y,0,t) = (w)_w$$

$$T(x,y,0,t) = T_\infty + (T_{wo} - T_\infty)R(t^*);$$

$$u(x,y,\infty,t) = u_e(x,t)$$

$$v(x,y,\infty,t) = v_e(y,t); \quad T(x,y,\infty,t) = T_\infty \qquad (3)$$

Semisimilar Equations. The set of partial differential equations (2) involving four independent variables x, y, z, and t can be reduced to semisimilar partial differential equations involving two independent variables η and t^* by applying the following transformations

$$\eta = (a/\nu)^{1/2}z, \quad t^* = at, \quad F = f_\eta(\eta,t^*), \quad S = s_\eta(\eta,t^*)$$

$$u = ax\varphi(t^*)F(\eta,t^*), \quad v = by\varphi(t^*)S(\eta,t^*)$$

$$w = -(a\nu)^{1/2}(f+cs)\varphi(t^*),$$

$$(T-T_\infty)/(T_{wo}-T_\infty) = G(\eta,t^*)$$

$$u_e = ax\varphi(t^*), \quad v_e = by\varphi(t^*),$$

$$c = b/a = (dv_e/dy)_0/(du_e/dx)_0$$

$$\alpha = \mathrm{Gr}/\mathrm{Re}_L^2, \quad \mathrm{Re}_L = aL^2/\nu,$$

$$\mathrm{Gr} = \beta g(T_{wo} - T_\infty)L^3/\nu^2 \qquad (4)$$

We find that $(2a)$ is identically satisfied and equations $(2b)$ to $(2d)$ can be expressed in dimensionless form as

$$F_{\eta\eta} + \varphi[(f+cs)F_\eta + 1 - F^2] + \varphi^{-1}\varphi_{t^*}(1-F)$$
$$-F_{t^*} + \varphi^{-1}\alpha G = 0 \qquad (5a)$$

$$S_{\eta\eta} + \varphi[(f+cs)S_\eta + c(1-S^2)] + \varphi^{-1}\varphi_{t^*}(1-S)$$
$$-S_{t^*} + \varphi^{-1}\alpha G = 0 \qquad (5b)$$

$$\mathrm{Pr}^{-1}G_{\eta\eta} + \varphi(f+cs)G_\eta - G_{t^*} = 0 \qquad (5c)$$

The appropriate boundary conditions are

$$\left. \begin{array}{ll} F=S=0, & G=R(t^*) \text{ at } \eta=0 \\ F=S=1, & G=0 \text{ as } \eta \to \infty \end{array} \right\} \text{ for } t^* \geq 0 \qquad (6)$$

Here

$$f = \int_0^\eta F \, d\eta + f_w, \quad s = \int_0^\eta S \, d\eta, \quad s_w = 0$$

$$f_w = -(w_w/u_e)(\mathrm{Re}_x)^{1/2}, \quad \mathrm{Re}_x = ax^2/\nu \qquad (7)$$

It has been assumed here that the flow is initially $(t^* = 0)$ steady and changes to unsteady for $t^* > 0$. Therefore, the initial conditions for F, S, and g at $t^* = 0$ are given by the steady-flow equations obtained by putting

$$\varphi(t^*) = R(t^*) = 1, \quad \varphi_{t^*} = 0, \quad \partial/\partial t^* = 0 \qquad (8)$$

in (5). These steady-state equations for $\alpha = 0$ (i.e., in the absence of buoyancy forces) represent three-dimensional stagnation-point forced convection flow which has been studied by Horwarth [14], and Hayday and Howlus [15]. The set of equations (5) for $\alpha = 0$ represents the unsteady three-dimensional stagnation point forced convection flow which has been studied by Kumari [16].

Here φ is an arbitrary function of t^* representing the nature of unsteadiness in the inviscid flow and has a continuous first derivative for $t^* \geq 0$. Also $R(t^*)$ is an arbitrary function of t^*, which represents the nature of unsteadiness in the wall temperature. If the normal velocity at the wall w_w is chosen in such a manner that $(w_w/u_e)(\mathrm{Re}_x)^{1/2}$ is a constant, then the surface mass transfer parameter f_w will be a constant (i.e., $f_w = A$) and $A \gtreqless 0$, according to whether there is suction or injection.

Nomenclature

a,b = velocity gradients at the edge of the boundary layer in the x and y directions, respectively, when $t^* = 0$

A = constant

c = ratio of the velocity gradients at the edge of the boundary layer when $t^* = 0$

$C_f, \bar{C}_f$ = skin-friction coefficients at the wall in the x and y directions, respectively

f,s = dimensionless stream functions

f_w = dimensionless mass-transfer parameter

F,S = dimensionless velocity components in the x and y directions, respectively

$(f_\eta)_w, (S_\eta)_w$ = skin-friction parameters in the x and y directions, respectively

g = acceleration due to gravity

G = dimensionless temperature

$(G_\eta)_w$ = heat-transfer parameter at the wall

Gr = Grashof number

L = characteristic length

Nu = Nusselt number

p = pressure

Pr = Prandtl number

$R(t^*)$ = function of t^*

Re_L = Reynolds number defined with respect to L

$\mathrm{Re}_x, \overline{\mathrm{Re}}_x$ = local Reynolds numbers

t, t^* = dimensional and dimensionless times, respectively

T = temperature

T_{wo} = wall temperature at $t = 0$ (or $t^* = 0$)

It may be noted that for $T_{wo} > T_\infty$ (i.e., when the wall temperature at $t^* = 0$ is greater than the free-stream temperature), the buoyancy force which arises due to the temperature difference will aid the forced flow. On the other hand, if $T_{wo} < T_\infty$, the resulting buoyancy force will oppose the forced flow. Consequently, the buoyance parameter $\alpha > 0$ for $T_{wo} > T_\infty$ (i.e., for aiding force) and $\alpha < 0$ for $T_{wo} < T_\infty$ (i.e., for opposing force).

The skin-friction coefficients in the x and y directions and the heat-transfer coefficient can be expressed in the form

$$C_f = 2\tau_x/\rho \bar{u}_e^2 = 2(\text{Re}_x)^{-\frac{1}{2}} \varphi(t^*)(F_\eta)_w \tag{9a}$$

$$\bar{C}_f = 2\tau_y/\rho \bar{u}_e^2 = 2(\text{Re}_x)^{-\frac{1}{2}} (v_e/u_e) \varphi(t^*)(S_\eta)_w$$

$$\text{Nu} = x(T_z)_w / (T_{wo} - T_\infty) = (\text{Re}_x)^{\frac{1}{2}} (G_\eta)_w \tag{9b}$$

Self-Similar Equations. The self-similar solution of the set of equations (2) exist if the free-stream velocity varies inversely as a linear function of time and the surface wall temperature as a quadratic function of time. Applying the following transformations

$$\eta = (a/\nu)^{\frac{1}{2}} (1 - \lambda t^*)^{-\frac{1}{2}} z, \quad t^* = at, \quad \lambda < t^{*-1} \tag{10a}$$

$$u = ax(1 - \lambda t^*)^{-1} F(\eta), \quad v = by(1 - \lambda t^*)^{-1} S(\eta),$$

$$w = -[(a\nu)^{\frac{1}{2}} (1 - \lambda t^*)^{-\frac{1}{2}} (f + cs)] \tag{10b}$$

$$(T - T_\infty)/(T_{wo} - T_\infty) = (1 - \lambda t^*)^{-2} G(\eta),$$

$$(T_w - T_\infty)/(T_{wo} - T_\infty) = (1 - \lambda t^*)^{-2} \tag{10c}$$

$$u_e = ax(1 - \lambda t^*)^{-1}, \quad v_e = by(1 - \lambda t^*)^{-1},$$

$$F_\eta = F, \quad s_\eta = S, \quad f = \int_0^\eta F \, d\eta + f_w,$$

$$f_w = -(w_w/u_e)(\text{Re}_x)^{\frac{1}{2}}, \quad s_w = 0 \tag{10d}$$

to equations (1), we get

$$F_{\eta\eta} + (f + cs)F_\eta + 1 - F^2 + \lambda(1 - F - 2^{-1}\eta F_\eta) + \alpha G = 0 \tag{11a}$$

$$S_{\eta\eta} + (f + cs)S_\eta + c(1 - S^2) + \lambda(1 - S - 2^{-1}\eta S_\eta) + \alpha G = 0 \tag{11b}$$

$$\text{Pr}^{-1} G_{\eta\eta} + (f + cs)G_\eta - 2\lambda(G - 4^{-1}\eta G_\eta) = 0 \tag{11c}$$

The boundary conditions are

$$F = S = 0, \quad G = 1 \text{ at } \eta = 0$$

$$F = S = 1, \quad G = 0 \text{ as } \eta \to \infty \tag{12}$$

Here f_w is also a constant (i.e., $f_w = A$) if w_w is selected in such a way that $(w_w/u_e)(\text{Re}_x)^{\frac{1}{2}}$ is a constant. The skin-friction and heat-transfer coefficients are now given by

$$C_f = 2\tau_x/\rho \bar{u}_e^2 = 2(\overline{\text{Re}}_x)^{-\frac{1}{2}} (F_\eta)_w$$

$$\bar{C}_f = 2\tau_y/\rho \bar{u}_e^2 = 2(\overline{\text{Re}}_x)^{-\frac{1}{2}} (v_e/u_e)(S_\eta)_w$$

$$\text{Nu} = x(T_z)_w / (T_w - T_\infty) = (\overline{\text{Re}}_x)^{\frac{1}{2}} (G_\eta)_w \tag{13}$$

$$\overline{\text{Re}}_x = ax^2/[(1 - \lambda t^*)\nu]$$

The set of equations (11) for $\alpha = 0$ represents unsteady forced flow with time-dependent wall temperature. The unsteady forced flow problem with constant wall temperature has been studied by Teipel [12]. For this case, the equations are same as (11) with $\alpha = 0$, except that G in (11c) is not present.

It may be remarked that when $\lambda > 0$, we have an accelerating flow provided $\lambda t^* < 1$. This, however, does not restrict the validity of the results because of the arbitrary scale factor included in the definition of t^*. When $\lambda < 0$, we get a decelerating flow. Although no lower limit of λ can be fixed mathematically, due to decelerating nature of the flow field, the solution may not exist below a certain value of λ when the flow separates from the boundary. For example, for the opposing flow ($\alpha = -0.25$), the separation $((F_\eta)_w = 0)$ occurs when $\lambda \sim -1.2$. Here the results have been presented for the range $-1 \le \lambda \le 1$.

Results and Discussion

Semi-Similar Case. The set of partial differential equations (5) under initial conditions obtained by using the relations (8) in (5) and boundary conditions (6) have been solved numerically using an implicit finite-difference scheme. Since the method is described in great detail in [13], for the sake of brevity, it is not presented here. The step sizes $\Delta\eta$ and Δt^* as well as η_∞ (i.e., the edge of the boundary layer) have been optimized. The results presented here are independent of step sizes or η_∞ up to the 4th decimal place. Computations have been carried out for various values of the parameters using two forms of the free-stream velocity distributions: (i) a constantly accelerating flow represented by $\varphi(t^*) = 1 + \epsilon t^{*2}$ and (ii) a periodic fluctuating flow given by $\varphi(t^*) = 1 + \epsilon_1 \sin^2(\omega^* t^*)$. The variation of the wall temperature has been assumed to be of the form $R(t^*) = 1 - \epsilon_2 t^*$. Since most three-dimensional body shapes of practical interest lie between a cylinder ($c = 0$) and a sphere ($c = 1$), we have confined our studies to the range $0 \le c \le 1$.

In order to test the accuracy of the method, we have compared our skin-friction and heat-transfer results for the steady forced convection flow ($t^* = 0$, $\alpha = 0$) with those of Howarth [14] and Hayday and Bowlus [15] and for the unsteady forced convection flow ($t^* > 0$, $\alpha = 0$) for $\varphi(t^*) = 1$

Nomenclature (cont.)

T_∞	=	free-stream temperature (constant)		
u,v,w	=	velocity components in the x, y, and z directions respectively		
$\bar{u}_e$	=	value of u_e at $t^* = 0$		
x,y,z	=	principle, transverse, and normal directions, respectively		
α	=	ratio of Grashof number to Reynolds number squared		
β	=	bulk coefficient of thermal expansion		
γ	=	angle which the		

direction of gravity makes with y-axis

$\epsilon, \epsilon_1, \epsilon_2$ = positive constants
η = dimensionless independent variable
λ = dimensionless parameter denoting the unsteadiness in the free-stream velocity
ν = kinematic viscosity
ρ = density
τ_x, τ_y = shear stresses at the wall in the x and y directions, respectively
$\varphi(t^*)$ = function of t^*
ω^* = frequency parameter

Subscripts

e, w = denote conditions at the edge of the boundary layer and on the surface, respectively
i = denotes initial conditions
0 = denotes conditions at the stagnation point
$t, t^*, x, y,$ = denote derivatives
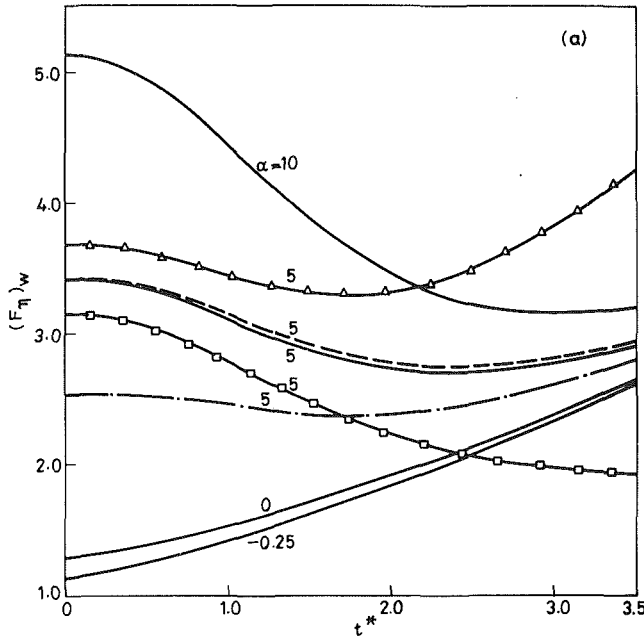z, η = with respect to t, t^*, x, y, z, and η, respectively

Fig. 1(a) Skin-friction parameter in the x direction, $(F_\eta)_w$

Fig. 1(b) Skin-friction parameter in the y direction, $(S_\eta)_w$
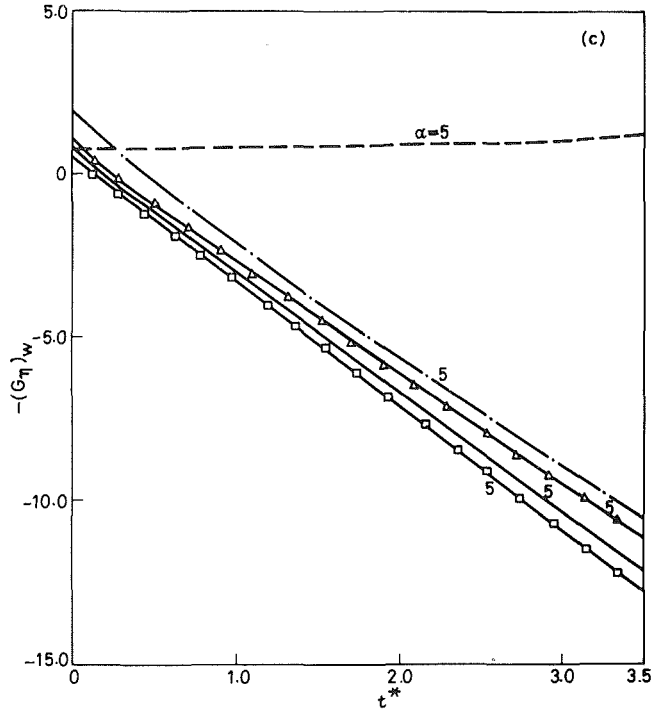

Fig. 1(c) Heat-transfer parameter $(G_\eta)_w$ for $\varphi(t^*) = 1 + \epsilon t^{*2}$ semi-similar flow)

Fig. 1 $c = 0.5, \epsilon = 0.25, \epsilon_2 = 0.05;$ ——, $A = 0, \text{Pr} = 0.72, R(t^*) = 1 - \epsilon_2 t^*;$ —△—, $A = 0.5, \text{Pr} = 0.72, R(t^*) = 1 - \epsilon_2 t^*;$ —□—, $A = -0.5, \text{Pr} = 0.72, R(t^*) = 1 - \epsilon_2 t^*;$ —·—, $A = 0, \text{Pr} = 10.0, R(t^*) = 1 - \epsilon_2 t;$ ----, $A = 0, \text{Pr} = 0.72, R(t^*) = 1$

+ t^* with those of Kumari [16]. Furthermore, we have also compared our results for skin friction, heat transfer, velocity, and temperature profiles for steady mixed convection flow ($t^* = 0$, $\alpha > 0$) for $c = 1$ (axisymmetric case) with those of Chen and Mucoglu [11]. All these results are found to be in excellent agreement. In fact, they are found to differ only in the fourth decimal place. Hence, these comparisons are not shown here for the sake of brevity. The results for constantly accelerating flow represented by $\varphi(t^*) = 1 + \epsilon t^{*2}$ are shown in Figs. 1–2 and Table 1.

The effects of buoyancy force represented by the parameter, α, Prandtl number, Pr, and mass transfer, A, on the skin friction and heat transfer $((F_\eta)_w, (S_\eta)_w, -(G_\eta)_w)$ have been presented in Figs. 1(a)–1(c). It is evident from Figs.

1(a)–1(b) that for small t^*, $(F_\eta)_w$ and $(S_\eta)_w$ increase appreciably when the buoyancy force which assists the forced flow ($\alpha > 0$) increases. This is due to the fact that the buoyancy force ($\alpha > 0$) gives rise to favourable pressure gradient which accelerates the fluid in the boundary layer and thereby increases both the skin friction and heat transfer. However, for large t^*, the effect of α ($\alpha > 0$) tends to diminish because the forced convection forces become equally important as the buoyancy forces which results in weak effect of α for large t^* (for small t^*, buoyancy forces dominate over the forced convection forces). For buoyancy assisted forced flow ($\alpha > 0$), $(F_\eta)_w$ and $(S_\eta)_w$ first decrease as t^* increases from zero until a minimum value is reached and then they begin to increase as t^* further increases. On the other hand, for purely forced flow ($\alpha = 0$) or for buoyancy opposed forced flow ($\alpha < 0$), $(F_\eta)_w$ and $(S_\eta)_w$ continuously increase as t^* increases. This is because for a given α ($\alpha > 0$), as t^* increases from zero, the skin friction parameters reduce due to buoyancy effect, but increase due to forced convection effect, but as the buoyancy effect is dominant over forced convection effect for small t^*, the net result is the reduction in the skin friction.

It is evident from Figs. 1(a)–1(c) that the heat transfer parameter $-(G_\eta)_w$ is strongly affected by the variation of the wall temperature with time ($R(t^*) = 1 - \epsilon_2 t^*$), whereas the skin friction is rather little affected by it. The reason for such a behaviour is that the variation of the wall temperature with time is the dominant force for the heat-transfer rate, but plays a minor role as far as the skin friction is concerned. Also, for $R(t^*) = 1 - \epsilon t^*$, it is observed that for small t^* ($t^* \approx 0.2$), the heat-transfer parameter $(G_\eta)_w$ is negative, but subsequently changes to positive values. This implies that for small times, the heat is transferred from the wall to the fluid, but after a certain instant t^*, the heat is transferred from the fluid to the wall as the wall becomes colder than the fluid due to the reduction in the wall temperature with time t^*. When the wall

Table 1 Heat transfer parameter $(G_\eta)_w$ for $\varphi(t^*) = 1 + \epsilon t^{*2}$, $R(t^*) = 1 - \epsilon_2 t^*$, $c = 0.5$, $A = 0$, $Pr = 0.72$, $\epsilon = 0.25$, $\epsilon_2 = 0.05$

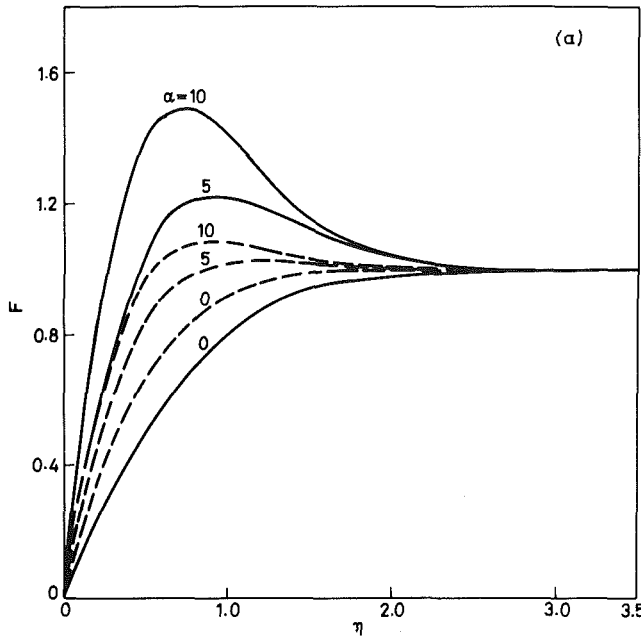| α	t^* 0	1	2	3	4
-0.25	-0.5711	3.1906	6.8060	10.3473	13.8843
0	-0.5854	3.1768	6.7981	10.3446	13.8831
4	-0.7554	3.0189	6.6950	10.2975	13.8611
10	-0.8497	2.9317	6.6296	10.2587	13.8414

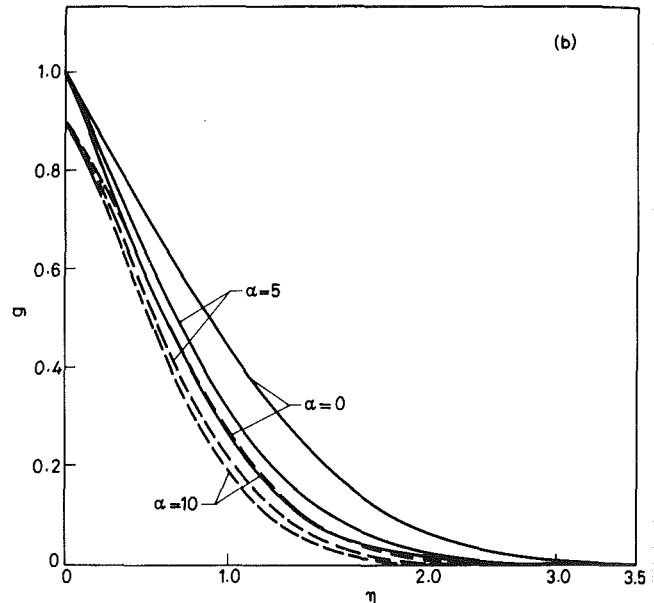Fig. 2(a)   Velocity profiles in the x direction F

Fig. 2(b)   Temperature profiles G for $\varphi(t^*) = 1 + \epsilon t^{*2}$, semisimilar flow

Fig. 2 $R(t^*) = 1 - \epsilon_2 t^*$, $c = 0.5$, $Pr = 0.72$, $\epsilon = 0.25$, $\epsilon_2 = 0.05$, $A = 0$;
——, $t^* = 0$; – – – –, $t^* = 2$

temperature is constant for all times $(R(t^*) = 1)$, $(G_\eta)_w < 0$ for all t^* which implies that the heat is transferred from the wall to the fluid. We also observe that the effect of buoyancy parameter α is more pronounced on the skin friction than on the heat transfer (see Figs. 1(a)–1(c) and Table 1). This is because the buoyancy force gives rise to favourable pressure gradient for $\alpha > 0$ and adverse pressure gradient for $\alpha < 0$ and as the skin friction is more dependent on the pressure gradient and the heat transfer is weakly dependent on it, the skin friction is affected by α more than the heat transfer.

Figures 1(a)–1(c) also show the effect of mass transfer (injection and suction), and Prandtl number on the skin friction and heat transfer $((F_\eta)_w, (S_\eta)_w, -(G_\eta)_w$. It is found that injection $(A < 0)$ reduces the skin friction and heat transfer and suction $(A > 0)$ does the reverse. This is due to thickening of both velocity and thermal boundary layers with injection which causes deceleration in the fluid with the result that both skin friction and heat transfer decrease with injection. For suction, the opposite trend is observed. We also observe that the skin friction $((F_\eta)_w, (S_\eta)_w)$ decreases as Pr increases. This is because of the increase of the velocity boundary layer thicknesses with Pr (higher Pr implies more viscous fluid), which results in deceleration of the fluid and a reduction of the skin friction. On the other hand, the heat transfer $-(G_\eta)_w$ is found to increase with Pr. This is to be expected, because a larger Prandtl number results in a thinner thermal boundary layer with a corresponding large temperature gradient at the wall, and hence a large surface heat transfer. The effect of c, the parameter characterizing the nature of the stagnation point, on the skin friction and heat transfer $((F_\eta)_w, (S_N)_w), -(G_\eta)_w)$ has also been studied, although not shown in the figures. It is found that both the

skin friction and heat transfer decrease as c decreases from 1 to zero whatever may be the values of α, t^* and A. The reason for this trend is that the fluid is decelerated due to the reduction in the favourable gradient as c decreases from 1 to zero, and, thereby, both the skin friction and heat transfer are reduced.

The effect of buoyancy force α on velocity and temperature profiles (F, G) are shown in Figs. 2(a)–(b). Since profiles for S are qualitatively similar to those of F, they are not shown here to reduce the number of figures. We find that there is a velocity overshoot in both the velocity components F and S for buoyancy assisted flow $(\alpha > 0)$, and the velocity overshoot increases as α increases (Fig. 2(a)). However, it decreases as t^* increases. There is no velocity overshoot either for purely forced flow $(\alpha = 0)$ or for buoyance opposed flow $(\alpha < 0)$. The velocity overshoot is because buoyancy force $(\alpha > 0)$ gives rise to a favourable pressure gradient resulting in velocity which adds to the forced convection velocity. The buoyancy opposed flow $(\alpha < 0)$ gives rise to adverse pressure gradient which reduces the forced convection velocity. As mentioned earlier, the net effect of buoyancy force $\alpha > 0$ and forced convection force decreases with time which results in reduction in the velocity overshoot with time. The temperature profiles (Fig. 2(b)) show that for the case of aiding flow $(\alpha > 0)$, an increase in buoyancy force α results in an increase in the temperature gradient at the wall due to the decrease in the thermal boundary layer thickness. The opposite trend is evident for the case of opposing flow $(\alpha < 0)$.

The skin friction and heat transfer for the periodic free stream velocity distribution $(\varphi(t^*) = 1 + \epsilon_1 \sin^2(\omega^* t^*))$ have also been obtained, but for the sake of brevity, they are not presented here. It is found that the skin friction responds
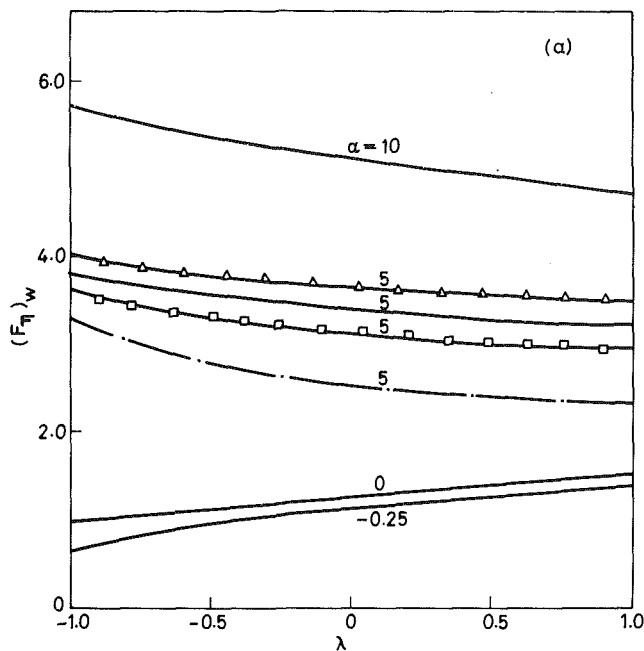
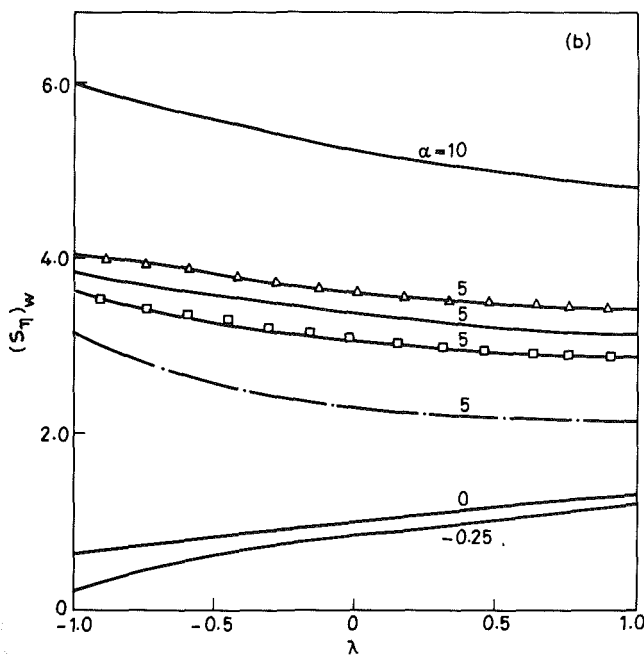Fig. 3(a)   Skin-friction parameter in the x direction, $(F_\eta)_w$

Fig. 3(b)   Skin-friction parameter in the y direction, $(S_\eta)_w$

Fig. 3(c)   Heat-transfer parameter − $(G_\eta)_w$ for self-similar flow

Fig. 3   c = 0.5; ——, A = 0, Pr = 0.72;— □ —, A = −0.5, Pr = 0.72; —·—, A = 0, Pr = 10.0; —△—, A = 0.5, Pr = 0.72

more to the fluctuations of the free stream velocity than the heat transfer, whereas the heat transfer is strongly affected by the variation of the wall temperature with time. This is because the variations of heat transfer and skin friction with time explicitly depend on the time-dependent wall temperature and the velocity induced by the fluctuations of the free-stream velocity, respectively.

Self-Similar Case. The set of equations (11) under boundary conditions (12) has also been solved using the implicit finite-difference scheme as mentioned earlier. The results for $\alpha = 0$, and Pr = 1 and 0.7 obtained by solving the set of equations (11) without the term $-2\lambda G$ in (11c) (the reason has been mentioned earlier) have been compared with those of Teipel [17], and they are found to be in excellent agreement (they differ only in the fourth decimal place). Computations have been carried out for various values of the parameters.
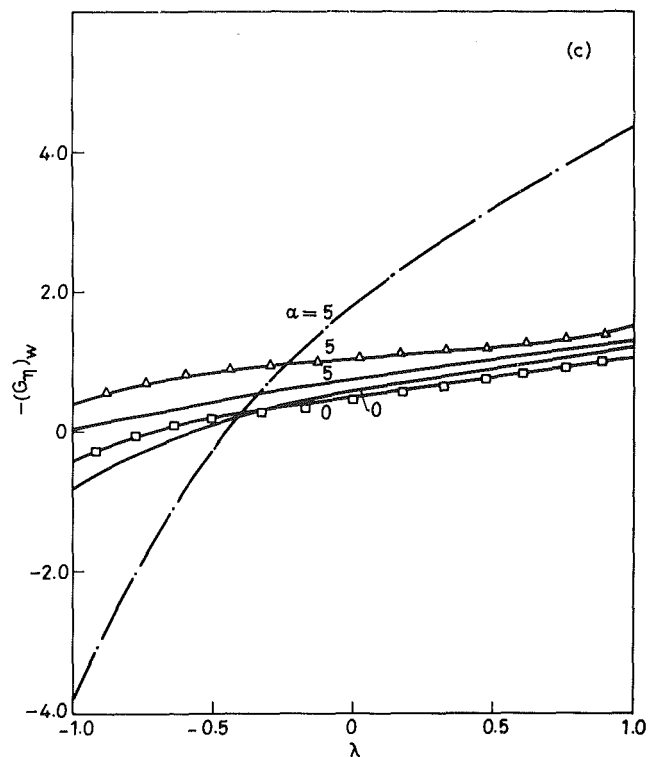
However, for the sake of brevity, only some representative results are presented.

Figures 3(a)–3(c) display the effect of buoyancy parameter, α, Prandtl number, Pr, mass transfer parameter, A, and the parameter, λ, representing the unsteadiness in the free-stream velocity on the skin friction and heat transfer ($(F_\eta)_w$, $(S_\eta)_w$, $-(G_\eta)_w$. As mentioned earlier, the buoyancy parameter α ($\alpha > 0$) gives rise to favourable pressure gradient which accelerates the fluid. Consequently, the skin friction and heat transfer are increased. We notice that the increase in the Prandtl number Pr results in the increase of thermal energy which increases the heat transfer for $\lambda > \lambda^*$ ($\lambda^* < \lambda \le 1$, $\lambda^* \simeq -0.5$). For $\lambda < \lambda^*$, the reverse behaviour is observed. This is due to the increase in the velocity and thermal boundary layer thicknesses because of the deceleration of the fluid as $\lambda < 0$ implies adverse pressure gradient. However, the skin friction ($(F_\eta)_w$, $(S_\eta)_w$) is reduced due to the increase in the velocity boundary layer thickness caused by higher viscosity as a result of increase in Pr. This behaviour is true, for all values of λ. Also the skin friction and heat transfer are reduced due to injection and the effect of suction is just the reverse. This is because of the increase in the thickness of both the velocity and thermal boundary layers due to injection, while suction does the reverse. Also the skin-friction parameters $(F_\eta)_w$ and $(S_\eta)_w$ for $\alpha > 0$ decrease as the parameter λ increases, whereas for $\alpha \le 0$ the trend is opposite (Figs. 3(a)–3(b)). On the other hand, the heat-transfer parameter $-(G_\eta)_w$ decreases as λ increases whatever may be the values of α (Fig. 3(c)). The heat transfer $(G_\eta)_w$ also shows that for $\alpha \ge 5$, $(G_\eta)_w < 0$ for all values of λ, implying that heat is transferred from the wall to the fluid, whereas for $\alpha = 0$, $(G_\eta)_w \gtrless 0$ according to whether $\lambda \lessgtr \lambda^*$ ($\lambda^* \simeq -0.58$ for $\alpha = 0$). This implies that heat is transferred from the fluid to the wall for $\lambda < \lambda^*$ and from the wall to the fluid for $\lambda > \lambda^*$. Also, no transfer of heat either from the fluid or from the wall takes place when $\lambda = \lambda^*$. The foregoing behaviour of the

heat-transfer parameter is due to the variation of the wall temperature with time represented by $(T_w - T_\infty)/(T_{wo} - T_\infty) = (1 - \lambda t^*)^{-2}$, $(T_{wo} - T_\infty) > 0$. We further observe that both the skin friction and heat transfer decrease as c decreases from 1 to zero. The reason for such a trend is that the fluid is decelerated due to the reduction in the favourable pressure gradient as c decreases from 1 to zero, and, thereby, both the skin friction and heat transfer are reduced.

The effect of the buoyancy paramter α and the parameter λ representing the unsteadiness in the free-stream velocity on the velocity and temperature profiles (F, S, G) has been studied, but in order to conserve space are not shown here. It is observed that for a given λ, there is a velocity overshoot in both the velocity components (F, S) for buoyancy parameter which assists the forced flow ($\alpha > 0$), and it increases when α ($\alpha > 0$) increases or λ decreases. However, there is no velocity overshoot either in F or in S for pure forced convection flow ($\alpha = 0$) or for opposing flow ($\alpha < 0$) whatever may be the values of λ. Therefore, it can be concluded that the velocity overshoot is caused by the buoyancy force which assists the forced flow ($\alpha > 0$), because it gives rise to a favourable pressure gradient resulting in velocity which adds to the forced convection velocity. The reason for the increase in the velocity overshoot as λ decreases can be explained as follows. From equation (10a), it follows that a small value of λ implies a large value of z for a given η and t^* (a and ν being fixed), which corresponds to a large value of F and S, thus increasing the magnitude of the velocity overshoot as λ decreases. The temperature profiles (G) show that, for a given buoyancy parameter α, an increase in the parameter λ results in an increase in the magnitude of the temperature gradient $(G_\eta)_w$ ($(G_\eta)_w < 0$ for $\alpha \geq 5$) due to the reduction in the thermal boundary layer thickness, and this causes the temperature profiles to become more steep as λ increases.

Conclusions

For constantly accelerating free-stream velocity, the buoyancy force strongly affects the skin friction both in the principal and transverse directions, whereas its effect on the heat transfer is comparatively less. The effect of buoyancy force both on the skin friction and heat transfer tends to diminish for large times. The heat transfer is significantly changed due to the effect of the wall temperature which varies with time, whereas the skin friction is little affected by it. The skin friction and heat transfer are also significantly affected by the mass transfer and the effect is more pronounced for large times than for small times. Also, the Prandtl number appreciably affects both the heat transfer and skin friction. The buoyancy force which assists the flow causes velocity overshoot in both the velocity profiles.

For the case of oscillatory free-stream velocity, the skin friction responds more to the fluctuations in the free-stream velocity than the heat transfer, but the heat transfer is strongly affected by the variation of the wall temperature with time although the skin friction is very little affected by it.

For the self-similar flow also, the effect of the buoyancy parameter is more on the skin friction than on the heat transfer. But the effect of the unsteady parameter on the skin

friction is comparatively less than that of the buoyancy parameter. However, the heat transfer is nearly equally sensitive both to buoyancy and unsteady parameters. Both the heat transfer and skin friction are significantly affected by the Prandtl number and mass transfer. The buoyancy force (which aids the flow) causes velocity overshoot in both the velocity profiles and the overshoot is appreciably affected by the unsteady parameter.

Acknowledgment

References

1 Ede, A. J., "Advances in Free Convection," *Advances in Heat Transfer*, edited by T. F. Irvine and J. P. Hartnett, Jr., Vol. 4, Academic Press, New York, 1967, pp. 1–64.

2 Morgan, V. T., "The Overall Convective Heat Transfer from Smooth Circular Cylinders," *Advances in Heat Transfer*, edited by T. F. Irvine and J. P. Hartnett Jr., Vol. 11, Academic Press, New York 1975, pp. 199–264.

3 Shah, R. K., and London, A. L., "Laminar Flow Forced Convection in Ducts," *Advances in Heat Transfer*, edited by T. F. Irvine and J. P. Hartnett Jr., Vol. 14, Academic Press, New York, 1978, pp. 1–477.

4 Oosthuizen, P. H. and Hart, A., "A Numerical Study of Laminar Combined Convective Flow Over Flat Plates," ASME JOURNAL OF HEAT TRANSFER, Vol. 95, No. 1, Feb. 1973, pp. 60–63.

5 Gryzagoridis, J., "Combined Free and Forced Convection from an Isothermal Vertical Plate," *International Journal of Heat and Mass Transfer*, Vol. 18, 1975, pp. 911–916.

6 Chen, T. S., Sparrow, E. M., and Moutsoglou, A., "Mixed Convecton in Boundary-Layer Flow on a Horizontal Plate," ASME JOURNAL OF HEAT TRANSFER, Vol. 99, 1977, pp. 66–71.

7 Pop, I., "Unsteady Laminar Combined Convection Near the Lower Stagnation Point of an Isothermal Circular Cylinder," *Archives of Mechanics*, Vol. 27, 1974, pp. 109–114.

8 Chen, T. S., and Moutsoglou, A., "Buoyancy Effects on Forced Convection along a Vertical Cylinder," ASME JOURNAL OF HEAT TRANSFER, Vol. 97, 1975, pp. 198–203.

9 Merkin, T. H., "Mixed Convection from a Horizontal Circular Cylinder," *International Journal of Heat and Mass Transfer*, Vol. 20, 1977, pp. 73–78.

10 Moutsoglou, A. and Chen, T. S., "Analysis of Combined Forced and Free Convection across a Horizontal Cylinder," *Canadian Journal of Chemical Engineering*, Vol. 55, 1977, pp. 265–271.

11 Chen, T. S. and Moutsoglou, A., "Analysis of Mixed Forced and Free Convection about a sphere," *International Journal of Heat and Mass Transfer*, Vol. 20, 1977, pp. 867–876.

12 Katagiri, M. and Pop, I., "Unsteady Combined Convection from an Isothermal Circular Cylinders," *Zeitschrift für angewandte Mathematic and Mechanik*, Vol. 59, 1979, pp. 51–60.

13 Marvin, J. G. and Sheaffer, Y. S., "A Method for Solving Nonsimilar Laminar Boundary-Layer Equations Including Foreign Gas Injection," NASA Tech. Note D-5516, 1969.

14 Howarth, L., "The Boundary Layer on Three-Dimensional Flow, Part 2. The Flow Near a Stagnation Point," *Philosophical Magazine*, Series 7, Vol. 42, No. 335, 1951, pp. 1433–1440.

15 Hayday, A. A. and Bowlus, D. A., "Integration of Coupled Nonlinear Equations in Boundary Layer Theory with Specific Reference to Heat Transfer Near the Stagnation Point in Three-Dimensional Flow," *International Journal of Heat and Mass Transfer*, Vol. 10, 1967, pp. 415–426.

16 Kumari, M., "Investigation of Laminar Boundary-Layer Flows Using Finite-Difference Method," Ph.D. thesis, Indian Institute of Science, Bangalore, chapter II, 1980.

17 Teipel, I., "Heat Transfer in Unsteady Laminar Boundary Layers at an Incompressible Three-Dimensional Stagnation Flow," Mechanics Research Communications, Vol. 6, 1979, pp. 27–32.

An Experimental Study of Mixed, Forced, and Free Convection Heat Transfer From a Horizontal Flat Plate to Air

X. A. Wang[1]

Department of Power Engineering,
Shanghai Mechanical Engineering
Institute
Shanghai, 200093
China

A heated flat plate is tested in a wind tunnel to study mixed convection in both upward and downward positions. It is found that the local heat transfer coefficient is strongly dependent on the free stream velocity and the temperature difference between the surface and the free stream. The buoyancy effect is more pronounced for the heated plate facing upward. This paper correlates the experimental data in terms of Nusselt, Grashof, and Reynolds numbers. The points of onset of instability caused by the buoyancy effect are also examined and correlated in terms of the dimensionless groups. Experimental data are compared with analysis documented in the literature, and the agreement is found satisfactory.

Introduction

The study of the mixed, forced-free convection problem is difficult because of the need to consider both inertia and buoyancy forces in the analysis. In fact, the heat transfer rate for such a problem is a function of many parameters including the relative magnitude and direction of the inertia and buoyancy forces, the instability of the boundary layer, among others. In the case of mixed convection over a horizontal flat plate, the buoyancy force is perpendicular to the inertia force. For such a problem, no similarity solutions can be found. Although approximate numerical solutions are still possible for a laminar, mixed convection problem, and such solutions have been documented in the literature [1–5], correlations and measurements of local heat transfer coefficients appear to be lacking. This prompts the presentation of this paper which addresses an experimental determination of the mixed, convective heat transfer coefficient for a horizontal, heated flat plate in both upward and downward positions. The experiment is carried out in a wind tunnel, covering a range of air velocities from 0.1 to 25 m/s, while the temperature differences between the plate and the free stream range from 19 to 106°C. For the ease of application, the experimentally determined convective coefficients given in this paper are also correlated in terms of the Nusselt number and expressed as functions of the Reynolds and Grashof numbers.

A review of the literature reveals that the mixed, forced-free convection on a horizontal flat plate has been a subject of several recent studies. The emphasis of these studies has been on the stability caused by the buoyancy effect. Wu and Cheng [6] employed a nonparallel flow model and obtained the critical values for vortex instability. Chen and Mucoglu [7] solved the linear, plane-wave instability of the laminar,

mixed, forced-free convection problem and also obtained the critical parameters. There is a scarcity of the experimental studies dealing with the subject [8, 9]. As will also be shown in this paper, Wu and Chen's instability criteria [6, 7] can actually be verified by the data given in this paper.

Experiment

The test is performed inside an open loop, low speed, wind tunnel whose nozzle section has a contraction ratio of 10 to 1. The dimensions of the test section are 0.25 × 0.3 × 1.5 m, width by height by length. As a means of cutting down on the radiative heat losses from the test plate, the test-section wall is made of aluminum and is highly polished in order to raise its reflectivity.

The construction of the flat plate is shown in Fig. 2. The plate measures 1.2 m (length) × 0.25 m (width) × 0.02 m (thickness). In the longitudinal (air flow) direction, the plate is beveled at its leading edge with an angle of 10 deg. The center portion of the plate is made of a main heater of stainless steel ribbon measuring 100 mm wide and 0.5 mm thick. Two guard heaters are placed alongside the main heater in order to compensate for the lateral heat losses. These three heaters are supported by two layers of reinforced plastic panels which are, in turn, housed inside an aluminum frame. The plate assembly is supported at its two ends inside the wind tunnel. In the experiment, the main heater is powered by a DC current supplied by a motor-generator set. The DC current is measured by a calibrated shunt and a potentiometer. AC power is used for the guard heaters, which is controlled by an autotransformer.

The surface temperatures of the plate are measured using 18 sets of 0.19 mm copper-constantan thermocouples installed along the center line of the plate (thermocouple locations marked in Fig. 1). Another 8 sets of thermocouples are placed at strategic locations along two cross sections of the panel in order to estimate the conductive heat losses. The guard heater

---

Fig. 1 Test plate construction

I MAIN HEATER
2 ALUMINUM FRAME
3 THERMOCOUPLE WIRES
4 REINFORCED PLASTICS PANEL
5 GUARD HEATER
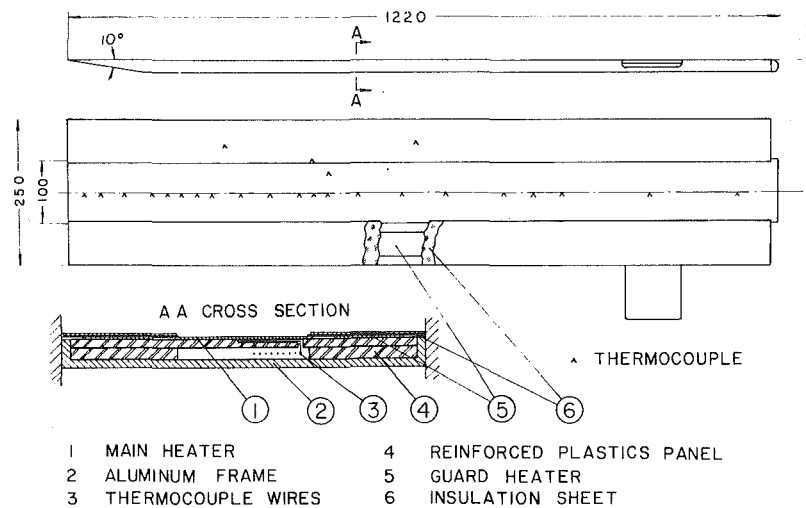**6** INSULATION SHEET

temperatures are measured using two thermocouples. Another two thermocouples are instrumented to measure the wall temperature of the wind tunnel. The free stream air velocities in the experiment are measured using a 3 mm OD pitot tube (for U > 8 m/s) and a hot-wire anemometer (for lower velocities) at three positions located 0.2, 0.5, and 0.9 m from the leading edge of the plate. The free stream air temperature is measured at the entrance of the wind tunnel. The test is carried out under a steady-state condition, with the plate first tested in the upward position. After this is done, the entire test section is rotated 180 deg to mount in a downward position, and the series of tests repeated for this new orientation.

The heat transfer coefficient is calculated using an energy balance equation given as follows:

$$h = \frac{P - Q_l}{A(T_w - T_\infty)} = \frac{I^2 R - Q_c - Q_r}{A(T_w - T_\infty)} \qquad (1)$$

where $I^2 R$ accounts for the electric power input to the main heater. Q_c refers to the conductive heat loss and is estimated using the following equation:

$$Q_c = Q_{c,x} + Q_{c,yz} \qquad (2)$$

where $Q_{c,x}$ is the conductive heat loss in the stainless steel ribbon in the longitudinal direction; $Q_{c,yz}$ denotes the heat loss through the backing plastic panel in the transverse direction. Based on the measured temperature readings, $Q_{c,x}$ is found to be negligibly small. The heat transfer along the heater plane in the transverse direction is also small because of the use of guard heaters. The conductive heat loss is only important across the backing panel, which can be treated as one dimensional in the analysis.

The radiative heat loss from the plate can be estimated using

$$Q_r = \frac{A\sigma(T_w^4 - T_0^4)}{\frac{1}{\epsilon_w} + \frac{A}{A_0}\left(\frac{1}{\epsilon_0} - 1\right)} \qquad (3)$$

where notations in this equation have been defined in the Nomenclature.

Results and Discussion

The variation of the convective heat-transfer coefficient, h, with position, x, is plotted in Fig. 2. In the legend, the free-stream velocity, U, and the wall /free-stream temperature differential $T_w - T_\infty$, are measured at a distance of $x = 0.5$ m from the leading edge of the plate. As is shown in the figure, the convective coefficient is a strong function of these parameters. Starting from the leading edge (Fig. 2(a)), the convective coefficient decreases with increasing x, and the coefficient is higher for a high speed flow, which trends are typical for a forced convection over a flat plate. As the air flows downstream, the free convection sets in, which is demonstrated by the slight rise of the curves in the figure. In these regions where the curves level off, the temperature of the plate plays a leading role; the higher the temperature, the larger the convective coefficient. Such a trend also characterizes the buoyancy effect in the flow.

Some observations can be made with regard to the position of the rise of the h curves. When the free-stream velocity is small, the x position of the valley (first minimum point along the curve) is found to be insensitive to the temperature difference. However, when the velocity is increased, the position of the valley shifts to the right. This trend can be ascribed to the relative magnitude of the inertia and buoyancy forces in the boundary layer. For a larger free-stream velocity, the buoyancy effect is felt further downstream.

Nomenclature

						Subscripts		

A = area
Gr = Grashof number
h = heat transfer coefficient
I = electric current
Nu = Nusselt number
P = electric power
Q = heat flow
R = electrical resistance
Re = Reynolds number

T = temperature
$\dot{T}_w$ = mid-point surface temperature
U = free stream velocity
x,y = coordinates
Δ = uncertainty
ϵ = emissivity
σ = Stefan-Boltzmann constant

Subscripts
c = conduction
e = free convection
f = forced convection
l = heat loss
o = wall of wind tunnel
r = radiation
x,y,z = coordinates
w = surface
∞ = free stream
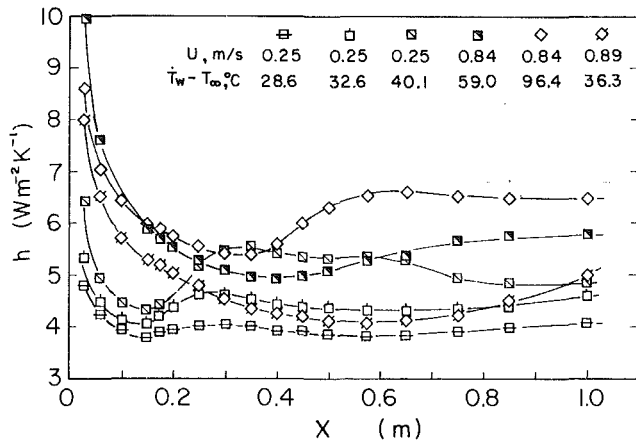
(a) upward facing plate
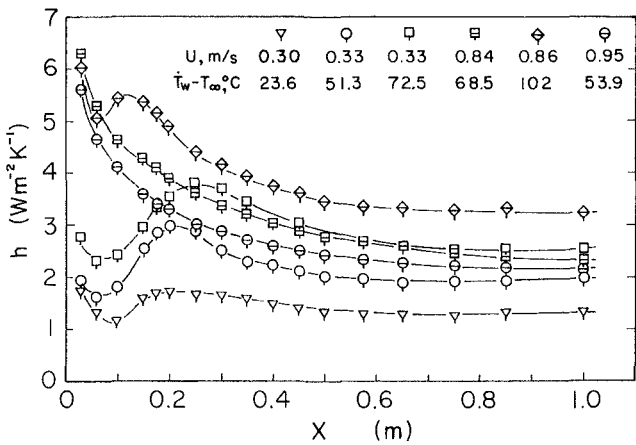
(b) downward facing plate

Fig. 2 Local heat transfer coefficients along horizontal heated plate

Fig. 3 Mixed convection from upward facing heated horizontal plate, Nu_x versus Re_x

Fig. 4 Mixed convection from downward facing heated horizontal plate, Nu_x versus Re_x

For the heated plate facing downward, the aforementioned trends repeat themselves (see Fig. 2(b)). However, a peak point is found on the h curves when the flow velocity is small; this point also rises with the temperature difference. When the flow velocity is large, the buoyancy effect becomes smaller, and this h rise disappears. In the meantime, the convective coefficient curve characterizes the condition of a forced flow over a flat plate, which is not unexpected. It is also noted that, in general, the convective coefficient is smaller for a heated plate facing downward.

A plot of the local Nu_x versus Re_x numbers is shown in Figs. 3 and 4. Here the local Grashof number Gr_x is chosen as a parameter. As is shown in both figures, the family of the Gr_x curves merge into a singular curve when Re_x is large. This merged curve can be divided into three segments as follows. When Re_x is small, Nu_x is related to Re_x according to

$$Nu_x = 0.295 Re_x^{0.5} \qquad (4)$$

which is known to be the relation of Nu_x for laminar, forced flow over a flat plate [10]. When Re_x is large, the Nu_x function characterizes a turbulent, forced-flow condition and its representative equation becomes

$$Nu_x = 0.0256 Re_x^{0.8} \qquad (5)$$

In between these two extremes is the curve for the present correlation,

$$Nu_{xf} = 3 + 0.0253 Re_x^{0.8} \qquad (6)$$

which is valid for the heated plate in both upward and downward positions (see Figs. 3 and 4). As is shown in both figures, the correlated Nu_x (equation (6)) is able to duplicate
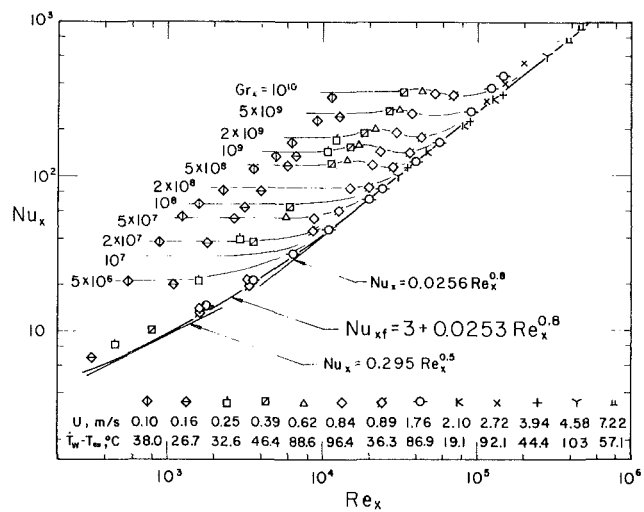
Nu_x for the entire Re_x range shown. This equation can thus be considered as a general equation for the forced flow condition.

It is also interesting to note that the Gr_x curves shown in Figs. 3 and 4 merge into those limiting curves following different paths. For a heated plate facing upward, Gr_x curves merge from above. Such a trend is, nevertheless, reversed for the plate facing downward. Another point of interest is that a dip is found in the Gr_x curves for the plate in both orientations. This dip is more pronounced for the heated plate facing downward. Physically, this could be attributed to a pseudointerference effect caused by the deceleration of the flow and the piling up of the boundary layer. A combination of these effects tends to thicken the boundary layer and suppress the Nu_x values. It is also noted that these trends can also be found in the case of mixed convection over horizontal cylinders and vertical plates as reported in [11, 12].

Figures 5 and 6 present plots of Nu_x versus Gr_x curves. This time, Re_x is chosed as a parameter. The family of the Re_x curves again merge asymptotically as before. It is interesting to note that, for the heated plate facing upward, the exponent in the asymptotic equation

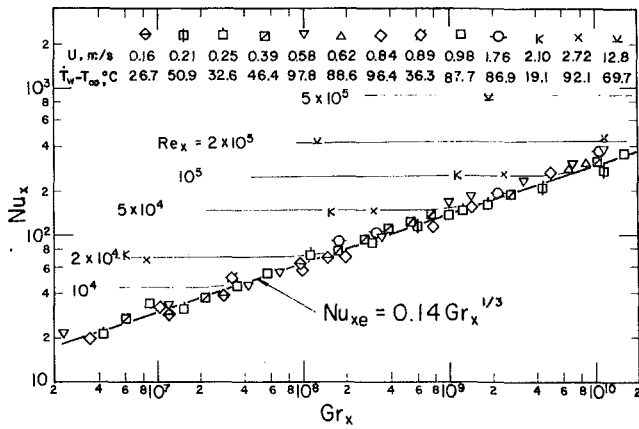$$Nu_x = 0.14 Gr_x^{1/3} \qquad (7)$$

Fig. 5 Mixed convection from upward facing heated horizontal plate, Nu_x versus Gr_x
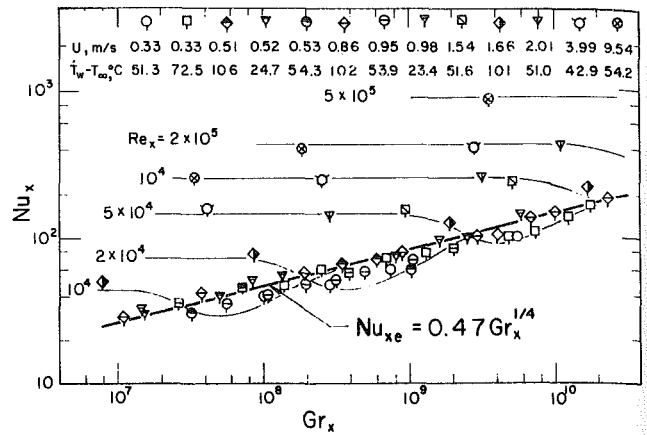

Fig. 6 Mixed convection from downward facing heated horizontal plate, Nu_x versus Gr_x
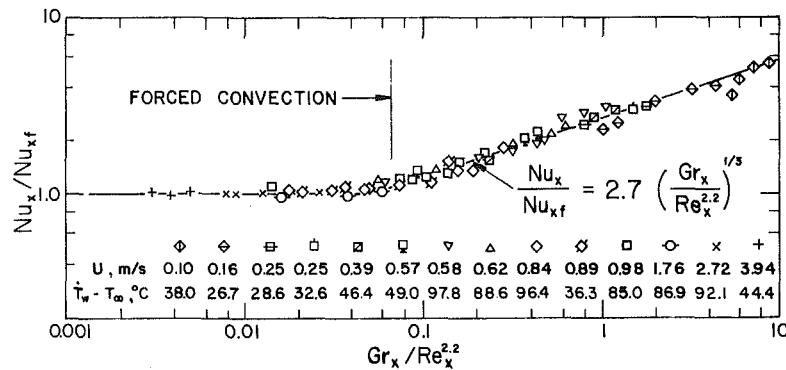

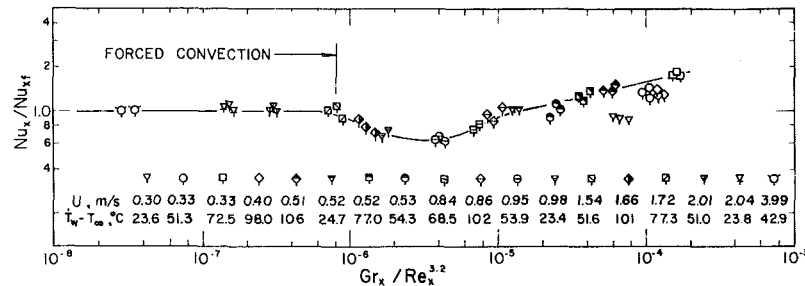**Fig. 7** Nusselt number ratio for mixed convection from upward facing heated plate

Fig. 8 Nusselt number ratio for mixed convection from downward facing heated plate

is in good agreement with that of a similar, free-convection equation without forced-convection contribution, both exponents being 1/3. Such an agreement is also found in the case of the heated plate facing downward (1/4 dependancy) [13] (see Fig. 6). The dips in the Re_x curves now replace the dips in the Gr_x curves seen earlier in Fig. 4, their reasons being similar.

In order to assess the effect of the buoyancy force on the heat transfer coefficient, a plot of the Nusselt-number ratio of the local Nusselt number, Nu_x, to the local Nusselt number for a forced flow over a flat plate, Nu_{xf}, (equation (6)) versus $Gr_x/Re_x^{2.2}$ curves, is made and shown in Fig. 7. For a heated plate facing upward, the ratio of the Nusselt numbers is nearly 1 for $Gr_x/Re_x^{2.2} \leq 0.068$, which signifies that the buoyancy effect is practically negligible in this region. The effect of the buoyancy force is felt when $Gr_x/Re_x^{2.2} > 0.068$. For this region, the experimental data can be correlated as

$$\frac{Nu_x}{Nu_{xf}} = 2.7 \left(\frac{Gr_x}{Re_x^{2.2}} \right)^{1/3} \qquad (8)$$

A slightly different state of affairs occurs when the heated plate faces downward (see Fig. 8). Although the forced convection region still exists as demonstrated by the flat portion of the curve, above $Gr_x/Re_x^{3.2} = 8 \times 10^{-7}$ the Nu_x/Nu_{xf} curve bends downward to form a large dip. This trend once again illustrates the pseudointerference effect mentioned earlier. In comparison with Fig. 7, this effect is seen to be more pronounced for the plate in downward position.

It is desirable to identify the mixed convection region for a heated plate facing upward by plotting the Re_x versus Gr_x curves as shown in Fig. 9. In this plot, the forced convection region identified earlier in Fig. 7 is used to separate the forced from the mixed convection region, this dividing line being

$$Gr_x = 0.068Re_x^{2.2} \qquad (9)$$

In a attempt to separate the mixed and free convection regions, it is felt logical to consider the transition being the points of inflection on the curves in Fig. 2 (a). Then, if these inflection points are plotted, a relation of
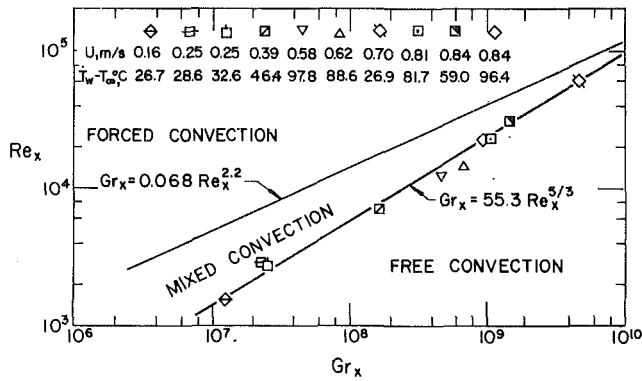
Fig. 9 Mixed convection regime for upward facing heated horizontal plate

$$Gr_x = 55.3 \, Re_x^{5/3} \qquad (10)$$

can be obtained. This line divides the mixed and free convection regions.

The convection regions examined in Fig. 9 are for a heated plate facing upward. For the plate facing downward, the convection coefficient becomes smaller. Consequently, the experimental uncertainty becomes larger. This forbids the use of similar schemes to identify convection regions. The division of convection regions is thus not attempted for the plate in a downward position.

It is now possible to summarize the correlated equations as follows:

$$Nu_{xf} = 3 + 0.0253 \, Re_x^{0.8} \quad \text{for } Gr_x < 0.068 \, Re_x^{2.2} \qquad (11)$$

$$Nu_x = 2.7 \left(\frac{Gr_x}{Re_x^{2.2}} \right)^{1/3} (3 + 0.0253 \, Re_x^{0.8})$$

$$\text{for } 0.068 \, Re_x \leq Gr_x \leq 55.3 Re_x^{5/3} \qquad (12)$$

$$Nu_{xe} = 0.14 \, Gr_x^{1/3} \quad \text{for } Gr_x > 55.3 \, Re_x^{5/3} \qquad (13)$$

where equations (11), (12) and (13) refer to the forced, mixed and free-convections regions, respectively.

As a final note to close this section, it is interesting to compare the present experimental data with the analytical results reported in [6, 7]. In these papers, the buoyancy effect has been studied and considered in terms of the instability. The problem of instability is now being studied and this calls for the reexamination of the h curve given in Fig, 2 (a). It is noted that, from the mechanics of convection, the inflection points on these curves in the figure can also be considered as the points of onset of instability induced by the buoyancy effect as referred to by the authors of [6, 7]. Following this approach, it is possible to construct Fig. 10, where the theoretical curves in [6, 7] are also plotted for contrast purposes. As is shown in this figure, the agreement between the present investigation and the theoretical curves is good. In order to further substantiate this point, the velocity fluctuation was measured by a hot-wire anemometer and recorded using a oscilloscope. The oscillograms are now used to identify the source of instability. As shown in Fig. 11, the velocity fluctuation is seen to be a function of both position (x) and temperature difference ($\dot{T}_w - T_\infty$). For the flow in the free convection region shown in Fig. 9, the velocity fluctuation is very pronounced (see traces on the upper right of the figure). This can certainly be attributed to the vortex effect in the flow.

Error Analysis

The uncertainites in the experiment are given in this section. The temperature uncertainties are given as follows:

$$\Delta T_w < 0.3\,°C$$

$$\Delta T_\infty < 0.1\,°C$$
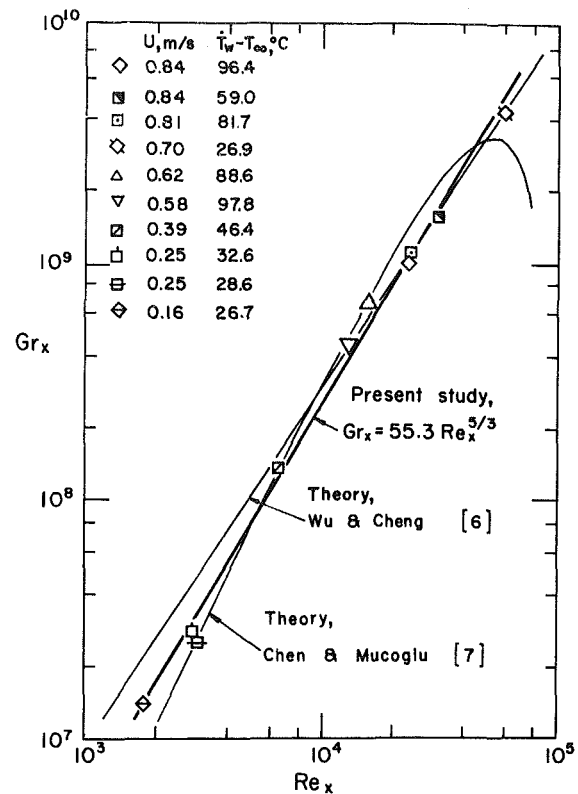
Fig. 10 Correlation for the onset points of air flow above a heated horizontal plate

U ≐ 0.3 m/s, Y = 30 mm
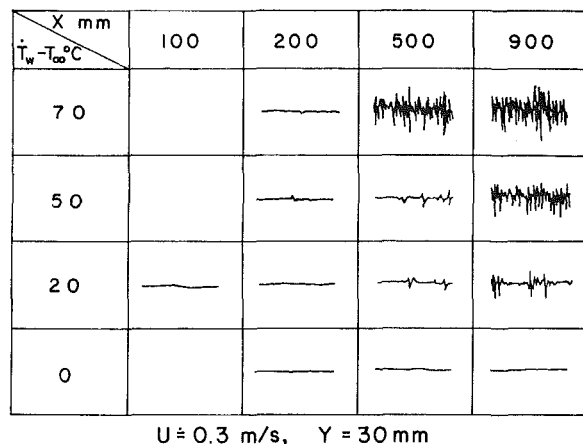
Fig. 11 Oscillograms of the velocity fluctuation in the air stream flowing above a heated horizontal plate

which are estimated based on the accuracy of the potentiometers used in the experiment.

The uncertainties of the air velocity are given as follows:

$$\frac{\Delta U}{U} < 2 \text{ percent} \quad \text{for } U > 8 \text{ m/s}$$

$$\frac{\Delta U}{U} < 5 \text{ percent} \quad \text{for } 2 \text{ m/s} \leq U \leq 8 \text{ m/s}$$

$$\frac{\Delta U}{U} < 8 \text{ percent} \quad \text{for } 0.1 \text{ m/s} \leq U < 2 \text{m/s}$$

The uncertainty decreases as the velocity is increased.

The uncertainties of the dc power measurement are estimated based on Ohm's law, given as

$$\frac{\Delta P}{P} = \sqrt{\left(2\frac{\Delta I}{I}\right)^2 + \left(\frac{\Delta R}{R}\right)^2} < 2.2 \text{ percent} \qquad (14)$$

Based on the uncertainties cited above, the uncertainty of the heat transfer coefficient can be calculated as

$$\frac{\Delta h}{h} = \sqrt{\frac{(\Delta P)^2 + (\Delta Q_l)^2}{(P - Q_l)^2} + \frac{(\Delta T_w)^2 + (\Delta T_\infty)^2}{(T_w - T_\infty)^2}} < 7 \text{ percent} \qquad (15)$$

for the plate facing upward. This uncertainty is increased to 13 percent for the plate facing downward. A detailed error estimation is given in [5].

Acknowledgment

The author acknowledges the guidance from Professor J.H. Sun, which makes this study possible. The author also wishes to thank Professor C.K. Hsieh, University of Flordia, U.S.A., for his critical comments and encouragement to publish this paper.

References

1 Mori, Y., "Buoyancy Effects in Forced Laminar Convection Flow Over a Horizontal Flat Plate," ASME JOURNAL OF HEAT TRANSFER, Vol. 83, 1961, pp. 479-482.

2 Sparrow, E. M., and Minkowycz, W. J., "Buoyancy Effects on Horizontal Boundary Layer Flow and Heat Transfer," International Journal of Heat and Mass Transfer, Vol. 5, 1962, pp. 505-511.

3 Hieber, C. A., "Mixed Convection Above a Heated Horizontal Surface," International Journal of Heat and Mass Transfer, Vol. 16, 1973, pp. 769-785.

4 Chen, T. S., Sparrow, E. M., and Mucoglu, A., "Mixed Convection in Boundary Layer Flow on a Horizontal Plate," ASME JOURNAL OF HEAT TRANSFER, Vol. 99, 1977, pp. 66-71.

5 Wang, X. A., "Mixed Forced and Free Convective Heat Transfer From Horizontal Plate to Air and The Investigation of Hot-wire Anemometer," Master thesis, Nanking Institute of Technology, China, 1966.

6 Wu, R. S., and Cheng, K. C., "Thermal Instability of Blasius Flow Along Horizontal Plates," International Journal of Heat and Mass Transfer, Vol. 19, 1976, pp. 907-913.

7 Chen, T. S., and Mucoglu, A., "Wave Instability of Mixed Convection Flow Over a horizontal Flat Plate," International Journal of Heat and Mass Transfer, Vol. 22, 1979, pp. 185-196.

8 Hayashi, Y., Takimoto, A., Hori, K., "Heat Transfer in Laminar, Mixed Convection Flow Over a Horizontal Flat Plate," (in Japanese), Proceeding of the 14th Japan Heat Transfer Symposium, 1977, pp. 4-6.

9 Gilpin, R. R., Imura, H., and Cheng, K. C., "Experiments on the Onset of Logitudinal Vorteces in Horizontal Blasius Flow Heated From Below," ASME JOURNAL OF HEAT TRANSFER, Vol. 100, 1978, pp. 71-77.

10 Holman, J. P., Heat Transfer, 3rd ed., McGraw-Hill, New York, 1971, pp. 153.

11 Oosthuizen, P. H., and Bassey, M., "An Experimental Study of Combined Forced-and-Free Convective Heat Transfer From Flat Plate to Air at Low Reynolds Numbers," ASME JOURNAL OF HEAT TRANSFER, Vol. 95, 1973, pp. 120-121.

12 Seiichi, N., and Takuro, O., "Heat Transfer From a Horizontal Circular Wire at Small Reynolds and Grashof Numbers - II, Mixed Convection," International Journal of Heat and Mass Transfer, Vol. 18, 1975, pp. 397-413.

13 Gebhart, B., Heat Transfer, McGraw-Hill, New York, 1971, pp. 375.

Free Convection Effects on Laminar Forced Convective Heat Transfer in a Horizontal Isothermal Tube

W. W. Yousef

Nuclear Studies and Safety Department,
Ontario Hydro,
Toronto, Ontario,
Canada M5G 1X6

J. D. Tarasuk

Faculty of Engineering Science,
The University of Western Ontario,
London, Ontario,
Canada N6A 5B9

The influence of free convection due to buoyancy on forced laminar flow of air in the entrance region of a horizontal isothermal tube was investigated. The Graetz numbers ranged form 2.5 to 110.0, the Reynolds numbers ranged from 120 to 1200, the Grashof numbers ranged from 0.8×10^4 to 8.7×10^4, and the ratio L/D was varied from 6 up to 46. The average Nusselt numbers based on the log-mean temperature difference, ranged from 2.0 to 25.9. The heat transfer data were correlated according to the influence of free convection which was found to have a significant effect at points close to the entrance to the tube.

Introduction

The influence of free convection on forced convective heat transfer can be significant. In many practical situations where the buoyancy force is high and the forced flow is low, the free and forced convection effects can be of comparable order of magnitude. This occurs in heat exchangers designed for viscous liquids, pipelines used for transporting oil, and heat exchangers for gas flows. When heat is transferrred through the wall of a horizontal tube, the warmer fluid moves upward along the side walls, and, by continuity, the heavier fluid near the center of the tube flows downward. As a result, a two symmetrical spiral-like motion is formed. This secondary flow is driven by the radial temperature variation. For a uniform wall temperature, the secondary flow develops to a maximum and then diminishes gradually as the wall-fluid temperature difference decreases.

A summary of the available experimental data and correlations which pertain to the current study is given in chronological order, in Table I.

A comparison between the different correlations reveal the following:

1 The forced convection term is represented by the Graetz number, Gz, in all correlations.

2 The term representing the free convection differs between the derived correlations. Eubank and Proctor [2] introduced the ratio D/L in the free convection term (it should be borne in mind that Eubank and Proctor's correlations were derived for heavy oils which is characterized by high viscous to buoyancy forces ratio). In the Jackson et al. [3] correlation, the ratio D/L does not exist, which suggest that the ratio is not needed. Oliver [4] suggested the ratio L/D in the free convection term such that when the Grashof number is multiplied by the L/D ratio, a term D^2 is produced which Oliver found to be more realistic than a term in D^4 if the D/L ratio is used. Oliver [4] mentioned that the power of the L/D term is provisional and that his correlation becomes inac-

curate for L/D below 70. Brown and Thomas [5] showed that the effect of free convection does increase with increasing flow rate and thus they introduced the flow rate, as represented by the Graetz number, into the free convection term. Finally, Depew and August [6] introduced the Prandtl number to account for fluids with large variations in viscosity. It should be noted that all the correlations, except that of Jackson et al. [3], were derived under the conditions of fully developed flow at the onset of heating.

A composite plot of the available experimental data for 4 different fluids is shown in Fig. 1. The average Nusselt number from Graetz analytical solution (GrPr = 0)[7] and from asymptote $Nu_a = 1/2X$ are shown in Fig. 1.

The experimental data obtained by the authors could not be reconciled with any of the above mentioned formulae. The major differences are:

1 The existing data were obtained for fully developed flow before the heated section of the tube.

2 The existing data do not extend to tubes with $L/D < 28$ or Gz < 7.0.

3 The existing data deal mainly with fluids having Pr larger than unity.

The analytical investigations include series expansion [17, 18], finite difference methods [7, 16, 19, 20] and boundary layer analysis [21].

This investigation, which is a continuation of the work published in reference [8], summarizes the experimental work on the free convection effects for laminar flow of air in a horizontal isothermal tube without a flow development section.

Experiment

The apparatus is shown diagrammatically in Fig. 2. The test section shown in Fig. 3, consists of an entry section, a tube and an exit section, all made of aluminum with a 25.103 mm inside dia and 25.0 mm wall thickness. The tube was formed of interchangeable segments bolted together. Segment lengths

Table I Data and correlations used in combined free and forced convection in an isothermal horizontal tube

REFERENCE	FLUID	TUBE DIAMETER MM-(INCHES)	$\frac{L}{D}$	Gr	Gz	Pr	CORRELATION	PERCENTAGE DEVIATION
Colburn [1] 1933	Air, Water, Light Oils	5.0 (0.2)- 95.9(3.78)	24-400	$3.7 \times 10^3 - 3.0 \times 10^8$		0.76-160 (heating)	$Nu_a \left[\frac{\mu_f}{\mu_b}\right]^{1/3} = 1.75\ Gz^{1/3}\left[1 + 0.015\ Gr_f^{1/3}\right]$	
Eubank and Proctor [2] 1951	Petroleum Oils	12.55(0.494)- 62.74(2.47)	61-235	$GrPr = 3.3 \times 10^5 - 8.6 \times 10^8$	12-4900	140-15200	$Nu_a\left(\frac{\mu_w}{\mu_b}\right)^{0.14} = 1.75\left[Gz + 12.6\left(Gr \cdot Pr \cdot \frac{D}{L}\right)^{0.40}\right]^{1/3}$	-32 +43
Jackson et al [3] 1961	Air	98.425(3 $\frac{7}{8}$)	31	$1.57 \times 10^6 - 3.14 \times 10^6$	33-1300	0.71	$Nu_m = 2.67\left[\left(Gz_b\right)^2 + (0.0087)^2\left(Gr_{1m} \cdot Pr\right)_w^{1.5}\right]^{1/6}$	
Oliver [4] 1962	Water Ethyl Alcohol Glycerol-water	12.7 ($\frac{1}{2}$)	72	$1.0 \times 10^4 - 1.1 \times 10^5$ $4.9 \times 10^4 - 1.6 \times 10^5$ $2.9 \times 10^1 - 6.4 \times 10^1$	7-11 24-187 20-176	1.9-3.7 4.8-7.0 62-326	$Nu_a\left(\frac{\mu_w}{\mu_b}\right)^{0.14} = 1.75\left[Gz + 5.6 \times 10^{-4}\left(Gr \cdot Pr \cdot \frac{L}{D}\right)^{0.70}\right]^{1/3}$	-25 +110
Brown and Thomas [5] 1965	Water	25.4 (1) 12.7 ($\frac{1}{2}$) 12.7 ($\frac{1}{2}$)	36 72 108	$3.1 \times 10^5 - 4.9 \times 10^6$ $7.1 \times 10^4 - 8.9 \times 10^5$ $2.9 \times 10^4 - 7.3 \times 10^5$	28-112 27-41 19-39	4.0-7.4 3.5-5.7 4.0-6.8	$Nu_a\left(\frac{\mu_w}{\mu_b}\right)^{0.14} = 1.75\left[Gz + 0.012\left(Gz \cdot Gr^{1/3}\right)^{4/3}\right]^{1/3}$	±50
Depew and August [6] 1971	Water Ethyl Alcohol Glycerol-water	19.05 ($\frac{3}{4}$)	28.4	$0.7 \times 10^5 - 5.8 \times 10^5$ $2.7 \times 10^5 - 9.9 \times 10^5$ $5.1 \times 10^2 - 9.0 \times 10^2$	25-338 36-712 53-188	5.7-8.0 14.2-16.1 328-391	$Nu_a\left(\frac{\mu_w}{\mu_b}\right)^{0.14} = 1.75\left[Gz + 0.12\left(Gz \cdot Gr^{1/3} \cdot Pr^{0.36}\right)^{0.88}\right]^{1/3}$	±40

were 50, 100, 150, 200, 300 and 400 mm, which, when assembled in different combinations, could give L/D ratios of approximately 2, 4, 6 . . . 46, 48. The tube segments were heated electrically through an electric heating cable which was wrapped tightly in the spiral groove machined around the tube. A d-c current was employed for heating. In order to achieve isothermal heating, the tube segments at both ends of the tube were heated independently by a power supply. At midway of each tube segment, three thermocouple wells were drilled radially 90 deg apart and 3 mm from the inside tube surface. The axial and circumferential variations in the wall temperature did not exceed 0.5 percent. The entry piece was designed to prevent flow separation at the tube inlet by having a radius of curvature at the tube inlet of the same order of magnitude as the diameter [9]; and to minimize the end effects by forcing air through a collar around the entry piece. A laminae of Celeron insulation was used to insulate the entry piece from the rest of the tube. Because no flow development section was used, the velocity and temperature profiles were developing simultaneously. The exit piece was designed so as to ensure even withdrawal of air and good mixing. Four shielded thermocouples were set 90 deg apart at the locations shown in Fig. 3 to measure exit air temperature. Sufficient mixing of the exit air was achieved, as the temperatures recorded by the four thermocouples varied by no more than 2.0 percent from the average temperature in most runs. The difference in the temperatures recorded by the four thermocouples reached 5.0 percent at low flow rates (Re < 200).

——————— Nomenclature ———————

A, B = the constants in equation (6)
A = surface area of tube πDL
A', B' = the constants in equation (8)
C_p = specific heat at constant pressure
D = inside tube diameter
Gr = Grashof number, $g\beta D^3 (\Delta t_{lm})/v^2$
Gz = Graetz number, $\frac{\pi}{4}\ RePr\frac{D}{L}$
g = gravitational acceleration
h_{lm} = average heat transfer coefficient based on log-mean temperature difference
h_x = local heat transfer coefficient
k = thermal conductivity
L = tube length
$\dot{m}$ = mass flow rate
m = the exponent in equation (6)
Nu_m = average Nusselt number, $h_{lm}D/k$

Nu_x = local Nusselt number, h_xD/k
Nu_∞ = Nusselt number determined analytically for fully developed flow, = 3.658
Nu_a = average Nusselt number based on arithmetic mean temperature difference
Pr = Prandtl number, $C_p\mu/k$
Q = heat transferred to air
Re = Reynolds number, $4\dot{m}/\pi D\mu$
t_1 = air bulk temperature at tube inlet
t_2, t_3 = air bulk temperature at tube exit
t_w = tube wall temperature
t_b = air mean bulk temperature
T = absolute temperature in °K, $t + 273.15$
Δt_{lm} = logarithmic mean temperature difference
X = nondimensional axial distance, $\dfrac{x/D}{RePr}$

X_t = nondimensional axial distance when thermal boundary layers merge
x = axial distance measured from tube inlet
β = coefficient of thermal expansion, $1/T$
θ_w = temperature difference, $t_w - t_1$
μ = dynamic viscosity
ν = kinematic viscosity, μ/ρ
ρ = density

Subscripts

1 = inlet conditions
2, 3 = outlet conditions
a = evaluated at arithmetic mean temperature
b = evaluated at mean bulk temperature
f = evaluated at film temperature
m = average or mean value
x = local value
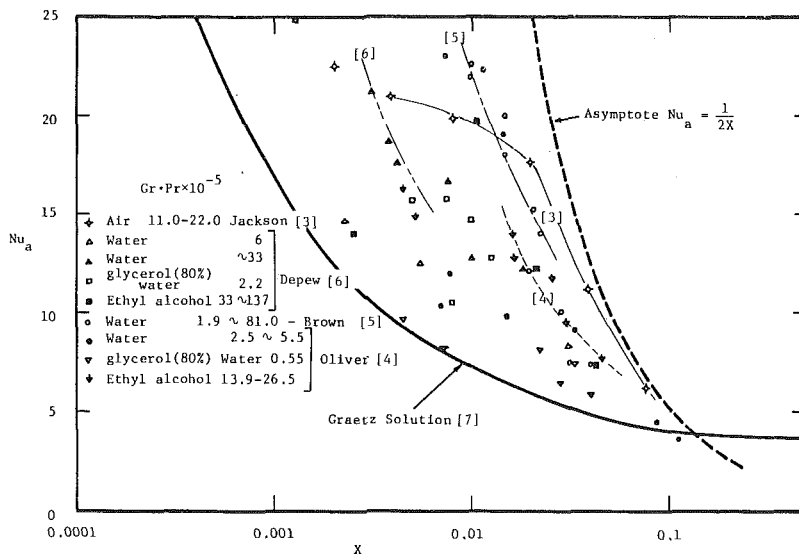w = evaluated at wall temperature

Fig. 1 Average Nusselt number for laminar flow heat transfer in tubes obtained from experimental data
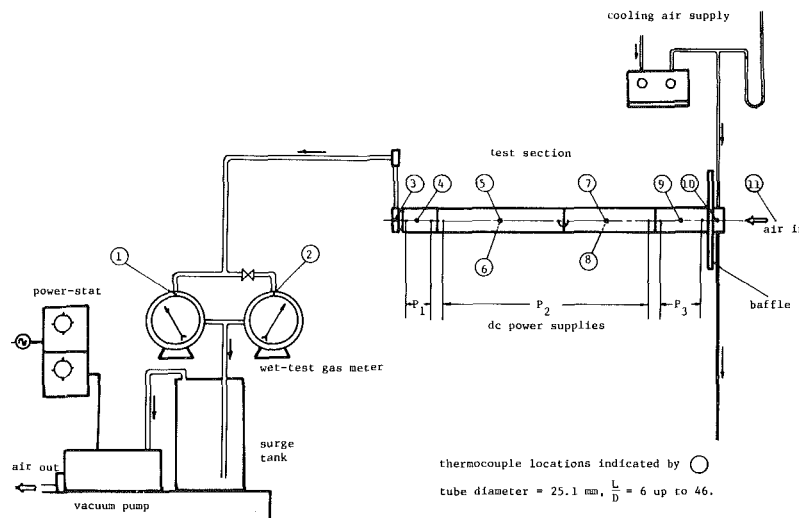

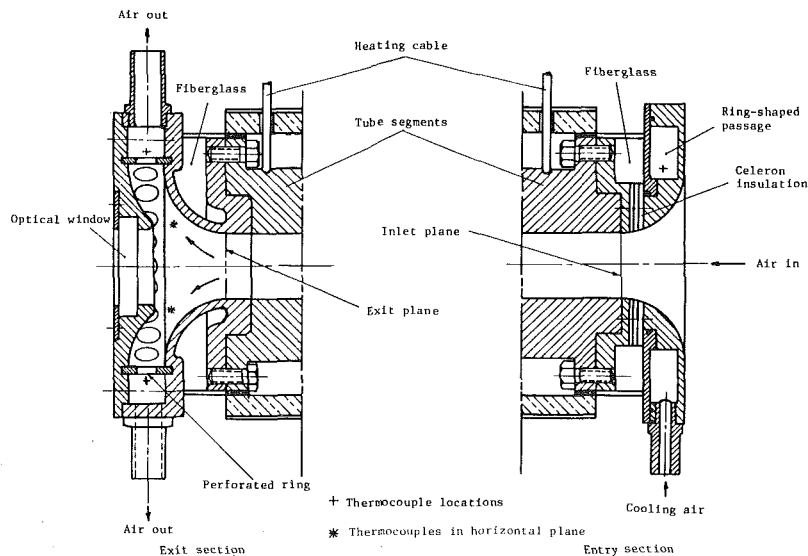**Fig. 2 Schematic layout of the test apparatus**

Fig. 3 Test section

This is mainly due to the poor mixing and stratification effect at such low flow rates.

A laminar flow of air was produced by withdrawing the air through the tube by a variable speed pump. The volumetric air flow was measured by a precision wet-test gas meter with a capacity range of 1.13 to 11.33 L/min and a resolution of 0.01 L. A surge tank of 45 L capacity was used to dampen any flow or pressure fluctuations especially at low flow rates. Air and tube wall temperatures were measured by 28-gauge, copper-constantan thermocouples and a Doric 220 data acquisition system with a 0.1°C resolution and a ±0.4°C accuracy. Detailed description of the experimental apparatus is given in reference [10].

By choosing different combinations of tube segments, eight different L/D ratios were used for the test runs, namely 6, 10, 14, 18, 24, 30, 38 and 46. The wall-minus-air temperatures $\theta_w = t_w - t_1$ were taken as 12, 23, 34, 49, 63, 81 and 102°C. The experiment proceeded by increasing the flow rate while holding the tube wall at constant temperature. This necessitated a fine adjustment for the electrical power especially in the segments at both ends of the tubes. A period of 3 hrs was allowed for warm-up and a period of half an hour was required to reach steady-state conditions before each run. Upon reaching steady-state conditions, room temperature, tube wall temperature, inlet and exit air temperature and barometric pressure were recorded.

The Nusselt numbers were based on heat transfer coefficients derived from energy balance over the tube length L:

$$Q = h_{lm} \pi D L \cdot \Delta t_{lm} = \dot{m} \cdot C_p \cdot (t_2 - t_1) \qquad (1)$$

where Δt_{lm} represents the log-mean temperature difference Thus

$$\Delta t_{lm} = \frac{t_2 - t_1}{ln \frac{t_w - t_1}{t_w - t_2}} \qquad (2)$$

$$\mathrm{Nu}_m = \frac{h_{lm} D}{k} = \dot{m} C_p \frac{\ln \frac{t_w - t_1}{t_w - t_2}}{\pi k L} \qquad (3)$$

The Graetz numbers ranged from 2.5 to 110.0, the Grashof numbers ranged from 0.8×10^4 to 8.7×10^4.

Correlation of Data

The mean bulk temperature based on the log-mean temperature difference was used to evaluate the air physical properties, average Nusselt number, Grashof and Graetz numbers. The viscosity variation of air was accounted for by introducing the empirical correction factor $(\mu_w/\mu_b)^{0.14}$ where μ_w is the viscosity at the wall temperature and μ_b is the viscosity at the mean bulk temperature [22]. The wall-to-bulk viscosity ratio for the air data in the present study ranged from 1.0016 to 1.020 which is small when compared with other fluids such as water and ethyl alcohol. The viscosity correction factor was mainly included to allow for comparison between the air data given here and other fluids with large variation in viscosity ratio. The only correlation, where the viscosity effect was not included, is the one developed by Jackson et al. [3].

The experimental data of the 228 test runs utilized to derive the required correlations are listed in reference [10]. A representative sample of the data is given in Table II.

The average Nusselt numbers of this study [10] are plotted against the nondimensional distance X on Fig. 4. On the same figure, the following analytical solutions are presented for comparison:

(a) The asymptote $\mathrm{Nu}_a = 1/2X$, representing the condition

where the fluid is heated nearly to the tube wall temperature [11]

(b) Kays solution [7], where the development of the velocity profile was considered in the solution of the momentum and energy equations

(c) Graetz solution [7], where the velocity profile is fully developed at the tube inlet. It can be seen from Fig. 4 that the average Nusselt number increases substantially due to the secondary flow or free convection in the region near the tube inlet where $X \leq 0.04$. At $X = 0.01$, the average Nusselt number from this study is about 2½ times the value predicted analytically by Kays [7].

The experimental data of different researchers, as listed in Table I, with two liquids namely water and ethyl alcohol are also plotted on Fig. 4.

The glycerol data was not included in Table I, mainly because the free convection in glycerol has a minor influence on heat transfer when compared with forced convection [4, 6].

The influence of free convection on the average Nusselt number is well illustrated in Fig. 5. The ratio $\mathrm{Gr}/\mathrm{Re}^{2.5}$ represents the relative magnitude of the buoyancy force to the viscous force [23]. Three sets of data are plotted in this Figure, namely with $L/D = 6$, 10 and 38 and θ_w ranging from 12 to 102°C. For a given L/D and X an increase in the ratio $\mathrm{Gr}/\mathrm{Re}^{2.5}$ implies directly an increase in Grashof number as Reynolds number remains constant. Thus, for example $L/D = 6$ and $X = 0.0128$, Fig. 5 shows that an increase in Grashof number results in an increase in the average Nusselt number. The region, where the free convection is effective, can be seen for $0.0077 < X < 0.045$. The maximum free convection effect as measured by the maximum slope of the constant X lines occurs at approximately $X = 0.020$ which confirms the conclusion obtained in a previous study by the authors [8, 10]. Beyond $X = 0.0450$, the free convection effect diminishes gradually as the increase in the average Nusselt number becomes less noticeable as the ratio $\mathrm{Gr}/\mathrm{Re}^{2.5}$ increases at a given X.

The fact that the constant X lines extend without discontinuity or change of slope at different L/D ratios, proves that the free convection does not depend on the L/D ratio. Figure 5 shows that the free convection effect, as measured by the slope of X lines, does depend not only on Gr but also on X (or $\mathrm{Gz} = \pi/4X$). This conclusion is supported by the study of Depew and August [6] and Brown and Thomas [5].

According to the relative effect of free convection upon forced convection, the heat-transfer data within the entry length of an isothermal horizontal tube are grouped into three regions:

a) Region I $0.0073 < X < 0.040$
                $20 < \mathrm{Gz} < 110$
                $1 \times 10^4 < \mathrm{Gr} < 8.7 \times 10^4$

In this region the free convection is dominant and its effect reaches a maximum at approximately $X = 0.020$ [8, 10]. Beyond $X = 0.040$, the free convection influence diminishes gradually.

Based on dimensional analysis, the equation which describes free and forced convection is

$$\mathrm{Nu}_m = f(\mathrm{Gz}, \mathrm{Gr}) \qquad (4)$$

Equation (4) was further developed by Brown and Thomas [5] to take the form

$$\mathrm{Nu}_m \left(\frac{\mu_w}{\mu_b} \right)^{0.14} = 1.75[\mathrm{Gz} + f(\mathrm{GzGr})]^{1/3} \qquad (5)$$

To determine the free convection term, equation [5] was expressed in the form

$$\left[0.572 \, \mathrm{Nu}_m \left(\frac{\mu_w}{\mu_b} \right)^{0.14} \right]^3 - \mathrm{Gz} = A(\mathrm{Gz}^m \mathrm{Gr}^{1/3})^B \qquad (6)$$

Run No	$\frac{L}{D}$	t_w °C	t_1 °C	t_2 °C	$\dot{m}$ Kg/s x 10^4	Nu_m	Re	Gz	Gr x10^{-4}
1	6	64.2	29.2	59.1	0.665	9.69	173.0	15.84	2.258
2	6	92.3	29.9	73.7	1.975	17.78	505.7	46.25	4.763
3	6	110.5	29.9	72.6	4.584	25.93	1179.2	107.88	7.815
4	6	131.6	30.3	84.2	4.364	24.39	1105.7	101.08	8.738
5	10	40.7	28.5	38.9	0.869	7.67	233.7	11.88	0.973
6	10	78.6	28.6	72.0	0.719	6.48	183.8	10.08	2.781
7	10	92.2	29.2	71.0	3.116	15.35	801.4	44.35	5.122
8	10	110.3	28.3	93.0	1.747	11.77	434.7	23.81	4.631
9	14	78.0	30.0	62.4	3.767	13.77	979.7	38.43	4.118
10	14	92.1	29.6	82.8	1.418	8.47	356.5	13.96	3.255
11	14	109.8	30.4	81.7	4.518	14.83	1145.1	44.85	6.056
12	14	129.5	29.9	101.7	3.609	14.14	889.5	34.78	5.824
13	18	78.1	28.2	71.8	1.120	6.16	306.3	9.34	2.752
14	18	92.3	28.5	81.6	2.042	8.94	515.2	15.69	3.629
15	18	111.3	29.3	94.6	2.445	9.36	606.5	18.45	4.575
16	18	131.1	28.5	116.9	0.578	2.65	138.6	4.21	4.048
17	24	63.3	29.0	58.7	2.015	7.65	524.8	12.01	2.143
18	24	78.4	29.5	72.6	0.646	2.54	164.6	3.76	2.523
19	24	92.9	29.9	82.6	2.631	8.72	661.8	15.12	3.354
20	24	110.1	29.1	97.9	2.311	7.83	568.8	12.97	3.695
21	30	53.4	29.3	50.8	1.339	4.56	352.9	6.47	1.508
22	30	62.2	27.9	58.5	0.851	2.89	221.7	4.06	1.997
23	30	78.7	29.9	71.8	2.667	7.73	680.8	12.45	2.743
24	30	110.7	29.6	100.3	0.973	2.86	238.5	4.35	3.502
25	38	40.1	26.3	38.8	1.349	3.72	362.6	5.25	0.826
26	38	63.5	29.3	59.7	0.817	2.15	212.2	3.07	1.977
27	38	79.3	29.6	74.5	0.718	1.95	182.2	2.63	2.382
28	38	93.0	31.3	86.4	2.303	5.90	573.5	8.27	2.727
29	46	51.8	29.9	49.4	2.620	5.79	691.6	8.26	1.424
30	46	61.8	30.1	59.0	0.978	2.33	254.0	3.03	1.747
31	46	78.4	29.1	72.8	0.911	1.91	232.0	2.77	2.616
32	46	92.4	29.0	85.4	1.035	2.15	258.8	3.08	3.001

The influence of mass flow, as expressed by the Graetz number, on the free convection was analyzed by assigning different values to the exponent m, namely 0.75, 1.0, 1.50 and 1.75. A linear regression by the method of least squares was employed to find the constants A and B.

A value of $m = 1.50$ was found to give the least scatter in correlating the current results. The constants were determined as $A = 0.245$ and $B = 0.882$ where all the data points were weighted equally as the error in the measurements was distributed equally. The coefficient of determination, which is a measure of the goodness-of-fit, was found to be 0.969. Thus equation (6) can be rewritten as

$$\mathrm{Nu}_m \left(\frac{\mu_w}{\mu_b} \right)^{0.14} = 1.75[\mathrm{Gz} + 0.245(\mathrm{Gz}^{1.5}\mathrm{Gr}^{1/3})^{0.882}]^{1/3} \qquad (7)$$

The experimental data of this research as well as selected published data [i.e., within the same range of Gz and Gr as the present data] by Brown and Thomas [5] for water and Depew and August [6] for water and ethyl alcohol are plotted on Fig. 6. Equation (7) correlates the present data to within + 3 percent and − 11 percent and correlates the previous data to within + 3 percent and − 30 percent. Equation (7) is the

best of several schemes that were attempted to correlate the data. Equation (7), which represents the recommended correlation in the present study, differs from either the correlation developed by Brown and Thomas [5] or the correlation developed by Depew and August [6] (see Table I) in the following ways:

1 Equation (7) is for a simultaneous development of the temperature and the velocity profiles. Brown's [5] and Depew's [6] correlations are for a fully developed flow at the onset of heating. The free convection has more influence in the present study since the Graetz number in the free convection term is raised to the power 1.5, whereas the similar term in Brown's and Depew's correlations was raised to the power 1.0.

2 Equation (7) is based upon the log-mean temperature difference, while Brown's and Depew's correlations are based on the arithmetic mean temperature difference. The data reported by Jackson et al. [3] was at much higher Graetz numbers and Grashof numbers (see Table I) and therefore could not be used for comparison.

The average Nusselt numbers which represent the upper bound in Fig. 6 were determined from runs with $L/D = 6$ and
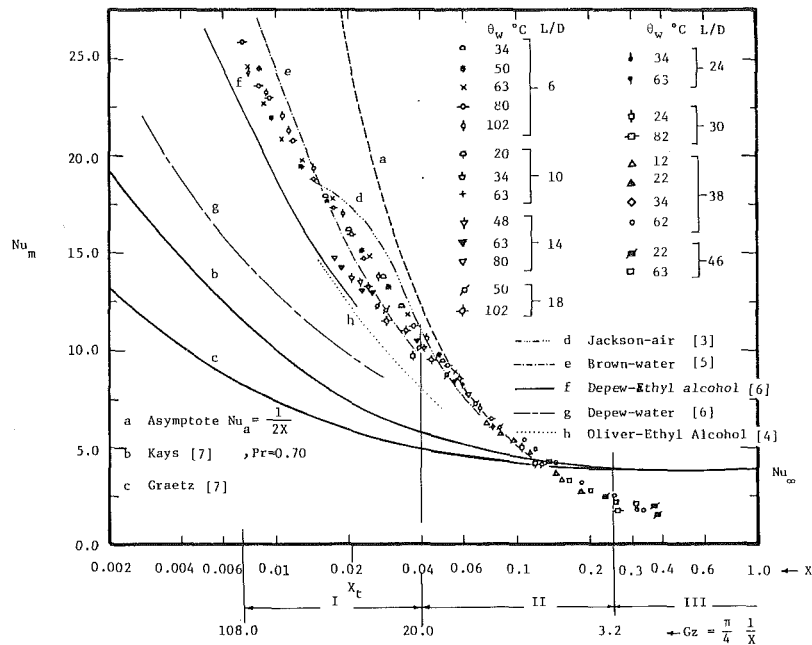
Fig. 4 Average Nusselt number obtained as compared with existing correlations and previous experimental results
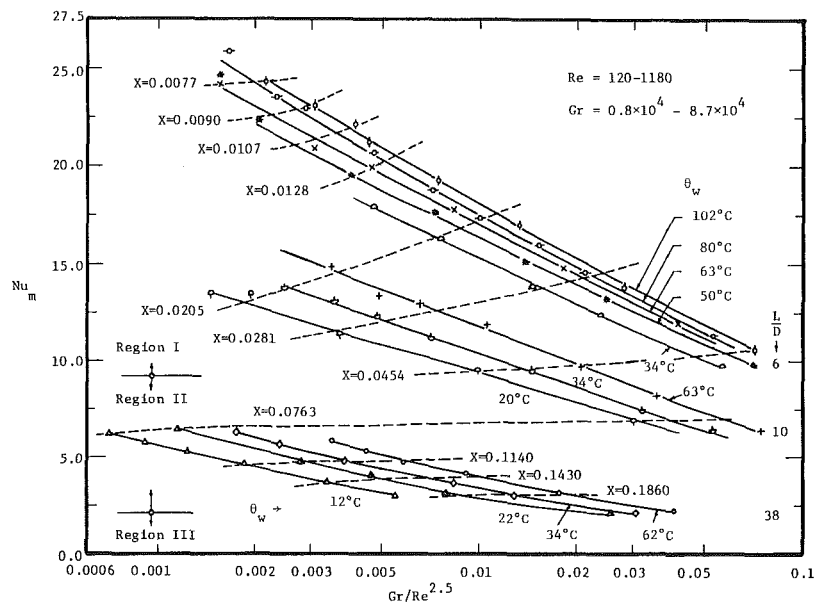

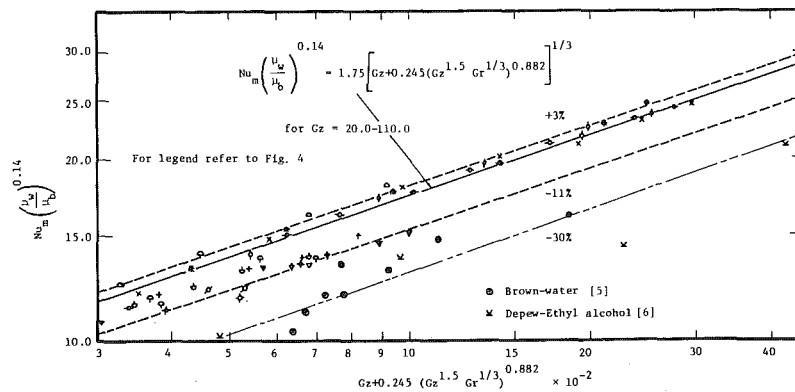**Fig. 5 Free convection effect on average Nusselt number**

Fig. 6 Experimental data plotted against the suggested correlation (7)—Region I

10 where the heat transfer coefficients are expected to be high for such relatively short tubes. The average Nusselt numbers determined by Depew and August [6] and Brown and Thomas [5] can be seen to be on the lower bound in Fig. 6. This is mainly due to the use of fully developed velocity profile at the tube section where heating starts [7].

(b) Region II $0.04 < X < 0.25$
                     $3.2 < Gz < 20$
                     $0.8 \times 10^4 < Gr < 4 \times 10^4$

Forced convection is dominant in this region, thus

$$Nu_m = f(Gz)$$

which may be expressed in the form

$$Nu_m \left(\frac{\mu_w}{\mu_b} \right)^{0.14} = A'(Gz)^{B'} \qquad (8)$$

where the constants A' and B' were determined by linear regression and were found to be $A' = 0.969$ and $B' = 0.82$.

Thus equation (8) becomes

$$Nu_m \left(\frac{\mu_w}{\mu_b} \right)^{0.14} = 0.969(Gz)^{0.82} \qquad (9)$$

The average Nusselt number as determined from equation (9) is slightly higher than the asymptote $Nu_a = 2Gz/\pi$ for Graetz number less than 6. This was caused by the use of the arithmetic mean temperature difference to drive the asymptotic solution [11]. The present data are well correlated by equation (9), as can be seen in Fig. 7. The maximum deviation was found to be +7.8 percent and −6.1 percent. The percentage difference between Nu_m as determined from equation (9) and that determined from interferogram analysis in a previous study [8] did not exceed ±7 percent. No available data relevant to region II could be found in literature to compare against the derived correlation (9).

c) Region III $x > 0.25$
                     $Gz < 3.2$

As $(t_w - t_b)$ diminishes so does the influence of free convection, and forced convection becomes more effective. An average Nusselt number of approximately 2.0 was determined [10] in 7 test runs which extended from $X = 0.255$ to $X = 0.314$. Although the data suggest that the average Nusselt number approaches a constant value of approximately 2.0 in Region III, more experimental work is required to obtain more data and establish clearly the trend of the average Nusselt numbers at $X \geq 0.250$.

The average Nusselt number in this region is well below the pure forced convection prediction of 3.658 for an isothermal tube [7]. This reduction in heat transfer is partly attributed to free convection effects which linger downstream, especially when the ratio $Gr/Re^{2.5}$ is high. A second reason for this reduction in heat transfer is the thermal stratification which develops at the top portion of tube as the flow proceeds. In a thermally stratified field, the heat is transferred from the wall to the fluid mainly by conduction. In fluids with $Pr \simeq 1$, the conduction mode of heat tranfer is low. Because in an isothermal tube the fluid bulk temperature approaches the wall temperature as the flow proceeds, the heat-transfer process becomes self-diminishing. Thus while the free convection tends to enhance the heat transfer near the tube inlet (region I), it decreases the heat transfer far from the tube inlet (region III).

Oliver and Rao [12] in their experimental investigation with highly viscous oils flowing in an isothermal horizontal tube reported Nusselt numbers as low as 1.5. A similar reduction in Nusselt number from the analytically predicated value for the constant heat flux at the wall was also reported [13, 14, 15] under comparable conditions, i.e. the same range of Graetz numbers and Grashof numbers as in the present study.
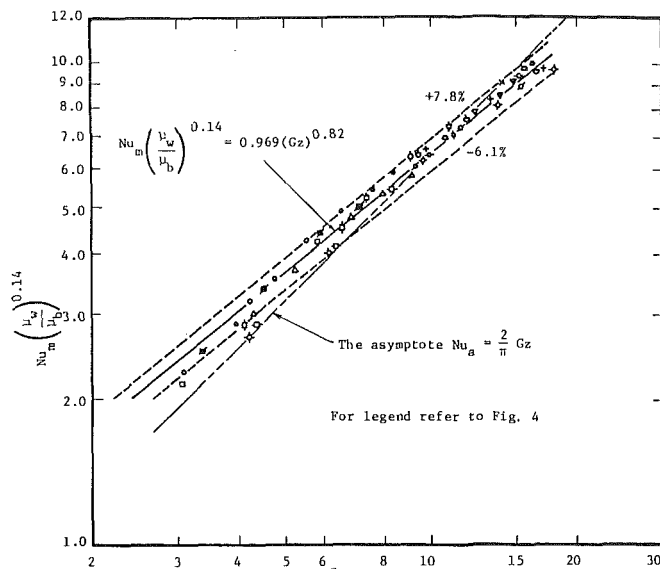

Fig. 7 Experimental data plotted against the suggested correlation (9)—Region II

An error analysis of all sources of errors showed an uncertainty of −1.5 percent and +4 percent in Nu_m.

The possibility that the average Nusselt number may increase at points further downstream of region III ($X > 0.32$) should be investigated. Such a recovery in Nusselt number was reported by Hussain and McComas [13] for air flowing in a uniformly heated tube with $L/D \simeq 118$ and by Shannon and Depew [15] for water flowing in a uniformly heated tube with $L/D \simeq 700$. The Nusselt numbers reported in references [13, 15] showed an increase with the axial distance beyond $L/d \simeq 90$. This strongly suggests the need to extend the present work with tubes having $L/d > 50$ in order to look into the possible increase in Nu_m.

Local Nusselt Number

First, an energy balance over a tube length L was carried out

$$Q_L = \dot{m} C_p (t_2 - t_1) = (h_{lm} A \Delta t_{lm})_L \qquad (10)$$

Adding a tube segment of length ΔL and maintaining the same flow rate, tube wall and air inlet temperatures, a second energy balance over the length $L + \Delta L$ gives

$$Q_{L+\Delta L} = \dot{m} C_p (t_3 - t_1) = (h_{lm} A \Delta t_{lm})_{L+\Delta L} \qquad (11)$$

where t_3 represents the air bulk temperature at exit from the tube of length $L + \Delta L$. The right side of equation (11) can be rewritten in the form

$$(h_{lm} A \Delta t_{lm})_{L+\Delta L} = (h_{lm} A \Delta t_{lm})_L + (hA \Delta t)_{\Delta L} \qquad (12)$$

By subtracting equation (10) from equation (11),

$$\dot{m} C_p (t_3 - t_2) = (hA \Delta t)_{\Delta L} \qquad (13)$$

in which $(h)_{\Delta L}$ represents the local heat-transfer coefficient h_x at a distance $L + \Delta L/2$ from tube inlet as averaged over a length ΔL, and Δt represents the mean temperature difference based on $(t_w - t_2)$ and $(t_w - t_3)$.

$$h_x \left(@x = L + \frac{\Delta L}{2} \right) = \dot{m} C_p \frac{(t_3 - t_2)}{\pi D \Delta L} \cdot \frac{1}{[(t_w - t_2) + (t_w - t_3)]/2} \qquad (14)$$

Equation (14) can be expressed in the differential form

$$h_x = \frac{\dot{m} C_p}{\pi D} \cdot \frac{dt_b}{dx} \cdot \frac{1}{t_w - t_b} \qquad (15)$$

where t_b denotes the bulk temperature at distance x.

The local heat transfer coefficient h_x as expressed by

equation (14) or equation (15) necessitated that the 2 test runs considered for the determination of h_x must fulfill the following conditions:

(*a*) the same wall temperature
(*b*) the same air inlet temperature
(*c*) the same mass flow rate

The above mentioned conditions were neeeded to ensure a continuation of the bulk temperature profile from the tube length L to the length $L+\Delta L$. These conditions were also needed to minimize the uncertainty in determining h_x. The above mentioned conditions were rather restrictive and resulted in a limited data points on the local heat-transfer coefficients.

The local heat-transfer coefficients expressed as Nusselt numbers are shown in Fig. 8. There were no experimental data in the literature concerning the local Nusselt numbers, which could be used for comparison.

The scatter of the data points representing the local Nusselt numbers shows the difficulty of obtaining precise data. An error analysis for the test runs utilized to determine Nu_x showed an uncertainty of ± 20 percent in Nu_x.

The local Nusselt numbers obtained in this study, as presented in Fig. 8, still offer a semiquantitive overall trend which shows that:

1 The value of X at which the local Nusselt number reaches its limiting value (i.e., the location of the fully developed temperature profile) is further downstream from the location where the thermal boundary layer merge ($X_t = 0.0212$ as determined in a previous study [8]).

2 Most of the local Nusselt numbers determined at $X>0.04$ were below 3.658, which is the asymptotic value as predicted analytically for pure forced convection [7].

The analytical results of Ou and Cheng [16], as shown in Fig. 8, seem to overpredict the Nusselt numbers. This may be attributed to the large Prandtl number assumption made in their analytical solution.

Because the data in Fig. 8 does not extend beyond $X=0.05$, neither the location at which Nu_x becomes constant nor the asymptotic value of Nu_x could be determined with certainty. Further work is required to determine Nu_x beyond $X=0.05$.

Conclusions

The heat transfer data in the entrance region of a horizontal isothermal tube were correlated according to the influence of the free convection. The tube entry length was divided into three regions: region I near the tube inlet where the free convection is dominant, region II further downstream where the free convection diminishes and the forced convection becomes dominant, and region III far from the tube inlet where Nu_m becomes constant. The free convection enhances the heat transfer, by up to a factor of 2.5 from the analytical predictions, which account for forced convection only. At points far from the tube inlet the free convection had a deleterious effect on heat transfer.

References

1 Colburn, A. P., "A Method of Correlating Forced Convection Heat Tranfer Data and a Comparison with Fluid Friction," *Transaction of the American Institute of Chemical Engineers*, Vol. 29, 1933, pp. 174–210.

2 Eubank, C. C., and Proctor, W. S., MS thesis in Chemical Engineering M.I.T., Cambridge, Mass., 1951.

3 Jackson, T. W., Spurlock, J. M., and Purdy, K. R., "Combined Free and Forced Convection in a Constant Temperature Horizontal Tube," *Journal of the American Institute of Chemical Engineers*, Vol. 7, 1961, pp. 38–45.

4 Oliver, D. R., "The Effect of Natural Convection on Viscous-Flow Heat Transfer in Horizontal Tubes," *Chemical Engineering Science*, Vol. 17, 1962, pp. 335–350.

5 Brown, A. R. and Thomas, M. A., "Combined Free and Forced Convection Heat Transfer for Laminar Flow in Horizontal Tubes," *Journal of Mechanical Engineering Science*, Vol. 7, No. 4, 1965, pp. 440–448.

6 Depew, C. A. and August, S. F., "Heat Transfer Due to Combined Free
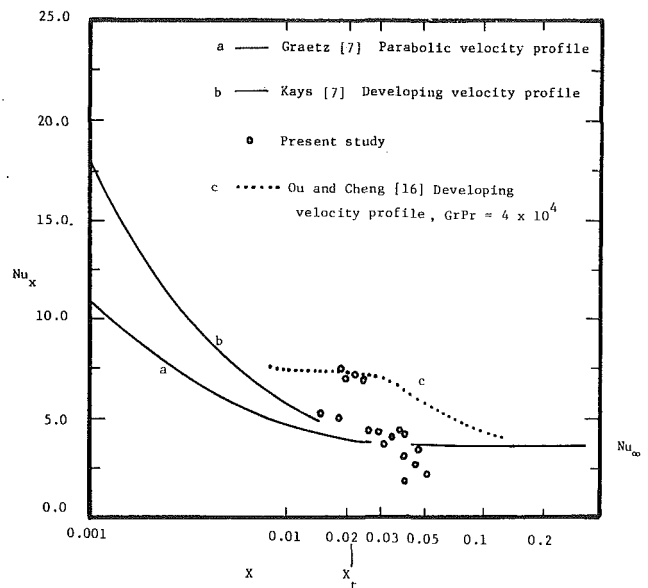
Fig. 8 Local Nusselt number obtained as compared with existing analytical solutions

and Forced Convection in a Horizontal and Isothermal Tube," ASME JOURNAL OF HEAT TRANSFER, Vol. 93, 1971, pp. 380–384.

7 Kays, W. M., *Convective Heat and Mass Transfer*, McGraw-Hill, New York, 1966.

8 Yousef, W. W., and Tarasuk, J. D., "An Interferometric Study of Combined Free and Forced Convection in a Horizontal Isothermal Tube," ASME JOURNAL OF HEAT TRANSFER, Vol. 103, 1981, pp. 249–256.

9 Evenko, V. I. and Aleksandrov, N. A., "A Study of Local Heat Transfer in the Entry Section of a Tube with Different Radii of Curvature of the Inlet Edge," (Translated from *Teploenergetika*, Vol. 17, No. 7), as Thermal Engineering, 1970, pp. 107–110.

10 Yousef, W. W., "An Interferometric Study of Laminar Combined Free and Forced Convective Heat Transfer in the Entrance Region of an Isothermal Horizontal Tube," Ph.D. thesis, The University of Western Ontario, 1980.

11 McAdams, W. H., *Heat Transmission*, McGraw-Hill, 3rd ed., New York, 1954.

12 Oliver, D. R. and Rao, S. S., "Heat Transfer to Viscous Newtonian Liquids in Laminar Flow in Straight Horizontal Circular Tubes," *Transaction of the Institute of Chemical Engineers*, Vol. 56, 1978, pp. 62–66.

13 Hussain, N. A. and McComas, S. T., "Experimental Investigation of Combined Convection in a Horizontal Circular Tube with Uniform Heat Flux," *Proceedings of the Fourth International Heat Transfer Conference*, NC 3.4, Paris, 1970, pp. 1–11.

14 Bergman, P. D. and Koppel, L. B., "Uniform Flux Heat Transfer to a Gas in Laminar Forced Convection in a Circular Tube," *Journal of the American Institute of Chemical Engineers*, Vol. 12, No. 4, 1966, pp. 648–655.

15 Shannon, R. L. and Depew, C. A., "Combined Free and Forced Laminar Convection in a Horizontal Tube with Uniform Heat Flux," ASME JOURNAL OF HEAT TRANSFER, Vol. 90, 1968, pp. 353–357.

16 Ou, J. W. and Cheng, K. C., "Natural Convection Effects on Graetz Problem in Horizontal Isothermal Tube," *International Journal of Heat and Mass Transfer*, Vol. 20, 1977, pp. 953–960.

17 Sellars, J. R., Tribus, M., and Klein, J. S., "Heat Transfer to Laminar Flow in a Round Tube or Flat Conduit—The Graetz Problem Extended," Trans. ASME, Vol. 78, 1956, pp. 441–448.

18 Yao, L. S., "Free-Forced Convection in the Entry Region of a Heated Straight Pipe," ASME JOURNAL OF HEAT TRANSFER, Vol. 100, 1978, pp. 212–219.

19 Ulrichson, D. L. and Schmitz, R. A., "Laminar-Flow Heat Transfer in the Entrance Region of Circular Tubes," *International Journal of Heat and Mass Transfer*, Vol. 8, 1965, pp. 253–258.

20 Grigull, U. and Tratz, H., "Thermischer Einlauf in Ausgebildeter Laminarer Rohrströmung," *International Journal of Heat and Mass Transfer*, Vol. 8, 1965, pp. 669–678.

21 Hieber, C. A. and Sreenivasan, S. K., "Mixed Convection in an Isothermally Heated Horizontal Pipe," *International Journal of Heat and Mass Transfer*, Vol. 17, 1974, pp. 1337–1348.

22 Shannon, R. L. and Depew, C. A., "Forced Laminar Flow Convection in a Horizontal Tube with Variable Viscosity and Free-Convection Effects," ASME JOURNAL OF HEAT TRANSFER, Vol. 91, 1969, pp. 251–258.

23 Gebhart, B., *Heat Transfer*, 2nd ed., McGraw-Hill, New York, 1971, pp. 388–390.

Combined Forced and Free Convection in the Entrance Region of an Isothermally Heated Horizontal Pipe

Mikio Hishida
Professor.

Yasutaka Nagano
Assoc. Professor.
Department of Mechanical Engineering,
Nagoya Institute of Technology,
Showa-ku, Nagoya, Japan

M. S. Montesclaros
Instructor,
Cebu Institute of Technology,
Cebu, Philippines

Numerical solutions are given without the aid of a large Prandtl number assumption for combined forced and free laminar convection in the entrance region of a horizontal pipe with uniform wall temperature. The steady-state solutions have been obtained from the asymptotic time solutions of the time-dependent equations of momentum and energy with the Poisson equation for pressure. Results are presented for the developing primary and secondary velocity profiles, developing temperature fields, local wall shear stress, and local and average Nusselt numbers, which reveal how the developing flow and heat transfer in the entrance region are affected by the secondary flow due to buoyancy forces.

1 Introduction

Analytical studies on combined forced and free laminar convection in the entrance region of a horizontal pipe can be classified into two categories: studies on mixed convection in the thermal entrance region, and those in the hydrodynamically and thermally developing flow region. Detailed results have been reported by several investigators [1–3] for the case of mixed convection in the thermal entrance region where the velocity field is hydrodynamically fully developed.

For combined forced and free convection in the entrance region where the velocity and temperature fields are developing simultaneously, on the other hand, solutions are available only in a limited case, due to the attendant complexities arising from the three-dimensionality of the flow. Hieber and Sreenivasan [4] obtained the solution of the entry flow problem by using the large Prandtl number assumption. This assumption was needed to neglect the nonlinear inertia terms in the governing momentum equations, thus avoiding the chief difficulty in obtaining a numerical solution [1-3]. Yao [5, 6] proposed as asymptotic solution of the developing entry flow by perturbing the solution of the developing flow in an unheated pipe. Though these results are helpful in the understanding of the problem, they are practical only for limited situations. The former result is expected to be valid for large Prandtl number fluids and hence is obviously unsatisfactory to describe the characteristics of fluid flow and heat transfer for ordinary gases and even smaller Prandtl number fluids. The latter perturbation solution applies to the flow regime very near the pipe inlet where the free convection effect is sufficiently small. For moderate or small Prandtl number fluids, no analytical solution applicable throughout the entrance region is as yet available in the literature.

The present study presents numerical solutions of mixed convection in the entrance region of an isothermally heated horizontal pipe for an air flow which is assumed to represent fluids for which the aforementioned large Prandtl number assumption is no longer valid. The steady-state solutions have been obtained from the asymptotic time solutions of the time-dependent momentum and energy equations with Poisson equation for pressure. The results reveal the effects of buoyancy forces on the developing velocity and temperature fields and the related heat-transfer characteristics in the entrance region.

2 Governing Equations

Analysis is made of a hydrodynamically and thermally developing laminar flow in a heated horizontal circular pipe. The fluid enters the pipe with a uniform velocity w_0' and at a uniform temperature t_0'. The pipe wall temperature is held constant at t_w'.

The dimensionless governing equations of continuity, momentum, and energy with the Boussinesq approximation in cylindrical coordinates shown in Fig. 1 become:

Fig. 1 Coordinate system

$$\partial(ru)/\partial r + \partial v/\partial \phi + \partial(rw)/\partial x = 0 \qquad (1)$$

$$\frac{\partial u}{\partial \tau} + u \frac{\partial u}{\partial r} + \frac{v}{r} \frac{\partial u}{\partial \phi} + w \frac{\partial u}{\partial x} - \frac{v^2}{r}$$

$$= -\frac{1}{2} \left(\frac{\mathrm{Re}}{2}\right)^2 \frac{\partial p}{\partial r} + \nabla^2 u - \frac{u}{r^2} - \frac{2}{r^2} \frac{\partial v}{\partial \phi}$$
$$- \mathrm{Gr}\theta \cos \phi \qquad (2)$$

$$\frac{\partial v}{\partial \tau} + u \frac{\partial v}{\partial r} + \frac{v}{r} \frac{\partial v}{\partial \phi} + w \frac{\partial v}{\partial x} + \frac{uv}{r}$$

$$= -\frac{1}{2} \left(\frac{\mathrm{Re}}{2}\right)^2 \frac{1}{r} \frac{\partial p}{\partial \phi} + \nabla^2 v - \frac{v}{r^2} + \frac{2}{r^2} \frac{\partial u}{\partial \phi}$$
$$+ \mathrm{Gr}\theta \sin \phi \qquad (3)$$

$$\frac{\partial w}{\partial \tau} + u \frac{\partial w}{\partial r} + \frac{v}{r} \frac{\partial w}{\partial \phi} + w \frac{\partial w}{\partial x} = -\frac{1}{2} \frac{\partial p}{\partial x} + \nabla^2 w \qquad (4)$$

$$\frac{\partial \theta}{\partial \tau} + u \frac{\partial \theta}{\partial r} + \frac{v}{r} \frac{\partial \theta}{\partial \phi} + w \frac{\partial \theta}{\partial x} = \frac{1}{\mathrm{Pr}} \nabla^2 \theta \qquad (5)$$

where the Laplacian operator is defined as:

$$\nabla^2 = \partial^2/\partial r^2 + (1/r)\partial/\partial r + (1/r^2)\partial^2/\partial \phi^2$$
$$+ (2/\mathrm{Re})^2 \partial^2/\partial x^2 \qquad (6)$$

The dimensionless variables are chosen as follows:

$$\left.\begin{array}{l} \tau = (\tau' w_0'/r_0')(2/\mathrm{Re}), \quad x = (x'/r_0')(2/\mathrm{Re}), \quad r = r'/r_0' \\[4pt] u = (r'/w_0')(\mathrm{Re}/2), \quad v = (v'/w_0')(\mathrm{Re}/2), \quad w = w'/w_0' \\[4pt] \theta = (t' - t_w')/(t_0' - t_w'), \quad p = p'/(\rho w_0'^2/2) \end{array}\right\} \quad (7)$$

The inertia terms such as v^2/r and uv/r in equations (2) and (3) lead to some numerical instability for the finite-difference solutions in the neighbourhood of the origin of the polar coordinates. To ensure stability and a faster rate of convergence, a transformation of the variable is then introduced:

$$U = ru, \quad V = rv, \quad W = rw \qquad (8)$$

A transformation is also used to make the axial boundary finite. Also it is desired to expand the coordinate in the inlet region. Thus:

$$\xi = 1 - 1/\{1 + (30x)^{0.95}\} \qquad (9)$$

With the transformations of equations (8) and (9), rewriting equations (1–5) gives:

$$\partial U/\partial r + \partial V/r\partial \phi + (\partial W/\partial \xi)(d\xi/dx) = 0 \qquad (10)$$

$$\frac{\partial U}{\partial \tau} + \frac{1}{r} \left(U \frac{\partial U}{\partial r} + \frac{V}{r} \frac{\partial U}{\partial \phi} + W \frac{\partial U}{\partial \xi} \frac{d\xi}{dx} - \frac{U^2 + V^2}{r}\right)$$

$$= -\frac{r}{2} \left(\frac{\mathrm{Re}}{2}\right)^2 \frac{\partial p}{\partial r} + \nabla^2 U - \frac{2}{r} \frac{\partial U}{\partial r} - \frac{2}{r^2} \frac{\partial V}{\partial \phi}$$
$$- \mathrm{Gr} r\theta \cos \phi \qquad (11)$$

$$\frac{\partial V}{\partial \tau} + \frac{1}{r} \left(U \frac{\partial V}{\partial r} + \frac{V}{r} \frac{\partial V}{\partial \phi} + W \frac{\partial V}{\partial \xi} \frac{d\xi}{dx}\right)$$

$$= -\frac{1}{2} \left(\frac{\mathrm{Re}}{2}\right)^2 \frac{\partial p}{\partial \phi} + \nabla^2 V - \frac{2}{r} \frac{\partial V}{\partial r} + \frac{2}{r^2} \frac{\partial U}{\partial \phi}$$
$$+ \mathrm{Gr} r\theta \sin \phi \qquad (12)$$

$$\frac{\partial W}{\partial \tau} + \frac{1}{r} \left(U \frac{\partial W}{\partial r} + \frac{V}{r} \frac{\partial W}{\partial \phi} + W \frac{\partial W}{\partial \xi} \frac{d\xi}{dx} - \frac{UW}{r}\right)$$

$$= -\frac{r}{2} \frac{\partial p}{\partial \xi} \frac{d\xi}{dx} + \nabla^2 W - \frac{2}{r} \frac{\partial W}{\partial r} + \frac{W}{r^2} \qquad (13)$$

$$\frac{\partial \theta}{\partial \tau} + \frac{1}{r} \left(U \frac{\partial \theta}{\partial r} + \frac{V}{r} \frac{\partial \theta}{\partial \phi} + W \frac{\partial \theta}{\partial \xi} \frac{d\xi}{dx}\right)$$

$$= \frac{1}{\mathrm{Pr}} \nabla^2 \theta \qquad (14)$$

where the Laplacian operator ∇^2 is written as:

$$\nabla^2 = \frac{\partial^2}{\partial r^2} + \frac{1}{r} \frac{\partial}{\partial r} + \frac{1}{r^2} \frac{\partial^2}{\partial \phi^2}$$

$$+ \left(\frac{2}{\mathrm{Re}}\right)^2 \left\{\left(\frac{d\xi}{dx}\right)^2 \frac{\partial^2}{\partial \xi^2} + \frac{d^2\xi}{dx^2} \frac{\partial}{\partial \xi}\right\} \qquad (15)$$

The above set of equations is sufficient to obtain solutions for U, V, W, θ, and P. For the pressure, however, a more accurate solution can be determined from the Poisson form of the pressure equation, which is derived from the continuity and momentum equations and is expressed as follows:

$$\nabla^2 p = -2 \left(\frac{2}{\mathrm{Re}}\right)^2 \left[\frac{1}{r} \left\{\frac{\partial D}{\partial \tau} + \frac{1}{r} \left(U \frac{\partial D}{\partial r} + \frac{V}{r} \frac{\partial D}{\partial \phi}\right.\right.\right.$$

$$\left.\left.+ W \frac{\partial D}{\partial \xi} \frac{d\xi}{dx} - \frac{UD}{r}\right) - \nabla^2 D + \frac{2}{r} \frac{\partial D}{\partial r} - \frac{D}{r^2}\right\}$$

$$+ \mathrm{Gr} \left(\cos\phi \frac{\partial \theta}{\partial r} - \sin\phi \frac{1}{r} \frac{\partial \theta}{\partial \phi}\right) + \frac{1}{r^2} \left\{\left(\frac{\partial U}{\partial r}\right)^2 + \left(\frac{1}{r} \frac{\partial V}{\partial \phi}\right)^2\right.$$

$$\left.+ \left(\frac{\partial W}{\partial \xi} \frac{d\xi}{dx}\right)^2\right\}$$

$$+ \frac{U^2 + V^2}{r^2} + \frac{2}{r} \left(\frac{U}{r} \frac{\partial V}{\partial \phi} - \frac{V}{r} \frac{\partial U}{\partial \phi}\right) - \frac{\partial}{\partial r} \left(\frac{U^2 + V^2}{r}\right)$$

───── **Nomenclature** ─────

Gr = Grashof number = $g\beta(t_\omega' - t_0')r_0'^3/\nu^2$
g = gravitational acceleration
Nu_ϕ = local Nusselt number, equation (21)
$\overline{\mathrm{Nu}}$ = circumferential average Nusselt number, equation (23)
P = dimensionless pressure, equation (18)
Pr = Prandtl number
p = dimensionless pressure = $p'/(\rho w_0'^2/2)$
p' = pressure
Re = Reynolds number = $2r_0' w_0'/\nu$
r, ϕ, x = dimensionless cylindrical coordinates, $[r = r'/r_0', \ x = (x'/r_0')(2/\mathrm{Re})]$
r', ϕ, x' = cylindrical coordinates
r_0' = pipe radius
t' = local fluid temperature
t_0' = uniform entrance fluid temperature
t_w' = uniform wall temperature

U, V, W = dimensionless velocity components, equation (8)
u, v, w = dimensionless velocity components in r, ϕ, x directions, equations (7)
u', v', w' = velocity components in r', ϕ, x' directions
w_0' = uniform entrance velocity
β = coefficient of thermal expansion
θ = dimensionless temperature difference = $(t' - t_w')/(t_0 - t_w')$
θ_b = dimensionless bulk temperature, equation (22)
λ = thermal conductivity
μ = dynamic viscosity
ν = kinematic viscosity
ξ = dimensionless axial coordinate, equation (9)
ρ = density
τ = dimensionless time = $(\tau' w_0'/r_0')(2/\mathrm{Re})$
$\tau_{w\phi}$ = local wall shear stress, equation (20)
τ' = time

$$-\frac{2W}{r}\frac{\partial U}{\partial \xi}\frac{d\xi}{dx}$$

$$+\frac{2}{r}\frac{\partial U}{\partial \phi}\frac{\partial V}{\partial r}+\frac{2}{r}\frac{\partial W}{\partial \phi}\frac{\partial V}{\partial \xi}\frac{d\xi}{dx}$$

$$+2\frac{\partial U}{\partial \xi}\frac{d\xi}{dx}\frac{\partial W}{\partial r}\biggr\}\biggr] \qquad (16)$$

Where D, called the dilatation term, is:

$$D=\partial U/\partial r+\partial V/r\partial \phi+(\partial W/\partial \xi)\,(d\xi/dx)$$

The continuity equation (10) just states that $D = 0$, yet incompatible initial conditions or incomplete iterative solutions of the Poisson equation eventually lead to the nonzero value of the finite-difference of D. The dilation term could still be set equal to zero in equation (16) without changing the order of the truncation error, but because the Poisson equation is solved iteratively, the error accumulates. The final result would not only be inaccurate: it would also reflect a nonlinear instability in the momentum equations. The inclusion of D could eliminate this nonlinear instability, as has been observed in other studies [7].

The boundary conditions for equations (10–14) and (16) at pipe inlet, at infinite downstream, at pipe wall, and at vertical centerline are, respectively, as follows:

$$\xi=0, 0\le r<1: U=V=0, w=W/r=1, \theta=1$$

$$p=2(2/\mathrm{Re})^2\mathrm{Gr}(1-r\,\cos\phi)$$

$$\xi=1, 0\le r<1: U=V=0, w=W/r=2(1-r^2), \theta=0$$

$$(\partial p/\partial \xi)\,(d\xi/dx)=-16$$

$$0\le \xi\le 1, r=1: U=V=W=0, \theta=0$$

$$\partial p/\partial r=2(2/\mathrm{Re})^2(\partial^2 U/\partial r^2-\partial U/\partial r)$$

$$0\le \xi\le 1, 0\le r\le 1, \phi=0, \pi: V=0 \qquad (17)$$

As seen from the boundary conditions, equation (17), the pressure changes linearly with axial distance in the fully developed region. Hence, let the asymptotic pressure solution be P. Then we can write P as:

$$P(r,\phi,x)=p+16x \qquad (18)$$

Upon simply replacing p by P the boundary condition for P becomes equal to equation (17) at the pipe inlet and wall, and is written at infinite downstream as:

$$\xi=1, 0\le r<1:\ \partial P/\partial \xi=0 \qquad (19)$$

Note that the upstream heat conduction may affect the temperature profile at the pipe inlet. We neglect, however, this effect using the same inlet temperature condition as that adoped in related problems [1–6].

3 Numerical Method of Solution

The solutions for U, V, W, θ, and P can be obtained from numerical solution of the finite-difference forms of the governing equations (11-16) with associated boundary conditions (17) and (19). With a view to reducing a truncation error and improving numerical stability, Euler's modified method and the Crank-Nicolson method are employed to evaluate the first and second-order derivatives in the time-dependent momentum and energy equations, respectively [7]. The forward time and centered space differences are used to evaluate the derivatives except the advection terms which are approximated by upwind differencing.

As mentioned previously, due to incompatible initial conditions or an incomplete iterative solution of the Poisson equation, the continuity eqution is not satisfied exactly, in finite-difference form, i.e., $D \ne 0$. A nonlinear instability of the pressure term results, which may be corrected by retaining $\partial D/\partial \tau$ as in equation (16). Since the inclusion of D in the

Table 1 Locations where velocity and temperature profiles are given

	x	x'/r_0'
A	1.18×10^{-3}	5.88×10^{-2}
B	1.23×10^{-2}	6.17×10^{-1}
C	3.06×10^{-2}	1.53
D	6.11×10^{-2}	3.05
E	1.91×10^{-1}	9.55
F	4.36×10^{-1}	21.8
G	∞	∞

spatial terms of equation (16) is not expected to be as important as the $\partial D/\partial \tau$ term [7], we set $D = 0$ in the spatial terms and evaluate the time derivative $\partial D/\partial \tau$ by forcing $D^{(\eta+1)} = 0$ so that $\partial D/\partial \tau = -D^{(n)}/\Delta \tau$. The boundary conditions for the pressure P are, as seen from equations (17) and (19), the Neumann boundaries at pipe wall and at infinite downstream. These boundary conditions are evaluated by applying Miyakoda's scheme [7], wherein the derivative boundary condition is incorporated directly into the SOR (successive over-relaxation) difference scheme at interior points adjacent to the boundaries in order to eliminate the drifting behavior of the pressure solution.
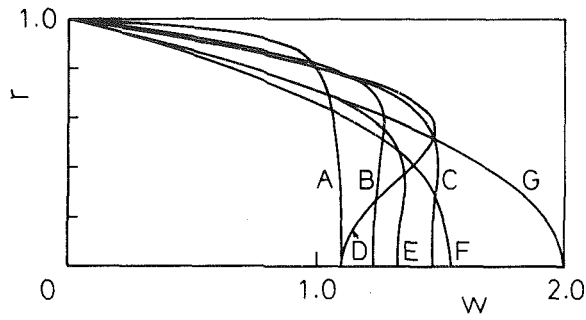
Because of symmetry, the problem is solved in one-half of the circular region by using the SOR method at each time level. The mesh size of $26 \times 27 \times 26$ (r, ϕ, ξ) is used. To confirm the numerical accuracy, the mesh size is cut in half for the pure forced convection case. No significant differences are seen in the results. The maximum value for the time-step size $\Delta \tau$ is determined by trial computations to facilitate the stable computation. The computations continue with increasing time levels until the steady-state profiles are obtained. The criterion for convergence is $|Q^{n+1} - Q^n|/$ Max $|Q^n| < 10^{-5}$ (Q: U, V, W, etc.). The present problem has been solved on the FACOM M-200 system. For one set of Re, Pr, and Gr, the computing time required is about four hours.
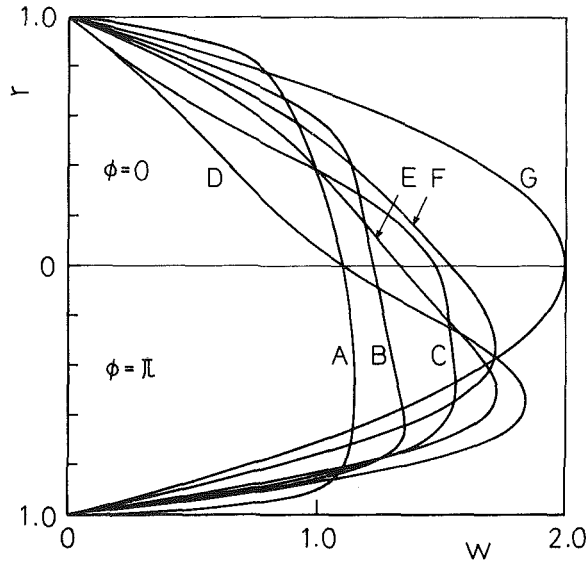
4 Results and Discussion

The numerical analysis has been made without the large Prandtl number assumption, and the results are presented for the following conditions: Pr $= 0.71$, Re $= 100$, Gr $= 5000$ and 10000. The difference between Gr $= 5000$ and 10000 causes no qualitative change on the Nu profile (Fig. 10), and thus the following discussion is mostly concerned with the result for Gr $= 5000$. The velocity and temperature profiles labeled A - G in the succeeding figures are those at the typical axial locations given in Table 1.

4.1 Velocity Profiles. The developing profiles of axial velocity w are illustrated in Fig. 2. The axial-velocity profile for pure forced convection is symmetric about the center. With addition of the free convection effect, the symmetric velocity profile is still retained along the horizontal centerline (Fig. 2(a)). However, this symmetry is lost along the vertical centerline, as evidenced in Fig. 2(b), with maximum velocity displaced toward the bottom pipe wall. This clearly starts to occur very near the pipe inlet. The asymmetric velocity profile is the most pronounced at the axial location marked D ($x = 6.11 \times 10^{-2}$, $x'/r_0' = 3.05$). Here the free convection effect becomes the strongest, as will be discussed later. At far downstream positions, the asymmetry in the velocity profile diminishes gradually with increasing distance from the entrance, as demonstrated by the profiles marked E, F, and G. Ultimately, it vanishes altogether, and the flow eventually becomes the Poiseuille flow.

The direction of the radial velocity component u for pure forced convection is toward the center, that is $u < 0$, throughout the entrance region, which is induced by the boundary-layer displacement. However, for combined forced

Journal of Heat Transfer

FEBRUARY 1982, Vol. 104 / 155

Downloaded 19 Dec 2010 to 194.27.225.72. Redistribution subject to ASME license or copyright; see http://www.asme.org/terms/Terms_Use.cfm

(a) horizontal centerline ($\phi = \pi/2$)

(b) vertical centerline ($\phi = 0, \pi$)

Fig. 2 Developing axial-velocity profiles for Re = 100 and Gr = 5000 along horizontal and vertical centerlines
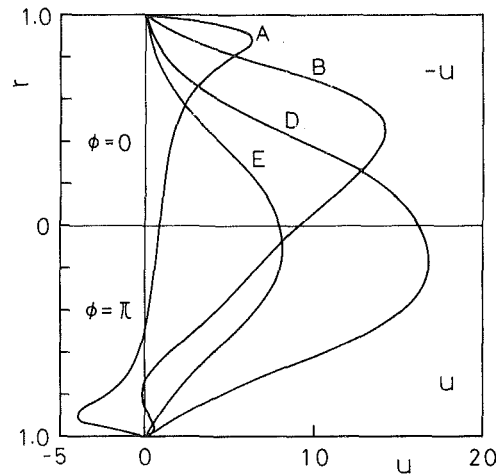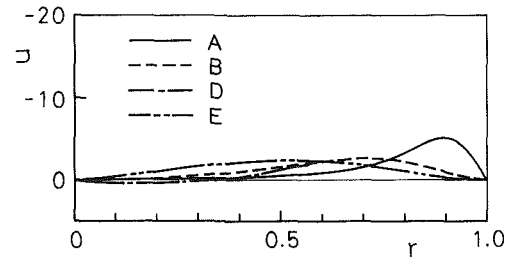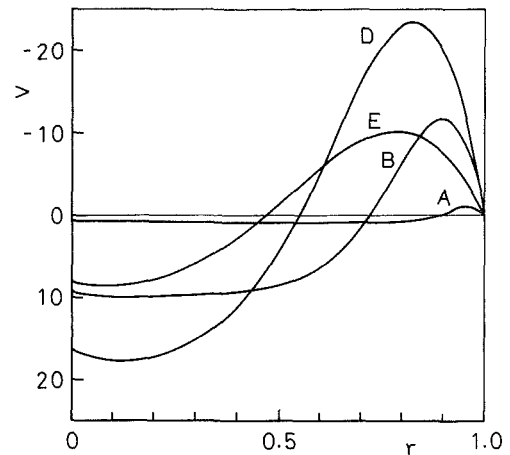

Fig. 3 Development of radial-velocity profiles along vertical centerline (Re = 100, Gr = 5000; ϕ = 0, π)

(a) radial velocity component u

(b) tangential velocity component v

Fig. 4 Development of secondary velocity profiles along horizontal centerline (Re = 100, Gr = 5000; ϕ = $\pi/2$)

and free convection, the radial stream toward the center is visible only very near the pipe inlet, say at the location A ($x = 1.18 \times 10^{-3}$, $x'/r_0' = 5.88 \times 10^{-2}$). This can be seen from the development of radial-velocity profiles along the vertical centerline shown in Fig. 3. Further downstream ($x = 1.23 \times 10^{-2}$) this radial stream is no longer in evidence, which indicates the onset of the secondary flow due to free convection effects. Hence, at the downstream location B, the downward stream from the upper region attendant on the secondary flow controls the boundary layer development along the bottom wall. At the further downstream location D, the inherent displacement effect associated with the boundary layer development along the lower wall is completely suppressed and the downward stream alone predominates in the secondary flow along the vertical axis. The downward flow, however, is seen to become weaker again at sufficiently far downstream locations, which may result from the disappearance of free convection effects.

The features of secondary flow are more clearly understood by investigating the development of secondary velocity profiles along the horizontal centerline ($\phi = \pi/2$). The developing radial-velocity profiles shown in Fig. 4(a) reveal that the fluid motion toward the center due to the displacement effect is apparent only in close proximity to the pipe inlet. As seen from the developing tangential-velocity profiles given in Fig. 4(b), the warmer fluid near the wall moves upward ($v < 0$) and the cooler fluid in the core region moves downward ($v > 0$) once the secondary flow is produced by free convection effects. Thus, in the upper region along the

vertical axis, the low momentum fluid near the top is constantly transported downward toward the center. In the lower region, the high momentum fluid at the core is continually transported downward toward the bottom of the pipe, eventually distorting the axial-velocity profiles as shown in Fig. 2(b).

4.2 Growth and Decay of Secondary Flow. In order to examine the secondary flow, velocity vectors at a series of downstream axial positions are plotted in Fig. 5. Only the arrowhead is drawn to show the direction of secondary motion when $|u| < 1$. It is seen from Fig. 5(a) that the secondary flow is not present very near the pipe inlet, however the fluid motion toward the center due to the boundary-layer displacement is already affected here by buoyance forces. The
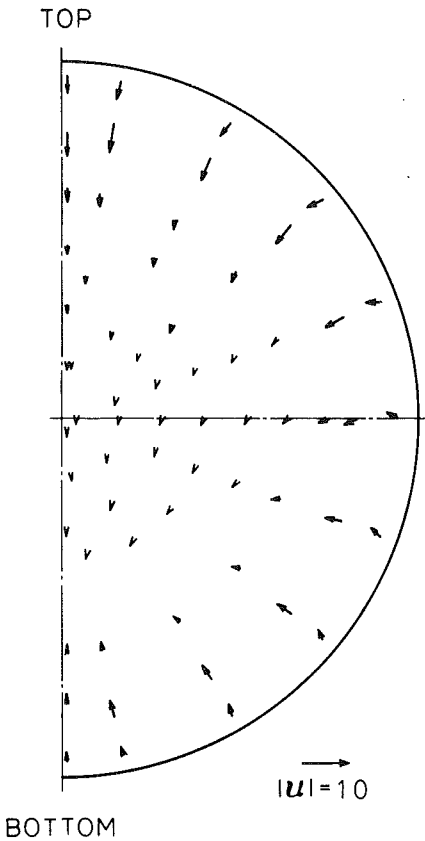
Fig. 5(a)   A $(x'/r_0' = 0.0588)$
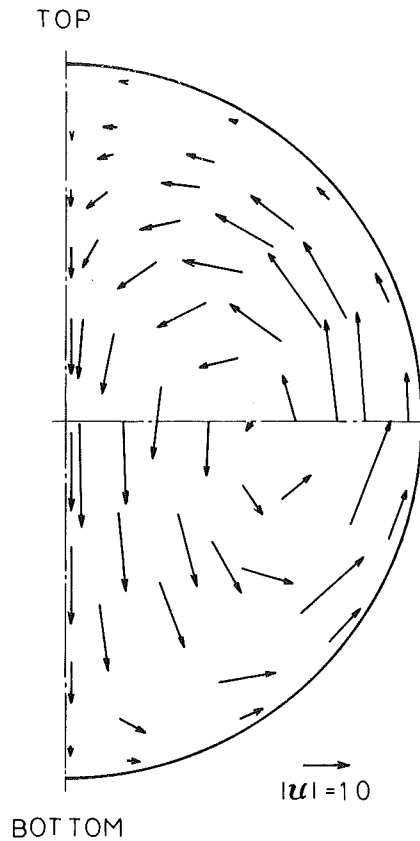
Fig. 5(c)   D $(x'/r_0' = 3.05)$

Fig. 5   Secondary flow pattern (Gr = 5000) at axial locations
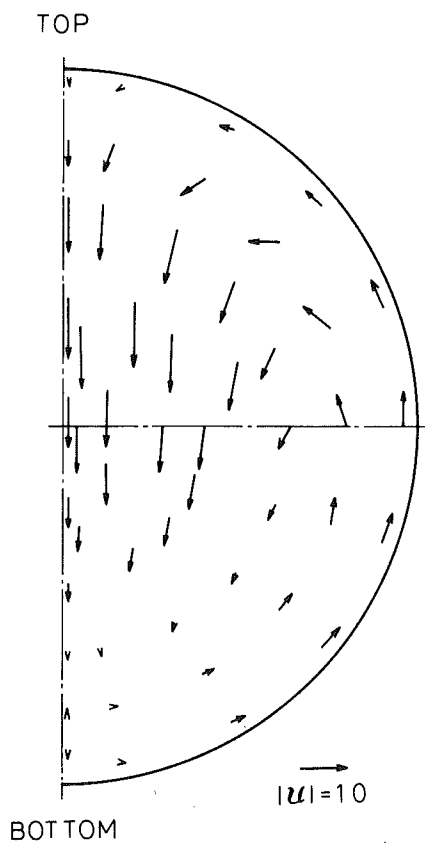
Fig. 5(b)   B $(x'/r_0' = 0.617)$

notable secondary flow pattern is observed in Fig. 5(b), where the axial distance from the entrance is still very short ($x' = 0.617\ r_0'$). The secondary velocity in the upper region is initially higher than that in the lower region where the stream looks somewhat sluggish. The center of circulation first appears in the lower region. Further down the pipe, as shown in Fig. 5(c), this center tends to move upward with some movement toward the pipe center. At this time the secondary velocity increases from zero at $x = 0$ to maximum nearly at $x \simeq 6.0 \times 10^{-2}$ ($x'/r' \simeq 3.0$), and then decreases further downstream. At sufficiently far downstream locations, the secondary flow disappears completely and the velocity becomes fully developed.

4.3 Wall Shear Stress. The dimensionless local shear stress at the wall $\tau_{w\phi}$ is obtained by:

$$\tau_{w\phi} = -\mu(\partial w'/\partial r')_{r'=r_0',\phi} / (\rho w_0'^2/2)$$
$$= -(4/\mathrm{Re})(\partial w/\partial r)_{r=1,\phi} \qquad (20)$$

As seen from Fig. 6, the local wall shear stress varies along the circumferential position with a maximum at the pipe bottom and a minimum at the top. This is because the main flow is forced down toward the pipe bottom by the secondary flow, thereby increasing velocity gradients at the wall for the lower region and vice versa for the upper region. The axial variation of shear stress at the lower and upper walls clearly exhibits the presence of a local peak and valley at some downstream positions where the intensity of the secondary motion due to free convection effects is prominent. At a far downstream position, say $x = 1.0$ ($x'/r' = 50$), the free convection effect almost disappears and the limiting value of $\tau_w \mathrm{Re} = 16$ for the Poiseuille flow is approached asymptotically.

4.4 Temperature Profiles. The temperature developments in the entrance region are shown in Fig. 7. The developing
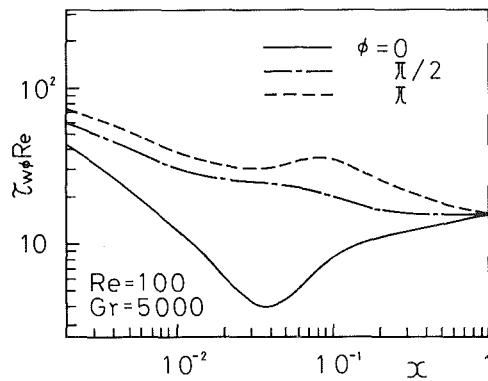
Fig. 6 Local wall shear stress variations at locations $\phi = 0, \pi/2, \pi$
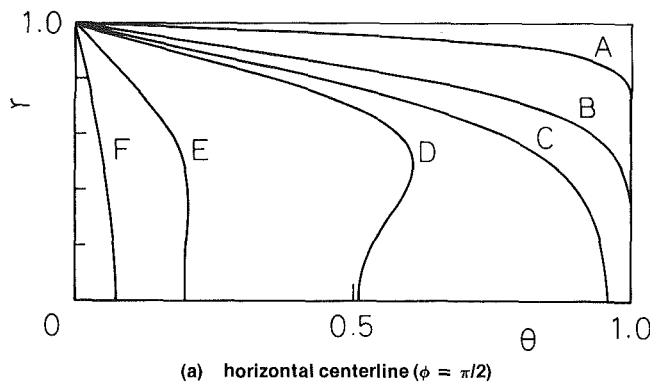
(a) horizontal centerline ($\phi = \pi/2$)
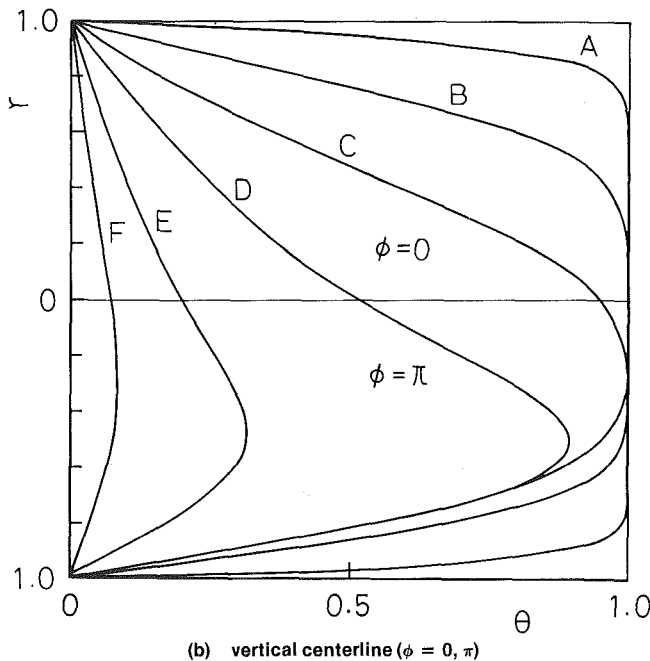
(b) vertical centerline ($\phi = 0, \pi$)

Fig. 7 Developing temperature profiles for Re = 100 and Gr = 5000 along horizontal and vertical centerlines

temperature profiles along the horizontal centerline are symmetric about the center. On the other hand, the vertical central temperature profiles in Fig. 7(b) are distorted by free convection effects just like the velocity profiles given in Fig. 2. The top fluid temperature near the wall is higher than the bottom fluid temperature and the temperature minimum shifts toward the pipe bottom. This is expected because in the upper region the warmer fluid near the wall is constantly transported upward along the pipe wall by convection due to secondary flows. Near the bottom of the pipe, however, the
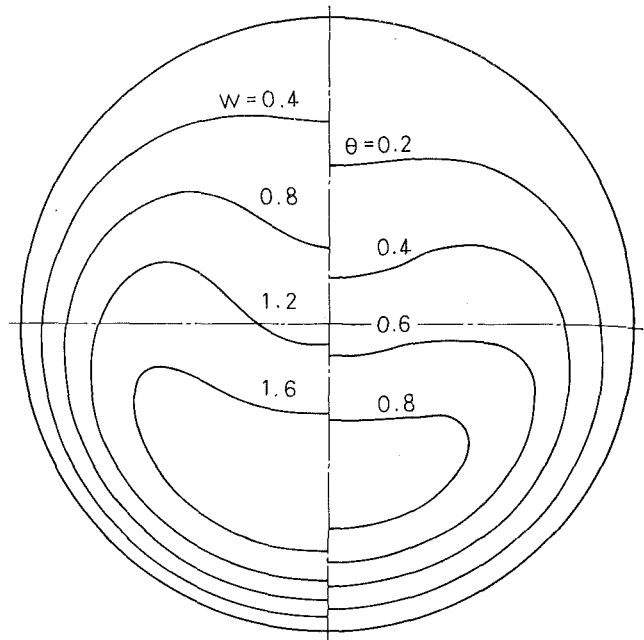
Fig. 8 Axial-velocity contours and isotherms (at location D: x = 6.11 × 10^{-2})

cooler fluid in the core region is continually transported downward. Once the secondary flow occurs, the velocity profile is distorted over the entire pipe section. In contrast, the temperature of the core flow near the pipe inlet is the same as the entry fluid temperature. Thus it appears to be unaffected by the intense secondary flow, as can be readily seen from the curve labelled B.

Further insight may be gained by contrasting the axial-velocity contours with the isotherms at the location where the free convection effect is prominent. From Fig. 8 it is seen that the axial-velocity maximum and the corresponding temperature minimum occur at about the same point on the vertical centerline below the pipe center. Here, there exists a close similarity in the two profiles. In the upper region, the velocity contours and isotherms are sparsely spaced. These spacings change considerably in the circumferential direction. Consequently, in the upper section, pronounced peripheral variations occur in the radial gradient of velocity and temperature. This is evidenced by the local wall shear stress values (Fig. 6) and the following local Nusselt number results.

4.5 Heat Transfer. The Nusselt number behavior is of special importance in many industrial applications. The local Nusselt number is given by:

$$\text{Nu}_\phi = 2r_0'h_\phi/\lambda = -(2/\theta_b)\,(\partial\theta/\partial r)_{r=1,\phi} \qquad (21)$$

in which h is the heat-transfer coefficient and θ_b denotes the dimensionless bulk temperature written as:

$$\theta_b = \int_0^1 \int_0^{2\pi} \theta wr\, d\phi\, dr \Big/ \int_0^1 \int_0^{2\pi} wr\, d\phi\, dr \qquad (22)$$

The circumferential average Nusselt number can be obtained by

$$\overline{\text{Nu}} = \frac{1}{2\pi} \int_0^{2\pi} \text{Nu}_\phi d_\phi \qquad (23)$$

The variations of the local Nusselt number are shown in Fig. 9 together with the perturbation solution obtained by Yao [6] for comparison. The overall behavior of the local Nusselt number is similar to the wall shear stress variation shown in Fig. 6, and the wall heat-transfer is larger in the lower region and smaller in the upper region. The difference in Nu_ϕ between above and below the horizontal axis reaches
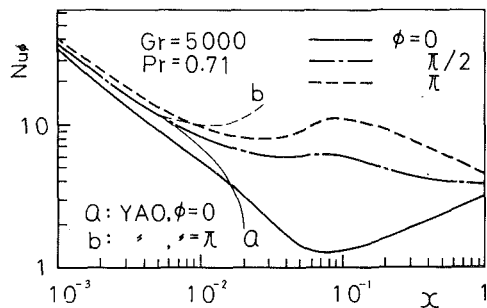
Fig. 9 Local Nusselt number variations at locations $\phi = 0$, $\pi/2$, and π

Fig. 10 Circumferential average Nusselt number values for Gr = 0, 5000, and 1000

maximum somewhere in the region $x \simeq 4 \times 10^{-2} - 10^{-1}$ ($x'/r_0' \simeq 2$–5) where the intensity of the secondary flow due to free convection effects is at its peak. With the decay of the secondary flow, the local Nusselt numbers at peripheral positions approach the asymptotic value of $Nu_\phi = 3.66$ for the pure forced convection further downstream. It is clear that Yao's perturbation solution is only applicable in close proximity to the pipe inlet.

The variations of the circumferential average Nusselt number $\overline{Nu}$ are presented in Fig. 10 in which the result for Gr = 0, 5000, and 10,000 are plotted to show the effects of Grashof number magnitude. With the addition of free convection effects, the average Nusselt number becomes higher than that for the pure forced convection (Gr = 0). As described previously in the context of velocity and temperature profiles, the free convection effect starts to appear at the start of the entrance region somewhere around $x = 10^{-3}$ ($x'/r_0' = 0.05$). The deviation of $\overline{Nu}$ for combined flow from that for the pure forced convection is also observed from the vicinity of the pipe inlet. The location of the local maximum for $\overline{Nu}$ is closely related to the appearance of the maximum secondary flow intensity. After reaching a local maximum value, the average Nusselt number decreases again until the limiting value of $\overline{Nu} = 3.66$ is approached. It is seen that increasing Grashof number decreases the entrance length prior to the onset of significant free convection effects. It also increases the local maximum for $\overline{Nu}$.

5 Conclusions

Numerical predictions of flow and heat transfer have been performed for combined forced and free convection in the entrance region of a horizontal pipe. Though the solution is presented for an air flow of Prandtl number 0.71, the solution procedure described here involves no questionable assumptions or approximations. Hence it is expected to be applicable to fluid of arbitrary Prandtl number. The results can be summarized in the following conclusions:

1 Without the aid of a large Prandtl number assumption, the steady-state solutions for the entry-flow problem with buoyancy effects can be calculated from numerical asymptotic time solutions of the time-dependent momentum and energy equations, and the Poisson equation for pressure.

2 The secondary flow due to free convection appears at the start of the pipe entrance region. This secondary velocity is initially higher in the upper region of the pipe, and increases throughout the cross section until its intensity reaches a maximum at a certain downstream position which depends on Grashof number. Further downstream, the secondary flow diminishes gradually, and ultimately vanishes altogether.
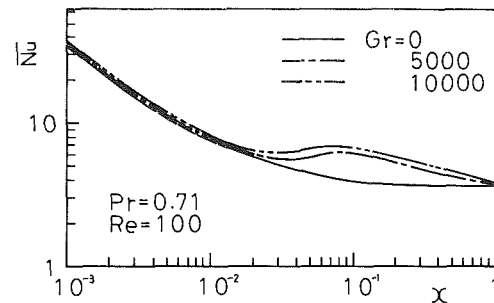
3 The secondary flow distorts the axial-velocity and temperature profiles with maximum velocity and minimum fluid temperature displaced toward the pipe bottom instead of at the center.

4 The temperature in the core flow near the pipe inlet is the same as the entry fluid temperature, unaffected by the intense secondary flow.

5 At axial locations where the secondary motion is prominent, the local Nusselt number as well as the local wall shear stress becomes higher below the horizontal axis than above the horizontal axis.

6 The circumferential average Nusselt number for combined flow reaches a local maximum value, which is considerably larger than the Nusselt number for pure forced convection. This maximum occurs at an axial location of maximum secondary flow intensity.

7 Increasing Grashof number decreases the entrance length prior to the onset of marked free convection effects. It also increases the local maximum Nusselt number.

References

1 Hong, S. W., Morcos, S. M., and Bergles, A. E., "Analytical and Experimental Results for Combined Forced and Free Laminar Convection in Horizontal Tubes," *Proceedings of the Fifth International Heat Transfer Conference*, Vol. 3, 1974, pp. 154–158.

2 Cheng, K. C. and Ou, J. W., "Free Convection Effects on Graetz Problem for Large Prandtl Number Fluids in Horizontal Tubes with Uniform Wall Heat Flux," *Proceedings of the Fifth International Heat Transfer Conference*, Vol. 3, 1974, pp. 159–163.

3 Ou, J. W. and Cheng, K. C., "Natural Convection Effects on Graetz Problem in Horizontal Isothermal Tubes," *International Journal of Heat and Mass Transfer*, Vol. 20, 1977, pp. 953–960.

4 Hieber, C. A. and Sreenivasan, S. K., "Mixed Convection in an Isothermally Heated Horizontal Pipe," *International Journal of Heat and Mass Trasnfer*, Vol. 17, 1974, pp. 1337–1348.

5 Yao, L. S., "Entry Flow in a Heated Straight Tube," ASME *Journal of Fluid Mechanics*, Vol. 88, 1978, pp. 465–483.

6 Yao, L. S., "Free-Forced Convection in the Entry Region of a Heated Straight Pipe," ASME JOURNAL OF HEAT TRANSFER, Vol. 100, 1978, pp. 212–219.

7 Roache, P. J., *Computational Fluid Dynamics*, Hermosa, 1976.

C. W. Somerton

I. Catton

Nuclear Energy Laboratory,
University of California,
Los Angeles, Calif. 90024

On the Thermal Instability of Superposed Porous and Fluid Layers

A solution is presented for the problem of predicting the onset of convection for a system consisting of a volumetrically heated porous bed saturated with and overlaid with a fluid, heated or cooled from below. Results are presented in graphical form in terms of the external Rayleigh number based on the fluid layer, which is shown to be the sole stability parameter of the problem. A wide range of independent parameters are investigated and physical justification for the behavior of the instability with respect to them is given. Finally, the results are compared with the two bounding cases of the problem and are found to be in agreement with them.

Introduction

Currently, interest in natural convection in porous media has been renewed due to its application to energy related problems. From these applications, a variety of new problems have arisen in the field. This present study deals with predicting the onset of convection when there is a fluid-saturated porous medium with internal heat generation, heated or cooled from below, and overlaid with a finite layer of fluid. The physical situation is shown in Fig. 1.

Recently, two experimental investigations dealing with measuring the heat transfer of the compound layer configuration of the present work have been conducted at UCLA by Rhee [1] and Cherng [2]. The stability limits presented in these works consider the onset of motion only in the porous layer, at which point convection in the overlying fluid has begun and has been going on for some time. Stability limits obtained from the present analysis are based on the total system. As seen in the results, the onset of motion in the fluid layer will penetrate into the porous bed and induce motion in it. Hence, a decoupling of the layers as done by Rhee [1] and Cherng [2] appears to be inappropriate.

Sun [3] and Nield [4] have looked at the same physical situation as presented in this work, except that they do not allow for internal heating in the porous medium. The significant differences between the present work and Sun's analysis are in the viscous shear term of the momentum equation for the porous layer and the form of the corresponding matching conditions at the interface. Sun uses D'Arcy's law for the viscous shear term, $(-\mu/\kappa \, \vec{u}_{II})$, and the corresponding Beavers and Joseph [5] boundary conditions at the interface,

$$\frac{\partial u_I}{\partial z} = \frac{\bar{\alpha}}{\sqrt{\kappa}} \, (u_I - u_{II}), \frac{\partial v_I}{\partial z} = \frac{\bar{\alpha}}{\sqrt{\kappa}} \, (v_I - v_{II}) \qquad (1)$$

The present analysis uses Brinkman's extension of D'Arcy's
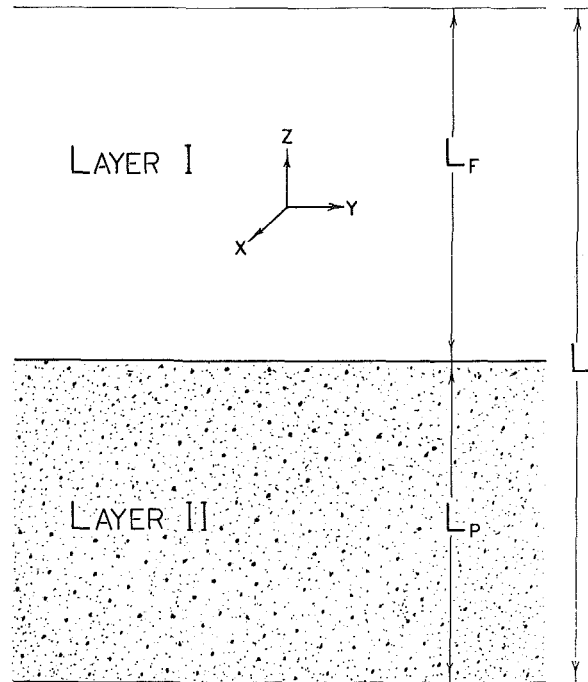
Fig. 1 Physical model and coordinate system

law, as suggested by Neale and Nadar [6]. Hence, the viscous shear term becomes, $-\bar{\mu}/\kappa \, \vec{u}_{II} + \bar{\mu}\nabla^2 \vec{u}_{II}$, with the following boundary conditions:

$$u_{II} = u_I, \qquad v_I = v_{II},$$

$$\mu\frac{\partial u_I}{\partial z} = \bar{\mu}\frac{\partial u_{II}}{\partial z}, \quad \text{and} \quad \mu\frac{\partial v_I}{\partial z} = \bar{\mu}\frac{\partial v_{II}}{\partial z} \qquad (2)$$

The "effective viscosity" in the porous bed, $\bar{\mu}$, is not, in general, equal to the fluid viscosity. Various models, such as

Copyright © 1982 by ASME

Downloaded 19 Dec 2010 to 194.27.225.72. Redistribution subject to ASME license or copyright; see http://www.asme.org/terms/Terms_Use.cfm

Lundgren's [7], have been postulated in order to predict the effective viscosity. These models are quite elaborate and it has been found that by simply letting $\mu = \tilde{\mu}$ experimental data may be fairly well reproduced [6]. The use of Brinkman's extension imposes the physically real no-slip velocity condition at the interface. On the other hand, although it gives identical predictions in the fluid layer for boundary layer porous flat plate flow, D'Arcy's law forces a discontinuity in the velocity at the interface.

Nield [4] follows the same approach as Sun and applies D'Arcy's law with the Beavers and Joseph boundary conditions. However, he uses more generalized boundary conditions at the upper and lower surfaces of the system.

Governing Equations and Boundary Conditions

The governing equations for this problem are written separately for the porous bed and overlying fluid layer. The two sets of equations are then coupled by applying the proper interface conditions. The undisturbed flow solution is given for region I by:

$$\vec{u}\,^0_{\rm I} = 0$$

$$T^0_{\rm I} = \frac{(T_T - T_M)z}{L_f} + T_M \tag{3}$$

$$\vec{\nabla} P^0_{\rm I} = -\rho_c g(1 - \beta T^0_{\rm I})\hat{e}_z$$

and for region II by:

$$\vec{u}\,^0_{\rm II} = 0$$

$$T^0_{\rm II} = -\frac{Q_v z^2}{2k_m} - \left[\frac{T_B - T_M}{L_p} + \frac{Q_V L_p}{2k_m}\right]z + T_M \tag{4}$$

$$\nabla P^0_{\rm II} = -\rho_c g(1 - \beta T^0_{\rm II})\hat{e}_z$$

where T_M is the interface temperature and is seen to be,

$$T_M = \frac{k_f L_p T_T + L_f k_m T_B - Q_v L_p^2 L_f/2}{k_f L_p + k_m L_f} \tag{5}$$

Assuming that all parameters can be expressed as a sum of the undisturbed flow solution and a small perturbation, the perturbation equations result when the products of the small terms are neglected.

Assuming that all disturbances are of the form

$$f(Z)\exp\{a_x X + a_y Y\} \tag{6}$$

and carrying out the normal stability manipulations (see Somerton [8]) the following equations result with $D = d/dz$ and $a^2 = a_x^2 + a_y^2$,

$$(D^2 - a^2)^2 W_{\rm I} = a^2 \theta_{\rm I} \tag{7a}$$

$$(D^2 - a^2)\theta_{\rm I} = \frac{-W_{\rm I}}{(\eta + \gamma)(1 + \eta)}[{\rm Ra}_E(1 + \eta)^2 + {\rm Ra_I}] \tag{7b}$$

and

$$(D^2 - a^2)^2 W_{\rm II} - \frac{1}{Da}(D^2 - a^2)W_{\rm II} = a^2 \theta_{\rm II} \tag{8a}$$

$$(D^2 - a^2)\theta_{\rm II} = -W_{\rm II}\left\{\frac{\gamma^2}{(\eta + \gamma)(1 + n)}[{\rm Ra}_E(1 + \eta)^2 + {\rm Ra_I}] + 2Z\gamma{\rm Ra_I}\right\} \tag{8b}$$

where the internal and external Rayleigh numbers are given by:

$$\mathrm{Ra}_E = \frac{g\beta\Delta T L^3}{\nu_f \alpha_f} \tag{9}$$

$$\mathrm{Ra_I} = \frac{g\beta Q_v L^5}{2k_m \nu_f \alpha_f} \tag{10}$$

The corresponding matching conditions at $Z = 0$ are given by:

$$\left.\begin{array}{l} \theta_{\rm I} = \theta_{\rm II}, \gamma D\theta_{\rm I} = D\theta_{\rm II}, W_{\rm I} = W_{\rm II}, \\[4pt] DW_{\rm I} = DW_{\rm II}, D^2 W_{\rm I} = D^2 W_{\rm II}, \text{ and} \\[4pt] (D^2 - a^2)DW_{\rm I} = (D^2 - a^2){\rm DW}_{\rm II} - \frac{1}{\rm Da}DW_{\rm II} \end{array}\right\} \tag{11}$$

and the boundary conditions by at $Z = \eta/(1 + \eta)$

$$W_{\rm I} = DW_{\rm I} = \theta_{\rm I} = 0, \tag{12}$$

and at $Z = -1/(1 + \eta)$

$$W_{\rm II} = DW_{\rm II} = \theta_{\rm II} = 0 \tag{13}$$

where θ is the temperature perturbation and the temperature, velocity, distance, and pressure have been scaled by $T_B - T_T$, $g\beta(T_B - T_T)L^2/\nu_f$, L, $g\beta\rho_f(T_B - T_L)L$, respectively. The above equations form an eigenvalue problem for $\mathrm{Ra_I}$ with parameters γ, ν, Da, a, and Ra_E.

Method of Solution

The equations derived above are solved approximately by using the Galerkin method. This is accomplished by assuming that the temperature perturbation takes the form:

Nomenclature

a = dimensionless wavenumber

Da = D'Arcy number, $\dfrac{\kappa}{L^2}$

$\hat{e}_z$ = unit vector in the z direction
g = gravitational acceleration
k = thermal conductivity
L = layer thickness
Q_v = volumetric heat generation rate
Ra_E = external Rayleigh number, $g\beta\Delta T L^3/\alpha_f \nu_f$
Ra_I = internal Rayleigh number, $g\beta Q_v L^5/2k_m \alpha_f \nu_f$
T = temperature
$\underset{\sim}{u}$ = vector velocity
u, v, w = x, y, z components of velocity, respectively
U, V, W = dimensionless x, y, z components of velocity
x, y, z = coordinates
Z = dimensionless z coordinate, z/L
α = thermal diffusivity
$\tilde{\alpha}$ = Beavers and Joseph velocity jump parameter
β = coefficient of thermal expansion

γ = thermal conductivity ratio, k_f/k_m
κ = permeability
η = layer thickness ratio, L_f/L_p
μ = viscosity
$\tilde{\mu}$ = effective viscosity of the porous medium
ρ = density
θ = dimensionless temperature disturbance

Subscripts

f = fluid
m = porous material-fluid mixture
p = porous layer
M = interface
I = upper fluid layer
II = lower porous medium layer
T = top
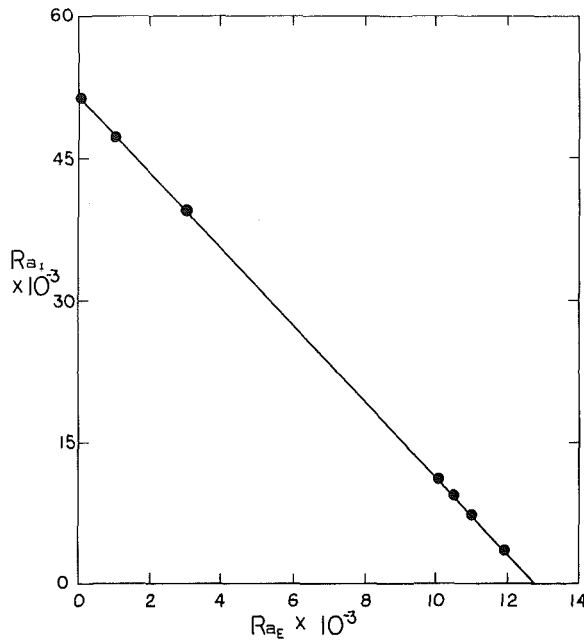B = bottom

Overscores

- = vector
= = two dimensional matrix

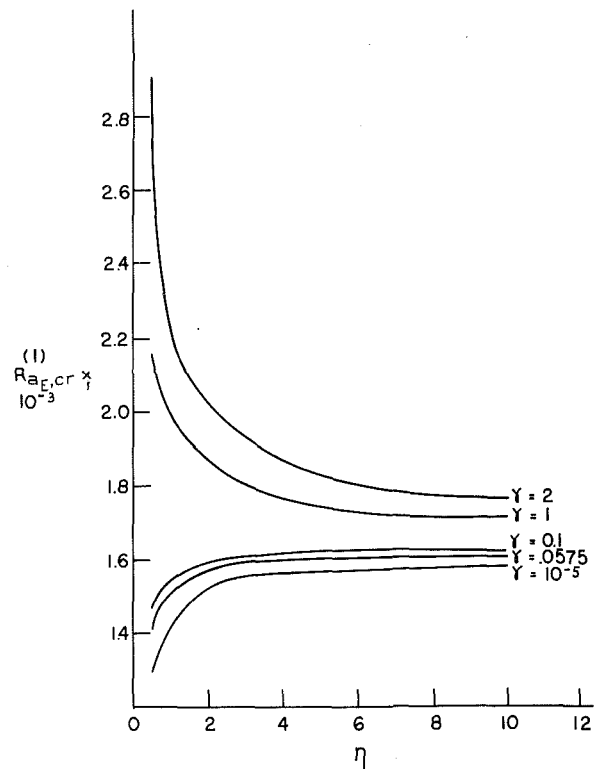Fig. 2 Relationship between internal and external Rayleigh numbers

Fig. 3(a) Critical external Rayleigh number based on the fluid layer for $Da = 3.775 \times 10^{-4}$
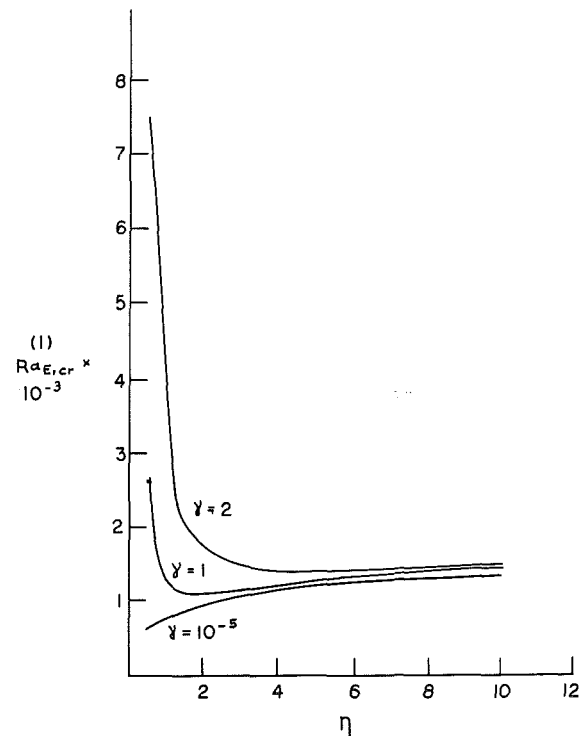
Fig. 3(b) Critical external Rayleigh number based on the fluid layer for $Da = 10^{-2}$

$$a^2\theta_I = \sum_k A_{k,1} \cos(\alpha_k^I Z) + \sum_k A_{k,2}\sin(\beta_k^I Z)$$

$$a^2\theta_{II} = \sum_k A_{k,1}\cos(\alpha_k^{II}Z) + \frac{\gamma}{\eta}\sum_k A_{k,2}\sin(\beta_k^{II}Z) \qquad (14)$$

where

$$\alpha_k^I = \frac{(2k-1)}{2}\pi\frac{(1+\eta)}{\eta} \qquad \beta_k^I = k\pi\frac{(1+\eta)}{\eta}$$

$$\alpha_k^{II} = \eta\alpha_k^I \qquad \beta_k^{II} = \eta\beta_k^I \qquad (15)$$

The boundary and matching conditions on temperature have been satisfied by the assumed series representation.

The corresponding perturbation velocities are found by solving Equations (7a) and (8a). The solution for $W_I^{(1)}$ is

$$W_I^{(1)} = \sum_k A_{k,1}\left[\frac{\cos(\alpha_k^I(\alpha_k^I Z))}{(\alpha_k^{I^2}+a^2)^2}\right.$$

$$+ B_{k,1}^{(1)}\cosh(aZ) + B_{k,1}^{(2)} Z\cosh(aZ)$$

$$\left. + C_{k,1}^{(1)}\sinh(aZ) + C_{k,1}^{(2)} Z\sinh(aZ)\right] \qquad (16)$$

Similar expressions for $W_I^{(2)}$, $W_{II}^{(1)}$, and $W_{II}^{(2)}$ can easily be found and are given in reference [8]. The constants of integration are obtained by requiring that the perturbation velocities satisfy the boundary and matching conditions.

Substituting for θ_I and W_I in equation (7b), multiplying by $\sin(\beta_k^I Z)$, and integrating over Z from 0 to $\eta/1 + \eta$ yields an equation of the form:

$$\left[\bar{\bar{P}}_1 + \frac{a^2(\mathrm{Ra}_E(1+\eta)^2+\mathrm{Ra}_I)}{(\gamma+\eta)(1+\eta)}\bar{\bar{R}}_1\right]\bar{A}_{k,1}$$

$$+ \left[\bar{\bar{S}}_1 + \frac{a^2(\mathrm{Ra}_E(1+\eta)^2+\mathrm{Ra}_I)}{(\gamma+\eta)(1+\eta)}\bar{\bar{T}}_1\right]\bar{A}_{k,2} = 0 \qquad (17)$$

Similarly, substituting for θ_{II} and W_{II} in equation (8), multiplying by $\sin(\beta_k^{II} Z)$, and integrating over Z from $-1/(1+\eta)$ to 0 yields:

$$\left[\bar{\bar{P}}_2 + \frac{a^2\gamma^2(\mathrm{Ra}_E(1+\eta)^2+\mathrm{Ra}_I)}{(\gamma+\eta)(1+\eta)}\bar{\bar{R}}_{2a} + 2a^2\gamma\mathrm{Ra}_I\bar{\bar{R}}_{2b}\right]\bar{A}_{k,1}$$

$$+ \left[\frac{\gamma}{\eta}\bar{\bar{S}}_2 + \frac{a^2\gamma^2(\mathrm{Ra}_E(1+\eta)^2+\mathrm{Ra}_I)}{(\gamma+\eta)(1+\eta)}\bar{\bar{T}}_{2a} + 2a^2\gamma\mathrm{Ra}_I\bar{\bar{T}}_{2b}\right]\bar{A}_{k,2} = 0 \qquad (18)$$

Equations (17) and (18) can be represented by:

$$\bar{\bar{M}}\cdot\bar{A} = 0 \qquad (19)$$
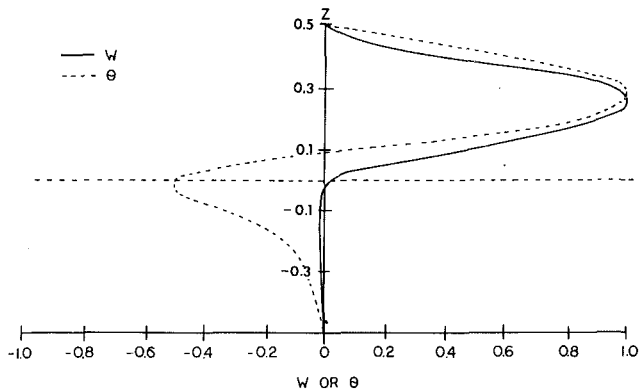
Fig. 4(a) Perturbation profiles for $\gamma = 2.0$, $\eta = 1.0$, and Da $= 3.775 \times 10^{-4}$
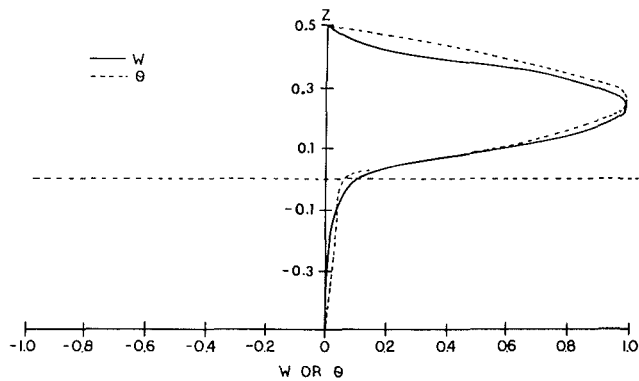
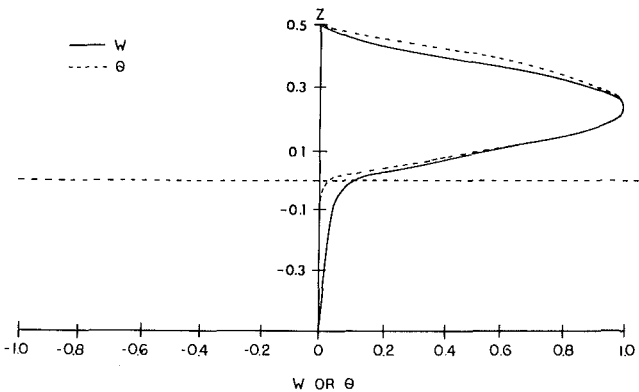Fig. 4(b) Perturbation profiles for $\gamma = 10^{-1}$ $\eta = 1.0$, and Da $= 3.775 \times 10^{-4}$

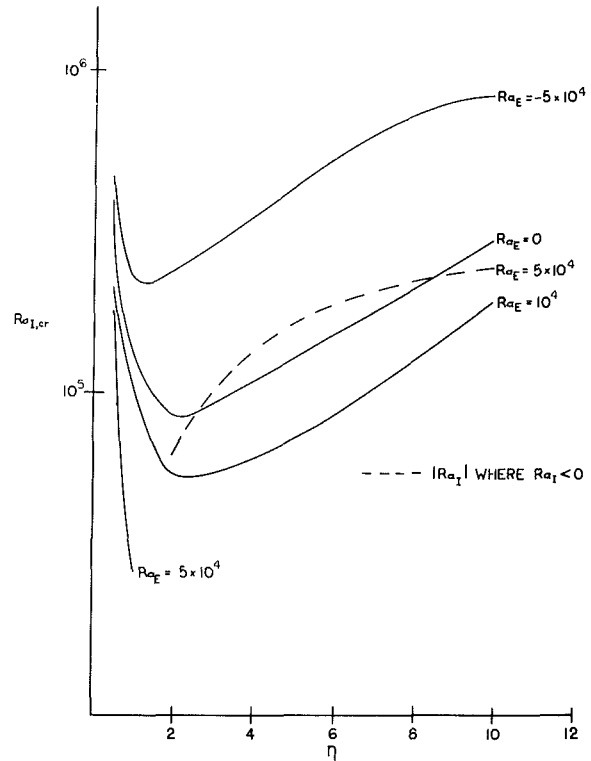Fig. 4(c) Perturbation profiles for $\gamma = 10^{-5}$, $\eta = 1.0$, and Da $= 3.775 \times 10^{-4}$

Fig. 5 The effect of applied temperature gradients on the critical internal Rayleigh number for $\gamma = 1.0$ and Da $= 3.775 \times 10^{-4}$
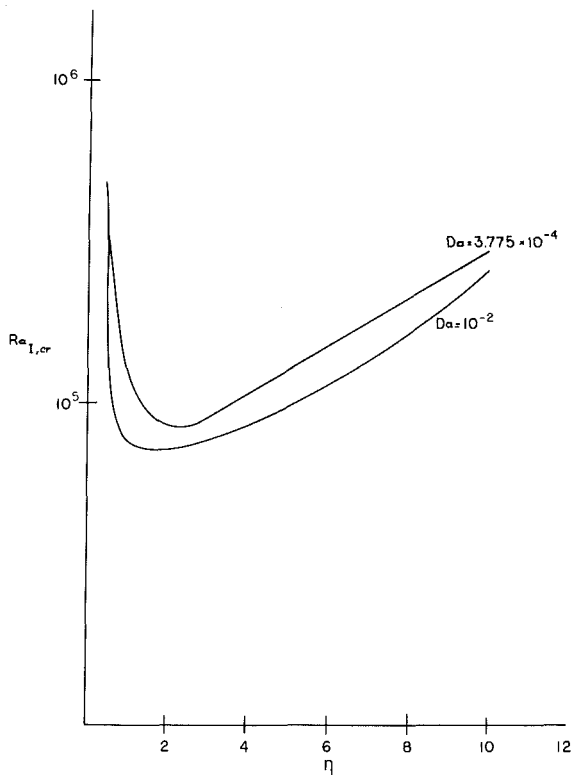

Fig. 6 The effect of the D'Arcy number on the critical internal Rayleigh number for $\gamma = 1.0$ and Ra$_E = 0$

In order to have a nontrivial solution to equation (19), one must have

$$\mathrm{DET}(\bar{\bar{M}}) = 0 \qquad (20)$$

For given values of a, γ, η, Da, and Ra$_E$, Ra$_I$ is determined from the above condition. The smallest real positive value of Ra$_I$ that satisfies equation (20) is taken to be the value at which fluid motion will occur. A first order Newton method is used to determine the critical Ra$_I$ at the most dangerous wavelength, namely that at which

$$\frac{d\mathrm{Ra}_I}{da} = 0 \qquad (21)$$

The solution algorithm was tested for a range of values of the independent parameters. It was found that a five term solution (N = 5) was always within 1 percent of a ten term solution (N = 10). Therefore, five terms were assumed to be sufficient for this work.

Results and Discussion

From the governing equations, it can be seen that the critical values of Ra$_I$, Ra$_E$, and a are function of γ, η, and Da. The solutions of the equations show that the critical wavenumber is only a function of γ, η, and Da and does not
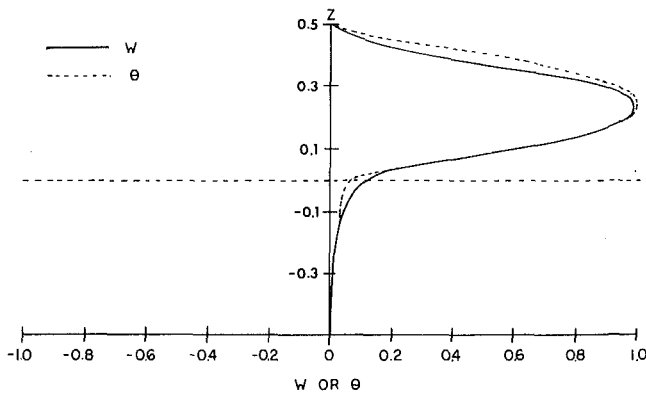
Fig. 7(a) Perturbation profiles for $\gamma = .0575$, $\eta = 1.0$ and Da $= 3.775 \times 10^{-4}$
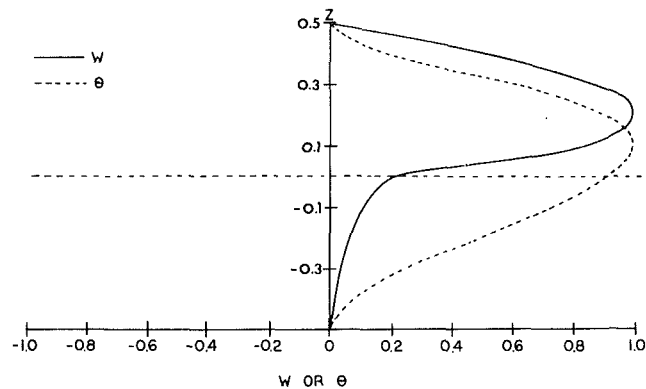
Fig. 7(b) Perturbation profiles for $\gamma = .0575$, $\eta = 1.0$, and Da $= 10^{-1}$

depend on the values of Ra_E and Ra_I. That is, given values of γ, η, and Da, the critical wavenumber is fixed. This implies that the two Rayleigh numbers cannot be independent of each other, and there must exist a unique relationship between them. One expects that from this relationship a universal stability parameter would emerge that is only a function of γ, η, and Da and corresponds to the critical wavenumber evaluated at those values of the independent parameters. The conjecture that such a universal stability parameter exists is borne out by the results of this analysis. The external Rayleigh number based on the fluid layer and defined by:

$$Ra_E^{(l)} = \frac{g\beta(T_M - T_T)\left(\frac{\eta L}{1+\eta}\right)^3}{\alpha_f \nu_f} \qquad (22)$$

is found to be the universal stability parameter. Correspondingly, there is an internal Rayleigh number based on the fluid layer defined by:

$$Ra_I^{(l)} = \frac{g\beta \Delta T_{Qv}\left(\frac{\eta L}{1+\eta}\right)^3}{\alpha_f \nu_f} \qquad (23)$$

where

$$\Delta T_{Qv} = \frac{Qv}{2k_m}\left(\frac{L}{1+\eta}\right)\left[\frac{1 + \frac{\gamma\eta}{2}}{\gamma + \eta} - 1\right] \qquad (24)$$

If one plots $Ra_{E,cr}^{(l)}$ versus $Ra_{I,cr}^{(l)}$ from the results of this analysis, one finds that $Ra_{E,cr}^{(l)}$ is independent of $Ra_{I,cr}^{(l)}$ which demonstrates that $Ra_{E,cr}^{(l)}$ is the sole stability parameter of the problem. In terms of the Rayleigh numbers for the entire system, $Ra_{E,cr}^{(l)}$ may be written as:
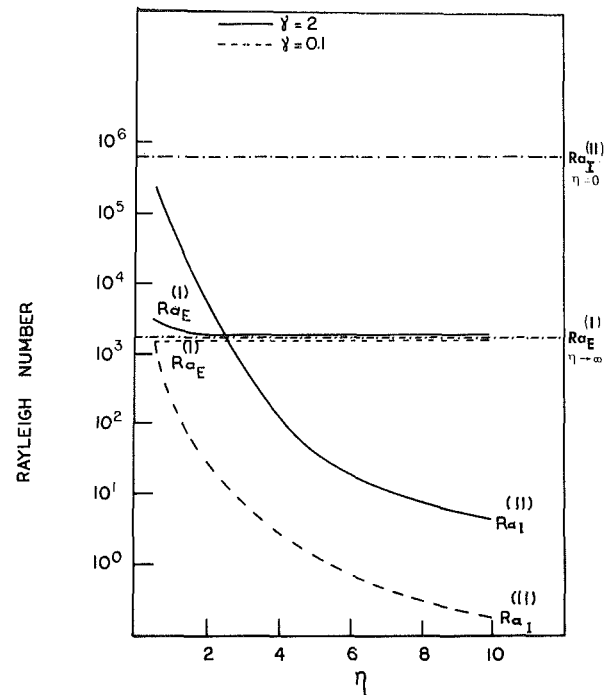
Fig. 8 Comparison with bounding cases for Da $= 3.775 \times 10^{-4}$

$$Ra_{E,cr}^{(l)} = \frac{\eta^4}{(1+\eta)^5(\gamma+\eta)}[Ra_{E,cr}(1+\eta)^2 + Ra_{I,cr}] \qquad (25)$$

Figure 2 shows a plot of $Ra_{E,cr}$ versus $Ra_{I,cr}$ for the calculated data points and the curve given by equation (25), where $Ra_{E,cr}^{(l)}$, evaluated at $Ra_{E,cr} = 0$, is determined from the calculations. One sees that equation (25) does indeed give the correct relation between $Ra_{E,cr}$ and $Ra_{I,cr}$.

The results of this analysis are presented in Figs. 3(a) and 3(b), which have $Ra_{E,cr}^{(l)}$ plotted against η for various values of γ and Da. Immediately, one sees some peculiarities in the behavior of $Ra_{E,cr}^{(l)}$. What needs to be remembered is that $Ra_{E,cr}^{(l)}$ is simply being used as a convenient way to present data and that physical interpretations should be drawn from the behaviors of $Ra_{E,cr}$ and $Ra_{I,cr}$.

One comment that can be made about Figs. 3(a) and 3(b) deals with the behavior of $Ra_{E,cr}^{(l)}$ as η becomes large. In this limit, one expects $Ra_{E,cr}^{(l)}$ to approach 1707 and be independent of γ. In the limit $\eta \to \infty$, there is just a horizontal layer of fluid heated from below, which is the Benard problem. However, though $Ra_{E,cr}^{(l)}$ becomes constant at large η it is still a function of γ. The reason for this can be seen in the velocity and temperature profiles presented in Figs. 4(a), 4(b) and 4(c). The velocity profiles are almost identical for the cases where $\gamma = 10^{-1}$ and 10^{-5}. There is one convection roll in the liquid layer with only slight motion of fluid in the porous layer. For $\gamma = 2$, there is not only a convection roll in the fluid layer, but, in addition, a small convection roll in the porous medium. Correspondingly, there are now moderate perturbation temperatures in the porous layer. It is reasonable to expect that the higher mode of two convection rolls is harder to attain and hence the large γ systems should be more stable. In view of this, the trend in $Ra_{E,cr}^{(l)}$ with the thermal conductivity appears correct. For the smaller values of γ, one sees that the temperature perturbation in the porous bed is small and approaches zero as γ becomes very small. This is physically reasonable, since as γ approaches zero the porous bed behaves like a perfect conductor.

There is some question as to the validity of using the profiles derived from a linear stability analysis. It is

reasonable to expect that at the onset of convection the temperature and velocity profiles should take a form similar to the eigenfunctions of the linear stability analysis.

The effect that stabilizing or destabilizing temperature gradients have on the problem is seen in Fig. 5, where $Ra_{I,cr}$ is plotted against η for various values of $Ra_{E,cr}$. First note that all of the curves take the same shape. When η is large $Ra_{I,cr}$ increases with increasing η. As η approaches 2, $Ra_{I,cr}$ decreases rapidly and tends toward a minimum. $Ra_{I,cr}$ decreases because decreasing η corresponds to increasing the heat generating volume. Since $Ra_{I,cr}$ is based on the volumetric heating rate, Q_v, and the heat generating volume has increased, one expects that lower values of Q_v (hence $Ra_{I,cr}$ smaller) will lead to the incipience of motion. Once the minimum is reached, $Ra_{I,cr}$ increases sharply with decreasing η. This is analogous to the behavior of ΔT when L is decreased in the Benard problem.

The behavior of $Ra_{I,cr}$ with respect to Ra_E follows the pattern established by equation (25). For stabilizing applied temperature gradients, $Ra_E < 0$, a larger Ra_I is required to cause convection. For destabilizing applied temperature gradients, $Ra_E > 0$, $Ra_{I,cr}$ is reduced. In fact, for very large values of Ra_E the critical internal Rayleigh number is negative. It is also seen that as η becomes small the effect of Ra_E on $Ra_{I,cr}$ is very slight.

In Fig. 6, the dependence of $Ra_{I,cr}$ on the D'Arcy number is shown. As Da increases the porous bed becomes more permeable. This increase in permeability allows greater fluid motion in the porous bed. Because it is easier for the fluid to move at larger Da, there is a decrease in $Ra_{I,cr}$ as seen in the results. This increase in fluid motion in the porous layer as Da increases is seen in Figs. 7(a) and 7(b) which are velocity profiles at different values of Da.

Finally, the results of this analysis are compared with the bounding cases of the problem which have been previously investigated. Figure 8 shows $Ra_{E,cr}^{(I)}$ and $Ra_{I,cr}^{(II)}$ (the external Rayleigh number based on the fluid layer and the internal Rayleigh number based on the porous layer, respectively) versus η. The internal Rayleigh number based on the porous layer is defined as:

$$Ra_{I,cr}^{(II)} = \frac{g\beta Q_v L_p^5}{2k_m \alpha_f \nu_f} = \frac{1}{(1+\eta)^5} Ra_{I,cr} \qquad (26)$$

The bounding case of the Benard problem results when $\eta \rightarrow \infty$, and the bounding case of the porous bed problem, as studied by Gasser and Kazimi [9], results when $\eta \rightarrow 0$. It can be seen that both limits are favorably reproduced by the method used in this work.

Conclusions

The major conclusions of this study are as follows:

1 The fluid layer and the porous bed cannot be uncoupled, as far as heat transfer is concerned.

2 Large γ leads to a more stable fluid layer than small γ, and therefore Rhee's [1] and Cherng's [2] results must be used with caution for other than a water saturated bed of steel particles.

3 Large Da leads to a less stable fluid layer than small Da, due to the increased freedom for fluid motion in the porous layer allowed by the increase in permeability.

4 The effect of a stabilizing temperature gradient is to increase the critical internal Rayleigh number, while a destabilizing temperature gradient causes a decrease in the critical Rayleigh number.

5 A fluid layer above the porous bed is destabilizing and can drive the motion in the porous bed.

Acknowledgments

References

1 Rhee, S. J., "Natural Convection Heat Transfer in Beds of Inductively Heated Particles," M. S. thesis, UCLA, 1977.

2 Cherng, J. C., "Effect of Bottom Cooling on Natural Convection in Beds of Inductively Heated Particles," M. S. thesis, UCLA, 1978.

3 Sun, W. J., "Convective Instability in Superposed Porous and Free Layers," Ph.D. Dissertation, University of Minnesota, Minneapolis, 1973.

4 Nield, D. A., "Onset of Convection in a Fluid Layer Overlying a Porous Medium," ASME *Journal of Fluid Mechanics*, Vol. 81, 1977, pp. 513-522.

5 Beavers, G. S., and Joseph, D. D., "Boundary Conditions of a Naturally Permeable Wall," ASME *Journal of Fluid Mechanics*, Vol. 30, 1967, pp. 2197-2207.

tension of Darcy's Law: Coupled Parallel Flow within a Channel and a Bounding Porous Medium," *Canadian Journal of Chemical Engineering*, Vol. 52, Aug. 1974, pp. 475-478.

7 Lundgren, T. S., "Slow Flow Through Stationary Random Beds and Suspensions of Spheres," ASME *Journal of Fluid Mechanics*, Vol. 51, 1972, pp. 273-299.

8 Somerton, C. W., "Convective Instability of a Volumetrically Heated Porous Bed with Applied Temperature Gradients," M.S. thesis, UCLA, 1979.

9 Gasser, R. D., and Kazimi, M. S., "Onset of Convection in a Porous Medium with Internal Heat Generation," ASME JOURNAL OF HEAT TRANSFER, Vol. 98, Feb. 1976, pp. 48-54.

Low Rayleigh Number Thermal Convection in a Vertical Cylinder Filled With Porous Materials and Heated From Below

H. H. Bau[1]

K. E. Torrance
Mem. ASME

Sibley School of Mechanical and
Aerospace Engineering,
Cornell University,
Ithaca, NY 14853

Low Rayleigh number ($R<500$) thermal convection is examined experimentally and analytically for a vertical circular cylinder filled with saturated porous materials. The cylinder is heated from below and cooled from above. The upper boundary is permeable to flow. Results are reported for the critical Rayleigh number at the onset of convection (R_c) and the Nusselt (Nu) versus Rayleigh (R) number correlation. The convective structure is deduced from temperature measurements. The lateral walls have a stabilizing effect and tend to increase R_c relative to the case of a laterally unbounded porous layer. The preferred convective patterns in the cylinder tend to be nonaxisymmetric. The experimental results are in good agreement with analytical predictions. A linear stability analysis is used to calculate R_c and the structure of the convective modes for a range of aspect ratios (radius/height). An integral technique is applied to obtain heat transfer rates for 1 < R/R_c < 5.5.

Introduction

The onset of convection in a porous layer of infinite horizontal extent with various top and bottom boundary conditions has been studied extensively [1-4]. In many applications, such as geothermal phenomena, it is important to consider the effect of lateral walls on the convective process. Analytical predictions of the critical Rayleigh number and the most unstable modes are available for a porous layer confined in rectangular parallelepipeds [5,6], circular cylinders [7,8], and annular cylinders [9]. The forenamed studies conclude that the lateral walls have a stabilizing effect. That is, the critical Rayleigh number for the onset of convection in relatively slender cavities is well above the corresponding value for a laterally unbounded layer. The lateral walls also control the shape of the convective structure. For example, Zebib [7] found that asymmetric flows are usually preferred in a circular cylinder with an impermeable top and bottom. Wooding [10] observed asymmetric flows in experiments on saline convection in an infinite vertical tube. Nevertheless, there appears to be no direct comparison of experimental and analytical results for a laterally confined, porous medium. The present paper provides such a comparison. The comparison embraces conditions both at and after the onset of convection.

We consider in this paper a vertical, circular cylinder filled with water-saturated, porous media. The cylinder is heated from below and cooled from above; the bottom is isothermal
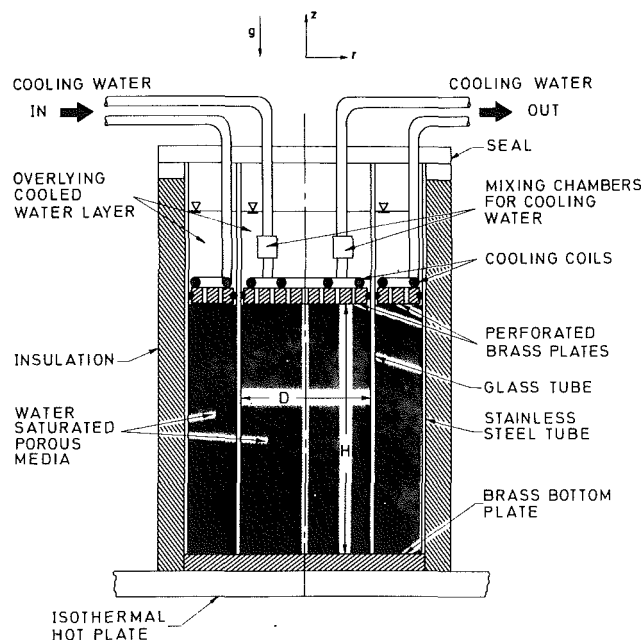
Fig. 1 Schematic diagram of the experimental apparatus

and impermeable; and the top is isothermal and permeable. The lateral walls are insulated and impermeable. Since our boundary conditions differ from those applied in [7], we calculate the critical Rayleigh number at the onset of convection and the preferred convective modes. An integral technique is used to extend the results to finite-amplitude convection and to determine the heat transfer rate. Finally, we

Copyright © 1982 by ASME

Table 1 Properties of the granular materials

Material	Grain size distribution (mm)	Average diameter (mm)	Porosity ϕ	Permeability $\lambda(m^2)$	Thermal conductivity k_e(W/mK)	Supplier
Silica sand	.21- .31	.25	.40	64×10^{-12}	2.60	Fisher Scientific
Ottawa sand	.85-1.27	1.06	.42	1374	2.15	"
Glass beads	1.41-1.68	1.54	.42	2625	0.92	Cataphote-Ferro

present a direct comparison of experimental results and analytical predictions.

Experimental Apparatus and Procedure

The experimental apparatus is shown schematically in Fig. 1. The apparatus consists of an inner Pyrex tube of inner diameter D = 95 mm and an outer, coaxial, stainless steel tube (178-mm i.d.). Both tubes are 318 mm high and are sealed at the bottom to a brass plate (13 mm thick). Two cavities are formed this way. The inner cavity is a vertical, circular cylinder; the outer cavity is a vertical, annular cylinder. The inner cavity is used as the test section; the outer cavity forms an insulating thermal guard.

The inner and outer cavities are filled to the same height with water-saturated permeable media. The water is distilled and degassed. Brass plates (13 mm thick) are placed on top of the porous beds. The plates are perforated (3.2-mm holes on 13-mm centers) to allow flow, and have a negligible pressure drop compared to an equivalent thickness of the porous media. The height of the bed, H, can be varied. The porous media are tamped to aid settling. A water layer of 1 to 2 cm is maintained above the perforated plates.

The apparatus is placed on an isothermal hot plate using a heat-conducting grease to ensure good thermal contact. The apparatus is leveled. The two compartments are cooled by passing tap water through separate copper coils located above the brass top plates. The water layer is covered with a seal to minimize evaporation. The entire apparatus is wrapped with a 15-mm thick layer of fiberglass insulation.

The temperature rise and the flow rate of the cooling water are measured with a thermopile and a rotameter, respectively. These measurements allow the heat flow through the system to be calculated. As a check, the measured heat flux is compared to a conductive heat flux using saturated glass beads of known conductivity in the cavities. The agreement is to within ± 20 percent. This uncertainty is attributed to difficulties in measuring small temperature differences in the cooling water, and to possible heat exchange between the

inner and outer cavities. A network of 36 gauge copper-constantan thermocouples is embedded at various locations within the porous matrix. Additional thermocouples are soldered to the base and top plates. Temperatures are recorded continuously with a multichannel strip chart recorder and may also be displayed on a digital voltmeter.

Commercially available granular materials are used for the permeable beds. They include glass beads and silica sands as listed in Table 1. The porosity (ϕ) is measured experimentally to ± 2 percent by displacing water as a bed is packed, and the permeability (λ) is obtained by using the Kozeny-Carman formula [11, p. 166]:

$$\lambda = \frac{d^2}{180} \frac{\phi^3}{(1-\phi)^2} \qquad (1)$$

where d is the average grain diameter. The effective thermal conductivity of the fluid saturated porous medium, k_e, is found by applying a known temperature gradient and measuring the heat flux in a conductive regime.

Experiments are carried out by starting from a quiescent initial state. The heating rate at the lower boundary is changed in a sequence of small steps (see Fig. 4). After each step, a period of several hours (about twice the diffusion time across the cavity) is allowed in order to achieve a steady state.

Preliminary experiments revealed that the temperature variation across both the top and bottom boundaries is less than 2 percent of the bottom-to-top temperature difference. Hence, we regard those boundaries as isothermal. It is somewhat more difficult to assess the nature of the lateral boundary conditions. We are aware of possible interactions between convective processes in the test section (the inner cavity) and the thermal guard (the outer cavity). Indeed, the convective structure in the outer cavity is asymmetric and the critical Rayleigh number is lower than the corresponding value in the inner cavity [9]. In order to estimate the severity of this effect, we measure the temperature variation over horizontal cross-sections in the test section (the inner cavity). Prior to the onset of convection, the above variations are smaller than 1 percent of the average temperature over the

_____ Nomenclature _____

A = amplitude of the disturbance
c_p = specific heat, Ws/kgK
d = average diameter of the solid particles in the porous bed, m
D = inside diameter of the cylinder, m
g = acceleration of gravity, m/s^2
H = height of the porous bed, m (Fig. 1)
k_e = thermal conductivity of the saturated porous matrix, W/mK
Nu = Nusselt number
q = heat flux, W/m^2
r = radial coordinate
R = Rayleigh number (equation 3)
R_c = critical Rayleigh number

R_l = Rayleigh number for an infinite cylinder
t = time, s
T = temperature, °C
T_0 = top temperature, °C
$\underline{u}$ = velocity vector, m/s
v = radial velocity, m/s
w = vertical velocity, m/s
z = vertical coordinate

Greek Symbols

β = thermal expansion coefficient, 1/K
γ = aspect ratio = D/2H
θ = nondimensional temperature
κ = wavelength of the disturbance

λ = permeability, m^2
$\underline{u}$ = velocity vector, m/s
ν = kinematic viscosity, m^2/s
ρ = density, kg/m^3
ϕ = porosity
ψ = azimuthal coordinate

Special Notation

* = dimensional quantity
$\simeq$ = (subscript tilde) vectorial quantity
∇^2 = Laplace operator
∇_1^2 = two-dimensional Laplace operator
D = d/dz

Journal of Heat Transfer

cross-section. Consequently, we conclude that the lateral walls can be regarded as insulated.

Further details about the experimental apparatus and procedures are available in reference [12].

Analysis

Formulation. Consider a vertical circular cylinder with diameter, D, height, H, and coordinate system (r^*, z^*, ψ as shown in Fig. 1). The vertical walls and the base are impermeable to flow. A fluid saturated medium of permeability λ fills the cylinder. The upper boundary ($z^* = 0$) is permeable. The horizontal boundaries at $z^* = 0$ and $z^* = -H$ are kept at constant temperatures T_0 and T_1, respectively. The vertical boundaries are adiabatic.

The linearized, steady-state, Darcy-Oberbeck-Boussinesq equations [13] in nondimensional form are:

$$\nabla \cdot \underline{u} = 0$$

$$\nabla^2 w = R^{1/2} \nabla_1^2 \theta \qquad (2)$$

$$\nabla^2 \theta = -R^{1/2} w$$

where $\underline{u}$ is the velocity vector, w is the vertical component of velocity, θ is the deviation from the linear conduction temperature profile,

$$\theta = \frac{T - T_0}{T_1 - T_0} + z^*/H$$

and $\nabla_1^2 = \nabla^2 - \partial^2/\partial z^2$. The Rayleigh number is defined by

$$R = \frac{g \lambda \beta (T_1 - T_0) H}{\nu (k_e / \rho_f \, c_{p_f})} \qquad (3)$$

where k_e is the thermal conductivity of the saturated medium, and β, ν, ρ_f, and c_{p_f} are, respectively, the volume thermal expansion coefficient, the kinematic viscosity, the density, and the specific heat of the fluid. Reference quantities for the nondimensionalization are H for the length, $(T_1 - T_0)$ for the temperature, and $R^{-1/2} k_e / \rho_f \, c_{p_f} H$ for the velocity. Variables with asterisks are dimensional; the same variables without asterisks are nondimensional.

The boundary conditions associated with (2) are

$$v = \frac{\partial \theta}{\partial r} = 0 \quad \text{at } r = D/2H = \gamma$$

$$w = \theta = 0 \qquad \text{at } z = -1$$

$$\frac{\partial w}{\partial z} = \theta = 0 \qquad \text{at } z = 0 \qquad (4)$$

The last boundary condition on $\partial w/\partial z$ corresponds to a constant pressure condition at the permeable upper boundary. At the adiabatic vertical walls, the boundary condition on the radial velocity, $v = 0$, is equivalent to $\partial w/\partial r = 0$.

The Critical Rayleigh Number. The onset of convection in the present case is characterized by a monotonic growth of disturbances in time. This is the principle of exchange of stabilities [14]. Thus, the marginal state is time independent, and the steady-state equations (2) are applicable.

The governing equations and boundary conditions may be reduced to

$$\nabla^4 \theta + R \nabla_1^2 \theta = 0$$

$$\frac{\partial \theta}{\partial r} = \nabla^2 \left(\frac{\partial \theta}{\partial z} \right) = 0 \qquad \text{at } r = \gamma$$

$$\theta = \nabla^2 \theta = 0 \qquad \text{at } z = -1$$

$$\theta = \nabla^2 \left(\frac{\partial \theta}{\partial z} \right) = 0 \qquad \text{at } z = 0 \qquad (5)$$

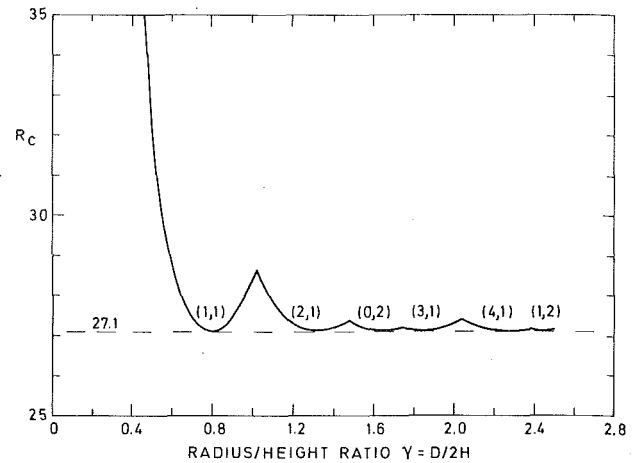Separation of variables leads to the following solution:

Fig. 2 Critical Rayleigh number (R_c) and the preferred convective modes (m,p) at the onset of convection. The dashed line indicates the result for an infinite horizontal layer.

$$\theta = \Theta(z) J_m (Z_{mp} \, r/\gamma) \cos (m\psi) \qquad (6)$$

where m and p are integers, J_m is a Bessel function of the first kind, and Z_{mp} is the pth zero of:

$$\frac{\partial}{\partial r} J_m (Z_{mp}) = 0. \qquad (7)$$

The zeroes of (7) are available in standard mathematical tables [16].

The linear stability eigenvalue problem is expressed in terms of $\Theta(z)$ after substituting (6) into (5).

$$(D^2 - \kappa_{mp}^2) \Theta - \kappa_{mp}^2 R \Theta = 0 \qquad (8)$$

where $D = d/dz$ and $\kappa_{mp} = Z_{mp}/\gamma$. The boundary conditions are:

$$\Theta = D(D^2 - \kappa_{mp}^2) \Theta = 0 \quad \text{at } z = 0$$

$$\Theta = (D^2 - \kappa_{mp}^2) \Theta = 0 \qquad \text{at } z = -1 \qquad (9)$$

In order to obtain a nontrivial solution to equation (8) with boundary conditions (9) we have to satisfy the condition:

$$\xi \coth \xi + \eta \cot \eta = 0 \qquad (10)$$

where

$$\xi^2 = \kappa_{mp} (R^{1/2} + \kappa_{mp}) \text{ and } \eta^2 = \kappa_{mp} (R^{1/2} - \kappa_{mp}).$$

Equation (10) is the characteristic equation for R. The zeroes of (10) are denoted by n. There are an infinite number of such zeroes for each value of κ_{mp}. Clearly R satisfies

$$(n-1)^2 \pi^2/4\kappa_{mp}^2 + \kappa_{mp} < R^{1/2} < n^2 \pi^2/\kappa_{mp} + \kappa_{mp}. \qquad (11)$$

For a given aspect ratio (γ), the critical Rayleigh number (R_c) is evaluated from:

$$R_c = \min_{m,n,p} R \qquad (12)$$

The (m,n,p) triplet corresponding to R_c represents the preferred convective mode at the onset of motion. We note from (11) that the minimum R value always occurs for the $n = 1$ vertical mode. Thus we search for the horizontal (m,p) modes which satisfy (12).

We note in passing that equation (10) also describes conditions at the onset of convection in a vertical cylinder with an isothermal top and a uniform-heat-flux bottom, both of which are impermeable. The critical Rayleigh numbers and the preferred convective modes from the present study also apply to this case.

The critical Rayleigh number (R_c) is shown in Fig. 2 for various aspect ratios (γ). For large values of the aspect ratio, R_c asymptotically approaches the value for an infinite horizontal layer of 27.1 [1]. It is readily shown that this is also the lower bound for R_c, which is achieved at discrete values of

Table 2 Geometry, aspect ratio, critical Rayleigh number and Nusselt versus Rayleigh number correlation for the experiments

Material	Bed height H(mm)	Radius/height γ	$(R_c)_{th}$	$(R_c)_{ex}$	$(Nu-1)/(1-R_c/R)$
Silica sand	217	.219	88.6	—	2.47
Ottawa sand	170	.280	61.1	79.6	2.55
Ottawa sand	200	.238	77.7	72.0	2.49
Glass beads	226	.211	95.0	75.5	2.45
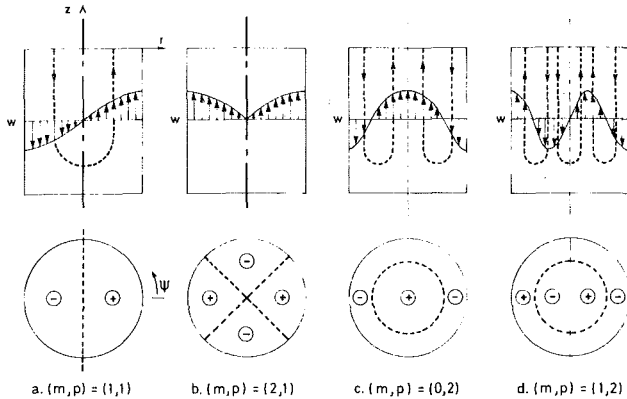
Fig. 3 Schematic description of four convective modes. Profiles of vertical velocity (w) and streamlines (dashed lines) are shown in the radial cross section (top). Regions of upflow (+) and downflow (−) are shown in the horizontal cross-sections (bottom).
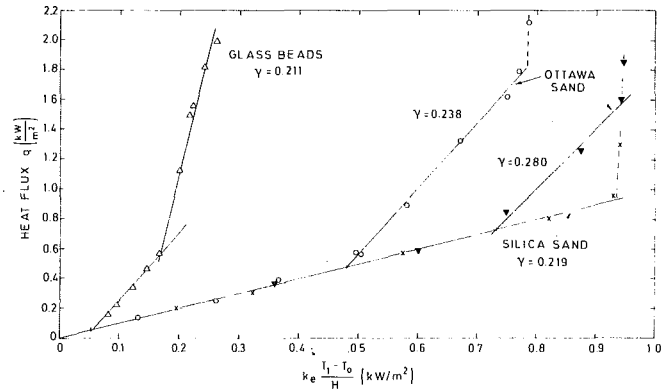

Fig. 4 The measured heat flux (q) versus the bottom-to-top temperature difference ($T_1 - T_0$). The first change of slope for the Ottawa sand and the glass beads indicates the onset of convection. The first change of slope for the silica sand and the second for the Ottawa sand indicate boiling. The second change of slope in the case of the glass beads indicates a transition to another convective regime.

γ. The stabilizing effect of the vertical walls is especially significant for low aspect ratios.

For very tall cylinders (low aspect ratios) it is convenient to redefine the Rayleigh number in the form

$$R_1 = \frac{\beta g \lambda (-\partial T/\partial z^*)D^2}{\nu(k_e/\rho_f c_{p_f})} \tag{13}$$

where $-\partial T/\partial z^*$ is the vertical temperature gradient (dimensional) and D is the cylinder diameter. For very tall cylinders, we find that the critical Rayleigh number is 13.56. This value is independent of the top boundary conditions [12].

The Convective Structure. The derivation of the previous sections reveals the preferred convective modes (m,p) at the onset of convection. In this section we examine the spatial form of several modes.

The disturbance temperature field (θ) is given by (6). The vertical structure function $\Theta(z)$ appearing therein is found as the solution to equations (8) and (9). The result is:

$$\Theta(z) = \frac{\sin \eta(z+1)}{\sin \eta} - \frac{\sinh \xi(z+1)}{\sinh \xi} \tag{14}$$

The vertical velocity component (w) obtained from (2) is

$$w = W(z) J_m (\kappa_{mp} r) \cos (m\psi) \tag{15}$$

where

$$W(z) = \frac{\kappa_{mp}}{R^{1/2}} \left(\frac{\sin \eta(z+1)}{\sin \eta} + \frac{\sinh \xi(z+1)}{\sinh \xi} \right) \tag{16}$$

The preferred convective modes (m,p) for various aspect ratios (γ) are indicated in Fig. 2. The structure of four of those modes is shown schematically in Fig. 3. The top row of Fig. 3 illustrates the vertical velocity profiles (arrows) and the streamlines (dashed lines) in a radial cross-section. The lower row of Fig. 3 shows the regions of downflow(−) and upflow (+) in a horizontal cross-section.

The (m,p) = (1,1) mode appears in Fig. 3 (a). This mode has a vertical component of velocity (15) which is proportional to cos ψ. This corresponds to, say, ascending flow in

the range of $-\pi/2\pi < \psi < \pi/2$ and descending flow elsewhere. Hence, the mode (1,1) consists of a single cell, whose axis of rotation coincides with the cylinder diameter.

The (m,p) = (2,1) mode is shown in Fig. 3 (b). This mode has a vertical component of velocity proportional to cos 2ψ. This corresponds to ascending and descending flow in alternate azimuthal quadrants. Hence, we have four counter-rotating cells whose axes of rotation lie in radial planes. The convective modes (m,p) = (3,1), (4,1), . . . , (m,1) are of similar structure and correspond respectively to 6, 8, . . . 2m counter-rotating vortices.

All of the above modes are clearly nonaxisymmetric. Axisymmetric modes correspond to m = 0. Only one such mode appears in Fig. 2; namely, the (m,p) = (0,2) mode. This is, for example, the preferred mode for a cylinder with aspect ratio γ = 1.6 and is shown in Fig. 3 (c). A single toroidal roll is apparent in the radial cross section. The flow is two-dimensional since the azimuthal velocity is zero everywhere. The direction of rotation of the toroidal vortex is arbitrary, but is shown ascending in the interval $0 < r < 1.0$ and descending in the interval $1.0 < r < 1.6$.

Higher modes result in complex, three-dimensional structures. The (m,p) = (1,2) mode is sketched in Fig. 3 (d). The upper graph shows three cells in the radial cross-section. The lower graph reveals the horizontal structure of the flow.

The Amplitude of the Convective Motion. The linear theory is unable to predict the amplitude of the convective motion. The amplitude may be found by using an integral technique derived by Malkus and Veronis [15]. A derivation of the integral equations for a viscous fluid is given, for example, in Chandresekhar [14, Appendix I]. We have extended his formulation for the case of Darcy flow in a permeable medium [12]. For the sake of brevity, we do not reproduce the derivation here, but only quote the main results.

The disturbance amplitude, A, may be introduced as an additional multiplicative coefficient in equation (6). The square of the amplitude is given by:

$$A^2 = -\kappa_{mp}^2 (R - R_c)$$

$$\frac{\displaystyle \int_{-1}^{0} FW \, dz}{\displaystyle \int_{-1}^{0} F^2 W^2 \, dz - \left(\int_{-1}^{0} FW \, dz \right)^2} \tag{17}$$

where $F = (D^2 - \kappa_{mp}^2) W$. With the amplitude known, the mean vertical heat flux per unit area, q, may be found. This is expressed in terms of a layer Nusselt number, Nu $= qH/k_e (T_1 - T_0)$, by the equation:

$$\frac{Nu - 1}{1 - R_c/R} =$$

$$\frac{\left(\displaystyle \int_{-1}^{0} FW \, dz \right)^2}{\displaystyle \int_{-1}^{0} F^2 W^2 \, dz - \left(\int_{-1}^{0} FW \, dz \right)^2} \tag{18}$$

In turn, the local temperature (T) is given by

$$\frac{T - T_0}{T_1 - T_0} = \frac{A}{R} \Theta(z) J_m (\kappa_{mp} r) \cos (m\psi) + \frac{A^2}{R} \int_0^z W\Theta \, dz - Nuz \tag{19}$$

Thus equations (18) and (19) describe the heat flow and temperature field based on a finite amplitude extension of the first unstable convective mode.

Results and Discussion

Experimental measurements include the temperature field within, and the vertical heat flux across, the inner cylinder shown in Fig. 1. Results are reported in this section for the four beds listed in Table 2. Each bed was packed with a particular granular material to a height, H, or bed aspect ratio $\gamma = D/2H$. For the aspect ratios listed, Fig. 2 suggests that convective mode (1,1) is the preferred mode at the onset of convection. The corresponding spatial structure is given in Fig. 3(a). Other entries in Table 2 will be discussed in the following subsections. We shall also compare the experimental data with the analytical predictions of the previous section.

Critical Rayleigh Number (R_c). The measured heat flux (q) is plotted in Fig. 4 against the bottom-to-top temperature difference, expressed as $k_e (T_1 - T_0)H$. Straight lines are drawn through the data points. The straight line passing through the origin corresponds to the conductive regime. The first change of slope for the glass beads and the Ottawa sand indicates the onset of convection. The first change of slope for the silica sand and the second change of slope for the Ottawa sand are due to the initiation of boiling. The second change of slope for the glass beads results from a transition to another convective regime, which will be discussed later.

Experimental and analytical values of R_c, denoted, respectively, by $(R_c)_{ex}$ and $(R_c)_{th}$, are listed in Table 2. The experimental value is calculated using equation (3). The temperature difference $(T_1 - T_0)$ is determined from the location of the first change of slope in Fig. 4. The physical properties of the fluid are evaluated at the average bed temperature. The experimental value for $(R_c)_{ex}$ is believed to be correct to within ± 30 percent. This range is due to uncertainties in estimating the permeability, and to the effects of temperature variations on viscosity.

The differences between the experimental and theoretical results in Table 2 are within the experimental error. Although we cannot conclude anything about the dependence of $(R_c)_{ex}$ on the aspect ratio $(D/2H)$, we note that the experimental and theoretical values of R_c are well above the value 27.1, which corresponds to a laterally unbounded layer [1]. This indicates the stabilizing effect of the lateral walls.
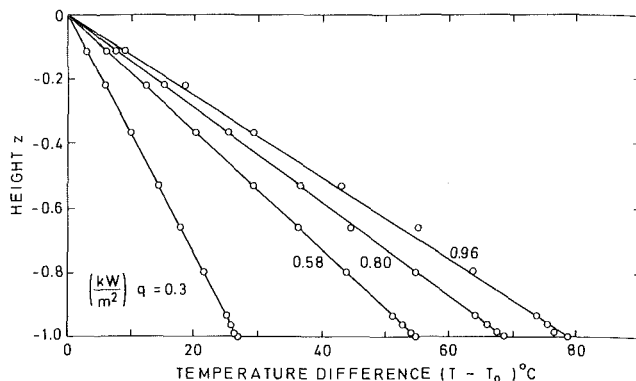

Fig. 5 Silica sand — temperature profiles at the cylinder axis for various input heat fluxes (q). The straight lines are evidence of the absence of convection.
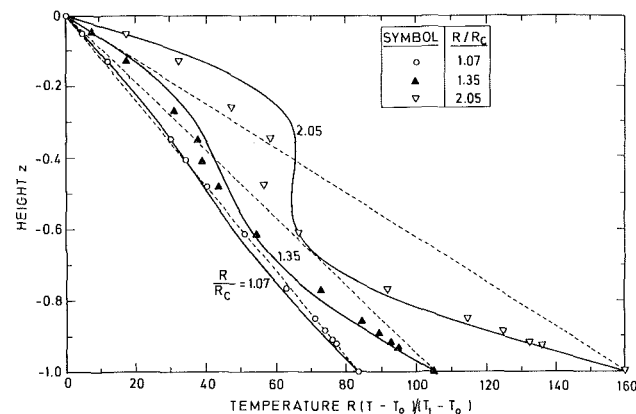

Fig. 6 Ottawa sand ($\gamma = 0.238$) — axial temperature profile — comparison between analysis (solid lines) and experiment for various values of R/R_c. The solid lines are from equation (19).

Temperature Profiles. Experimental and analytical temperature profiles along the cylinder axis are shown in Figs. 5, 6 and 7 for the silica sand, the Ottawa sand ($\gamma = 0.238$), and the glass beads, respectively. These figures are in order of increasing permeability. The analytical results (solid lines) are derived from equation (19).

Results for the silica sand (Fig. 5) are shown with the temperature difference $(T - T_0)$ on the abscissa, the nondimensional height (z) on the ordinate, and the dimensional heat flux q as the curve parameter. Linear temperature profiles are observed up to the onset of boiling and confirm the dominance of conduction. The bottom temperature reaches saturation at a heat flow of about 0.96kW/m^2. The lack of convection up to the onset of boiling is in accord with results in the previous section.

Centerline temperature profiles for the Ottawa sand (Fig. 6) and the glass beads (Fig. 7) show the influence of convection. In those figures, all parameters are nondimensional. The curve parameter is the ratio between the actual Rayleigh number (R) and the critical Rayleigh number at the onset of convection (R_c). This ratio is essentially independent of the permeability and is given by:

$$\frac{R}{R_c} = \frac{T_1 - T_0}{(T_1 - T_0)_c} \frac{\nu_c}{\nu} \tag{20}$$

where subscript c denotes conditions at the onset of convection. The nondimensional temperature on the abscissa is $R(T - T_0)/(T_1 - T_0)$. For the experimental data, it is calculated in the following way:

$$R \frac{T - T_0}{T_1 - T_0} = \frac{T - T_0}{(T_1 - T_0)_c} \frac{(R_c)_{th} \nu_c}{\nu} \tag{21}$$

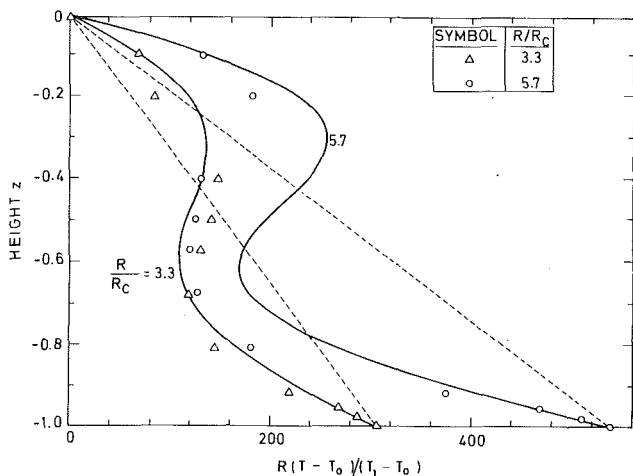Again, the permeability (λ) does not appear in the calculation.

Fig. 7 Glass beads – axial temperature profile – comparison between analysis (solid lines) and experiment for various values of R/R_c. The solid lines are from equation (19).
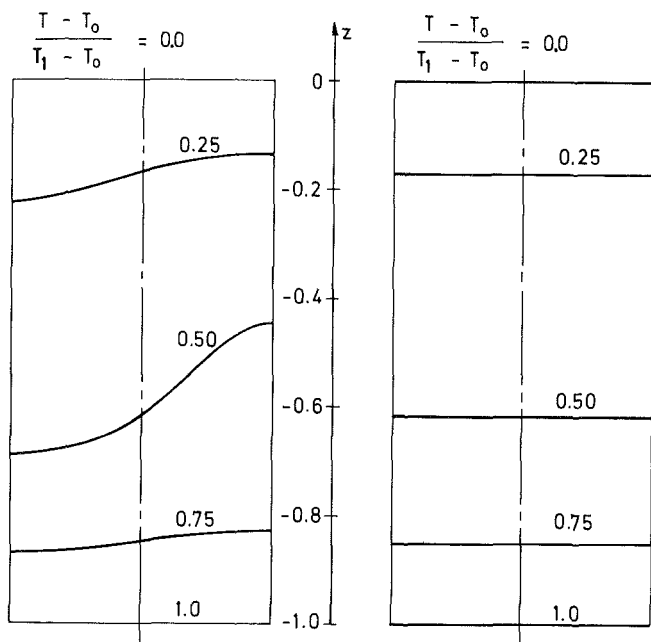

Fig. 8 Ottawa sand ($\gamma = 0.238$) – isotherms (nondimensional temperature $(T - T_0)/(T_1 - T_0)$) shown in two perpendicular-radial cross-sections for $R/R_c = 1.46$.
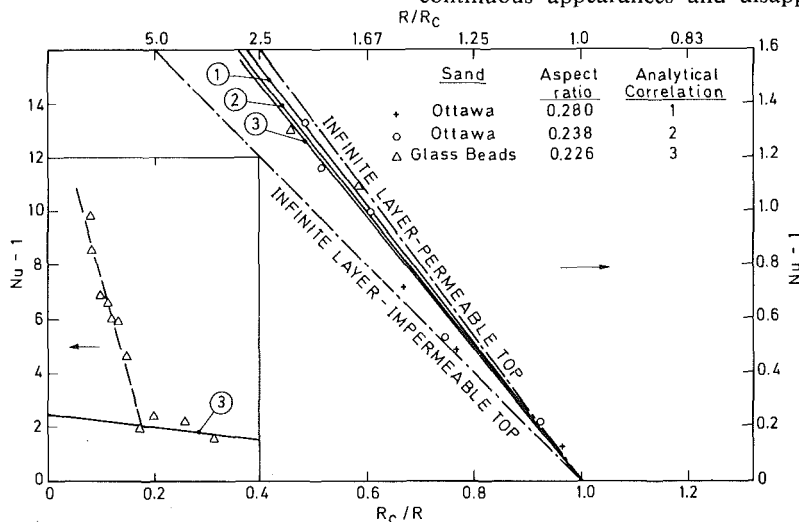
To facilitate comparisons, dashed lines are drawn to illustrate the linear conduction state.

For values of R/R_c close to unity in Fig. 6, the centerline temperature profile is nearly linear. Heat transfer is primarily by conduction. As R/R_c increases above unity, convection becomes more significant and the temperature profile becomes increasingly S-shaped (Figs. 6 and 7). Descending cold fluid causes the temperature near the bottom to fall below the conduction value, while ascending warm fluid causes the opposite effect near the top. A reversal of the vertical temperature gradient occurs on the axis for $R/R_c \approx$ 1.8. The reversal becomes more pronounced as R/R_c is increased above this value. Note that the temperature profiles are not symmetric about the $z = -0.5$ plane. This is a result of the different boundary conditions at the top and bottom, with the top being permeable and in contact with a reservoir at T_0 while the bottom is impermeable. As a result of the cold inflow, the mean temperature is less than the arithmetic average of the top and bottom temperatures.

The temperature profiles in Figs. 6 and 7 strongly suggest that the convective motion is in the form of a single, nonaxisymmetric cell. This assertion is also supported by temperature measurements made away from the centerline and shown in Fig. 8. This figure illustrates isotherms in two orthogonal, vertical cross-sections. The left graph suggests a nonaxisymmetric structure with descending and ascending flow to the left and right of the cylinder centerline, respectively. The horizontal isotherms shown in the right graph suggest a single convection cell. The structure of the implied convection cell is consistent with the (1,1) mode sketched in Fig. 3(a).

Analytical and experimental temperature profiles along the axis of the cylinder are in reasonable agreement in Figs. 6 and 7 for $R/R_c \leq$ 3.3. However, significant deviations are apparent for $R/R_c = $ 5.7 in Fig. 7. These deviations are associated with the onset of oscillatory convection. For $R/R_c \leq$ 5.5, the measured temperatures are time steady. Above this value, aperiodic oscillations are observed. The onset of oscillations is associated with the second change of slope prior to the onset of boiling in Fig. 4. For the glass beads, the change of slope occurs at $R/R_c = 5.5$

We conclude that there is a change in the nature of the convection at $R/R_c \approx 5.5$. This is in agreement with Combarnous and Bories [17], and Gupta and Joseph [18], who report experimental and analytical results, respectively, on the onset of oscillatory motion in a laterally-unbounded porous layer. The fluctuations were interpreted as mode shifts (i.e., continuous appearances and disappearances of convection
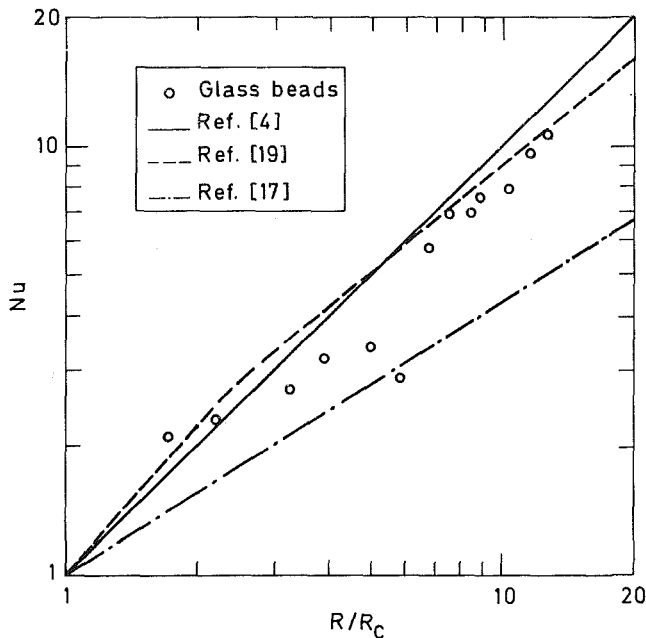

Fig. 9 Nusselt number (Nu) versus Rayleigh number ratio (R/R_c) – comparison of experiment and analysis. The solid lines are from equation (18).

Fig. 10 Nusselt number (Nu) versus Rayleigh number ratio (R/R$_c$) — comparison of experimental results for glass beads with existing correlations taken from Elder [4], Combarnous and Bories [17], and Burreta and Berman [19]

cells). The transition points ranged from $R/R_c = 6.1$ to 7.1 in the experiments [17], and occurred at $R/R_c = 5.61$ in the analysis [18]. These $R \times R_c$ values are close to those observed at the onset of oscillations in the present experiments.

Heat Transfer Rates. Measured heat transfer rates for the glass beads and the Ottawa sands are compared with the finite amplitude analysis in Fig. 9. The ordinate is Nu-1, where Nu is the Nusselt number, and the abscissa is the ratio R_c/R. An insert is used to show all of the data for the glass beads.

The coordinates of Fig. 9 are based on the finite amplitude analysis, equation (18), which suggests that the group (Nu-1)/$(1 - R_c/R)$ should be constant for each porous bed. This group corresponds to a straight line with negative slope which intersects the abscissa at $R_c/R = 1$. Numerical values for this group for the four porous beds considered in this study are listed in Table 2. Analytical results for three of the four beds are shown by solid lines (labeled 1 to 3). The scatter of the experimental results is well within the range of experimental error. Both the experimental and analytical results fall below the prediction for an infinite layer with a permeable top. This illustrates the effect of lateral confinement in reducing convection (and thus heat transfer). Over the range of aspect ratios considered, the rate of heat transfer decreases as the aspect ratio is decreased. In the case of the glass beads, the heat transfer suddenly increases above the predicted value at $R_c/R = 0.18$ (see insert). This corresponds to the second change of slope in Fig. 4, and the data in this range appear to scatter about a straight line — the dashed line in the insert in Fig. 9.

A comparison of our experimental results for the glass beads with existing correlations for laterally unbounded layers [4, 17, 19] has been carried out in Fig. 10. For low Rayleigh numbers, $(R/R_c < 5.5)$ the correlations do not describe our data; thus the analysis given by (18) is to be preferred. For $R/R_c > 5.5$, our data is reasonably close to the correlation of Burreta and Berman [19].

Summary

Results from the present study of single-phase convection in a vertical circular cylinder containing a saturated porous medium heated from below may be summarized:

(*a*) Lateral walls are stabilizing, especially in the case of relatively tall cavities, where the critical Rayleigh number at the onset of convection is well above the corresponding value for an unbounded layer.

(*b*) The geometry of the lateral walls dictates the convective structure. In the case of slender circular cylinders the convective modes are nonaxisymmetric.

(*c*) A weak nonlinear theory, based on the first unstable convective mode, supplies reasonable predictions for the temperature field and for the Nusselt number for $R/R_c < 5.5$.

(*d*) A change in the convective nature (oscillatory bifurcation) occurs at $R/R_c \approx 5.5$. This ratio is close to corresponding values in the literature for an unbounded horizontal layer.

Acknowledgments

References

1 Lapwood, E. R., "Convection of a Fluid in a Porous Medium," *Proc. Cambridge Phil. Soc.,* Vol. 44, 1948, pp. 508–521.

2 Nield, D. A., "Onset of Thermohaline Convection in a Porous Medium," *Water Resour. Res.*, Vol. 4, 1968, pp. 553–560.

3 Katto, Y. and Masuoka, T., "Criterion for Onset of Convective Flow in a Fluid in a Porous Medium," *International Journal of Heat and Mass Transfer,* Vol. 10, 1967, pp. 297–309.

4 Elder, J. W., "Steady Free Convection in a Porous Medium Heated from Below," *Journal of Fluid Mechanics,* Vol. 27, 1967, pp. 29–48.

5 Beck, J. L., "Convection in a Box of Porous Material Saturated with Fluid," *Phys. Fluids,* Vol. 15, 1972, pp. 1377–1383.

6 Holst, P. H. and Aziz, K., "Transient Three-Dimensional Natural Convection in Confined Porous Media," *International Journal of Heat and Mass Transfer,* Vol. 15, 1972, pp. 73–90.

7 Zebib, A., "Onset of Natural Convection in a Cylinder of Water Saturated Porous Media," *Phys. Fluids,* Vol. 21, 1978, pp. 699–700.

8 Bories, S. and Deltour, A., "Influence des Conditions aux Limites sur la Convection Naturelle dans un Volume Poreux Cylindrique," *International Journal of Heat and Mass Transfer,* Vol. 23, 1980, pp. 765–771.

9 Bau, H. H. and Torrance, K. E., "Onset of Convection in a Permeable Medium between Vertical Coaxial Cylinders," *Phys. Fluids,* Vol. 24, 1981, pp. 382–385.

10 Wooding, R. A., "The Stability of a Viscous Liquid in a Vertical Tube Containing Porous Material," *Proc. Royal Society London A*, Vol. 252, 1955, pp. 120–134.

11 Bear, J., *Dynamics of Fluids in Porous Media,* Elsevier, New York, 1972.

12 Bau, H. H., "Experimental and Theoretical Studies of Natural Convection in Laboratory-Scale Models of Geothermal Systems," Ph.D. Thesis, Cornell University, Ithaca, NY, 1980.

13 Joseph, D. D., *Stability of Fluid Motion*, Chapter 10, Springer Verlag, Berlin, 1976.

14 Chandrasekhar, S., *Hydrodynamic and Hydromagnetic Stability*, Chapter 2, Oxford University Press, London, 1961.

15 Malkus, W. V. R. and Veronis, G., "Finite Amplitude Cellular Convection," *Journal of Fluid Mechanics,* Vol. 4, 1958, pp. 225–260.

16 Abramowitz, M. and Stegun, L. A., *Handbook of Mathematical Functions,* National Bureau of Standards, 1964, pp. 411.

17 Combarnous, M. A. and Bories, S. A., "Hydrothermal Convection, in Porous Media," *Advances in Hydroscience,* Vol. 10, edited by Ven Ten Chow, Academic Press, 1975, pp. 231–307.

18 Gupta, V. P. and Joseph, D. D., "Bounds for Heat Transport in Porous Layer," *Journal of Fluid Mechanics,* Vol. 57, 1973, pp. 491–514.

19 Burreta, R. J. and Berman, A. S., "Convection Heat Transfer in a Liquid Saturated Porous Layer," *Journal of Applied Mechanics,* Vol. 98, 1976, pp. 249–253.

20 Eckert, E. R. G. and Drake, R. M., *Analysis of Heat and Mass Transfer,* Appendix B, McGraw-Hill, NY, 1972.

C. A. Oster

Battelle Pacific Northwest Laboratory,
P.O. Box 999,
Richland, Wash. 99352

W. A. Scheffler

Joint Center for Graduate Study,
University of Washington,
Richland, Wash. 99352

Temperature Profiles and Aquifer Mass Transfer in a Circulating Well

A method is described for determining the temperature distribution in a circulating drilling fluid when aquifers are present in the formation. The depth of an aquifer relative to the well depth is shown to be an important parameter. An aquifer near the surface has much less influence on the temperature distributions than one located near the bottom of the well. If the drilling fluid has much greater density than the entering formation water, then the temperature distributions are altered significantly.

Introduction

The prediction of temperature distributions in rock formations through which a well is being drilled is an important task. An accurate prediction of the depth at which temperatures are high enough to cause steam flashing, e.g. in geothermal exploratory drilling, permits the driller to safely operate for longer periods with less pressure control and, thus, with less cost. Because the ambient rock temperature is disturbed by the drilling muds and other fluids flowing in the well, it is difficult to predict the temperature changes. A quasisteady-state model is used to predict the temperature distributions in the drill pipe, annulus, and in the rock formation when water from the rock formation is entering the annulus and/or where drilling fluid is flowing from the annulus to the formation. An aquifer is defined here to be any region of the formation from which water enters the annulus or where drilling fluid flows to the formation. Previous studies have addressed various aspects of the problem studied here. Raymond [1][1], Tragesser et al. [2] and Holmes and Swift [3] studied the case where no aquifer flow occurs. Ramey [4] and Wooley [5] consider the problem of coolant flow to the aquifer in the context of an injection well. Here we study also the problem of aquifer flows into the annulus. This mixing of formation water and drilling fluid alters the fluid in the annulus which in turn alters the heat transfer characteristics of the annulus region. An earlier version of this work was reported by Oster and Scheffler [6], who also reported on a parametric study using the same model in reference [7].

Mathematical Model

The temperature distribution in rock surrounding a well is modeled in cylindrical coordinates with axial symmetry. The origin of this coordinate system is located at the earth's surface with the z axis coinciding with the centerline of the well. The z axis is positive in the downward direction, as indicated in Fig. 1. The mathematical model is applicable to

the region defined by $0 < r < R$ and $0 < z < Z$. Three regions are assumed. Region one is a pipe of radius r_1, extending to the well bottom with no openings except at the endpoints. Region two is an annulus between the well wall and the pipe. (The well has a constant radius, r_2.) The bore hole wall may have openings into the surrounding rock. Region three is the surrounding rock. Regions two and three are further divided into J "control volumes" or "layers" which may coincide with the various rock layers.

We assume a drilling fluid (this fluid is referred to as coolant hereafter) is pumped through the drill pipe to the hole
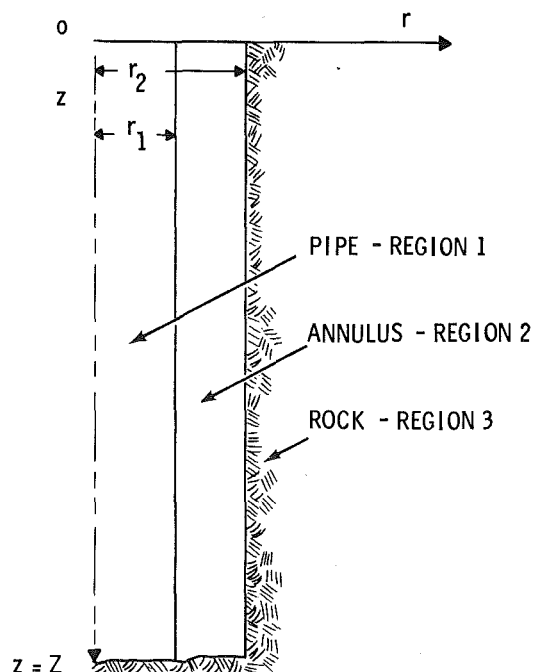

Fig. 1 The well-rock formation geometry

---

[1] Number in brackets designate references at the end of the paper.

Copyright © 1982 by ASME

bottom and is returned through region two, where it may mix with water from one or more aquifers. The possibility of the coolant being lost into the rock formation is also covered.

Let the subscripts 1, 2, and R refer to regions one, two, and three, respectively. The model is based on the following assumptions:

- The flow is single phase and incompressible.
- The temperature distribution in the annulus is uniform radially and at the bulk temperature of the fluid.
- Axial condition of heat in the fluid is negligible relative to axial convection.
- No fluid enters the annulus at the surface.
- Fluid entering the annulus through an aquifer is perfectly mixed with annulus fluid at the point of entry.
- Mass flow rates from (to) the formation into (from) the annulus are known.
- Heat generation by viscous dissipation in the fluid is negligible.
- The temperature drop across drilling pipe is negligible.
- Heat is transferred by conduction alone in the formation.
- Coolant entering the formation does not affect the formation temperature.

The temperature distribution is governed by the following equation in region one,

$$\dot{m}_0 c_{pc} \frac{dT_1}{dz} = 2\pi r_1 h (T_2 - T_1), \tag{1}$$

and for the annulus (region two), control volume j with no aquifer flow present

$$-\dot{m}_j c_{pj} \frac{dT_{2j}}{dz} = 2\pi r_1 h (T_{2j} - T_{1j}) - 2\pi r_2 k_j \frac{\partial T_{Rj}}{\partial r} \bigg|_{r=r_2} + g(z,t). \tag{2}$$

The function $g(z,t)$ is defined as 0 except at $z = Z$. The specific heat, c_{pj}, is determined by the mixture of coolant and entrained water flowing into the control volume j.

If aquifer flow is present in control volume j, the following relationship which neglects annulus-drill pipe heat transfer, is used

$$(\dot{m}_d c_{pj}) T_{2j} = (\dot{m} c_p T_2)_u + 1/2 (\dot{m}_{hj} + |\dot{m}_{hj}|) c_{ph} T_{hj} \tag{3}$$

where the subscripts d and u denote downstream (i.e. leaving the control volume) and upstream (i.e. entering the control volume), respectively. The subscript h denotes water from the aquifer. Attention is called to the factor $1/2(\dot{m}_{hj} + |\dot{m}_{hj}|)$ in the above equation. This factor reduces to $\dot{m}_{hj}$ when the flow is *from* the aquifer *into* the annulus, and is zero if the flow is *to* the aquifer *from* the annulus (see Fig. 2).

For the rock (region three), layer j

$$\frac{1}{\alpha_{Rj}} \frac{\partial T_{Rj}}{\partial t} = \frac{\partial^2 T_{Rj}}{\partial r^2} + \frac{1}{r} \frac{\partial T_{Rj}}{\partial r} + \frac{\partial^2 T_{Rj}}{\partial z^2}. \tag{4}$$

Initial and boundary conditions for $0 < r < R$ and $0 < z < Z$ are

$$T_R(r,z,0) = f(r,z) \tag{5}$$

$$\frac{\partial T_R}{\partial z} \bigg|_{z=0} = (q/k_R)_{surface} \tag{6}$$

$$T_R(r_2,z,t) = T_2(z,t) \tag{7}$$

$$T_R(r > R, z, t) = f(r,z) \tag{8}$$

$$T_R(r, z > Z, t) = f(r,z) \tag{9}$$

$$T_1(z=0, t) = T_0 \tag{10}$$

$$T_2(z=Z, t) = T_1(z=Z, t) \tag{11}$$

The function $f(r,z)$ is assumed known, as are (q/k_R), the surface temperature gradient, with q the surface heat flow, T_0 the temperature of the coolant at the drill pipe inlet, and $g(z,t)$ the temperature rise due to energy released by the drill bit during drilling. At the bottom of the well, the depth is $z = Z$.

A numerical solution of the model described in the foregoing is obtained by imposing an r-z grid on the three regions and replacing equations (1-4) with appropriate finite difference equations. By specifying T_0, A, $g(z,t)$, at specific points in time, it is possible to obtain time dependent solutions. At any fixed time, the temperatures in regions one and two are obtained iteratively. This then determines the boundary conditions needed to obtain T_R. The rock temperatures are then determined by the Crank-Nicolson procedure [8]. The calculation sequence just described produces an annulus temperature based on the preceding rock temperature. This annulus temperature is then used to determine the new rock temperature. To obtain a truly consistent set of temperatures, one could repeat this calculation sequence until no significant change occurs in the calculated temperatures. However, the thermal conductivity of rock is generally much larger than that of the coolant, so iteration is not usually required.

The fluid in the annular control volume j is made up of two components, the coolant and any formation water that may be present. Denote the coolant by the subscript c and let the subscript h denote water from the formation at the current control volume. Finally, let the subscript H denote formation water *already* mixed with the coolant. The two fluid components are determined by the following procedure based on a mass balance for the jth control volume (see Fig. 2). The values of $\dot{m}_{hj}$ for $j = 1, 2, \ldots, J$ are assumed known. The values of $\dot{m}_{cj}$ and $\dot{m}_{Hj}$ are determined in reverse order.

_____ Nomenclature _____

A = annulus cross sectional area
c_p = specific heat
$g(z,t)$ = a function defined at the well bottom to allow for heat generated by the drilling process
h = heat transfer coefficient
J = number of control volumes in a z-direction for annulus and rock regions, maximum value of j.
k = thermal conductivity
$\dot{m}$ = mass flow rate
q = surface heat flow per unit area
R = maximum radial distance

r = radial measurement
T = temperature
t = time
x = coolant mass fraction
Z = maximum depth
z = depth measurement
α = thermal diffusivity
ΔP = hydrostatic head
μ = viscosity
ξ = a constant used in correcting the viscosity due to pressure difference
π = 3.141593
ρ = density

Subscripts

c = coolant or drilling fluid
d = downstream
H = formation water mixed with coolant
h = horizontal flow to and/or from formation
i = radial index
j = depth index
R = rock formation
S = surface
u = upstream
0 = surface, i.e. top of well
1 = drill pipe
2 = annulus

REGION 1   REGION 2   REGION 3
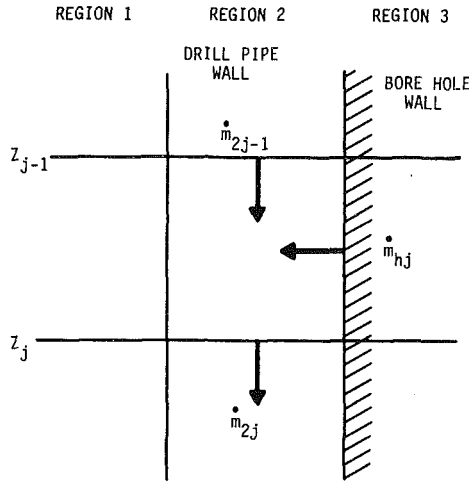
ARROWS SHOW DIRECTION OF POSITIVE FLOW

Fig. 2   Control volume in the annular region

Table 1   Generalized fluid viscosity function

$T^2(\cdot)$	μ (Pa·s)
1	100
2	0.5
3	0.035
4	0.005
5	0.0013
6	0.0006
7	0.00035
8	0.00020
9	0.00015
10	0.00010

Starting with $\dot{m}_{cJ} = -\dot{m}_0$, $\dot{m}_{HJ} = 0$ then for $j = J-1, J-2,$ . . . , 1 $\dot{m}_{cj}$ is given by

$$\dot{m}_{cj} = \begin{cases} \dot{m}_{cj+1} & \text{if } \dot{m}_{hj+1} \geq 0 \\ \min\left[0, \dot{m}_{cj+1}\left(1 - \frac{\dot{m}_{hj+1}}{\dot{m}_{cj+1} + \dot{m}_{Hj+1}}\right)\right] & \text{if } \dot{m}_{hj+1} < 0 \end{cases}$$

(12)

and $\dot{m}_{Hj}$ is calculated from

$$\dot{m}_{Hj} = \dot{m}_{Hj+1} + \dot{m}_{cj+1} - \dot{m}_{cj} - \dot{m}_{hj+1}$$ (13)

If after all the $\dot{m}_{cj}$ and $\dot{m}_{Hj}$ are computed by the foregoing formulas, and $\dot{m}_{c0} > 0$ and/or $\dot{m}_{H0} > 0$ (fluid cannot enter the annulus from the surface), then set

$$\dot{m}_{cj} = \dot{m}_{Hj} = 0$$ (14)

for $j = 1, 2, \ldots, j^* - 1$ where j^* is the smallest value of j such that both

$$\dot{m}_{cj} \leq 0 \text{ and } \dot{m}_{Hj} \leq 0.$$ (15)

Once all flow rates are known, the mass fraction of coolant within each control volume can be determined. The mass of coolant flowing through control volume j during time Δt is given by

$$m_{cj} = [\dot{m}_{cj-1} + |\dot{m}_{cj-1}| - \dot{m}_{cj} + |\dot{m}_{cj}|]\left(\frac{\Delta t}{2}\right)$$ (16)

Similarly, $\dot{m}_{Hj}$ is given by

$$m_{Hj} = [\dot{m}_{Hj-1} + |\dot{m}_{Hj-1}| - \dot{m}_{Hj} + |\dot{m}_{Hj}| + \dot{m}_{hj}$$
$$+ |\dot{m}_{hj}|]\left(\frac{\Delta t}{2}\right)$$ (17)

Then the mass fraction of coolant is given by $x_j = m_{cj}/(m_{cj}$

²T is a dimensionless temperature.
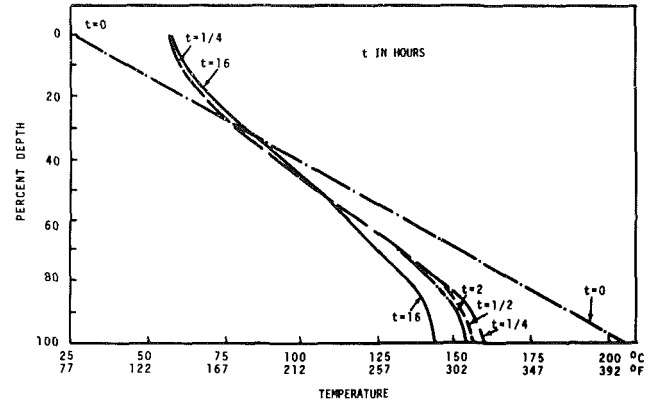
Fig. 3   Drill pipe temperature (no aquifers)

$+ m_{Hj})$. With x_j known, the specific heat capacity, c_p, the thermal conductivity, k, and fluid density, ρ, are computed from

$$c_{pj} = x_j c_{pc} + (1 - x_j) c_{pH}$$ (18)

$$k_j = x_j k_c + (1 - x_j) k_H$$ (19)

$$\rho_j = \frac{1}{\dfrac{x_j}{\rho_c} + \dfrac{1 - x_j}{\rho_H}}$$ (20)

The heat transfer coefficient, h_c, is calculated from standard correlations with Sieder-Tate modifications for both heating and cooling [9, 10]. The correlations used here are for Newtonian fluids and well drilling coolant is generally non-Newtonian. The choice of these relations is based on lack of adequate data representing a generic drilling fluid. Friend and Metzner [11] discuss this problem at length. The equations used are

$$h_c = 1.86\frac{k_c}{\Delta r_2}\left(\frac{\dot{m}\Delta r_2}{A\mu}\right)^{1/3}\left(\frac{\mu}{k_c c_p}\right)^{1/3}\left(\frac{\mu}{\mu_1}\right)^{0.14}$$
$$\times \left(\frac{r_2}{r_1}\right)^{0.15}$$ (21)

if

$$\frac{\dot{m}\Delta r_2}{A\mu} < 2300$$ (22)

and

$$h_c = 0.023\frac{k_c}{\Delta r_2}\left(\frac{\dot{m}\Delta r_2}{A\mu}\right)^{0.8}\left(\frac{\mu}{k_c c_p}\right)^{1/3}\left(\frac{\mu}{\mu_1}\right)^{0.14}$$
$$\times \left(\frac{r_2}{r_1}\right)^{0.15}$$ (23)

otherwise. In the foregoing equations, Δr_2 is the hydraulic diameter and defined as $\Delta r_2 = r_2 - r_1$. The viscosity, μ_1, is determined from the temperature of the drillpipe, whereas μ is determined from the temperature at the control volume center. The drill pipe temperature is obtained by linear interpolation from the pipe fluid and annulus fluid temperature.

The coolant viscosity is assumed to be a function of both temperature and pressure [12, 13]. The pressure is computed as a hydrostatic head which, in turn, requires the fluid density. The viscosity is temperature dependent and satisfies the tabular function in Table 1. With the viscosity and temperature of the coolant at the inlet, a reference point on this function is established. Then, for any other temperature, this function is interpolated relative to this initial reference
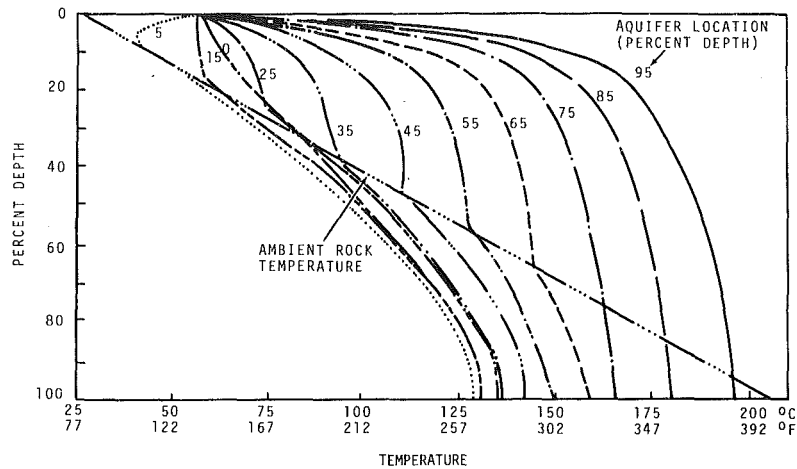
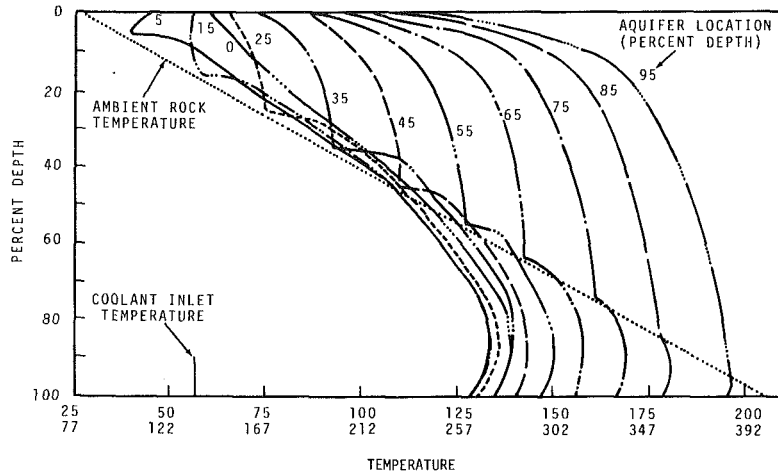**Fig. 4 Drill pipe temperature as a function of aquifer location**

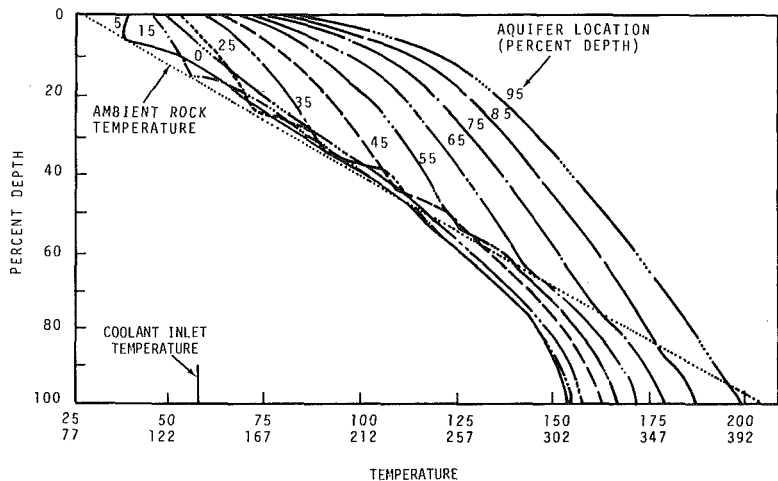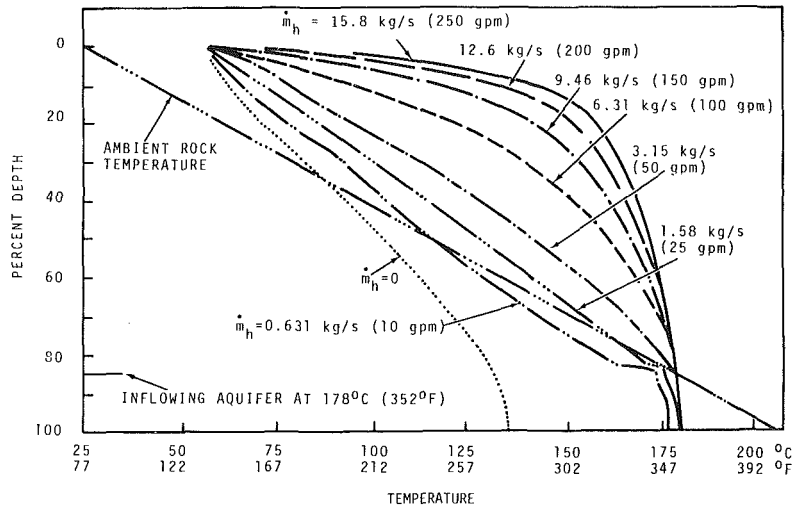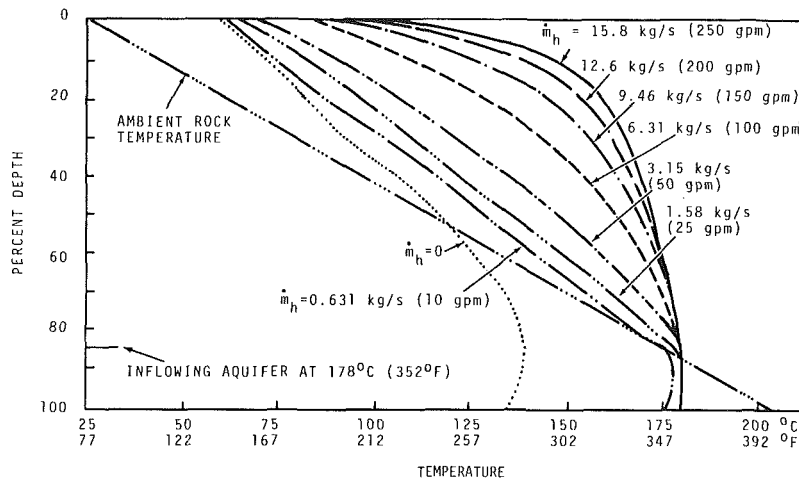**Fig. 5 Annulus temperature as a function of aquifer location**

**Fig. 6 Bore-hole wall temperature as a function of aquifer location**

point. The value obtained from Table 1 is further modified by the hydrostatic pressure to yield

$$\mu = \mu_{table}(1-\xi\Delta P) \qquad (24)$$

where ξ is a constant in the range of 1.71×10^{-7} to 2.84×10^{-7}, and where ΔP is the annulus hydrostatic head in N/m^2.

Well Data

The mathematical model discussed in the foregoing has been implemented on a computer. Data for a hypothetical well is listed in Table 2. The well is studied during circulation only, i.e., $g(z,t) = 0$, and Z remains fixed at the maximum

depth of 6096 m (20,000 ft). A heavy oil base mud with a density of 2157 kg/m³ (18 lb/gal) is assumed. The well is studied both with and without acquifer flows present. The influence of both mass flow rate and location of an acquifer were studied. The initial temperature distribution is that of the ambient rock. The finite difference grid used for the example is defined by radial and depth boundaries. The radial boundaries are at .1708 ($=r_1$), .359 ($=r_2$), 1, 2, 3, 4, 5, 6.5, 8, 10 ft. For the nominal system (i.e. no aquifers present) the region between 500 and 19,500 ft is divided into 19 layers, each 1000 ft thick. Other boundaries were placed at 200, 19,800, 20,200, and 20,400 ft. An extra layer lying entirely

below the well is included to isolate the well bottom from the boundary of the system.

The aquifers included in this study were all restricted to the region where the layers are of uniform thickness. Each aquifer is 100 ft thick and centered at the midpoint of one of these layers. A layer containing an aquifer is replaced with three layers, the aquifer layer being sandwiched between two layers each 450 ft thick. The results of this study are discussed in the following section.

Results of Example

Figure 3 shows for various times expressed in hours, the temperature profiles for the drill pipe when no aquifer flow is present. This figure is similar to those given by Raymond [1] and is included here because it shows the drill pipe temperature behavior when no aquifer is present.

Initially, the coolant is warmer than the surrounding surface rock. As the coolant passes down the drill pipe, energy

Fig. 7 Drill pipe temperature as a function of aquifer flow rate

Fig. 8 Annulus temperature as a function of aquifer flow rate
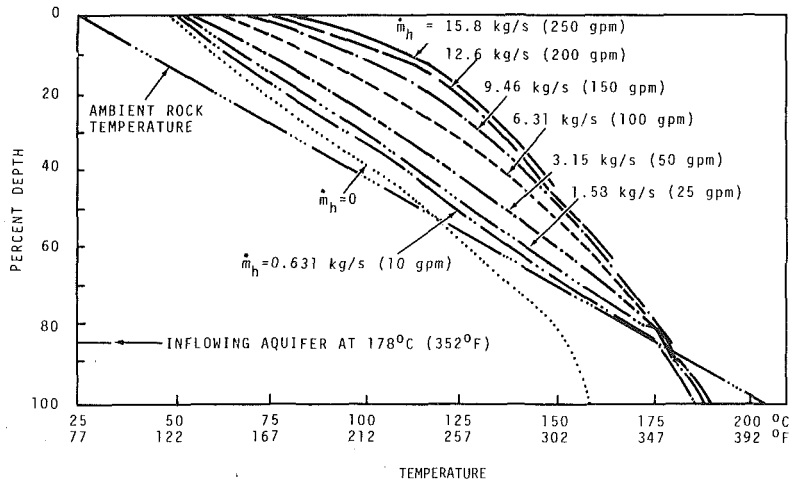
Fig. 9 Bore-hole wall temperature as a function of aquifer flow rate

Fig. 10   Drill pipe temperature as a function of time, with two aquifers

Fig. 11   Annulus temperature as a function of time, with two aquifers
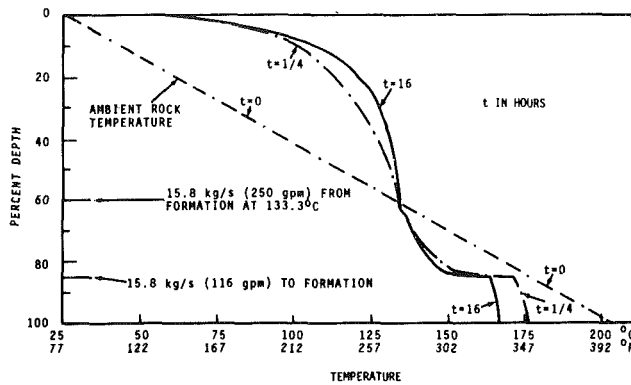
Fig. 12   Bore-hole wall temperature as a function of time, with two aquifers

is lost to fluid in the annulus and to the surrounding formation. At some depth, the formation temperature exceeds that of the coolant in the drill pipe. From this point on, the energy transfer is reversed. The drill pipe fluid is heated and the formation is cooled. The coolant proceeds down the pipe and, on entering the annulus, begins the return to the surface. For some distance, the coolant in the annulus continues to receive more energy from the formation than is lost to the drill pipe resulting in the characteristic maximum fluid temperature occurring at about 80 percent depth. This same characteristic was reported by Raymond [1].

Figures 4–6 show the drill pipe, annulus and bore-hole wall temperature distributions, respectively, when an aquifer flow is present. The aquifer flow rate is taken as 15.8 kg/s (250 gpm). The temperature curves shown are after equilibrium has been achieved (about 16 hr). The aquifer depth is varied from 5 to 95 percent of total well depth in increments of 10 percent. The aquifer enters only one control volume, i.e. the one located at the specified depth. The inflowing water temperature is that of the ambient rock at corresponding depth.

Two interesting points may be seen in Figs. 4–6. First, when no aquifer is present, the drilling fluid is hotter than the surrounding rock formation near the earth's surface. At the well bottom, the fluid is cooler than the rock. Hence, the aquifer water tends to cool the well fluid if the aquifer is not very deep, while a deep aquifer tends to heat the well fluid. The phenomenon is displayed in the top 25 percent depth of the well as plotted in Figs. 4 and 6.

The second point of interest is closely related to the first. The change in well fluid temperature is less abrupt as the aquifer depth is increased. The deep aquifer increases the total amount of heat transferred from the rock (and drill pipe) which is carried up the annulus to the surface. This increase is due to the increased mass flow rate in the annulus and a longer transit time from the aquifer to the surface.

Figures 7–9 show the effect of a variable mass flow rate from an aquifer located at 85 percent of the well depth, i.e. 5180 m (17,000 ft). The dramatic change in bottom-hole fluid temperature between when an aquifer is, and is not present, is startling. We note also that the curves for no mass flow from the aquifer in Figs. 7–9 correspond to the equilibrium of Raymond [1].

Table 3 shows the mass fraction of coolant in the well for the flow rates used to produce the plotted data in Figs. 7–9. Even when the mass fraction of formation water is as small as 3 percent, the temperature distribution is greatly changed. This phenomenon leads to the conclusion that an aquifer tends to dominate the temperature distribution when it is present. Additional support for this idea is given in the following discussion.

Figures 10–12 show the temperature distributions of the drill pipe, annulus and bore hole wall, respectively, when two aquifers are encountered by the coolant as it passes from the
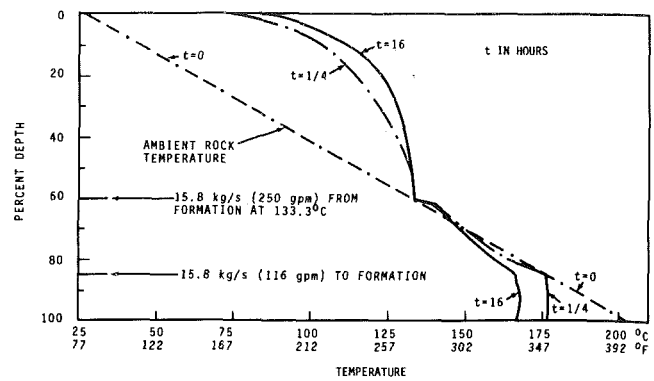
well bottom to the surface. The first aquifer is located at 85 percent of the well depth 5180 m (17,000 ft) and is removing coolant from the annulus at a rate of 15.8 kg/sec (116 gpm). The second aquifer is located at 60 percent of the well depth 3660 m (12,000 ft) and is pouring 15.8 kg/sec (250 gpm) of the water into the annulus. The time, t, is expressed in hours. Dilution of the coolant by formation water greatly influences the temperature distribution in the annulus. The first aquifer simply causes a slowdown in the coolant flow rate, and does not result in the dramatic change observed with the second aquifer which introduces water at the ambient rock temperature.

The inflowing formation water essentially fixes the temperature of the annulus fluid at the point of entry. The mixture proceeds up the annulus where it is effectively cooled by the surrounding rock and the drill pipe.

Table 2   Data used in well simulations

	SI units	U.S. customary units
Surface temperature	26.7°C	80°F
Surface heat flow per unit area	0.817 W/m²	0.259 Btu/hr-ft²
Formation thermal conductivity	1.68 W/mK	0.068 Btu/hr-ft-°F
Formation thermal diffusivity	1.18×10^{-6} m²/s	0.0457 ft²/hr
Drill-pipe diameter	0.1041 m	4.099 in.
Bore-hole diameter	0.2189 m	8.616 in.
Depth	6,096 m	20,000 ft
Geothermal gradient	0.02916°C/m	1.6°F/100 ft
Coolant		
Mass flow rate	27.2 kg/s	200 gal/min
Density	2,157 kg/m³	18 lb/gal
Inlet temperature	57.2°C	135°F
Thermal conductivity	0.0374 W/mK	0.0216 Btu/hr-ft-°F
Specific heat capacity	886 J/kg-K	0.2116 Btu/1b-F
Inlet viscosity	0.118 Pa-s	118 cp
Viscosity correction factor	2.28×10^{-7} m³/N	16%/1000 psi

Table 3 Mass fraction of coolant in annulus above the aquifer for various aquifer flow rates

Aquifer flow rate		Coolant mass fraction
(kg/s)	(gal/min)	
0.631	10	0.98
1.58	25	0.95
3.15	50	0.90
6.31	100	0.82
9.46	150	0.75
12.6	200	0.69
15.8	250	0.64

Conclusion

The example studied shows the temperature distributions in a circulating well to be quite sensitive to any formation water entering the annulus of the well. An aquifer near the well bottom has a much greater influence on the pipe and annulus temperature than when the aquifer is located near the earth's surface. In the case of a drilling fluid of much greater density than the entering formation water, only a few percent dilution can alter the bottom-hole temperature significantly, yet the fluid discharged at the well top does not change significantly.

Acknowledgment

References

1 Raymond, L. R., "Temperature Distribution in a Circulating Drilling Fluid," *Journal of Petroleum Technology*, Mar. 1969, pp. 333–341.

2 Tragesser, A. F., Crawford, P. B., and Crawford, H. R., "A Method for Calculating Circulating Temperatures," *Journal of Petroleum Technology*, Nov. 1967, pp. 1507–1512.

3 Holmes, C. S., and Swift, S. C., "Calculation of Circulating Mud Temperatures," *Journal of Petroleum Technology*, June 1970, pp. 670–674.

4 Ramey, H. J., Jr. "Wellbore Heat Transmission," *Journal of Petroleum Technology*, Apr. 1962, pp. 427–435.

5 Wooley, G. R., "Computing Temperatures in Circulation, Injection and Production Wells," *Journal of Petroleum Technology*, Sept. 1980, pp. 1509–1522.

6 Oster, C. A., and Scheffler, W. A., "Well-Hole Temperature Distributions in the Presence of Aquifers," BNWL-SA-5662, Jan. 1976. Presented at the 31st Annual Petroleum Mechanical Engineering Conference in Mexico City, Sept. 19-23, 1976. ASME Publication number 76-Pet-59.

7 Oster, C. A., and Scheffler, W. A., "Well-Hole Temperature Distributions in the Presence of Aquifers — A Parametric Study," BNWL-SA-6209, Feb. 1977. Presented at the Energy Technology Conference and Exhibition in Houston, Texas, Nov. 5-9, 1978. ASME Publication number 77-Pet-76.

8 von Rosenburg, D. U., *Methods for Numerical Solution of Partial Differential Equations*, Elsevier Publishing, New York, 1969.

9 Jakob, M., *Heat Transfer*, 1st ed., Vol. 1, Wiley, New York, 1949, pp. 543–47.

10 Brown, G. G., et al., "Transfer Coefficients Between Fluids and Tubes," Chapter 29 of *Unit Operations*, Wiley, New York, 1950, pp. 438–444.

11 Friend, W. L., and Metzner, A. B., "Turbulent Heat Transfer Inside Tubes and the Analogy Among Heat, Mass and Momentum Transfer," *AIChE Journal* Vol. 4, No. 4, Dec. 1958, pp. 393–402.

12 Rogers, W. F., *Composition and Properties of Oil Well Drilling Fluids*, 3rd Edition, Gulf Publishing Houston, Texas, 1963, pp. 586–588.

13 Perry, J. H., ed., *Chemical Engineer's Handbook*, 3rd ed. McGraw-Hill, New York, 1950, pp. 372–374.

S. W. Beyerlein[2]

H. C. Claiborne

Chemical Technology Division,
Oak Ridge National Laboratory,
Oak Ridge, Tenn. 37830

The Possibility of Multiple Temperature Maxima in Geologic Repositories for Spent Fuel From Nuclear Reactors[1]

Heat transfer studies for CANDU spent fuel repositories showed that two temperature maxima at the source could occur: one at ~ 60 and another one at $\sim 13,000$ yrs. Spent fuel from pressurized water reactors (PWRs) did not exhibit this phenomenon. Because CANDU spent fuels display a monotonically decreasing heat generation rate, it is not immediately obvious why such behavior occurs. This paper demonstrates that the "double-peak" phenomenon is due to the presence of the right mixture of short and long-lived nuclides in the fuel and that the second peak does not occur for repository sizes less than ~ 1 km^2. For larger repositories, radial and surface heat transfer reduces the magnitude of the second peak.

Introduction

At a conceptual design review meeting of Acres Consulting Services, Ltd. in April 1979, J. L. Ratigan presented thermal analyses [1] of a repository for unreprocessed spent fuels from a CANDU reactor that showed temperature peaks on the source plane at ~ 60 and 13,000 yrs with the latter peak being a little higher (later reported in [2]). This double-peaking phenomenon was first identified by Osnes and Brandschaug [3] using the finite element heat transfer code TRANCO [4] and verified by Ratigan with an analytical solution that utilized an infinite plane source model with exponential term fits of the source term. The phenomenon of late temperature peaking had never been observed in the thermal modeling of repositories containing spent fuels from U.S. light water reactors (LWRs).

Because of implications to the U.S. program, an investigation was begun in order to determine whether the behavior resulted from the composition of the spent fuel, an inadequacy in the plane source model, or both. In this report, a two-nuclide source term with half-lives of 30 yrs (^{137}Cs and ^{90}Sr) and 24,000 yrs (^{239}Pu) was used to show how the double-peak phenomenon can occur and to demonstrate the effects of surface and radial heat transfer from a finite repository.

Thermal Characteristics of Spent Fuel and Rock Medium

The thermal properties of the medium were assumed in-

variant with temperature, which permitted analytical solutions. The rock medium was granite with a thermal conductivity of 2.64 W/m°C and a thermal diffusivity of 37 m^2/yr.

For comparison with the original analysis by Ratigan [1] on an absolute as well as a relative basis, 32 W/m^2 (130 kW/acre) was chosen as the thermal loading for all calculations. The final conceptual design [2] for a Canadian spent fuel repository used 14.2 W/m^2 (57 W/m^2).

The conceptual design assumes an immobilized package of spent fuel from the CANDU reactor with an outside diameter of 0.91 m and a height of 1.15 m that generates 269 W at 10 yrs after reactor discharge [2]. D. R. Prowse considered fission products, plutonium, and other actinides (reported in reference [5]) in fitting the heat generation rate of
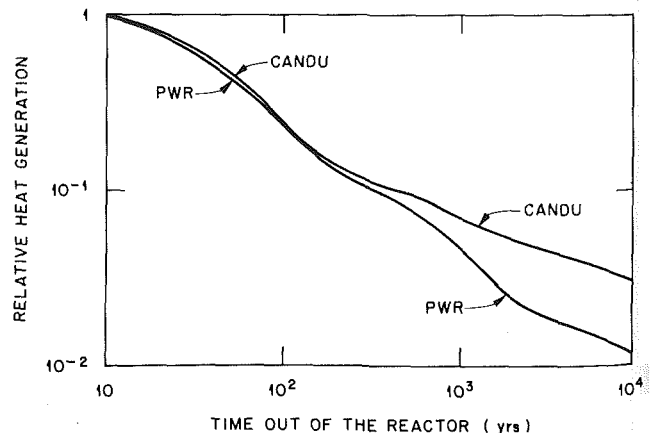
Fig. 1   Relative heat generation rates of PWR and CANDU spent fuels

Copyright © 1982 by ASME

unreprocessed spent fuel from CANDU reactors with exponential terms that can be resolved into the form

$$g(t) = F \sum_{j=1}^{N} A_j e^{-\lambda_j t}, \qquad (1)$$

where $N = 9$.

A least squares fit of ORIGEN data [6] for PWR unreprocessed spent fuel was made, and a fit was obtained with 5 terms having a standard deviation of 1.1 percent for times between 10 and 10^5 yrs.

The fitted source terms (normalized to a sum of unity) for both the CANDU and PWR spent fuels are presented in Table 1 for burnups of 7000 and 33,000 MWd/t for the CANDU and PWR fuels, respectively.

The heat generation rate (as a function of time) for each fuel, normalized to unity at 10 yrs after reactor discharge, is shown in Fig. 1.

Theory of Multiple Temperature Peaking

Ratigan [1] has demonstrated a reasonable argument for the possibility of multiple peaks. For a source represented by equation (1), the temperature rise on the infinite source plane in an infinite medium is

Table 1 Fit constants for source terms for CANDU and PWR spent fuels

	CANDU		PWR	
Term	$\lambda_j,$ y^{-1}	$A_j,$ dimen.	$\lambda_j,$ y^{-1}	$A_j,$ dimen.
1	1.04E-4	3.072E-2	1.796E-1	1.262E-1
2	2.80E-5	2.439E-2	2.130E-2	7.015E-1
3	7.90E-3	9.252E-3	1.704E-2	1.402E-1
4	4.80E-2	-5.507E-2	8.459E-5	1.606E-2
5	1.60E-3	8.900E-2	1.901E-5	5.840E-3
6	2.30E-2	8.398E-1		
7	6.93E-1	1.499E-2		
8	3.47E-1	2.810E-2		
9	8.88E-2	1.880E-2		

$$\Delta T(0,t) = \frac{F\sqrt{\alpha}}{k\sqrt{\pi}} \sum_{j=1}^{N} \frac{A_j}{\lambda_j} D(\sqrt{\lambda_j}t) \qquad (2)$$

(See Appendix for derivation of equations.)

The points of inflection can be obtained by differentiating equation (2) with respect to time and setting it equal to zero. On differentiating, rearranging, and noting that the sum of A_j is unity, we have

$$\sum_{j=1}^{N} A_j \sqrt{\lambda_j} t D(\sqrt{\lambda_j}t) - 1/2 = 0 \qquad (3)$$

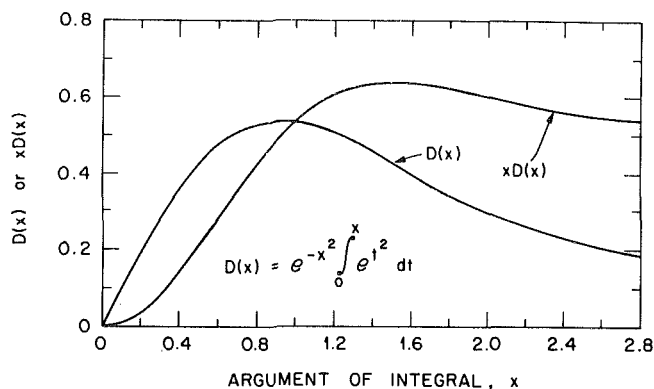Examination of equations (2) and (3) shows the possible

Fig. 2 Plot of Dawson's integral

existence of multiple roots and multiple peaks, depending on values of the constants, since Dawson's integral (reference [7], p. 319), as well as the product of the integral and its argument, has a maximum (see Fig. 2). If the fit constants, λ_j, are widely different, a maximum of nine peaks is theoretically possible for CANDU fuels. Since only two have occurred, we suspect dominance by two nuclides, which the following discussion suggests to be the fission products ^{90}Sr and ^{137}Cs, with 30-yr half-lives, and the longer-lived plutonium isotopes.

To understand the thermal history of the infinite plane source, consider a simple hypothetical case in which only two radionuclides are present, one having a half-life of tens of years and the other having a half-life of thousands of years.

Applying equation (2) for the two-nuclide system,

$$\Delta T(0,t) = \frac{\sqrt{\alpha}}{2k\sqrt{\pi}} \left[\frac{F_1}{\sqrt{\lambda_1}} D(\sqrt{\lambda_1}t) + \frac{F_2}{\sqrt{\lambda_2}} D(\sqrt{\lambda_2}t) \right] \qquad (4)$$

Assume that nuclide 1 has a half-life of 30 yr and is distributed uniformly over an infinite plane, with an intensity of 1 W/m^2. For nuclide 2, assume the corresponding values to be 24,000 yrs and 0.05 W/m^2, which is higher than usual, but this emphasizes the effect of the long-lived nuclide. During the first few hundred years, the first term of equation (4) will dominate; the second term will dominate after several thousand years, when nuclide 1 has effectively disappeared. Two peaks will be evident from these conditions. A maximum of Dawson's integral (reference [7], p. 298) occurs for an argument of 0.9241. Therfore, $\lambda_j t = 0.9241$ identifies the occurrence times for the two maxima, t_1 and t_2. For the two nuclide half-lives assumed, $t_1 = 37$ yr and $t_2 = 30,000$ yrs.

In the nine-term fit to the CANDU fuel, the intermediate peaks are suppressed because of the overlapping contributions from many terms and because the ^{240}Pu (half-life = 6540 yr) contributes to decreasing the plutonium peak to $\sim 13,000$ yrs.

Inspection of equations (3) and (4) reveals that the occurrence of multiple peaks is a function only of the relative half-life for each nuclide. Because the value of the Dawson's integral for the two terms of equation (4) is the same at their

_____ Nomenclature _____

A = fit constant, dimensionless

$D(X)$ = Dawson's integral of argument X (reference [7], p. 319)

F = total emplacement thermal loading, W/m^2

i = complex operator, $\sqrt{-1}$

$g(t)$ = thermal source function, W/m^2

k = thermal conductivity, W/m·K

L = depth, m

N = number of terms

R = radius of repository, m

r = radial coordinate, m

T = temperature, °C

t = time after emplacement, yrs

U = real part of error function with complex argument (reference [7], p. 325)

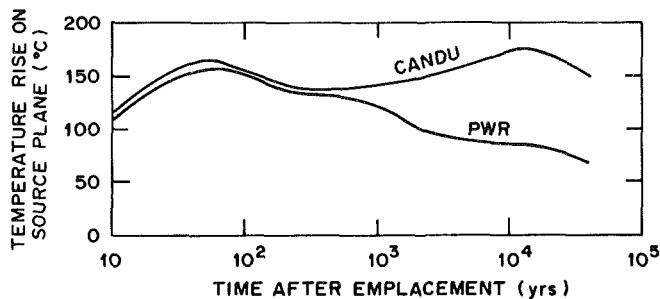V = imaginary part of error function with complex

argument (reference [7], p. 325)

$w(z)$ = error function of complex argument z, when $z = x + iy$ or x, y (reference [7], p. 297)

x,y,z = Cartesian coordinates, m

α = thermal diffusivity, m^2/yrs

λ = fit constant equivalent to decay constant yrs^{-1}

Fig. 3 Comparison of CANDU and PWR temperature rise histories for an infinite plane source

1. INFINITE PLANE SOURCE, INFINITE MEDIUM
2. INFINITE PLANE SOURCE BURIED AT 1000 m
3. INFINITE PLANE SOURCE BURIED AT 800 m
4. INFINITE PLANE SOURCE BURIED AT 600 m

Fig. 4 Effect of burial depth on the temperature rise histories for CANDU spent fuels

1. INFINITE DISK SOURCE
2. 170-m-diam DISK SOURCE (150 x 150 m)
3. 1130-m-diam DISK SOURCE (1000 x 1000 m)
4. 2260-m-diam DISK SOURCE (2000 x 2000 m)
5. 4510-m-diam DISK SOURCE (4000 x 4000 m)

Fig. 5 Effects of source plane area on the temperature rise histories

respective peaks, the ratio of the temperature peaks for the two-nuclide spent fuel is given by

$$\Delta T_2/\Delta T_1 = F_2\sqrt{\lambda_1}/F_1\sqrt{\lambda_2}, \qquad (5)$$

Therefore, for the second peak to exceed the first peak,

$$F_2/F_1 < \lambda_2/\lambda_1 \qquad (6)$$

which is the case for our example because $F_2/F_1 = 0.05$, and $\lambda_2/\lambda_1 = 0.035$.

Results of Model Calculations

Calculations were made for the CANDU fuels using plane sources, arrays of point and spherical sources, and computer models with homogenized source regions. However, only the infinite plane source calculation was made for the PWR spent fuels since they did not exhibit the double peak phenomenon.

Figure 3 presents a comparison of temperature histories for CANDU and PWR spent fuel repositories for a plane source in an infinite homogeneous medium.

A marked difference occurs in the behavior of the CANDU and the PWR spent fuels after ~300 yrs. At ~60 yrs, a thermal peak arises from the decay of ^{137}Cs and ^{90}Sr. The initial temperature rise due to PWR fuel is slightly less than that for CANDU fuel, because of its lower relative heat generation rate. After 300 yrs, however, the CANDU repository temperature begins to increase, whereas the temperature in the PWR repository slowly declines. Because of the higher relative amounts of transuranium elements in the CANDU spent fuel, a second peak, higher than the first, occurs at ~13,000 yrs. The relatively smaller amounts of longer-lived transuranics in the PWR spent fuel apparently cause an overlapping of the individual contributions that damp out the second peak.

To ascertain whether the double-peak phenomenon was inherent to CANDU spent fuel or whether it was a deficiency in the plane source model, effects of heat transfer from the earth's surface and radial heat transfer were considered.

Figure 4 portrays the temperature rise histories for CANDU spent fuels at burial depths of 600, 800, and 1000 m for an infinite plane source compared with the infinite medium case. Disposal nearer the surface lowers the second peak and causes it to occur earlier; however, even at 600 m the effect of surface leakage is not noticeable before 3000 yrs — long after repository temperatures have begun to increase. Deeper emplacement of spent fuel postpones the onset of surface heat leakage, leading to higher secondary temperature peaks.

Radial heat transfer was investigated by representing the repository as a finite disk. The temperature rise histories at the center of repositories with radii ranging from 85 to 2260 m are shown in Fig. 5 in comparison with the infinite plane or disk source case. For a disk source less than ~1200 m in diameter, only one temperature peak appears because of the heat escaping from the side of the repository. It appears that only in a repository larger than ~1 km² could two maxima
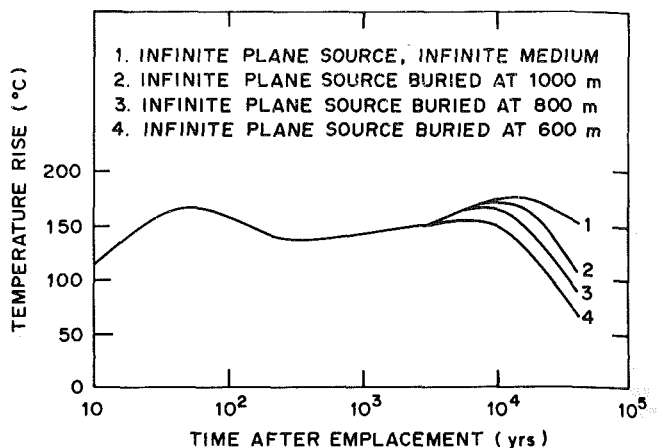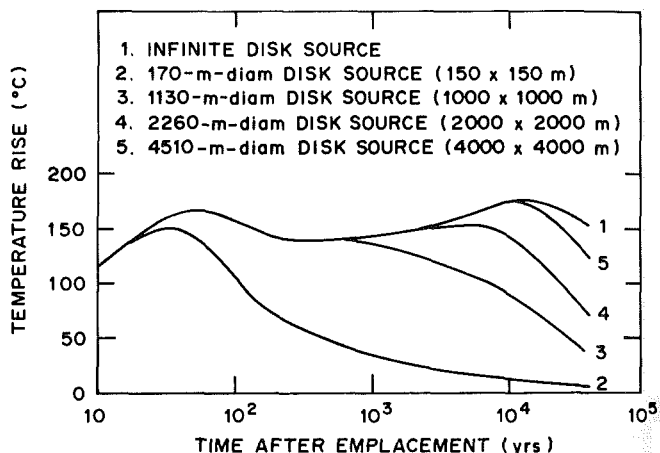
occur, and only in a repository larger than ~4 km² would the second temperature peak exceed the first.

Two numerical models of the 170-m-dia disk source were solved using the finite difference program HEATINGS [8]; these agreed quite well with the analytical result.

In the actual repository, waste will be contained in canisters that are situated at some distance from each other. The source is then discrete rather than continuous.

Modeling the repository as an array of point sources should represent a lower bound for the temperatures of the abiabatic interfaces at the disposal horizon, and modeling the repository as an array of spheres should produce an approximate upper bound for a real case (but lower than for a plane source model). For CANDU spent fuel that is to be stored in canisters 1.15 m high and 0.91 m in diameter, an assumed sphere diameter of 1.0 m should represent a reasonably accurate approximation. The temperature at any point in the array can be obtained by superimposing the effects of the constituent points or spherical sources, because the problem is linear when the thermal properties are invariant.

Calculations for arrays of sources represented by points and spheres gave results almost identical to those from disk sources encompassing the same areas. The long-term differences were not distinguishable on the scale of the graphs used here. A unit-cell calculation for the CANDU conditions was also made with the HEATING 5 computer code and the results were within a small percentage of the infinite source plane temperatures. More details of these results are given in reference [9].

Conclusions

Multiple temperature maxima are theoretically possible for certain spent fuels, depending on the relative quantities of radioactive nuclides, their half-lives, and the dimensions of the repository horizon.

For spent fuel from CANDU reactors, thermal peaks can occur at ~60 and 13,000 yrs, with the second peak being greater if the repository is relatively large. Double temperature peaks will not occur if the repository is smaller than ~1 km². Even for very large repositories, double thermal peaks will not occur with spent fuel from PWRs because of the relatively smaller quantities of transuranics present.

In modeling spent fuel repositories, the superiority of disk and spherical sources rather than an infinite plane source was demonstrated for long burial times. For shorter times (<100 yrs), all models are in close agreement; after ~1000 yrs, the long-term edge and surface effects become important, and an infinite plane source/infinite medium model is progressively less applicable.

Acknowledgments

References

1 Ratigan, J. L., RE/SPEC, Inc., private communication to H. C. Claiborne, Oak Ridge National Laboratory, 1979.

2 Mayman, S. A., Charlwood, R. G., and Ratigan, J. L., "Long-Term Response of a CANDU Fuel Disposal Vault," AECL Report TR-134, Dec. 1980.

3 Osnes, J. D., and Brandschaug, T., RE/SPEC, Inc., private communication to J. L. Ratigan, RE/SPEC, Inc., 1978.

4 Callahan, G. D., "Documentation of the Heat Transfer Code TRANCO," Report RSI-0037, ORNL/SUB-4269/15, RE/SPEC, Inc., Aug. 1975.

5 Charlwood, R. G., and Burgess, A. S., "Irradiated Fuel and Immobilized Waste Vaults: Design Specifications and Scope of Work," AECL Report TR-47, 1980.

6 Bell, M. J., ORIGEN-The ORNL Isotope Generation and Depletion Code, ORNL-4628, May 1973.

7 Gautschi, W., "Error Function and Fresnel Integrals," Handbook of Mathematical Functions, Abramowitz and Stegun, eds., National Bureau of Standards, 1964.

8 Turner, W. D., Elrod, D. C., and Siman-Tov, I. I., HEATING5-An IBM 360 Heat Conduction Program, ORNL/CSD/TM-15, March 1977.

9 Beyerlein, S. W., and Claiborne, H. C., "The Possibility of Multiple Temperature Maxima in Geologic Repositories for Spent Fuel from Nuclear Reactors," presented at the annual winter meeting of the ASME, Chicago, Illinois, Nov. 16-21, 1980, HTD-Vol. II. Also given in more detail in ORNL/TM-7024, Jan. 1980.

10 Carslaw, H. S., and Jaeger, J. C., Conduction of Heat in Solids, Oxford University Press, 1959.

11 Nichols, J. P., Oak Ridge National Laboratory, private communication to H. C. Claiborne, Oak Ridge National Laboratory, 1971.

APPENDIX: DERIVATION OF EQUATIONS

A solution to the heat transfer equation for an instantaneous point source of heat in an infinite medium, initially at uniform temperature, is a Green's function. If the source is located at (x', y', z', t'), the Green's function giving the temperature or temperature rise (reference [10], p. 353) for the heat conduction equation is

$$G(x,y,z,t) = \frac{\alpha g(t) e^{-[(x-x')^2 + (y-y')^2 + (z-z')^2]/4\alpha(t-t')}}{k[4\pi\alpha(t-t')]^{3/2}} \tag{A1}$$

This expression was used to develop the solutions for time-dependent point, plane, and spherical sources by integrating over time and space.

The total temperature rise can be determined by superimposing the rises resulting from the solutions for each individual source term as given by equation (1).

Point Source, Infinite Medium

Applying equations (A1) and (1) and expressing in radial coordinates, the temperature rise for a continuous point source at $r' = 0$ is

$$\Delta T_j = \frac{\alpha F A_j}{k} \int_0^t \frac{e^{-\lambda_j t'} e^{-r^2/4\alpha(t-t')}}{[4\pi\alpha(t-t')]^{3/2}} dt' \tag{A2}$$

On letting

$t-t' = 1/u^2$, $a = r/\sqrt{4\alpha}$, and $b = \sqrt{\lambda_j}$,

$$\Delta T_j = \frac{\alpha F A_j e^{-\lambda_j t}}{4k(\alpha\pi)^{3/2}} \int_{1/\sqrt{t}}^{\infty} e^{-a^2 u^2 + b^2/u^2} du \tag{A3}$$

The solution to equation (A3) (reference [6], p. 304) is

$$f_1 = \frac{\sqrt{\pi}}{2\alpha} e^{-(a^2/t) + \lambda_j t} [w(\sqrt{\lambda_j t}, a/\sqrt{t}) + w(-\sqrt{\lambda_j t}, a/\sqrt{t})], \tag{A4}$$

where f_1 is the integral in equation (A3).

The second term of equation (A4) is the negative of the conjugate, or

$$-x + iy = -(x - iy) = w(-\bar{z}) \tag{A5}$$

Complex functions can be expressed in terms of a real part and an imaginary part, represented by

$$w(z) = U + iV \tag{A6}$$

It also can be shown (reference [7], p. 297) that

$$w(-\bar{z}) = \overline{w(z)} = U - iV \tag{A7}$$

The first term of equation (A4) is of the same form as equation (A6), and the second term is of the same form as equation (A7). Therefore, combining these with equation (A3) yields

$$\Delta T_j = \frac{F A_j e^{-r^2/4\alpha t}}{4k\pi r} U(\sqrt{\lambda_j t}, r/\sqrt{4\alpha t}) \tag{A8}$$

Infinite Plane Source, Infinite Medium

The temperature rise resulting from a continuous and time-dependent infinite plane source in an infinite medium may be obtained by integrating equation (A1) from $-\infty$ to $+\infty$ in the x and y directions and over time. On integrating with respect to x' and y',

$$\Delta T_j = \frac{F A_j \alpha}{k} \int_0^t \frac{e^{-\lambda_j t e^{-(z-z')^2/4\alpha(t-t')}}}{\sqrt{4\pi\alpha(t-t')}} dt' \tag{A9}$$

Letting

$x = t-t'$, $\alpha = (z-z')/\sqrt{4\alpha}$, and
$b = \sqrt{\lambda_j}$, then

$$\Delta T_j = \frac{F A_j \sqrt{\alpha} e^{-\lambda_j t}}{2K\sqrt{\pi}} \int_0^t \frac{e^{-(a^2/x) + b^2 x}}{\sqrt{x}} dx \tag{A10}$$

In solving equation (A10), we follow the technique outlined by Nichols [11] by noting that the integral of equation (A10) is the derivative with respect to λ_j of f_1 in equation (A4). Therefore,

$$\frac{df_1}{d\lambda_j} = \frac{\sqrt{\pi}}{2a} e^{-(a^2/t) + \lambda_j t} \{ tw(z) + tw(-z)$$

$$+ (1/2)t/\lambda_j [w'(z) - w'(-z)] \}, \tag{A11}$$

where

$$z = \sqrt{\lambda_j} t + ia/\sqrt{t} = (\sqrt{\lambda_j t}, a/\sqrt{t})$$

The differential of the complex error function (reference [7], p. 298) is

$$w'(z) = -2zw(z) + 2i/\sqrt{\pi}, \tag{A12}$$

and

$$w'(-\bar{z}) = 2\bar{z}w(-\bar{z}) + 2i(\sqrt{\pi}) \tag{A13}$$

Subtracting equation (A13) from (A12) and combining with equations (A5), (A6), and (A7) yields

$$w'(z) - w'(-\bar{z}) = 4(-\sqrt{\lambda_j}tU + aV/\sqrt{t}) \tag{A14}$$

Combining equations (A10), (A11), and (A14),

$$\Delta T_j = \frac{FA_j\sqrt{\alpha}}{2k\sqrt{\lambda_j}} e^{-(z-z')^2/4\alpha t} V(\sqrt{\lambda_j}t,(z-z')/\sqrt{4\alpha t}) \tag{A15}$$

For the special case of the temperature rise on the source plane $(z - z' = 0)$, equation (A15) becomes

$$\Delta T_j = \frac{FA_j\sqrt{\alpha}}{2K\sqrt{\lambda_j}} V(\sqrt{\lambda_j}t,0), \tag{A16}$$

which can be expressed in terms of Dawson's integral. Therefore,

$$\Delta T_j(0,t) = \frac{FA_j\sqrt{\alpha}}{k\sqrt{\lambda_j}\sqrt{\pi}} D(\sqrt{\lambda_j}t) \tag{A17}$$

Tabulated values of the imaginary part (V) of the complex error functions and Dawson's integral are available (reference [7], pp. 325 and 319).

Disk or Finite Plane Source, Infinite Medium

The temperature rise resulting from a continuous disk source in an infinite medium can be obtained by integrating equation (A1) over time and over a source plane of radius R, using the cylindrical coordinate system. For the source plane at $z' = 0$,

$$\Delta T(r,z,t) = \frac{2\pi\alpha FA_j}{k} \int_0^t dt'$$

$$\times \int_0^R \frac{e^{-\lambda_j t'} e^{-[(r-r')^2 + 3^2]/4\alpha(t-t')}}{[(4\pi\alpha(t-t')]^{3/2}} r'dr' \tag{A18}$$

By letting $y = r - r'$, integrating with respect to r', and applying the Faltung or integral theorem, it can be shown that two integral terms are produced that are identical in form to the integral in equation (A10). For the special case at $r = 0$, the solution to equation (A18) becomes

$$\Delta T_j(0,z,t) = \frac{FA_j\sqrt{\alpha}}{2k\sqrt{\lambda_j}} [e^{-z^2/4\alpha t} V(\sqrt{\lambda_j}t,z/\sqrt{4\alpha t})$$

$$-e^{p^2/4\alpha t} V(\sqrt{\lambda_j}t,p/\sqrt{4\alpha t})], \tag{A19}$$

where $p^2 = R^2 + z^2$.

Continuous Spherical Source, Infinite Medium

The temperature rise at radius r in an infinite medium, external to a spherical source of radius R (reference [10], p. 263), is given by

$$\Delta T_j = \frac{\alpha FA_j}{4\pi krR'}$$

$$\times \int_0^t \frac{e^{-\lambda_j t} e^{-(r-R')^2/4\alpha(t-t')} - e^{-(r-R')^2/4\alpha(t-t')}}{4\pi\alpha(t-t')} dt' \tag{A20}$$

Applying the Faltung or convolution integral theorem and setting

$$a_1 = (r-R')/\sqrt{4\alpha t'}, x = t',$$

$$a_2 = (r+R')/\sqrt{4\alpha t'}, \text{ and } b = \sqrt{\lambda_j}t',$$

it can be shown that two integral terms are obtained that are identical in form to the integral in equation (A10) and that the solution to equation (A20) becomes

$$\Delta T_j = \frac{FA_j\sqrt{\alpha}}{k\pi rR'\sqrt{\lambda_j}} [e^{-a_1^2/t} V(\sqrt{\lambda_j}t,a_1/\sqrt{t})$$

$$-e^{-a_2^2/t} V(\sqrt{\lambda_j}t + a_2/\sqrt{t})] \tag{A21}$$

Infinite Plane Source, Semi-Infinite Medium

An estimate of the effect of thermal leakage through the earth's surface can be made by adapting the solution to the infinite medium case by employing the method of images (reference [10], p. 273).

The solution to the problem of a source plane at a depth $z' = L$, a surface at $z = 0$, and a uniform initial temperature can be obtained by superimposing a negative source at $z' = L$ and subtracting the result from the solution given by equation (A15); that is,

$$\Delta T_j(z,t) = \frac{FA_j\sqrt{\alpha}}{2k\sqrt{\lambda_j}} \left\{ e^{-(z-L)^2/4\alpha t} V\left[\sqrt{\lambda_j}t, \frac{(z-L)}{\sqrt{4\alpha t}}\right] \right.$$

$$\left. -e^{-(z+L)^2/4\alpha t} V\left[\sqrt{\lambda_j}t, \frac{(z+L)}{\sqrt{4\alpha t}}\right] \right\} \tag{A22}$$

D. Ramkrishna

School of Chemical
Engineering,
Purdue University,
West Lafayette, Ind. 47907

N. R. Amundson

Department of Chemical
Engineering,
University of Houston,
Houston, Texas 77004

A Non-Self-Adjoint Problem in Heat Conduction

A non-self-adjoint heat conduction problem is solved by an expansion in terms of the root vectors of the conduction operator and its adjoint using their biorthogonality properties. The completeness of the root vectors follows from the fact that the non-self-adjoint boundary conditions satisfy a regularity condition, which is sufficient to guarantee it.

Introduction

Linear boundary value problems in heat conduction have been investigated extensively for a diverse variety of boundary conditions, but almost invariably these have been of the type that produce self-adjoint problems. The property of self-adjointness makes it possible to obtain readily the solution of steady and unsteady-state heat conduction problems in the form of a series expansion of orthogonal eigenfunctions. Fortunately, in a good many situations, the boundary conditions fit the physics naturally. For example, in one-dimensional heat conduction problems the boundary conditions at the ends are always "unmixed" in the sense that each boundary condition involves only one or the other end-point. Boundary value problems of this type are always self-adjoint. A situation, in which, self-adjointness arises from boundary conditions featuring both endpoints is that which employs the familiar 'periodicity' criteria characteristic of circular domains. In general, however, "mixed" boundary conditions produce non-self-adjoint problems, for which orthogonal eigenfunctions do not exist so that the solution to the problem cannot be obtained by the technique applicable to the self-adjoint problems. Frequently, the non-self-adjoint problem defines an adjoint problem with a common set of eigenvalues and sets of eigenvectors which are biorthogonal. If each of the above sets of biorthogonal vectors is complete, then a solution to the non-self-adjoint problem is possible in the form of a series solution. Completeness can certainly not be taken for granted since non-self-adjoint problems can display very strange behavior in regard to their eigenvalues and eigenvectors. It is sometimes possible to test for completeness of the eigenvectors by rather powerful theorems (see Chapter V of [1]).

In this paper, we consider a non-self-adjoint boundary value problem in heat conduction, which could be of significance in *controlled* heating or cooling of a solid object. Naturally such considerations would extend as well to corresponding situations of diffusive mass transport. We obtain the eigenvalues and the biorthogonal sets of eigenvectors or more generally root vectors[1] by analyzing also the

---

[1] A root vector is defined in the next section.

adjoint system. Although the boundary conditions lead to a non-self-adjoint problem, they satisfy a somewhat complicated regularity criterion, which guarantees the completeness of the root vectors [2]. The solution to the boundary value problem is then obtained as a biorthogonal expansion in terms of the root vectors of the original and the adjoint problems.

Our organization consists of an initial discussion of the boundary value problem (which defines a differential operator) followed by a spectral analysis of the differential operator and its adjoint and, subsequently, the solution of the problem as an expansion in terms of the biorthogonal sets of root vectors.

Boundary Value Problem

Consider a slab of finite thickness along the x'-direction but infinite in the other two directions y and z, initially at a temperature, which is uniform with respect to y and z. The slab is to be heated from both ends in such a way that the heating rate at one end is to be adjusted depending on the heating rate at the other end, where the temperature is specified. Evidently, such a problem may be inherent to situations in which some controlled heating (or cooling) is required to accomplish a desired objective. It is not our purpose to dilate on the nature of such objectives here, for there could be a number of them, the exact nature of which is of no consequence to this work. It is assumed that conduction is one-dimensional so that the unsteady-state energy is given by

$$\alpha \frac{\partial^2 T}{\partial x'^2} = \frac{\partial T}{\partial t} \qquad 0 < x' < l \quad t > 0 \tag{1}$$

where we have used x' as the coordinate variable to make a subsequent switch to a dimensionless distance $x = x'/l$. The boundary condition at $x' = 0$, where the temperature is assumed to be specified is given by

$$T(0,t) = T_0 g_1(t) \tag{2}$$

Since the heating rate at $x' = l$ is to be adjusted in accordance with that at $x' = 0$, we assume that

$$k \frac{\partial T}{\partial x'}(l,t) = -k \frac{\partial T}{\partial x'}(0,t) + h_1(t) T_0 \tag{3}$$

where $h_1(t)$ is taken to be a known function. When the specific objective of control is identified, it would then be possible to obtain an equation for $h_1(t)$ from the solution for the temperature profile, which is developed here. The initial temperature profile of the slab is expressed as

$$T(x',0) = T_0 f_1(x') \qquad (4)$$

In order to solve this boundary value problem, we consider the eigenvalue problem

$$-u'' = \lambda u \qquad (5)$$

$$u(0) = 0 \qquad (6)$$

$$u'(0) + u'(1) = 0 \qquad (7)$$

where primes denote differentiation with respect to x, and the boundary conditions (6) and (7) represent the homogeneous versions of (2) and (3) respectively. The differential expression $L \equiv \{-d^2/dx^2\}$ with the domain $D(L) = [\mathbf{u} \equiv \{u(x)\}: u(0) = 0; \; u'(0) + u'(1) = 0]$ defines an operator $\mathbf{L}$.[2] L is a formally self-adjoint differential expression.

However $\mathbf{L}$ is a non-self-adjoint operator. Its adjoint operator L^* can be easily seen to be composed of the differential expression $L^* = L = \{-d^2/dx^2\}$ and the domain $D^*(L)$ given by

$$D^*(L) = [v \equiv \{\mathbf{v}(x)\}: v'(1) = 0; \; v(0) + v(1) = 0]$$

In what follows we denote $D(L)$ more simply by D and $D^*(L)$ by D^*. If it is agreed that $\mathbf{L}$ automatically operates on $u\epsilon D$ and $\mathbf{L}^*$ operates on $v\epsilon D^*$, then we may write

$$<\mathbf{L}\mathbf{u},\mathbf{v}> = <\mathbf{u},\mathbf{L}^*\mathbf{v}> \qquad (8)$$

At this point, we digress to make some observations about non-self-adjoint operators in general. This digression is essential, since the above operator $\mathbf{L}$ exhibits certain features somewhat unfamiliar to engineering analysis.

It is well known to engineers that real symmetric matrices have certain desirable properties. These are that the eigenvalues are real and regardless of the number of times any of the eigenvalues is repeated there is always a complete set of eigenvectors in terms of which arbitrary vectors can be ex-

___

[2] The boldface symbol $\mathbf{u}$ is to denote the function $\{u(x)\}$ as a vector. Here $D(L)$ is a dense subspace of L_2 [0,1], which is the set of functions $u(x)$ such that

$$\int_0^1 u^2(x)\,dx < \infty$$

pressed as linear combinations. The familiar Sylvester's formula is available for forming functions of the matrix. However, this property does not always extend to unsymmetric matrices, whose eigenvalues could be real or complex and the eigenvectors may or may not be complete. When the eigenvectors are not complete (a situation which may arise in the case of repeating eigenvalues) the ordinary form of Sylvester's theorem is not applicable. Instead a "confluent" form of Sylvester's theorem is available, the use of which leads to a simple solution of linear differential equations featuring unsymmetric matrices. Self-adjoint boundary value problems are analogous to symmetric matrices and as pointed out earlier, unsteady-state, one-dimensional heat conduction problems with unmixed boundary conditions come within the foregoing category. The solution to such problems is obtained as an expansion in terms of eigenfunctions. Non-self-adjoint problems, on the other hand, are analogous to nonsymmetric matrices. Thus it is not certain that solutions can be obtained as expansions in terms of eigenfunctions because the latter may not be complete. In the development here the biorthogonal expansions of solutions in terms of the root vectors (to be defined presently) are analogous to using the confluent form of Sylvester's theorem in dealing with unsymmetric matrices with repeated eigenvalues.

Let $\mathbf{L}$ be a general non-self-adjoint differential operator, whose adjoint is $\mathbf{L}^*$. In this case, it is not possible to make definite assertions about the spectrum of $\mathbf{L}$ in regard to whether or not it is empty, discrete, continuous, or generates a complete set of eigenvectors. A further complication that can arise with non-self-adjoint operators is that associated with repeating eigenvalues. This eventuality comes up when one or more eigenvalues are multiple roots of the characteristic equation. With self-adjoint operators, an eigenvalue, which repeats, say, n times, generates n linearly independent eigenvectors. Such is not necessarily the case with non-self-adjoint operators. Thus it is possible that only one eigenvector may be associated with an eigenvalue that is repeated n times. In the foregoing situation, the set of all eigenvectors of the non-self-adjoint operator, $\mathbf{L}$, cannot be expected to be complete. The difficulty is partially overcome by generalizing the concept of an eigenvector. This generalization consists of what has been referred to as a root vector (see for example p. 5 of [1]), which is defined as follows. A vector $\mathbf{u}$ is called a root vector of operator $\mathbf{L}$, corresponding to an eigenvalue λ, if there exists an integer n such that

___

Nomenclature

D,D^*	=	domain of differential operators $\mathbf{L}$ and $\mathbf{L}^*$, respectively
$\mathbf{D}(\lambda)$	=	characteristic matrix defined by equation (15)
f, f_1	=	initial dimensionless temperature distribution in the slab
g, g_1	=	time dependent dimensionless temperature at slab end, $x = 0$
h, h_1	=	time dependent inhomogenieties in the boundary conditions (3) and (42), respectively
k	=	thermal conductivity of slab material
$\mathbf{k}(u(x))$	=	Wronskian vector of function $u(x)$ defined above equation (13)

$\mathbf{K}(\mathbf{U}(x))$	=	Wronskian matrix of vector $\mathbf{U}(x)$ defined belows equation (15)
L	=	differential expression
$\mathbf{L}$	=	differential operator defined by L and homogeneous boundary conditions, $\mathbf{L}^* \equiv$ adjoint operator of $\mathbf{L}$
t	=	time
T	=	temperature of the slab, $T_o \equiv$ constant with dimension of temperature
T_l	=	coolant temperature
$\mathbf{u}, \mathbf{v}$	=	typical vectors, usually $\mathbf{u} \epsilon D$, $\mathbf{v} \epsilon D^*$
$\mathbf{U}$	=	vector defined by equation (16) containing

		linearly independent solutions of equation (11)
$\mathbf{u}_\lambda, \mathbf{v}_\lambda$	=	root vectors satisfying $(\mathbf{L} - \lambda\mathbf{I})^2\,\mathbf{u}_\lambda = \mathbf{0}$ and $(\mathbf{L}^* - \lambda\mathbf{I})^2\,\mathbf{v}_\lambda = \mathbf{0}$
x, x'	=	dimensionless and dimensional distance along slab axis

Greek symbols

α	=	thermal diffusivity of slab material
α_j, β_j	=	coefficients of expansion in equation (26)
λ_j	=	Eigenvalue, j^{th}
ϕ	=	dimensionless coolant temperature
Θ	=	dimensionless temperature defined above equation (40)
τ	=	dimensionless time

$$(\mathbf{L} - \lambda \mathbf{I})^n \mathbf{u} = \mathbf{0} \tag{9}$$

While an eigenvector is also a root vector, the converse is clearly not true. When $\mathbf{L}$ is a differential operator consisting of the differential expression L and its domain $D(L)$, then equation (9) implies that

$$(L - \lambda)^n \mathbf{u} = \mathbf{0} \tag{10}$$

and that $\mathbf{u} \epsilon D(L)$. When root vectors exist for a differential operator, they can be obtained in an interesting manner. Thus, for example, let $u_1(x,\lambda)$ and $u_2(x,\lambda)$ be the linearly independent solutions of the differential equation

$$(L - \lambda)\mathbf{u} = 0, \qquad 0 < x < 1 \tag{11}$$

in which the differential expression L involves differentiation w.r.t.x. We let the boundary conditions defining the domain of L be given by

$$\beta^0 \mathbf{k}(u(0,\lambda)) + \beta^1 \mathbf{k}(u(1,\lambda)) = 0 \tag{12}$$

where β^0 and β^1 are (2×2) matrices of constant coefficients (See Cole [3] for such a representation of boundary conditions); $\mathbf{k}(u(x,\lambda))$ is the Wronskian column vector, with the first component $u(x,\lambda)$ and the second $u'(x,\lambda)$, the prime denoting differentiation with respect to x. If the solution $u(x,\lambda)$ is expressed as

$$u(x,\lambda) = c_1 u_1(x,\lambda) + c_2 u_2(x,\lambda) \tag{13}$$

then the characteristic equation for the eigenvalues is given by

$$|\mathbf{D}(\lambda)| = 0 \tag{14}$$

where $|\mathbf{D}(\lambda)|$ is the determinant of the matrix

$$\mathbf{D}(\lambda) = \beta^0 \mathbf{K}(\mathbf{U})(0,\lambda)) + \beta^1 \mathbf{K}(\mathbf{U}(1,\lambda)) \tag{15}$$

in which $\mathbf{U}(x,\lambda)$ and $\mathbf{K}(\mathbf{U}(x,\lambda))$ are given by

$$\mathbf{U}(x,\lambda) = \begin{bmatrix} u_1(x,\lambda) \\ u_2(x,\lambda) \end{bmatrix},$$

$$\mathbf{K}(\mathbf{U}(x,\lambda)) = \begin{bmatrix} u_1(x,\lambda) & u_2(x,\lambda) \\ u_1'(x,\lambda) & u_2'(x,\lambda) \end{bmatrix}$$

If an eigenvalue $\lambda = \lambda_0$ is repeated once then this implies that

$$\frac{d|\mathbf{D}(\lambda)|}{d\lambda} \bigg|_{\lambda = \lambda_0} = 0 \tag{16}$$

If $D(\lambda_0)$ has rank 1, then only one linearly independent solution can be obtained for the equation

$$\mathbf{D}(\lambda_0)\mathbf{c} = \mathbf{0} \tag{17}$$

where

$$\mathbf{c} = \begin{bmatrix} c_1 \\ c_2 \end{bmatrix}$$

consists of the constants in equation (13). This development of the characteristic equation (14) and calculation of the eigenvector (17) is given in detail by Cole [3] for the general differential operator of even order. In the foregoing situation, only one eigenvector is obtained for eigenvalue λ_0 (with multiplicity 2) through equations (13) and (17). However, a root vector for $\lambda = \lambda_0$ may exist if it happens that

$$\left| \frac{d}{d\lambda}[\mathbf{D}(\lambda)]_{\lambda = \lambda_0} \right| = 0 \tag{18}$$

which is distinct from equation (16) and is not, in general, implied by it. The existence of a root vector, given equation (18) is established as follows. Differentiating equation (11) w.r.t. λ we have

$$(L - \lambda) \frac{\partial u}{\partial \lambda}(x,\lambda) = u(x,\lambda) \tag{19}$$

Again using equation (11) on (19) we obtain

$$(L - \lambda)^2 \frac{\partial u}{\partial \lambda}(x,\lambda) = 0 \tag{20}$$

Thus the candidate for the root vector from equation (10) with $n = 2$ is given by

$$w(x,\lambda) \equiv \gamma_1 \frac{\partial u_1}{\partial \lambda}(x,\lambda) + \gamma_2 \frac{\partial u_2}{\partial \lambda}(x,\lambda) \tag{21}$$

where $u_1(x,\lambda)$ and $u_2(x,\lambda)$ are the solutions of (11). For $w(x, \lambda_0)$ to be a root vector it must satisfy equation (14), which implies that

$$\left| \beta^0 \mathbf{K} \left(\frac{\partial \mathbf{U}}{\partial \lambda}(0,\lambda_0) \right) + \beta^1 \mathbf{K} \left(\frac{\partial \mathbf{U}}{\partial \lambda}(1,\lambda_0) \right) \right| = 0 \tag{22}$$

Since the Wronskian matrix $\mathbf{K}$ is linear in its argument, we infer the validity of equation (18) from (22). The coefficients γ_1 and γ_2 in equation (21) are obtained from the algebraic equations

$$\frac{d}{d\lambda}[\mathbf{D}(\lambda)]_{\lambda = \lambda_0} \gamma = \mathbf{0} \tag{23}$$

where

$$\gamma \equiv \begin{bmatrix} \gamma_1 \\ \gamma_2 \end{bmatrix}.$$

The generalization of the foregoing procedure to determining the root vector for higher order repetitions of an eigenvalue is self-suggestive; furthermore, it is not required for the present paper. Thus considerations are henceforth restricted to the case for which each eigenvalue is repeated at most once. Denoting the eigenvectors of $\mathbf{L}$ by $\mathbf{u}_j$ and the root vectors by $\mathbf{u}_{\lambda_j}$, we have the set $\mathbf{u}_j$, $\mathbf{u}_{\lambda_j}$, which could conceivably be a basis in $L_2[0, 1]$.

Furthermore, the adjoint operator, $\mathbf{L}^*$, has the same eigenvalues $\{\lambda_j\}$ and a corresponding set of eigenvectors and root vectors $\{\mathbf{v}_j, \mathbf{v}_{\lambda_j}\}$. A number of theorems are proved in the appendix of this paper, the results of which are stated here. Firstly, (from Theorem 1) $\mathbf{u}_j$ and $\mathbf{u}_{\lambda_j}$ are linearly independent vectors. Secondly, (from Theorem 2) for $j \neq k$

$$<\mathbf{u}_j, \mathbf{v}_k> = <\mathbf{u}_{\lambda_j}, \mathbf{v}_k< = <\mathbf{u}_j, \mathbf{u}_{\lambda_k}> = <\mathbf{u}_{\lambda_k} \mathbf{v}_{\lambda_k}> = 0 \tag{24}$$

Thirdly, (from Theorem 3) we show that

$$<\mathbf{u}_j, \mathbf{v}_j> = 0 \tag{25}$$

Fourthly, based on the presumption of completeness of the sets of root vectors $\{\mathbf{u}_j, \mathbf{u}_{\lambda_j}\}$ and $\{\mathbf{v}_j, \mathbf{v}_{\lambda_j}\}$ and expansion formula may be derived for an arbitrary vector $f \epsilon L_2[0, 1]$. This derivation is presented below.

We let

$$\mathbf{f} = \sum_{j=1}^{\infty} (\alpha_j \mathbf{u}_j + \beta_j \mathbf{u}_{\lambda_j}) \tag{26}$$

Forming the inner product of equation (26) with $\mathbf{v}_k$

$$<\mathbf{f}, \mathbf{v}_k> = \sum_{j=1}^{\infty} (\alpha_j <\mathbf{u}_j, \mathbf{v}_k> + \beta_j <\mathbf{u}_{\lambda_j}, \mathbf{v}_k>) \tag{27}$$

The use of equations (24) and (25) on equation (27) yields

$$\beta_k = \frac{<\mathbf{f}, \mathbf{v}_k>}{<\mathbf{u}_{\lambda_k}, \mathbf{v}_k>} \tag{28}$$

Further, we take the inner product of equation (26) with $\mathbf{v}_{\lambda_k}$

$$<\mathbf{f}, \mathbf{v}_{\lambda_k}> = \sum_{j=1}^{\infty} (\alpha_j <\mathbf{u}_j, \mathbf{v}_{\lambda_k}> + \beta_j <\mathbf{u}_{\lambda_j}, \mathbf{v}_{\lambda_k}>) \tag{29}$$

We again use the biorthogonality conditions (24) to obtain from equation (29)

$$\alpha_k <\mathbf{u}_k,\mathbf{v}_{\lambda_k}> + \beta_k <\mathbf{u}_{\lambda_k},\mathbf{v}_{\lambda_k}> = <\mathbf{f},\mathbf{v}_{\lambda_k}> \qquad (30)$$

Since β_k is known from (28), α_k is found to be

$$\alpha_k = \frac{<\mathbf{f},\mathbf{v}_{\lambda_k}> - <\mathbf{u}_{\lambda_k},\mathbf{v}_{\lambda_k}> <\mathbf{f},\mathbf{v}_k>/<\mathbf{u}_{\lambda_k},\mathbf{v}_k>}{<\mathbf{u}_k,\mathbf{v}_{\lambda_k}>} \qquad (31)$$

so that the expansion formula (26) is completely established

$$\mathbf{f} = \sum_{j=1}^{\infty}$$

$$\frac{\{<\mathbf{f},\mathbf{v}_{\lambda_j}> - <\mathbf{u}_{\lambda_j},\mathbf{v}_{\lambda_j}> <\mathbf{f},\mathbf{v}_j>/<\mathbf{u}_{\lambda_j},\mathbf{v}_j<\}\mathbf{u}_j + <\mathbf{f},\mathbf{v}_j>\mathbf{u}_{\lambda_j}}{<\mathbf{u}_{\lambda_j},\mathbf{v}_j>}$$
$$(32)$$

Of course, whether or not the root vectors are complete requires proof and is discussed later.

Returning to the problem of specific interest, we solve equations (5)–(7) to obtain $u(x,\lambda) = \sin\sqrt{\lambda}x$. The characteristics equation is given by

$$(1 + \cos\sqrt{\lambda}) = 0 \qquad (33)$$

which has the roots $\sqrt{\lambda} = (2n-1)\pi$, each repeated one because

$$\frac{d}{d\lambda}(1 + \cos\sqrt{\lambda})\bigg|_{\sqrt{\lambda}=(2n-1)\pi} = -\frac{1}{2(2n-1)\pi}\sin(2n-1)\pi = 0 \quad (34)$$

There is only one eigenvector $\mathbf{u}_n = \{\sin(2n-1)\pi x\}$. There exists, however a root vector

$$\mathbf{u}_{\lambda_n} = \left\{\frac{d}{d\lambda}\sin\sqrt{\lambda}x\bigg|_{\sqrt{\lambda}=(2n-1)}\right.$$

$$\left. = \frac{x}{2(2n-1)\pi}\cos(2n-1)\pi x\right\} \qquad (35)$$

which can be readily shown to satisfy the boundary conditions (6) and (7). Thus $\mathbf{u}_{\lambda_n} \epsilon D(L)$.

Similarly for the adjoint problem, we have

$$\mathbf{v}_n = \{\cos(2n-1)\pi(1-x)\} \qquad (36)$$

$$\mathbf{v}_{\lambda_n} = \left\{-\frac{(1-x)}{2(2n-1)\pi}\sin(2n-1)\pi(1-x)\right\} \qquad (37)$$

The vectors $\mathbf{v}_n$ and $\mathbf{v}_{\lambda_n}$ satisfy the adjoint boundary conditions constituting $D^*(L)$. It is now possible to make a direct verification of the orthogonality conditions (24), which is a straightforward procedure. An additional feature of interest, however, is the relationship

$$<\mathbf{u}_{\lambda_n},\mathbf{v}_{\lambda_n}> = \frac{1}{4(2n-1)^2\pi^2}$$

$$\int_0^1 x(1-x)\cos(2n-1)\pi x\sin(2n-1)\pi(1-x)dx = 0 \qquad (38)$$

which appears to be a result specific to the problem. The expansion formula simplifies in this case to

$$\mathbf{f} = \sum_{n=1}^{\infty} \frac{<\mathbf{f},\mathbf{v}_{\lambda_n}>\mathbf{u}_n + <\mathbf{f},\mathbf{v}_n>\mathbf{u}_{\lambda_n}}{<\mathbf{u}_{\lambda_n},\mathbf{v}_n>} \qquad (39)$$

It is this expansion, which leads to the solution of the boundary value problem of interest. The validity of the expansion is contingent on the completeness of the root vectors $\{\mathbf{u}_n,\mathbf{u}_{\lambda_n}\}$. Mathematical research on non-self-adjoint differential operators [2] has established that the boundary conditions (6) and (7) ensure the required completeness. The boundary value problem is non dimensionalized, using the customary dimensionless variables

$$x \equiv \frac{x'}{l}, \tau = \frac{\alpha t}{l^2}, \Theta(x,\tau) \equiv \frac{T}{T_0} ;$$

$$h(\tau) \equiv \frac{h_1(t)l}{k}; f(x) \equiv f_1(x'); g(\tau) \equiv g_1(t)$$

Thus the dimensionless form of (1) is

$$\frac{\partial^2\Theta}{\partial x^2} = -\frac{\partial\Theta}{\partial\tau} \quad 0<x<1, \tau>0 \qquad (40)$$

with the boundary conditions

$$\Theta(0,\tau) = g(\tau) \qquad (41)$$

$$\frac{\partial\Theta}{\partial x}(1,\tau) + \frac{\partial\Theta}{\partial x}(0,\tau) = h(\tau) \qquad (42)$$

The initial condition transforms to

$$\Theta(x,0) = f(x) \qquad (43)$$

The differential equation (40) may be written as

$$L\Theta(\tau) = -\frac{d}{d\tau}\Theta(\tau) \qquad (44)$$

where $\Theta(\tau) = \{\Theta(x,\tau)\}$, and $L \equiv -d^2/dx$. We seek a solution of the form (39), i.e.,

$$\Theta(\tau) = \sum_{n=1}^{\infty} \frac{<\Theta(\tau),\mathbf{v}_{\lambda_n}>\mathbf{u}_n + <\Theta(\tau),\mathbf{v}_n>\mathbf{u}_{\lambda_n}}{<\mathbf{u}_{\lambda_n},\mathbf{v}_n>} \qquad (45)$$

In order to obtain $<\Theta(\tau), \mathbf{v}_n> \kappa\psi\mu <\Theta(\tau),\mathbf{v}_{\lambda_n}>$, we first recognize that for $\mathbf{v}\epsilon D^*(L)$

$$<L\Theta(\tau),\mathbf{v}> - <\Theta(\tau),L\mathbf{v}$$

$$= \left[\Theta(x,\tau)\mathbf{v}'(x) - \frac{\partial\Theta}{\partial x}(x,\tau)v(x)\right]_{x=0}^{x=1}$$

$$= \frac{\partial\Theta}{\partial x}(1,\tau)v(1) - \Theta(0,\tau)v'(0) + \frac{\partial\Theta}{\partial x}(0,\tau)v(0)$$

$$= v(0)h(\tau) - v'(0)g(\tau) \qquad (46)$$

which results from $v'(1) = 0$, $v(0) = -v(1)$ and the boundary conditions (41) and (42). Equation (46) may be used to find the quantities $<\Theta(\tau), \mathbf{v}_n>$ and $\Theta(\tau), \mathbf{v}_{\lambda_n}>$ in the expansion (45). Thus we form the inner product of (44) with $\mathbf{v}_n$ to obtain in the light of (46)

$$<\Theta(\tau),L\mathbf{v}_n> + \mathbf{v}_n(0)h(\tau)$$

$$-\mathbf{v}_n'(0)g(\tau) = -\frac{d}{d\lambda}\Theta(\tau),\mathbf{v}_n> \qquad (47)$$

Since $L\mathbf{v}_n = \lambda_n\mathbf{v}_n$ and $\Theta(0) = \mathbf{f}$ from (43) the solution of (47) is written as

$$<\Theta(\tau),\mathbf{v}_n> = <\mathbf{f},\mathbf{v}_n>e^{-\lambda_n\tau}$$

$$+\int_0^\tau e^{-\lambda_n(\tau-\tau')}[v_n'(0)g(\tau') - v_n(0)h(\tau')]d\tau' \qquad (48)$$

Similarly, the inner product of (44) with $\mathbf{v}_{\lambda_n}$ yields

$$<\Theta(\tau),L\mathbf{v}_{\lambda_n}> + \mathbf{v}_{\lambda_n}(0)h(\tau)$$

$$-\mathbf{v}_{\lambda_n}'(0)g(\tau) = -\frac{d}{d\tau}<\Theta(\tau),\mathbf{v}_{\lambda_n}> \qquad (49)$$

The equation $L\mathbf{v}_n = \lambda_n\mathbf{v}_n$ implies that $L\mathbf{v}_{\lambda_n} + \lambda_n\mathbf{v}_{\lambda_n}$, which when inserted into (49) obtains

$$<\Theta(\tau),\mathbf{v}_n> + \lambda_n<\Theta(\tau),\mathbf{v}_{\lambda_n}>$$

$$+\mathbf{v}_{\lambda_n}(0)h(\tau) - \mathbf{v}'_{\lambda_n}(0)g(\tau)$$

$$= -\frac{d}{d\tau}<\Theta(\tau),\mathbf{v}_{\lambda_n}> \qquad (50)$$

Equation (50) is solved subject to (43) producing

$$<\Theta(\tau),\mathbf{v}_{\lambda_n}> = <\mathbf{f},\mathbf{v}_{\lambda_n}>e^{-\lambda_n\tau}$$

$$+\int_0^\tau [\mathbf{v}_{\lambda'_n}(0)g(\tau') - \mathbf{v}_{\lambda_n}(0)h(\tau')$$

$$-<\Theta(\tau),\mathbf{v}_n>]e^{-\lambda_n(\tau-\tau')}d\tau' \qquad (51)$$
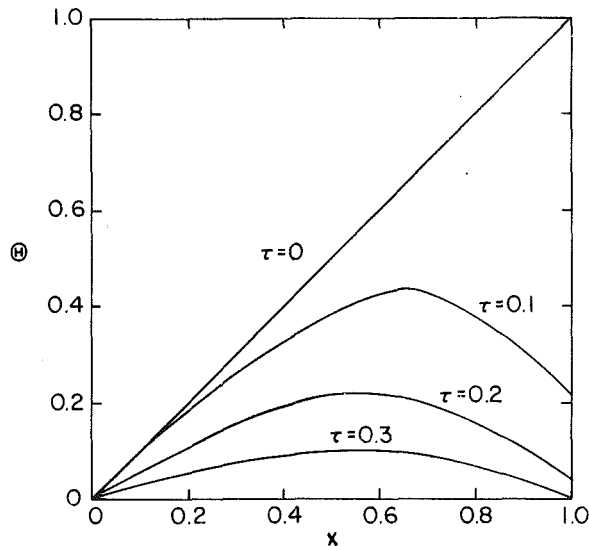
Fig. 1 Evolution of dimensionless temperature profiles

Fig. 2 Dimensionless coolant temperature program

Equation (48) may be substituted into (51), which leads to

$$< \Theta(\tau), \mathbf{v}_{\lambda_n} > = [< \mathbf{f}, \mathbf{v}_{\lambda_n} > - \tau < \mathbf{f}, \mathbf{v}_n >] e^{-\lambda_n \tau}$$

$$+ \int_0^\tau d\tau' [v_{\lambda'_n}(0) g(\tau') - v_{\lambda_n}(0) h(\tau')$$

$$- \int_0^{\tau'} e^{-\lambda_n}(\tau - \tau'') \{ v_n{}'(0) g(\tau'') - v_n(0) h(\tau'') \} d\tau''] \quad (52)$$

Of particular interest is the first term on the right side of (52), which displays the coefficient $\tau e^{-\lambda_n \tau}$ characteristic of repeating eigenvalues. The solution is now essentially complete except for the details of evaluating the known terms in equations (48) and (52). Thus, we have

$$u_n(0) = \cos(2n-1)\pi = -1, v'_n(0) = 0, u_{\lambda_n}(0) = 0$$

$$v_{\lambda'_n}(0) = + \frac{1}{2} \cos(2n-1)\pi = - \frac{1}{2}$$

$$< \mathbf{u}_{\lambda_n}, \mathbf{u}_n > = \int_0^1 \frac{x}{2(2n-1)\pi} \cos(2n-1)\pi$$

$$x \cos(2n-1)\pi(1-x)dx = - \frac{1}{8(2n-1)\pi}$$

from which the solution to the boundary value problem for $\Theta(x,\tau)$ may be written as

$$\Theta(x,\tau) = \sum_{n=1}^\infty - 8\sqrt{\lambda_n} e^{-\lambda_n \tau} \left[\frac{x}{2\sqrt{\lambda_n}} \cos\sqrt{\lambda_n} x \right.$$

$$\times \int_0^1 f(x')\cos\sqrt{\lambda_n}(1-x')dx' + \int_0^\tau e^{\lambda_n \tau'} h(\tau')d\tau'$$

$$- \sin\sqrt{\lambda_n} x \left\{ \int_0^1 f(x')(1-x') \frac{1}{2\sqrt{\lambda_n}} \sin\sqrt{\lambda_n}(1-x')dx' \right.$$

$$+ \tau \int_0^1 f(x')\cos\sqrt{\lambda_n}(1-x')dx'$$

$$\left. \left. - \int_0^\tau \left[\frac{1}{2} g(\tau') + \int_0^{\tau'} e^{\lambda_n \tau''} h(\tau'')d\tau'' \right] d\tau' \right\} \right] \quad (53)$$

where $\lambda_n = (2n-1)^2 \pi^2$. Thus the complete solution to the non-self-adjoint boundary value problem is obtained.

As a demonstration of the solution, we present calculations for the case $g(\tau) = h(\tau) = 0$, which implies that the slab is equally cooled (or h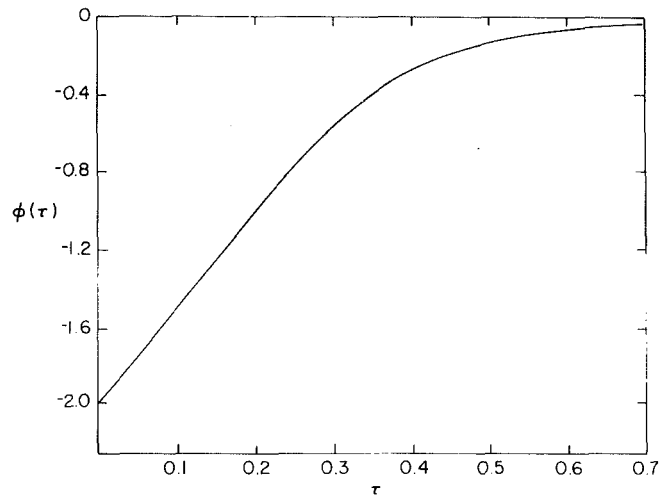eated) from both ends and that the end at $x = 0$ is constrained to be at zero temperature. Furthermore, we assume that the initial temperature distribution $f(x) = x$ (see Fig.1). The solution (53) becomes

$$\Theta(x,\tau) = 8 \sum_{n=1}^\infty e^{-\lambda_n \tau} \left[- \frac{x}{\lambda_n} \cos\sqrt{\lambda_n} x \right.$$

$$\left. + \frac{2}{\sqrt{\lambda_n}} \sin\sqrt{\lambda_n} x \left(\tau + \frac{1}{\lambda_n} \right) \right] \quad (54)$$

If the heat transfer coefficient at $x = 1$ is known, it is possible to calculate a "temperature program" for the coolant at this end as function of time to maintain equal cooling rate at both ends. Thus letting

$$- k \frac{\partial T}{\partial x'}(l,t) = h_l [T(l,t) - T_l(t)] \quad (55)$$

where $t_l(t)$ is the temperature program to be calculated from the solution. By defining dimensionless variables

$$B \equiv \frac{h_l l}{k}, \phi(\tau) \equiv \frac{T_l(t)}{T_0} \quad (56)$$

we obtain from (55)

$$\phi(\tau) = \frac{1}{B} \frac{\partial}{\partial x} \Theta(1,\tau) + \Theta(1,\tau) \quad (57)$$

The solution (54) yields

$$\phi(\tau) = 8 \sum_{n=1}^\infty e^{-\lambda_n \tau} \left[\frac{1}{\lambda_n} \left(1 - \frac{1}{B} \right) - \frac{2\tau}{B} \right] \quad (58)$$

Figure 1 shows the evolution of the temperature profile. Figure 2 shows the required temperature program of the control end of the rod.

It is of interest to observe that the above boundary value problem could also have been solved by the method of Laplace transform, the solution emerging from an inversion of its transform, which requires contour integration. The procedure yields the same solution (53). Indeed, the method pf non-self-adjoint operator representation, which we have presented here, requires some discussion in regard to its merit relative to that of the method of Laplace transform. The two methods are in essence equivalent, except that the spectral theory of operators decomposes the procedure into units, each with a powerfully organized structure. Thus the spectral resolution of the operator $\mathbf{L}$ is a much deeper quest that the chore of determining the singularities of a complex integrand for the evaluation of its complex integral through the method of residues. The climax of the method of eigenvalues and eigenvectors is the expansion formula (32), a virtually instant

passport to construction of the solution to the boundary value problem. However, the equivalence of the two methods is a reflection of the profound generalization that the spectral resolution of operators (or analytic functions of them represents of the well-known Cauchy integral formula for an analytic function. This aspect of spectral theory is brought out in a elementary way by a superb exposition of the subject by Lorch [4].

Conclusions

The unsteady-state, heat-conduction problem of this paper has been solved by using the root vectors of the non-self-adjoint operator that appears in the problem with non-self-adjoint boundary conditions. The boundary conditions satisfy a regularity condition which assures the completeness of the root vectors.

Other variants of the boundary conditions (2) and (3) may also be envisaged. For example instead of boundary condition (7) one may have

$$u'(0) = \alpha u(0) \tag{59}$$

along with the boundary condition (6). This too leads to a complete set of eigenvectors[3] with eigenvalues $\{(2n-1)^2 n^2 \pi^2\}$ which occur as single roots, together with another set obtained from

$$\sqrt{\lambda} \tan \frac{\sqrt{\lambda}}{2} = \alpha$$

Note how the problem whose solution has been obtained is recovered from here letting $\alpha \to \infty$. Since none of the eigenvalues is repeated no root vectors are present and the eigenvectors are entirely adequate. We have pursued the problem for $\alpha = \infty$ because it accommodates the complication of repeated eigenvalues and the consequent necessity for including the root vectors. The problem for finite α is solved by a biorthogonal expansion including only the eigenvectors.

The methodology of this paper may be important for other non-self-adjoint problems, which may arise in heat conduction or mass diffusion.

Acknowledgment

We are thankful to Professor M.F. Malone of the University of Massachusetts who provided us with finite difference calculation of the problem for comparison.

References

1 Gohberg, I. C. and Krein, M. G., *Introduction to Theory of Linear Nonselfadjoint Operators,* American Mathematical Society, Providence, Rhode Island, 1969.

2 Dunford, N. and Schwartz, J. T., *Linear Operators, Part III, Spectral Operators,* Wiley-Interscience, New York, 1971, pp. 2344–2345.

---

[3] This assertion requires the establishment of the regularity condition with which we do not bother in this article.

3 Cole, R. H., *Theory of Ordinary Differential Equations,* Appleton-Century-Crafts, New York, 1968.

4 Lorch, E., "The Spectral Theorem" in *Studies in Mathematics,* Vol. I, Math. Assn. Amer., 1962, pp. 89–137.

APPENDIX

In the following theorems, it is understood that we are dealing with a non-self-adjoint operator, L whose adjoint operator is L^*. Further, L and L^* have the same eigenvalues which repeat, at most, once. (The generalization to higher order repetitions is self-suggestive). The eigenvalues are assumed to be real since the generalization to complex values is unnecessary here. u is an eigenvector of L and $u_\lambda \equiv \partial u / \partial \lambda$ is a root vector of L with $n = 2$. Similarly v is the eigenvector of L and v_λ is a root vector with $n = 2$.

Theorem 1: u and u_λ are linearly independent; so are v and v_λ.

Proof: Let α and β be numbers such that $\alpha u + \beta u_\lambda = 0$.
Then $0 = L(\alpha u + \beta u_\lambda) = \alpha L u + \beta L u_\lambda$.
From equation (19), the above equality yields

$$0 = \alpha \lambda u + \beta u + \beta \lambda u_\lambda.$$

But $0 = \alpha \lambda u + \beta \lambda u_\lambda$ so that $\beta u = 0$.
Thus $\beta = 0$. Hence, $\alpha = 0$ so that u and u_λ are linear independent.

Theorem 2: For $\lambda_j \neq \lambda_k$, each repeating once we have

$$<u_j, v_k> = <u_j, v_{\lambda_k}> = <u_{\lambda_j}, v_k> = <u_{\lambda_j}, v_{\lambda_k}> = 0.$$

Proof: That $<u_j, v_k> = 0$ is well known since u_j and v_k are eigenvectors of L and L^* for distinct eigenvalues. Now since $u_j \epsilon D, v_{\lambda_k} \epsilon D^*$

$$0 = <L u_j, v_{\lambda_j}> - <u_j, L^* v_k>$$
$$= \lambda_j <u_j, v_k> - <u_j, v_{\lambda_k}> \lambda_k <u_j, v_{\lambda_k}>$$

so that $(\lambda_j - \lambda_k) <u_j, v_{\lambda_k}> = $ and 0 and $<u_j, v_{\lambda_k}> = 0$.
Similary, $<u_{\lambda_j}, v_k> 0$.
To prove the last result, we write

$$0 = <L u_{\lambda_j}, u_{\lambda_k}> - <u_{\lambda_j}, L^* v_k>$$

or

$$0 = <u_j, v_{\lambda_k}> + \lambda_j <u_{\lambda_j}, v_{\lambda_k}>$$
$$- <u_{\lambda_j}, v_k> - \lambda_k <u_{\lambda_j}, v_{\lambda_k}>$$

so that $(\lambda_j - \lambda_k) <u_{\lambda_j}, v_{\lambda_k}> = 0$
from which $<u_{\lambda_j}, v_{\lambda_k}> = 0$ Q.E.D.

Theorem 3: $<u_j, v_j> = 0$ when λ_j repeats once and $<u_{\lambda_j}, v_j>$ are root vectors.

Proof: Since $L u_{\lambda_j} = u_j + \lambda_j u_{\lambda_j}$

$$<L u_{\lambda_j}, v_j> = <u_j, v_j> + \lambda_j <u_{\lambda_j}, v_j>$$

so that

$$\lambda_j <u_{\lambda_j}, v_j> = <u_j, v_j> + \lambda_j <u_{\lambda_j}, v_j>$$
$$\text{or} \quad <u_j, v_j> = 0 \quad \text{Q.E.D.}$$

Note that it is also easy to prove that $<u_{\lambda_j}, v_j> = <u_j, v_{\lambda_j}>$.
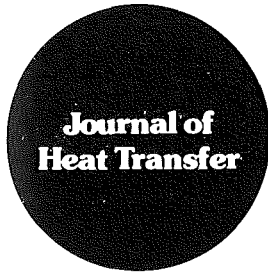
Technical Notes

This section contains shorter technical papers. These shorter papers will be subjected to the same review process as that for full papers.

Thermoeconomically Optimum Counterflow Heat Exchanger Effectiveness

D. K. Edwards[1] and R. Matavosian[2]

Nomenclature

A_c = cross-sectional flow area, m^2
C = cost, dollars/yr
$\dot{C}$ = flow capacity rate $\dot{m}c$, W/K
c = specific heat, J/kg K
D = hydraulic diameter, m
E = thermoeconomic factor, dimensionless
f = friction factor, dimensionless
h = specific enthalpy, J/kg
K = pressure loss coefficient, dimensionless
L = length of exchanger, m
L^* = dimensionless length, Eq. (9)
$\dot{m}$ = mass flow rate, kg/s
N_{tu} = number of transfer units, dimensionless
P = heat-transfer surface per unit length, m
R_c = flow capacity ratio $\dot{C}_{min}/\dot{C}_{max}$, dimensionless
R_o = temperature difference ratio, dimensionless
r = capital recovery factor, yr^{-1}
T = temperature, K
t = operating time per year, s/yr
U = overall heat-transfer coefficient, W/m^2 K
V = value of energy saved, dollars/yr
v = thermal energy cost, dollars/J
v_0 = fixed cost, dollars
v_s = heat-transfer surface cost for unit area, dollars/m^2
v_w = pumping work cost, dollars/J
η_w = pump efficiency, dimensionless
ΔT_f = feed outlet-inlet temperature difference, K
ΔT_i = difference in inlet temperature, K
ϵ = heat exchanger effectiveness, dimensionless
ρ = density, kg/m^3

Subscripts

a = annual
f = feed stream
i = inlet
min = minimum
o = outlet
p = purchased stream
w = pumping work

Introduction

Optimization of heat exchangers is a recurring problem [1–7]. Reference [8] treats a special case where the flow rates and inlet temperatures of both streams are known and introduces a dimensionless thermoeconomic parameter, E, that governs the optimum effectiveness and number of transfer units for a counterflow waste-heat-recovery unit. This note is to extend [8] by recommending a procedure for optimizing a counterflow heat exchanger with one prescribed feed rate with prescribed inlet and outlet temperatures and a purchased stream with prescribed inlet temperature but unknown flow rate.

Previous Work

In reference [8], the optimum waste-heat-recovery unit used as a preheater upstream of the main heater was determined subject to the following idealizations: (a) The annual ownership and operating cost was assumed to be linear in length L

$$C_a = rv_0 + rv_s PL$$

(b) The annual benefit was taken to be linear in the value of the mainheater energy saved

$$V_a = vt\dot{C}_{min}\Delta T_i\epsilon$$

where (c) the flow rates and inlet temperatures of both streams were prescribed in a counterflow heat exchanger with constant overall heat-transfer coefficient. The size of the exchanger was optimized by equating dC_a/dL with dV_a/dL, i.e., the exchanger was made larger as long as the incremental dollars per year saved exceeded the dollars per year of total costs added by a unit of incremental area. The result shown was that the optimum effectiveness occurs where

$$\frac{d\epsilon}{dN_{tu}} = E \equiv \frac{rv_s}{vtU\Delta T_i}$$

The expression for $d\epsilon/dN_{tu}$ (at constant R_c) was presented and permitted finding the optimum effectiveness ϵ and number of transfer units N_{tu}, hence the optimum size for the prescribed flow rates.

Present Analysis

The feed stream has known flow rate $\dot{m}_f$ and prescribed inlet and outlet temperatures $T_{f,i}$ and $T_{f,0}$. The purchased stream with known inlet temperature $T_{p,i}$ and unknown flow rate $\dot{m}_p$ is used to heat (or cool) the feed. For a chosen cross-sectional configuration of the exchanger, the annual cost of ownership and operation is assumed to be directly proportional to $\dot{m}_p$ and the heat-transfer surface PL. There is an optimum area of exchanger, because increasing area increases capital and operating costs but increases effectiveness ϵ and thus reduces the cost of the purchased stream. The annual cost of the purchased stream is

$$C_{pa} = \dot{m}_p t\Delta\hat{h}v = \dot{m}_p c_p \Delta T_i vt \quad (\Delta T_i \equiv T_{p,i} - T_{f,i}) \tag{1}$$

where t is the time of annual operation, $\Delta\hat{h}$ is the heating value defined arbitrarily as the enthalpy difference between inlet temperature $T_{p,i}$ and $T_{f,i}$ and v is the value of a unit of that thermal energy. The annual cost of ownership and operation of the exchanger is assumed to be linear in PL in the form

$$C_a = rv_0 + rv_s PL \tag{2}$$

where rv_0 is the annual fixed cost, and $rv_s PL$ is the annual cost that varies with exchanger area. In a simple application, r is the capital recovery rate, v_0 is the installation cost, and v_s is the cost of the exchanger per unit area of heat transfer surface. More generally, fixed annual maintenance costs and fixed pumping costs would be included in rv_0, and other area or length-dependent costs would be added to rv_s. For example, if the cost of pumping work is v_w and the pump-motor efficiency is η_w, the annual cost of pumping the feed is

$$C_{wfa} = \frac{v_w}{\eta_w} \left(\frac{\dot{m}_f t}{\rho_f}\right) \left[\frac{1}{2}\rho_f(\dot{m}_f/\rho_f A_{c,f})^2\right]\left[f_f \frac{L}{D_f} + \Sigma K\right] \tag{3}$$

The length-dependent and fixed terms are clearly discernible. A similar relation may hold for the purchased stream, if it must be pumped, but $\dot{m}_p$ is unknown. In that case an iterative procedure could be followed.

The optimum length is obtained from minimizing $C_{pa} + C_a$

$$\frac{d}{dL}[\dot{m}_p c_p \Delta T_i vt + rv_s PL] = 0 \tag{4}$$

The flow $\dot{m}_p$ is related to L through the heat exchanger effectiveness ϵ. Two cases exist, (a) $\dot{C}_p = (\dot{m}c)_p \le \dot{C}_f$ and (b) $\dot{C}_f < \dot{C}_p$. For case (a) the heat balance gives

$$\dot{m}_p = \frac{\dot{C}_f \Delta T_f}{c_p \Delta T_i \epsilon} \quad (\Delta T_f \equiv T_{f,0} - T_{f,i}) \tag{5}$$

where ϵ is related to L through the well-known ϵ-N_{tu} relationship [2,8],

$$\epsilon = \frac{1 - e^{-(1-R_c)N_{tu}}}{1 - R_c e^{-(1-R_c)N_{tu}}} \tag{6a}$$

$$N_{tu} = \frac{1}{1-R_c}\ln\frac{1-\epsilon R_c}{1-\epsilon} \tag{6b}$$

The flow capacity ratio R_c is $\dot{C}_p/\dot{C}_f$. From equation (5)

$$R_c = \frac{\Delta T_f}{\Delta T_i \epsilon} = \frac{R_0}{\epsilon} \tag{7}$$

The number of transfer units is

$$N_{tu} = \frac{UPL}{\dot{C}_p} = \frac{UP\Delta T_i L\epsilon}{\dot{C}_f \Delta T_f} = L^* \epsilon \tag{8}$$

where

$$L^* = \frac{UPL}{\dot{C}_f R_0} \tag{9}$$

With equations (5) and (9), equation (4) becomes

$$\frac{d}{dL^*}\left[\frac{1}{\epsilon} + EL^*\right] = 0 \tag{10}$$

where E is the thermoeconomic factor [8]

$$E = \frac{rv_s}{vtU\Delta T_i} \tag{11}$$

Equation (6b) with equations (7) and (8) relates L^* to ϵ

$$L^* = \frac{1}{\epsilon - R_0}\ln\frac{1-R_0}{1-\epsilon} \tag{12}$$

Hence, equation (10) is written

$$\frac{d\epsilon}{dL^*}\frac{d}{d\epsilon}\left[\frac{1}{\epsilon} + EL^*\right] = 0$$

$$\frac{1}{E} = \frac{\epsilon^2}{(\epsilon-R_0)(1-\epsilon)}\left[1 - \frac{(1-\epsilon)}{(\epsilon-R_0)}\ln\frac{1-R_0}{1-\epsilon}\right](\dot{C}_f \ge \dot{C}_p) \tag{13}$$

Equation (13) gives the optimum value of ϵ for a known thermoeconomic factor E and temperature difference ratio $R_0 = \Delta T_f/\Delta T_i$.

For case (2) where $\dot{C}_p > \dot{C}_f$ the effectiveness is known from the overall heat balance

$$\epsilon = R_0 = \Delta T_f/\Delta T_i \tag{14}$$

Then equation (6b) relates N_{tu} to the unknown flow capacity ratio R_c. Equation (4) becomes

$$\frac{dR_c}{dN_{tu}}\frac{d}{dR_c}\left[\frac{1}{R_c} + EN_{tu}\right] = 0$$

$$\frac{1}{E} = \frac{R_c^2}{(1-R_c)^2}\left[\ln\frac{1-R_0 R_c}{1-R_0} - \frac{R_0(1-R_c)}{1-R_0 R_c}\right](\dot{C}_f < \dot{C}_p) \tag{15}$$

Sample Result

After the designer selects a cross-sectional configuration and calculates the overall U coefficient and the pressure drop terms following standard heat transfer practice [1, 2, 8], the values rv_s, E and R_0 are found. Then equation (13) or (15) is used to find the unknown optimum effectiveness or flow capacity ratio. The optimum size of the heat exchanger may then be found from the N_{tu} relation, equation (6b), and the N_{tu} definition equation (8). In general, the designer would then iterate to reestablish overall heat-transfer coefficient and pumping costs. He would also examine different cross-sectional configurations.

For example, suppose a feed stream with $\dot{C}_f = 10^4$ W/K must be heated from 300 K to 500 K against a purchased stream with inlet temperature 800 K and $c_p = 1200$ J/kg K. For a trial configuration $U = 50$ W/m^2 K and $rv_s = 36$ dollars/m^2 yr. The unit operates $t = 7.2\times10^6$ s/yr, and the thermal energy cost is $v = 10^{-9}$ dollars/J. Thus

$$E = \frac{rv_s}{vtU\Delta T_i} = \frac{36}{(10^{-9})(7.2\times10^6)(50)(500)} = 0.20$$

$$R_0 = \frac{\Delta T_f}{\Delta T_i} = \frac{500\text{-}300}{800\text{-}300} = 0.40$$

Since E is small, we surmise that energy cost is high relative to capital cost, and a high-ϵ unit will be optimum. Since R_0 is less than the expected value of ϵ, we expect that equation (13) applies. Equation (13), solved iteratively with the aid of a programmable pocket calculator, gives $\epsilon = 0.836$, and $R_c = R_0/\epsilon = 0.40/0.836$ is found to be less than one, verifying that equation (13) rather than equation (15) does apply. Knowing $\epsilon = 0.836$ and $R_c = 0.478$ allows N_{tu} to be found to be 2.49 from equation (6b). Equation (8) shows that the required optimum heat exchanger area is $PL = 238$ m^2.

Concluding Remarks

Heat exchanger design will always require the specification of a large number of parameters and so involve experienced engineering judgment and iterative procedures. We propose that the analytical results derived here can simplify and speed the designer's task by relating the optimum size of heat exchanger to the governing thermoeconomic factor.

References

1 McAdams, W. H., *Heat Transmission*, McGraw-Hill, New York, 1954, Chapter 15.

2 Kays, W. M., and London, A. L., *Compact Heat Exchangers*, 2d ed., McGraw-Hill, New York, 1964.

3 Evans, R. B., "Thermoeconomic Isolation and Essergy Analysis," *Energy*, Vol. 5, 1980, pp. 805–821.

4 Palen, J. W., Cham, T. P., and Taborek, T., "Optimization of Shell-and-Tube Heat Exchangers by Case Study Method," *Chemical Engineering Progress Symposium Series*, Vol. 70, 1974, pp. 205–214.

5 Fax, D. H., and Mills, R. R., Jr., "Generalized Optimal Heat Exchanger Design," *Trans. ASME*, Vol. 79, 1957, pp. 653–661.

6 Shah, R. K., Afimiwala, K. A., and Mayne, R. W., "Heat Exchanger Optimization," *Proceedings Sixth International Heat Transfer Conference*, Toronto, Canada, Aug. 7-11, 1978, Vol. 4, pp. 185–191.

7 Cichelli, M. T., and Brinn, M. S., "Optimum Design of Shell-and-Tube Heat Exchangers," ASME Paper No. 54-A-125, Winter Annual Meeting of the ASME, Nov. 28-Dec. 3, 1954.

8 Edwards, D. K., Denny, V. E., and Mills, A. F., *Transfer Processes*, Hemisphere/McGraw-Hill, New York, 2d ed., 1979, pp. 292–296.

Solidification of a Conglomerate of Particles

B. Rubinsky[1]

Nomenclature

a = dimension of coal particle, m
A = cross-section area of flow channel, m^2
c = specific heat, J/(kg K)
k = thermal conductivity, W/mk
L = latent heat, J/kg
P = perimeter of flow channel, m
Ste = Stefan number, defined in equation (7)
t = time, s
T = temperature, K
T_0 = initial air temperature, K
v = air bulk flow velocity through the particles conglomerate, m/s
$\bar{v}$ = dimensionless velocity
v_1 = air bulk flow velocity prior to entering the particles conglomerate, m/s
x = space variable, m
α = thermal diffusivity, m^2/s
β = position of the frozen-partially frozen interface, m
$\bar{\beta}$ = dimensionless position of the frozen-partially frozen interface
γ = position of the partially frozen-unfrozen interface, m
$\bar{\gamma}$ = dimensionless position of the partially frozen-unfrozen interface, m
δ = position of the change of phase interface, m
$\bar{\delta}$ = dimensionless position of the change of phase interface
ρ = specific weight, kg/m^3
θ = dimensionless temperature
τ = dimensionless time
ξ = dimensionless space variable

[1] Department of Mechanical Engineering, University of California, Berkeley, Calif. 94720, Assoc. Mem. ASME

Subscripts

c = frozen coal
f = air
ph = phase transition

Introduction

Certain types of coal, when extracted from the mine, can have a water content of up to 50 percent by weight [1]. The water is dispersed uniformly throughout the porous structure of the coal particle. Moist coal, when exposed to low temperatures will freeze and the frozen particles will adhere to each other. One of the major problems encountered during the transportation of coal in winter time is the freezing of the coal load and the consequent difficulties in unloading [1, 2]. It is of importance to be able to predict the extent of the frozen region in the coal load and to identify the factors which influence the solidification process in the coal particles. The purpose of this work is to investigate through a first order model and analytical study the solidification process in a load of coal particles caused by the forced flow of exterior cold air through the load. This air flow occurs because coal loads are transported in open cars at high train velocities.

Heat transfer problems dealing with phase transformation have been studied extensively and recently several monographs have been published on this topic, [3, 4]. A great number of publications analyze the phase transformation processes in a homogeneous medium. Studies on phase transformation processes in a heterogeneous medium, e.g., a solid medium permeated by a fluid, have been performed in connection with the artificial freezing of soil and the thawing of permafrost [5–7]. In the studies mentioned above, the fluid permeating the solid medium undergoes phase transformation and the heterogeneous medium is modeled as homogeneous from a macroscopic point of view. A study on the thawing of frozen coal in which the frozen coal is described as a homogeneous medium can be found in reference [8].

In the problem discussed in this study the fluid permeating the solid medium, air, remains at all times in a gaseous phase.
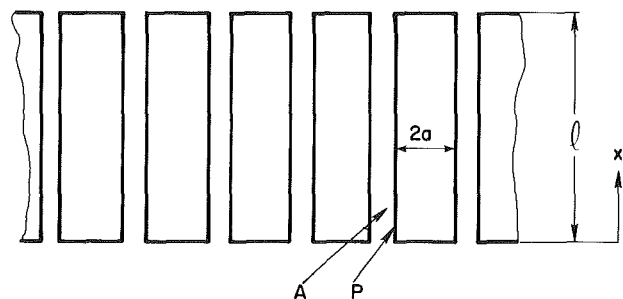

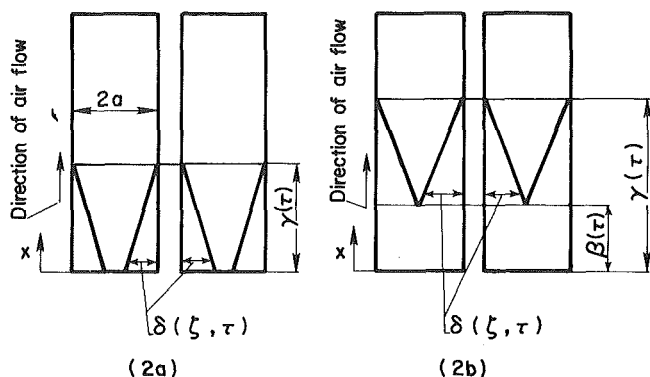Fig. 1 Schematic drawing of the discussed geometry

Fig. 2 Schematic drawing of the solidification process

3 Evans, R. B., "Thermoeconomic Isolation and Essergy Analysis," *Energy*, Vol. 5, 1980, pp. 805–821.

4 Palen, J. W., Cham, T. P., and Taborek, T., "Optimization of Shell-and-Tube Heat Exchangers by Case Study Method," *Chemical Engineering Progress Symposium Series*, Vol. 70, 1974, pp. 205–214.

5 Fax, D. H., and Mills, R. R., Jr., "Generalized Optimal Heat Exchanger Design," *Trans. ASME*, Vol. 79, 1957, pp. 653–661.

6 Shah, R. K., Afimiwala, K. A., and Mayne, R. W., "Heat Exchanger Optimization," *Proceedings Sixth International Heat Transfer Conference*, Toronto, Canada, Aug. 7-11, 1978, Vol. 4, pp. 185–191.

7 Cichelli, M. T., and Brinn, M. S., "Optimum Design of Shell-and-Tube Heat Exchangers," ASME Paper No. 54-A-125, Winter Annual Meeting of the ASME, Nov. 28-Dec. 3, 1954.

8 Edwards, D. K., Denny, V. E., and Mills, A. F., *Transfer Processes*, Hemisphere/McGraw-Hill, New York, 2d ed., 1979, pp. 292–296.

Solidification of a Conglomerate of Particles

B. Rubinsky[1]

Nomenclature

a = dimension of coal particle, m

A = cross-section area of flow channel, m^2

c = specific heat, J/(kg K)

k = thermal conductivity, W/mk

L = latent heat, J/kg

P = perimeter of flow channel, m

Ste = Stefan number, defined in equation (7)

t = time, s

T = temperature, K

T_0 = initial air temperature, K

v = air bulk flow velocity through the particles conglomerate, m/s

$\bar{v}$ = dimensionless velocity

v_1 = air bulk flow velocity prior to entering the particles conglomerate, m/s

x = space variable, m

α = thermal diffusivity, m^2/s

β = position of the frozen-partially frozen interface, m

$\bar{\beta}$ = dimensionless position of the frozen-partially frozen interface

γ = position of the partially frozen-unfrozen interface, m

$\bar{\gamma}$ = dimensionless position of the partially frozen-unfrozen interface, m

δ = position of the change of phase interface, m

$\bar{\delta}$ = dimensionless position of the change of phase interface

ρ = specific weight, kg/m^3

θ = dimensionless temperature

τ = dimensionless time

ξ = dimensionless space variable

[1] Department of Mechanical Engineering, University of California, Berkeley, Calif. 94720, Assoc. Mem. ASME

Subscripts

c = frozen coal

f = air

ph = phase transition

Introduction

Certain types of coal, when extracted from the mine, can have a water content of up to 50 percent by weight [1]. The water is dispersed uniformly throughout the porous structure of the coal particle. Moist coal, when exposed to low temperatures will freeze and the frozen particles will adhere to each other. One of the major problems encountered during the transportation of coal in winter time is the freezing of the coal load and the consequent difficulties in unloading [1, 2]. It is of importance to be able to predict the extent of the frozen region in the coal load and to identify the factors which influence the solidification process in the coal particles. The purpose of this work is to investigate through a first order model and analytical study the solidification process in a load of coal particles caused by the forced flow of exterior cold air through the load. This air flow occurs because coal loads are transported in open cars at high train velocities.

Heat transfer problems dealing with phase transformation have been studied extensively and recently several monographs have been published on this topic, [3, 4]. A great number of publications analyze the phase transformation processes in a homogeneous medium. Studies on phase transformation processes in a heterogeneous medium, e.g., a solid medium permeated by a fluid, have been performed in connection with the artificial freezing of soil and the thawing of permafrost [5–7]. In the studies mentioned above, the fluid permeating the solid medium undergoes phase transformation and the heterogeneous medium is modeled as homogeneous from a macroscopic point of view. A study on the thawing of frozen coal in which the frozen coal is described as a homogeneous medium can be found in reference [8].

In the problem discussed in this study the fluid permeating the solid medium, air, remains at all times in a gaseous phase.
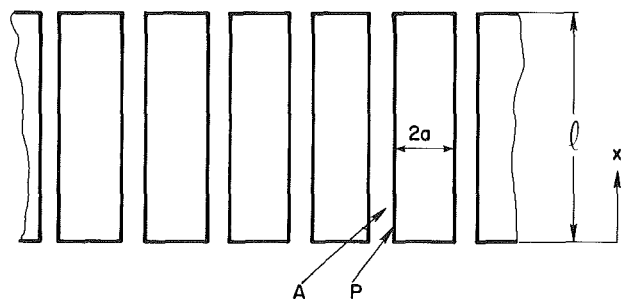

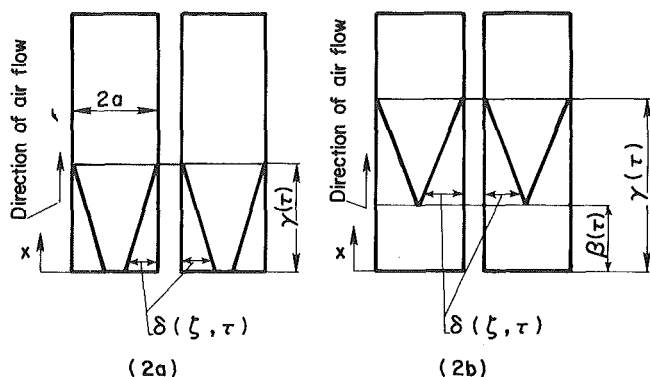Fig. 1 Schematic drawing of the discussed geometry

Fig. 2 Schematic drawing of the solidification process

Consequently, the discussed medium is regarded as heterogeneous and the heat-transfer process in air and coal will be analyzed separately.

Analysis

This study will deal with the solidification process in a conglomerate of solid coal particles with an overall slab like geometry. A number of simplifying assumptions will be made to obtain a first order solution to the problem. The coal particles conglomerate will be modelled by a slab-like succession of coal particles with a width $2a$, separated by channels with a constant perimeter, P, and cross-section area, A, through which air can flow. The values for a, P, and A can be correlated to the void fraction, sphericity and average size of the coal particles. The analysis will be performed from a macroscopic point of view in which the slab-like succession of coal particles will be regarded as a continuous medium. The discussed geometry is shown in a schematic way in Fig. 1. It is assumed that the initial temperature of a coal particle is the change of phase temperature for water. Air at a constant bulk flow velocity with a constant initial temperature below the change of phase temperature is flowing through the discussed medium. Since the water is distributed uniformly throughout the coal particle the solidification process occurs from the outer surface of each coal particle to its interior. As a first

order approximation it will be assumed that in the energy balance the sensible heat storage of coal and air is negligible relative to the latent heat of solidification for water. Because of the existence of a contact resistance between each coal particle and because of the solidification pattern in each coal particle described above, it will be assumed that the coal in the imaginary slab-like succession of coal particles behaves from a macroscopic point of view like an anisotropic material. The thermal conductivity of the coal will be taken to be finite in the direction normal to that of the air flow (x-axis) and zero in the direction of the air flow. Consequently, the dominant heat transfer mechanism in the direction of the bulk air flow is the forced convection of air, whereas the conduction heat transfer process in the coal occurs only in a direction normal to the direction of the bulk air flow. Further, it will be assumed that the air and the coal particle outer surface have the same temperature. (The method of solution presented here can be used with minor changes for problems in which the heat-transfer process between the air and the coal particle is correlated through a known heat-transfer coefficient.)

In accordance with the previous assumptions, that the sensible heat storage in the solid medium is negligible relative to the latent heat and that the coal behaves from a macroscopic point of view as an anisotropic medium, it will be assumed that at the instant the imaginary slab has frozen
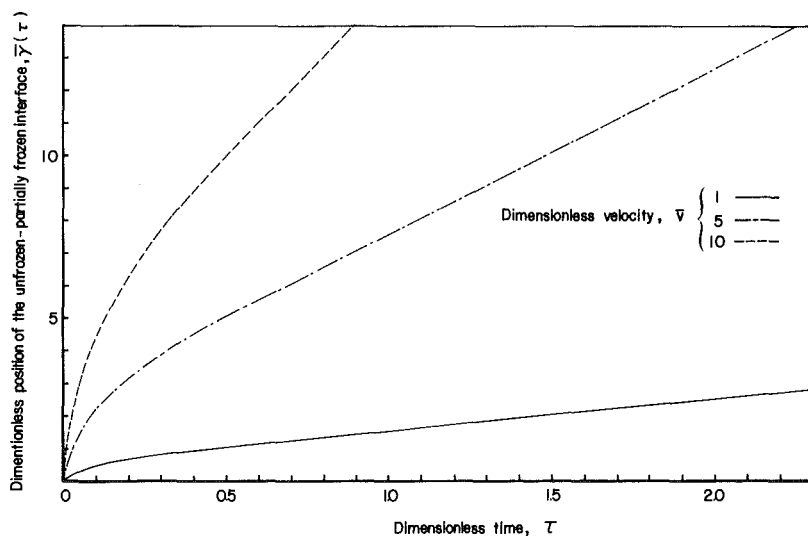
Fig. 3 Position of the frozen-unfrozen region interface as a function of time
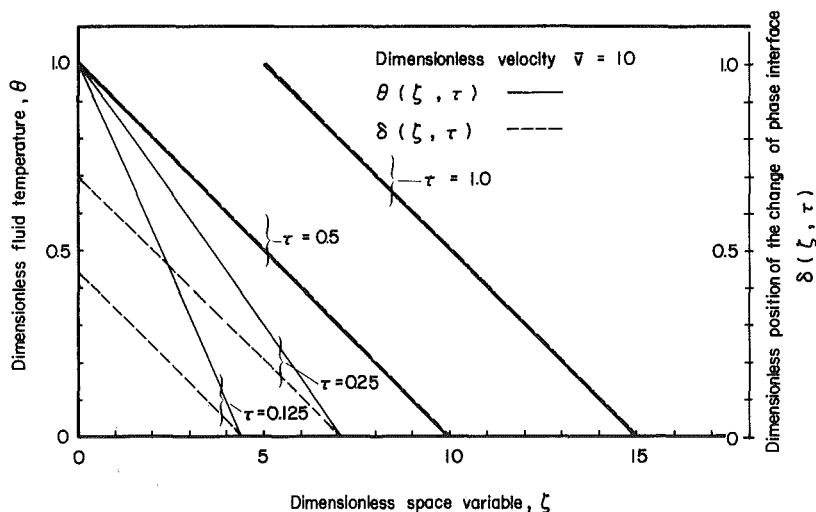
Fig. 4 Fluid temperature distribution and position of the change of phase interface

completely throughout its cross section, the coal temperature at that axial coordinate will change instantaneously and become equal to that of the surrounding air. Consequently, the solidification process will have two distinctive patterns. Initially, as shown in Fig. 2(a), the coal slab will solidify from its outer surface to the interior. Then, at the instant when at $x = 0$, the slab has frozen completely, and the interface between the completely frozen and partially frozen region will start to change its position in time as shown in a schematic way in Fig. 2(b).

A parameter of importance in this analysis is the position of the interface between the partially frozen and the unfrozen regions. This parameter gives an indication of the extent of the region in which the coal particles will adhere to each other and cause difficulties in the unloading process.

The first stage of the solidification process will now be analyzed. For the geometry discussed in this analysis, the bulk air flow velocity through the coal particles can be expressed by,

$$v = \frac{v_1 \left(a + \frac{A}{P} \right)}{\frac{A}{P}} \tag{1}$$

where v_1 is the bulk air flow velocity prior to entering the conglomerate of coal particles. According to the assumptions presented above, the energy balance for the air flow is given by,

$$A \cdot (\rho c)_f \cdot v \cdot \frac{\partial T_f}{\partial x} = k_c \cdot P \frac{(T_{ph} - T_f)}{\delta(x, t)}$$

$$0 \le x \le \gamma(t), \ 0 \le t \le t_1 \tag{2}$$

The energy balance on the change of phase interface is,

$$k_c \frac{(T_{Ph} - T_f)}{\delta(x, t)} = \rho_c \cdot L \cdot \frac{\partial \delta(x, t)}{\partial t} \tag{3}$$

$$0 \le x \le \gamma(t); \ 0 \le t \le t_1 \tag{3}$$

It should be emphasized that the solidification process analyzed above and illustrated in Figs. 2(a) and 2(b) regards the process from a macroscopic point of view in which the position of the change of phase interface and the temperature distribution are taken to be a continuous function of the space variable, x, and the time, t.

The initial conditions of the problem are,

$$T_c(x, 0) = T_{ph}, \ \delta(0,0) = 0 \tag{4}$$

The inlet air temperature is

$$T_f(0, t) = T_0 \tag{5}$$

The following dimensionless parameters and variable will be used in the analysis.

$$\zeta = \frac{x}{a}; \ \bar{v} = \frac{v \cdot A (\rho c)_f}{\alpha_c P (\rho c)_c}; \ \theta = \frac{T_f - T_{ph}}{T_0 - T_{ph}}; \ \bar{\delta} = \frac{\delta}{a}; \ \bar{\gamma} = \frac{\gamma}{a};$$

$$\bar{\beta} = \frac{\beta}{a}; \ \tau = \text{Ste} \cdot \frac{\alpha_c t}{a^2}; \ \text{Ste} = \frac{c_c (T_{ph} - T_0)}{L} \tag{6}$$

Equations (2–6) in a dimensionless form become,

$$\left. \begin{array}{l} -\bar{v} \cdot \dfrac{\partial \theta}{\partial \zeta} = \dfrac{\theta}{\bar{\delta}(\zeta, \tau)} \\[4mm] \dfrac{\theta}{\bar{\delta}(\zeta, \tau)} = \dfrac{\partial \bar{\delta}(\zeta, \tau)}{\partial \tau} \end{array} \right\} \begin{array}{l} 0 \le \zeta \le \bar{\gamma} \\[4mm] 0 < \tau \le \tau_1 \end{array} \tag{7}$$

$$\bar{\delta}(0,0) = 0, \ \theta(0, \tau) = 1$$

The solution of the equations, boundary, and initial conditions shown above can be obtained by combining the differential equations, to give:

$$-\frac{\bar{v}}{2} \frac{\partial^2 (\delta^2)}{\partial \zeta \partial \tau} = \frac{\partial \bar{\delta}}{\partial \tau} \tag{8}$$

and by assuming a superposition solution of the form

$$\delta = A(\tau) + B(\zeta) \tag{9}$$

Equation (9) was introduced into equation (8) and into the second differential equation in (7) and a solution was found which satisfies the boundary conditions in equation (7).

$$\left. \begin{array}{l} \delta = \left(\sqrt{2\tau} - \dfrac{\zeta}{\bar{v}} \right) \\[4mm] \theta = \left(\sqrt{2\tau} - \dfrac{\zeta}{\bar{v}} \right) \cdot \dfrac{1}{\sqrt{2\tau}} \end{array} \right\} \begin{array}{l} 0 \le \zeta \le \bar{\gamma} \\[4mm] 0 < \tau \le \tau_1 \end{array} \tag{10}$$

The extent of the region in which the freezing occurs and in which the solution is valid is given by the location at which $\bar{\delta}$ and θ are 0. From equation (10) this location is found to be

$$\bar{\gamma}(\tau) = \bar{v} \cdot \sqrt{2\tau} \tag{11}$$

The end of the first stage of the solidification process will occur when,

$$\bar{\delta}(0, \tau) = 1; \ \tau_1 = \frac{1}{2} \tag{12}$$

The second stage of the solidification process described by Fig. 2(b) will be presented next.

The following conditions have to be satisfied at the interface between the completely solidified and the partially solidified regions,

$$\bar{\delta}(\bar{\beta}(\tau), \tau) = 1 \quad \theta(\bar{\beta}(\tau), \tau) = 1 \tag{13}$$

The energy balance equations (2) and (3) are valid in the second stage of the solidification process. Assuming a superposition solution of the form given in equation (9) the solution which satisfies the boundary conditions in equation (13) is given by

$$\left. \begin{array}{l} \delta = \left(\tau - \dfrac{\zeta}{\bar{v}} + \dfrac{1}{2} \right) \\[4mm] \theta = \left(\tau - \dfrac{\zeta}{\bar{v}} + \dfrac{1}{2} \right) \end{array} \right\} \begin{array}{l} \bar{\beta}(\tau) \le \zeta \le \bar{\gamma}(\tau) \\[4mm] \dfrac{1}{2} \le \tau \end{array}$$

where

$$\bar{\gamma}(\tau) = \bar{v} \left(\tau + \frac{1}{2} \right) \tag{15}$$

and

$$\bar{\beta}(\tau) = \bar{v} \left(\tau - \frac{1}{2} \right) \tag{16}$$

Discussion

Equations (11) and (15) indicate that the extent of the frozen region for identical geometrical and thermophysical conditions is a direct function of the dimensionless $\bar{v}$. Figure 3 shows the dimensionless position of the unfrozen-partially frozen interface $\bar{\gamma}(\tau)$ as a function of time and illustrates the observation made above. The temperature distribution in the fluid as well as the extent of the frozen region in each coal particle are shown in Fig. 4 for a specific value of dimensionless velocity $\bar{v}$.

From equation (1) for small areas A between coal particles relative to the area of the coal particle the dimensionless velocity $\bar{v}$ becomes,

$$\bar{v} = \frac{v_1 a (\rho c)_f}{\alpha_c \cdot (\rho c)_c} \qquad (17)$$

Equations (6), (11), (15) and (17) indicate that for a constant velocity v_1, the extent of the frozen region is a direct function of the coal particle dimension, a. At long times following the onset of the freezing process the extent of the frozen region becomes, for practical considerations, independent of the particle size.

Conclusions

A first-order analysis has been performed for the solidification process in a conglomerate of moist coal particles where the dominant heat-transfer mechanism is forced convection through the conglomerate.

The analysis indicates that for identical geometrical and thermophysical conditions the extent of the frozen region is a strong function of the air bulk velocity.

For constant air flow rates through the solidifying medium and identical thermophysical properties an increase in the particle size will increase the extent of the frozen region.

The results indicate that it would be beneficial in order to decrease the extent of the frozen region in a coal load to minimize the flow of cold outside air through the load and during winter time to transport smaller sizes of coal particles.

Acknowledgment

References

1 *1971 Keystone Coal Industry Manual*, McGraw-Hill, 1979.

2 DeSteeze, J. D., "Identification and Priorization of Concerns in Coal Transportation, Now Through 2000," in *Critical Issues in Coal Transportation Systems, Proceedings of the Symposium of the Maritime Transportation Board Commission on Sociotechnical Systems*, National Academy of Science, Washington, D.C., 1979.

3 Ockendon, J. R., and Hodgkins, R., eds., *Moving Boundary Problems in Heat Flow and Diffusion*, Oxford University Press, Oxford, 1979.

4 Wilson, D. G., Solomon, A. D., and Boggs, P. T., eds., *Moving Boundary Problems*, Academic Press, 1978.

5 Hashemi, H. T., and Sliepcevich, C. M., "Effect of Seepage Stream on Artificial Soil Freezing," in J. of Solid Mech. and Found. Div., *Proceedings of the ASCE*, 1973, pp. 267–289.

6 Wheeler, J. A., "Simulation of Heat Transfer from a Warm Pipeline Buried in Permafrost," AIChE Symposium Series 135, Vol. 69, 1973, pp. 206–207.

7 Epstein, M., and Cho, D. H., "Melting Heat Transfer in Steady Laminar Flow Over a Flat Plate," ASME, JOURNAL OF HEAT TRANSFER, Vol. 99, No. 3, 1976, pp. 533–535.

8 *Oosthuizen, P. H., "A Numerical Study of the Surface Thawing of Coal Cars," ASME paper 77-WA/HT-33, 1977.*

Thermal Stresses During Solidification Processes

B. Rubinsky[1]

Introduction

When a liquid medium undergoes phase transformation to a solid phase, thermal stresses will develop in the solid medium. The stresses appear because of the transient temperature distribution in the solid medium.

The mathematical treatment of this problem is complicated by the nonlinear boundary conditions imposed on the solid-liquid interface. Several attempts to solve this problem have been reported in the technical literature [1–4]. The method of solution consists in solving first the uncoupled heat-transfer equation and then using the pertinent time dependent temperature distribution to find the thermal stresses in the solid region. The problems discussed in references [1–4] are limited to the solution of the uncoupled heat-transfer equation with several specific boundary conditions which include: constant outer-surface temperature [1], outer-surface temperature varying as a slow function of time [2] and as an exponential function of time.

The purpose of this work is to describe the use of a perturbation method to determine the thermal stresses which appear during the freezing of a slab-like region of water. The perturbation method, which can cope with any time-dependent boundary conditions, has been applied to the solution of the coupled heat-transfer equation. The results of the analysis indicate that the thermal stresses are a function of a specific dimensionless number in the solidification process, the Stefan number, and that the expression obtained by considering the coupling effect is different from that obtained by neglecting the coupling effect by a constant factor, which is independent of the thermal boundary conditions.

Analysis

This work will deal with the freezing of a slab-like medium. The geometry is presented in a schematic way in Fig. 1. It is assumed that the medium is water initially at the phase transition temperature. Although the perturbation method of solution can cope with any time-dependent thermal boundary condition, it will be assumed for illustration purpose, that the temperature on the outer surface changes with a constant cooling rate, H. The medium is assumed homogeneous and it is assumed that the ice behaves as an elastic medium with a constant Young's modulus. This behavior has been observed experimentally for small stresses and short times of application [5, 6]. It will be assumed that the frozen region is constrained against bending but otherwise free of traction on any of its surfaces.

In the solution presented here, the moving solid-liquid interface will be immobilized by a transform, proposed by Landau [7], which reduces the boundary conditions to a linear form and introduces the nonlinearity in the governing equations. The resulting nonlinear governing equations will be solved by a perturbation method similar to that used by Rubinsky and Cravalho [8].

The dimensionless variables employed in this analysis are:

$$\theta = \frac{T_{ph} - T}{T_{ph} - T_{min}} \; ; \; \zeta = \frac{x}{s(t)} \; ; \; \eta = \frac{y}{a} \; ; \; \mu = \frac{z}{a}$$

$$\tau = \text{Ste} \cdot \frac{\alpha \cdot t}{a^2} \; ; \; \bar{u} = \frac{u}{a} \; ; \; s = \frac{s}{a} \; ; \; \bar{\sigma} = \frac{\sigma(1-\nu)}{s \cdot E(T_{ph} - T_{min})} \quad (1)$$

While the dimensionless parameters used in the analysis are:

$$\text{Ste} = \frac{c(T_{ph} - T_{min})}{L} \; ; \; B = \frac{H \cdot a^2}{(T_{ph} - T_{min})\alpha} \; ; \; A = \frac{B}{\text{Ste}} \quad (2)$$

where T_{min} is the temperature on the outer surface at the instance the phase change interface has reached the center of the slab, $x = a$, c = specific heat, k = thermal conductivity, L = latent heat, s = temporal position of change of phase front, t = time, T = temperature, T_{ph} = change of phase temperature, x, y, z = space variables and α = thermal diffusivity.

[1] Assistant Professor, Department of Mechanical Engineering, University of California, Berkeley, Calif. 94720, Assoc. Mem. ASME

From equation (1) for small areas A between coal particles relative to the area of the coal particle the dimensionless velocity $\bar{v}$ becomes,

$$\bar{v} = \frac{v_1 a (\rho c)_f}{\alpha_c \cdot (\rho c)_c} \qquad (17)$$

Equations (6), (11), (15) and (17) indicate that for a constant velocity v_1, the extent of the frozen region is a direct function of the coal particle dimension, a. At long times following the onset of the freezing process the extent of the frozen region becomes, for practical considerations, independent of the particle size.

Conclusions

A first-order analysis has been performed for the solidification process in a conglomerate of moist coal particles where the dominant heat-transfer mechanism is forced convection through the conglomerate.

The analysis indicates that for identical geometrical and thermophysical conditions the extent of the frozen region is a strong function of the air bulk velocity.

For constant air flow rates through the solidifying medium and identical thermophysical properties an increase in the particle size will increase the extent of the frozen region.

The results indicate that it would be beneficial in order to decrease the extent of the frozen region in a coal load to minimize the flow of cold outside air through the load and during winter time to transport smaller sizes of coal particles.

Acknowledgment

References

1 *1971 Keystone Coal Industry Manual*, McGraw-Hill, 1979.

2 DeSteeze, J. D., "Identification and Priorization of Concerns in Coal Transportation, Now Through 2000," in *Critical Issues in Coal Transportation Systems, Proceedings of the Symposium of the Maritime Transportation Board Commission on Sociotechnical Systems*, National Academy of Science, Washington, D.C., 1979.

3 Ockendon, J. R., and Hodgkins, R., eds., *Moving Boundary Problems in Heat Flow and Diffusion*, Oxford University Press, Oxford, 1979.

4 Wilson, D. G., Solomon, A. D., and Boggs, P. T., eds., *Moving Boundary Problems*, Academic Press, 1978.

5 Hashemi, H. T., and Sliepcevich, C. M., "Effect of Seepage Stream on Artificial Soil Freezing," in J. of Solid Mech. and Found. Div., *Proceedings of the ASCE*, 1973, pp. 267–289.

6 Wheeler, J. A., "Simulation of Heat Transfer from a Warm Pipeline Buried in Permafrost," AIChE Symposium Series 135, Vol. 69, 1973, pp. 206–207.

7 Epstein, M., and Cho, D. H., "Melting Heat Transfer in Steady Laminar Flow Over a Flat Plate," ASME, JOURNAL OF HEAT TRANSFER, Vol. 99, No. 3, 1976, pp. 533–535.

8 Oosthuizen, P. H., "A Numerical Study of the Surface Thawing of Coal Cars," ASME paper 77-WA/HT-33, 1977.

Thermal Stresses During Solidification Processes

B. Rubinsky[1]

Introduction

When a liquid medium undergoes phase transformation to

[1] Assistant Professor, Department of Mechanical Engineering, University of California, Berkeley, Calif. 94720, Assoc. Mem. ASME

a solid phase, thermal stresses will develop in the solid medium. The stresses appear because of the transient temperature distribution in the solid medium.

The mathematical treatment of this problem is complicated by the nonlinear boundary conditions imposed on the solid-liquid interface. Several attempts to solve this problem have been reported in the technical literature [1–4]. The method of solution consists in solving first the uncoupled heat-transfer equation and then using the pertinent time dependent temperature distribution to find the thermal stresses in the solid region. The problems discussed in references [1–4] are limited to the solution of the uncoupled heat-transfer equation with several specific boundary conditions which include: constant outer-surface temperature [1], outer-surface temperature varying as a slow function of time [2] and as an exponential function of time.

The purpose of this work is to describe the use of a perturbation method to determine the thermal stresses which appear during the freezing of a slab-like region of water. The perturbation method, which can cope with any time-dependent boundary conditions, has been applied to the solution of the coupled heat-transfer equation. The results of the analysis indicate that the thermal stresses are a function of a specific dimensionless number in the solidification process, the Stefan number, and that the expression obtained by considering the coupling effect is different from that obtained by neglecting the coupling effect by a constant factor, which is independent of the thermal boundary conditions.

Analysis

This work will deal with the freezing of a slab-like medium. The geometry is presented in a schematic way in Fig. 1. It is assumed that the medium is water initially at the phase transition temperature. Although the perturbation method of solution can cope with any time-dependent thermal boundary condition, it will be assumed for illustration purpose, that the temperature on the outer surface changes with a constant cooling rate, H. The medium is assumed homogeneous and it is assumed that the ice behaves as an elastic medium with a constant Young's modulus. This behavior has been observed experimentally for small stresses and short times of application [5, 6]. It will be assumed that the frozen region is constrained against bending but otherwise free of traction on any of its surfaces.

In the solution presented here, the moving solid-liquid interface will be immobilized by a transform, proposed by Landau [7], which reduces the boundary conditions to a linear form and introduces the nonlinearity in the governing equations. The resulting nonlinear governing equations will be solved by a perturbation method similar to that used by Rubinsky and Cravalho [8].

The dimensionless variables employed in this analysis are:

$$\theta = \frac{T_{ph} - T}{T_{ph} - T_{min}} \; ; \; \zeta = \frac{x}{\delta(t)} \; ; \; \eta = \frac{y}{a} \; ; \; \mu = \frac{z}{a}$$

$$\tau = \text{Ste} \cdot \frac{\alpha \cdot t}{a^2} \; ; \; \bar{u} = \frac{u}{a} \; ; \; s = \frac{\delta}{a} \; ; \; \bar{\sigma} = \frac{\sigma(1-\nu)}{\delta \cdot E (T_{ph} - T_{min})} \quad (1)$$

While the dimensionless parameters used in the analysis are:

$$\text{Ste} = \frac{c(T_{ph} - T_{min})}{L} \; ; \; B = \frac{H \cdot a^2}{(T_{ph} - T_{min})\alpha} \; ; \; A = \frac{B}{\text{Ste}} \quad (2)$$

where T_{min} is the temperature on the outer surface at the instance the phase change interface has reached the center of the slab, $x = a$, c = specific heat, k = thermal conductivity, L = latent heat, δ = temporal position of change of phase front, t = time, T = temperature, T_{ph} = change of phase temperature, x,y,z = space variables and α = thermal diffusivity.
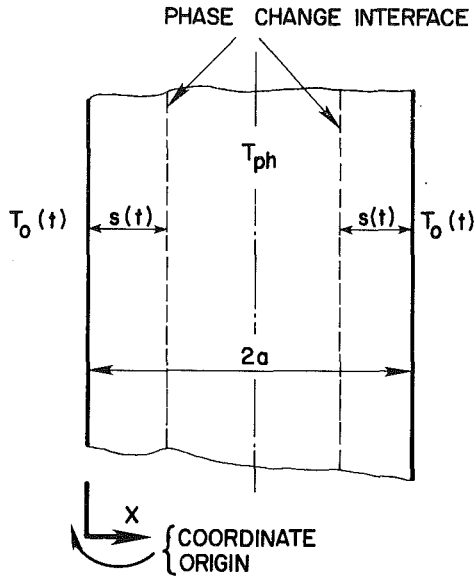
PHASE CHANGE INTERFACE

Fig. 1 Schematic drawing of the model

The mathematical formulation for the coupled energy equation in the frozen region [9–11] is given in terms of the dimensionless variables and parameters presented above,

$$\frac{\partial^2 \theta}{\partial \zeta^2} = \text{Ste} \cdot \left(s^2 \cdot \frac{\partial \theta}{\partial \tau} - \zeta \cdot s \cdot \frac{\partial \theta}{\partial \tau} \cdot \frac{ds}{d\tau} \right.$$

$$- \frac{\delta T_0 \cdot E \cdot s}{(1 - 2\nu) \cdot \rho \cdot c \cdot (T_{ph} - T_{min})} \cdot \left(s \cdot \frac{\partial^2 \bar{u}_x}{\partial \tau \partial \zeta} \right.$$

$$+ s^2 \cdot \left(\frac{\partial^2 \bar{u}_y}{\partial \tau \partial \eta} + \frac{\partial^2 \bar{u}_z}{\partial \tau \partial \mu} \right)$$

$$- \left[\frac{ds}{d\tau} \frac{\partial}{\partial \zeta} \left(\zeta \frac{\partial \bar{u}_x}{\partial \zeta} \right) + \frac{\partial}{\partial \eta} \left(\zeta \frac{\partial \bar{u}_y}{\partial \zeta} \right) \right.$$

$$+ \left. \left. \frac{\partial}{\partial \mu} \left(\zeta \frac{\partial \bar{u}_z}{\partial \zeta} \right) \right] \right) \right) 0 \le \zeta \le 1; \tau > 0 \qquad (3)$$

where T_0 is the environment temperature, u_x, u_y, u_z are the displacements in the x,y,z direction, respectively, δ = thermal expansion coefficient, ρ = specific weight, ν = Poisson modulus, E = Young's modulus. The initial and boundary conditions are

$$\theta(\zeta,0) = 0, \ \theta(0,\tau) = A \cdot \tau, \ \theta(1,\tau) = 0 \qquad (4)$$

The energy balance on the freezing front is

$$\frac{\partial \theta}{\partial \zeta}(1,\tau) = -s \cdot \frac{ds}{d\tau}, \ s(0) = 0 \qquad (5)$$

According to the text by Boley and Weiner [9], the thermal stresses, σ, and displacements, u, in a slab constrained against bending but otherwise free of traction are given by

$$\sigma_{xx} = \sigma_{xz} = \sigma_{yx} = \sigma_{zy} = 0 \qquad (6)$$

$$\sigma_{zz} = \sigma_{yy} = \frac{\delta E}{((1 - \nu)} \cdot \left((T_{ph} - T) - \frac{1}{\delta(t)} \int_0^{\delta(t)} (T_{ph} - T) dx \right.$$

$$\frac{3(2x - \delta(t))}{(\delta(t))^3} \int_0^{\delta(t)} (T_{ph} - T)(2x - \delta(t)) dx \right) \qquad (7)$$

and

$$\frac{\partial u_y}{\partial y} = \frac{\partial u_z}{\partial z} = -\delta \left(\frac{1}{\delta(t)} \int_0^{\delta(t)} (T_{ph} - T) \cdot dx \right.$$

$$+ \frac{3(2x - \delta(t))}{(\delta(t))^3} \int_0^{\delta(t)} (T_{ph} - T)(2x - \delta(t)) dx \right)$$

$$\frac{\partial u_x}{\partial x} = \left(\frac{1 + \nu}{1 - \nu} \right) \delta(T - T_{ph}) + \frac{2\nu\delta}{(1 - \nu)} \cdot \left(\frac{1}{\delta(t)} \int_0^{\delta(t)} (T_{ph} - T) dx \right.$$

$$+ \frac{3(2x - \delta(t))}{\delta(t)^3} \int_0^{\delta(t)} (T_{ph} - T)(2x - \delta(t)) dx \right) \qquad (8)$$

Although equation (3) is highly nonlinear, it should be noted that the nonlinear terms are multiplied by the Stefan number, Ste. The value for the Stefan number for water is smaller than 1 and decreases for higher minimal temperatures, T_{min}. Thus the Stefan number can be used as a perturbation parameter. Equation (3) suggests the following form for the variables in this problem. The solution is sought to an acuracy on the order $0(\text{Ste}^2)$.

$$\theta = \theta_0 + \text{Ste} \ \theta_1 + \ldots 0(\text{Ste}^2)$$

$$s = s_0 + \text{Ste} \ s_1 + \ldots 0(\text{Ste}^2)$$

$$\bar{u} = \bar{u}_0 + \text{Ste} \ \bar{u}_1 + \ldots 0(\text{Ste}^2)$$

$$\bar{\sigma} = \bar{\sigma}_0 + \text{Ste} \ \bar{\sigma}_1 + \ldots 0(\text{Ste}^2) \qquad (9)$$

Equation (9) was introduced into equations (3–8) and a set of regular differential equations and integrals was obtained by equating powers of the Stefan number. A set of equations for Ste^0 is given below to illustrate the method.

$$\frac{\partial^2 \theta_0}{\partial \zeta^2} = 0, \theta_0(0,\tau) = A\tau, \ \theta_0(1,\tau) = 0 \qquad (10)$$

$$\frac{\partial \theta_0}{\partial \zeta}(1,\tau) = -s_0 \cdot \frac{ds_0}{d\tau}, \ s_0(0) = 0 \qquad (11)$$

The solution was found by obtaining first an expression for the temperature distribution in the solid medium and then by solving the integral in equations (7) and (8) for the specific temperature distribution. It should be noted from equation (10) that the perturbation method has the effect of decoupling the heat transfer equation. The first order solution to the problem discussed in this work is given below in a dimensionless form:

$$\theta = A\tau(1 - \zeta) - \text{Ste} \cdot A^2 \cdot \tau^2 \cdot \left(1 + \frac{3\delta^2 T_0 E}{(1 - \nu)\rho c} \right) \zeta(1 - \zeta)$$

$$+ \ldots 0(\text{Ste}^2) \qquad (12)$$

$$\bar{\sigma} = \text{Ste} \cdot A^2 \cdot \tau^2 \cdot \left((1 + \frac{3\delta^2 T_0 E}{(1 - \nu)\rho c}) \left(\frac{1}{6} - \zeta(1 - \zeta) \right) \right.$$

$$+ \ldots 0(Ste^2) \qquad (13)$$

$$s = A^{1/2}\tau - \text{Ste} \frac{A^{3/2}}{3} \left(1 + \frac{3\delta^2 T_0 E}{(1 - \nu)\rho c} \right) \cdot \tau^2 + \ldots 0(\text{Ste}^2) \qquad (14)$$

$$\bar{\epsilon}_{zz} = \bar{\epsilon}_{yy} = A\tau(\zeta - 1) + \text{Ste} \ A^2\tau^2$$

$$\times \left(1 + \frac{3\delta^2 T_0 E}{(1 - \nu)\rho c} \right) + \ldots 0(\text{Ste}^2) \qquad (15)$$

$$\bar{\epsilon}_{xx} = A(\zeta - 1) + \text{Ste} A^2\tau^2$$

$$\times \left(1 + \frac{3\delta^2 T_0 E}{(1 - \nu)\rho c} \right) \left(\frac{3(1 + \nu) \zeta(1 - \zeta) - \nu}{3(1 - \nu)} \right) + \ldots 0(\text{Ste}^2) \qquad (16)$$

where ϵ is the strain.

The specific Stefan number in this analysis is defined using T_{min} the outer surface temperature at the instance the change of phase interface has reached the center of the slab.

The value for T_{min} in a specific freezing process can be obtained from the solution of equation (17) obtained from equation (14) for the instance the change of phase front has reached the center of the slab and the product $A \cdot \tau$ is equal to one.

Table 1 Thermophysical properties for ice

L, kJ/kg	α, cm²/min	ρc_p, J/m³K	E, Pa	ν	δ, K⁻¹	T_0, K
330	0.8	$1.8 \cdot 10^6$	10^{10}	0.33	0.55×10^{-4}	273

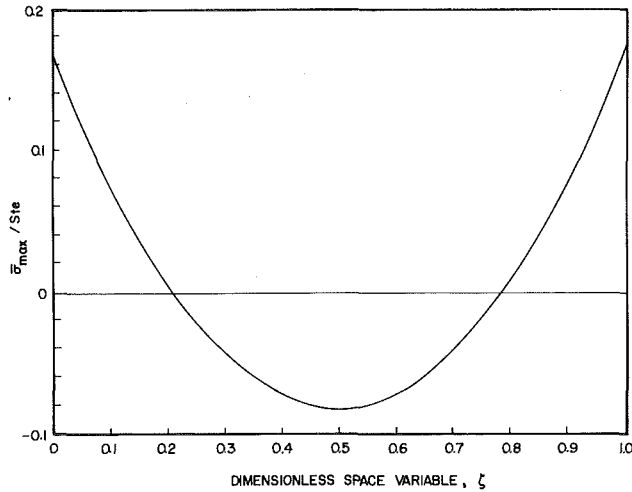Fig. 2 Dimensionless thermal stress distribution in the frozen medium

Fig. 3 Dimensionless thermal stress distribution in the frozen medium

$$1 = A^{1/2}\left(1 - \text{Ste}\left(1 + \frac{3\delta^2 T_0 E}{(1-\nu)\rho c}\right)\right) \qquad (17)$$

Discussion

The analytical results in equations (14) to (18) indicate that the coupling effect which contributes the second term in the expression

$$1 + \frac{3\delta^2 T_0 E}{(1-\nu)\rho c} \qquad (18)$$

does not change the general behavior of the solution. The only consequence of including the coupling effect in the analysis is to change the terms with an order of magnitude 0(Ste) by a certain constant factor. This factor is a function of the mechanical properties of the medium and is independent on the boundary conditions imposed on the outer surface. The analysis presented here does not exclude the possibility of imposing an infinitely fast cooling rate, H, on the outer surface of the frozen medium. This observation indicates that independent of the boundary conditions no thermal shock can be expected during a solidification process provided the term in equation (18) is on the order of magnitude of 1, 0(1) or smaller, and the specific Stefan number for the problem is smaller than one. If either of these conditions is not satisfied the perturbation method will fail.

A numerical analysis of the solution was performed for an ice slab whose mechanical and thermal properties are given in Table 1.

The following value is obtained for the second term in equation (18),

$$\frac{3\delta^2 T_0 E}{(1-\nu)\rho c_p} = 0.02$$

The numerical value given above indicates that the coupling effect can be neglected when analyzing the solidification process in water.

Since the maximal value for the product $A \cdot \tau$ is one, according to equation (18), the maximal value for the dimensionless stresses during a certain freezing process will be

$$\bar{\sigma}_{max} = \text{Ste} \cdot \left(1 + \frac{3\delta^2 T_0 E}{(1-\nu)\rho c}\right)\left(\frac{1}{6} - \zeta(1-\zeta)\right) + \ldots \; 0(\text{Ste}^2) \qquad (19)$$
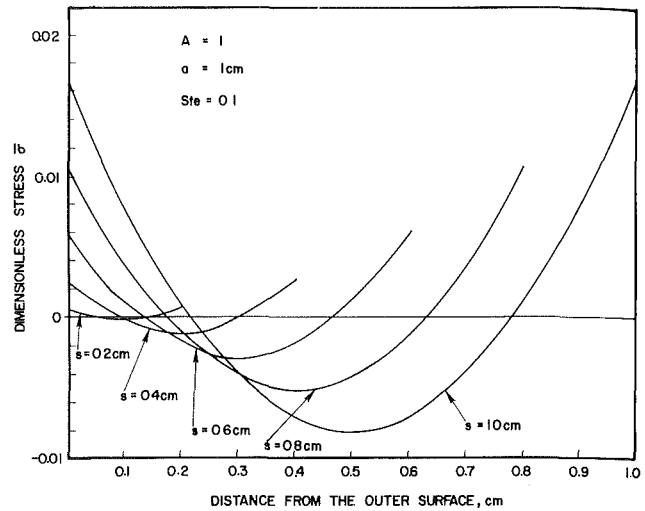
Equations (13) and (19) indicate that the magnitude of the thermal stresses during a solidification process is a function of the specific Stefan number for the discussed problem, and that the maximal stresses will appear on the outer surface of the solidifying medium.

In Fig. 2 the ratio $\bar{\sigma}_{max}/\text{Ste}$ is plotted as a function of the dimensionless space variable, ζ. The numerical results obtained from equation (19) indicates that at the instant the phase change interface will reach the center of the slab the stresses at the center and on the outer surface of the slab will be tensile, while the stresses midway between the center and the outer surface will be compressive. The special stress distribution obtained here is obviously a consequence of the mechanical boundary conditions used in this problem, which require a zero value for the force and momentum at the edges of the slab.

In Fig. 3, the dimensionless stresses in the frozen medium are shown as a function of the space variable, ζ, for different positions of the change of phase front. As the water at a certain location freezes, the ice in the vicinity of the change of phase interface will be exposed to tensile stresses. The stresses at that location will become compressive as the change of phase interface advances toward the center of the slab and can change to tensile again if the discussed location is in the vicinity of the outer surface of the slab.

Conclusions

A perturbation method has been presented to determine the thermal stresses in the solid region of a slab-like geometry of water frozen by imposing a constant cooling rate on the outer surface. The perturbation method described in this work can cope with any time-dependent thermal boundary conditions and the specific boundary conditions mentioned above have been chosen only for illustration purposes.

The solution to the coupled heat transfer equation indicates that the thermal stresses in the frozen region are a direct function of the specific Stefan number of the problem.

The analytical expression for the thermal stresses obtained by considering the coupling effect is different from that obtained by neglecting the coupling effect by a constant factor. This factor is a function of the mechanical properties of the medium and is independent of any time-dependent boundary conditions.

References

1 Weiner, J. H., and Boley, B. A., "Elasto-Plastic Thermal Stresses in a Soldifying Body," *Journal of Mechanical and Phys. Solids*, Vol. 11, 1963, pp. 145-154.

2 Richmond, O., and Tien, R. H., "Theory of Thermal Stresses and Air-Gaps Formation During the Early Stages of Solidification in a Rectangular Mold," *Journal of Mechanical and Phys. Solids*, Vol. 19, pp. 1971, 273-284.

3 Tien, R. H., and Koump, V., "Thermal Stresses During Solidification on Basis of Elastic Model," ASME *Journal of Applied Mechanics*, Dec. 1969, pp. 763-767.

4 Lewis, R. W., and Bass, B. R., "The Determination of Stresses and Temperatures in Cooling Bodies by Finite Elements," ASME JOURNAL OF HEAT TRANSFER, Aug. 1976, pp. 478-484.

5 Sinha, N. K., "Rheology of Columnar Grained Ice, Experimental Mechanics," Vol. 15, 1978, pp. 646-670.

6 Hobbs, P. V., *Ice Physics*, Clarendon Press, Oxford, England, 1974.

7 Landau, H. G., "Heat Conduction in a Melting Solid," *Quarterly of Applied Mathematics*, Vol. 8, 1950, pp. 81-95.

8 Rubinsky, B., and Cravalho, E. G., "The Determination of the Thermal History of a One-Dimensional Freezing System by a Perturbatioon Method," ASME JOURNAL OF HEAT TRANSFER, May 1979, pp. 326-330.

9 Boley, B. A., and Weiner, J. H., *Theory of Thermal Stresses*, John Wiley & Sons, Inc., New York, 1960.

10 Nowacki, W., *Thermoelasticity*, Pergamon Press, Inc., 1962.

11 Takeuti, Y., "Foundation for Coupled Thermoelasticity," *Journal of Thermal Stresses*, Vol. 2, 1979, pp. 232-325.

Downward Penetration of a Hot Liquid Pool Into the Horizontal Surface of a Solid[1]

R. Farhadieh[2] and M. Epstein[3]

Introduction

In the melting of a horizontal solid surface by an overlying hot, liquid pool, the melt, upon formation, is bounded in a thin layer between the solid and the liquid pool. The removal of the melt layer is dependent on the relative densities of the two superposed fluid layers (the liquid pool and the melt layer). For a melt layer lighter than the overlying liquid pool a gravitationally unstable system is encountered. This situation is of interest in the study of postulated meltdown accidents in nuclear reactors where molten core debris could form above structural steel, concrete or ceramic (sacrificial) material [1]. The molten phases of these materials are lighter than the overlying core-debris pool. A rigorous description of the downward penetration of molten core debris into such materials must include the effects of freeze-layer formation [2] and/or combined melting and dissolution [3]. For the purposes of this note, however, we consider instead the simplest case of melting heat transfer and motion within a melt film that is *immiscible* with the pool material, which provides an effective starting point for a study of the general behavior of molten reactor materials.

Several investigations have been made of the melting of a solid by an overlying hot, liquid pool immiscible with the molten phase of the solid. A qualitative experimental study of the melting of frozen benzene and frozen o-xylene under warm water was made by Alsmeyer and Reimann [4]. Tafreshi et al. [5] obtained detailed data on the melting of a slab of frozen olive oil placed beneath a pool of water. Their careful study of the structure of the melt film indicated that the melting process is best described as a Taylor instability. A
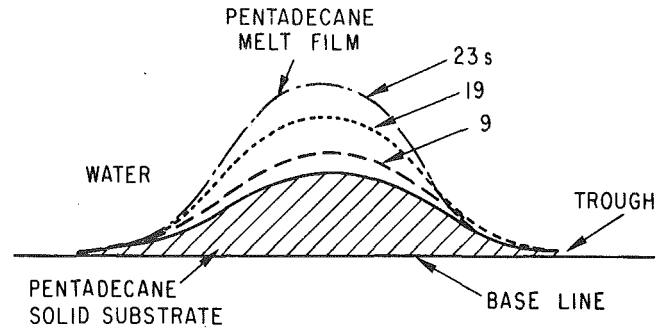
Fig. 1 Typical shape and quasi-steady growth of the melt layer

model was developed by these workers which showed that the melting rate or transport of heat across the melt film depends on the 1/4 power of a modified melt-layer Rayleigh Number (see below).

To establish the form of the dependence between melting rate and melt-layer Rayleigh number, it is important to make measurements of melting rates similar to those of Tafreshi et al., but under a wide variety of physical conditions. In the present experimental study, many pool-solid substrate material pairs were utilized, covering a wide range of density difference between the materials, melt-layer viscosity, and latent heat of melting. The melting rate data are compared with the theory of Tafreshi et al., [5], the film boiling model of Berenson [6], which shows melting rate-Rayleigh number functional dependence similar to that of [5], and with a theory by Gerstmann and Griffith [7], originally developed for film condensation on the underside of a horizontal surface.

Theoretical Considerations

From experimental observations made in [4, 5] and in the present study, the melt layer is best described as consisting of an array of cosine-shaped melt drops. One of these upside-down pendant drops, observed during the melting of frozen pentadecane by an overlying pool of water, is illustrated in Fig. 1. The flow within the melt layer initiates from the trough region between drops, where the thickness of the melt layer is minimal. The flow is directed radially inward toward the center of the drop. The continuous influx of the melt material into the drop increases its "amplitude," which eventually results in the release of the drop through a necking and pinching-off process. The film thickness in the trough region appears to remain constant throughout the period of droplet growth. The drops are stationary, due mainly to the fact that the melting process erodes the surface between drops at a faster rate than the surfaces beneath drops. This results in the formation of hills and valleys on the substrate surface (as shown in Fig. 1). New drops grow above the same hills vacated by released drops.

Tafreshi et al. [5] formulated a model of the melt film by assuming the melt layer to be covered with spherical segments of melt material separated by areas of uniform melt layer. The drop spacing was taken to be proportional to the Taylor wavelength, while the drop sizes were estimated with an averaging technique. The temperature difference across the melt layer, ΔT, was assumed constant and was determined from experimental observations. Their work resulted in the following heat transfer expression:

$$\mathrm{Nu} = 0.2\,\mathrm{Ra}^{1/4} \qquad (1)$$

where Ra is the modified melt-layer Rayleigh number:

$$\mathrm{Ra} \equiv \frac{(h_{sf} + 0.5c_p\Delta T)g(\rho_H - \rho)}{\nu k \Delta T} \cdot \left[\frac{\sigma}{g(\rho_H - \rho)}\right]^{3/2} \qquad (2)$$

and Nu, the Nusselt number, is defined to be

$$\mathrm{Nu} \equiv \frac{h}{k}\left[\frac{\sigma}{g(\rho_H - \rho)}\right]^{1/2} \qquad (3)$$

References

1 Weiner, J. H., and Boley, B. A., "Elasto-Plastic Thermal Stresses in a Soldifying Body," *Journal of Mechanical and Phys. Solids*, Vol. 11, 1963, pp. 145-154.

2 Richmond, O., and Tien, R. H., "Theory of Thermal Stresses and Air-Gaps Formation During the Early Stages of Solidification in a Rectangular Mold," *Journal of Mechanical and Phys. Solids*, Vol. 19, pp. 1971, 273-284.

3 Tien, R. H., and Koump, V., "Thermal Stresses During Solidification on Basis of Elastic Model," ASME *Journal of Applied Mechanics*, Dec. 1969, pp. 763-767.

4 Lewis, R. W., and Bass, B. R., "The Determination of Stresses and Temperatures in Cooling Bodies by Finite Elements," ASME JOURNAL OF HEAT TRANSFER, Aug. 1976, pp. 478-484.

5 Sinha, N. K., "Rheology of Columnar Grained Ice, Experimental Mechanics," Vol. 15, 1978, pp. 646-670.

6 Hobbs, P. V., *Ice Physics*, Clarendon Press, Oxford, England, 1974.

7 Landau, H. G., "Heat Conduction in a Melting Solid," *Quarterly of Applied Mathematics*, Vol. 8, 1950, pp. 81-95.

8 Rubinsky, B., and Cravalho, E. G., "The Determination of the Thermal History of a One-Dimensional Freezing System by a Perturbatioon Method," ASME JOURNAL OF HEAT TRANSFER, May 1979, pp. 326-330.

9 Boley, B. A., and Weiner, J. H., *Theory of Thermal Stresses*, John Wiley & Sons, Inc., New York, 1960.

10 Nowacki, W., *Thermoelasticity*, Pergamon Press, Inc., 1962.

11 Takeuti, Y ., "Foundation for Coupled Thermoelasticity," *Journal of Thermal Stresses*, Vol. 2, 1979, pp. 232-325.

Downward Penetration of a Hot Liquid Pool Into the Horizontal Surface of a Solid[1]

R. Farhadieh[2] and M. Epstein[3]

Introduction

In the melting of a horizontal solid surface by an overlying hot, liquid pool, the melt, upon formation, is bounded in a thin layer between the solid and the liquid pool. The removal of the melt layer is dependent on the relative densities of the two superposed fluid layers (the liquid pool and the melt layer). For a melt layer lighter than the overlying liquid pool a gravitationally unstable system is encountered. This situation is of interest in the study of postulated meltdown accidents in nuclear reactors where molten core debris could form above structural steel, concrete or ceramic (sacrificial) material [1]. The molten phases of these materials are lighter than the overlying core-debris pool. A rigorous description of the downward penetration of molten core debris into such materials must include the effects of freeze-layer formation [2] and/or combined melting and dissolution [3]. For the purposes of this note, however, we consider instead the simplest case of melting heat transfer and motion within a melt film that is *immiscible* with the pool material, which provides an effective starting point for a study of the general behavior of molten reactor materials.

Several investigations have been made of the melting of a solid by an overlying hot, liquid pool immiscible with the molten phase of the solid. A qualitative experimental study of the melting of frozen benzene and frozen o-xylene under warm water was made by Alsmeyer and Reimann [4]. Tafreshi et al. [5] obtained detailed data on the melting of a slab of frozen olive oil placed beneath a pool of water. Their careful study of the structure of the melt film indicated that the melting process is best described as a Taylor instability. A
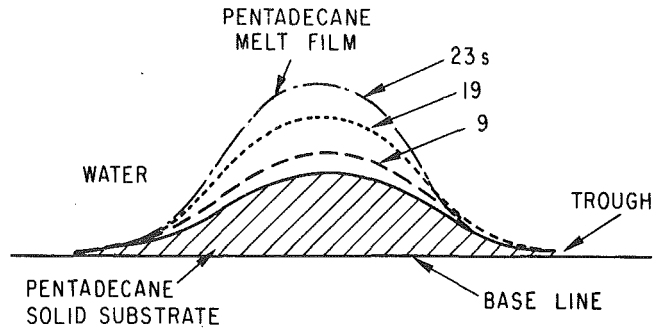
Fig. 1 Typical shape and quasi-steady growth of the melt layer

model was developed by these workers which showed that the melting rate or transport of heat across the melt film depends on the 1/4 power of a modified melt-layer Rayleigh Number (see below).

To establish the form of the dependence between melting rate and melt-layer Rayleigh number, it is important to make measurements of melting rates similar to those of Tafreshi et al., but under a wide variety of physical conditions. In the present experimental study, many pool-solid substrate material pairs were utilized, covering a wide range of density difference between the materials, melt-layer viscosity, and latent heat of melting. The melting rate data are compared with the theory of Tafreshi et al., [5], the film boiling model of Berenson [6], which shows melting rate-Rayleigh number functional dependence similar to that of [5], and with a theory by Gerstmann and Griffith [7], originally developed for film condensation on the underside of a horizontal surface.

Theoretical Considerations

From experimental observations made in [4, 5] and in the present study, the melt layer is best described as consisting of an array of cosine-shaped melt drops. One of these upside-down pendant drops, observed during the melting of frozen pentadecane by an overlying pool of water, is illustrated in Fig. 1. The flow within the melt layer initiates from the trough region between drops, where the thickness of the melt layer is minimal. The flow is directed radially inward toward the center of the drop. The continuous influx of the melt material into the drop increases its "amplitude," which eventually results in the release of the drop through a necking and pinching-off process. The film thickness in the trough region appears to remain constant throughout the period of droplet growth. The drops are stationary, due mainly to the fact that the melting process erodes the surface between drops at a faster rate than the surfaces beneath drops. This results in the formation of hills and valleys on the substrate surface (as shown in Fig. 1). New drops grow above the same hills vacated by released drops.

Tafreshi et al. [5] formulated a model of the melt film by assuming the melt layer to be covered with spherical segments of melt material separated by areas of uniform melt layer. The drop spacing was taken to be proportional to the Taylor wavelength, while the drop sizes were estimated with an averaging technique. The temperature difference across the melt layer, ΔT, was assumed constant and was determined from experimental observations. Their work resulted in the following heat transfer expression:

$$\text{Nu} = 0.2 \, \text{Ra}^{1/4} \tag{1}$$

where Ra is the modified melt-layer Rayleigh number:

$$\text{Ra} \equiv \frac{(h_{sf} + 0.5 c_p \Delta T) g (\rho_H - \rho)}{\nu k \Delta T} \cdot \left[\frac{\sigma}{g (\rho_H - \rho)} \right]^{3/2} \tag{2}$$

and Nu, the Nusselt number, is defined to be

$$\text{Nu} \equiv \frac{h}{k} \left[\frac{\sigma}{g (\rho_H - \rho)} \right]^{1/2} \tag{3}$$

In the above definitions, σ is the interfacial tension at the pool liquid/melt-layer interface; ρ, ν, k, and c_p are, respectively, the density, kinematic viscosity, thermal conductivity and heat capacity of the melt-layer material; h_{sf} is the latent heat of melting of the solid substrate material, h is the heat transfer coefficient which when multiplied by ΔT gives the heat transfer rate through the melt layer; and ρ_H is the density of the heavier, warm liquid pool. Note that the square-root of the bracketed term in the above definitions of Ra and Nu is the usual characteristic length for horizontal surfaces with phase change and is proportional to the Taylor wave length. It is interesting to compare equation (1) with that of Berenson [6] for film boiling above a horizontal surface with, of course, the vapor film properties replaced by those of the melt layer:

$$Nu = 0.43 \, Ra^{1/4} \tag{4}$$

The major difference is an increase in the Nusselt number by about a factor of two above that predicted by equation (1).

In a study of laminar film condensation on the underside of a horizontal surface by Gerstmann and Griffith [7], the condensation process was treated as a nonlinear interfacial instability with a rate so low that the flow everywhere beneath the (condensate) drop is quasi-steady. Theoretical analysis of this problem resulted in a fourth-order ordinary differential equation describing the entire shape of the condensate drop (peak and trough regions, see Fig. 1) and thus the Nusselt number for heat transfer. Except for the boundary condition on velocity at the pool liquid/melt-layer interface, Gerstmann and Griffith's analysis would appear to be equally valid for melting of a horizontal surface by a heavier pool of warm liquid. It can be readily shown that Gerstmann and Griffith's analysis, when applied to a melting system, results in the following expression for the Nusselt number:

$$Nu = 0.63 \, Ra^{1/5} \tag{5}$$

According to equation (5), the transport of heat depends on the 1/5 power of the Rayleigh number. Although the temperature drop across the melt layer, ΔT, drives the melting process it is interesting to note from the theory [5] or [7] the small effect which the numerical value of this quantity has on the melting rate; it is felt numerically only in the one-fourth [5] or one-fifth power [7].

Experimental Apparatus and Procedure

The experimental portion of this study was conducted with pairs of immiscible materials in which the upper liquid was heavier than the molten phase of the substrate solid. Materials selected for the solid phase were pentadecane, p-xylene, paraffin wax, frozen olive oil, and polyethylene glycol 6000 (poly 6000). The overlying liquid phases chosen were water, solutions of potassium iodide of different densities, and zinc bromide. With our choice of frozen substrate-liquid pool combinations, melting heat transfer observations were obtained for modified melt-layer Rayleigh numbers ranging from approximately 10^4 to 10^7.

The test section was an evacuated, clear-glass, double-wall cylindrical Dewar. The inside diameter and the height of the vessel were 152 and 250 mm, respectively. A 100-mm deep cast of the dyed substrate solid at a constant temperature of less than 10°C below its melting point was made inside the vessel, and the system was kept at this temperature for about 24 hr. Before the experiment was started, about 1400 cm³ of the upper fluid was prepared and its density was accurately determined. The liquid was preheated to 60°C above the melting point of the solid and poured on the top of the solid. The top of the vessel was covered by a 67-mm thick Styrofoam plate through which two iron-constantan thermocouples were passed. These thermocouples were used to measure the temperature of the solid, and the temperature of

the interface between the melt layer and the upper fluid. The uncertainty in the melt-film/pool interface temperature measurements was ±0.2°C. Temperature measurements, for the determination of the temperature drop across the melt layer, were made as soon as a melt drop was pinched off. A typical run generally lasted about 15 min, during which time the bulk temperature of the fluid dropped less than 5°C.

The downward heat flux was calculated from observations of the downward melting rate which was extracted from motion pictures taken of the process. That is, the linear rate of buildup in time of the thickness of melt material film at the free surface of the pool was monitored. Enough "initial time" was allowed to pass to ensure that the melting process was quasi-steady as manifested, for example, by the maintenance of a constant melt-film/pool interface temperature. This simple technique yielded mean melting rate measurements that were in close agreement with those reported in [5] for the olive oil-water system. The average heat transfer rate were taken to be the product of the latent heat of fusion and the melting rate measurements. Correction was made for the heat that must be supplied to raise the solid substrate temperature to its melting temperature. The uncertainty in the melting rate measurements is provided in Fig. 2 for one data point. This is typical of the uncertainty for all the measured melting rate values (or calculated heat transfer rates). Each point in Fig. 2 represents an average of several runs for fixed experimental conditions.
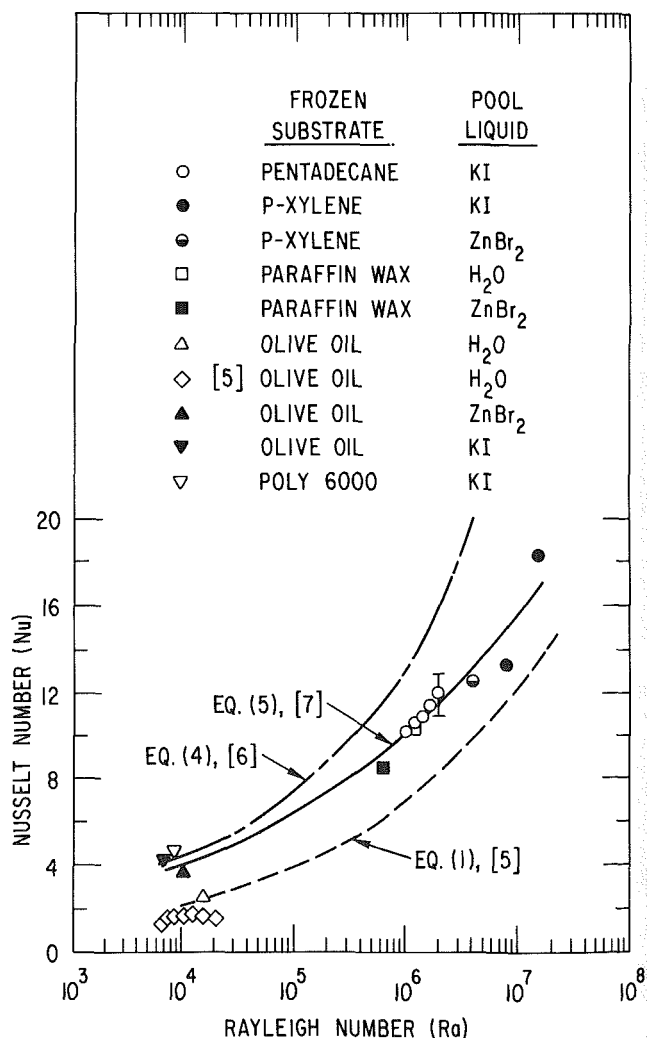

Fig. 2 Comparison of melting heat-transfer data with equations (1), (4) and (5)

The average rate of change of enthalpy of the stratified pool was of little interest in our study and, accordingly, it was not measured. The melting-rate measurement technique mentioned above does not require knowledge of the enthalpy of the pool. It is important to note here that as long as the melt-film/pool interface temperature is known and constant, it is not necessary to understand the motion of heat and mass in the overlying pool to understand or model the motion of heat and mass in the melt film, as these two liquid regions become uncoupled. The measured interface temperature, combined with the usual thermal boundary conditions at the melting surface, is sufficient to completely specify the distribution of temperature within the melt film. Moreover, it can readily be shown by using either of the models of [5] or [7] that the melting rate is quite insensitive to the choice of fluid mechanical condition at the melt-film/pool interface.

Discussion and Concluding Remarks

In Fig. 2 the heat transfer or melting-rate measurements are compared with equations (1), (4) and (5). The melt Rayleigh number was calculated using the measured temperature drop across the melt film, ΔT. The measurements indicated that $\Delta T = 5°C$ for all material pairs, except when frozen olive oil served as the solid substrate, in which case a value of $\Delta T \simeq 20°C$ was recorded. Almost all of the data are seen to lie between the two $Nu - Ra^{1/4}$ relations [5, 6]. While scatter in the available experimental data precludes a definitive judgement concerning the dependence of Nusselt number on Rayleigh number, the $Ra^{1/5}$ behavior predicted by Gerstmann and Griffith's theory [7] seems to best represent the data in term of absolute agreement with the measurements and thus appear to be valid for both laminar film condensation and melting in an unstable, horizontal orientation.

The heat-transfer data of the present study and that of reference [5] for frozen olive oil and water fall about 50 percent below the theoretical [7] and experimental results obtained with other material pairs. The main cause of this behavior appears to stem from the small $\Delta\rho = \rho_H - \rho$ (0.084 g cm^{-3}) for the frozen olive oil-water system. The fact that the observed heat-transfer data for the frozen olive oil/KI system ($\Delta\rho = 0.78$ g cm^{-3}) fall on the $Nu = Ra^{1/5}$ relation seems to support this conclusion.

To complete the theoretical model of melting of a horizontal surface by an overlying hot liquid pool, it is especially desirable to couple the motion in the melt-film with that in the overlying pool. In particular, the development of a method or correlation for making melting heat transfer predictions in terms of the difference between the average pool temperature and the melting temperature of the solid substrate would constitute a useful next step.

References

1 Gluekler, E. L., and Baker, L., Jr., "Post-Accident Heat Removal in LMFBRs," in *Symposium on the Thermal and Hydraulic Aspects of Nuclear Reactor Safety*, Vol. 2, *Liquid Metal Fast Breeder Reactors*, ASME New York, 1977, pp. 285-324.

2 Epstein, M., "Stability of a Submerged Frozen Crust," ASME JOURNAL OF HEAT TRANSFER, Vol. 99, 1977, pp. 527-532.

3 Farhadieh, R., and Baker, L., Jr., "Heat Transfer Phenomenology of a Hydrodynamically Unstable Melting System," ASME JOURNAL OF HEAT TRANSFER, Vol. 100, 1978, pp. 305-310.

4 Alsmeyer, H., and Reimann, M., "On the Heat and Mass Transport Processes of a Horizontal Melting or Decomposing Layer Under a Molten Pool," paper presented at the Nuclear Safety Heat Transfer Symposium, ASME Winter Annual Meeting, 1977; see also Alsmeyer, H., et al., *European Applied Research Reports*, Vol. 1, 1979, pp. 1516-1524.

5 Taghavi-Tafreshi, K., Dhir, V. K., and Catton, I., "Thermal and Hydrodynamic Phenomenon Associated with Melting of a Horizontal Substrate Placed Beneath a Heavier Immiscible Liquid," ASME JOURNAL OF HEAT TRANSFER, Vol. 101, 1979, pp. 318-325.

6 Berensen, P. J., "Film-Boiling Heat Transfer from a Horizontal Surface," ASME JOURNAL OF HEAT TRANSFER, Vol. 83, 1961, pp. 351-361.

7 Gerstmann, J., and Griffith, P., "Laminar Film Condensation on the Underside of Horizontal and Inclined Surfaces," *International Journal of Heat and Mass Transfer*, Vol. 10, 1967, pp. 567-580.

A Simpler Formulation for Radiative View Factors From Spheres to a Class of Axisymmetric Bodies

B. T. F. Chung[1] and M. H. N. Naraghi[2]

A simpler formulation is developed for radiative view factor from a sphere to a class of axisymmetric bodies. The new formulation is semianalytical in nature and only requires a single numerical integration at most.

Introduction

The mathematical expression for the view factor between two finite surfaces is a quadruple integral in terms of geometrical coordinates. Solutions to this integral are available in closed form for only a few cases. With the aid of a digital computer, the configuration factors of more complex three dimensional geometries have become available [1-7]. Most of these studies could not avoid multiple integration and the numerical integration procedures involved were extremely tedious. Furthermore, they are expensive due to large amounts of computer time needed for the small grid size required for suitable accuracy.

In the present note, a new and much simpler formulation is developed for the radiation shape factors between a sphere and a class of coaxial axisymmetric bodies such as a sphere, spherical cap, right circular cone, ellipsoid, and paraboloid. This technique not only reduces computer time but also improves the accuracy of the results substantially.

Formulation

The following procedure is employed to formulate the view factor between a sphere and an arbitrary coaxial axisymmetric body.

(a) The exact solution for the shape factor between a sphere and a differential element which is located in the axisymmetric surface is derived.

(b) An analytical expression for the view factor, $dF_{S-\delta r}$, is obtained from the sphere to a differential conical ring which is generated by rotating the above differential element around the axis passing through the center of the sphere.

(c) The above result is integrated over the surface of the axisymmetric body to give the view factor from a sphere to a coaxial axisymmetric body.

Using the contour integral method [8], the view factor from a differential element to a finite sphere is derived as [9] (see Fig. 1 for notation)

$$F_{dA_2-S} = \cos\theta/(1+S)^2 \qquad (1a)$$

when

$$\tan^{-1}(-A) \le \theta \le \tan^{-1}(A) \text{ and } -\pi/2 \le \theta \le \pi/2$$

and

$$F_{dA_2-S} = -\frac{A\sin\theta}{\pi(S+1)^2}(1-A^2\cot^2\theta)^{1/2} + \frac{1}{\pi}\tan^{-1}$$

____
[1] Professor, Department of Mechanical Engineering, The University of Akron, Akron, Ohio 44325, Mem. ASME

[2] Graduate Research Assistant, Department of Mechanical Engineering, The University of Akron, Akron, Ohio 44325, Student Mem. ASME

The average rate of change of enthalpy of the stratified pool was of little interest in our study and, accordingly, it was not measured. The melting-rate measurement technique mentioned above does not require knowledge of the enthalpy of the pool. It is important to note here that as long as the melt-film/pool interface temperature is known and constant, it is not necessary to understand the motion of heat and mass in the overlying pool to understand or model the motion of heat and mass in the melt film, as these two liquid regions become uncoupled. The measured interface temperature, combined with the usual thermal boundary conditions at the melting surface, is sufficient to completely specify the distribution of temperature within the melt film. Moreover, it can readily be shown by using either of the models of [5] or [7] that the melting rate is quite insensitive to the choice of fluid mechanical condition at the melt-film/pool interface.

Discussion and Concluding Remarks

In Fig. 2 the heat transfer or melting-rate measurements are compared with equations (1), (4) and (5). The melt Rayleigh number was calculated using the measured temperature drop across the melt film, ΔT. The measurements indicated that $\Delta T = 5°C$ for all material pairs, except when frozen olive oil served as the solid substrate, in which case a value of $\Delta T \simeq 20°C$ was recorded. Almost all of the data are seen to lie between the two $\mathrm{Nu} - \mathrm{Ra}^{1/4}$ relations [5, 6]. While scatter in the available experimental data precludes a definitive judgement concerning the dependence of Nusselt number on Rayleigh number, the $\mathrm{Ra}^{1/5}$ behavior predicted by Gerstmann and Griffith's theory [7] seems to best represent the data in term of absolute agreement with the measurements and thus appear to be valid for both laminar film condensation and melting in an unstable, horizontal orientation.

The heat-transfer data of the present study and that of reference [5] for frozen olive oil and water fall about 50 percent below the theoretical [7] and experimental results obtained with other material pairs. The main cause of this behavior appears to stem from the small $\Delta\rho = \rho_H - \rho$ (0.084 g cm^{-3}) for the frozen olive oil-water system. The fact that the observed heat-transfer data for the frozen olive oil/KI system ($\Delta\rho = 0.78$ g cm^{-3}) fall on the $\mathrm{Nu} = \mathrm{Ra}^{1/5}$ relation seems to support this conclusion.

To complete the theoretical model of melting of a horizontal surface by an overlying hot liquid pool, it is especially desirable to couple the motion in the melt-film with that in the overlying pool. In particular, the development of a method or correlation for making melting heat transfer predictions in terms of the difference between the average pool temperature and the melting temperature of the solid substrate would constitute a useful next step.

References

1 Gluekler, E. L., and Baker, L., Jr., "Post-Accident Heat Removal in LMFBRs," in *Symposium on the Thermal and Hydraulic Aspects of Nuclear Reactor Safety*, Vol. 2, *Liquid Metal Fast Breeder Reactors*, ASME New York, 1977, pp. 285–324.

2 Epstein, M., "Stability of a Submerged Frozen Crust," ASME JOURNAL OF HEAT TRANSFER, Vol. 99, 1977, pp. 527–532.

3 Farhadieh, R., and Baker, L., Jr., "Heat Transfer Phenomenology of a Hydrodynamically Unstable Melting System," ASME JOURNAL OF HEAT TRANSFER, Vol. 100, 1978, pp. 305–310.

4 Alsmeyer, H., and Reimann, M., "On the Heat and Mass Transport Processes of a Horizontal Melting or Decomposing Layer Under a Molten Pool," paper presented at the Nuclear Safety Heat Transfer Symposium, ASME Winter Annual Meeting, 1977; see also Alsmeyer, H., et al., *European Applied Research Reports*, Vol. 1, 1979, pp. 1516–1524.

5 Taghavi-Tafreshi, K., Dhir, V. K., and Catton, I., "Thermal and Hydrodynamic Phenomenon Associated with Melting of a Horizontal Substrate Placed Beneath a Heavier Immiscible Liquid," ASME JOURNAL OF HEAT TRANSFER, Vol. 101, 1979, pp. 318–325.

6 Berensen, P. J., "Film-Boiling Heat Transfer from a Horizontal Surface," ASME JOURNAL OF HEAT TRANSFER, Vol. 83, 1961, pp. 351–361.

7 Gerstmann, J., and Griffith, P., "Laminar Film Condensation on the Underside of Horizontal and Inclined Surfaces," *International Journal of Heat and Mass Transfer*, Vol. 10, 1967, pp. 567–580.

A Simpler Formulation for Radiative View Factors From Spheres to a Class of Axisymmetric Bodies

B. T. F. Chung[1] and M. H. N. Naraghi[2]

A simpler formulation is developed for radiative view factor from a sphere to a class of axisymmetric bodies. The new formulation is semianalytical in nature and only requires a single numerical integration at most.

Introduction

The mathematical expression for the view factor between two finite surfaces is a quadruple integral in terms of geometrical coordinates. Solutions to this integral are available in closed form for only a few cases. With the aid of a digital computer, the configuration factors of more complex three dimensional geometries have become available [1–7]. Most of these studies could not avoid multiple integration and the numerical integration procedures involved were extremely tedious. Furthermore, they are expensive due to large amounts of computer time needed for the small grid size required for suitable accuracy.

In the present note, a new and much simpler formulation is developed for the radiation shape factors between a sphere and a class of coaxial axisymmetric bodies such as a sphere, spherical cap, right circular cone, ellipsoid, and paraboloid. This technique not only reduces computer time but also improves the accuracy of the results substantially.

Formulation

The following procedure is employed to formulate the view factor between a sphere and an arbitrary coaxial axisymmetric body.

(a) The exact solution for the shape factor between a sphere and a differential element which is located in the axisymmetric surface is derived.

(b) An analytical expression for the view factor, $dF_{S-\delta r}$, is obtained from the sphere to a differential conical ring which is generated by rotating the above differential element around the axis passing through the center of the sphere.

(c) The above result is integrated over the surface of the axisymmetric body to give the view factor from a sphere to a coaxial axisymmetric body.

Using the contour integral method [8], the view factor from a differential element to a finite sphere is derived as [9] (see Fig. 1 for notation)

$$F_{dA_2-S} = \cos\theta/(1+S)^2 \qquad (1a)$$

when

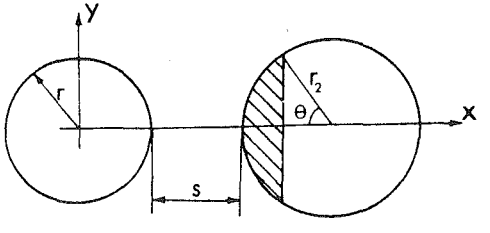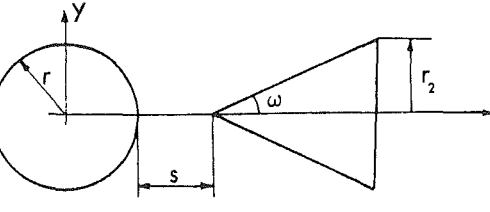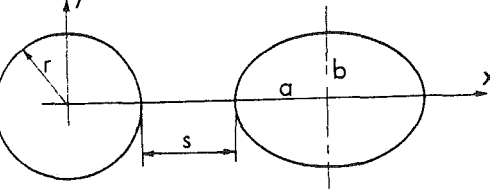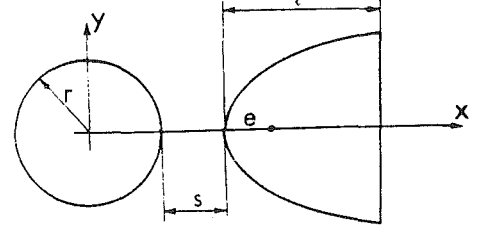$$\tan^{-1}(-A) \le \theta \le \tan^{-1}(A) \text{ and } -\pi/2 \le \theta \le \pi/2$$

and

$$F_{dA_2-S} = -\frac{A\sin\theta}{\pi(S+1)^2}(1 - A^2\cot^2\theta)^{1/2} + \frac{1}{\pi}\tan^{-1}$$

---
[1] Professor, Department of Mechanical Engineering, The University of Akron, Akron, Ohio 44325, Mem. ASME

[2] Graduate Research Assistant, Department of Mechanical Engineering, The University of Akron, Akron, Ohio 44325, Student Mem. ASME

Table 1 View factors from spheres to a class of axisymmetric bodies

Configuration and Function Generator of the axisymmetric body	View Factor Formulae[*]
Sphere to spherical cap[±] $f(x) = [r_2^2 - (x-r-r_2-s)^2]^{1/2}$	$F_{S-Sc} = F_{S-I} = \frac{1}{2}\left\{ 1 - \dfrac{1}{\sqrt{1 + \left[\frac{R\sin\theta}{1+S+(1-\cos\theta)R}\right]^2}} \right\}$ when $\theta \leq \cos^{-1}[(R+1)/(1+R+S)]$ $F_{S-Sc} = F_{S-I} + F_{S-II}$ when $\cos^{-1}[(R+1)/(1+R+S)] \leq \theta \leq \cos^{-1}[(R-1)/(1+R+S)]$ Note: In this case the upper limit of integration in equation (8b) changes to $x_e = r+s+(1-\cos\theta)r_2$ $F_{S-Sc} = F_{S-I} + F_{S-II}$ when $\theta \geq \cos^{-1}[(R-1)/(1+R+S)]$ where $R = r_2/r$, $S = s/r$ x_i & $x_e = s + r + r_2 - r_2(r_2 \pm r)/(s + r + r_2)$
Sphere to circular cone $f(x) = (x-r-s)\tan\alpha$	$F_{S-C} = F_{S-I} = \frac{1}{2}\left[1 - \dfrac{1}{\sqrt{1 + \left(\frac{R}{S+1+R\cot\omega}\right)^2}} \right]$ when $\omega \geq \csc^{-1}(1+S)$ $F_{S-C} = F_{S-I} + F_{S-II}$ when $\omega \leq \csc^{-1}(1+S)$ where $x_i = s + r$ and $x_e = r + s + r_2\cot\omega$
Sphere to ellipsoid[+] $f(x) = b\,[1-(x-r-s-a)^2/a^2]^{1/2}$	$F_{S-e} = F_{S-I} + F_{S-II}$
Sphere to paraboloid $f(x) = 2\,[e(x-s-r)]^{1/2}$	$F_{S-p} = F_{S-I} = \frac{1}{2}\left[1 - \dfrac{1}{\sqrt{1 + \frac{4e\,\ell}{(s+r+\ell)^2}}} \right]$ when $x_i \geq r+s+\ell$ $F_{S-p} = F_{S-I} + F_{S-II}$ when $x_i \leq r + s + \ell \leq x_e$ Note: In this case the upper limit of integration in equation (8b) changes to $x_e = r+s+\ell$ $F_{S-p} = F_{S-I} + F_{S-II}$ when $x_e \geq r+s+\ell$

[*] F_{S-I}, F_{S-II}, x_i and x_e are obtained from equations (8a), (8b), (9) and (10) respectively, unless otherwise noted.

[±] With sphere to sphere as its limiting case.

$$\left[\frac{(1-A^2\cot^2\theta)^{1/2}\sin\theta}{A} \right] + \frac{\cos\theta}{\pi(S+1)^2}[\pi - \cos^{-1}(A\cot\theta)]$$

when

$$\tan^{-1}(-A) \geq \theta \geq \tan^{-1}(A) \text{ and } 0 \leq \theta \leq \pi$$

(1b)

where $S = s/r$ and $A = [(S+1)^2 - 1]^{1/2}$; θ is the angle between the normal of the element and the line connecting the element and the center of the sphere. The same expressions were derived using different techniques [10–11]. Consider the radiation between the sphere and any differential element on the conical ring as shown in Fig. 1. From the reciprocal rule we have

$$dF_{S-dA_2} = \frac{dA_2}{4\pi r^2}F_{dA_2-S} = \frac{y\,d\xi\,ds}{4\pi r^2}F_{dA_2-S}$$

(2)

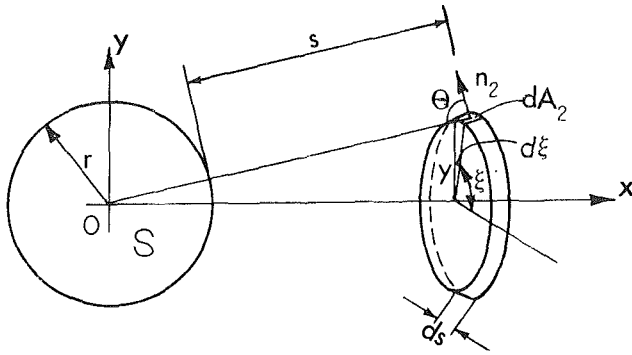where y is the radius of the differential ring. Integrating

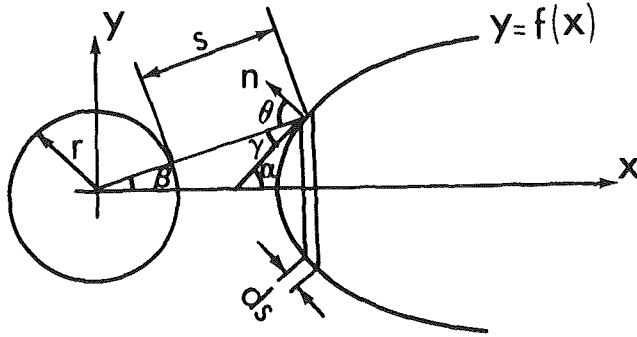Fig. 1   Sphere-differential coaxial conical ring view factor geometry

Fig. 2   Sphere-axisymmetric body view factor geometry

dF_{S-dA_2} with respect to ξ and noting that F_{dA_2-S} is independent of ξ due to the symmetrical configuration, we obtain an expression for the view factor from the sphere to the coaxial differential ring as

$$dF_{S-\delta r} = \int_0^{2\pi} \frac{y\,ds}{4\pi r^2} F_{dA_2-S}\,d\xi = \frac{y}{2r^2} F_{dA_2-S}\,ds \qquad (3)$$

where F_{dA_2-S} is given by equation (1).

Let the differential ring mentioned above be a differential section of an axisymmetric body which is generated from the rotation of the curve $y = f(x)$ around x-axis. Referring to Fig. 2, we have:

$$ds = (1 + [f'(x)]^2)^{1/2}\,dx \qquad (4)$$

$$\theta = \frac{\pi}{2} - \gamma = \frac{\pi}{2} - \tan^{-1} f'(x) + \tan^{-1}(f(x)/x) \qquad (5)$$

$$S + 1 = (x^2 + [f(x)]^2)^{1/2}/r \qquad (6)$$

Substituting equations (1a) and (1b) into equation (3) and making use of equations (4–6), we obtain the view factor from a sphere to a differential ring, $dF_{S-\delta r}$ in terms of r, x, $f(x)$ and $f'(x)$ (the expression for $dF_{S-\delta r}$ is not shown here to conserve space). In order to integrate $dF_{S-\delta r}$ over the entire axisymmetric surface, we divide the axisymmetric body under consideration into three regions as illustrated in Fig. 3.

Region I The region which can "see" the sphere and every tangent plane to the axisymmetric body in this region does not intersect the sphere, i.e., $(r + s) \leq x \leq x_i$, for every x in this region.

Region II The region which can "see" the sphere but every tangent plane to the axisymmetric body in this region intersects the sphere, i.e., $x_i \leq x \leq x_e$.

Region III The region on the axisymmetric body which can not "see" the sphere, i.e., $x > x_e$.

Integrating $dF_{S-\delta r}$ over the regions I and II mentioned above yields the radiation view factor from the sphere to the entire axisymmetric body, F_{S-ax}
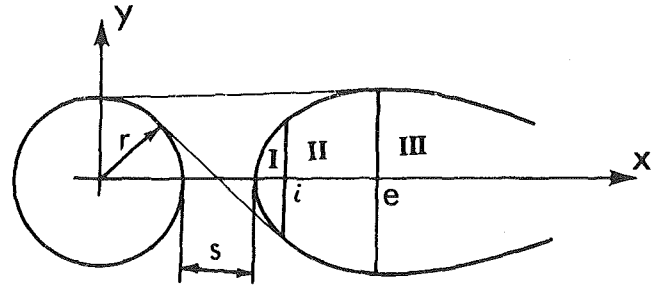

Fig. 3   Illustration of three regions in sphere-axisymmetric body view factor geometry

$$F_{S-ax} = \int_{r+s}^{x_i} dF_{(S-\delta r)\mathrm{I}} + \int_{x_i}^{x_e} dF_{(S-\delta r)\mathrm{II}} = F_{S-\mathrm{I}} + F_{S-\mathrm{II}} \qquad (7)$$

The first integral in equation (7) can be integrated exactly and is expressed by,

$$F_{S-\mathrm{I}} = \tfrac{1}{2}(1 - 1/[1 + (f(x_i)/x_i)^2]^{1/2}) \qquad (8a)$$

The second integral in equation (7) generally requires a numerical integration. It can be rewritten in the following compact form

$$F_{S-\mathrm{II}} = \frac{1}{2\pi r^2} \int_{x_i}^{x_e} f(x)\left[-\frac{r\eta\lambda}{\xi^3}(1-Q^2)^{1/2} \right.$$
$$\left. + \psi\tan^{-1}\left[\frac{r\lambda}{\psi\xi\eta}(1-Q^2)^{1/2} \right] + \frac{r^2\phi}{\xi^3}(\pi - \cos^{-1}Q) \right]dx$$

where

$$\eta = (x^2 + [f(x)]^2 - r^2)^{1/2}, \quad \phi = xf'(x) - f(x),$$
$$\xi = (x^2 + [f(x)]^2)^{1/2}, \quad \lambda = x + f'(x)f(x),$$
$$\psi = (1 + [f'(x)]^2)^{1/2} \text{ and } Q = (\eta\phi)/(r\lambda) \qquad (8b)$$

It can be easily shown that the integration limits in equation (8b) are determined from the following relationships

$$\frac{x_i f'(x_i) - f(x_i)}{x_i + f'(x_i)f(x_i)} = \frac{r}{\sqrt{x_i^2 + [f(x_i)]^2 - r^2}} \qquad (9)$$

$$\frac{-x_e f'(x_e) + f(x_e)}{x_e + f'(x_e)f(x_e)} = \frac{r}{\sqrt{x_e^2 + [f(x_e)]^2 - r^2}} \qquad (10)$$

Once $f(x)$ and r are specified, x_i and x_e can be solved from equations (9) and (10), respectively. It should be pointed out that not necessarily all axisymmetric bodies are consisted of all three regions mentioned above. For certain geometries region I does not exist while for some configurations, region II does not exist, i.e., $F_{S-\mathrm{II}} = 0$ which yields a closed form solution for $F_{S-ax} = F_{S-\mathrm{I}}$. Therefore, the solution for F_{S-ax} is semi-analytical and requires a single numerical integration under the worst condition (when $F_{S-\mathrm{II}} \neq 0$).

Applications and Discussion

Based on equations (7–10), the view factors from a sphere to a class of axisymmetric bodies are investigated which include sphere, spherical cap, right circular cone, ellipsoid and paraboloid. The resulting formulae for view factors are summarized in Table 1.

The application of the present technique is not restricted only to the geometries presented in Table 1. This method is applicable as long as the function generator of the axisymmetric body, $f(x)$, is continuous, $f'(x)$ exists and $f''(x)$ is less than or equal to zero everywhere in the region between x_i and x_e.

Extensive numerical results for the aforementioned geometries have been presented in graphical and tabulated forms elsewhere; the interested readers may refer to reference 9 for further details.

References

1 Jones, L. R., "Diffuse Radiation View Factor Between Two Spheres," *Journal of Heat Transfer*, Vol. 87, No. 3, 1965, pp. 421–422.

2 Juul, N. H., "Diffuse Radiation Configuration Factors Between Two Spheres and The Limits," *Letters in Heat and Mass Transfer*, Vol. 3, No. 3, 1976, pp. 205–211.

3 Grier, N. T., *Tabulations of Configuration Factors Between Any Two Spheres and Their Parts*, NASA SP-3050, 1969.

4 Campbell, J. P., and McConnell, D. G., *Radiant-Interchange Configuration Factors for Spherical and Conical Surfaces To Spheres*, NASA TN D-4457, 1968.

5 Minning, C. P., "Shape Factors Between Coaxial Annular Discs Separated by a Solid Cylinder," *AIAA Journal*, Vol. 17, No. 3, 1979, pp. 318–320.

6 Minning, C. P., "Calculation of Shape Factors Between Parallel Ring Sectors Sharing a Common Center Line," *AIAA Journal*, Vol. 14, No. 6, 1976, pp. 813–815.

7 Minning, C. P., "Calculation of Shape Factors Between Rings and Inverted Cones Sharing a Common Axis," *Journal of Heat Transfer*, Vol. 99, No. 3, 1977, pp. 492–494.

8 Sparrow, E. M., "A New and Simpler Formation for Radiative Angle Factors," *Journal of Heat Transfer*, Vol. 85, No. 2, 1963, pp. 81–88.

9 Chung, B. T. F., and Naraghi, M. H. N., "A Formulation for Radiative View Factors from Spheres to A Class of Axisymmetric Bodies" ASME Paper *80 WA/HT-58*, presented at ASME Winter Annual Meeting, Chicago, 1980.

10 Cunningham, F. G., "*Power Input to Small Flat Plate from a Diffusely Radiating Sphere, with Application to Earth Satellites*," NASA TN D-710, Aug. 1961.

11 Juul, N. H., "Diffuse Radiation View Factors from Differential Plane Source to Spheres," *Journal of Heat Transfer*, Vol. 101, No. 3, 1979, pp. 558–560.

Conjugate Forced Convection-Conduction Analysis of Heat Transfer in a Plate Fin

E. M. Sparrow[1] and M. K. Chyu[2]

Nomenclature

h = local heat transfer coefficient

$\bar{h}$ = average heat transfer coefficient

$\hat{h}$ = dimensionless local heat transfer coefficient, $hL/k\mathrm{Re}_L^{1/2}$

k = fluid thermal conductivity

k_f = fin thermal conductivity

L = fin length

N_{cc} = conduction-convection parameter, $(kL/k_f t)\mathrm{Re}_L^{1/2}$

Q = overall rate of fin heat transfer

q = local fin heat transfer rate

Re_L = Reynolds number, $u_\infty L/\nu$

Re_x = Reynolds number, $u_\infty x/\nu$

T_f = fin temperature at x

T_0 = fin base temperature

T_∞ = fluid temperature

t = fin half thickness

U = dimensionless velocity, u/u_∞

V = dimensionless velocity, $vL/\nu\mathrm{Re}_L^{1/2}$

u,v = velocity components

u_∞ = free stream velocity

X = dimensionless coordinate, x/L

Y = dimensionless coordinate, $(y/L)\mathrm{Re}_L^{1/2}$

x,y = coordinates

η = fin efficiency

θ = dimensionless temperature, $(T - T_\infty)/(T_0 - T_\infty)$

θ_f = dimensionless fin temperature, $(T_f - T_\infty)/(T_0 - T_\infty)$

ν = kinematic viscosity

Introduction

In the conventional approach to determining the heat-transfer characteristics of fins, the fin heat conduction equation is solved using a literature-given value of the convective heat-transfer coefficient that is assumed uniform all along the fin surface. This approach leads to uncertain results because, in general, the heat-transfer coefficient varies along the fin surface and also because the available literature information may not correspond to the actual fluid flow and/or thermal boundary conditions for the fin. The alternative to the aforementioned procedure is to simultaneously solve the conduction problem for the fin and the convective heat-transfer problem for the flowing fluid. This obviates the need to use literature information and ensures that the convective heat-transfer coefficients are truly appropriate for the specific problem under consideration.

Such a simultaneous solution is carried out here for a plate fin that is washed by a laminar forced-convection boundary layer flow. Heat-transfer results obtained from numerical solutions will be compared with those from the conventional approach.

The problem to be studied here is illustrated in the inset of Fig. 1. A uniform free stream (velocity, u_∞, temperature, T_∞) approaches a plate fin that is aligned parallel to the oncoming flow. The fin is of length L, thickness $2t$, and is attached to a base surface whose temperature is T_0. The temperature of the fin varies along its length (i.e., as a function of x), and this temperature distribution, which is not known *a priori*, serves as a boundary condition for the boundary-layer energy equation. It is well established that the heat-transfer coefficients for laminar boundary layer flow are affected by the nature of the temperature distribution on the bounding surface. Heat-transfer coefficients are available for certain special cases (e.g., variations of the surface temperature as a polynomial in x), but these results are not applicable here since the surface temperature variation is of arbitrary form and is unknown.

The present investigation bears a kinship to a prior study [1] of the interaction between a vertical plate fin and a natural-convection, boundary-layer flow. In fact, one of the motivations for undertaking the present work was to seek clarification of certain novel findings of [1]. To facilitate a compact presentation here, concepts and procedures which are already described in [1] will not be restated. The present problem also bears a distant relationship to a prior study [2] of heat transfer from a continuous moving sheet, where the boundary-layer equations were solved simultaneously with a conduction equation for the solid. However, in that case, the conduction equation was simplified by deleting the axial conduction term and adding a kind of pseudo axial convection term – which leads to a problem decisively different from that studied here.

Analysis and Solution

For the fin (subscript f), application of the widely accepted thin-fin model yields the energy balance

$$d^2 T_f/dx^2 = (h(x)/k_f t)(T_f(x) - T_\infty) \tag{1}$$

where the novel feature of the equation is that the heat-

[1] Department of Mechanical Engineering, University of Minnesota, Minneapolis, Minn., 55455, Fellow ASME
[2] Department of Mechanical Engineering, University of Minnesota, Minneapolis, Minn., 55455

References

1 Jones, L. R., "Diffuse Radiation View Factor Between Two Spheres," *Journal of Heat Transfer*, Vol. 87, No. 3, 1965, pp. 421–422.

2 Juul, N. H., "Diffuse Radiation Configuration Factors Between Two Spheres and The Limits," *Letters in Heat and Mass Transfer*, Vol. 3, No. 3, 1976, pp. 205–211.

3 Grier, N. T., *Tabulations of Configuration Factors Between Any Two Spheres and Their Parts*, NASA SP-3050, 1969.

4 Campbell, J. P., and McConnell, D. G., *Radiant-Interchange Configuration Factors for Spherical and Conical Surfaces To Spheres*, NASA TN D-4457, 1968.

5 Minning, C. P., "Shape Factors Between Coaxial Annular Discs Separated by a Solid Cylinder," *AIAA Journal*, Vol. 17, No. 3, 1979, pp. 318–320.

6 Minning, C. P., "Calculation of Shape Factors Between Parallel Ring Sectors Sharing a Common Center Line," *AIAA Journal*, Vol. 14, No. 6, 1976, pp. 813–815.

7 Minning, C. P., "Calculation of Shape Factors Between Rings and Inverted Cones Sharing a Common Axis," *Journal of Heat Transfer*, Vol. 99, No. 3, 1977, pp. 492–494.

8 Sparrow, E. M., "A New and Simpler Formation for Radiative Angle Factors," *Journal of Heat Transfer*, Vol. 85, No. 2, 1963, pp. 81–88.

9 Chung, B. T. F., and Naraghi, M. H. N., "A Formulation for Radiative View Factors from Spheres to A Class of Axisymmetric Bodies" ASME Paper 80 WA/HT-58, presented at ASME Winter Annual Meeting, Chicago, 1980.

10 Cunningham, F. G., "*Power Input to Small Flat Plate from a Diffusely Radiating Sphere, with Application to Earth Satellites*," NASA TN D-710, Aug. 1961.

11 Juul, N. H., "Diffuse Radiation View Factors from Differential Plane Source to Spheres," *Journal of Heat Transfer*, Vol. 101, No. 3, 1979, pp. 558–560.

Conjugate Forced Convection-Conduction Analysis of Heat Transfer in a Plate Fin

E. M. Sparrow[1] and M. K. Chyu[2]

Nomenclature

h = local heat transfer coefficient

$\bar{h}$ = average heat transfer coefficient

$\hat{h}$ = dimensionless local heat transfer coefficient, $hL/k\mathrm{Re}_L^{1/2}$

k = fluid thermal conductivity

k_f = fin thermal conductivity

L = fin length

N_{cc} = conduction-convection parameter, $(kL/k_f t)\mathrm{Re}_L^{1/2}$

Q = overall rate of fin heat transfer

q = local fin heat transfer rate

Re_L = Reynolds number, $u_\infty L/\nu$

Re_x = Reynolds number, $u_\infty x/\nu$

T_f = fin temperature at x

T_0 = fin base temperature

T_∞ = fluid temperature

t = fin half thickness

U = dimensionless velocity, u/u_∞

V = dimensionless velocity, $vL/\nu\mathrm{Re}_L^{1/2}$

u,v = velocity components

u_∞ = free stream velocity

X = dimensionless coordinate, x/L

Y = dimensionless coordinate, $(y/L)\mathrm{Re}_L^{1/2}$

x,y = coordinates

η = fin efficiency

θ = dimensionless temperature, $(T - T_\infty)/(T_0 - T_\infty)$

θ_f = dimensionless fin temperature, $(T_f - T_\infty)/(T_0 - T_\infty)$

ν = kinematic viscosity

Introduction

In the conventional approach to determining the heat-transfer characteristics of fins, the fin heat conduction equation is solved using a literature-given value of the convective heat-transfer coefficient that is assumed uniform all along the fin surface. This approach leads to uncertain results because, in general, the heat-transfer coefficient varies along the fin surface and also because the available literature information may not correspond to the actual fluid flow and/or thermal boundary conditions for the fin. The alternative to the aforementioned procedure is to simultaneously solve the conduction problem for the fin and the convective heat-transfer problem for the flowing fluid. This obviates the need to use literature information and ensures that the convective heat-transfer coefficients are truly appropriate for the specific problem under consideration.

Such a simultaneous solution is carried out here for a plate fin that is washed by a laminar forced-convection boundary layer flow. Heat-transfer results obtained from numerical solutions will be compared with those from the conventional approach.

The problem to be studied here is illustrated in the inset of Fig. 1. A uniform free stream (velocity, u_∞, temperature, T_∞) approaches a plate fin that is aligned parallel to the oncoming flow. The fin is of length L, thickness $2t$, and is attached to a base surface whose temperature is T_0. The temperature of the fin varies along its length (i.e., as a function of x), and this temperature distribution, which is not known *a priori*, serves as a boundary condition for the boundary-layer energy equation. It is well established that the heat-transfer coefficients for laminar boundary layer flow are affected by the nature of the temperature distribution on the bounding surface. Heat-transfer coefficients are available for certain special cases (e.g., variations of the surface temperature as a polynomial in x), but these results are not applicable here since the surface temperature variation is of arbitrary form and is unknown.

The present investigation bears a kinship to a prior study [1] of the interaction between a vertical plate fin and a natural-convection, boundary-layer flow. In fact, one of the motivations for undertaking the present work was to seek clarification of certain novel findings of [1]. To facilitate a compact presentation here, concepts and procedures which are already described in [1] will not be restated. The present problem also bears a distant relationship to a prior study [2] of heat transfer from a continuous moving sheet, where the boundary-layer equations were solved simultaneously with a conduction equation for the solid. However, in that case, the conduction equation was simplified by deleting the axial conduction term and adding a kind of pseudo axial convection term — which leads to a problem decisively different from that studied here.

Analysis and Solution

For the fin (subscript f), application of the widely accepted thin-fin model yields the energy balance

$$d^2 T_f/dx^2 = (h(x)/k_f t)(T_f(x) - T_\infty) \tag{1}$$

where the novel feature of the equation is that the heat-

[1] Department of Mechanical Engineering, University of Minnesota, Minneapolis, Minn., 55455, Fellow ASME

[2] Department of Mechanical Engineering, University of Minnesota, Minneapolis, Minn., 55455
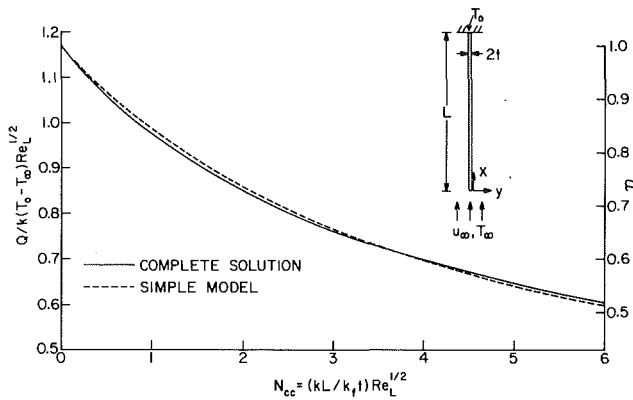
Copyright © 1982 by ASME

Fig. 1 Overall rate of fin heat transfer (left ordinate) and fin efficiency (right ordinate). Inset — schematic diagram of the physical problem.
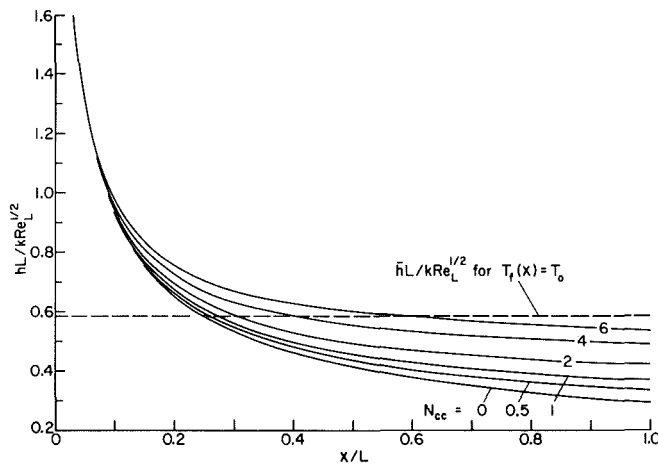

Fig. 2 Local heat transfer coefficients

transfer coefficient, h, may vary with x, in contrast with $h = $ constant, as is conventional. Introduction of dimensionless variables and parameters as indicated in the nomenclature leads to

$$d^2\theta_f/dX^2 = \hat{h}N_{cc}\theta_f \qquad (2)$$

For the boundary layer flow along the fin, the dimensionless form of the conservation equation is

$$\partial U/\partial X + \partial V/\partial Y = 0 \qquad (3)$$

$$U(\partial U/\partial X) + V(\partial U/\partial Y) = \partial^2 U/\partial Y^2 \qquad (4)$$

$$U(\partial\theta/\partial X) + V(\partial\theta/\partial Y) = (1/\text{Pr})\partial^2\theta/\partial Y^2 \qquad (5)$$

Equations (2–5) contain two dimensionless groups, the conduction-convection parameter, N_{cc}, and the Prandtl number, Pr. The former will be varied systematically during the computations, while the latter has been assigned a fixed value of 0.7 (air).

The boundary conditions that are specific to the fin are that $d\theta/dX = 0$ at $X = 0$ and $\theta = 1$ at $X = 1$. For the boundary layer flow, U and V are zero at $Y = 0$ (at the plate surface), while $U = 1$ and $\theta = 0$ as $Y \rightarrow \infty$ (in the free stream). Of particular interest is the thermal coupling between the fin and the boundary layer. The basic coupling is expressed by the requirement that the fin and fluid temperatures and heat fluxes be continuous at the plate-fluid interface, at all X. In the adopted solution methodology, the continuity conditions were fulfilled for the converged solutions obtained as the end result of an iterative process.

The solution methodology involves the execution of a succession of numerical solutions, alternately for the boundary layer and for the fin. To start, the boundary layer equations are solved subject to the thermal boundary con-

dition $\theta = 1$ at the plate surface, and from this solution $\hat{h}$ is evaluated from

$$\hat{h}(X) = -[(\partial\theta/\partial Y)/\theta]_{Y=0} \qquad (6)$$

The $\hat{h}(X)$ values are fed to the fin equation (2), which is solved to give $\theta_f(X)$. This θ distribution is then imposed as the surface boundary condition for the boundary layer problem, the solution of which is used to evaluate an updated $\hat{h}(X)$ from equation (6) and so on until convergence.

The numerical details are similar to those of [1], although a completely independent computer program was employed here. The Patankar-Spalding method was used for the boundary layer equations, while the fin equation was solved using the tridiagonal matrix algorithm (Thomas algorithm). Both methods possess speed and accuracy, and these characteristics are also attributes of the overall solution methodology.

The converged solutions for each assigned value of N_{cc} yielded the following results:

$$Q/k(T_0 - T_\infty)\text{Re}_L^{1/2} \text{ and } \eta \qquad (7a)$$

$$(hL/k)/\text{Re}_L^{1/2} \qquad (7b)$$

$$qL/k(T_0 - T_\infty)\text{Re}_L^{1/2} \qquad (7c)$$

$$(T_f - T_\infty)/(T_0 - T_\infty) \qquad (7d)$$

In equation (7a), Q denotes the overall rate of fin heat transfer (from both faces of the fin), while η, the fin efficiency, compares the fin heat transfer with that for an isothermal fin. For the isothermal fin, the local and average heat transfer coefficients, h and $\bar{h}$, respectively, are obtained from the widely available boundary layer solution for the isothermal flat plate (for Pr − 0.7)

$$hx/k = 0.2927\text{Re}_x^{1/2}, \quad \bar{h}L/k = 0.5854\text{Re}_L^{1/2} \qquad (8)$$

In equation (7b), h denotes the local heat-transfer coefficient corresponding to the (nonuniform) fin temperature distribution $T_f(x)$, which results from the solution of the governing equations, and q in equation (7c) is the corresponding local heat flux. The temperature distribution itself will be presented in terms of the dimensionless group of equation (7d).

The results from the numerical solutions will be compared with those of the conventional fin model which is based on the assumption of a uniform heat-transfer coefficient. In view of the fact that the coefficient is, in fact, nonuniform, it appears reasonable to take the *fictive* uniform heat-transfer coefficient for the conventional model as being equal to $\bar{h}$ of equation (8). With this, the results from the conventional model follow as

$$Q/k(T_0 - T_\infty)\text{Re}_L^{1/2}$$

$$= (1.530/N_{cc}^{1/2})\tanh(0.5854N_{cc})^{1/2} \qquad (9a)$$

$$\eta = (1.307/N_{cc}^{1/2})\tanh(0.5854N_{cc})^{1/2} \qquad (9b)$$

$$qL/k(T_0 - T_\infty)\text{Re}_L^{1/2} = 0.5854\theta_f \qquad (9c)$$

$$(T_f - T_\infty)/(T_0 - T_\infty) = \theta_f$$

$$= \cosh(0.5854N_{cc}X^2)^{1/2}/\cosh(0.5854N_{cc})^{1/2} \qquad (9d)$$

Results and Discussion

The overall rate of fin heat transfer, Q, and the fin efficiency, η, are presented in Fig. 1 (left and right ordinates, respectively) as a function of the conduction-convection parameter N_{cc}. The results of the present analysis are labeled *complete solution*, while those of the conventional approach, evaluated from equations (9a) and (9b), are identified as
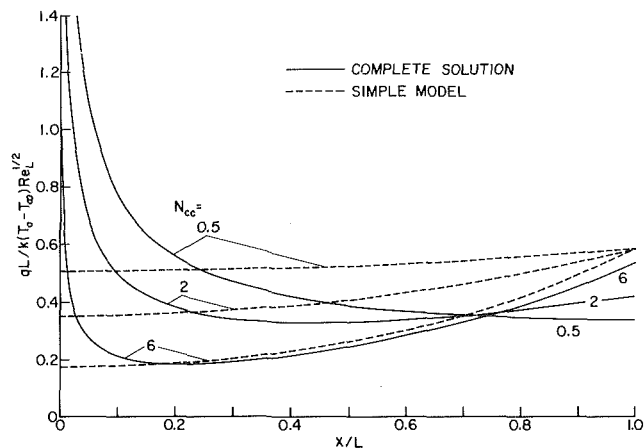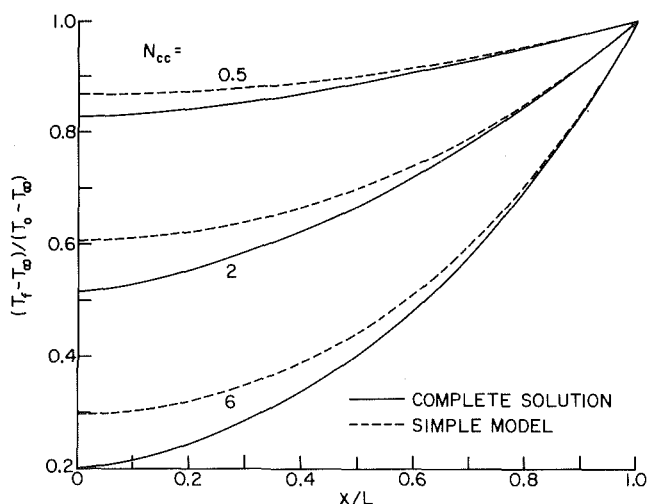
Fig. 3 Local heat flux at the fin surface

Fig. 4 Fin temperature distributions

simple model. Since the two ordinate variables differ only by a multiplicative constant, it is sufficient to discuss either one. Considering the fin efficiency, it may be noted that its departures from unity reflect departures of the fin temperature distribution from the uniform value T_0. The fin temperature drop, relative to T_0, is accentuated by higher convective coefficients (higher k and Re_L), longer fin lengths, L, and smaller fin conductances, $k_f t$. Taken together, these individual trends merge to yield a decrease of η with N_{cc}.

The agreement of the results from the simple model with those of the complete solution is truly remarkable, so that equations (9a) and (9b), which represent Q and η for the simple model, are altogether satisfactory for fin design. This near-perfect agreement should not be regarded as a validation of the simple model but only as an indication of its ability to accurately predict overall results.

The variation of the local heat transfer coefficient h along the fin is shown in Fig. 2. The lowermost curve ($N_{cc} = 0$) is for the isothermal fin, while the curves for $N_{cc} > 0$ are for nonisothermal fins, with larger temperature variations being evoked by larger N_{cc}. Thus, the more nonisothermal the fin, the higher the local heat-transfer coefficients. In all cases, the local heat-transfer coefficients decrease in the direction of fluid flow (from tip to base).

The dashed horizontal line appearing in Fig. 2 corresponds to the average heat transfer coefficient for an isothermal plate (or fin). It is this line (in reality, its algebraic counterpart from equation (8)) that was used for the fictive uniform heat-transfer coefficient for the simple model. Clearly, such a

uniform coefficient is not a very close approximation to the axially varying h values that actually prevail.

Whereas the h values of Fig. 2 monotonically decrease in the fluid flow direction, the natural convection coefficients computed in [1] for a vertical plate fin do not vary monotonically. In the direction from tip to base, those coefficients decrease at first, attain a minimum, and then increase. The existence of the minimum and the subsequent increase can be attributed to the increased buoyancy encountered by the fluid as it passes from the tip toward the base. Since buoyancy is not a factor in the present forced convection analysis, the nonmonotonic behavior observed in [1] is not in evidence here.

The local heat-flux variations presented in Fig. 3 also show a distinct difference between the results of the complete solution (solid lines) and of the simple model (dashed lines). The largest deviations are at small N_{cc}. For the largest N_{cc} of the figure, the q distribution for the simple model tracks that for the complete solution reasonably well, except at small x/L (i.e., near the tip).

Despite the significant errors in the local heat flux predicted by the simple model, the plus and minus errors tend to cancel almost perfectly, yielding an overall heat-transfer rate which is virtually exact.

Figure 4 presents fin temperature distributions for both the complete solution and the simple model. The latter predicts a smaller base-to-tip temperature variation than actually prevails.

To sum up, it may be noted that the conventional fin model based on a uniform input value of the heat-transfer coefficient yields very good predictions for the overall rate of fin heat transfer, but the local predictions can be substantially in error. These findings should continue to apply for Prandtl numbers that are not too different from Pr = 0.7, but it is uncertain whether or not they will be applicable at more deviant Prandtl numbers.

Acknowledgment

References

1 Sparrow, E. M. and Acharya, S., "A Natural Convection Fin with a Solution-Determined Nonmonotonically Varying Heat Transfer Coefficient," ASME JOURNAL OF HEAT TRANSFER, Vol. 103, 1981, pp. 218–225.

2 Erickson, L. E., Cha, L. C., and Fan, L. T., "The Cooling of a Moving Continuous Flat Sheet," *Chemical Engineering Progress Symposium Series,* Vol. 62, No. 64, 1966, pp. 157–165.

An Analytical Study of Bubble and Adjacent Tube Influence on Heat Transfer to a Horizontal Tube in a Gas Fluidized Bed

R. L. Adams[1] and J. R. Welty[2]

Introduction

In reference [1], Adams and Welty present a gas convection model of heat transfer to a horizontal tube immersed in a large particle fluidized bed. The heat transfer model is used

[1] Assistant Professor, Department of Mechanical Engineering, Oregon State University, Mem. ASME

[2] Professor, Department of Mechanical Engineering, Oregon State University, Corvallis, Ore. 97331. Mem. ASME
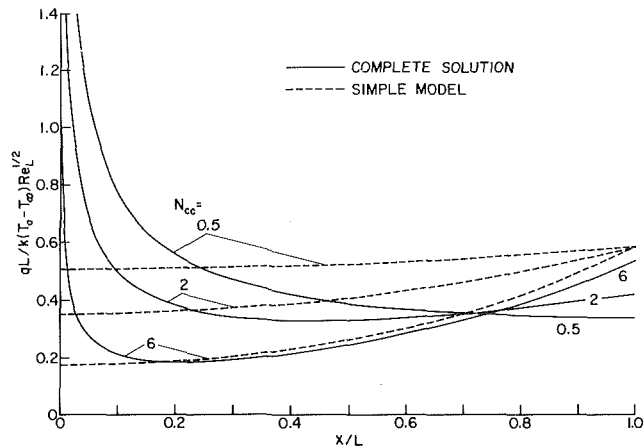
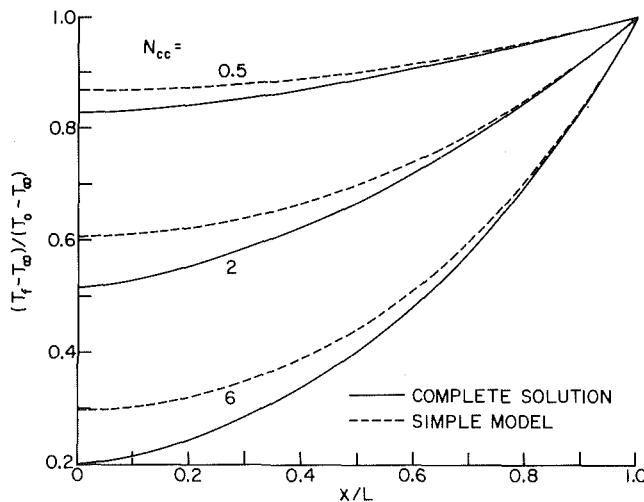**Fig. 3   Local heat flux at the fin surface**

Fig. 4   Fin temperature distributions

simple model. Since the two ordinate variables differ only by a multiplicative constant, it is sufficient to discuss either one. Considering the fin efficiency, it may be noted that its departures from unity reflect departures of the fin temperature distribution from the uniform value T_0. The fin temperature drop, relative to T_0, is accentuated by higher convective coefficients (higher k and Re_L), longer fin lengths, L, and smaller fin conductances, $k_f t$. Taken together, these individual trends merge to yield a decrease of η with N_{cc}.

The agreement of the results from the simple model with those of the complete solution is truly remarkable, so that equations (9a) and (9b), which represent Q and η for the simple model, are altogether satisfactory for fin design. This near-perfect agreement should not be regarded as a validation of the simple model but only as an indication of its ability to accurately predict overall results.

The variation of the local heat transfer coefficient h along the fin is shown in Fig. 2. The lowermost curve ($N_{cc} = 0$) is for the isothermal fin, while the curves for $N_{cc} > 0$ are for nonisothermal fins, with larger temperature variations being evoked by larger N_{cc}. Thus, the more nonisothermal the fin, the higher the local heat-transfer coefficients. In all cases, the local heat-transfer coefficients decrease in the direction of fluid flow (from tip to base).

The dashed horizontal line appearing in Fig. 2 corresponds to the average heat transfer coefficient for an isothermal plate (or fin). It is this line (in reality, its algebraic counterpart from equation (8)) that was used for the fictive uniform heat-transfer coefficient for the simple model. Clearly, such a

uniform coefficient is not a very close approximation to the axially varying h values that actually prevail.

Whereas the h values of Fig. 2 monotonically decrease in the fluid flow direction, the natural convection coefficients computed in [1] for a vertical plate fin do not vary monotonically. In the direction from tip to base, those coefficients decrease at first, attain a minimum, and then increase. The existence of the minimum and the subsequent increase can be attributed to the increased buoyancy encountered by the fluid as it passes from the tip toward the base. Since buoyancy is not a factor in the present forced convection analysis, the nonmonotonic behavior observed in [1] is not in evidence here.

The local heat-flux variations presented in Fig. 3 also show a distinct difference between the results of the complete solution (solid lines) and of the simple model (dashed lines). The largest deviations are at small N_{cc}. For the largest N_{cc} of the figure, the q distribution for the simple model tracks that for the complete solution reasonably well, except at small x/L (i.e., near the tip).

Despite the significant errors in the local heat flux predicted by the simple model, the plus and minus errors tend to cancel almost perfectly, yielding an overall heat-transfer rate which is virtually exact.

Figure 4 presents fin temperature distributions for both the complete solution and the simple model. The latter predicts a smaller base-to-tip temperature variation than actually prevails.

To sum up, it may be noted that the conventional fin model based on a uniform input value of the heat-transfer coefficient yields very good predictions for the overall rate of fin heat transfer, but the local predictions can be substantially in error. These findings should continue to apply for Prandtl numbers that are not too different from Pr = 0.7, but it is uncertain whether or not they will be applicable at more deviant Prandtl numbers.

Acknowledgment

References

1 Sparrow, E. M. and Acharya, S., "A Natural Convection Fin with a Solution-Determined Nonmonotonically Varying Heat Transfer Coefficient," ASME JOURNAL OF HEAT TRANSFER, Vol. 103, 1981, pp. 218–225.

2 Erickson, L. E., Cha, L. C., and Fan, L. T., "The Cooling of a Moving Continuous Flat Sheet," *Chemical Engineering Progress Symposium Series*, Vol. 62, No. 64, 1966, pp. 157–165.

An Analytical Study of Bubble and Adjacent Tube Influence on Heat Transfer to a Horizontal Tube in a Gas Fluidized Bed

R. L. Adams[1] and J. R. Welty[2]

Introduction

In reference [1], Adams and Welty present a gas convection model of heat transfer to a horizontal tube immersed in a large particle fluidized bed. The heat transfer model is used

[1] Assistant Professor, Department of Mechanical Engineering, Oregon State University, Mem. ASME

[2] Professor, Department of Mechanical Engineering, Oregon State University, Corvallis, Ore. 97331. Mem. ASME

together with an approximate hydrodynamic model to establish the influence of a single two-dimensional tube-sized slow bubble on the local and total heat transfer to the tube. The accuracy of the model has been established by an extensive experimental study of heat transfer and hydrodynamics in a two-dimensional cold bed (see Catipovic [2] and Catipovic et al. [3]). Based upon these two-dimensional results, the heat-transfer model seems to be valid for particle Reynolds number (based upon minimum fluidizing velocity) greater than 200, and reasonable results are obtained for Reynolds number as low as 50.

The purpose of this note is to report the results of a further analytical study of the effects of bubble size, position and velocity, and of adjacent tubes upon the heat transfer to a horizontal tube. To facilitate these calculations, the approximate hydrodynamic model presented in [1] has been modified to include the effect of bubble-induced particle motion and to improve the accuracy of both interstitial and bubble flow fields. The hydrodynamic model and, therefore, the heat transfer results are limited to the two-dimensional case for which approximate analytical solutions can be obtained, however the results should be qualitatively correct for three-dimensional situations as well.

Analysis

According to the heat transfer model of Adams and Welty [1], emulsion phase and bubble phase contributions are due to gas convection and are considered separately. The emulsion phase contribution is determined from an analysis of gas flow within interstitial channels bounded by particle surfaces and the tube wall. The geometry of this flow is simplified by using a boundary layer/inviscid core model with two-dimensional boundary layer flow near the channel center and three-dimensional but Stokes flow near particle contact points. The bubble phase heat transfer is determined by using conventional two-dimensional boundary layer theory. For both the emulsion phase and bubble phase, the model is formulated to include the effect of interstitial turbulence.

The analytical development of the emulsion phase heat transfer model can be found in Adams [4] and Adams and Welty [1]. Recently, Adams [5] showed that the emulsion

Fig. 1 Polar plot showing effect of bubble velocity on local Nusselt number

phase Nusselt number can be reduced to the following approximations

$$
\mathrm{Nu}_p \simeq \begin{cases} a \ \sqrt{\mathrm{Re}_{p_c}} + b + \mathrm{Nu}_{p_0} & \mathrm{Re}_{p_c} \geq \mathrm{Re}_{p_{cm}} \\ c \ \mathrm{Re}_{p_c} + \mathrm{Nu}_{p_0} & \mathrm{Re}_{p_c} < \mathrm{Re}_{p_{cm}} \end{cases} \quad (1)
$$

where a, b, c, $\mathrm{Re}_{p_{cm}}$ and Nu_{p_0} depend upon the local voidage, interstitial turbulence, bed and wall temperatures and Prandtl number of the gas (detailed expressions are given in [5]). In equation (1), Re_{p_c} is the Reynolds number based upon particle diameter and local interstitial gas velocity.

The bubble phase heat transfer is obtained using an integral method developed by Adams [4] which includes the effect of interstitial turbulence present within the bubble flow field. The approach follows the Pohlhausen approximation for velocity and temperature profiles with an integral transformation to absorb the interstitial turbulence effect and numerical integration of the resulting ordinary differential equations. The reader is referred to [1] and [4] for details of this anaylsis.

The essential parameter in the evaluation of the heat transfer is the local gas velocity within the interstitial passages of the emulsion phase and within contacting bubbles. As in [1], the interstitial gas velocity is obtained by reducing the momentum equations of Anderson and Jackson [6] and linearizing the Ergun equation for pressure drop in packed beds [7] to obtain

$$
\vec{\nabla} p = -K_D(\bar{Q}_g - \bar{Q}_s) \quad (2)
$$

where $\bar{Q}_g$ and $\bar{Q}_s$ are average gas and particle velocities, respectively, K_D is the drag parameter, and p is the gas pressure. In [1], the large particle bed was assumed to be operating near minimum fluidizing conditions so that bubble velocities and hence $\bar{Q}_s$ could be neglected.

When the voidage and K_D are constant, equation (2) and conservation of mass reveal that $-p/K_D$ serves as a potential for the velocity difference, $(\bar{Q}_g - \bar{Q}_s)$. Also the particle velocity field induced by rising bubbles is obtained using the potential flow model of Davidson [8] (note that the solutions of the complete particle momentum equation reported by Martin-Gautier and Pyle [9] offer no substantial increase in accuracy) so that the interstitial gas velocity field is based completely on potential flow.

When equation (2) is used to determine the local gas velocity at the tube surface, the parameter, K_D, is based upon local surface voidage except in the high voidage lower stagnation region of the tube where the approximation breaks down. In this region, a correlation based upon finite difference solutions by George et al. [10] is used to relate the potential flow, constant voidage pressure gradient to the actual variable voidage value.

For two-dimensional geometries, the required velocity potentials can be constructed using complex variable theory and the method of images. This approach was previously used by Adams and Welty [1], but only one image reflection was made and the particle velocity field was neglected as noted above. To allow for multiple reflections, an algorithm similar to that reported by Halsey [11] has been developed to treat the two types of boundary conditions on the flow. The condition of flow tangency for the gas at a tube surface and for particles relative to a moving bubble (i.e. constant stream function) is satisfied by complex functions of the form

$$
G(Z) = F(Z) + \bar{F}\left(\frac{b_i^2}{Z - Z0_i}\right) \quad (3)
$$

in accordance with the circle theorem (see Batchelor [12]), where b_i is the radius of the object and $Z0_i$ is the location of the center of the object. While the condition of constant
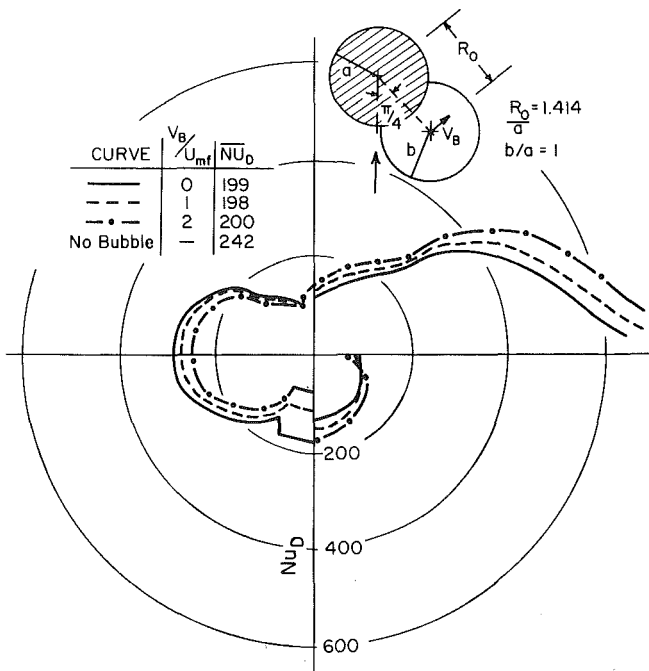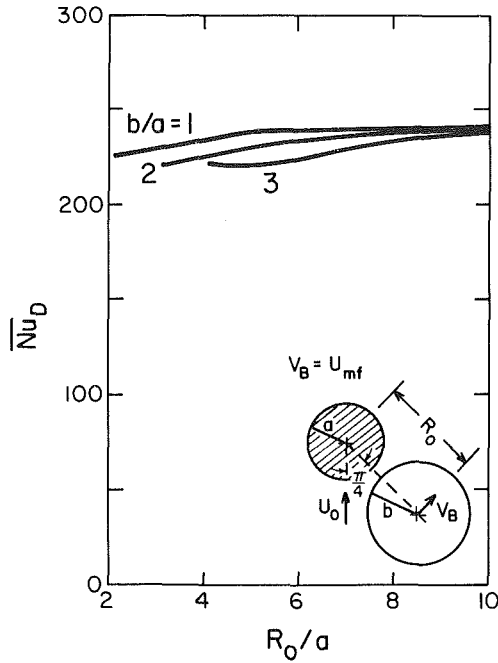
Fig. 2 Effect of bubble size and position on total Nusselt number for bubble at $\theta = \pi/4$ and $V_B = U_{mf}$
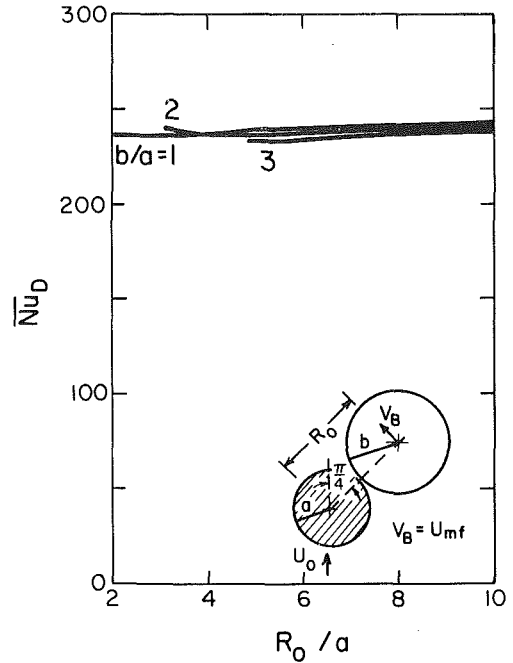

Fig. 4 Effect of bubble size and position on total Nusselt number for bubble at $\theta = 3\pi/4$ and $V_B = U_{mf}$
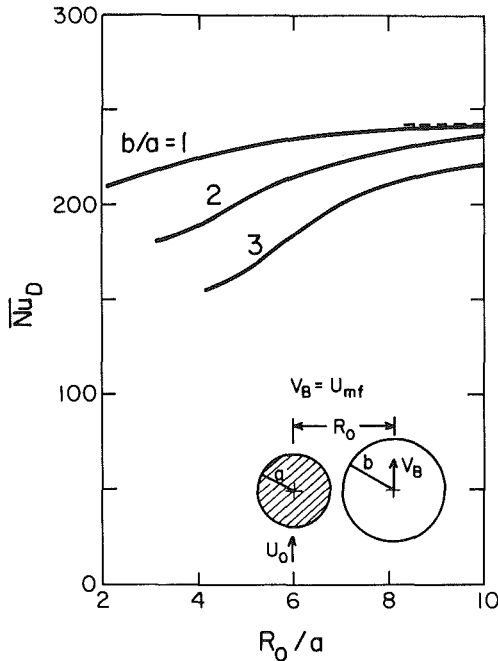

Fig. 3 Effect of bubble size and position on total Nusselt number for bubble at $\theta = \pi/2$ and $V_B = U_{mf}$

pressure along a bubble boundary (i.e. constant potential) is satisfied by functions of the form

$$H(Z) = F(Z) - \bar{F}\left(\frac{b_i{}^2}{Z - Z0_i}\right) \qquad (4)$$

The flow-field within contacting bubbles is assumed to be irrotational though unsteady. The normal component of interstitial gas velocity at the bubble surface is used as a boundary condition on this field and the complex potential describing the flow is assumed to be of the form

$$W_B = \sum_{n=0}^{N} \left(D_n Z^n + \bar{D}_n \left(\frac{a^2}{Z}\right)^{-n}\right) \qquad (5)$$

where a is the tube radius and the complex coefficients, D_n, are obtained by making a least-square fit to the boundary condition using the Householder transformation (see Ralston and Rabinowitz [13]). This represents an improvement over the mass flow averaged velocity used in [1].

The emulsion phase velocity field outside a contacting bubble requires special consideration because the bubble and tube boundaries intersect and the image method described above cannot be used. However, it has been found that successive application of the Joukowski transformation

$$\zeta = c\left(\frac{\tau+1}{\tau-1}\right) \qquad (6)$$

where $\tau = [(Z+c)/(Z-c)]^{1/\alpha}$, $\alpha = 3/2$, and c is half of the chord length of the intersected region, will produce two pseudocircles with a negligible region of intersection. This transformed geometry is approximated as two contacting circles and the image method is applied on the transform plane.

Generally 5 image reflections are required when bubbles contact the tube while two or three reflections are sufficient for object separations greater than 1/4 tube diameter for boundary-condition accuracy to within 5 percent.

Results

The combined hydrodynamic and heat-transfer model described above has been used to obtain the effects of bubble size, position and velocity and of adjacent tubes on local and total heat transfer to an immersed tube. In carrying out these calculations, the parameters of Catipovic's experiments for 4 mm particles [2] were selected since the gas convection heat-transfer model has been validated by those results. These parameters are listed in Table 1 and results of calculations are presented in Figs. 1–4 and Table 2.

Figure 1 shows the effect of the velocity of a single contacting bubble upon the Nusselt number (based upon tube diameter) distribution. The case of zero bubble velocity is essentially that reported previously [1] but with refinements to the hydrodynamic model discussed above. Note that local values of Nusselt number are affected by the velocity of the bubble, but the total heat transfer ($\bar{Nu}_D$) remains nearly

Table 1 Calculation parameters

Reynolds number (Re_D)	5900
Bed temperature	308 K
Wall temperature	376 K
Bed voidage	0.5
Surface voidage	
Lower stagnation point	0.90 ($\theta = 0$ to 0.452 rad)*
Side	0.55 ($\theta = 0.498$ to 2.29 rad)
Stack	0.44 ($\theta = 2.36$ to 3.1416 rad)
Turbulence intensity	0.2
Prandtl number	0.7
Particle dia/Tube dia	0.0787

*θ from lower stagnation point, linear interpolation between limits, e.g., 0.452–0.498

Table 2 Effect of adjacent tubes

Arrangement Spacing P/D	|←P→|		Total Nusselt number			
1.25	275.8	259.8	266.4	313.3	256.1	-
1.5	263.3	-	-	286.8	-	247.9
2	-	247.8	244.9	265.5	243.8	263.4
2.5	249.3	-	-	-	-	-
3	-	244.6	244.9	252.2	242.5	275.6
3.5	245.8	-	-	-	-	-
5	244.0	-	-	-	-	-
∞	242.4	242.4	242.4	242.4	242.4	286.8

Note: Tubes 1 and 2 are fixed at P/D = 1.5, while the position of 3 and 4 is varied as indicated.

constant as the bubble velocity increases from 0 to 2 U_{mf}. Since bubble velocity depends strongly upon superficial velocity, these results suggest that the Nusselt number ought to be independent of superficial velocity once the bed is fluidized and provided the bubble contact fraction is fixed. Also note that the presence of the bubble decreases the tube Nusselt number by about 20 percent relative to the level without bubbles present. These results agree qualitatively with experiments reported by Catipovic [2].

The effect of bubble size and position on the total heat transfer to a single tube is shown in Figs. 2, 3 and 4. For these calculations, the bubble velocity was fixed at U_{mf}, since bubble velocity has a small effect on total heat transfer. Again the bubble interaction effect was found to be small; the maximum change in total Nusselt number is 33 percent for a bubble 3 times tube size and nearly contacting the tube.

A summary of the effect of adjacent tubes upon total heat transfer in the absence of bubbles is presented in Table 2. The interstitial gas velocity for these cases was obtained using the criterion of equation (3). Generally, adjacent tubes were found to increase the heat transfer due to increases in the local interstitial gas velocity. The maximum increase was obtained with one tube on each side and as close as possible to the reference tube. But when the reference tube was surrounded by 4 tubes, very little change in Nusselt number was observed. This suggests that tubes should be placed in rows with close horizontal spacing between adjacent tubes and wide vertical spacing between adjacent rows. The benefit of such an arrangement is suggested by the last column of Table 2 which shows that a horizontal spacing of 1.5 and a vertical spacing of 3 diameters could provide an increase of 15 percent over the single tube level. According to the model, horizontal spacings of less than 1.5 dia would further improve this benefit but are impractical because of the poor fluidization characteristics (bridging of particles) reported by Lese and Kermode [14] and Zabrodsky et al. [15]. Zabrodsky et al. [15] obtained some data for the effect of tube spacing for an in-line tube array in a large particle bed (2 mm – 3 mm dia) and found that a horizontal spacing of 2–3 tube dia provided the best performance. However, these data and those of Catipovic [2] (with a pitch of 2 dia) show a slight decrease in total heat transfer relative to single tube data while the data reported by Chandran et al. [16] for intermediate (.650 mm) particles indicates a slight increase at a pitch of 3.3 dia. Without detailed hydrodynamic information, it is difficult to assess the accuracy of the model in this case. However the magnitude of the effect is comparable to that observed experimentally.

Acknowledgments

References

1 Adams, R. L. and Welty, J. R., "A Gas Convection Model of Heat Transfer in Large Particle Fluidized Beds," *AIChE Journal*, Vol. 25, May 1979, pp. 395–405.

2 Catipovic, N. M., "Heat Transfer to Horizontal Tubes in Fluidized Beds: Experiment and Theory," Ph.D. thesis, Oregon State University, Corvallis, Ore., 1979.

3 Catipovic, N. M., Fitzgerald, T. J., George, A. H., and Welty, J. R., "Experimental Validation of the Adams-Welty Model for Heat Transfer in Large-Particle Fluidized Beds," submitted to *AIChE Journal*, 1980.

4 Adams, R. L., "An Analytical Model of Heat Transfer to a Horizontal Cylinder Immersed in a Gas Fluidized Bed," Ph.D. thesis, Oregon State University, Corvallis, Ore., 1977.

5 Adams, R. L., "An Approximate Formula for Gas Convection Dominant Heat Transfer in Large-Particle Fluidized Beds," ASME JOURNAL OF HEAT TRANSFER, Vol. 103, 1981, pp. 395–397.

6 Davidson, J. F. and Harrison, D., eds., *Fluidization*, Academic Press, New York, 1971.

7 Kunii, D. and Levenspiel, O., *Fluidization Engineering*, Wiley, New York, 1962.

8 Davidson, J. F., "Symposium on Fluidization—Discussion, *Transaction Inst. of Chemical Engineering*, Vol. 39, p. 230, 1961.

9 Martin-Gautier, A. L. F. and Pyle, D. L., "The Fluid Mechanics of Single Bubbles," *Fluidization Technology*, Vol. I, edited by D. L. Keairns, Hemisphere Publishing, Washington, D.C., 1976.

10 George, A. H., Catipovic, N. M., and Welty, J. R., "An Analytical Study of Heat Transfer to a Horizontal Cylinder in a Large Particle Fluidized Bed," ASME Paper 79-HT-78, 1979.

11 Halsey, N. D., "Potential Flow Analysis of Multielement Airfoils Using Conformal Mapping," AIAA Paper 79-0271, 1979.

12 Batchelor, G. K., *An Introduction to Fluid Dynamics*, Cambridge University Press, England, 1967.

13 Ralston, A. and Rabinowitz, P., *A First Course in Numerical Analysis*, 2nd ed., McGraw-Hill, New York, 1978.

14 Lese, H. K. and Kermode, R. I., "Heat Transfer from a Horizontal Tube to a Fluidized Bed in the Presence of Unheated Tubes," *Canadian Journal of Chemical Engineering*, Vol. 50, 1972, pp. 44–48.

15 Zabrodsky, S. S., Epanov, Y. G., Galershtein, D. M., Saxena, S. C., and Kolar, A. K., "Heat Transfer in a Large-Particle Fluidized Bed with Immersed In-Line and Staggered Bundles of Horizontal Smooth Tubes," *International Journal of Heat and Mass Transfer*, Vol. 24, No. 4, 1981, pp. 571–579.

16 Chandran, R., Chen, J. C., and Staub, F. W., "Local Heat Transfer Coefficient Around Horizontal Tubes in Fluidized Beds," ASME JOURNAL OF HEAT TRANSFER, Vol. 102, 1980, pp. 152–157.

The Analysis of Fin Assembly Heat Transfer
by a Series Truncation Method

P. J. Heggs[1], D. B. Ingham[1], and M. Manzoor[2]

Nomenclature

· Aug = augmentation
Bi_1 = $h_1 P/k_w$, Biot number
Bi_2 = $h_2 P/k_w$, Biot number
h_1, h_2 = heat transfer coefficients
k_f, k_w = thermal conductivities
1 = fin length
L = $1/P$, aspect ratio
P = half fin pitch
t = half fin-base thickness
T = t/P, aspect ratio
w = wall thickness
W = w/P, aspect ratio
X = x/P
Y = y/P
κ = k_f/k_w
θ = temperature distribution
θ_1, θ_2 = fluid temperatures
ϕ = $(\theta - \theta_2)/(\theta_1 - \theta_2)$, dimensionless temperature distribution
* = approximate value

Subscripts

1 = plain side
2 = fin side
f = fin
w = wall

Introduction

The accurate prediction of the performance of finned heat exchangers is essential for compact and efficient design. However, the analysis of fin problems is conventionally based on the assumption that the heat flow is unidirectional because this, in general, facilitates an analytical treatment, e.g. [1, 2]. The early investigations into the applicability of the one-dimensional approximation restricted attention solely to the fin and concluded that two-dimensional effects are negligible provided the transverse Biot number, based on the fin-base thickness, is much less than unity [3, 4, 5]. Recent investigations of the combined fin and supporting surface have shown that the presence of fins induces two-dimensional effects within the supporting surface and these may in turn act to produce two-dimensional variations within the fin, e.g., [6–9]. Suryanarayana [7] has reported that the difference between heat transfer rates predicted by one and two-dimensional analyses can be as much as 80 percent. It is therefore essential for the effective design of finned heat exchangers to consider the complete fin assembly and to employ a multidimensional analysis.

The two-dimensional analysis of the conductive-convective heat flow through an assembly of longitudinal rectangular fins attached to a plane wall, as shown in Fig. 1, requires the solution of a Laplacian mixed boundary-value problem [7–9].
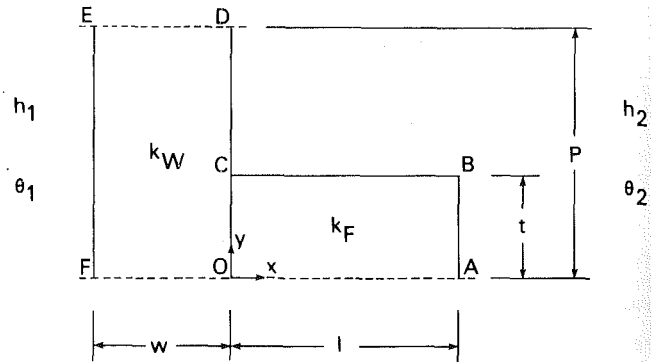
Fig. 1 Schematic representation of a fin assembly

In the previous examinations of this problem, solutions have been computed employing either the finite-difference method [7–9] or the finite-element method [9]. However, these methods necessitate the solution of very large systems of simultaneous linear algebraic equations in order to produce accurate solutions. Furthermore, Stones [9] has shown that for a particular range of the system parameters neither of these methods produces satisfactory solutions.

In this study it is shown that, contrary to the inferences of the previous investigations [7–9], this particular fin assembly problem is susceptible to an analytical treatment. An extension of the separation of variables technique is devised which enables the derivation of a truncated series solution. However, this solution is not in a closed form. The determination of the coefficients associated with the series expansions requires the solution of a system of linear algebraic equations. Nevertheless, in order to obtain solutions of comparable accuracy, the series truncation method requires the solution of considerably fewer equations than that required by either the finite-difference or the finite element methods. Thus, the series truncation method facilitates a considerable reduction in the computational storage and time requirements. Furthermore, it is shown that the series truncation method yields accurate solutions even for problems for which the finite-difference and finite-element methods fail to provide acceptable results.

Analysis

The following analysis is based upon the classical assumptions employed in the examination of conducting-convecting finned surfaces, namely, constant thermal conductivities, uniform heat transfer coefficients and perfect wall-to-fin contact.

The geometrical symmetry of an assembly of equally-spaced longitudinal rectangular fins attached to a plane wall indicates that it is only necessary to examine that section of the assembly shown schematically in Fig. 1. Thus, for steady-state, two-dimensional conductive heat flow, the determination of the assembly temperature distribution, $\phi(X, Y)$, involves the simultaneous solution of [8],

$$\frac{\partial^2}{\partial x^2} \phi_f + \frac{\partial^2}{\partial Y^2} \phi_f = 0 \quad \text{within the fin} \tag{1}$$

and

$$\frac{\partial^2}{\partial x^2} \phi_w + \frac{\partial^2}{\partial Y^2} \phi_w = 0 \quad \text{within the wall} \tag{2}$$

subject to the boundary conditions [8], on

$$OA \quad \frac{\partial \phi_f}{\partial Y} = 0 \tag{3a}$$

on

$$AB \quad \frac{\partial \phi_f}{\partial X} = -\frac{Bi_2}{\kappa} \phi_f \tag{3b}$$

on

$$BC \quad \frac{\partial \phi_f}{\partial Y} = -\frac{Bi_2}{\kappa} \phi_f \tag{3c}$$

on

$$CO \quad \phi_f = \phi_w \tag{3d}$$

and

$$\frac{\partial \phi_w}{\partial X} = \kappa \frac{\partial \phi_f}{\partial X} \tag{3e}$$

on

$$CD \quad \frac{\partial \phi_w}{\partial X} = -Bi_2 \phi_w \tag{3f}$$

on

$$DE \quad \frac{\partial \phi_w}{\partial Y} = 0 \tag{3g}$$

on

$$EF \quad \frac{\partial \phi_w}{\partial X} = -Bi_1(1 - \phi_w) \tag{3h}$$

on

$$FO \quad \frac{\partial \phi_w}{\partial Y} = 0. \tag{3i}$$

The heat flow through the assembly may therefore be parameterized by the Biot number, Bi_1 and Bi_2, the ratio of the thermal conductivities, κ, and the aspect ratios, L, T, and W.

Integrating equations (1) and (2) by the application of the separation of variables method [10] and then enforcing the boundary conditions (3a), (3b), (3c), (3g), (3h) and (3i) gives

$$\phi_f(X,Y) =$$

$$\sum_{n=1}^{\infty} \frac{a_n(\cosh\lambda_n(L-X) + \frac{Bi_2}{\kappa\lambda_n}\sinh\lambda_n(L-X))\cos\lambda_n Y}{\cosh\lambda_n L + \frac{Bi_2}{\kappa\lambda_n}\sinh\lambda_n L} \tag{4}$$

and

$$\phi_w(X,Y) = 1 + b_0(1 + Bi_1(W+X))$$

$$+ \sum_{n=1}^{\infty} \frac{b_n(\cosh\mu_n(W+X) + \frac{Bi_1}{\mu_n}\sinh\mu_n(W+X))\cos\mu_n Y}{\cosh\mu_n W + \frac{Bi_1}{\mu_n}\sinh\mu_n W} \tag{5}$$

where the eigenvalues λ_n and μ_n are defined by

$$\lambda_n \tan\lambda_n T = Bi_2/\kappa$$

and

$$\mu_n = n\pi$$

and the constant coefficients a_n and b_n are, as yet, un-determined.

Enforcing the remaining boundary conditions, (3c), (3d), and (3e), gives

$$0 = 1 - \sum_{n=1}^{\infty} a_n \cos\lambda_n Y + b_0(1 + Bi_1 W) + \sum_{n=1}^{\infty} b_n \cos\mu_n Y,$$

$$0 \le Y \le T \tag{6}$$

$$0 = \kappa \sum_{n=1}^{\infty} a_n L_n \cos\lambda_n Y + b_0 Bi_1 + \sum_{n=1}^{\infty} b_n M_n \cos\mu_n Y, 0 \le Y \le T$$

$$\tag{7}$$

and

$$0 = Bi_2 + b_0(Bi_1 + Bi_2(1 + Bi_1 W))$$

$$+ \sum_{n=1}^{\infty} b_n(Bi_2 + M_n)\cos\mu_n Y, T \le Y \le 1 \tag{8}$$

where

$$L_n = \lambda_n \left(\tanh\lambda_n L + \frac{Bi_2}{\kappa\lambda_n} \right) / \left(1 + \frac{Bi_2}{\kappa\lambda_n} \tanh\lambda_n L \right) \tag{9}$$

and

$$M_n = \mu_n \left(\tanh\mu_n W + \frac{Bi_1}{\mu_n} \right) / \left(1 + \frac{Bi_1}{\mu_n} \tanh\mu_n W \right). \tag{10}$$

Multiplying equation (7) by $\cos\lambda_m Y$ and then integrating over the range $0 \le Y \le T$ defines a relation between the a_n and b_n, namely,

$$a_m = \frac{-b_0 Bi_1 \frac{\sin\lambda_m T}{\lambda_m} - \sum_{n=1}^{\infty} b_n M_n \int_0^T \cos\lambda_m Y\cos\mu_n Y dY}{\frac{\kappa}{4\mu_m}(2\mu_m T + \sin 2\mu_m T)L_m},$$

$$m = 1, 2, \ldots \tag{11}$$

Thus, it remains to determine the coefficients b_n. However, the combined complexity of the governing relations, namely equations (6), (8) and (11), precludes the possibility of obtaining an explicit expression for the coefficients b_n. In fact, these coefficients can only be determined approximately. The temperature distributions $\phi_f(X,Y)$ and $\phi_w(X,Y)$ are approximated by the first N terms in each of the series expansions (4) and (5), respectively, and the relations (6) and (8) are accordingly modified to

$$0 = 1 + \sum_{n=1}^{N}$$

$$\frac{\left\{ b_0^* Bi_1 \frac{\sin\lambda_n T}{\lambda_n} - \sum_{m=1}^{N} b_m^* M_m \int_0^T \cos\lambda_n Y\cos\mu_m Y dY \right\}\cos\lambda_n Y}{\frac{\kappa}{4\mu_n}(2\mu_n T + \sin 2\mu_n T)L_n}$$

$$+ b_0^*(1 + Bi_1 W) + \sum_{n=1}^{N} b_n^* \cos\mu_n Y, 0 \le Y \le T \tag{12}$$

and

$$0 = Bi_2 + b_0^*(Bi_1 + Bi_2(1 + Bi_1 W))$$

$$+ \sum_{n=1}^{N} b_n^*(Bi_2 + M_n)\cos\mu_n Y, T \le Y \le 1 \tag{13}$$

where the coefficients a_n^* have been replaced using the approximate form of equation (11), namely,

$$a_m^* = \frac{-b_0^* Bi_1 \frac{\sin\lambda_m T}{\lambda_m} - \sum_{n=1}^{N} b_n^* M_n \int_0^T \cos\lambda_m Y\cos\mu_n Y dY}{\frac{\kappa}{4\lambda_m}(2\lambda_m T + \sin 2\lambda_m T)L_m},$$

$$m = 1, 2, \ldots, N$$

and the asterisk denotes the approximate value of the respective quantity.

In order to determine the $N+1$ unknown coefficients, b_0^*, $b_1^*, \ldots, b_N^*$, and therefore the solution, a system of linear algebraic equations is generated from the expressions (12) and (13). Equations (12) and (13) are multiplied by $\cos \mu_n Y$ and then equation (12) is integrated over the range $0 \leq Y \leq T$, and equation (13) is integrated over the range $T \leq Y \leq 1$. Combining the integrated relations and then collocating for $m = 1,2,\ldots,N$ generates N equations in the $N+1$ unknown b_n^*. An additional equation is obtained by integrating equation (12) over the range $0 \leq Y \leq T$ and equation (13) over the range $T \leq Y \leq 1$. The resulting system of simultaneous linear algebraic equations is solved employing a Gaussian elimination technique [10] and thus $\phi_f^*(X,Y)$ and $\phi_w^*(X,Y)$ are determined.

The heat flow through the fin assembly is most conveniently expressed in the form of an augmentation factor, Aug, defined as the ratio of the heat transfer rate of the fin assembly to that of the unfinned wall operating under the same conditions [9]. Corresponding to the approximate solutions $\phi_f^*(X,Y)$ and $\phi_w^*(X,Y)$, this augmentation factor may be obtained by integrating the heat flux at the surface EF, and is given by,

$$\text{Aug}^* = -b_0^* Bi_1 \left(\frac{1}{Bi_1} + W + \frac{1}{Bi_2} \right) \qquad (14)$$

Thus, the series truncation method enables the fin assembly heat transfer rate to be evaluated without actually computing the temperature distribution within the fin assembly. In contrast, the finite-difference and finite-element formulations automatically generate the temperature distribution throughout the fin assembly section OABCDEFO.

Results and Discussion

Solutions have been obtained for a wide range of the system parameters, Bi_1, Bi_2, κ, L, T and W. For each particular problem solutions were computed for the cases $N = 25, 50, 100$ and 200. In order to illustrate the performance of the series truncation method the results for three particular problems are presented here:

Aug*

Problem	$N=25$	$N=50$	$N=100$	$N=200$
A	5.1202	5.1167	5.1153	5.1149
B	1.0432	1.0433	1.0434	1.0434
C	1.1366	1.1371	1.1374	1.1375

These results correspond to the problems defined by:

Problem	Bi_1	Bi_2	κ	L	T	W
A	1.00	0.01	1.0	10.0	0.5	5.0
B	2.25	0.75	1.0	10.0	0.5	5.0
C	2.25	0.75	10.0	10.0	0.5	5.0

Problem A represents the performance of a stainless-steel finned heat exchanger with forced convection of water on the plain side and free convection of air on the fin side. The system parameters for the problems B and C lie in the range $Bi_1 > 2.0$ and $Bi_2 > 0.5$ for which Stones [9] has indicated that neither the finite-difference method nor the finite-element method provide acceptable solutions.

The results for the problems A, B and C illustrate various features of the series truncation technique and are characteristic of those observed for other values of the system parameters. In particular, in all cases, the augmentation factor, Aug*, displays a monotonic convergent behavior as the order of the approximation is improved, i.e. as more terms are taken in the approximate representations of

$\theta_f(X,Y)$ and $\theta_w(X,Y)$. Furthermore, the first three significant figures of the solution remain unchanged as the approximation is refined from $N = 50$ to $N = 200$.

Stones [9] performed a similar convergence study for the finite-difference and finite-element methods and concluded that even with as many as 991 nodes (requiring the solution of a system of 991 linear algebraic equations), these methods are usually only accurate to two significant figures. It is therefore apparent that the series truncation method facilitates substantial reductions in the computional requirements because for the case $N = 50$ the series truncation method only requires the solution of a system of 51 linear algebraic equations, but is accurate to at least three significant figures. The relative inaccuracy of the finite-difference and finite-element methods, in comparison to the series truncation method, in determining the augmentation factor, (which is a global quantity), is probably due to the fact that the series truncation method is a global technique whereas the finite difference and finite-element methods are discrete techniques.

Conclusions

A mathematically rigorous method has been devised for the solution of a fin assembly heat transfer problem. This method uses the separation of variables technique in order to integrate the governing differential equations exactly, and approximations are only introduced in order to satisfy the boundary conditions pertaining to the wall-to-fin interface. The results obtained indicate that this method is more accurate and computationally more economical than the finite-difference and finite-element methods. Furthermore, this method gives accurate solutions even for problems for which the finite-difference and finite-element methods fail to provide acceptable results, e.g., see the results for problems B and C given in the preceeding section.

Acknowledgment

References

1 Gardner, K. A., "Efficiency of Extended Surface," Transactions of the ASME, Vol. 67, 1945, pp. 621–631.

2 Mikk, I., "Convective Fin of Minimum Mass," International Journal of Heat and Mass Transfer, Vol. 23, 1980, pp. 707–711.

3 Irey, R. K., "Errors in the One-Dimensional Fin Solution," ASME JOURNAL OF HEAT TRANSFER, Vol. 90, 1968, pp. 175–176.

4 Levitsky, M., "The Criterion for the Validity of the Fin Approximation," International Journal of Heat and Mass Transfer, Vol. 15, 1972, pp. 1960–1963.

5 Lau, W., and Tan, C. W., "Errors in One-Dimensional Heat Transfer Analysis in Straight and Annular Fins," ASME JOURNAL OF HEAT TRANSFER, Vol. 95, 1973, pp. 549–551.

6 Sparrow, E. M., and Lee, L., "Effects of Fin Base-Temperature Depression in a Multifin Array," ASME JOURNAL OF HEAT TRANSFER, Vol. 97, 1975, pp. 463–465.

7 Suryanarayana, N. V., "Two-Dimensional Effects on Heat Transfer Rates from an Array of Straight Fins," ASME JOURNAL OF HEAT TRANSFER, Vol. 99, 1977, pp. 129–132.

8 Heggs, P. J., and Stones, P. R., "The Effects of Dimensions on the Heat Flow Rate through Extended Surfaces," ASME JOURNAL OF HEAT TRANSFER, Vol. 102, 1980, pp. 180–182.

9 Stones, P. R., Ph.D. Thesis, Leeds University, England, 1980.

10 Ralston, A., A First Course in Numerical Analysis, McGraw-Hill, New York, 1965.

Determination of Physical Properties of Heat Transfer Sensors From Vacuum Heat Loss Observations

M. R. Davis[1]

1 Introduction

A particular motivation for the work is that when observing small surface convective power loss rates in the presence of a relatively large conduction power loss to the mountings, it is necessary to ensure that the conduction loss is accurately accounted for. This depends critically upon using the correct material properties of the sensor so that the equilibrium case for zero heat-transfer coefficient ($h \rightarrow 0$) is satisfied. If this is not the case, solutions for small heat transfer coefficients become very inaccurate.

When fine wires or thin surface films are used as heat-transfer sensors, as described by Davis and Davies [1] and Davis [2], it is necessary to know the temperature variation of sensor electrical resistance and thermal conductivity if overall power loss is used to determine surface heat-transfer coefficients. Published data for material properties are not always reliable in particular when the metal is formed by different processes such as the cold drawing used in producing fine wires. In this note the measurement of pure conduction power loss for a set of elements is used as the basis for determining their physical properties. Whilst only fine wire elements will be discussed, similar principles can be applied to thin film elements and other heat transfer gauges. Although the material resistivity can be easily verified in a heated bath at different temperatures, other properties such as conductivity require alternative means of verification.

2 Analytical Method

The thermal equilibrium of a long cylindrical wire element is governed by the equation

$$\frac{\pi d^2}{4} \frac{d}{dx}\left(k\frac{dT}{dx}\right) + \frac{4i^2\rho}{\pi d^2} - \pi dh(T-T_f)$$
$$ + \sigma i \frac{dT}{dx} - \epsilon\sigma_0\pi d(T^4 - T_0{}^4) = 0 \qquad (1)$$

where ϵ = surface emissivity, σ_0 = Stefan-Boltzmann constant, σ = Seebeck thermoelectric coefficient, d is the wire diameter, T its temperature (°K), T_f the surrounding fluid temperature, i the heating current, h the average surface heat transfer coefficient, and k and ρ the temperature dependent thermal conductivity and resistivity of the wire material. Solution of equation (1) for the temperature distribution along the coordinate x along the wire axis must match the conditions of known end-temperature at the mountings. The radiation term was retained in the computation but was found to be less than 0.05 percent of the total power loss for the cases to be considered. The Seebeck thermoelectric term was also retained in the computation, although it too was small, being less than 0.1 percent of the total power loss. End temperature of the wire element were observed directly using thermocouples, being only slightly above ambient temperatures due to the relative massiveness of the mounting supports. Care was taken to select thermocouples which when mounted were relatively insensitive to induced voltages from heating current. The heating current was reversed and an average reading of the thermocouple voltage taken to
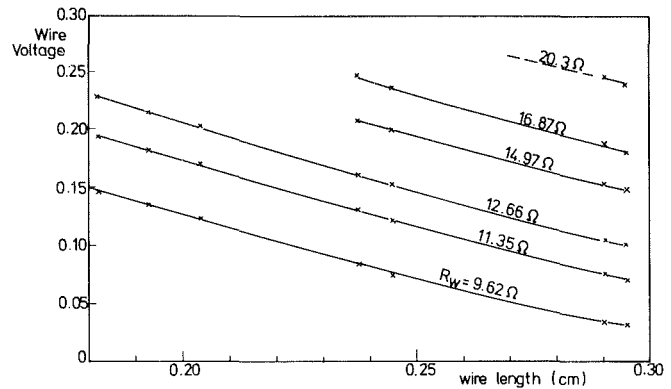
Fig. 1 Variation of power loss in vacuum with wire operating resistance and length (tungsten wires of diameter 5.0 μm), length = 2l

eliminate this effect. When a known current i is passed through the wire of resistance R_W ($i = E/R_W$), the heat-transfer coefficient h may be determined as described by Davis and Davies [1], provided that the wire total resistance and the variation of k and ρ with temperature are known. The wire current and voltage were observed using a high-precision, six-digit Solartron LM1440 voltmeter. The equation is solved by step-by-step numerical integration, over the whole length of the wire from $x = -1$ to $x = +1$ (total length = 2l), iterating for h and the end-temperature gradient (dT/dx) until the boundary conditions of end-temperature and the overall wire resistance and integrated resistance from the solution

$$\int_{-1}^{+1} \frac{4\rho}{\pi d^2}\, dx = R_W$$

are matched. When the wire is mounted in a vacuum, $h = 0$ and it is then possible to investigate from similar iterative numerical solutions what the wire properties k and ρ must be if the observed heating current and total wire resistance are known. By using a set of observations in vacuum of heating current and resistance for wires of differing length it is then possible to determine what parameters k and ρ produce consistent solutions for the whole set of wires and operating conditions.

3 Experimental Observations

Observations were made with a set of tungsten wires of lengths between 1.5 and 3mm, measured using a traversing microscope. The wire diameter (5.0 μm) was checked using a electron microscope and calibrated diffraction grating. The wires were made of tungsten for which the resistivity and conductivity of the pure material are given in an extensive review by Smithells [3] in terms of a dimensionless temperature $\tau = (T-54)/237$, as

$$\rho = (\rho_a\tau + \rho_b\tau^2)\times 10^{-6} \text{ ohm cm}$$
$$k = k_a(\tau + \tau_a)(\rho_a\tau + \rho_b\tau^2) \text{ watt/cm}°C$$

where $\rho_a = 5.53$, $\rho_b = 0.227$, $k_a = 6.92$, $\tau_a = 0.228$. The tungsten wires were attached to nickel mounting prongs by copper plating and soldering. During this process it was quite possible that the wire was mechanically damaged, and undamaged wires were selected on the basis that damage would raise the element resistance. Thus a smaller heating current would be needed to heat a damaged element to a prescribed resistance. Figure 1 shows the variation of voltage applied to the wires which were selected as undamaged; wires whose applied voltage to attain a prescribed resistance was more than 2 percent below the various curves were rejected. Checks were made by observing the variation of heat loss with surrounding gas pressure to ensure that the surface heat loss was negligible, an absolute pressure of 3 μm of mercury being sufficient to introduce an error of less than 0.05 percent in the

power loss. The wires were operated in a conventional constant resistance anemometer [Davis, [4]],, and attained maximum temperature of approximately 500°C.

Numerical integration of equation (1) was carried out for $h = 0$ and, using the above property values, a solution beginning at ambient temperature. The initial temperature gradient (dT/dx) was varied until the solution passed through
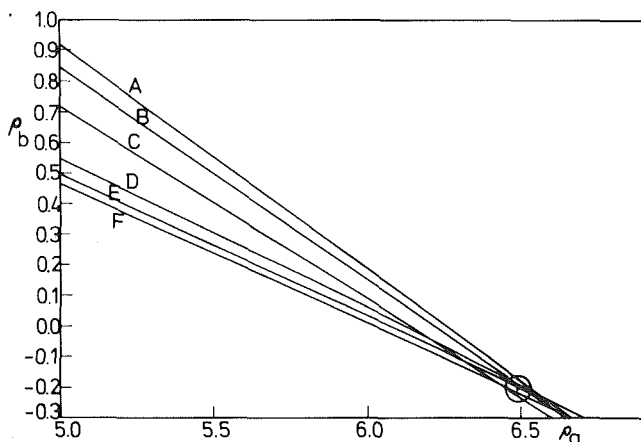

Fig. 2 Resistivity properties required to match vacuum thermal equilibrium solution (other properties have nominal values); wire length and resistance: (A) 0.295 cm, 13 Ω; (B) 0.240 cm, 11 Ω; (C) 0.200 cm, 10 Ω; (D) 0.200 cm, 13 Ω; (E) 0.240 cm, 16.5 Ω; (F) 0.295 cm, 20.3 Ω. Circle denotes properties which are consistent with all observations of power loss.
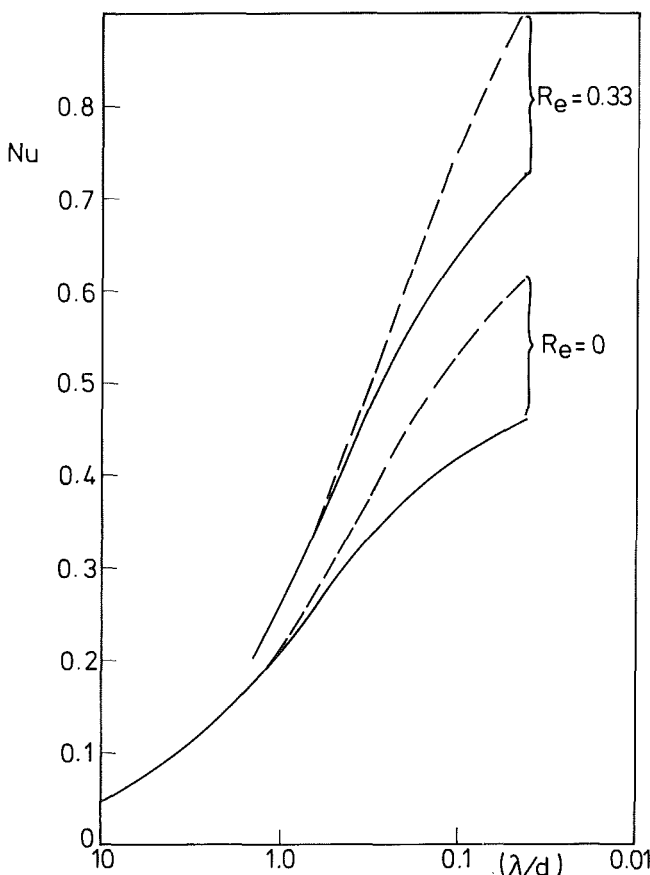

Fig. 3 Variation of sensor heat loss with Knudsen number (λ/d), Reynolds number and wire temperature (observed in a flow of argon gas at 20°C and reduced pressure using a 1.79 mm long tungsten wire of diameter 5.0 μm operated in the range 9.6 Ω < R_W < 15 Ω). Solid lines: T_W = 160°C; dashed lines: T_W = 393°C; Vertical scale: Nusselt number based on ambient gas conditions and wire diameter (Each curve based on approximately 100 observed points).

ambient temperature again at the other end of the wire ($x = +1$). At this stage the resistance calculated by integration along the solution was checked, and then changes were made to one of the property parameters and further solutions obtained until the correct value of resistance was obtained. The process was repeated for 6 conditions obtained from Fig. 1, corresponding to extremes of length and wire operating temperature and with differing combinations of the parameters ρ_a, ρ_b, k_a and τ_a, which define the material properties. Using the nominal values of k_a and τ_a, Fig. 2 shows the values of ρ_a and ρ_b, which were required to match the wire resistance and temperature boundary conditions. As can be seen, the curves intercept closely at $\rho_a = 6.49$, $\rho_b = -0.20$, and indicate that these values will match the complete set of tested elements with only a small variation of ± 0.02 in each of these parameters. It thus appears that the observations of power loss indicate that these values are the correct property values for the batch of wires used.

Solution, of the wire temperature distribution requires that values of wire length and diameter, end temperature, heating current and resistance, as well as of k_a and τ_a be used, and the influence of varying all of these other parameters in conjunction with variation of ρ_a was investigated. None of the other parameters showed a convergence similar to that of Fig. 2, and it was concluded that the material of the batch deviated from the nominal published resistivity behaviour. As a check on this conclusion observations of the temperature dependence of the resistance of a wire element were made directly by immersing it in a heated oil bath in the range 20°C–150°C. It was found that the observed resistivity variation deviated from that expected by the convergence of lines in Fig. 2 by approximately 5 percent. By comparison, the nominal published data for tungsten deviated by 21 percent, the published data having a stronger increase of resistivity with temperature. It is concluded that the process by which the very fine wires are cold drawn modifies the material properties from their bulk values.

The applications of heat transfer sensors whose properties are known to the observation of heat transfer mechanisms in slip flow is illustrated in Fig. 3. The sensor heating current has been computed as a function of surface heat-transfer coefficient, determined from numerical solutions of equation (1) as described above. The local heat-transfer coefficient, h, at any position on the wire was assumed to vary linearly with the local temperature, the variation being adjusted until solutions for different wire operating resistances were all matched. Because the sensor properties have been determined on the basis of vacuum power loss observations, the limit $h \to 0$ is accurately approached by these calculations, and thus allows the sensors to be used reliably over a wide range of surface heat loss rates. It is seen that there is a steady increase of temperature sensitivity of the Nusselt number as the Knudsen number is reduced for both forced and natural convective cooling. This demonstrates that temperature dependence of the Nusselt number is determined by the temperature dependence of the gas with thermal conductivity, which increasingly affects the cooling process as continuum conditions are approached. Under free molecular conditions the Nusselt number is found to be independent of wire temperature. The form of the transition curves through the range $0.1 < Kn < 10$ is consistent with that predicted analytically by Madden and Piret [5] for Re = 0, although their analysis assumed a constant (temperature independent) conductivity for the gas and did not indicate the temperature dependence of the Nusselt number demonstrated here. A fuller discussion of heat transfer in the slip region is given by Davis and Davies [1].

References

1 Davis, M. R. and Davies, P.O.A.L., "Factors Influencing the Heat

Transfer from Cylindrical Anemometer Probes," *International Journal of Heat and Mass Transfer*, Vol. 15, 1972, pp. 1659–1677.

2 Davis, M. R., "Application of Hot Wires to Measurements in Freely Expanding Jets," *AIAA Journal*, Vol. 11, No. 1, 1973, pp. 113–115.

3 Smithells, C. J., *Tungsten*, Chapman and Hall, 3rd ed. 1952.

4 Davis, M. R., "The Dynamic Response of Constant Resistance Anemometers," *Journal of Physics E: Scientific Instruments*, Vol. 3 No. 1, 1970, pp. 15–20.

5 Madden, A. J. and Piret, E. L., *Heat Transfer from Wires to Gases at Sub-atmospheric Pressures Under Natural Convection Conditions*. Institute of Mechanical Engineers, London, 1951, p. 328.

Effect of Fluid Carryover on Regenerator Performance

P. J. Banks[1]

1 Introduction

A regenerative heat exchanger or regenerator transfers sensible heat between two fluid streams by means of a porous matrix through which the fluid streams are passed alternately. In a rotary regenerator the matrix is rotated through the fluid streams, while in a fixed-bed regenerator the matrix is divided into two halves and the fluid streams are switched through the halves alternately by means of valves. Heat is transferred from one fluid stream to the matrix and then from the matrix to the other fluid stream. Transfer also occurs via the fluid contained in the matrix passages, since this fluid is carried from one fluid stream to the other by the rotation of the matrix, or the switching of the fluid streams.

Longstanding theoretical predictions of regenerator transfer performance are for transfer via the matrix [1-3]. However, in recent years the effect of fluid carryover has been included in finite difference solutions of the governing equations obtained utilizing digital computers [4-7]. Results have been presented for the effect of carryover on the effectiveness of a symmetric balanced counterflow regenerator for certain values and ranges of the parameters determining effectiveness. In this note, the effect is shown on a design chart applicable for all operating conditions of such a regenerator of practical design for transfer between gas streams. The chart was obtained using digital computer programs developed by Maclaine-cross [3, 6, 8] for calculating regenerator effectiveness both including and neglecting the effect of carryover.

The parameter carryover effect is introduced. It is defined as the increase in regenerator effectiveness resulting from fluid carryover divided by the carryover ratio, which is the ratio of the thermal capacity rates of fluid carryover and the fluid stream with minimum thermal capacity rate. Carryover effect is shown to be closely independent of the carryover ratio for regenerators of practical design for gas streams, enabling it to be presented on design chart which uses the parameters determining regenerator effectiveness neglecting the effect of carryover, and thus supplements the existing chart [2, 3] for this effectiveness.

The design chart for carryover effect achieves the objective of including an additional parameter for carryover with a small number of charts, for which Maclaine-cross [6] has provided another design method. He showed that the effect of carryover may be included approximately in predictions neglecting the effect by modifying the values of matrix specific heat and matrix to fluid heat-transfer coefficient. A comparison of this design method with the use of carryover effect is made in section 4 which follows.

[1] Division of Energy Technology, Commonwealth Scientific and Industrial Research Organization, Highett, Victoria 3190, Australia

The formulation of the design chart for carryover effect was stimulated by the similarity between fluid carryover and fluid flows through a regenerator that bypass the matrix [9], suggested to the author by a colleague [10].

Consideration is given to symmetric balanced counterflow regenerators. "Balance" means equal thermal capacity rates in the two fluid streams between which heat transfer is effected by the regenerator, and "symmetry" means equal numbers of heat-transfer units between fluid stream and regenerator matrix in the two streams. It is assumed that the specific heats and densities of fluid and matrix and the matrix to fluid heat-transfer coefficient are constant. Counterflow regenerators are considered rather than those of the unidirectional type, since the former type can give higher performance and is widely used.

Carryover flow rates less than that of a fluid stream are considered, since with greater carryover none of either fluid stream passes through the regenerator, and it ceases to act as a normal regenerator. Cryogenic regenerators may operate otherwise [4, 7].

In air-conditioning regenerators used for energy recovery by transfer between fresh and exhaust air streams, the carryover flow from the exhaust air stream is usually separated from the fresh air stream leaving the regenerator, in what is termed a "purge" arrangement. This arrangement prevents contaminant transfer by carryover, however energy transfer between the air streams is reduced. Regenerators without purge arrangements are considered here.

2 Parameters

The transfer performance of a regenerator is described by the ratio of the transfer rate achieved and the maximum possible transfer rate, and this ratio is termed the effectiveness of the regenerator. Thus for a balanced regenerator, the effectiveness is given by

$$\epsilon = \frac{(t_0 - t_i)}{(t_n - t_i)} \tag{1}$$

where t_i and t_0 denote the temperature of a fluid stream at inlet to and outlet from the matrix, respectively, and t_n that of the other fluid stream at inlet. The outlet temperatures are bulk mean values because of the periodic nature of heat storage in the matrix.

The effectiveness is denoted ϵ_m when t_0 is evaluated considering only transfer via the matrix. For a symmetric balanced regenerator, ϵ_m is determined by two parameters [1-3]. The two parameters used here are the modified number of heat-transfer units and the matrix to fluid stream thermal capacity-rate [2], given respectively for such a regenerator by

$$N_{tu,0} = \frac{hAL}{2c_f v} \quad \text{and} \quad C_r^* = \frac{\mu \sigma L}{v \tau} \tag{2}$$

where h is the heat-transfer coefficient between matrix and fluid, A, the heat-transfer surface area-per-unit-mass of fluid in the matrix, L, the matrix dimension in the fluid flow direction, c_f, the fluid specific heat at constant pressure, v, the mean velocity of fluid flow through the matrix passages, μ, the matrix to contained fluid mass ratio, σ, the matrix to fluid specific heat ratio, and τ, the period of time that the matrix spends in each fluid stream.

The effectiveness ϵ, which includes the effect of transfer via fluid carried over, depends also on a parameter defined by the rate of fluid carryover [4-7]. This dependence is presented here in terms of the carryover ratio, which for balanced flow and constant c_f is given by

$$K = \frac{L}{v \tau} \tag{3}$$

The parameters used by others to present the effect of

Transfer from Cylindrical Anemometer Probes," *International Journal of Heat and Mass Transfer*, Vol. 15, 1972, pp. 1659–1677.

2 Davis, M. R., "Application of Hot Wires to Measurements in Freely Expanding Jets," *AIAA Journal*, Vol. 11, No. 1, 1973, pp. 113–115.

3 Smithells, C. J., *Tungsten*, Chapman and Hall, 3rd ed. 1952.

4 Davis, M. R., "The Dynamic Response of Constant Resistance Anemometers," *Journal of Physics E: Scientific Instruments*, Vol. 3 No. 1, 1970, pp. 15–20.

5 Madden, A. J. and Piret, E. L., *Heat Transfer from Wires to Gases at Sub-atmospheric Pressures Under Natural Convection Conditions*. Institute of Mechanical Engineers, London, 1951, p. 328.

Effect of Fluid Carryover on Regenerator Performance

P. J. Banks[1]

1 Introduction

A regenerative heat exchanger or regenerator transfers sensible heat between two fluid streams by means of a porous matrix through which the fluid streams are passed alternately. In a rotary regenerator the matrix is rotated through the fluid streams, while in a fixed-bed regenerator the matrix is divided into two halves and the fluid streams are switched through the halves alternately by means of valves. Heat is transferred from one fluid stream to the matrix and then from the matrix to the other fluid stream. Transfer also occurs via the fluid contained in the matrix passages, since this fluid is carried from one fluid stream to the other by the rotation of the matrix, or the switching of the fluid streams.

Longstanding theoretical predictions of regenerator transfer performance are for transfer via the matrix [1-3]. However, in recent years the effect of fluid carryover has been included in finite difference solutions of the governing equations obtained utilizing digital computers [4-7]. Results have been presented for the effect of carryover on the effectiveness of a symmetric balanced counterflow regenerator for certain values and ranges of the parameters determining effectiveness. In this note, the effect is shown on a design chart applicable for all operating conditions of such a regenerator of practical design for transfer between gas streams. The chart was obtained using digital computer programs developed by Maclaine-cross [3, 6, 8] for calculating regenerator effectiveness both including and neglecting the effect of carryover.

The parameter carryover effect is introduced. It is defined as the increase in regenerator effectiveness resulting from fluid carryover divided by the carryover ratio, which is the ratio of the thermal capacity rates of fluid carryover and the fluid stream with minimum thermal capacity rate. Carryover effect is shown to be closely independent of the carryover ratio for regenerators of practical design for gas streams, enabling it to be presented on design chart which uses the parameters determining regenerator effectiveness neglecting the effect of carryover, and thus supplements the existing chart [2, 3] for this effectiveness.

The design chart for carryover effect achieves the objective of including an additional parameter for carryover with a small number of charts, for which Maclaine-cross [6] has provided another design method. He showed that the effect of carryover may be included approximately in predictions neglecting the effect by modifying the values of matrix specific heat and matrix to fluid heat-transfer coefficient. A comparison of this design method with the use of carryover effect is made in section 4 which follows.

[1] Division of Energy Technology, Commonwealth Scientific and Industrial Research Organization, Highett, Victoria 3190, Australia

The formulation of the design chart for carryover effect was stimulated by the similarity between fluid carryover and fluid flows through a regenerator that bypass the matrix [9], suggested to the author by a colleague [10].

Consideration is given to symmetric balanced counterflow regenerators. "Balance" means equal thermal capacity rates in the two fluid streams between which heat transfer is effected by the regenerator, and "symmetry" means equal numbers of heat-transfer units between fluid stream and regenerator matrix in the two streams. It is assumed that the specific heats and densities of fluid and matrix and the matrix to fluid heat-transfer coefficient are constant. Counterflow regenerators are considered rather than those of the unidirectional type, since the former type can give higher performance and is widely used.

Carryover flow rates less than that of a fluid stream are considered, since with greater carryover none of either fluid stream passes through the regenerator, and it ceases to act as a normal regenerator. Cryogenic regenerators may operate otherwise [4, 7].

In air-conditioning regenerators used for energy recovery by transfer between fresh and exhaust air streams, the carryover flow from the exhaust air stream is usually separated from the fresh air stream leaving the regenerator, in what is termed a "purge" arrangement. This arrangement prevents contaminant transfer by carryover, however energy transfer between the air streams is reduced. Regenerators without purge arrangements are considered here.

2 Parameters

The transfer performance of a regenerator is described by the ratio of the transfer rate achieved and the maximum possible transfer rate, and this ratio is termed the effectiveness of the regenerator. Thus for a balanced regenerator, the effectiveness is given by

$$\epsilon = \frac{(t_0 - t_i)}{(t_n - t_i)} \tag{1}$$

where t_i and t_0 denote the temperature of a fluid stream at inlet to and outlet from the matrix, respectively, and t_n that of the other fluid stream at inlet. The outlet temperatures are bulk mean values because of the periodic nature of heat storage in the matrix.

The effectiveness is denoted ϵ_m when t_0 is evaluated considering only transfer via the matrix. For a symmetric balanced regenerator, ϵ_m is determined by two parameters [1-3]. The two parameters used here are the modified number of heat-transfer units and the matrix to fluid stream thermal capacity-rate [2], given respectively for such a regenerator by

$$N_{tu,0} = \frac{hAL}{2c_f v} \text{ and } C_r^* = \frac{\mu \sigma L}{v \tau} \tag{2}$$

where h is the heat-transfer coefficient between matrix and fluid, A, the heat-transfer surface area-per-unit-mass of fluid in the matrix, L, the matrix dimension in the fluid flow direction, c_f, the fluid specific heat at constant pressure, v, the mean velocity of fluid flow through the matrix passages, μ, the matrix to contained fluid mass ratio, σ, the matrix to fluid specific heat ratio, and τ, the period of time that the matrix spends in each fluid stream.

The effectiveness ϵ, which includes the effect of transfer via fluid carried over, depends also on a parameter defined by the rate of fluid carryover [4-7]. This dependence is presented here in terms of the carryover ratio, which for balanced flow and constant c_f is given by

$$K = \frac{L}{v \tau} \tag{3}$$

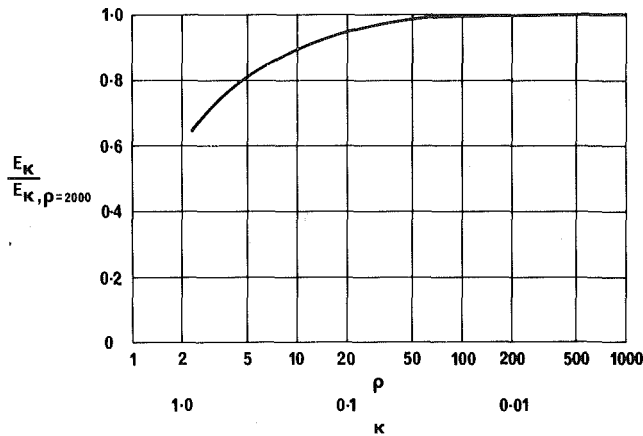The parameters used by others to present the effect of

Fig. 1 Variation of carryover effect with thermal capacity ratio and carryover ratio, for $N_{tu,0} = 5$ and $C_r^* = 2$

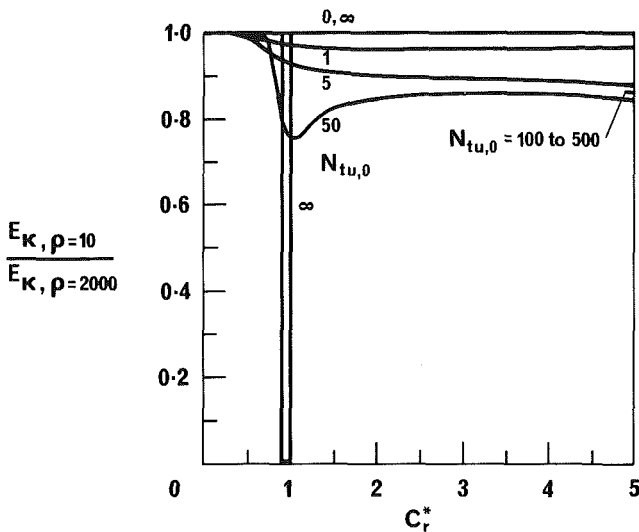Fig. 2 Variation of carryover effect for $\rho = 10$ with operating parameters
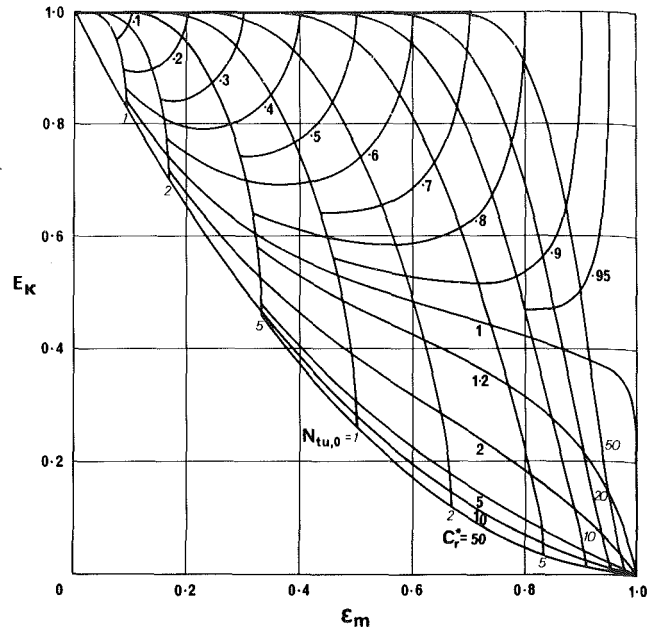

Fig. 3 Design chart showing carryover effect for a symmetric balanced counterflow regenerator, for $\rho \geq 150$ and within 0.01 in E_κ for $\rho > 50$

carryover, together with their relationship to K, are as follows: $SR = (2N_{tu,0}/C_r^*)\kappa$ and $SR/\mathrm{II} = \kappa$, [4]; $\delta\mathrm{II}/\mathrm{II} = \kappa/(1 - \kappa)$, [5]; $\mu\sigma = C_r^*/\kappa$, [6]; $Hu = \kappa$, [7].

The parameter $\mu\sigma$ is also used here, and denoted ρ. It equals the ratio of the matrix mass to the mass of fluid contained in it multiplied by the specific heat ratio of matrix and fluid, an so is the matrix to contained fluid thermal capacity ratio. In practical regenerators for transferring sensible heat between gas streams, the value of ρ is large compared to 10.

For balanced flow and constant c_f, carryover ratio κ is the rate of carryover of fluid between the fluid streams through the regenerator as a fraction of fluid stream flow rate. It is also the residence time of fluid in the matrix as a fraction of the period of time that the matrix spends in each fluid stream, equation (3). Necessarily, K < 1 for normal regenerator operation, since otherwise the fluid streams do not pass through the regenerator. Furthermore, to avoid excessive carryover, it is desirable to keep κ < 0.01.

The parameter carryover effect introduced here is given by

$$E_\kappa = \frac{(\epsilon - \epsilon_m)}{\kappa} \qquad (4)$$

3 Carryover Effect

Digital computer programs developed by Maclaine-Cross [3, 6, 8] have been used to compute effectivenesses ϵ and ϵ_m for a symmetric balanced counterflow regenerator, enabling

values of carryover effect E_k to be obtained for constant values of the thermal capacity ratio ρ and the parameters determining ϵ_m, namely $N_{tu,0}$ and C_r^*.

The effect on E_κ of a change in ρ was found to be small for ρ large compared to 10, as in practial regenerators for gas streams, except for an unusual operating condition. This effect is illustrated in Fig. 1 for $N_{tu,0} = 5$ and $C_r^* = 2$, which are typical values. Values of κ corresponding to those of ρ, from equations (2) and (3), are given, showing that the effect increases with κ but is still small when κ reaches the excessive value of 0.1. Figure 2 gives the variation of the effect for $\rho = 10$ with $N_{tu,0}$ and C_r^*, showing that the effect becomes large only for the unusual operating condition with $N_{tu,0}$ very large and C_r^* just less than unity. The curves for $N_{tu,0} = 0$ and ∞ were derived from the results for these limiting cases, which are described subsequently. Curves for $N_{tu,0} = 100$ to 500 are shown only close to $C_r^* = 5$. Values of C_r^* less than 5 are considered, since for greater values κ exceeds a half, a really excessive value, with ρ equal to 10.

Curves of E_κ versus ϵ_m for $\rho \geq 150$ are presented in Fig. 3. The curves for $\rho = 50$ differ by less than 0.01 in E_κ, giving errors in ϵ of less than 0.1 percent for $\kappa < 0.1$. For $\rho < 50$, the errors are greater, as indicated by Figs. 1 and 2. The unusual operating condition, which gives a large effect of change in ρ, occurs in a very narrow strip along the upper part of the right hand edge of Fig. 3.

Figure 3 shows the variation of the dependance of E_κ on ϵ_m with the well known parameters determining ϵ_m. Thus the figure provides a design chart for evaluating the effect of carryover on regenerator effectiveness that supplements the existing design chart for ϵ_m, [2, 3], presented also in table form by Kays and London [2].

Results from Maclaine-cross's finite difference computer program for ϵ, [6], were not available for $N_{tu,0} < 0.1$ and $N_{tu,0} > 50$ due to limitations in the program. However, results can be deduced from first principles for $N_{tu,0} = 0$ and ∞, and Maclaine-cross's approximate method [6] is accurate for large $N_{tu,0}$.

For $N_{tu,0} = 0$, there is no transfer between fluid streams and matrix, so that $\epsilon_m = 0$ and $\epsilon = \kappa$, giving $E_\kappa = 1$.

For $N_{tu,0} = \infty$ and $(C_r^* + \kappa) \leq 1$ it may be deduced from a wave diagram for the matrix ([3], Fig. 7, with wave at fluid velocity [11] added) that $\epsilon_m = C_r^*$ and $\epsilon = (C_r^* + \kappa)$, giving E_κ

= 1, in accord with the computed results shown in Fig. 3. Similarly, for $C_r^* < 1 < (C_r^* + \kappa)$, $\epsilon_m = C_r^*$ and $\epsilon = 1$, giving $E_\kappa = (1 - \epsilon_m)/\kappa$. Also, for $C_r^* \geq 1$, $\epsilon_m = \epsilon = 1$, giving $E_\kappa = 0$. It follows from these results that the relation between E_κ and ϵ_m for $N_{tu,0} = \infty$ is given by

$$
\begin{aligned}
E_k &= 1, & \text{for } 0 \leq \epsilon_m \leq \rho/(1+\rho) \\
E_k &= \rho(1 - \epsilon_m)/\epsilon_m, & \text{for } \rho/(1+\rho) < \epsilon_m < 1 \\
E_k &= 0, & \text{for } \epsilon_m = 1
\end{aligned}
$$

This relation is in accord with the trend with increasing $N_{tu,0}$ of the curves at constant $N_{tu,0}$ on Fig. 3. The dependence of the relation on ρ for ϵ_m close to unity confirms the already noted sensitivity to change in ρ of Fig. 3 for this unusual operating condition.

The maximum value of C_r^* for which results are shown in Fig. 3 is 50, which corresponds for $\rho > 50$ to $\kappa < 1.0$, the upper limit for normal regenerator operation.

For $C_r^* \rightarrow \infty$, the curves at constant $N_{tu,0}$ in Fig. 3 are seen to tend to approach $E_\kappa = 0$ at a value of ϵ_m equal to its value for $C_r^* = \infty$, given by $N_{tu,0}/(1 + N_{tu,0})$, [2]. The indicated absence of an effect of carryover in this limiting case is in accord with the equivalence to a recuperator of this case.

For $N_{tu,0} < 0.5$ and $C_r^* > 10$ in Fig. 3, E_k increases with increase in C_r^*, whereas the opposite trend occurs in the remainder of the figure. The magnitude of this trend is small, of the same order as that due to change in ρ for $\rho > 50$.

A carryover effect chart like Fig. 3 has the value of showing how the increase in regenerator effectiveness caused by a certain carryover ratio varies with the operating parameters. Thus Fig. 3 shows that carryover increases effectiveness most at low values of effectiveness, except when the capacity-rate ratio is nearly unity.

4 Comparison of Design Methods for Including Effect of Carryover

Regenerator effectiveness including the effect of carryover could be obtained from digital computer programs [4-7] and presented as design tables and charts. A parameter additional to those determining effectiveness neglecting the effect would be needed, making the presentation very lengthy.

A way of avoiding this problem has been presented in section 3. The effect of carryover is presented there as carryover effect E_κ, which is shown to be closely independent of an additional parameter for values of additional parameter ρ greater than 50, for a symmetric balanced counterflow regenerator.

Maclaine-cross [6] evaluates another way of avoiding the additional parameter problem, that of suitably modifying the parameters determining effectiveness neglecting carryover. The accuracy of this approach appears to be as close as that of Fig. 3 only for $N_{tu,0} > 5$, that is for the numbers of transfer units used in high performance regenerators.

Maclaine-cross [6] has shown that his approach is applicable to regenerators with unbalanced flow. Maclaine-cross's digital computer programs [3, 6, 8] have been used to obtain E_κ for unbalanced flow, and a significant effect of unbalance found. Therefore, the approach presented here requires a carryover effect chart for each degree of unbalance, to match the existing effectiveness chart for this degree of unbalance [2, 3],

The effect of regenerator asymmetry on ϵ_m is small and neglected in design charts [2, 3]. Therefore its effect on ϵ was not considered by Maclaine-Cross [6]. The effect of asymmetry on carryover effect remains to be explored.

5 Conclusion

The description of the effect of carryover on regenerator effectiveness by the quantity E_κ has been shown to enable the effect for practical designs of symmetric balanced counterflow regenerator for gas streams to be presented on a single chart, which supplements the existing chart for effectiveness neglecting the effect.

References

1 Hausen, H., *Wärmeübertragung im Gegenstrom, Gleichstrom und Kreuzstrom,* 2nd ed., Springer-Verlag, Berlin, 1976.

2 Kays, W. M. and London, A. L., *Compact Heat Exchangers,* 2nd ed., McGraw-Hill, New York, 1964.

3 Maclaine-cross, I. L. and Banks, P. J., "Coupled Heat and Mass Transfer in Regenerators-Prediction Using an Analogy with Heat Transfer," *International Journal of Heat and Mass Transfer,* Vol. 15, No. 6, 1972, pp. 1225–1242.

4 Heggs, P. J. and Carpenter, K. J., "The Effect of Fluid Hold-Up on the Effectiveness of Contraflow Regenerators," *Transactions of The Institution of Chemical Engineers,* Vol. 54, No. 4, Oct. 1976, pp. 232–238.

5 Willmott, A. J., "A Comment on the Paper (The Effect of Gas Heat Storage Upon the Performance of the Thermal Regenerator) [1]" *International Journal of Heat and Mass Transfer,* Vol. 20, No. 11, Nov. 1977, p. 1267.

6 Maclaine-cross, I. L., "Effect of Interstitial Fluid Heat Capacity on Regenerator Performance," ASME JOURNAL OF HEAT TRANSFER, Vol. 102, No. 3, Aug. 1980, pp. 572–574.

7 Harness, J. B. and Neumann, P.E.L., "Digital Computer Simulation of Voidage in a Regenerator," in *Advances in Cryogenic Engineering,* Vol. 25, Plenum, New York, 1980, pp. 438–445.

8 Maclaine-cross, I. L., "A Theory of Combined Heat and Mass Transfer in Regenerators," Ph.D. thesis, Department of Mechanical Engineering, Monash University, Australia, 1974.

9 Banks, P. J. and Ellul, W. M. J., "Predicted Effects of By-Pass Flows on Regenerator Performance," *Mechanical and Chemical Engineering Transactions of The Institution of Engineers Australia,* Vol. MC 9, Nos. 1 & 2, 1973, pp. 10–14.

10 Dunkle, R. V., Personal communication, 1969.

11 van Leersum, J. G. and Banks, P. J., "Equilibrium Heat and Mass Transfer in Regenerators in which Condensation Occurs," *International Journal of Heat and Mass Transfer,* Vol. 20, No. 9, Sept. 1977, pp. 927–934.

Strongly Implicit Algorithm for Use in Three-Dimensional National Convection Studies[1]

P. M. Beckett.[2]
Pepper and Cooper[1] proposed a strongly implicit method for dealing with three-dimensional flow problems in terms of a vector potential. This short discussion does not suggest there are errors in their results or that the numerical scheme is without merit, the point which needs to be emphasised is that care is needed when solving problems in this way.

The numerical solution of three-dimensional flow problems is often formulated in terms of a vector potential, and though the deviation of the differential equation is a simple matter there has been considerable controversy about the precise boundary conditions which must be imposed on the vector potential. Although these differences of opinion have now been resolved, it is not uncommon to see the vector potential method applied without an appreciation of the background argument, and it is the purpose of this short article to highlight two points which, when overlooked, can lead to errors.

Formulation of the equation for the Vector Potential. For incompressible flow the solenoidal nature of the velocity field **v** can be ensured by introducing a vector potential ψ by

$$\mathbf{v} = \Delta \times \psi. \qquad (1)$$

There is a certain amount of flexibility in the selection of ψ, and it is usual to insist that ψ itself is solenoidal. As a result, on taking the curl of the steady form of the Navier-Stokes equation, ψ is found to satisfy

$$\nabla^4 \psi = f(\psi, x_1, x_2, x_3), \qquad (2)$$

where ∇^4 is the Cartesian biharmonic operator and f accounts for the nonviscous terms. Alternatively, the fourth order equation is often split to yield

$$\nabla^2 \psi = -f \text{ and } \nabla^2 \psi = -\zeta \qquad (3)$$

where $\zeta = $ curl **v** is the vorticity.

The boundary conditions. The controversy over the boundary conditions which must be imposed on (2) or (3) is partially reviewed by Ames [1] with reference to the problem of convection inside a box ($x_1 = \pm a, x_2 = \pm b, x_3 = \pm c$), as considered by Azia and Hellums [2] and by Ozoe et al. [3]. The accepted set of conditions for the coupled equations (3) relevant to the no-slip condition on $x_1 = \pm a$ are given as

$$\frac{\partial \psi_1}{\partial x_1} = \psi_2 = \psi_3 = 0, \qquad (4)$$

$$\zeta_1 = 0, \ \zeta_2 = -\frac{\partial v_3}{\partial x_1}, \ \zeta_3 = \frac{\partial v_2}{\partial x_1}, \qquad (5)$$

where ψ_i, ζ_i, v_i are the components of ψ, ζ and **v**. Similar conditions apply on the outer surfaces. The set (4) follows from a very complex paper by Hirasaki and Hellums [4] concerned with generally shaped boundaries, a paper which was later simplified by the same authors to deal with plane boundaries [5]. The conditions (5) follow directly from the boundary condition $v_1 = 0$ on $x = \pm a$.

The first point which should be noted is that these conditions do *not* ensure that the tangential components of velocity vanish on each face. Aziz and Hellums recognized this fact and imposed the conditions $v_2 = v_3 = 0$ on $x = \pm a$ through the finite representation of the boundary conditions of ζ_2 and ζ_3. This point is completely overlooked by Ames in his description of the method and it also appears to be the reason why the second method described in [3] does not work.

However the major point which is often overlooked is that the particular form of equation (3) only holds because $\nabla \cdot \psi = 0$, and it is therefore necessary to ensure that the numerical solution of (3) for ψ is constructed in such a way that ψ is everywhere solenoidal. Hirasaki and Hellums [4] state this condition is ensured by applying the boundary condition (4) and (5) so naturally anyone using these will have a suitable result, but perhaps without realizing the significance; however, anyone using alternative sets must ensure these also automatically lead to a vector potential satisfying $\nabla \cdot \psi = 0$. While Pepper and Cooper's numerical method is commendable they do not seem to ensure the solenoidal nature of ψ nor test for it. Unlike Aziz and Hellums whose test of accuracy is made by calculating $\nabla \cdot \psi$, Pepper and Cooper compute the size of $\nabla \cdot \mathbf{v}$ and conclude their methods satisfactory because this is small. However, since it is quite possible for $\nabla \cdot \mathbf{v} = 0$ but $\nabla \cdot \psi = 0$ a solution satisfying the Pepper and Cooper test may not be meaningful.

Additional References

1 Ames, W. F., *Non-linear Partial Differential Equations in Engineering Sciences*, Vol. 2, Academic Press, 1972.

2 Aziz, K. and Hellums, J. D., "Numerical Solution of the Three-Dimensional Equations of Motion for Laminar Natural Convection," *Physics of Fluids*, Vol. 10, 1967, pp. 314–324.

3 Ozoe, H., Yamamoto, K., Churchill, S. W., and Sayama, H., "Three-Dimensional Numerical Analysis of Laminar Natural Convection in a Confined Fluid Heated from Below," ASME JOURNAL OF HEAT TRANSFER, Vol. 99, 1976, p. 202–207.

4 Hirasaki, G. J. and Hellums, J. D., "A General Formulation of the Boundary Conditions on the Vector Potential in Three-Dimensional Hydrodynamics," *Quat. Appl. Math.*, Vol. 26, 1969, pp. 331–342.

5 Hirasaki, G. J. and Hellums, J. D., "Boundary Conditons on the Vector and Scalar Potentials in Viscous Three-Dimensional Hydrodynamics," *Quart. Appl. Math.*, Vol. 28, No. 2, 1970, pp. 293–296.

Author's Closure

Dr. Beckett's observations on the use of a vector potential

---

posed, and care must be taken to properly ensure that the tangential velocities vanish at the surfaces. We agree with Dr. Beckett that ψ must be everywhere solenoidal; likewise, the flow should be divergence free, i.e. $\nabla \cdot \bar{u} = 0$. This condition is not readily guaranteed when using numerical methods, irrespective of the accuracy of the method. Even the use of variational methods (e.g., Langrangian multipliers) to correct the velocity filed in not always satisfactory. However, a good indication of the effectiveness of the numerical solution to obtain a converged solution is to check for divergence. Our computation of the size of $\nabla \cdot \bar{u}$ was obtained by first expressing the velocity components as the gradients of ψ, then computing the gradients of $\bar{u}$. The reason for this is that only

ψ and ω values need to be solved in the solution sequence, avoiding the solution of the primitive equations and the troublesome Poisson equation for pressure. Hence, our test for $\nabla \cdot \bar{u}$ (although in terms of ψ) does not necessarily ensure that $\nabla \cdot \psi$ is conserved within the solution domain. It is easy to in solving three-dimensional flows are well-taken. The formulation of boundary conditions for the vector potential can be troublesome, and is certainly more involved than the constraints imposed when using the primitive equations. It is particularly important that the boundary conditions be well-include a test for $\nabla \cdot \psi$ along with $\nabla \cdot \bar{u}$; testing for $\nabla \cdot \bar{u}$ provides an overall perspective of the solution accuracy of the "numerical" governing equations.

ERRATA

Corrections to "Heat Transfer in Two-Component Dispersed Flow," K. Mastanaiah and E. N. Ganic, published in the May 1981 issue of the ASME JOURNAL OF HEAT TRANSFER, pp. 300–306.

1 In the nomenclature, d_{mn} should be defined:

d_{mn} = generalized characteristic drop size,

$$= \int_0^\infty d_p^m \, P(d_p) \, d(d_p) \Big/ \int_0^\infty d_p^n \, P(d_p) \, d(d_p)$$

(m,n = 1,2, or 3)

2 Equation (13a) should read:

$$q_{gd} = q_{gds} \cdot \pi d_{20}^2 \tag{13a}$$